



Adam Mickiewicz University, Poznań
Faculty of Physics and Astronomy
Institute of Spintronics and Quantum Information

DOCTORAL THESIS

**Novel approaches to control spin waves
using structuring and complex geometry
of ferromagnetic nanostructures**

Mateusz Gołębiewski

Supervisor: **prof. dr hab. Maciej Krawczyk**

Assistant supervisor: **dr hab. Paweł Gruszecki, prof. UAM**

Poznań 2025

To my loving parents and to my dearest Marta,

In recognition of your unwavering support,
patience, and encouragement throughout the course
of my academic journey.

Declaration


Declaration of the author of this dissertation

I hereby declare that except where specific reference is made to the work of others, the contents of this dissertation are original and have not been submitted in whole or in part for consideration for any other degree or qualification in this, or any other university. This dissertation is my own work and all the contents of the dissertation have been obtained by legal means.


.....
mgr Mateusz Gołębiewski

Declaration of the thesis Supervisor

This dissertation is ready to be reviewed.


.....
prof. dr hab. Maciej Krawczyk

Abstract

Magnetism, a fundamental phenomenon of nature, drives many technologies ranging from data storage to energy conversion. At the heart of modern magnetism is the ability to control the dynamics of magnetization, which is governed by the complex interplay of exchange interactions, magnetic anisotropies, and demagnetizing fields. As devices continue to miniaturize and increase in functionality, understanding these dynamics becomes critical – especially for applications in spintronics and magnonics. The latter focuses on the propagation of magnetization perturbations known as spin waves, which show promise for information processing at low energy levels.

The study of magnetic domains has evolved from the macroscopic bulk materials to the miniaturized systems, allowing the investigation of spin-wave phenomena in confined geometries. Low-dimensional structures, such as thin films (2D) and nanowires (1D), have enabled scientists to study spin-wave control through boundary effects, chirality, and periodic texturing, leading to applications such as frequency filtering and signal processing. However, the recent development of three-dimensional nanostructures (3D) introduced an entirely new research direction. The nanoscale periodicity in complex geometries, such as gyroids or scaffold-like networks, enables the unprecedented control of spin-wave localization, dispersion, band structure, and other essential dynamic properties. These advances represent a natural progression toward using highly complex and small structural elements to fine-tune magnetization dynamics in all spatial directions.

The rapid growth of this field is fueled not only by innovations in nanofabrication methods, such as atomic layer deposition or self-assembly techniques, but also by improved computational capabilities that enable advanced numerical methods. Theoretical tools such as finite difference and finite element methods are essential to solve the complex magnetization dynamics described by the Landau–Lifshitz–Gilbert equation. The ability to model magnetic phenomena with high precision further supports the simulation of high-resolution 3D systems that were previously considered too computationally expensive. They allow researchers to study how complex 3D nanostructures affect the control of spin waves, opening up new possibilities for the design of new magnonic and spintronic devices. From bulk materials to nanostructures, and from planar systems to complex three-dimensional nanoarchitectures, the field of magnetism is pushing the boundaries of magnetization control, driving innovation in dynamic phenomena for next-generation technologies.

This dissertation investigates the control of spin waves in ferromagnetic materials through multidimensional structuring, with an emphasis on micromagnetic simulations as a central

research tool. It begins by presenting the basic theoretical concepts of magnetism, especially micromagnetism, to explain some of the key aspects of spin-wave dynamics, including exchange interactions, demagnetizing fields, and the Landau–Lifshitz–Gilbert equation. A substantial part of the thesis then discusses the numerical methods used for these simulations, describes the special features of software tools such as MuMax3, COMSOL Multiphysics, and tetmag, and shows how they can be used to design, simulate, and analyze complex magnetic systems.

The fundament of this thesis is a collection of published research papers demonstrating new strategies for controlling spin waves by progressively increasing the geometric complexity of structured ferromagnetic media. Knowing the advances in manufacturing and using numerical simulation, I demonstrate how geometry and dimensionality affect spin-wave propagation, dispersion, and localization. I study one-dimensional gratings, two-dimensional antidot lattices, and fully three-dimensional magnetic nanostructures to show how higher-dimensional systems enable new magnonic functionalities and define future trends. The main goal was to connect theoretical spin-wave optics with practical magnonic applications, and to show that geometric structuring can be as important as intrinsic material properties in controlling interference, diffraction, nonreciprocity, and localization. Through theoretical modeling, large-scale micromagnetic simulations, and close collaboration with experimental groups, my work ensures both computational accuracy and experimental feasibility, aiming to advance next-generation magnonic circuits, logic architectures, and hybrid spintronic devices.

An important result of my Ph.D. research is the first micromagnetic demonstration of the Talbot effect for spin waves, revealing self-imaging phenomena emerging in systems patterned with periodic 1D gratings. Using MuMax3 simulations and convolution-based computational tools, I show how Talbot “carpets” can be harnessed to perform logic operations, introducing a reconfigurable and scalable framework for magnonic computing. MuMax3 and COMSOL simulations of two-dimensional antidot lattices with a predetermined defect show that the periodic structuring modifies the band structure of the spin waves and enhances the induction of higher harmonics suitable for fast information processing. Further studies on crescent-shaped waveguides show that the localization of spin waves depends on the chirality of the profile, demonstrating how shape anisotropies lead to unidirectional propagation. The most advanced aspect of my research involves three-dimensional nanostructures, where spatial modulation in all three dimensions allows unprecedented control of magnetization dynamics. Through COMSOL Multiphysics and tetmag simulations, I study gyroid networks to show that complex geometries combined with crystallographic orientation produce strongly field-dependent ferromagnetic responses and spin-wave mode localization. Notably, the surface-localized ferromagnetic resonance modes found in gyroids and scaffold-like lattices exhibit field-switchable high-magnetization states, opening new possibilities for reconfigurable magnonic waveguides and functional spin-wave devices.

In short, my main contributions include:

- the first micromagnetic demonstration of the Talbot effect for spin waves and the introduction of spin-wave self-imaging as a novel computing paradigm;
- the investigation of edge modes in crescent-shaped waveguides, establishing a link between structural chirality and spin-wave localization;
- the adaptation and optimization of finite-element solvers and numerical methods to enable efficient large-scale 3D micromagnetic simulations;
- the coordination and contribution to an international collaboration exploring gyroidal structures as platforms for unconventional magnetization dynamics;
- the discovery of tunable, surface-localized ferromagnetic resonance modes in three-dimensional magnetic networks.

Overall, this work contributes to the expanding field of magnonics by demonstrating how dimensionality and geometry can create new functionalities in spin-wave dynamics. By combining theoretical modeling, advanced micromagnetic simulations, and collaborations with international experimental groups, it highlights promising strategies for spin-wave control. As 3D magnonics continues to evolve, the findings presented in this thesis can support future efforts to design devices for energy-efficient information processing, storage, and communication systems.

Streszczenie

Magnetyzm, fundamentalne zjawisko natury, odgrywa kluczową rolę w wielu technologiach, od przechowywania danych po konwersję energii. Sercem nowoczesnego magnetyzmu jest kontrola dynamiki magnetyzacji, która jest regulowana przez wzajemne oddziaływania wymienne, anizotropie i pola rozmagnesowujące. W miarę jak urządzenia stają się coraz mniejsze i bardziej wydajne, zrozumienie dynamiki magnetyzacji staje się niezbędne – szczególnie w zastosowaniach w spintronice i magnonice. Druga z tych dziedzin koncentruje się na propagujących zaburzeniach magnetyzacji, zwanych falami spinowymi, które wykazują potencjał do przetwarzania informacji przy bardzo niskim zużyciu energii.

Badania nad domenami magnetycznymi ewoluowały od analiz objętościowych (makro)materiałów do zminiaturyzowanych systemów, umożliwiając eksplorację fal spinowych w ograniczonych geometriach. Struktury o niższych wymiarach, takie jak ultracienkie warstwy (2D) i nanodruty/nanopręty (1D), umożliwiły naukowcom manipulację falami spinowymi poprzez efekty brzegowe, chiralność i periodyczne teksturowanie, prowadząc do zastosowań takich jak filtrowanie częstotliwości i przetwarzanie sygnałów. Jednakże, niedawny rozwój badań nad nanostrukturami trójwymiarowymi (3D) sygnalizuje rozwijający się trend, który otwiera zupełnie nowe możliwości dla badań nad falami spinowymi. Periodyczności w złożonych geometriach, takich jak gyroidy czy kaskadowe matryce nanoprętów, pozwalają uzyskać niespotykaną dotąd kontrolę nad lokalizacją fal spinowych, ich dyspersją oraz strukturą pasmową, a także innymi kluczowymi właściwościami dynamicznymi. Postępy te stanowią naturalny krok w kierunku wykorzystania niezwykle małych i złożonych struktur do precyzyjnego strojenia dynamiki magnetyzacji we wszystkich kierunkach przestrzennych.

Szybki rozwój tej dziedziny jest napędzany nie tylko innowacjami w technikach nanofabrykacji, takimi jak osadzanie warstw atomowych i metody samo-organizacji, ale również rosnącymi możliwościami obliczeniowymi, które umożliwiają stosowanie coraz bardziej zaawansowanych metod numerycznych. Narzędzia teoretyczne, takie jak metody różnic i elementów skończonych, są niezbędne do rozwiązania złożonej dynamiki opisanej równaniem Landaua–Lifshitz–Gilberta. Wzrost dostępnych zasobów obliczeniowych przełożył się również na możliwość precyzyjnego modelowania zjawisk magnetycznych w trójwymiarowych układach o wysokiej rozdzielczości, które do niedawna były zbyt wymagające. Metody numeryczne pozwalają badaczom odkrywać, w jaki sposób nanostruktury 3D mogą kontrolować fale spinowe, otwierając nowe możliwości projektowania urządzeń magnonicznych i spintronicznych. Od układów objętościowych po nanostruktury i od cienkich warstw po skomplikowane nanoarchitektury 3D, dziedzina magnetyzmu

stale rozszerza możliwości kontroli magnetyzacji, napędzając innowacje w zakresie zjawisk dynamicznych dla technologii nowej generacji.

Niniejsza rozprawa doktorska bada kontrolę fal spinowych w materiałach ferromagnetycznych poprzez wielowymiarową strukturyzację, koncentrując się na symulacjach mikromagnetycznych jako głównym narzędziu badawczym. Pracę otwierają niezbędne podstawy teoretyczne z magnetyzmu, w szczególności mikromagnetyzmu, w celu wyjaśnienia kluczowych aspektów dynamiki fal spinowych, takich jak oddziaływania wymienne, pola rozmagnesowujące i równanie Landaua–Lifshitz–Gilberta. Znaczna część pracy poświęcona jest następnie metodom numerycznym stosowanym w symulacjach. Przedstawiono szczegółowe analizy metod różnic i elementów skończonych zaimplementowanych w środowiskach obliczeniowych takich jak MuMax3, COMSOL Multiphysics i tetmag, oraz pokazano ich zastosowanie w projektowaniu, symulowaniu i analizowaniu złożonych układów magnetycznych.

Podstawą rozprawy jest zbiór opublikowanych artykułów naukowych, które przedstawiają nowe strategie kontroli fal spinowych poprzez stopniowe zwiększanie złożoności geometrycznej nośników ferromagnetycznych. Znając postępy w technikach ich wytwarzania oraz wykorzystując metody numeryczne demonstruję, w jaki sposób geometria i wymiarowość wpływają na propagację, dyspersję i lokalizację fal spinowych. Badam jednowymiarowe siatki dyfrakcyjne, dwuwymiarowe sieci dziur kołowych, a także w pełni trójwymiarowe nanostruktury magnetyczne aby pokazać, w jaki sposób układy o wyższej wymiarowości i złożonej strukturyzacji mogą prowadzić do nowych funkcjonalności magnonicznych, definiując przyszłe kierunki rozwoju tej dziedziny. Głównym celem było połączenie teoretycznej optyki fal spinowych z praktycznymi zastosowaniami magnonicznymi, oraz pokazanie, że strukturyzowanie geometryczne może być równie istotne jak właściwości materiałowe w kontrolowaniu interferencji, dyfrakcji, asymetrycznej propagacji i lokalizacji fal spinowych. Poprzez modelowanie teoretyczne, wielkoskalowe symulacje mikromagnetyczne oraz ścisłą współpracę z grupami eksperymentalnymi, moja praca zapewnia zarówno dokładność obliczeniową, jak i możliwość realizacji laboratoryjnej, dążąc do rozwoju nowej generacji układów magnonicznych, architektur logicznych i hybrydowych technologii spintronicznych.

Ważnym rezultatem mojej pracy doktorskiej jest pierwsza mikromagnetyczna demonstracja efektu Talbota dla fal spinowych, ujawniająca samo-obrazowanie zaburzenia magnetyzacji po przejściu przez periodyczną jednowymiarową przeszkodę. Wykorzystując symulacje w MuMax3 oraz narzędzia obliczeniowe oparte na mnożeniu splotowym (konwolucji), pokazuję również, w jaki sposób „dywany” Talbota umożliwiają przeprowadzanie operacji logicznych, proponując rekonfigurowalny i skalowalny model do przeprowadzania obliczeń magnonicznych. Symulacje dwuwymiarowych periodycznych sieci nanodziur z odgórnie zaprojektowanym defektem w MuMax3 i COMSOL wykazały, że takie układy modyfikują strukturę pasmową fal spinowych i umożliwiają generację wyższych harmonicznnych, korzystnych w technologiach przetwarzania informacji o wysokiej częstotliwości. Badania nad falowodami o przekroju poprzecznym w kształcie półksiężyca ujawniają natomiast zależną od chiralności profilu lokalizację fal spinowych, podkreślając rolę anizotropii kształtu we wzbudzaniu jednokierunkowej propagacji.

Najbardziej zaawansowany aspekt moich badań obejmuje trójwymiarowe nanostruktury, w których modulacja przestrzenna we wszystkich trzech wymiarach umożliwia niespotykaną dotąd kontrolę nad dynamiką magnetyzacji. Korzystając z COMSOL Multiphysics oraz tetmag, badam sieci gyroidalne aby pokazać, że złożona geometria i orientacja krystalografii prowadzą do silnie zależnych od pola odpowiedzi ferromagnetycznych i lokalizacji modów fal spinowych. Demonstruję w szczególności, że zlokalizowane przy powierzchni mody rezonansu ferromagnetycznego, zaobserwowane w strukturach gyroidalnych oraz kaskadowych matrycach nanoprętów (przypominających rusztowanie), wykazują stan silnej magnetyzacji przełączalny zewnętrznym polem, co otwiera nowe perspektywy dla rekonfigurowalnych falowodów i funkcjonalnych urządzeń magnonicznych.

W skrócie, moje główne osiągnięcia obejmują:

- pierwszą mikromagnetyczną demonstrację efektu Talbota dla fal spinowych oraz wprowadzenie samo-obrazowania fal spinowych jako nowego paradygmatu obliczeniowego;
- identyfikację modów krawędziowych w falowodach o przekroju półksiężycowym, łączącą chiralność strukturalną z lokalizacją fal spinowych;
- dostosowanie i optymalizację metod elementów skończonych oraz technik numerycznych w celu umożliwienia wydajnych, wielkoskalowych symulacji mikromagnetycznych w trzech wymiarach;
- koordynację i aktywny udział we współpracy międzynarodowej dotyczącej badań nad strukturami gyroidalnymi jako platformami dla niekonwencjonalnej dynamiki magnetyzacji;
- odkrycie powierzchniowo zlokalizowanych modów rezonansu ferromagnetycznego w trójwymiarowych nanostrukturach, oferujących możliwość projektowania kontrolowalnych urządzeń magnonicznych.

Niniejsza praca wnosi wkład w rozwijającą się dziedzinę magnoniki badając, w jaki sposób wymiarowość i geometria nośników magnetycznych mogą być wykorzystane do uzyskania nowych funkcjonalności fal spinowych. Łącząc modelowanie teoretyczne, zaawansowane symulacje numeryczne oraz międzynarodową współpracę z grupami eksperymentalnymi, podkreślono obiecujące strategie kontroli fal spinowych. W miarę dalszego rozwoju trójwymiarowej magnoniki, zaprezentowane tutaj wyniki mogą stanowić wsparcie dla przyszłych działań ukierunkowanych na projektowanie urządzeń do energooszczędnego przetwarzania, przechowywania i przesyłania informacji.

Contents

Abstract ENG	v
Abstract PL (Streszczenie)	ix
Acknowledgments	xvii
Preface	xix
List of publications included in the Thesis	xxi
1 Introduction	1
1.1 Shape related effects on spin waves	1
1.2 From patterned thin films to intricate 3D ferromagnetic nanostructures	2
2 Fundamentals of magnetism	7
2.1 Historical overview	7
2.2 Magnetic moments and magnetic fields	10
2.3 Types of magnetism	13
2.4 Magnetic materials: properties and hysteresis behavior	15
2.5 The quantum theory of magnetism	17
2.6 Magnetic domains and domain walls	20
2.7 Magnetic anisotropy	22
2.8 Magnetostatics and demagnetizing fields	24
3 Micromagnetism	27
3.1 Gibbs free energy	28
3.1.1 Exchange interactions	28
3.1.2 Dipolar interactions	29
3.1.3 Anisotropic contributions	31
3.1.4 Zeeman energy	32
3.1.5 Dzyaloshinskii–Moriya interactions	32
3.1.6 Effective field	33
3.2 Magnetization dynamics and spin waves	33

3.2.1	Gyromagnetic (Larmor) precession	34
3.2.2	Landau–Lifshitz–Gilbert equation	36
3.2.2.1	Normalization	37
3.2.2.2	Equilibrium state and linearization	38
3.2.3	Ferromagnetic resonance and the Kittel formula	40
3.2.4	Spin-wave spectra	41
3.2.4.1	Kalinikos–Slavin theory of spin waves in thin films	44
3.3	Chirality effects	47
3.4	Magnonic crystals	48
3.5	Localization of spin waves	50
3.6	Spin-wave optics	51
4	Numerical methods and micromagnetic simulations	53
4.1	Spatial and temporal discretization methods	54
4.1.1	Finite difference method	55
4.1.2	Finite element method	56
4.1.2.1	Weak formulation and variational principle	56
4.1.3	Boundary element method	57
4.2	Time-stepping approaches	58
4.2.1	Runge–Kutta methods	60
4.2.2	Adams–Bashforth method	62
4.2.3	Euler methods	63
4.2.4	Backward differentiation formulas	64
4.2.5	Generalized- α method	65
4.3	Boundary conditions	66
4.4	Overview of software tools for micromagnetic simulations	67
4.4.1	MuMax3 (used in P1, P2, P3, P6)	67
4.4.2	Tetmag (used in P7)	69
4.4.2.1	Hierarchical \mathcal{H}^2 -matrices algorithm.	70
4.4.3	COMSOL Multiphysics (used in P4, P5, P8, P9)	71
4.4.3.1	Coefficient Form PDE	71
4.4.3.2	Implementation of boundary conditions in COMSOL	73
4.4.3.3	Time-domain solver	74
4.4.3.4	Frequency-domain solver	74
4.4.3.5	Eigenfrequency solver	75
4.4.3.6	Linear and nonlinear methods	76
4.4.3.7	Termination criteria	77
4.4.4	Concluding comparison	78

5 Research	81
5.1 One-dimensional nanostructures	81
5.1.1 Demonstration of spin-wave self-imaging effect (P1)	82
5.1.2 Spin-wave Talbot effect in various multimode waveguides (P2)	94
5.1.3 Concept of a magnonic logic device based on the self-imaging phenomenon (P3)	100
5.1.4 Experimental demonstration of spin-wave self-imaging (P6)	115
5.2 Two-dimensional systems	127
5.2.1 Spin-wave localization and dynamics in crescent cross-section nanorods under geometric and field manipulations (P4)	127
5.2.2 Thin-film magnonic crystals for high-frequency spin-wave generation (P5)	139
5.3 Three-dimensional architectures	148
5.3.1 Theoretical and experimental investigation of gyroid networks: localized spin-wave excitations and crystallography-dependent ferromagnetic responses (P7)	149
5.3.2 Comprehensive overview of state-of-the-art research on magnetic gyroid structures: from mathematical foundations and fabrication to experimental characterization and numerical simulations (P8)	167
5.3.3 Theoretical demonstration of a new type of FMR mode localization in 3D nanostructures (P9)	200
5.4 Co-authorship statements	218
Scientific perspectives	245
Summary	249
Bibliography	253
About the Author	261

Acknowledgments

My academic journey would not have been possible without the tremendous support I have received at every stage along the way.

First and foremost, I would like to express my profound gratitude to my supervisor, Prof. Maciej Krawczyk, for instilling in me a passion for science. His approach to research, vast knowledge, openness, and insight have been a constant source of inspiration since we began working together during my undergraduate studies. No words can truly capture the depth of the guidance and support I have received from him over the years. I remain deeply grateful and hopeful that my scientific work will prove worthy.

I strongly believe that teamwork is essential in scientific research. Therefore, I would like to express my sincere gratitude to the entire Department of Physics of Nanostructures (at the Faculty of Physics and Astronomy, AMU) for their kindness and for fostering an atmosphere conducive to both stimulating scientific discussions and enjoyable everyday interactions. In particular, I would like to thank my assistant supervisor, Prof. Paweł Gruszecki, for generously sharing his knowledge and for familiarizing me with the MuMax3 software. I am also especially grateful to Dr. Mateusz Zelent for his invaluable technical support, as well as for his patience and always friendly attitude. I would also like to thank Dr. Piotr Graczyk and Dr. Krzysztof Szulc for introducing me to COMSOL Multiphysics, which formed the core of my scientific work. To all my colleagues at the Department: thank you for the countless coffee-time conversations and for the opportunity to relax in good company over chess (and more recently, darts).

Alongside domestic teamwork, I was fortunate to build valuable international collaborations during my studies. I would like to thank Prof. Riccardo Hertel for welcoming me into his lab, where I had the pleasure of completing a six-month research internship. I am also particularly thankful to Prof. Justin Llandro for pointing me toward the field of 3D nanostructures as a promising medium for magnonic phenomena, and for many valuable scientific discussions.

Finally, I would like to express my appreciation to the funding institutions, without whose support none of this research would have been possible. I thank the National Science Centre of Poland (NCN) for awarding me the PRELUDIUM grant (2023/49/N/ST3/03032) and for the financial support within the projects: 2015/17/B/ST3/00118, 2018/30/Q/ST3/00416, 2019/33/B/ST5/02013, 2019/35/D/ST3/03729, 2020/39/I/ST3/02413. I am also grateful to the AMU Foundation for awarding me a scholarship for Ph.D. students, and to the Polish National Agency for Academic Exchange (NAWA) for funding my research stay at the University of Strasbourg.

Preface

In the current era of widespread digitization and increasing computing demands, the scientific community is focused on discovering new ways to perform logical operations, store data, and transport information.

As we approach the physical limits of traditional electronic circuits – challenged by quantum effects, heat dissipation, and the resulting decrease in device efficiency and longevity – the need for alternative information carriers becomes essential. This dissertation, entitled “Novel approaches to control spin waves using structuring and complex geometry of ferromagnetic nanostructures,” seeks to contribute to one of the promising research fields addressing these challenges: *magnonics*.

The main objective of magnonics is to analyze magnetism in solid states by studying the propagation of spin waves. Spin waves, as carriers of angular momentum without charge transport, offer a bypass of traditional electronic constraints. With their ability to transmit signals without thermal loss, while offering a broad frequency spectrum and dual amplitude and phase information encoding capabilities, spin waves show potential for next-generation information carriers. This thesis investigates spin-wave properties through one-, two-, and three-dimensional material structures, which represents an innovative approach in the field of magnonics. By studying magnetization dynamics and spin-wave responses throughout complex multidimensional magnetic systems (including their edges, surfaces, and bulk regions) this research reveals interesting phenomena that deepen our understanding of spin-wave behavior and offer new opportunities for functional magnonic design.

List of publications included in the Thesis

- [P1] **Gołębiewski, M.**; Gruszecki, P.; Krawczyk, M.; Serebryannikov, A. E.
Spin-wave Talbot effect in a thin ferromagnetic film
Physical Review B **102**, 13, 134402 (2020)
- [P2] **Gołębiewski, M.**; Gruszecki, P.; Krawczyk, M.
Self-imaging of spin waves in thin, multimode ferromagnetic waveguides
IEEE Transactions on Magnetics **58**, 8, 1–5 (2022)
- [P3] **Gołębiewski, M.**; Gruszecki, P.; Krawczyk, M.
Self-imaging based programmable spin-wave lookup tables
Advanced Electronic Materials **8**, 10, 2200373 (2022)
- [P4] **Gołębiewski, M.**; Reshetniak, H.; Makartsou, U.; Krawczyk, M.; van den Berg, A.; Ladak, S.; Barman, A.
Spin-Wave Spectral Analysis in Crescent-Shaped Ferromagnetic Nanorods
Physical Review Applied **19**, 6, 2200373 (2023)
- [P5] Kumar, N.; Gruszecki, P.; **Gołębiewski, M.**; Kłos, J. W.; Krawczyk, M.
Exciting High-Frequency Short-Wavelength Spin Waves using High Harmonics of a Magnonic Cavity Mode
Advanced Quantum Technologies 2400015 (2024)
- [P6] Makartsou, U.; **Gołębiewski, M.**; Guzowska, U.; Stognij, A.; Gieniusz, R.; Krawczyk, M.
Spin-Wave Self-Imaging: Experimental and Numerical Demonstration of Caustic and Talbot-like Diffraction Patterns
Applied Physics Letters **124**, 19, 192406 (2024)
- [P7] **Gołębiewski, M.**; Hertel, R.; d'Aquino, M.; Vasyuchka, V.; Weiler, M.; Pirro, P.; Krawczyk, M.; Fukami, S.; Ohno, H.; Llandro, J.
Collective Spin-Wave Dynamics in Gyroid Ferromagnetic Nanostructures
ACS Applied Materials & Interfaces **16**, 17, 22177–22188 (2024)
- [P8] **Gołębiewski, M.**; Krawczyk, M.
Gyroid ferromagnetic nanostructures in 3D magnonics
arXiv preprint arXiv:2407.05851 (2024)
- [P9] **Gołębiewski, M.**; Szulc, K.; Krawczyk, M.
Magnetic field controlled surface localization of ferromagnetic resonance modes in 3D nanostructures
Acta Materialia **283**, 120499 (2025)

Chapter 1

Introduction

Harnessing and controlling spin waves is a major focus in the growing field of magnonics. Their ability to transport signals without heat dissipation [1–4] provides high energy efficiency without compromising the processing speed [1, 5–7]. The wavelength spectrum of spin waves (from micrometers to tens of nanometers) corresponds to frequencies from a few to several hundred gigahertz [8–10]. In addition, the ability to control the dispersion and group velocity of spin waves greatly increases their potential applications [11–14]. These properties make spin waves an attractive alternative to conventional charge-based electronics in computing, memory and microwave technologies. Recent advances have also demonstrated the need to reduce the size of magnonic devices, such as majority gates [15], down to nanometer levels. This approach allows the use of ferromagnetic materials with moderate Gilbert damping, which remain suitable at the nanoscale where its low value is not essential [15]. Moreover, the interaction between spin waves and different magnetization textures, such as skyrmions and domain walls, leads to chiral effects that enable advanced magnonic applications, e.g., nonreciprocal waveguides (diode-like behavior), directional spin-wave couplers, or reconfigurable logic gates and memory devices [16, 17]. The development of magnonic systems requires precise control of the magnetization dynamics through static factors such as geometry and material, as well as dynamic parameters such as excitation frequency and external magnetic field. This thesis focuses on novel design of (nano)structures and geometries as a method to control and improve functional performance of spin waves.

1.1 Shape related effects on spin waves

In ferromagnetic materials, spin waves are shaped by the interplay between strong isotropic exchange interactions and anisotropic long-range magnetostatic effects. The miniaturization of magnonic systems together with improved magnetization control has made spin-wave localization a fundamental property of nanoscale operations. Edge modes, driven by a geometry and boundary effects, represent a well-documented example of localization [18–30], where spin waves are confined or propagate along the edges of the system. The inhomogeneous internal magnetic

field near the edges becomes essential for wave confinement as waveguide dimensions decrease. This localization at the boundaries allows the trapped spin-wave modes to function as sensitive probes [31, 32], revealing the magnetic properties of the entire system.

Despite recent progress, the study of geometric properties affecting spin-wave propagation in complex magnonic systems remains at an early stage. In my study, I implemented such geometries to simulate the spin-wave Talbot effect, also known as self-imaging. This phenomenon occurs when a plane wave passes through a one-dimensional array of periodic obstacles, such as nanodots, creating a distinctive near-field diffraction pattern that reconstructs the periodic structure at some specific intervals. Furthermore, the circular antidots have shown growing interest [33] due to their potential to excite spin waves at higher harmonic frequencies through nonlinear effects – an aspect I also explore in this thesis. The intentional design of nanoscale geometries in planar magnonic systems offers exciting possibilities for controlling spin-wave behavior.

In addition to planar systems, this thesis also investigates more complex, higher-dimensional structures for advanced spin-wave manipulation. Particularly intriguing are nanowires with a crescent-shaped cross section, which – when arranged in a diamond-bond network – show promise for studying near-degenerate magnetic states and developing reconfigurable magnonic devices [34, 35]. However, in this work, the research focuses exclusively on single crescent-shaped nanowires to study their fundamental spin-wave properties.

Even more structurally complex are gyroids – fully interconnected three dimensional periodic networks, composed entirely of chiral triple junctions [36–39]. The magnetic gyroidal nanostructures, with at least one dimension in the nanoscale, show potential to demonstrate monopole-type excitations, which have been observed so far only in 2D systems [40, 41]. Furthermore, the unit cell of a 3D gyroid is not only intrinsically chiral, but also exhibits continuous curvature, providing a rich platform for the development of controllable, nonlinear, and spatially localized spin textures [42–44].

The structures and phenomena discussed in this dissertation are in line with current trends in magnonics, particularly the growing interest in the use of nontrivial shapes to control spin-wave properties. While many challenges remain, the results presented here can contribute to this growing area of research and suggest exciting paths for further investigation, both in fundamental studies and potential applications.

1.2 From patterned thin films to intricate 3D ferromagnetic nanostructures

The primary objective of this dissertation is to develop prototypes of novel, geometrically complex magnonic nanostructures that have the potential for experimental realization and offer promising spin-wave control properties.

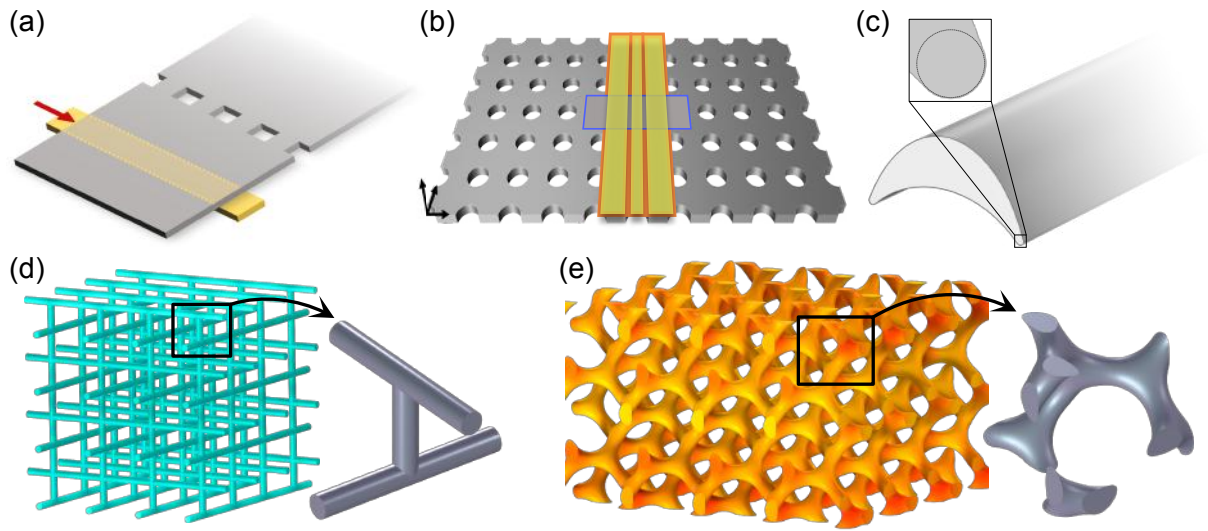


Figure 1.1 Schematic representation of the main systems studied in this thesis, presented in a sequence based on their increasing dimensional complexity. In (a), a one-dimensional antidot diffraction grating is shown (publications P1, P2, P3, and P6). In (b), there is a two-dimensional antidot lattice (ADL) with a defect in the center (publication P5). In (c), a crescent-shaped waveguide is shown, occupying a transitional regime between two- and three-dimensional structures. Although the simulations assume a two-dimensional geometry of infinite length, the resulting magnetic effects extend into the third dimension, as highlighted in publication P4. In (d) a scaffold-like three-dimensional lattice structure is shown, which was investigated in publication P9. Finally, (e) illustrates the gyroidal nanostructure presented in publications P7, P8 and P9.

The examination of nanostructures with complex shapes and nontrivial curvature brings multiple potential advantages to magnonics. First, it enhances our knowledge about magnon interactions with local magnetic properties, which might enable new methods for spin-wave manipulation. Second, the strategic implementation of different textures can enhance stronger magnonic band gaps and asymmetric spin-wave propagation, paving the way for the creation of efficient magnonic devices such as spin-wave-based logic circuits. Finally, these geometries provide a platform to study nonlinear and quantum effects that may drive progress in quantum magnonics and spintronics research. By investigating these nanostructures, this work aims to increase the theoretical knowledge of magnonic phenomena and ultimately support the development of magnon-based technologies for information processing. However, the design and development of complex material nanoarchitectures faces major obstacles. The fabrication of structures with lattice dimensions below 100 nm is particularly demanding and represents a significant technical challenge, which is being addressed by the efforts of the collaborating experimental groups. From a theoretical perspective, modeling and simulating of complex geometric systems demands advanced computational methods. To address these issues, my research has employed state-of-the-art micromagnetic simulations that allow reliable numerical investigations through the careful selection of parameters to optimize both the design and functionality of the simulated prototypes.

By means of the simulations, I have systematically studied magnetization dynamics, distribution, and localization in various metastructures, uncovering the mechanisms that drive these phenomena, developing methods to control them, and identifying their most effective applications. The term *metamaterial* refers here to engineered structures that exhibit unique, often unconventional magnetic properties not found in natural materials. The designed structural features allow precise and tunable control of wave propagation through their mutual interactions. The proposed geometric models were developed in the context of existing research, building on and extending the findings of other groups. This work focuses on five types of ferromagnetic metastructures (see Fig. 1.1) across different spatial dimensions:

- **one-dimensional nanodot arrays** that act as spin-wave diffraction gratings, giving rise to the Talbot (self-imaging) effect (Fig. 1.1a);
- **two-dimensional planar nano-ADLs**, where the structured geometry supports the formation of edge modes and enables nonlinear spin-wave excitation (Fig. 1.1b);
- **crescent-shaped waveguides**, studied for their influence on spin-wave dynamics, including curvature-induced localization effects (Fig. 1.1c);
- **scaffold-like three-dimensional lattices**, providing a fully interconnected probe for spin-wave modes localization in complex spatial environments (Fig. 1.1d);
- **three-dimensional gyroidal networks**, investigated for how their crystallographic orientation influences the ferromagnetic resonance (FMR) frequency and facilitates spin-wave modes localization (Fig. 1.1e).

One of the key tasks was to use structured ferromagnetic thin films with antidots to verify theoretically and numerically the induction of the Talbot effect for spin waves (see P1 in Sec. 5.1.1, and P2 in Sec. 5.1.2). The self-imaging has been successfully described and demonstrated by micromagnetic simulations, and the results have also been experimentally verified by collaborating partners (see P6 in Sec. 5.1.4). The control of spin-wave interference patterns by phase adjustments at the apertures between antidots led to the design of a yttrium iron garnet (YIG)-based logic device using the Talbot effect (see P3 in Sec. 5.1.3).

Another important research direction was the generation of high-frequency spin waves by exploiting nonlinear effects and localized cavity modes in the ADL (see P5 in Sec. 5.2.2). This study allowed for the excitation of magnons with very short wavelengths, a critical element in the development of compact magnonic devices.

Crescent-shaped waveguides also form a significant part of this study (see P4 in Sec. 5.2.1). The distribution of spin-wave modes in such systems depends on the precise control of the magnetic energies determined by the structural geometry. Here, I investigated how the curvature and edge sharpness of crescent-shaped nanowires affect the spin-wave dynamics in single nanorods. This particular design allows the distinction between edge-localized and volume-confined modes, which produce different spatial profiles and alter the spin-wave propagation properties.

Gyroids, while still relatively unexplored within the field of magnonics, represent a promising and novel direction of research (see P8 in Sec.5.3.2). Building on studies primarily concerned with their magnetostatic properties, I have conducted an extensive theoretical and numerical investigation of these structures. This involved systematic modification of parameters such as material filling fraction, structure size, and crystallographic orientation relative to external magnetic fields. These efforts were coordinated with the experiments of partner groups that measured the gyroid samples (see P7 in Sec.5.3.1).

The research also focused on an significant aspect of spin-wave localization in three-dimensional systems. The gyroid stands out as a promising example because it represents a periodic chiral network of nanorods that combines natural curvature with crystallographic symmetry. These geometric and structural features guided my research to design 3D gyroid architectures which demonstrate a novel form of surface-localized spin-wave FMR modes (see P9 in Sec. 5.3.3). Interestingly, the study revealed a similar localization effect in scaffold-like nanostructures, suggesting that this phenomenon is general. The comparative analysis of gyroids and scaffold-like lattices not only established the robustness of the localization effect across different 3D geometries, but also identified essential structural parameters needed for this phenomenon to occur.

The most difficult part of this research was to integrate multiple interrelated challenges into a single, comprehensive computational strategy. Besides, I was responsible for implementing specialized numerical methods for solving both frequency-domain and time-domain problems in complex multidimensional structures (see Ch. 4). These methods were crucial for obtaining the relaxed magnetization states and for capturing the spin-wave dynamics in noncollinear configurations. Using simulation environments such as MuMax3, COMSOL Multiphysics, and tetmag, I was able to systematically study how metamaterials, especially 3D architectures, allow for the unprecedented control of spin-wave propagation and localization. With new experimental techniques enabling the fabrication and measurement of these complex nanosystems, the numerical framework I use serves as a bridge between theoretical modeling and practical application in next-generation magnonic devices.

Chapter 2

Fundamentals of magnetism

2.1 Historical overview

The history of magnetism spans thousands of years, beginning with ancient observations of magnetic properties in materials and evolving into a scientific discipline. The first recorded mentions date back to ancient Greece, where magnetite (Fe_3O_4) was first discovered in the region of Magnesia, from which the term *magnetism* is derived. The ancient Greeks and Chinese recognized the unique properties of lodestone, a naturally magnetized form of Fe_3O_4 . While the former primarily observed and studied its magnetic behavior as a subject of curiosity and natural philosophy as early as the 2nd century BC¹, the latter later developed and used it as a navigational tool. The earliest confirmed use of the compass for navigation in China dates to around the 11th century AD² [45].

The scientific study of magnetism began as a systematic discipline in the late Middle Ages. In 1269, Petrus Peregrinus de Maricourt described the behavior of magnetic materials in his book *Epistola de Magnete*, introducing the idea of magnetic poles and describing how magnets interact [46]. A major advance came in 1600 when William Gilbert published *De Magnete*, which separated magnetism from static electricity, and also explained that the Earth itself acts as a giant magnet. Gilbert established the basic principles of magnetism as a property of matter and created concepts that remain important in modern science [47].

In the 19th century, a major breakthrough deepened our understanding of the relationship between electricity and magnetism. In 1820, Hans Christian Ørsted discovered that an electric current generates a magnetic field – a finding that directly contributed to the foundation of electromagnetism. André-Marie Ampère further quantified these findings by articulating Ampère’s law, which details how electric currents produce magnetic fields [48]. This development continued with Michael Faraday, who discovered electromagnetic induction in 1831, showing that time-varying magnetic fields could induce electric currents [49]. These groundbreaking findings

¹BC means ‘Before Christ’ and refers to years before year 1.

²AD stands for *Anno Domini*, Latin for “in the year of the Lord,” and refers to years after year 1.

were eventually combined by James Clerk Maxwell in 1873 into Maxwell's equations [50], which unified electricity and magnetism into a framework known as electromagnetism.

Although classical theories successfully described macroscopic magnetic phenomena, they were insufficient to explain the microscopic origins of magnetism. The development of quantum mechanics in the early 20th century revolutionized the entire field. The discovery of the intrinsic angular momentum of the electron (spin) by George Uhlenbeck and Samuel Goudsmit in 1925 [51], along with the introduction of quantum mechanical spin theory by Wolfgang Pauli [52], represented fundamental breakthroughs. These discoveries enabled the formulation of the Heisenberg model [53], which describes ferromagnetism in terms of exchange interactions. Werner Heisenberg's model also extended the concept of the Curie temperature (above which thermal energy disrupts magnetic order) by explaining that spontaneous magnetization above it vanishes due to thermal excitation overcoming the exchange interaction [54]. The Ising model, developed by Ernst Ising in 1925, provided further insights into magnetic order and phase transitions [55].

Building on earlier pioneering research, significant developments in the mid-20th century greatly deepened our understanding of the electronic origins of magnetism. Felix Bloch presented his seminal work on electrons in periodic potentials in 1929 [56], where he introduced the concept that the wavefunction of an electron in a crystalline lattice can be expressed as the product of a plane wave and a lattice periodic function. This became known as Bloch's theorem and is a principle of modern band theory of solids. By characterizing the allowed and forbidden energy bands within a periodic potential, Bloch's framework enabled systematic studies of how the quantum properties of electrons drive both conduction and magnetic effects. In the 1930s, John C. Slater built on these band theoretic concepts to develop an explanation of ferromagnetism in terms of exchange-induced splitting of electronic states [57]. Slater's key insight was that the Pauli exclusion principle, coupled with Coulomb interactions, can shift the energies of spin-up and spin-down bands differently. This splitting leads to unequal populations of electrons with opposite spins, creating a spontaneous net magnetic moment. His model linked the quantum-mechanical properties of electrons to the macroscopic ferromagnetic behavior observed in materials such as iron (Fe), cobalt (Co), and nickel (Ni). Subsequently, in the 1960s, John Hubbard introduced a more comprehensive framework to explain strong electron–electron correlations [58]. The Hubbard model captures local Coulomb repulsion by balancing two competing effects: the tendency of electrons to delocalize and form energy bands, and their tendency to localize due to strong interactions. By adjusting parameters such as hopping amplitude and local repulsion, the model shows how electrons can switch between moving freely (itinerant) and staying in place (localized). This has become a key tool for understanding effects such as metal–insulator transitions.

In the 20th century, scientists also made important breakthroughs in creating new magnetic materials. Although the naturally occurring magnetite mentioned above has been known since ancient times, the industrial synthesis of ferrites by Takeshi Takei and colleagues in the 1930s [59] led to the development of materials that combine high magnetic permeability with

low electrical conductivity. The engineered ferrites proved essential to transformer and inductor technology. The discovery of samarium–cobalt (SmCo) magnets in the late 1960s, followed by the introduction of neodymium–iron–boron ($\text{Nd}_2\text{Fe}_{14}\text{B}$) magnets in the early 1980s [60], revolutionized the field with permanent magnets offering exceptional power and thermal stability, enabling a wide range of applications in motors, sensors, and data storage.

Louis Néel’s pioneering research on antiferromagnetism and ferrimagnetism, for which he was awarded the Nobel Prize in Physics in 1970, revolutionized the understanding of complex magnetic ordering in solids [61]. Néel explained how interactions between different magnetic sublattices govern these phenomena, and showed that the net magnetic moment of a material can vanish when neighboring atomic spins are arranged in opposite configurations. These findings laid the groundwork for future spin-based technologies.

In parallel, the formalism of magnetization dynamics took shape. Building on Bloch’s quantum-mechanical treatment of electrons in crystalline lattices described above, in 1935 Lev Landau and Evgeny Lifshitz introduced a differential equation describing how the magnetization of a material evolves with time under external fields [62]. This equation was extended by T. L. Gilbert [63] in the mid-1950s, by adding a damping term to account for energy losses during magnetization precession. The resulting Landau–Lifshitz–Gilbert (LLG) equation is a fundamental tool in micromagnetism for modeling magnetization dynamics.

Major experimental milestones during this period also changed the practical applications of magnetism. Albert Fert and Peter Grünberg made an independent discovery of giant magnetoresistance (GMR) in 1988 [64, 65], showing that the electrical resistance in thin magnetic multilayers can change drastically with applied magnetic fields when electron scattering depends on spin orientation. This effect allowed engineers to reduce the size of magnetic sensors while revolutionizing data storage by increasing the density of hard drives. This was soon followed by the discovery of tunnel magnetoresistance (TMR) in magnetic tunnel junctions [66, 67], where electron tunneling across an insulating barrier also depends on spin orientation. TMR’s larger magnetoresistance ratios have further advanced the efficiency and scalability of spintronic devices.

Alongside spintronics, the closely related field of magnonics uses collective excitations of spin waves to transfer and process information. The study of spin-wave dynamics began with Bloch’s work on ferromagnet spin-wave excitations [68] and Néel’s research on antiferromagnet collective modes in multi-sublattice systems. The development of micromagnetic theory through the LLG equation established predictive methods for the control and design of spin-wave propagation in various media. In the late 20th century, the phenomenon of spin-transfer torque (STT) became the link between spintronics and magnonics by demonstrating how spin-polarized electric currents can generate torques on local magnetization states. In parallel research, J. C. Slonczewski and L. Berger demonstrated how STT enables electrical switching of magnetization – essential for high-speed, low-energy magnetic memory and other spin-based devices [69, 70]. These discoveries revealed the complex relationship between electron spin, charge transport, and collective magnetic excitations, opening new avenues for both fundamental

research and technological innovation. In recent decades, the study of magnetism has broadened its scope to include quantum magnetism, exploring new phenomena in nanoscale and complex magnetic structures. The discovery of topological insulators and magnetic skyrmions has opened new perspectives on magnetic materials, focusing on the interaction between topology, spin textures, and electronic properties [71]. These recent breakthroughs demonstrate the potential to develop energy-efficient non-volatile memory and logic devices.

Overall, the evolution of magnetism reflects a journey from early empirical observations to a deep theoretical understanding that includes both classical and quantum aspects. This development has advanced our knowledge of fundamental physical principles and stimulated technological progress in many fields of human activity.

2.2 Magnetic moments and magnetic fields

The magnetic moment $\boldsymbol{\mu}$ is a fundamental concept of magnetism at both the microscopic and macroscopic levels. It arises from the motion of electric charges, mainly the electron's orbital motion around the nucleus (acting like a current loop) and its intrinsic spin magnetic moment. The orbital magnetic moment $\boldsymbol{\mu}_{\text{orb}}$ is given by

$$\boldsymbol{\mu}_{\text{orb}} = -\frac{e}{2m_e}\mathbf{L}, \quad (2.1)$$

where \mathbf{L} is the orbital angular momentum of the electron, e is the elementary charge³ ($\approx 1.602 \times 10^{-19}$ C), and m_e is the electron mass ($\approx 9.109 \times 10^{-31}$ kg) [72]. As mentioned above, electrons also have an intrinsic angular momentum known as *spin*. The magnetic moment associated with it, $\boldsymbol{\mu}_s$, is defined as

$$\boldsymbol{\mu}_s = g_e \mu_B \mathbf{S}, \quad (2.2)$$

where g_e is the electron spin g -factor (approximately -2 ; see Sec. 3.2.1 for details), and \mathbf{S} denotes the spin angular momentum [73] (further discussed in Sec. 2.5). The *Bohr magneton* μ_B is a fundamental physical constant that represents the magnetic moment of an electron resulting from its spin or orbital motion. It is defined as

$$\mu_B = \frac{e\hbar}{2m_e} \approx 9.274 \times 10^{-24} \text{ J/T}, \quad (2.3)$$

where \hbar is the reduced Planck constant ($\approx 1.055 \times 10^{-34}$ J·s) [74]. The Bohr magneton sets the natural scale for magnetic moments in atomic and solid-state physics.

The total magnetic moment of an atom, $\boldsymbol{\mu}$, is the vector sum of the magnetic moments resulting from the orbital and spin contributions. When viewed from a distance, a localized magnetic moment behaves like a magnetic dipole, producing a magnetic field similar to that of a

³Although the charge of the electron is negative, e is conventionally defined as the *positive* elementary charge. The negative sign in Eq. 2.1 accounts for the electron's actual charge.

tiny bar magnet – hence, in the literature, it is often referred to as a dipole magnetic moment. This leads to the concept of magnetization, \mathbf{M} , which quantifies the magnetic moment per unit volume. For a discrete system with n atoms per unit volume, the magnetization is expressed as

$$\mathbf{M} = n\boldsymbol{\mu}, \quad (2.4)$$

and describes how a material responds to an external magnetic field, making it one of the most important quantities in determining the magnetic properties of materials [45]. In ferromagnets, the alignment of the magnetic (dipole) moments leads to a net magnetization even in the absence of an external field, a phenomenon known as spontaneous magnetization, which is discussed in detail in Sec. 2.3. The magnetic field, in turn, can be described in two different but related forms: as the magnetic flux density \mathbf{B} and as the magnetic field intensity \mathbf{H} ⁴. The flux density \mathbf{B} is defined as the force per unit charge per unit velocity acting on a charged particle moving through a magnetic field and is measured in tesla (T). The field intensity (or strength) \mathbf{H} , characterizes the magnetic field produced by free currents and external sources, and it is measured in amperes per meter (A/m). The relationship between \mathbf{B} and \mathbf{H} in a material is given by

$$\mathbf{B} = \mu_0(\mathbf{H} + \mathbf{M}), \quad (2.5)$$

where μ_0 is the permeability of free space (vacuum permeability, $= 4\pi \times 10^{-7}$ H/m). Outside the magnetic material, however, $\mathbf{M} = 0$, and the Eq. 2.5 simplifies to $\mathbf{B} = \mu_0\mathbf{H}$ [75]. The field \mathbf{H} is particularly useful for describing the influence of external (free) currents on the magnetic field within a material or in free space, and under magnetostatic conditions (i.e., when fields and currents are time-independent), it is governed by Ampère’s law:

$$\nabla \times \mathbf{H} = \mathbf{J}_{\text{ext}}. \quad (2.6)$$

If a given region of vacuum contains no free currents, then $\mathbf{J}_{\text{ext}} = 0$ and the equation reduces to $\nabla \times \mathbf{H} = 0$, indicating that \mathbf{H} is curl-free there. However, if charged particles or current-carrying wires pass through the vacuum, then $\mathbf{J}_{\text{ext}} \neq 0$, and $\nabla \times \mathbf{H}$ remains equal to that current density.

The interaction between a magnetic moment and an external magnetic field plays a key role in determining the magnetic behavior of materials and, as noted above, can be approximated as the dipole–field interaction. For a single magnetic dipole $\boldsymbol{\mu}$ in an external magnetic flux density \mathbf{B} , the potential energy is defined as

$$U_{\text{dipole}} = -\boldsymbol{\mu} \cdot \mathbf{B}, \quad (2.7)$$

which is minimized when both vectors are aligned. However, in most physical systems there is a continuous distribution of magnetic dipoles, $\boldsymbol{\mu}(\mathbf{r})$, rather than a single one. Transforming the Eq. 2.4 into a derivative expression, the magnetization $\mathbf{M}(\mathbf{r})$ can be introduced to represent the

⁴The terms \mathbf{B} and \mathbf{H} are often used interchangeably in the literature – the convention used in this work is to refer to both symbols as ‘magnetic field’ representations unless a distinction is necessary.

continuous⁵ magnetic moment per unit volume:

$$\mathbf{M}(\mathbf{r}) = \frac{d\boldsymbol{\mu}(\mathbf{r})}{dV}. \quad (2.8)$$

Consequently, the total magnetic potential energy can be expressed as an integral over the volume V of the material:

$$U_{\text{mag}} = - \int_V \mathbf{M}(\mathbf{r}) \cdot \mathbf{B} dV. \quad (2.9)$$

This formulation generalizes Eq. 2.7 from a single dipole to a continuum of dipoles, which reflects the behavior of real magnetic materials. Regardless of whether one uses \mathbf{B} or \mathbf{H} (see Eq. 2.5), the physical picture remains the same: the system lowers its energy when the dipoles, or equivalently the magnetization, align with the external field. This alignment leads to a stable magnetic configuration, influencing phenomena such as hysteresis, domain formation, and other key aspects of magnetic materials described in the following sections.

Magnetic susceptibility is a dimensionless quantity that measures how strongly a material becomes magnetized in response to an external magnetic field. In the most general formulation, the susceptibility is expressed as a second-order tensor, denoted $\bar{\chi}$, which relates the magnetization \mathbf{M} to the applied⁶ magnetic field \mathbf{H} via

$$\mathbf{M} = \bar{\chi} \mathbf{H}. \quad (2.10)$$

This form is essential for the description of anisotropic materials, where \mathbf{M} is not necessarily aligned with the applied field \mathbf{H} (more in Sec. 2.7). The tensor $\bar{\chi}$ is then a 3×3 matrix whose elements depend on the crystal symmetry or other anisotropic properties of the material. However, in many practical cases, the magnetic medium can be approximated as isotropic and linear in its response to an external field. Under these conditions, $\bar{\chi}$ reduces to a single, dimensionless scalar χ , simplifying the Eq. 2.10 to $\mathbf{M} = \chi \mathbf{H}$. Here, \mathbf{M} is strictly parallel (or antiparallel) to \mathbf{H} , and the value of χ does not change as long as the material remains in its linear response regime.

Materials are classified into different categories based on their susceptibility values, e.g., diamagnets with a negative χ (indicating magnetic moments in opposite directions to the applied field), paramagnets with a small positive χ (slight alignment with the field), and ferromagnetic materials with large positive χ , indicating strong alignment [72] – more details in Sec. 2.3. The permeability μ (not to be confused with the magnetic moment vector $\boldsymbol{\mu}$) of a material is related to its susceptibility by

$$\mu = \mu_0(1 + \chi). \quad (2.11)$$

⁵For clarity, \mathbf{M} denotes the magnetization in both discrete and continuous forms; when necessary, the spatial dependence is given explicitly as $\mathbf{M}(\mathbf{r})$.

⁶In this chapter, the distinction between the applied and general magnetic fields is not needed, so the symbol \mathbf{H} is used throughout. In the following chapters, where several magnetic field components appear, the applied field will be denoted explicitly as \mathbf{H}_0 .

2.3 Types of magnetism

As outlined in the previous section, materials can be categorized into different types based on their response to external magnetic fields. These types include diamagnetism, paramagnetism, ferromagnetism, antiferromagnetism, and ferrimagnetism, each arising from different microscopic mechanisms and exhibiting unique material behaviors, as shown in Fig. 2.1.

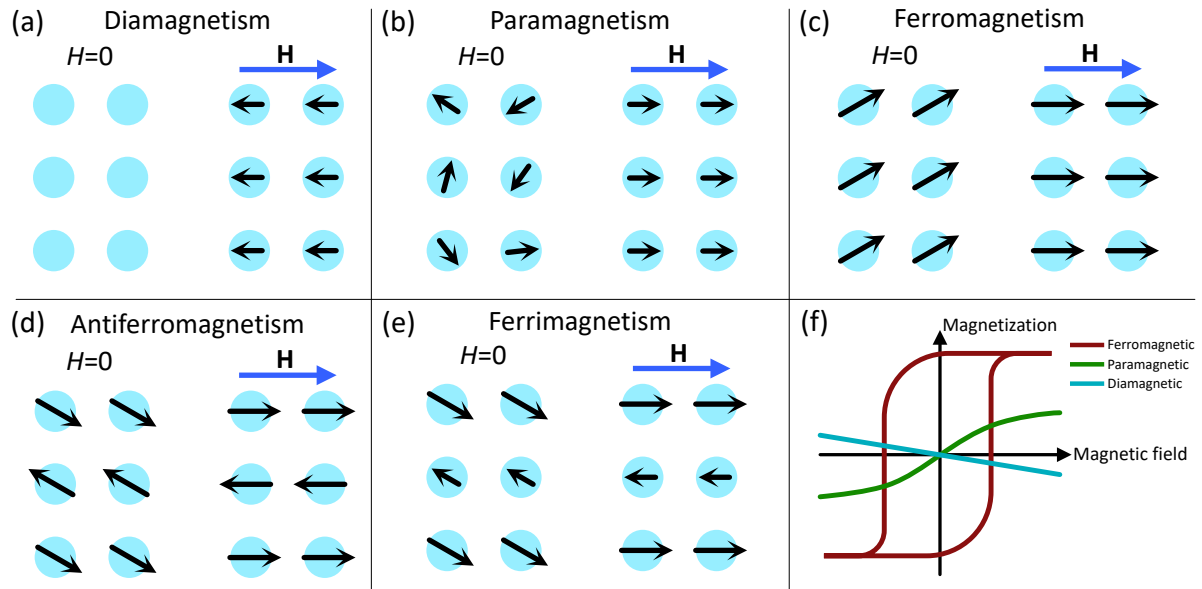


Figure 2.1 Schematic illustration of different types of magnetic responses to an external magnetic field, from (a) to (e): diamagnetism, paramagnetism, ferromagnetism, antiferromagnetism, and ferrimagnetism. Black arrows represent magnetic moment vectors, while blue arrows indicate the direction of the applied magnetic field (if present). The last panel (f) shows model hysteresis loops for ferromagnetic, paramagnetic and diamagnetic materials to illustrate their different magnetic behavior. Note: Under sufficiently strong external fields, some antiferromagnets and certain ferrimagnets can undergo spin-flop transitions, where the antiparallel spins reorient to a tilted configuration. The configurations shown in (d) and (e) reflect field strengths below this threshold.

Diamagnetism (Fig. 2.1a) is the basic form of magnetism that exists in all materials regardless of temperature [72, 73]. It results from the response of electrons to an applied magnetic field, where their orbital motion generates small currents that create a magnetic field in the opposite direction. This effect is typically very weak, meaning that diamagnetic materials are only slightly repelled by external magnetic fields. A special case of diamagnetism occurs in superconductors, which exhibit perfect diamagnetism below a critical temperature due to the Meissner effect [76]. In this state, superconductors completely expel magnetic flux from their interior, making their diamagnetic response much stronger than in typical materials [77].

Paramagnetism occurs in materials containing unpaired electrons, i.e., electrons whose spins are not canceled out by a partner with the opposite spin. Although each unpaired electron has its own magnetic moment, in the absence of an external field these are randomly oriented due to thermal fluctuations, resulting in zero net magnetization (Fig. 2.1b). When an external magnetic

field is applied, these magnetic moments tend to align with it, resulting in a small positive net magnetization. The strength of this response decreases as temperature T increases, following Curie's law:

$$\chi = \frac{C}{T}, \quad (2.12)$$

where C is a material-specific Curie constant. This inverse relationship between susceptibility χ and T is due to thermal oscillations that perturb the alignment of the magnetic moments. Common examples of paramagnetic materials include aluminum (Al) and platinum (Pt) [72, 78].

In my research, I focus on ferromagnetism – a type of magnetic ordering characterized by the spontaneous alignment of magnetic moments within the material, even in the absence of an external magnetic field (Fig. 2.1c). This behavior is driven by strong exchange interactions in these materials (overlapping electron orbitals), which force the spins of neighboring atoms to align parallel to each other, resulting in a strong collective magnetization. This alignment persists up to a critical temperature, known as the Curie temperature (T_C), beyond which thermal energy disrupts the ordered state and the material becomes paramagnetic. Fe, Co, and Ni are classic examples of ferromagnetic materials, and their alloys are widely used in various technological applications [45, 73].

Antiferromagnetism occurs when adjacent magnetic moments align in opposite directions (Fig. 2.1d), effectively canceling each other out and resulting in zero net magnetization. This arrangement is energetically favorable because of the antiferromagnetic exchange interaction. The characteristic temperature at which the antiferromagnetic order is lost is called the Néel temperature (T_N). Below T_N the material shows no macroscopic magnetization, but above this temperature it behaves like a paramagnet. Manganese oxide (MnO) and chromium (Cr) are typical examples of antiferromagnetic materials [54, 73].

Ferrimagnetism (Fig. 2.1e) is similar to antiferromagnetism in that it involves inversely oriented magnetic moments. However, the magnitudes of these moments are not equal, resulting in a net magnetization. This behavior occurs in materials with multiple magnetic sublattices, each contributing differently to the total magnetization. A well-known example is magnetite (Fe_3O_4), where the unequal magnetic contributions of different Fe ions result in a non-zero overall magnetization. Analogous to ferromagnets, ferrimagnets have a Curie temperature, above which they lose their ordered magnetic state [61, 78].

Altermagnetism: a novel magnetic phase

Altermagnetism is a recently recognized magnetic phase that integrates properties of ferromagnetism and antiferromagnetism [79]. In altermagnetic materials, adjacent electron spins are antiparallel, resulting in zero net magnetization, similar to conventional antiferromagnets. However, unlike them, altermagnets exhibit significant *spin splitting* in their electronic band structures, a characteristic typically associated with ferromagnets.

Spin splitting is the separation of electronic energy levels or bands according to their spin orientation. In magnetic materials, this effect usually arises from exchange interactions, where

one spin channel (e.g., spin-up) is energetically favored over the other (spin-down), producing separate band structures. In conventional ferromagnets, this splitting underlies a net magnetization, whereas in altermagnets a substantial spin splitting coexists with collinear antiparallel spins. This combination leads to unique magnetic and electronic properties, positioning altermagnets as promising candidates for next-generation spintronic applications [80]. Experimental evidence for altermagnetism has been reported in compounds such as manganese telluride (MnTe) and ruthenium dioxide (RuO₂) [81–83].

2.4 Magnetic materials: properties and hysteresis behavior

The previous section explained the basic types of magnetism by showing how different materials respond to external magnetic fields based on their intrinsic electronic and magnetic properties. Among these, the complex response of ferromagnetic (and ferrimagnetic) materials to cyclic magnetic fields (see Fig. 2.1f) is characterized by magnetic hysteresis behavior, which will be the focus of this section.

Magnetic materials can be broadly classified as *soft* or *hard* magnets. Soft magnetic materials are characterized by their low *coercivity*, meaning that they can reverse their magnetization in response to small changes in external magnetic field. As a result, they have a relatively narrow hysteresis loop (see Fig. 2.2), which typically corresponds to relatively low remanent (residual) magnetization and minimal energy loss over repeated magnetization cycles. Soft magnets are mostly used in applications that require rapid magnetization and demagnetization, such as transformers and inductors [73, 84]. It also makes them important for studying and exploiting fast magnetization dynamics in magnonics – more details in Sec. 3.2.

Examples of soft magnetic materials include:

- **soft Fe**, often used in transformer cores due to its low coercivity and high magnetic permeability,
- **ferrites**, oxide materials commonly used in high-frequency transformers and inductors due to their low eddy current losses and ease of magnetization,
- **permalloy (Ni₈₀Fe₂₀)**, widely used in read heads and magnetic sensors due to its high permeability and low coercivity. Its good soft-magnetic properties, negligible magnetostriction and low Gilbert damping [84] make it a preferred material for magnonic waveguides and spintronic devices (used in my publications P1–P6),
- **Ni**, which has a relatively low coercivity and is often used in thin films or multilayer structures for magnetic sensing and spintronic applications (used in P7–P9).

In contrast, hard magnets are high coercivity materials that maintain their magnetization even in relatively strong opposing magnetic fields. Their wide hysteresis loops (Fig. 2.2) indicate strong remanence properties and high energy requirements for demagnetization. Hard magnets

are used in applications where permanent magnetization is required, such as in motors, generators, and magnetic storage devices [85]. Examples of hard magnetic materials include:

- **alnico (acronym from Al–Ni–Co) alloys**, being one of the first commercially significant permanent magnet material, offering high remanence and relatively good thermal stability. Although surpassed by modern alloys, alnico magnets remain valuable for certain high-temperature applications,
- **rare-earth magnets**, like neodymium–iron–boron (NdFeB) and samarium–cobalt (SmCo), are known for their exceptional coercivity, making them ideal for high-power applications such as electric motors, wind turbines, and magnetic data storage,
- **layered systems with L_{10} -ordering**, where the tetragonal structure provides very high magnetocrystalline anisotropy. As a result, thin-film L_{10} FePt or CoPt materials are particularly relevant for advanced data storage technologies (e.g., perpendicular magnetic recording) and other applications requiring high coercivity [86].

In addition to coercivity, a typical hysteresis loop describes how the magnetization of a material responds to an external magnetic field, as shown in Fig. 2.2. It is plotted as the magnetization component (or projection) M versus the applied field value H , with both quantities typically aligned with one of the “easy” magnetization axes of the material. Under these conditions, the hysteresis loop reveals several key material properties, such as the previously mentioned coercivity, remanence, saturation magnetization, and energy loss (given by the area of the loop).

In materials with significant magnetocrystalline anisotropy (see Sec. 2.7), hysteresis loops can look different when measured along different crystallographic orientations. The easy axis (or axes) typically exhibits higher remanence and coercivity than other directions, due to the presence of anisotropy energy barriers. As a result, hysteresis loops measured with the field applied along the easy axis tend to be more “square” in shape and enclose larger areas. In contrast, loops measured along a hard axis have lower remanence and reduced coercivity. Understanding these orientation-dependent behaviors is critical for designing magnetic materials tailored to specific applications.

Coercivity (H_c), as outlined above, is defined as the magnitude of the reverse (negative) magnetic field required to reduce the net magnetization of a material to zero after it has been magnetically saturated. In essence, it quantifies the material’s resistance to demagnetization, reflecting how robustly it retains magnetization when subjected to an opposing external field.

Remanence (M_r) is the residual magnetization that remains in a material after the external magnetic field has been reduced to zero (from saturated state), i.e., it quantifies the ability of the material to remain magnetized in the absence of an external field. High remanence is advantageous in hard magnetic materials (e.g., permanent magnets) because it indicates that a substantial magnetic field can be maintained without distortion. In contrast, soft magnets tend to have relatively low remanence. While it is consistent with easy magnetization cycling, it is mostly the low coercivity that enable rapid switching of magnetization [85].

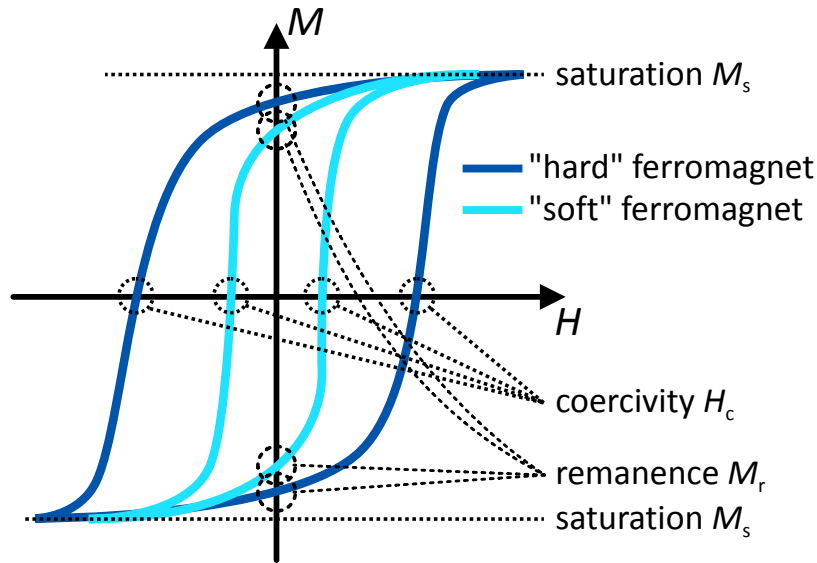


Figure 2.2 Representative magnetic hysteresis loops for soft and hard magnets (light and dark blue curves, respectively), illustrating key parameters such as coercivity field (H_c), remanence magnetization (M_r), and saturation magnetization (M_s).

Saturation magnetization (M_s) is the maximum magnetization that a material can reach. Beyond this point, increasing the field will not result in any additional magnetic induction because all the moments are already aligned in the direction of the field. Saturation magnetization is a fundamental material property and is strongly dependent on the type of magnetic material and its temperature. Materials with high saturation are preferred in applications where strong magnetic fields are required, such as in electromagnets and permanent magnets [73, 84].

The energy loss in magnetic materials during a magnetization cycle is proportional to the area enclosed by the hysteresis loop. This energy loss, often referred to as hysteresis loss, is dissipated in the form of heat. It becomes significant in applications such as transformers and induction motors, where materials are exposed to rapidly changing magnetic fields. Reducing hysteresis loss is a key goal in the design of efficient soft magnetic materials for such applications [87].

2.5 The quantum theory of magnetism

To understand the diverse behavior of magnetic materials, one must delve into their quantum-mechanical foundations. Although classical approaches can successfully describe many macroscopic properties such as magnetic susceptibility and hysteresis, they cannot fully explain the microscopic origins of magnetism, including the exchange interactions and the role of electron spin at the atomic level. The quantum theory of magnetism addresses these limitations. A prominent example of the interplay between quantum origins and classical descriptions is found in magnonics. Although *magnons* (the quanta of spin waves) originate from quantum spin interactions, their propagation through a magnetic medium can often be described by classical

wave models. Remarkably, this approach remains valid down to the nanometer scale, linking quantum many-body physics with classical continuum models.

As introduced in Sec. 2.2, the basis of quantum magnetism lies in electron spin that generates a magnetic moment (see Eq. 2.2). Unlike orbital magnetic moments, which result from the motion of the electron around the nucleus, the spin magnetic moment is an intrinsic property of the electron, analogous to a tiny bar magnet [72, 73]. It can be represented by the spin angular momentum operator $\hat{\mathbf{S}}$, which obeys:

$$\hat{\mathbf{S}}^2|S, m\rangle = \hbar^2 S(S+1)|S, m\rangle, \quad (2.13)$$

where the quantum number $S = 1/2$ for the electron, and m is the spin projection quantum number.

Spin arises from the quantum field theory, and its associated magnetic moment underlies many of the physical phenomena observed in magnetic materials [73]. However, many macroscopic and mesoscale theories treat it as a classical vector, especially when studying collective spin behavior. For example, in micromagnetism, the magnetization $\mathbf{M}(\mathbf{r})$ in any infinitesimal volume (Eq. 2.8) is modeled as a continuous vector field satisfying the LLG equation [62, 63, 88] – more in Ch. 3.

Another key concept in quantum magnetism is the exchange interaction, which is a direct consequence of the Pauli exclusion principle and the Coulomb repulsion between electrons. It determines how adjacent spins in a material are aligned, either parallel or antiparallel. In ferromagnetic materials, the positive exchange interaction favors parallel alignment of spins, resulting in a net macroscopic magnetization. In contrast, antiferromagnetic materials exhibit a negative exchange interaction, which causes neighboring spins to align antiparallel, effectively canceling out the overall magnetization [74]. These behaviors are described quantitatively by the Heisenberg model developed in the late 1920s [53], which is based on the Heisenberg exchange Hamiltonian:

$$\mathcal{H} = -2J \sum_{\langle i, j \rangle} \mathbf{S}_i \cdot \mathbf{S}_j, \quad (2.14)$$

where J is the exchange integral, and \mathbf{S}_i and \mathbf{S}_j are the spin operators of neighboring atoms i and j . The sign and magnitude of the exchange constant J determine how the neighboring spins are aligned. For a simple quantum Heisenberg model with spin S , a rough mean-field approximation [89, 90] relates the exchange constant J to the Curie or Néel temperature, with the coordination number z capturing the lattice geometry and interaction strength. This relationship takes the form:

$$T_{C,N} \sim \frac{zS(S+1)|J|}{k_B}, \quad \begin{cases} T_C & \text{ferromagnets} \\ T_N & \text{antiferromagnets} \end{cases} \quad (2.15)$$

where the Boltzmann constant $k_B \approx 1.3806 \times 10^{-23}$ J/K. In essence, the stronger the exchange coupling (larger $|J|$), the more thermal energy is required to disorder the spins (transition to a paramagnetic phase), leading to higher T_C or T_N .

Among quantum approaches to describing ferromagnetism is the itinerant electron (band) model [90], often associated with the Stoner criterion [91]. In this framework, electrons are treated as delocalized quasiparticles occupying conduction bands, and the interplay of exchange interactions with the band structure can induce a spontaneous splitting between spin-up and spin-down bands, thereby leading to ferromagnetism. In contrast to localized spin models, such as the Heisenberg model, this approach emphasizes the importance of the electronic structure in driving the magnetic order.

An even more rigorous quantum description that includes electron–electron correlations is the Hubbard model, briefly introduced in Sec. 2.1. By integrating local interactions, it provides a unified framework capable of describing both localized and itinerant limits of magnetism.

In addition to the Heisenberg and band models, the Ising framework provides insight into magnetic phase transitions and critical phenomena. Here, the spin of each atom is constrained to be either parallel or antiparallel along a chosen axis, which simplifies the analysis of magnetic ordering in one- and two-dimensional systems. The Ising model was originally developed to describe ferromagnets, but it has been extended to study complex behavior also in systems with competing interactions, such as spin glasses and frustrated magnets [55].

An important aspect of quantum magnetism is also the role of spin-orbit coupling (SOC), which arises from the interaction between an electron’s spin and its orbital motion around the nucleus. SOC is a relativistic effect that links the electron’s spin degree of freedom to its orbital angular momentum. From a quantum-mechanical perspective, this coupling originates from the Dirac equation, but it is commonly described using an effective interaction Hamiltonian:

$$\mathcal{H}_{\text{SOC}} = \lambda \hat{\mathbf{L}} \cdot \hat{\mathbf{S}}, \quad (2.16)$$

where λ is an effective SOC constant, and $\hat{\mathbf{L}}$ is the orbital angular momentum operator [72, 92]. In a more detailed approach (e.g., for atoms with spherical symmetry), the radial coordinate function, $\lambda = \zeta(r)$, indicates that the coupling strength can change with the distance r of the electron from the nucleus. Solids modify this interaction through their crystal environment, affecting both electronic band structures and the resulting magnetic properties. A key consequence of SOC in magnetic materials is a *magnetic anisotropy*, which means that the total energy of a system depends on the direction of magnetization relative to the crystallographic axes – more in Sec. 2.7.

A semi-classical framework provides accurate and convenient analyses of spin-wave dynamics in many magnetic materials, but certain regimes require a fully quantum-mechanical formalism. For example, at low temperatures, thermal excitations may be dominated by few-magnon processes, making classical approximations insufficient. In materials with strong electron correlations, topological band structures cannot be captured by purely classical spin-wave theory. Also, when describing ultrafast or ultralow energy processes, including single-magnon excitations or quantum-entangled spin states, methods like the Holstein–Primakoff transformation and exact diagonalization are necessary [90, 93].

2.6 Magnetic domains and domain walls

To minimize their free energy, ferromagnetic and ferrimagnetic materials tend to split into *domains* – subregions where spins are uniformly aligned in the same direction (see Fig. 2.3). While exchange interactions favor uniform spin alignment across the entire material, this is opposed by the magnetostatic (dipolar) field, which promotes flux closure. Additionally, magnetocrystalline anisotropy introduces a directional preference for the magnetization based on the crystal structure. The balance among exchange, magnetostatic, and anisotropy energies leads to the formation of a mosaic of domains with different magnetization directions, rather than a single, uniformly magnetized state. The boundaries between these domains, known as *domain walls*, represent continuous rotations of the local spin orientation (see Fig. 2.3). Although domain walls carry an energy cost – primarily due to exchange and anisotropy – they help reduce the overall magnetostatic energy by minimizing stray fields. Consequently, key magnetic properties such as coercivity, remanence, and hysteresis behavior in ferromagnetic and ferrimagnetic materials are largely governed by the nucleation, growth, and stability of domains and their walls.

The concept of magnetic domains was first introduced in the early 20th century by Pierre Weiss, who proposed that ferromagnetic materials are composed of small, uniformly magnetized regions – even in the absence of an external magnetic field. While the magnetization within each domain is aligned, the overall magnetization of the material remains zero due to the random orientation of the domains relative to one another [84]. This domain structure helps reduce the system's magnetostatic energy, as the presence of multiple domains with different orientations lowers the stray magnetic fields generated by the material.

There are two primary types of domain walls, distinguished by how the magnetization transitions across them: Bloch and Néel walls (Fig. 2.3). In a Bloch wall, the magnetization rotates within the plane of the domain wall (the surface that separates the two domains), resulting in a spiral-like transition of the magnetic moments from one domain to the other. This type of wall typically occurs in bulk materials with moderate/low magnetic anisotropy. The width of a Bloch wall, δ_B , is determined by the competition between exchange energy, which favors a gradual change in spin direction, and anisotropy energy, which favors alignment along easy axes [87], and can be determined as

$$\delta_B = \sqrt{\frac{A_{\text{ex}}}{K_u}}, \quad (2.17)$$

where A_{ex} is the exchange stiffness constant (introduced in Sec. 3.1.1) and K_u is the uniaxial anisotropy constant (more in Sec. 2.7). A larger A_{ex} or smaller K_u leads to a wider Bloch wall, reflecting a smoother transition between domains.

Néel walls, on the other hand, are characterized by a rotation of magnetization that occurs perpendicular to the domain wall plane. This type of wall is commonly observed in thin films and nanostructures, where surface effects and demagnetizing fields play a dominant role. The

width of a Néel wall, denoted as δ_N , is typically smaller than that of a Bloch wall and, like it, is governed by the balance between exchange and anisotropy energies [87].

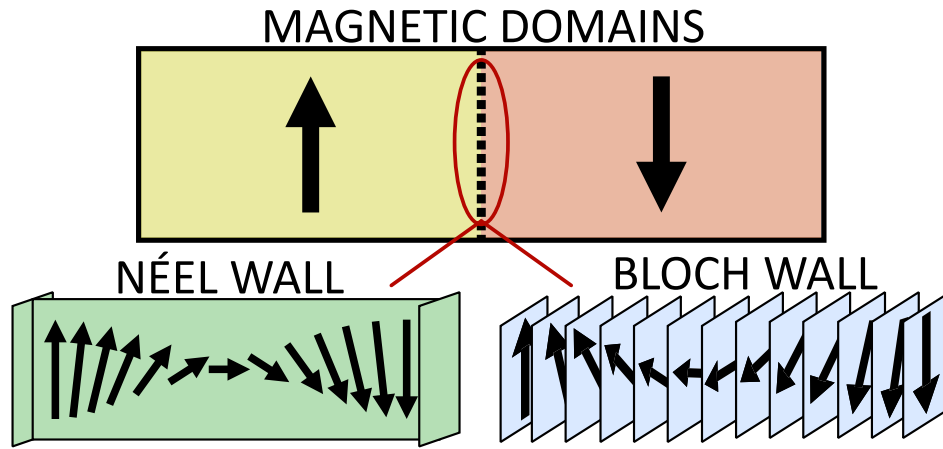


Figure 2.3 Schematic illustration of a two-domain magnetic system, with domain walls separating regions of opposite magnetization. The left panel shows a Néel domain wall where the magnetization rotates perpendicular to the wall plane. The right panel shows a Bloch domain wall where the magnetization rotates within the wall plane. Both configurations provide a continuous transition between different domains.

The stability and mobility of magnetic domain walls are governed by their domain wall energy per unit area, approximated by

$$\sigma \approx 4\sqrt{A_{\text{ex}}K_{\text{u}}}, \quad (2.18)$$

that holds under certain assumptions:

- a single-axis or easy-axis anisotropy (described by Eq. 2.20);
- a uniform rotation of the magnetization across the wall width, (ignoring in-plane variations or complex curling);
- magnetostatic contributions within the wall region itself do not significantly affect the fundamental scaling behavior. However, in practice, especially in thin films, magnetostatic energy can influence which type of domain wall is energetically preferred;
- a micromagnetic continuum approximation.

A lower σ generally indicates that domain walls are easier to form and require less energy to move. In contrast, a higher wall energy tends to stabilize domain configurations against external fields or perturbations. Table 2.1 summarizes typical values of domain wall energies and widths for selected materials, highlighting the differences between Bloch and Néel wall types.

Domain wall dynamics, including nucleation, motion, and pinning, are influenced by external magnetic fields, temperature, and material defects. Understanding these factors is crucial for the development of advanced magnetic devices. A prominent example is racetrack memory, where

Table 2.1 Typical domain wall energies (σ) and approximate domain wall widths (δ_{DW}) for selected ferromagnetic and ferrimagnetic materials. Reported values may vary depending on factors such as microstructure, temperature, and sample preparation. Lattice structures: hcp = hexagonal close-packed, fcc = face-centered cubic, bcc = body-centered cubic.

Material	Wall type	σ (mJ/m ²)	δ_{DW} (nm)	Refs.
Fe (bcc, bulk)	Bloch	50–100	20–40	[85, 87]
Ni (fcc, bulk)	Bloch	10–30	50–70	[73]
Co (hcp, bulk)	Bloch	100–200	10–20	[87]
Ni ₈₀ Fe ₂₀ (fcc, thin film)	Néel	2–10	100–150	[85, 87]
YIG (garnet, bulk)	Néel	1–5	100–300	[73]

information is stored in domain wall regions within magnetic nanowires [94]. In such devices, precise control over domain wall motion is essential for achieving fast and reliable operation.

2.7 Magnetic anisotropy

Magnetic anisotropy refers to the directional dependence of magnetic properties, meaning that the energy required to magnetize a material varies with the direction of magnetization. This property influences the behavior of magnetic domains, domain walls, and the overall magnetization dynamics. It also plays a key role in magnetization reversal processes (see the hysteresis loops in Fig. 2.2). When an external magnetic field is applied, the magnetization tends to rotate in the direction of the field. However, anisotropy introduces energy barriers that must be overcome for complete reversal. The stronger the uniaxial or cubic anisotropy, the higher the external field is required [73]. In addition, the orientation of the applied field relative to the easy axis significantly changes the shape of the hysteresis loop, as explained in Sec. 2.4.

Magnetic anisotropy results from several factors such as crystal structure, shape, and mechanical stress, each affecting the magnetic response in a different way.

Crystalline anisotropy

This specific type of anisotropy results from the interaction between the crystal lattice and the magnetic moments of the electrons, that are affected by SOC. In such materials, certain crystallographic directions require less energy to orient the magnetization (easy axes). This dependence can be captured by the general expression for the anisotropy energy:

$$E_{\text{crystal}} = K_1 f(\alpha_i) + K_2 f(\alpha_i) + \dots, \quad (2.19)$$

where K_1 , K_2 , and higher-order terms are anisotropy constants, and $f(\alpha_i)$ represents a function of the direction cosines α_i of the magnetization with respect to the crystal axes. This equation is general, and specific cases such as uniaxial and cubic anisotropies, represent different realizations of this form [73, 84].

Uniaxial anisotropy occurs when the material has a single preferred direction of magnetization (easy axis). Crystalline hcp systems or certain tetragonal structures often exhibit strong uniaxial anisotropy due to their lattice symmetry and SOC effects (for example hcp-Co, L₁₀ FePt or CoPt alloys [72, 73]). Similarly, many rare-earth–transition-metal compounds (e.g., SmCo₅, Nd₂Fe₁₄B) have a strong uniaxial anisotropy axis that dominates their macroscopic magnetic behavior. Beyond crystallographic origins, engineered thin films or nanostructures can also exhibit uniaxial anisotropy due to epitaxial strain, surface effects, or shape anisotropy in elongated geometries. The energy associated with this type of anisotropy is often described by the simplified form of Eq. 2.19:

$$E_{\text{uniaxial}} = K_u \sin^2 \theta, \quad (2.20)$$

where K_u is the uniaxial anisotropy constant and θ is the angle between the magnetization and the easy axis. Materials with positive K_u , such as Co, tend to orient their magnetization along the easy axis, while materials with negative K_u prefer alignment perpendicular to it [95].

Cubic anisotropy is observed in materials with cubic crystal symmetry, such as Fe and Ni [84]. For this type of crystalline anisotropy, the associated energy is given by

$$E_{\text{cubic}} = K_{c1} (\alpha_1^2 \alpha_2^2 + \alpha_2^2 \alpha_3^2 + \alpha_3^2 \alpha_1^2) + K_{c2} \alpha_1^2 \alpha_2^2 \alpha_3^2, \quad (2.21)$$

where K_{c1} and K_{c2} are the cubic anisotropy constants. Physically, these terms originate from SOC in a crystal field with cubic symmetry. The spin–orbit interaction induces certain degeneracies in the electronic states, favoring specific orientations of electron spins – and hence, the magnetization – along particular crystallographic directions. In contrast to uniaxial crystals, which have a single easy axis, cubic systems can exhibit multiple equivalent easy directions, depending on the signs and magnitudes of K_{c1} and K_{c2} .

Shape anisotropy

Shape anisotropy originates from magnetostatic interactions: the geometry of a magnetic body influences the distribution of magnetic charges (poles) on its surfaces, thereby creating an internal demagnetizing field [87, 95]. In essence, any geometry – whether an elongated nanowire, a thin film, or a bulk ellipsoid – has different *demagnetization factors* (N_x, N_y, N_z) along its principal axes (more in Sec. 2.8). The magnetization \mathbf{M} thus adopts an orientation that minimizes the total magnetic energy, often along the direction of the smallest demagnetization factor. For example, in thin films and nanowires, the magnetization is typically parallel to the long axis, thus reducing the demagnetizing field. Such geometry-induced anisotropy becomes more pronounced at the nanoscale, where the high surface-to-volume ratio enhances the influence of surface magnetic poles.

Stress-induced anisotropy

Stress-induced anisotropy arises from the inverse magnetostrictive effect (also known as inverse magnetostriction or the Villari effect), where mechanical strain influences the orientation of magnetization [84]. When a material is subjected to stress, the magnetization tends to align along directions that minimize the magnetoelastic energy – typically those associated with either tensile or compressive strain. The magnetic strain energy can be expressed as

$$E_{\text{mag-str}} = \frac{3}{2} \Lambda \sigma \sin^2 \theta, \quad (2.22)$$

where Λ is the magnetostriction constant, σ is the applied stress, and θ is the angle between the magnetization and the direction of the applied stress [85]. This type of anisotropy is especially important in thin films and nanostructures, where stresses from the substrate or fabrication process can strongly affect the magnetic properties.

2.8 Magnetostatics and demagnetizing fields

Magnetostatics is the branch of classical electromagnetism that deals with magnetic fields in systems where both currents and fields are constant in time. In this regime, magnetic fields arise from stationary currents or static distributions of magnetic dipoles (magnetization). The governing principles start from Maxwell's equations, especially Gauss's law for magnetism, which states that the net magnetic flux through any closed surface must be zero. This condition underlies the distribution of magnetic flux lines in static field configurations.

The *magnetostatic approximation* is also widely used and important framework in magnonics. Certain components of the internal magnetic field can evolve on much slower timescales (thus remaining quasi-static), when compared to the rapid precessional motion of the spins. As a result, calculations often use magnetostatic boundary conditions and field distributions to simplify the analysis of spin-wave modes and their interactions – more in Sec. 3.2.

Gauss's law for magnetism

As noted above, Gauss's law states that the net magnetic flux through any closed surface is zero, which means that magnetic field lines do not originate from or terminate at any point, unlike electric field lines, which begin and end on charges. This law reflects the fact that there are no magnetic monopoles and is expressed mathematically as

$$\nabla \cdot \mathbf{B} = 0. \quad (2.23)$$

This equation shows that the divergence of the magnetic flux density is always zero, meaning magnetic field lines form closed loops [46]. In integral form, Gauss's law for magnetism states

$$\oint_{\partial V} \mathbf{B} \cdot d\mathbf{A} = 0, \quad (2.24)$$

where the surface integral is taken over the closed surface ∂V , and $d\mathbf{A}$ is the infinitesimal area element on the surface.

Demagnetizing field and demagnetizing tensor

In addition to externally applied fields, magnetic materials generate their own *demagnetizing field* \mathbf{H}_d . This field arises from surface (and sometimes interface) magnetic charges that appear when the magnetization \mathbf{M} is non-uniform or terminates at a boundary. On a microscopic level, these so-called magnetic poles create stray fields that oppose the internal magnetization. The net effect is a reduction of the internal magnetic field – hence the term “demagnetizing field.” In many theoretical treatments, it is expressed in a linearized form:

$$\mathbf{H}_d = -\bar{\bar{N}}\mathbf{M}, \quad (2.25)$$

where $\bar{\bar{N}}$ is the demagnetizing tensor, a real symmetric 3×3 matrix whose elements depend solely on the sample's geometry and orientation, assuming uniform magnetization. For special shapes with high symmetry, such as ellipsoids, the magnetization can be assumed to be uniform at equilibrium, allowing an analytical derivation of the tensor components. In this case, one can define the principal axes x, y, z along the three major directions of an ellipsoid, making $\bar{\bar{N}}$ diagonal:

$$\bar{\bar{N}} = \begin{pmatrix} N_x & 0 & 0 \\ 0 & N_y & 0 \\ 0 & 0 & N_z \end{pmatrix}, \quad \text{with } N_x + N_y + N_z = 1. \quad (2.26)$$

Each diagonal component N_i ($i = x, y, z$) is the demagnetizing factor for magnetization aligned along the i -th principal axis, and these factors sum to unity for ellipsoids [95, 96]. Often, a simplified scalar form of Eq. 2.25 is used:

$$\mathbf{H}_d = -N\mathbf{M}, \quad (2.27)$$

but this holds strictly for geometries where the magnetization is uniform and the shape is ellipsoidal, or in one-dimensional approximations (e.g., infinite cylinders). Non-ellipsoidal shapes (like rectangular prisms) introduce inhomogeneous internal fields that invalidate a simple uniform N factor, though approximate formulas or numerical methods can still be used.

Demagnetizing factors in standard shapes

- **Ellipsoids:** In an ellipsoid, each principal axis i has a corresponding demagnetization factor N_i , satisfying the condition $N_x + N_y + N_z = 1$. For a prolate spheroid (needle-like shape), the demagnetization factor along the elongated axis (e.g., N_z) is much smaller than those in the transverse directions (N_x and N_y). In contrast, for an oblate spheroid (disc-like shape), the in-plane demagnetization factors (e.g., N_x, N_y) are small, while the factor perpendicular to the plane (N_z) becomes large.
- **Spheres:** Due to the perfect symmetry of a shape, the demagnetization factors are equal along all principal directions: $N_x = N_y = N_z = 1/3$. As a result, the magnetization experiences the same demagnetizing effect regardless of its orientation.
- **Cylinders (long rods):** An extremely elongated cylinder aligned along the z -axis has $N_z \approx 0$, while $N_x + N_y \approx 1$, indicating a negligible demagnetizing field along the length of the rod. As a result, the magnetization tends to align with the long axis in order to minimize the magnetostatic (demagnetizing) energy.
- **Thin films:** For a thin film with negligible thickness along the z -direction, the demagnetization factor satisfies $N_z \approx 1$, while $N_x \approx N_y \approx 0$. This results in a strong demagnetizing field normal to the film plane, effectively confining the magnetization to lie in-plane unless a sufficiently large external field is applied perpendicular to the surface.

Why Ellipsoids? Ellipsoids, of which spheres, rods, and discs are special cases, are convenient because a uniform magnetization \mathbf{M} mathematically satisfies Maxwell's equations within such a shape. For more complex geometries (e.g., rectangular prisms, polycrystals with irregular boundaries, or multilayer thin-film stacks), the demagnetization tensor $\bar{\bar{N}}$ can only be estimated or computed by numerical methods (see Ch. 4).

The chapter has provided a historical perspective on the development of magnetism and presented the basic theoretical concepts of the field, starting with the microscopic origins of magnetic moments. Various types of magnetic order have been reviewed, followed by a discussion of magnetic domains and domain walls. In exploring these energetic contributions, this chapter has considered both discrete, atomic-level perspectives on spin interactions as well as the classical continuum framework used to describe magnetization behavior in extended media.

Building on these foundations, the next chapter addresses *magnetization dynamics*, moving from static and quasi-static domain configurations to time-dependent processes occurring on micro- and nanoscales. It employs a continuum formulation of the Gibbs free energy, which in our investigations includes exchange, anisotropy, and magnetostatic contributions, to model spin-wave excitations and support the description of my micromagnetic simulations. This approach bridges the discrete quantum origins of magnetism with classical field-based descriptions, allowing a detailed analysis of magnetization dynamics.

Chapter 3

Micromagnetism

Micromagnetism is a theoretical framework that describes magnetism at the continuum level, linking the atomic-scale interactions with macroscopic magnetic behavior [88]. This approach goes beyond traditional “classical models” of magnetism, which often treat a magnetic medium either as a single, uniform macrospin or rely on bulk-averaged properties without capturing spatial variations. In contrast, micromagnetism uses a continuum description in which the magnetization $\mathbf{M}(\mathbf{r})$ is treated as a smoothly varying vector field throughout the material. This refinement makes it possible to analyze magnetic structures and phenomena on the submicrometer or nanometer length scale – much smaller than what can be handled by simplistic approaches. It also avoids the impracticality of full atomic or quantum mechanical simulations, which require tracking the states and interactions of an astronomically large number of individual spins. As a result, micromagnetism provides a powerful framework for studying domain-wall motion, spin-wave excitations, topologically protected spin textures, and many other effects arising from the interplay of exchange, anisotropy, and magnetostatic energies. — The primary objective of micromagnetism is to determine both the equilibrium configuration and the dynamic behavior of the magnetization vector by minimizing the total free energy of a system. This energy includes several key contributions: exchange interactions, magnetostatic (dipolar) interactions, magnetocrystalline anisotropy, the Zeeman energy due to external magnetic fields, and, in some cases, additional effects such as Dzyaloshinskii–Moriya interactions (DMI) or thermal fluctuations. The interplay among these energy terms governs the resulting magnetic structure and its evolution over time.

This chapter outlines the fundamentals of micromagnetic theory, beginning with the continuum formulation of the Gibbs free energy and its constituent energy terms. It then introduces the dynamics of magnetization as described by the LLG equation and examines how these principles underpin spin-wave propagation and its manipulation. This theoretical framework is essential for understanding modern applications in spintronics and magnonic crystals, where precise control of nanoscale magnetization is critical to technological advancement. In this thesis, micromagnetic simulations serve as the primary tool for investigating advanced ferromagnetic systems and for analyzing how various energy contributions influence both their static configurations and dynamic behavior.

3.1 Gibbs free energy

The Gibbs free energy represents the total energy of a magnetic system in the presence of an external magnetic field and serves as the central quantity in micromagnetic theory for determining stable magnetic configurations [88, 95]. As mentioned above, the magnetization \mathbf{M} is treated as a continuous field that varies spatially and evolves to minimize the total energy. The interplay between competing energy contributions determines whether the static magnetization aligns uniformly, forms complex domain patterns, or gives rise to more exotic textures [87].

The total Gibbs free energy, G , of a magnetic system is generally expressed as the sum of several contributions, the most prominent of which are:

$$G = E_{\text{exchange}} + E_{\text{dipolar}} + E_{\text{anisotropy}} + E_{\text{Zeeman}} + E_{\text{DMI}} + \dots, \quad (3.1)$$

where each term corresponds to a distinct physical interaction that influences the magnetization dynamics and equilibrium state [73, 88]. Determining the stable magnetic configuration requires minimizing G while accounting for the material's geometry and any applied external fields.

The following subsections systematically describe the individual energy terms from Eq. 3.1 most relevant to my research. Each of them is important in determining the magnetization distribution and its time-evolution. Moreover, understanding these contributions allows the interpretation of the magnetic phenomena observed in micromagnetic simulations and in real materials.

3.1.1 Exchange interactions

The exchange interaction in magnetically ordered materials reflects a fundamental tendency for adjacent spins to align. In a discrete, atomic-level picture, this behavior can be captured by the Heisenberg Hamiltonian (Eq. 2.14) introduced in Sec. 2.5. There, the energy increases when neighboring spins deviate from parallel alignment, reflecting the quantum-mechanical origin of the interaction.

For macroscopic or mesoscopic descriptions, where the atomic lattice is not resolved, the spins are replaced by a smoothly varying magnetization field $\mathbf{M}(\mathbf{r})$. Physically, large spin–spin misalignments in the discrete model correspond to rapid spatial changes of \mathbf{M} in the continuum model. By adapting the discrete Heisenberg energy to a spatially averaged description, one can obtain the exchange energy term in the continuum model:

$$E_{\text{exchange}} = A_{\text{ex}} \int_V \left[(\nabla m_x)^2 + (\nabla m_y)^2 + (\nabla m_z)^2 \right] dV, \quad (3.2)$$

where m_x, m_y, m_z are the components of the normalized magnetization $\mathbf{m} = \mathbf{M}/M_s$. In the discrete model (Eq. 2.14), J describes the exchange coupling between spins at sites i and j . When transitioning to a continuum description, the sum over discrete sites becomes an integral, and spin dot products are replaced by spatial gradients of the magnetization field. Consequently,

A_{ex} contains the net effect of all the J terms and acts as the effective coupling constant in the continuum limit. Conceptually, it encodes the strength of the interaction between infinitesimal volume elements, just as J does for spins in the discrete lattice (see Eq. 2.14).

This formulation shows that any spatial variation in the magnetization profile will increase the total exchange energy. Therefore, in the absence of other competing effects (e.g., anisotropy or dipolar fields), the exchange interaction causes the magnetization to remain as uniform as possible throughout the material [87, 88]. Mathematically, the gradient terms $(\nabla m_i)^2$ measure the “strain” or local deviation from a perfectly parallel spin configuration. The integral in Eq. 3.2 sums these deviations over the entire volume V , penalizing nonuniform orientations. In the total Gibbs free energy, this contribution serves as a local force favoring smooth magnetization textures and suppressing abrupt changes.

The exchange stiffness constant A_{ex} measures the intensity of the exchange interaction in a magnetic material. The larger A_{ex} the stronger the preference for uniformly aligned spins, while a smaller value indicates that other energies (magnetostatic or anisotropy) can more easily induce non-uniform magnetization. A very useful parameter related to A_{ex} is the *exchange length* ℓ_{ex} , defined as

$$\ell_{\text{ex}} = \sqrt{\frac{2A_{\text{ex}}}{\mu_0 M_s^2}}. \quad (3.3)$$

Physically, ℓ_{ex} sets the characteristic distance over which the exchange interaction dictates the spin orientation. If a magnetic feature (e.g., a domain wall, a vortex core, or a spin-wave wavelength) is smaller than ℓ_{ex} , the exchange energy dominates and effectively “overrides” the competing magnetostatic energy, forcing the spins to align uniformly. Thus, on length scales larger than ℓ_{ex} , magnetostatic fields (as well as anisotropy and other long-range interactions) become increasingly important, potentially allowing more variation in the magnetization structure.

Thus, ℓ_{ex} can be viewed as the distance at which exchange determines spin orientation relative to magnetostatic effects, making it an important parameter in the design and understanding of nanoscale magnetic systems. For example, the exchange interaction resists abrupt changes in magnetization direction between magnetic domains, leading to the formation of a finite width domain wall (see Sec. 2.6). Similarly, in systems with noncollinear magnetization textures, such as spin spirals or skyrmions, the exchange interaction stabilizes them by moderating local variations in spin orientation [87].

3.1.2 Dipolar interactions

Dipolar (magnetostatic) interactions are a significant component of the total Gibbs free energy in micromagnetic systems. Unlike exchange interactions, which act mainly between neighboring spins, dipolar interactions extend over large distances and arise from the fact that each magnetic dipole creates a stray field that affects other dipoles [73, 87, 97].

From a microscopic perspective, a single magnetic dipole moment \mathbf{m} generates a magnetic field that typically decays as $1/r^3$. When two dipoles, \mathbf{m}_1 and \mathbf{m}_2 , are separated by a vector \mathbf{r} of magnitude $r = |\mathbf{r}|$, the dipolar interaction energy between them is given by

$$E_{\mathbf{m}_1, \mathbf{m}_2} = \frac{\mu_0}{4\pi r^3} \left[\mathbf{m}_1 \cdot \mathbf{m}_2 - 3 (\mathbf{m}_1 \cdot \hat{\mathbf{r}}) (\mathbf{m}_2 \cdot \hat{\mathbf{r}}) \right], \quad (3.4)$$

where $\hat{\mathbf{r}} = \mathbf{r}/r$ is the unit vector pointing from one dipole to the other. This energy depends not only on the distance between the dipoles, but also on their relative orientations, reflecting the long-range and anisotropic nature of dipolar interactions.

In the macroscopic (continuum) approach, the demagnetizing field $\mathbf{H}_d(\mathbf{r})$ can be derived by solving Maxwell's equations for magnetostatics. In particular, Gauss's law 2.23, discussed in Sec. 2.8, provides the foundation for this derivation and leads to

$$\nabla \times \mathbf{H}_d = \mathbf{0}, \quad \nabla \cdot \mathbf{B} = 0, \quad \mathbf{B} = \mu_0 (\mathbf{H}_d + \mathbf{M}). \quad (3.5)$$

From these relations, the magnetostatic potential $\varphi(\mathbf{r})$ can be defined such that

$$\mathbf{H}_d(\mathbf{r}) = -\nabla \varphi(\mathbf{r}), \quad (3.6)$$

and

$$\nabla^2 \varphi(\mathbf{r}) = -\nabla \cdot \mathbf{M}(\mathbf{r}). \quad (3.7)$$

Equations 3.6–3.7 represent a general formulation of the demagnetizing field derived from the magnetostatic potential, in contrast to the specific tensor form introduced in Sec. 2.8. As described there, for certain geometries such as ellipsoids with uniform magnetization, solving the magnetostatic boundary-value problem for $\varphi(\mathbf{r})$ yields a constant internal field proportional to $-\mathbf{M}$. In these cases, the gradient of the scalar potential, $\nabla \varphi$, remains uniform throughout the sample, and the demagnetizing factors N_x, N_y, N_z appear as the diagonal elements of the demagnetizing tensor $\overline{\overline{N}}$ (see Eq. 2.26). The negative sign in Eq. 3.6 is often chosen by convention.

In the magnetostatic formulation, it is convenient to introduce the concept of hypothetical magnetic charges. These arise mathematically from the distribution of magnetization in a material and can be categorized as volume or surface types [95]. The volume magnetic charge density is defined by

$$\rho_m(\mathbf{r}) = -\nabla \cdot \mathbf{M}(\mathbf{r}), \quad (3.8)$$

while the surface magnetic charge density is

$$\sigma_m(\mathbf{r}) = \mathbf{M}(\mathbf{r}) \cdot \hat{\mathbf{n}}, \quad (3.9)$$

where $\hat{\mathbf{n}}$ is the outward unit normal vector at the surface of the magnetic body. Although these quantities do not represent actual physical charges, they provide a convenient way to visualize the sources of magnetostatic potential and field within a material (especially where $\nabla \cdot \mathbf{M} \neq 0$).

From the perspective of magnetic charge densities, the magnetic scalar potential at a point \mathbf{r} in space can be expressed as the sum of the contributions from both volume and surface charge densities [95]:

$$\varphi(\mathbf{r}) = \frac{1}{4\pi} \int_V \frac{\rho_m(\mathbf{r}')}{|\mathbf{r} - \mathbf{r}'|} dV' + \frac{1}{4\pi} \int_S \frac{\sigma_m(\mathbf{r}')}{|\mathbf{r} - \mathbf{r}'|} dS'. \quad (3.10)$$

The integrals run over the volume V and the surface S of a magnetic body. By treating variations and discontinuities of the magnetization $\mathbf{M}(\mathbf{r})$ as sources of a scalar potential, the magnetostatic boundary-value problem can be formulated and solved more systematically.

Once $\mathbf{H}_d(\mathbf{r})$ is known (from substituting Eq. 3.10 to Eq. 3.6), the magnetostatic/dipolar energy (generalized form of Eq. 3.4) can be written as

$$E_{\text{dipolar}} = \frac{\mu_0}{2} \int_V \mathbf{H}_d(\mathbf{r}) \cdot \mathbf{M}(\mathbf{r}) dV, \quad (3.11)$$

where the factor of $1/2$ prevents double-counting of dipole–dipole interactions [73, 95, 98]. Physically, this energy penalizes configurations that produce large stray fields outside the sample and thus favors magnetization arrangements that minimize surface poles. This means that the demagnetizing field is strongly dependent on the magnetization distribution, making the magnetostatic energy particularly sensitive to the shape and size of the sample.

In micromagnetic simulations, the computation of $\mathbf{H}_d(\mathbf{r})$ is often the most challenging step, since it involves solving the Poisson-like boundary-value problem for the magnetostatic potential (more in Sec. 4.1.3). Nevertheless, understanding how the demagnetizing field emerges from the magnetization distribution is crucial for accurately modeling domain structures, spin-wave excitations, and other magnetic phenomena that rely on long-range dipolar interactions.

3.1.3 Anisotropic contributions

Magnetic anisotropies (introduced in Ch. 2, Sec. 2.7), play a fundamental role in shaping the magnetic behavior of materials. In micromagnetism, anisotropy energies interact and compete with exchange and dipolar contributions as part of the total Gibbs free energy (Eq. 3.1).

As described earlier, (magneto)crystalline anisotropy arises from SOC, causing the magnetization to align preferentially along certain crystallographic axes (hence, called easy axes). Within a micromagnetic model, this anisotropy term serves as a local energy well, that can stabilize magnetic configurations near an easy axis, thereby influencing the formation and evolution of magnetic domains [95].

Shape anisotropy, on the other hand, is a purely magnetostatic effect that depends on the geometry of the sample. As discussed in detail in Sec. 2.7, it arises from the demagnetizing field generated by surface poles whenever the magnetization distribution meets the material boundary. This is particularly relevant at the nanoscale, where large surface-to-volume ratios amplify the role of magnetostatic interactions. Thus, shape anisotropy is inherently contained in the dipole energy term of the micromagnetic free energy.

In summary, crystalline anisotropy tends to align the magnetization along specific crystallographic axes, while shape anisotropy favors alignment along directions dictated by the sample geometry. The interplay between these anisotropies – along with exchange and dipolar interactions – governs the formation of complex domain patterns and magnetization configurations [73].

3.1.4 Zeeman energy

The interaction between magnetization and an external magnetic field is described by the Zeeman energy, which originates from the Zeeman effect – first observed by Pieter Zeeman in 1896 [99].

This energy term, E_{Zeeman} , describes how an applied magnetic field \mathbf{H}_0 tends to align the magnetization vector $\mathbf{M}(\mathbf{r})$ along its direction [73, 95], and is given by

$$E_{\text{Zeeman}} = -\mu_0 \int_V \mathbf{M}(\mathbf{r}) \cdot \mathbf{H}_0 dV. \quad (3.12)$$

The negative sign and the dot product indicate that the energy is minimized when \mathbf{M} and \mathbf{H}_0 are aligned – that is, when the magnetization points in the direction of the applied field.

In magnetic systems, the Zeeman energy serves as a driving force that promotes full alignment of the magnetization with the external field. However, exchange interactions, magnetic anisotropies, and dipolar effects counteract this tendency – particularly in complex geometries and for field strengths below the saturation magnetization M_s [87].

The Zeeman energy governs not only static magnetization configurations but also plays a key role in magnetization dynamics, particularly under time-dependent applied fields. The LLG equation, discussed in the following sections, incorporates the Zeeman term as an effective torque that drives the magnetization toward alignment with the external field. The rate of this alignment depends on the intrinsic damping of the system and the influence of competing interactions.

3.1.5 Dzyaloshinskii–Moriya interactions

DMI is an antisymmetric exchange interaction that is significant in systems with broken inversion symmetry, either in the crystal lattice (bulk DMI) or at interfaces between materials (interfacial DMI). It promotes noncollinear spin configurations, favoring chiral magnetic textures such as spin spirals, domain walls with fixed chirality, and skyrmions.

In the context of the total Gibbs free energy, the DMI adds a new term that competes with the symmetric exchange interaction, which favors parallel or antiparallel alignment of spins, as explained in Sec. 3.1.1. The Dzyaloshinskii–Moriya energy is defined as

$$E_{\text{DMI}} = D \int_V \mathbf{M}(\mathbf{r}) \cdot [\nabla \times \mathbf{M}(\mathbf{r})] dV, \quad (3.13)$$

where D is the DMI constant that quantifies the strength of the interaction [73, 100]. The cross product term introduces a preference for twisted spin configurations by favoring spins that rotate continuously rather than uniformly aligned. DMI also modifies the structure of domain walls by

imposing a fixed chirality, leading to Néel-type domain walls instead of Bloch walls in certain systems [101].

3.1.6 Effective field

To describe the magnetization behavior in micromagnetic models and simulations, it is necessary to calculate an effective magnetic field \mathbf{H}_{eff} . This effective field is a major component of the LLG equation, as it captures the cumulative influence of all energy contributions at each point within the system. It thus determines how the magnetization evolves under internal forces and external perturbations [102], and can be derived directly from the Gibbs free energy:

$$\mathbf{H}_{\text{eff}} = -\frac{1}{\mu_0} \frac{\delta G}{\delta \mathbf{M}}. \quad (3.14)$$

As mentioned above, at equilibrium the magnetization is aligned with this field, minimizing the total energy of the system. However, when perturbed by an external magnetic field, thermal fluctuations, or other stimuli, the magnetization starts to precess around \mathbf{H}_{eff} , leading to dynamic phenomena such as spin-wave propagation or magnetization reversal [73, 87].

In short, the exchange energy promotes uniformity, anisotropies favor specific magnetization orientations, and the magnetostatic interaction creates long-range effects that lead to domain formation. The Zeeman energy, if present, adds a directional force from external fields, while the DMI introduces chiral structures into the system [95]. All of this is captured in the effective field, which serves as the main parameter in the LLG equation describing the magnetization dynamics.

The energy terms described in this section cover the primary contributions typically addressed in micromagnetism, but it is important to recognize other interactions that exist but are beyond the scope of this thesis. For example, in systems where indirect exchange coupling occurs through conduction electrons (e.g., magnetic multilayers), the Ruderman–Kittel–Kasuya–Yosida (RKKY) energy term should be included in the analysis [103–108]. This interaction can induce the spatially-variable coupling between ferromagnetic or antiferromagnetic layers, depending on the distance between them. Other effects, such as thermal fluctuations or relativistic corrections like magnetoelectric coupling, can also influence the total energy in certain cases.

3.2 Magnetization dynamics and spin waves

The static configuration of the magnetization, obtained by minimizing the total Gibbs free energy, is only one aspect of magnetic systems. In many practical scenarios, magnetic materials experience external stimuli – such as applied magnetic fields, spin-polarized currents, or thermal fluctuations – that perturb them away from energetic equilibrium. Even the magnetization relaxation is a dynamic process. Consequently, the magnetization vector $\mathbf{M}(\mathbf{r}, t)$ typically evolves with time under the influence of exchange, magnetostatic, anisotropy, and other energy contributions.

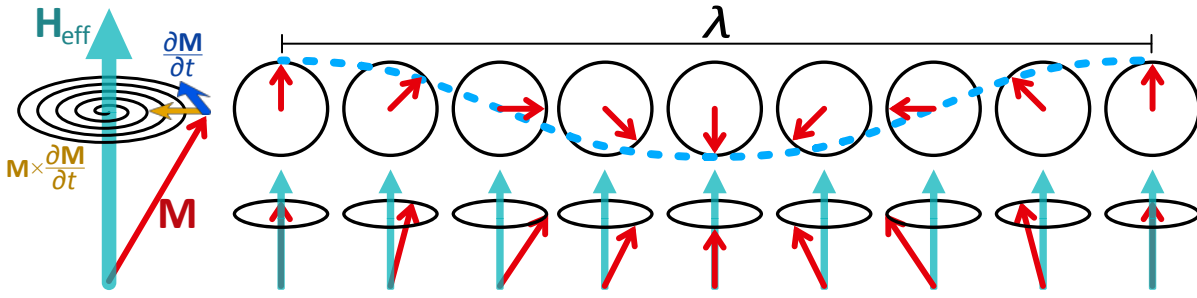


Figure 3.1 Schematic representation of a magnon, illustrating the precession of the magnetization vector \mathbf{M} around the effective magnetic field \mathbf{H}_{eff} . On the left, the precession components are shown with Gilbert damping ($\mathbf{M} \times \partial \mathbf{M} / \partial t$), causing the magnetization to gradually spiral toward equilibrium. On the right are time-frames for a complete spin-wave precession over a wavelength λ , capturing its oscillatory nature.

Spin waves are collective excitations involving spatially and temporally correlated precessions of magnetic moments throughout the material. Contrary to a common misconception, a single magnetic moment undergoing precessional motion around an effective field is not itself a spin wave – this scenario simply reflects the gyromagnetic precession of a localized spin. Classically, a spin wave can be understood as a propagating disturbance in the local magnetization vectors, characterized by a wavelength λ and frequency ω . From a quantum-mechanical perspective, these wave-like excitations are quantized into particles known as *magnons* – the spin-wave analogues of photons in electromagnetic waves or phonons in lattice vibrations [5, 109]. Figure 3.1 illustrates this concept: each magnetic moment precesses slightly out of phase with its neighbors, forming a collective oscillatory pattern. A single magnon corresponds to one quantum of spin-wave energy.

As mentioned above, in micromagnetism the time evolution of $\mathbf{M}(\mathbf{r}, t)$ results from its precession around an effective magnetic field \mathbf{H}_{eff} . When the magnetization is perturbed – for example, by a small thermal fluctuation – it does not immediately return to equilibrium. Instead, it precesses around \mathbf{H}_{eff} , with the possibility of exciting spin waves if the disturbance has spatial structure or if the system couples to neighboring spins in a coherent manner. Once excited, these spin waves carry both angular momentum and energy through the material.

The foundation of magnetization dynamics and the LLG equation lies in the *gyromagnetic precession* proposed by Joseph Larmor [110], which describes how a magnetic moment precesses around an external magnetic field.

3.2.1 Gyromagnetic (Larmor) precession

Gyromagnetic precession, also known as Larmor precession, is the fundamental motion that determines the dynamic properties of magnetization in response to an external magnetic field. When \mathbf{M} is displaced from its equilibrium orientation, it experiences a torque that causes it to precess around the direction of \mathbf{H}_{eff} . This precession is at the heart of many dynamic magnetic phenomena, including spin-wave generation.

The gyromagnetic ratio is defined as the proportionality constant between a magnetic moment and its angular momentum. For an isolated electron, this is a well-defined parameter, often denoted as γ_e . As introduced in Sec. 2.2, in free space $g_e \approx -2.0023$ ¹, yielding

$$\gamma_e = \frac{g_e \mu_B}{\hbar} \approx -1.76086 \times 10^{11} \text{ rad} \cdot \text{s}^{-1} \cdot \text{T}^{-1}. \quad (3.15)$$

In classical terms, when a magnetic moment (such as that of an electron) is placed in a static magnetic field, it experiences a torque that causes it to precess around the field direction at a characteristic angular frequency. This is known as the Larmor frequency ω_L , and is given by

$$\omega_L = |\gamma_e| \mu_0 H_0. \quad (3.16)$$

In other words, the magnetic moment precesses around the external field at a rate proportional to its magnitude. The Larmor frequency sets a fundamental timescale for magnetization dynamics in magnetic materials and underpins many spin-related phenomena.

In the micromagnetic approach, the gyromagnetic ratio is often treated as a material-dependent effective parameter. While the free-electron value, γ_e , serves as a useful reference, real magnetic materials may exhibit g -factors that deviate from exactly -2 due to crystal field effects and SOC. Therefore, in this work, the subscript is omitted, and the material-dependent gyromagnetic ratio is simply denoted as γ . This convention reflects the fact that while the concept of the gyromagnetic ratio remains consistent, its numerical value can vary across different materials.

It is also important to clarify the sign convention for γ . Although the gyromagnetic ratio of the electron is inherently negative – reflecting the negative g -factor and the antiparallel alignment between the magnetic moment and angular momentum – this thesis adopts the convention of treating γ as a positive quantity, $|\gamma|$, with an explicit negative sign included in equations where appropriate. This practice is common in the literature because it provides practical clarity: by making the sign of the precession term explicit, it removes ambiguity regarding the sign of γ , avoids non-intuitive negative magnitudes of physical variables (such as the frequency in Eq. 3.16), and reduces potential confusion when interpreting the direction of magnetization precession. This formulation preserves the correct physical behavior – namely, that the magnetization precesses in a direction consistent with the negative electron gyromagnetic ratio – while improving the consistency and readability of the mathematical expressions. It also facilitates comparison with numerical implementations and standard micromagnetic software packages, many of which adopt the same convention.

¹The electron g -factor has been determined to an extraordinary precision of fourteen decimal places by precise measurements of a single electron in a Penning trap [111]: $g_e/2 = -1.001\,159\,652\,180\,59(13)$. This experimental value is in excellent agreement with the theoretical predictions of quantum electrodynamics.

The relationship between the torque experienced by the magnetization and the rate of change of the magnetization vector [63] is given by

$$\frac{\partial \mathbf{M}}{\partial t} = -|\gamma|\mu_0 \mathbf{M} \times \mathbf{H}_{\text{eff}}. \quad (3.17)$$

This equation describes the gyromagnetic precession of the magnetization around the effective field, where the torque $\mathbf{M} \times \mathbf{H}_{\text{eff}}$ acts to change the orientation of the magnetization vector without affecting its magnitude.

Physically, gyromagnetic precession can be understood as a consequence of the conservation of angular momentum. The magnetization vector, associated with the collective magnetic moments of individual spins, responds to the external magnetic field by undergoing a precessional motion. This motion occurs because the torque generated by the cross product $\mathbf{M} \times \mathbf{H}_{\text{eff}}$ is perpendicular to both the magnetization vector and the applied field, creating a circular path for the magnetization (see Fig. 3.1). In the absence of damping (discussed in the next section), this motion would continue indefinitely at a constant rate. In real magnetic materials, however, damping mechanisms cause the magnetization to gradually align with the direction of the effective magnetic field, leading to the relaxation of the system to its equilibrium state.

3.2.2 Landau–Lifshitz–Gilbert equation

To fully capture the dynamics of magnetization $\mathbf{M}(\mathbf{r}, t)$ under the influence of internal and external magnetic fields, the classical description of gyromagnetic precession (Eq. 3.17) was extended by incorporating a damping term. This modification allows the magnetization to relax toward energetically favorable equilibrium states, rather than precessing indefinitely.

In 1935, Lev Landau and Evgeny Lifshitz introduced an equation that describes the precession of magnetization around an effective field, supplemented by a damping term to account for energy dissipation [62]. Thus, the Landau–Lifshitz (LL) equation was the first significant theoretical step in describing magnetization dynamics beyond simple precession. The phenomenological damping term was introduced in a form that depends on the instantaneous effective field. In International System of Units (SI) form, the original LL equation is defined as

$$\frac{\partial \mathbf{M}}{\partial t} = -|\gamma|\mu_0 (\mathbf{M} \times \mathbf{H}_{\text{eff}}) - \lambda [\mathbf{M} \times (\mathbf{M} \times \mathbf{H}_{\text{eff}})], \quad (3.18)$$

where λ is a phenomenological constant characteristic of a material. The first term on the right is responsible for the gyromagnetic precession around \mathbf{H}_{eff} (known from Eq. 3.17), while the second part models the dissipation. Although this framework was a major advance, its damping torque being proportional to \mathbf{H}_{eff} led to unphysical behavior when the field was very large.

About 20 years later (in unpublished work from 1955, and made widely known in 2004 [63]), Thomas Gilbert refined this formalism by proposing that the damping should be proportional to the time derivative of \mathbf{M} , rather than to the instantaneous magnetization itself. This proposition

has been accepted as more physically accurate, and is now referred to as the LLG equation:

$$\frac{\partial \mathbf{M}}{\partial t} = -|\gamma|\mu_0(\mathbf{M} \times \mathbf{H}_{\text{eff}}) + \frac{\alpha}{M_s} \left(\mathbf{M} \times \frac{\partial \mathbf{M}}{\partial t} \right), \quad (3.19)$$

where α is the dimensionless Gilbert damping constant of a material [63, 73, 95]. Gilbert's approach resolves certain inconsistencies in the original LL form and has become the standard in modern micromagnetism.

Building on the LLG equation, it is sometimes useful to explicitly isolate the time derivative $\partial \mathbf{M} / \partial t$ as a function of \mathbf{M} and \mathbf{H}_{eff} . This step is especially practical for numerical integration, where the magnetization dynamics must be cast into a standard first-order ordinary differential equation (ODE) form (more in Sec. 4.2). The explicit version of the LLG is:

$$\frac{\partial \mathbf{M}}{\partial t} = -\frac{|\gamma|\mu_0}{1+\alpha^2} (\mathbf{M} \times \mathbf{H}_{\text{eff}}) - \frac{\alpha|\gamma|\mu_0}{(1+\alpha^2)M_s} [\mathbf{M} \times (\mathbf{M} \times \mathbf{H}_{\text{eff}})]. \quad (3.20)$$

In this form, both the precession and damping terms are rescaled by $1/(1+\alpha^2)$, preserving the physics of the LLG equation but allowing a direct integration approach. The representations 3.18 and 3.20 are related by the following substitutions:

$$|\gamma| \rightarrow \frac{|\gamma|}{1+\alpha^2}, \quad \lambda \rightarrow \frac{\alpha|\gamma|\mu_0}{(1+\alpha^2)M_s}. \quad (3.21)$$

Microscopically, the damping term and the associated energy dissipation processes result primarily from:

- spin–lattice (magnon–phonon) interactions, where spin excitations exchange energy with lattice vibrations;
- spin–electron (magnon–electron) scattering, which can be enhanced by SOC;
- defects or impurities, acting as channels for energy relaxation via scattering.

The dimensionless parameter α thus reflects how effectively the magnetic system couples to its environment and loses energy during precession. Typical experimental values of α range from 10^{-4} to 10^{-1} , depending on material composition, spin–orbit strength, and temperature [73, 112].

3.2.2.1 Normalization

For numerical and analytical convenience, it is common to normalize the dynamic magnetization by M_s and measure time in units of $|\gamma\mu_0 M_s|^{-1}$. Dividing the Eq. 3.19 by $|\gamma|\mu_0 M_s^2$, yields

$$\frac{1}{|\gamma|\mu_0 M_s^2} \frac{\partial \mathbf{M}}{\partial t} = -\frac{1}{M_s^2} (\mathbf{M} \times \mathbf{H}_{\text{eff}}) + \frac{\alpha}{|\gamma|\mu_0 M_s^3} \left(\mathbf{M} \times \frac{\partial \mathbf{M}}{\partial t} \right), \quad (3.22)$$

The normalized quantities are now defined as

$$\mathbf{m} = \frac{\mathbf{M}}{M_s}, \quad \mathbf{h}_{\text{eff}} = \frac{\mathbf{H}_{\text{eff}}}{M_s}, \quad \tau = |\gamma|\mu_0 M_s t, \quad (3.23)$$

and by substituting them into Eq. 3.22, the following dimensionless form is obtained:

$$\frac{\partial \mathbf{m}}{\partial \tau} = -(\mathbf{m} \times \mathbf{h}_{\text{eff}}) + \alpha \left(\mathbf{m} \times \frac{\partial \mathbf{m}}{\partial \tau} \right). \quad (3.24)$$

Here, \mathbf{m} and \mathbf{h}_{eff} are dimensionless vectors, and τ is a dimensionless time variable that advances in units of one radian of precession per field of magnitude M_s . This form isolates α as the primary parameter controlling the relaxation rate. Equation 3.24 is also useful for simulations because, by working in normalized units, the algorithm deals with numerically stable quantities. The single dimensionless parameter α then determines how fast (or slow) the system relaxes to equilibrium.

The LLG equation is fundamental to the understanding of dynamic magnetic phenomena in a wide range of materials and applications. It underlies the study of FMR, domain wall motion, and the propagation of spin waves, all of which are critical for the development of modern magnetic technologies such as magnetic random-access memory (MRAM), spintronic devices, and magnonic crystals [5, 109].

3.2.2.2 Equilibrium state and linearization

Linearization is particularly useful for studying small-amplitude magnetization dynamics, such as spin waves. For minor deviations from equilibrium, the nonlinear terms in the governing equations can be neglected, allowing the system to be described by linear differential equations. This greatly simplifies the mathematical treatment and thus reduces the computational complexity in numerical simulations.

It is important to emphasize, that this technique is only valid around an equilibrium state, i.e. it assumes a magnetic system in which the magnetization $\mathbf{M}(\mathbf{r})$ is aligned with the effective magnetic field \mathbf{H}_{eff} . It can be expressed by the equilibrium magnetization configuration \mathbf{M}_0 , which satisfies

$$\mathbf{M}_0 \times \mathbf{H}_{\text{eff}}(\mathbf{M}_0) = \mathbf{0}, \quad (3.25)$$

where $\mathbf{H}_{\text{eff}}(\mathbf{M}_0)$ is the static, equilibrium part of the effective field.

Next, let $\delta \mathbf{M}(\mathbf{r})$ and $\delta \mathbf{H}_{\text{eff}}$ represent the small transverse deviation of the magnetization and the effective magnetic field, respectively. In this context, the following can be written:

$$\mathbf{M}(\mathbf{r}, t) = \mathbf{M}_0 + \delta \mathbf{M}(\mathbf{r}, t) \quad \Longleftrightarrow \quad |\delta \mathbf{M}| \ll |\mathbf{M}_0|, \quad (3.26)$$

$$\mathbf{H}_{\text{eff}}(\mathbf{r}, t) = \mathbf{H}_{\text{eff}}(\mathbf{M}_0) + \delta \mathbf{H}_{\text{eff}}(\mathbf{r}, t) \quad \Longleftrightarrow \quad |\delta \mathbf{H}_{\text{eff}}| \ll |\mathbf{H}_{\text{eff}}(\mathbf{M}_0)|. \quad (3.27)$$

The goal is to keep only first-order terms in $\delta\mathbf{M}$ and $\delta\mathbf{H}_{\text{eff}}$, discarding their products or higher powers. Substituting Eqs. 3.26 and 3.27 into Eq. 3.19 gives

$$\begin{aligned} \frac{\partial(\mathbf{M}_0 + \delta\mathbf{M})}{\partial t} = & -|\gamma|\mu_0 [(\mathbf{M}_0 + \delta\mathbf{M}) \times (\mathbf{H}_{\text{eff}}(\mathbf{M}_0) + \delta\mathbf{H}_{\text{eff}})] \\ & + \frac{\alpha}{M_s} \left[(\mathbf{M}_0 + \delta\mathbf{M}) \times \frac{\partial(\mathbf{M}_0 + \delta\mathbf{M})}{\partial t} \right]. \end{aligned} \quad (3.28)$$

Since the vector \mathbf{M}_0 is constant in time, $\partial\mathbf{M}_0/\partial t = 0$, and the term $\mathbf{M}_0 \times \mathbf{H}_{\text{eff}}(\mathbf{M}_0)$ vanishes due to equilibrium (Eq. 3.25). To eliminate second-order terms in small quantities, cross products such as $\delta\mathbf{M} \times \delta\mathbf{H}_{\text{eff}}$, and $(\delta\mathbf{M} \times \partial\delta\mathbf{M}/\partial t)$ can be neglected. Thus, the Eqs. 3.26 and 3.27 are concretized to

$$\mathbf{M}_0 + \delta\mathbf{M} \longrightarrow \mathbf{M}_0 + (\text{1st-order term } \delta\mathbf{M}), \quad (3.29)$$

$$\mathbf{H}_{\text{eff}}(\mathbf{M}_0) + \delta\mathbf{H}_{\text{eff}} \longrightarrow \mathbf{H}_{\text{eff}}(\mathbf{M}_0) + (\text{1st-order term } \delta\mathbf{H}_{\text{eff}}), \quad (3.30)$$

and the precessional term is simplified to

$$-|\gamma|\mu_0 [(\mathbf{M}_0 + \delta\mathbf{M}) \times (\mathbf{H}_{\text{eff}}(\mathbf{M}_0) + \delta\mathbf{H}_{\text{eff}})] \approx -|\gamma|\mu_0 (\mathbf{M}_0 \times \delta\mathbf{H}_{\text{eff}} + \delta\mathbf{M} \times \mathbf{H}_{\text{eff}}(\mathbf{M}_0)). \quad (3.31)$$

The damping term, in turn, yields

$$\frac{\alpha}{M_s} \left[(\mathbf{M}_0 + \delta\mathbf{M}) \times \frac{\partial(\mathbf{M}_0 + \delta\mathbf{M})}{\partial t} \right] \approx \frac{\alpha}{M_s} \left(\mathbf{M}_0 \times \frac{\partial\delta\mathbf{M}}{\partial t} \right). \quad (3.32)$$

Thus, collecting only the first-order terms of $\delta\mathbf{M}$ and $\delta\mathbf{H}_{\text{eff}}$ returns

$$\frac{\partial(\delta\mathbf{M})}{\partial t} = -|\gamma|\mu_0 (\mathbf{M}_0 \times \delta\mathbf{H}_{\text{eff}} + \delta\mathbf{M} \times \mathbf{H}_{\text{eff}}(\mathbf{M}_0)) + \frac{\alpha}{M_s} \left[\mathbf{M}_0 \times \frac{\partial(\delta\mathbf{M})}{\partial t} \right]. \quad (3.33)$$

In practical linearized treatments, $\delta\mathbf{H}_{\text{eff}}$ depends linearly on $\delta\mathbf{M}$. Symbolically:

$$\delta\mathbf{H}_{\text{eff}} \approx \hat{\Gamma} \delta\mathbf{M}, \quad (3.34)$$

where $\hat{\Gamma}$ is a suitable linear operator. Substituting Eq. 3.34 into Eq. 3.33 results in a linear partial differential equation for $\delta\mathbf{M}(\mathbf{r}, t)$:

$$\frac{\partial(\delta\mathbf{M})}{\partial t} = -|\gamma|\mu_0 [\mathbf{M}_0 \times (\hat{\Gamma} \delta\mathbf{M}) + \delta\mathbf{M} \times \mathbf{H}_{\text{eff}}(\mathbf{M}_0)] + \frac{\alpha}{M_s} \left[\mathbf{M}_0 \times \frac{\partial(\delta\mathbf{M})}{\partial t} \right], \quad (3.35)$$

which can be solved using standard techniques (Fourier transforms, eigenmode expansions, etc.), greatly simplifying the analysis of small-angle precession modes.

The linearization shows that small fluctuations behave as damped precessional modes around \mathbf{M}_0 . In spin-wave theory, these modes propagate with wavevectors determined by the system

geometry and the operator $\hat{\Gamma}$ (e.g., from exchange stiffness, anisotropy fields, or magnetostatic boundary conditions). In many small-amplitude oscillation analyses, it is also convenient to consider the dynamical component of Eq. 3.26 in the form of a monochromatic wave $e^{i\omega t}$:

$$\mathbf{M}(\mathbf{r}, t) = \mathbf{M}_0 + \delta\mathbf{M}(\mathbf{r})e^{i\omega t}, \quad (3.36)$$

where ω is the angular frequency of the oscillation. In particular, assume that the static applied magnetic field along \hat{z} dominates the effective field at equilibrium, such that $\mathbf{M}_0 \approx M_s \hat{z}$ and $\mathbf{H}_{\text{eff}}(\mathbf{M}_0) \approx H_0 \hat{z}$, with $\delta\mathbf{M}(\mathbf{r}) = (m_x, m_y, 0)$ representing small transverse components. Substituting this into the linearized LLG equation (3.33, neglecting the damping part), results in two coupled frequency-domain equations:

$$\begin{aligned} i\omega m_x &= |\gamma|\mu_0(H_0 m_y - M_s h_y), \\ i\omega m_y &= |\gamma|\mu_0(-H_0 m_x + M_s h_x). \end{aligned} \quad (3.37)$$

Here, h_x and h_y are small transverse components of an external excitation field. These linear equations capture the essential precessional spin-wave dynamics around the z -axis, ignoring dissipative effects [73, 113].

3.2.3 Ferromagnetic resonance and the Kittel formula

FMR is a fundamental phenomenon in which a coherently precessing magnetization in a ferromagnetic material absorbs electromagnetic radiation at a characteristic resonant frequency determined by the material's magnetic properties and the applied field. Resonant (coherent) precession arises from the dynamic response of the magnetization to an external radio-frequency (RF) magnetic field $\mathbf{h}_{\text{RF}}(t)$. The applied static magnetic field \mathbf{H}_0 sets the resonance condition, with the strongest excitation occurring when $\mathbf{h}_{\text{RF}}(t) \perp \mathbf{H}_0$. FMR provides a key method for probing internal fields, anisotropies, and damping in magnetic materials [85, 114].

A concise way to analyze FMR starts with the gyromagnetic precession (Eq. 3.17). At equilibrium, the magnetization \mathbf{M} is static and aligned with the effective field \mathbf{H}_{eff} . Small oscillations around this equilibrium are described by the linearized Eqs. 3.37, which provide the resonance condition – namely, the angular frequency ω_{FMR} when the mode is uniform. This is given by the well-known Kittel formula [114], expressed in SI units as

$$\omega_{\text{FMR}}^2 = |\gamma|^2 \mu_0^2 (H_0 + (N_y - N_z)M_{\text{eff}})(H_0 + (N_x - N_z)M_{\text{eff}}), \quad (3.38)$$

where H_0 is a magnetic field large enough to saturate the magnetization, and M_{eff} is an effective magnetization term that can include contributions from internal anisotropies. In simple cases without significant anisotropy, $M_{\text{eff}} \approx M_s$. The demagnetizing factors N_x, N_y, N_z introduced in Sec. 2.8 enable the calculation of FMR frequencies for various geometries directly from Eq. 3.38. Examples include:

- sphere ($N_x = N_y = N_z = 1/3$): $\omega_{\text{FMR}} = |\gamma|\mu_0 H_0$;
- thin film magnetized out-of-(xy)-plane ($N_x = N_y = 0, N_z = 1$): $\omega_{\text{FMR}} = |\gamma|\mu_0(H_0 - M_s)$;
- thin film magnetized in-(xy)-plane ($N_x = 1, N_y = N_z = 0$): $\omega_{\text{FMR}} = |\gamma|\mu_0\sqrt{H_0(H_0 - M_s)}$.

FMR measurements not only identify the resonant frequency, but also provide information about the linewidth or damping – indicators of energy losses due to spin–lattice relaxation and other dissipation channels. Consequently, FMR has become a standard technique in magnetic materials research, revealing intrinsic properties such as g -factors, anisotropy constants, and spin-pumping effects. In magnonics, FMR underpins the study of uniform precessional modes and serves as a foundation for understanding more complex spin-wave excitations.

3.2.4 Spin-wave spectra

In the magnetostatic limit, the spin-wave wavelength is much larger than the exchange length. When $\lambda \gg \ell_{\text{ex}}$, the exchange interaction can be neglected, and the spin-wave dynamics are dominated by dipolar (magnetostatic) interactions. In this regime, the resonance condition and dispersion relation can be derived by solving the linearized LL equation (Eq. 3.17) without the exchange term. This leads to the description of so-called *magnetostatic modes*.

If the magnetic medium is a bulk sample in which boundary effects can be neglected, the spin-wave frequency is given by [102]

$$\omega = |\gamma|\mu_0\sqrt{H_0(H_0 + M_s \sin^2 \theta_{\mathbf{k}})}, \quad (3.39)$$

where $\theta_{\mathbf{k}}$ is the angle between the magnetization direction and the spin-wave wavevector \mathbf{k} . The wavevector defines both the propagation direction and the spatial periodicity of the spin wave. In three dimensions, its components (k_x, k_y, k_z) represent the projections along the Cartesian axes, and its magnitude – commonly referred to as the wavenumber k – is given by $k = |\mathbf{k}| = \sqrt{k_x^2 + k_y^2 + k_z^2}$.

Notably, in Eq. 3.39, the spin-wave frequency depends solely on the direction of propagation, not on the magnitude of the wavevector. The frequency is maximal when the spin wave propagates perpendicular to the magnetization direction and minimal when the propagation is parallel.

In a thin film, the magnetization dynamics are influenced by both exchange and dipolar (magnetostatic) interactions. The presence of surfaces at $z = 0$ and $z = d$ (for a film of thickness d extending in the xy -plane) introduces boundary conditions that constrain the behavior of the dynamic magnetization. This leads to a series of discrete thickness modes, referred to as perpendicular standing spin waves (PSSWs). Each mode is indexed by an integer n , which corresponds to the number of half-wavelengths that fit between the film surfaces [1, 5]:

$$k_{z,n} \approx \frac{n\pi}{d}, \quad (3.40)$$

where $k_{z,n}$ is the quantized wavevector component along the film thickness. The approximation symbol (\approx) indicates that corrections from finite interface effects – such as surface anisotropy – are neglected in this expression.

In the thin-film scenario, out-of-plane quantization is treated separately by discrete standing modes rather than a continuous wavevector component k_z . Therefore, in cases where the magnetization is assumed to be uniform across the film thickness (i.e., the fundamental thickness mode with $k_{z,0} = 0$), the wavenumber k refers to the magnitude of the in-plane wavevector, defined as $k = \sqrt{k_x^2 + k_y^2}$. The standing modes overlap with the in-plane propagation, resulting in a full 3D dispersion that depends on both the exchange stiffness and the dipolar interactions. At small wavevectors (long wavelength), dipolar interactions dominate, giving a nearly linear $\omega(k)$ relationship (see inset in Fig. 3.2). For larger k the exchange takes over, bending the dispersion into a quadratic form. This crossover between dipolar- and exchange-like regimes is a feature of thin-film spin waves (Fig. 3.2).

In addition to the thickness quantization, spin-wave dispersion is strongly affected by the orientation of the magnetization vector \mathbf{M} relative to the wavevector \mathbf{k} . Three standard configurations are often distinguished in thin films [113]:

1. **Damon–Eshbach (DE) geometry**, where the film is magnetized in-plane, and \mathbf{k} is perpendicular to \mathbf{M} , both confined to the film plane [115]. In the magnetostatic limit (i.e., at long wavelengths), these modes evolve into surface spin waves whose amplitudes are localized near the film boundaries. This localization can reduce scattering from the interior of the film, often resulting in lower damping for long-wavelength modes. Experiments have shown that the DE geometry often supports efficient spin-wave propagation [116, 117]. In practice, however, the range still depends mostly on material-specific damping (α), as well as on structural imperfections and surface roughness. In addition, the orthogonal arrangement of \mathbf{M} and \mathbf{k} facilitates stronger coupling to external RF fields, allowing more efficient excitation and detection of spin waves [118].
2. **Backward volume (BV) geometry**, where the film is magnetized in-plane and \mathbf{k} is parallel to \mathbf{M} . A characteristic feature of this configuration is that the group velocity can be opposite to the phase velocity – hence the name *backward volume wave*. As a result, increasing the wavenumber k can lead to a decrease in spin-wave frequency, a behavior linked to the magnetostatic boundary conditions for $\mathbf{M} \parallel \mathbf{k}$. The close alignment between the wavevector and magnetization also enhances the coupling of the spin precession ellipse to external fields, which facilitates nonlinear spin-wave phenomena such as three-magnon splitting. These effects are valuable for advanced signal processing, broad tunability of spin-wave spectra, and spin-wave comb generation [119, 120].
3. **Forward volume (FV) geometry**, where the magnetization is oriented perpendicular to the film plane (out-of-plane), while \mathbf{k} lies in-plane. In an ideal, uniformly magnetized film with \mathbf{M} out-of-plane, the dispersion is fully isotropic, which, combined with relatively high group velocities for moderate wavevectors, is a favorable scenario for magnonic

circuits [121]. The out-of-plane \mathbf{M} also allows greater control over perpendicular fields, which can be integrated with standard perpendicular magnetic anisotropy systems (such as CoFeB/MgO). Finally, the FV spin waves can interact with other quasiparticles (phonons, photons) across the (small) thickness of the film, offering the prospect of hybrid magnon–photon or magnon–phonon coupling [4, 122].

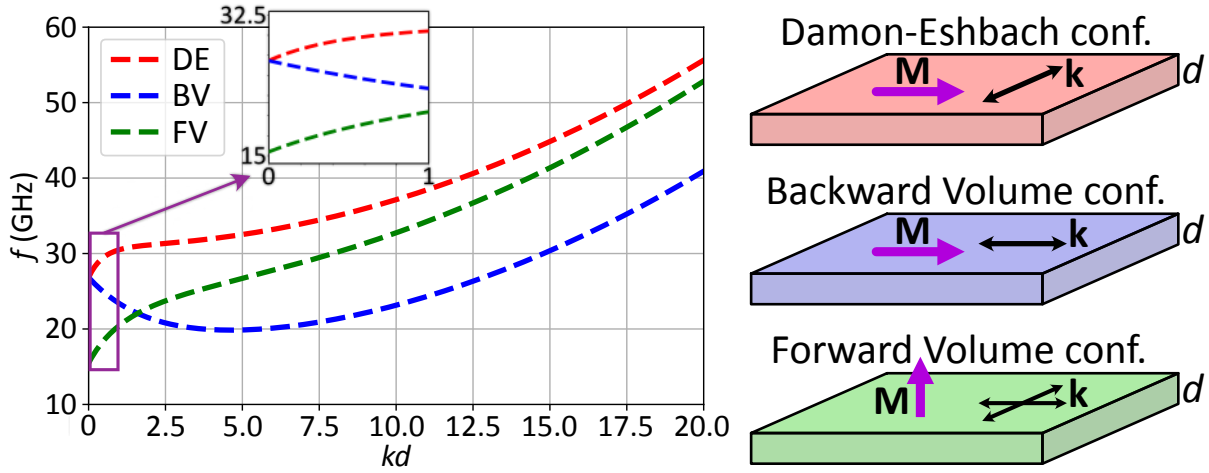


Figure 3.2 Spin-wave dispersion relations in the dipolar–exchange regime for thin films, shown for the three primary configurations, plotted as a function of the dimensionless parameter kd . The frequency f dependence on kd illustrates the transition from the dipolar-dominated linear regime at low wavevectors to the exchange-dominated quadratic regime at higher k values. The inset provides a magnified view of the magnetostatic regime, emphasizing the behavior of long-wavelength spin waves. On the right, schematic illustrations of the thin-film configurations show the orientations of the magnetization vector \mathbf{M} (magenta arrows) and wavevector \mathbf{k} (black arrows): DE with $\mathbf{k} \perp \mathbf{M}$, both in-plane; BV with $\mathbf{k} \parallel \mathbf{M}$, both in-plane; and FV with \mathbf{M} out-of-plane and \mathbf{k} in-plane. The dispersion curves were calculated using material parameters $M_s = 800$ kA/m, $A_{\text{ex}} = 8$ pJ/m, $d = 100$ nm, with external magnetic fields set to $H_0 = 0.5 M_s$ for the DE and BV configurations, and $H_0 = 1.5 M_s$ for the FV configuration.

The dominance of dipolar or exchange interactions in spin-wave dynamics depends on the spin-wave wavelength (λ), wavenumber ($k = 2\pi/\lambda$), and the material’s exchange length (ℓ_{ex} – see Eq. 3.3). The dipolar interaction dominates in the long-wavelength limit ($\lambda \gg \ell_{\text{ex}}$ or $k \ll 1/\ell_{\text{ex}}$). In this regime (i.e., for small k), spin-wave dynamics are dominated by magnetostatic interactions, resulting in a linear dispersion relation, $\omega(k) \propto k$. As the wavelength decreases and approaches the exchange length ($\lambda \lesssim \ell_{\text{ex}}$, or equivalently $k \gtrsim 1/\ell_{\text{ex}}$), the exchange interaction becomes significant. Under these conditions, the dispersion relation transitions to a quadratic form, $\omega(k) \propto k^2$. Exchange interactions stabilize magnetization at the nanoscale, which is critical for high-frequency spin waves. The reciprocal of the exchange length, often referred to as the *exchange wavenumber*, $k_{\text{ex}} = 1/\ell_{\text{ex}}$, provides a useful criterion for distinguishing between dipolar- and exchange-dominated regimes of spin-wave excitations. In typical ferromagnetic materials, ℓ_{ex} ranges from a few to several tens of nanometers, corresponding to k_{ex} on the order of 10^7 – 10^8 m $^{-1}$.

The crossover between the dipolar and exchange regimes, along with the discrete thickness modes, is critical in the design of spin-wave based devices. By adjusting film thickness, saturation magnetization, and applied field, one can tailor where this crossover occurs and which modes are most effectively excited.

3.2.4.1 Kalinikos–Slavin theory of spin waves in thin films

The Kalinikos–Slavin theory provides a well-known approximate analytical framework for describing spin-wave dispersion in uniformly magnetized thin ferromagnetic films [123]. It takes into account both dipolar and exchange interactions, as well as finite-thickness boundary effects. The spin-wave angular frequency ω depends on the in-plane wavevector magnitude k , the angle ϕ between \mathbf{k} and the magnetization direction \mathbf{M} , and the polar angle θ of \mathbf{M} relative to the film normal. It is expressed as

$$\omega(k, \phi, \theta) = |\gamma|\mu_0 \sqrt{\left(H_{\text{eff}} + M_s \ell_{\text{ex}}^2 k^2\right) \left(H_{\text{eff}} + M_s \ell_{\text{ex}}^2 k^2 + M_s F(k, \phi, \theta)\right)}, \quad (3.41)$$

where $F(k, \phi, \theta)$ is the dipolar interaction factor given by

$$F(k, \phi, \theta) = P(k) + \sin^2 \theta \left[1 - P(k)(1 + \cos^2 \phi) + \sin^2 \phi \frac{M_s(1 - e^{-2kd})}{4(H_0 + M_s \ell_{\text{ex}}^2 k^2)} \right], \quad (3.42)$$

and $P(k)$ is related to the surface conditions:

$$P(k) = 1 - \frac{1 - e^{-kd}}{kd}. \quad (3.43)$$

The exchange length ℓ_{ex} was defined in Eq. 3.3, while the term $M_s \ell_{\text{ex}}^2 k^2$ in Eq. 3.41 captures the exchange contribution, growing with k^2 and dominating at short wavelengths.

The Eq. 3.43 represents decoupled approximations for individual spin-wave modes quantized along the thickness of the film. In reality, solving the full spin-wave problem in a finite-thickness system leads to a set of matrix equations involving thickness quantization and potential coupling between higher-order modes [113, 123]. The formulas here assume each mode can be treated separately, which is valid when the mode–mode coupling is weak.

Kalinikos–Slavin theory applies over a wide range of angles for \mathbf{M} relative to \mathbf{k} . Three common special cases in thin films are, as described above, DE, BV, and FV geometries, each offering different dispersion characteristics [102].

DE configuration. Here, $\theta = 90^\circ$ corresponds to the in-plane magnetization, and $\phi = 90^\circ$ indicates that the wavevector is perpendicular to \mathbf{M} . Assuming that the static applied field H_0 dominates the internal fields, the effective field at equilibrium can be approximated as $H_{\text{eff}} \approx H_0$. In this case the dipolar interaction factor $F(k, 90^\circ, 90^\circ)$ simplifies to $M_s(1 - e^{-2kd})/4(H_0 + M_s \ell_{\text{ex}}^2 k^2)$. Substituting this expression into Eq. 3.41 yields the dispersion relation [115] for surface spin

waves:

$$\omega_{\text{DE}}(k) = |\gamma|\mu_0 \sqrt{\left(H_0 + M_s \ell_{\text{ex}}^2 k^2\right)^2 + \frac{M_s^2}{4} \left(1 - e^{-2kd}\right)}. \quad (3.44)$$

For large k (short wavelength), the dipolar part $(1 - e^{-2kd})$ saturates to 1, and exchange dominates:

$$\omega_{\text{DE}}(k \rightarrow \infty) = |\gamma|\mu_0 \sqrt{\left(H_0 + M_s \ell_{\text{ex}}^2 k^2\right)^2 + \frac{M_s^2}{4}}. \quad (3.45)$$

BV configuration. Here $\theta = 90^\circ$ (in-plane magnetization) but $\phi = 0^\circ$, meaning the wavevector is parallel to the magnetization direction ($\mathbf{k} \parallel \mathbf{M}$). Assuming $H_{\text{eff}} \approx H_0$ (same reasoning as in the DE case), the dipolar interaction factor becomes $F(k, 0^\circ, 90^\circ) = (1 - e^{-kd})/kd$. Substituting this into Eq. 3.41 yields

$$\omega_{\text{BV}}(k) = |\gamma|\mu_0 \sqrt{\left(H_0 + M_s \ell_{\text{ex}}^2 k^2\right) \left(H_0 + M_s \ell_{\text{ex}}^2 k^2 + M_s \frac{1 - e^{-kd}}{kd}\right)}. \quad (3.46)$$

As $k \rightarrow \infty$, the term $(1 - e^{-kd})/kd \rightarrow 0$ (see the proof in the gray box below), indicating that the dipolar interaction becomes negligible and the exchange interaction dominates the spin-wave behavior:

$$\omega_{\text{BV}}(k \rightarrow \infty) = |\gamma|\mu_0 \left(H_0 + M_s \ell_{\text{ex}}^2 k^2\right). \quad (3.47)$$

As mentioned earlier, BV modes often exhibit a backward dispersion (group velocity opposite to phase velocity) at lower k in the dipolar regime [113]. They also exhibit propagation anisotropy, but differ from DE in that $\mathbf{k} \parallel \mathbf{M}$ can result in a narrower angular bandwidth for low-damping propagation.

For all $k > 0$ and $d > 0$, the following inequality holds

$$0 \leq 1 - e^{-kd} \leq 1.$$

Dividing through by $kd > 0$ gives

$$0 \leq \frac{1 - e^{-kd}}{kd} \leq \frac{1}{kd}.$$

Since $\lim_{k \rightarrow \infty} 1/kd = 0$, the squeeze (sandwich) theorem [124] implies that

$$\lim_{k \rightarrow \infty} \frac{1 - e^{-kd}}{kd} = 0.$$

FV configuration. In the FV geometry, the magnetization is oriented out-of-plane ($\theta = 0^\circ$). In this case, the dipolar interaction factor $F(k, \phi, 0^\circ)$ becomes independent of the in-plane wavevector angle ϕ , and simplifies to $1 - (1 - e^{-kd})/kd$. As a result, the dispersion relation of this configuration is isotropic within the in-plane propagation directions (see Fig. 3.3b). Here, the effective magnetic field is typically approximated as $H_{\text{eff}} \approx H_0 - M_s$, accounting for the full demagnetizing field produced by the out-of-plane magnetization. Substituting this into Eq. 3.41

yields the corresponding dispersion relation:

$$\omega_{\text{FV}}(k) = |\gamma|\mu_0 \sqrt{\left(H_0 - M_s + M_s \ell_{\text{ex}}^2 k^2\right) \left(H_0 + M_s \ell_{\text{ex}}^2 k^2 - M_s \frac{1 - e^{-kd}}{kd}\right)}. \quad (3.48)$$

The finite-thickness factor $(1 - e^{-kd})/(kd)$ still governs the dipolar corrections, but at large k , where the exchange dominates, Eq. 3.48 is simplified to

$$\omega_{\text{FV}}(k \rightarrow \infty) = |\gamma|\mu_0 \sqrt{\left(H_0 - M_s + M_s \ell_{\text{ex}}^2 k^2\right) \left(H_0 + M_s \ell_{\text{ex}}^2 k^2\right)}. \quad (3.49)$$

When studying spin-wave propagation in thin ferromagnetic films, it is common to analyze *isofrequency contours* in the two-dimensional wavevector space (k_x, k_y) at a fixed spin-wave frequency f . Each contour represents all in-plane wavevector directions and magnitudes that satisfy the film's dispersion relation at a given frequency. They provide insight into the anisotropy of spin-wave propagation: circular contours imply isotropic behavior, while highly distorted contours indicate strong directional dependence – see Fig. 3.3.

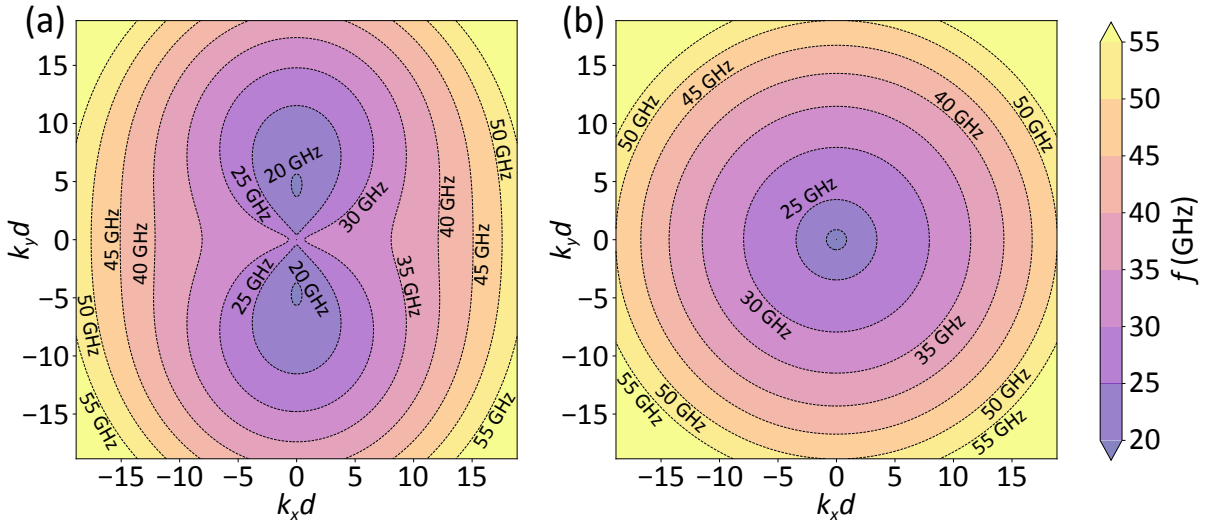


Figure 3.3 Isofrequency contours for spin waves in thin ferromagnetic films. For in-plane magnetization (a), the external magnetic field is oriented along the y -axis, which denotes the DE configuration along k_x and BV for k_y . For out-of-plane magnetic field and magnetization (b), the circular contours typical of the FV configuration are shown. The magnetic parameters used here are consistent with those in Fig. 3.2 ($M_s = 800$ kA/m, $A_{\text{ex}} = 8$ pJ/m, $d = 100$ nm, $H_0 = 0.5 M_s$ for DE and BV, and $H_0 = 1.5 M_s$ for FV).

Figure 3.3a shows an eight-shaped (or lemniscate-like) isofrequency contour for a film magnetized in-plane. At low wavenumbers, dipolar contributions dominate the dispersion and give rise to a strong angular dependence. At larger k (shorter wavelengths), exchange interactions gradually reduce the influence of dipolar anisotropy, and the isofrequency contours become more elliptical. Figure 3.3b shows circular isofrequency contours for a film magnetized out-of-plane. In this configuration, each in-plane direction of \mathbf{k} experiences similar boundary and internal field conditions, resulting in isotropic dispersion.

3.3 Chirality effects

Chirality, broadly defined as the property by which an object or configuration cannot be superimposed on its mirror image (lack of mirror symmetry), appears in various contexts within magnonics. In some cases, chirality emerges from specific magnetostatic textures, in others it reflects dynamical or topological aspects of magnetization similar to those recognized in photons, phonons, and electrons. There is also a class of chirality arising from antisymmetric exchange DMI (described in Sec. 3.1.5). Each type affects the behavior of spin waves in a different way, giving rise to phenomena such as topologically protected modes or directional propagation.

As mentioned above, chiral effects appear not only in specific magnetization textures, such as chiral domain walls and spiral states, but also in the dynamics. Even in saturated systems, the time evolution of the dynamic magnetization can follow a trajectory that breaks the mirror symmetry. This form of dynamical chirality is inherent to spin waves, which have an intrinsic sense of rotation around the equilibrium magnetization direction.

A well-known route to chiral properties in magnetism involves the DMI, that favors tilted spin alignments that do not map onto their mirror images [11] (see Sec. 3.1.5). From a wave-dynamics perspective, it induces an asymmetric dispersion relation in which spin waves acquire different energies (frequencies) for forward and backward propagation. The resulting *nonreciprocal* propagation can be used to design magnonic diodes and isolators [125].

Magnetically chiral textures can also arise in artificial nanostructures, where chirality is imposed by the physical geometry rather than by magnetic interactions [126]. A notable example is the gyroid structure (introduced in Sec. 5.3), which features a three-dimensional periodic network of interconnected curved channels that imposes the intrinsic geometric chirality. As a result, spin-wave dynamics in such architectures can be strongly affected by complex magnetic interactions, leading to nontrivial dispersion characteristics and mode localization. Furthermore, gyroids are predicted to support the interplay between geometric chirality and DMI [127], or with topological effects, broadening the design space of 3D magnonics.

Beyond magnetostatic and dynamical considerations, topological chirality has also been extensively studied in various quasiparticle systems [128, 129]. It can arise from topologically nontrivial band structures, leading to protected magnon edge states, or from spin textures, such as skyrmions, which exhibit real-space topological winding of the magnetization. These topologically protected chiral spin textures host unique localized eigenmodes that are sensitive to their topology. Furthermore, propagation through a skyrmion lattice can quantize spin waves into discrete modes and enable robust, chiral magnon properties [130].

In summary, chirality in magnonics can arise from several sources: magnetostatic textures, dynamic magnetization processes, topological band structures, and antisymmetric DMI interactions. While nonreciprocity is often associated with chiral states, it is not always due to chirality alone. Nevertheless, its presence typically enriches the magnonic spectrum with directional propagation, topological protection, and novel domain-wall or skyrmion-based functionalities.

3.4 Magnonic crystals

Magnonic crystals are periodic magnetic structures that enable the control of spin waves by exploiting wave interference effects analogous to those found in photonic and phononic crystals [5, 6]. In these systems, the periodicity in one, two, or three dimensions modifies the spin-wave dispersion relation, often leading to band gaps where certain frequencies are forbidden. The theoretical basis for understanding these band structures is Bloch's theorem [56], which states that for a medium with discrete translational symmetry (periodic structure), wave solutions $\psi(\mathbf{r})$ can be expressed as the product of a plane wave and a periodic function $u(\mathbf{r})$:

$$\psi(\mathbf{r}) = e^{i\mathbf{k}\cdot\mathbf{r}} u(\mathbf{r}), \quad (3.50)$$

where $u(\mathbf{r})$ has the same periodicity as the underlying lattice or crystal. Importantly, this description introduces an equivalence between wavevectors, since \mathbf{k} and $\mathbf{k} + \mathbf{K}$, where \mathbf{K} is any reciprocal lattice vector, describe the same Bloch state. This equivalence occurs because the periodic lattice symmetry ensures that the same physical properties are represented for wavevectors that differ by reciprocal lattice vectors.

To eliminate redundancy and ensure a unique representation of all Bloch states, the wavevectors are restricted to the *first Brillouin zone*, a region in reciprocal space where each \mathbf{k} uniquely represents an equivalence class of states related by reciprocal lattice translations. This region is defined as the Wigner–Seitz cell of the reciprocal lattice [131]. For any wavevector \mathbf{k} lying outside the first Brillouin zone, there exists an equivalent wavevector $\mathbf{k}' = \mathbf{k} - \mathbf{K}$, such that \mathbf{k}' lies within the zone. This convention ensures that each Bloch state is uniquely represented by a wavevector confined to the first Brillouin zone.

The same principles apply to magnonic crystals in one, two and three dimensions (see Fig. 3.4). Periodicity in the magnetic structure gives rise to a reciprocal lattice in spin-wave dynamics, making the first Brillouin zone the natural framework for describing magnonic band structures. The periodic modulations in magnonic crystals can be achieved in the following ways:

- *geometry modulation* – periodic structuring of the geometry of a magnetic medium (e.g., an array of dots, stripes, or antidots);
- *material modulation* – periodic changes in the magnetic properties, such as magnetization or anisotropy (e.g., layered structures with different materials);
- *magnetization texture modulation* – repeating spin textures, such as strip domains, skyrmion lattices, or vortex arrays, can locally modify the effective magnetic fields and thus act as a spatially varying potential for spin waves [132–134]. Such magnetization textures can be stabilized by balancing multiple material or geometry parameters, providing reconfigurable magnonic functionalities.

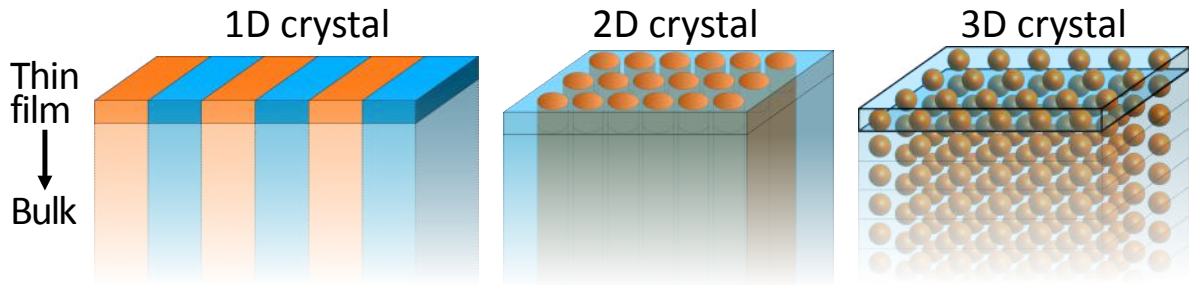


Figure 3.4 Classification of magnonic crystals based on the dimensionality of periodic variation in their material parameters. The figure shows 1D, 2D, and 3D magnonic crystals from left to right. Thin-film magnonic crystals (upper part of each) are laterally patterned structures, confined in the vertical direction with periodic modulation within the plane. On the other hand, bulk magnonic crystals (lower part) occupy the entire three-dimensional volume, with internal periodicity that depends on the specific crystal type.

In one-dimensional magnonic crystals (Fig. 3.4, left), periodic modulation of properties such as film thickness or material composition gives rise to Bragg reflections for spin waves propagating along the direction of periodicity, particularly for wavelengths matching the lattice constant. These reflections lead to the formation of band gaps in the spin-wave spectrum, which can be tuned by varying the lattice period, the applied magnetic field, or the magnetic anisotropy.

When the periodicity is extended to two dimensions, a richer band structure emerges, often supporting localized edge modes and multiple gap openings. In particular, ADLs – periodic arrays of holes etched into thin magnetic films – have become a model system for the study of 2D magnonic crystals (Fig. 3.4 in the center) [7, 135, 136]. The geometry of the holes (size, spacing, and shape) has a strong influence on the resulting band gaps and can also lead to nonreciprocal propagation. However, the results of the ADL study included in this thesis (P5) highlight the versatility of these structures for controlling and inducing higher harmonic spin waves through edge or defect modes.

The concept of three-dimensional magnonic crystals has attracted growing interest in recent years. In that case, the magnetic material is periodically modulated along all three spatial directions (Fig. 3.4 on the right), either by forming intricate networks (like the gyroid structures) or by stacking multilayers with patterned in-plane periodicities [5]. Bloch’s theorem still applies in full 3D, resulting in a band structure that is even more complex than in lower dimensions. Three-dimensional nanocrystals are a major focus of ongoing magnonic research, as they enable novel spin-wave phenomena such as multidirectional band gaps and complex mode hybridization. These features can lead to advanced functionalities, including broadband filters, low-crosstalk waveguides, and spin-wave ‘cavities’ capable of confining modes in all spatial directions. The thesis places special emphasis on 3D magnonic crystals, where curvature, connectivity, and volume constraints open new frontiers for exploring spin-wave dynamics and potential applications in three-dimensional logic or sensor nanoarchitectures.

3.5 Localization of spin waves

Spin-wave localization refers to the confinement of spin-wave propagation to specific regions in a magnetic medium. Several mechanisms can induce this localization, including structural or chemical disorder, engineered geometry, and boundary/surface effects.

An important class of localization phenomena arises from engineered periodic structures, such as ADLs in thin films (see Sec. 3.4 or 5.2.2). This structuring significantly alters the local internal magnetic field around each hole, resulting in a periodically modulated effective potential landscape for spin waves [7, 136]. The resulting spin-wave band structure often features modes that are spatially confined either within the antidot cavities or along the narrow connecting “corridors.” While the periodicity of the lattice can give rise to Bragg band gaps, even slight variations in geometry (like a defect) or the introduction of additional structural complexity can enhance the localization of certain modes within specific antidot regions. This type of geometry-induced localization is fundamentally different from the Anderson localization observed in disordered media [137–139]. Here, it is the intentional lattice design that constrains spin-wave propagation.

Related, but more general form of spin-wave localization occurs at interfaces between two magnetic phases – when a spin wave encounters a mismatch in material parameters such as magnetization, exchange stiffness, anisotropy, or simply the physical edge (which is the extreme case of parameter difference). These interfaces act as effective potential barriers, resulting in the confinement of spin waves to specific regions (e.g., around antidot edges). In some cases, this leads to distinct boundary modes with characteristic frequencies and damping. When the magnetostatic and exchange interactions break the inversion symmetry at the interface, the propagation of these modes can become nonreciprocal, meaning that the spin waves travel more efficiently in one direction along the interface [6]. Such localized modes have been exploited in magnonic devices, where one-way propagation along domain walls or interfaces facilitates spin-wave routing [140–142].

Three-dimensional magnonic crystals also offer opportunities for spin-wave localization. By periodically modulating material parameters in all three spatial dimensions, it is possible to partially or completely confine bulk modes to specific regions or ‘layers’ of the structure. This thesis focuses on 3D architectures such as gyroid-based magnonic crystals, where the complex, chiral network of struts can potentially guide spin waves along specific channels. As shown in P9 (Sec. 5.3.3), this curvilinear geometry gives rise to localized FMR modes at the surfaces, leading to novel types of spin-wave phenomena.

Spin-wave localization underlies many advanced magnonic functionalities. For example, ADLs can support the generation of higher-order harmonics, while domain walls containing localized modes show potential for reconfigurable spin-wave waveguides. The ability to spatially confine spin waves with high precision enables logic operations based on interference and phase manipulation. Importantly, these concepts extend beyond planar systems: three-dimensional nanostructures introduce additional degrees of freedom for tailoring mode confinement, opening new avenues for functional and compact magnonic devices.

3.6 Spin-wave optics

Magnonics, by its wave-based nature, shares a profound conceptual similarity with optics. Just as electromagnetic waves follow Maxwell's equations, spin waves in ferromagnets obey a wave equation that exhibits interference, diffraction, and other canonical wave phenomena [6, 113]. The magnetodynamic equations can be rearranged [143] into a form that reveals parallels to Fresnel and Fraunhofer diffraction theory, the Huygens–Fresnel principle, and the Talbot effect.

When spin waves propagate in a thin ferromagnetic film, their amplitude and phase evolution can often be described using methods similar to those used in scalar or vector wave optics. Writing the small transverse components of the magnetization as a complex amplitude $\Psi(\mathbf{r}, t) = \Psi(\mathbf{r}) e^{-i\omega t}$, it satisfies a Helmholtz-type differential equation:

$$\nabla_{\perp}^2 \Psi(\mathbf{r}) + k^2(\omega) \Psi(\mathbf{r}) = 0, \quad (3.51)$$

where ∇_{\perp}^2 is the in-plane Laplacian (for a thin film) and $k(\omega)$ depends on frequency, local effective fields, and exchange stiffness [113]. This is analogous to the wave equation

$$\nabla_{\perp}^2 E(\mathbf{r}) + n^2(\omega) \left(\frac{\omega}{c}\right)^2 E(\mathbf{r}) = 0 \quad (3.52)$$

in optics, where E is the electric field and $n(\omega)$ is the refractive index. The effective ‘index’ for spin waves can be strongly anisotropic, including dipolar fields, exchange contributions, and possible DMI, thereby leading to wave-optical effects with distinct magnetic properties [116].

Just as light diffracts around apertures and interferes when it encounters multiple slits, spin waves exhibit the same phenomena. Narrow apertures in a thin magnetic waveguide diffract spin waves in patterns determined by wavevector-dependent phase accumulation, and coherent superposition of two spin-wave beams produces interference fringes known from conventional optics [144]. A particularly compelling demonstration of spin-wave optics is the Talbot effect (P1–P3, P6). The discrete wavevector spectrum generated by the periodic grating leads to interference that reproduces the initial pattern (more in Sec. 5.1.1). These findings confirm that conventional optical diffraction integrals can be effectively applied to describe spin-wave fields.

The wave-theoretical framework allows researchers to design resonators, gratings, or couplers using the same conceptual toolkit as in photonics. This unified approach accelerates device prototyping, by allowing proven and well-established optical designs such as lens shapes, gradient indices, and multi-slit interferometers, to inspire magnonic analogues [6].

The field of micromagnetism provides a deep understanding of the fundamental principles governing magnetization dynamics in magnetic materials. The core concepts of the micromagnetic model have been explored throughout this chapter, with particular emphasis on the contributions to the Gibbs free energy – namely exchange interactions, magnetostatic (dipolar)

interactions, various forms of magnetic anisotropy, and the Zeeman energy. Together, these terms form the basis for exploring complex magnetic phenomena, even in systems with reduced dimensions and patterned nanostructures.

The evolution of micromagnetic theory has been followed by the development of advanced magnetic nanostructures, where the control of magnetization occurs on length scales from tens of nanometers to a few micrometers. Initially, the manipulation of spin waves was mainly studied in homogeneous materials, but the introduction of 1D and 2D patterned nanostructures marked a significant advance in the ability to control these magnetic excitations. In such systems, the confinement of magnetic moments along one or two spatial directions allowed the first insights into localized spin-wave modes and their band gap formation.

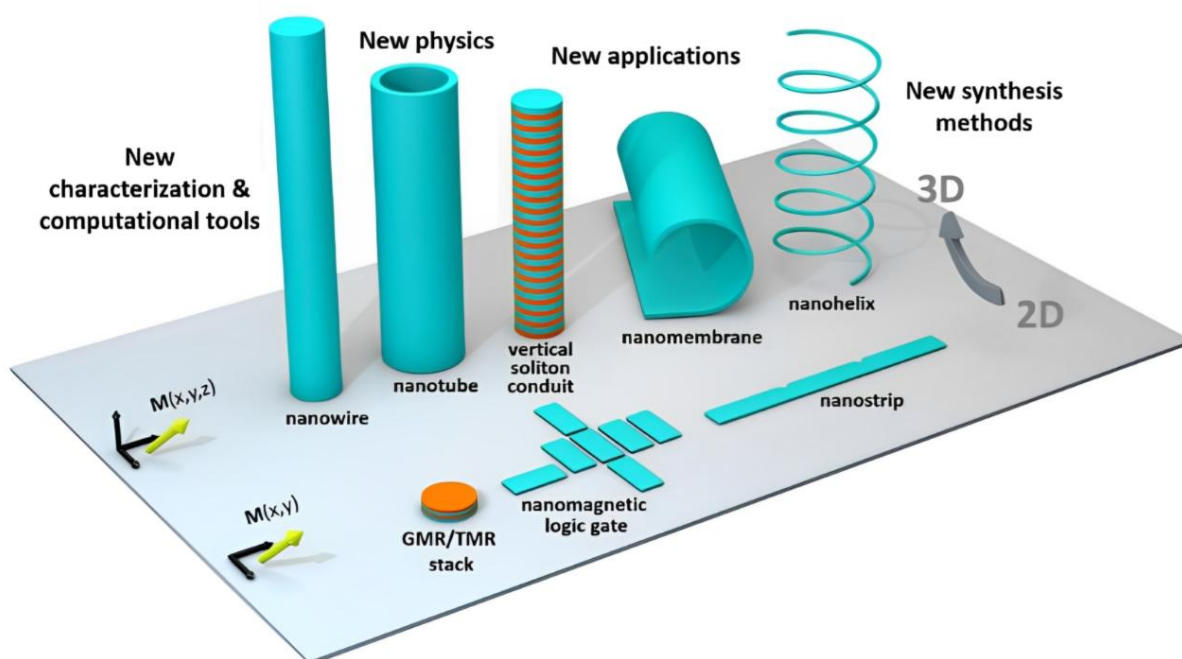


Figure 3.5 The transition from 2D to 3D nanomagnetic systems requires advanced fabrication, characterization, and sophisticated modeling tools, enabling the discovery of new phenomena driven by complex geometries and nanoscale magnetization dynamics. Credit: Sanz-Hernández, D. et al. *Nanomaterials* 2018, **8**, 483 [145]. © 2018 by the Authors. Licensee MDPI, Basel, Switzerland.

The latest frontier in micromagnetism is the exploration of 3D complex magnetic nanostructures where the periodicity and connectivity of the material extend into all three spatial dimensions (Fig. 3.5). Gyroidal magnonic crystals, with their complex chiral geometry, are a state-of-the-art example of these structures. In 3D systems, the curvature and chirality of the lattice offer new possibilities for controlling the spin-wave dynamics, and the ability to localize it in such complex geometries enables the development of novel, advanced magnonic devices.

In conclusion, this chapter lays the theoretical foundation for understanding the rich variety of magnetic phenomena observed in magnetic nanostructures, while also highlighting the future research in magnonic crystals and the use of geometry to control magnetization dynamics.

Chapter 4

Numerical methods and micromagnetic simulations

Micromagnetic simulations are at the heart of my research, serving as a powerful tool to gain deep insight into spin-wave dynamics in ferromagnetic nanostructures, as well as a compelling research topic in its own right. My expertise spans different simulation frameworks, from finite difference methods (FDM) used in MuMax3 [146] to finite element methods (FEM) implemented in tools such as COMSOL Multiphysics [147] and tetmag [148]. Alongside FDM and FEM, the boundary element method (BEM) is also investigated within the tetmag environment as a complementary technique. This broad experience with different numerical approaches allows me to tailor simulations to the specific needs of the systems I investigate, taking into account complex geometries, boundary conditions, and material properties. These methods not only provide theoretical predictions but also serve as a bridge to experimental research, enabling the design and optimization of magnonic devices that are often difficult or costly to fabricate and test directly.

One of the key equations governing the systems studied in this work is the LLG equation, already introduced in Sec. 3.2.2. This is a nonlinear partial differential equation (PDE) and due to its nonlinearity and the spatial dependence of the effective magnetic field, analytical solutions are impractical except for the simplest geometries and conditions. This is where numerical methods come in. Tools such as FDM and FEM discretize both space and time, breaking down the continuous magnetization field and its associated interactions into small, manageable steps. In essence, these methods transform the PDE into a system of algebraic equations that can be solved iteratively.

However, performing these simulations is a multidisciplinary process that, in addition to a solid understanding of physics, integrates programming expertise, mathematical modeling, and even elements of visual and geometric design. Accurate representation of three-dimensional nanostructures often requires the use of computer-aided design (CAD) software, where precise geometric definitions must be established as a critical basis for initiating simulations. Once the geometries are defined (with proper computational meshes), the simulation process involves implementing the governing equations (such as LLG) and specifying material parameters and

boundary conditions, all of which are essential for obtaining accurate and physically meaningful results (see Fig. 4.1). In addition, the post-processing stage requires proficiency in data analysis and visualization techniques to transform the large amounts of raw simulation data into meaningful interpretations of the system’s magnetic behavior.

The demand for computational power in micromagnetic simulations is increasing as we push the boundaries of what can be modeled, especially in complex three-dimensional nanostructures. High quality simulations require fine spatial discretization to accurately capture key phenomena such as domain wall motion or spin-wave propagation. Ironically, we need immense computing power to simulate devices that are themselves intended to reduce energy demands by utilizing spin waves for logic operations. This paradox is reflected in the humorous quote attributed to Bill Gates: “The computer was born to solve problems that did not exist before” [149]. In the case of micromagnetic simulations, researchers are in a unique position to understand this irony. However, the paradigm-shifting potential of magnonic technology, which promises energy-efficient computing solutions that can meet the growing demands on conventional architectures, justifies these efforts.

As mentioned above, simulations play an increasingly important role in guiding and optimizing experimental procedures. However, they also serve as effective tools for interpreting experimental data – especially in cases where measurements are affected by imperfections, noise, or limited resolution. For example, simulations can reveal how spin waves scatter from defects or interact with domain walls – phenomena that may be challenging to observe directly, but can be understood through indirect experimental indicators when supported by accurate modeling.

In this context, micromagnetic simulations have become indispensable in the modern research and development of magnonic devices. Despite all the advantages, however, the combination of high computational demands and the inherently interdisciplinary nature of numerical modeling highlights the complexity and sophistication of these studies. The following sections provide a detailed examination of the specific numerical methods I have used, with a focus on their implementation in MuMax3, tetmag, and COMSOL Multiphysics.

4.1 Spatial and temporal discretization methods

This section introduces the spatial and temporal discretization methods used throughout my research – FDM, FEM, and BEM. These methods form the numerical basis for solving the LLG equation and related micromagnetic problems. Their inclusion here is justified by their widespread use, established theoretical background, and compatibility with frequency- and time-domain formulations. Presentation of these methods provides a foundation for understanding the simulation strategies and computational frameworks discussed in later sections.

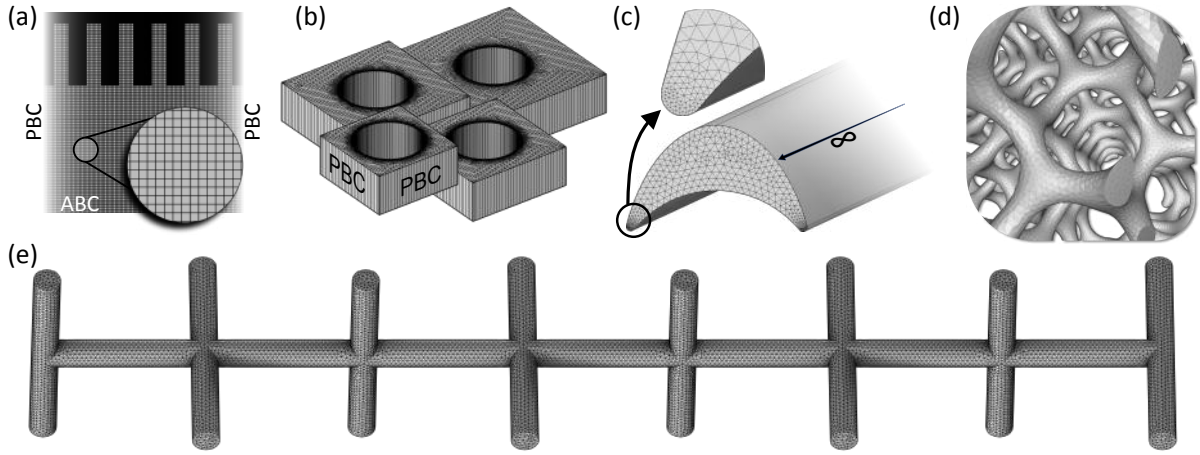


Figure 4.1 Illustration of the discretization meshes used in various models in this thesis, highlighting mesh adaptations tailored to specific simulation goals. (a) A homogeneous cubic FDM-based mesh used in the model with a single-cell thickness, representing an array of narrow waveguides entering a wider multimode waveguide – studied in the context of the Talbot effect (publications P1–P3 and P6). (b) An antidot structure discretized with a tetrahedral FEM mesh, also with a single-cell thickness. For visualization purposes, the mesh is stretched in the out-of-plane direction. High-resolution meshing around the antidots is essential to capture edge-localized spin-wave modes (publication P5). (c) A triangular FEM mesh used to model the cross section of a crescent-shaped waveguide, representing an infinitely long structure in a 2D simulation (publication P4). (d) A tetrahedral FEM mesh used to simulate the full three-dimensional geometry of the gyroid structure (publications P7–P9). (e) A scaffold-like structure discretized by FEM, specifically designed for the FMR mode simulations presented in publication P9.

4.1.1 Finite difference method

The FDM is a widely used approach in micromagnetic simulations for numerically solving PDEs governing magnetization dynamics [87, 113]. The graphics processing unit (GPU)-based micromagnetic solver MuMax3 [146] provides an exemplary FDM-grounded implementation, extensively used in publications P1, P2, P3, and P6.

In FDM-based micromagnetism, a computational system is divided into a three-dimensional Cartesian mesh with cell sizes Δx , Δy , and Δz . The continuous magnetization $\mathbf{M}(x, y, z, t)$ becomes discrete, $\mathbf{M}_{i,j,k}(t)$, at each mesh cell (i, j, k) . Finite difference approximations replace spatial derivatives in the effective field \mathbf{H}_{eff} . For example, a first-order derivative along x is approximated by

$$\left. \frac{\partial \mathbf{M}_{i,j,k}}{\partial x} \right|_{x_i} \approx \frac{\mathbf{M}_{i+1,j,k} - \mathbf{M}_{i,j,k}}{\Delta x}, \quad (4.1)$$

and the second-order derivative (for exchange interactions¹) becomes

$$\left. \frac{\partial^2 \mathbf{M}_{i,j,k}}{\partial x^2} \right|_{x_i} \approx \frac{\mathbf{M}_{i+1,j,k} - 2\mathbf{M}_{i,j,k} + \mathbf{M}_{i-1,j,k}}{\Delta x^2}. \quad (4.2)$$

¹In micromagnetism, exchange interactions are modeled by the term proportional to $\nabla^2 \mathbf{M}$ (see Eq. 3.2), requiring second-order spatial derivatives.

Similar discretization schemes apply to y and z . An appropriate grid resolution must be chosen to resolve critical magnetic length scales (e.g., the exchange length ℓ_{ex} – Eq. 3.3) to accurately capture subtle magnetization features.

Time is discretized into intervals of length Δt . The magnetization is updated iteratively from \mathbf{M}^n at time t_n to \mathbf{M}^{n+1} at $t_{n+1} = t_n + \Delta t$. The numerical scheme uses an explicit solver for the LLG equation:

$$\mathbf{M}_{i,j,k}^{n+1} = \mathbf{M}_{i,j,k}^n + \Delta t \mathbf{f}(\mathbf{M}_{i,j,k}^n, \mathbf{H}_{\text{eff}}(\mathbf{M}_{i,j,k}^n)), \quad (4.3)$$

where \mathbf{f} includes precession and damping terms. Common time integrators based on these discretization methods are described in Sec. 4.2.

4.1.2 Finite element method

FEM is a versatile numerical approach often used in micromagnetism to handle complex geometries, irregular boundaries, and spatially varying material properties [87, 113]. Unlike the regular Cartesian discretization of the FDM, FEM uses meshes composed of arbitrary elements (often triangles in 2D or tetrahedra in 3D, see Fig. 4.1). Each element approximates the magnetization $\mathbf{M}(x, y, z)$ within its volume or area using local basis functions. This flexibility ensures accurate modeling in regions with curved edges or intricate shapes.

Let Ω be the entire simulation domain, partitioned into N finite elements Ω_e :

$$\Omega = \bigcup_{e=1}^N \Omega_e. \quad (4.4)$$

Within each element, the magnetization $\mathbf{M}(x, y, z)$ is approximated as a linear (or higher-order polynomial) combination of basis functions $N_i(x, y, z)$ that interpolate the nodal values $\mathbf{M}_i(t)$. Thus, for element Ω_e ,

$$\mathbf{M}_e(x, y, z, t) = \sum_{i=1}^{n_e} N_i(x, y, z) \mathbf{M}_i(t), \quad (4.5)$$

where n_e is the number of nodes in the element. Each node has a time-dependent magnetization vector. By assembling the elementwise approximations (local solutions within each finite element), one constructs a global representation of $\mathbf{M}(\mathbf{r}, t)$ across the entire domain.

4.1.2.1 Weak formulation and variational principle

The core of FEM lies in the transformation of a PDE (here LLG) into its ‘weak form’ [87, 113]. The LLG equation is multiplied by appropriate test functions (often the same basis functions N_i) and integrated over Ω . This procedure leads to an elementwise system of equations that, when assembled, yields a global system describing the magnetization evolution. Symbolically, the weak form of the LLG equation can be expressed as

$$\int_{\Omega} \left(\frac{\partial \mathbf{M}}{\partial t} + |\gamma| \mu_0 \mathbf{M} \times \mathbf{H}_{\text{eff}} - \frac{\alpha}{M_s} \mathbf{M} \times \frac{\partial \mathbf{M}}{\partial t} \right) \cdot N_i d\Omega = 0 \quad \forall i. \quad (4.6)$$

Within each element Ω_e , one obtains a local system of the form

$$\mathbf{K}_e \mathbf{M}_e = \mathbf{F}_e, \quad (4.7)$$

where \mathbf{K}_e captures elementwise stiffness-like relations (incorporating exchange, anisotropy, or dipolar contributions), \mathbf{M}_e holds nodal magnetization values, and \mathbf{F}_e includes effects from external magnetic fields and boundaries. Compilation of these elementwise contributions over all elements results in a global system, which has to be solved at each time step.

4.1.3 Boundary element method

BEM is a numerical approach that, in contrast to volume-based discretization techniques such as FEM or FDM, solves certain boundary value problems by transforming the governing PDEs into boundary integral equations [150, 151]. This allows only the domain boundary to be discretized, making BEM particularly effective for problems involving large or unbounded regions. A scalar potential φ is defined to satisfy the Poisson equation:

$$\Delta \varphi = f \quad \text{in } \Omega, \quad (4.8)$$

where f is a source term, and Δ is the Laplace operator ($\nabla \cdot \nabla$ or ∇^2). Let $\Omega \subset \mathbb{R}^n$ be a domain that may be finite, semi-infinite, or infinite, and let $\partial\Omega$ denote its boundary. For $\varphi(\mathbf{x})$ governed by the Poisson equation, Green's functions provide a fundamental framework for expressing the solution in terms of boundary values and source distributions within the domain Ω .

Green's function. A Green's function $G(\mathbf{x}, \mathbf{y})$ for the Poisson equation (4.8) satisfies

$$-\Delta G(\mathbf{x}, \mathbf{y}) = \delta(\mathbf{x} - \mathbf{y}) \quad \text{in } \Omega, \quad (4.9)$$

along with the appropriate boundary conditions on $\partial\Omega$. Here, $\delta(\mathbf{x} - \mathbf{y})$ is the Dirac delta function² centered at \mathbf{y} . In physical terms, $G(\mathbf{x}, \mathbf{y})$ describes the effect at the field point $\mathbf{x} \in \Omega$ due to a unit point source placed at $\mathbf{y} \in \Omega$.

An integral representation of $\varphi(\mathbf{x})$ in terms of the boundary values can be written by using Green's theorem [152] and the Green's function:

$$\varphi(\mathbf{x}) = \int_{\partial\Omega} \left(G(\mathbf{x}, \mathbf{y}) \frac{\partial \varphi}{\partial n}(\mathbf{y}) - \varphi(\mathbf{y}) \frac{\partial G(\mathbf{x}, \mathbf{y})}{\partial n} \right) dS(\mathbf{y}), \quad (4.10)$$

²The Dirac delta function $\delta(\mathbf{x} - \mathbf{y})$ is a generalized function (or distribution) that is zero everywhere except at $\mathbf{x} = \mathbf{y}$, where it is infinitely large in such a way that its integral over the entire domain is unity. It is commonly used to represent a point source in PDEs.

where $\mathbf{x} \in \Omega$ and $\mathbf{y} \in \partial\Omega$. The operator $\partial/\partial n$ denotes the normal derivative on the boundary. In other words, if \mathbf{n} is the outward unit normal to the surface $\partial\Omega$, then

$$\frac{\partial \varphi}{\partial n} = \nabla \varphi \cdot \mathbf{n}. \quad (4.11)$$

Equation 4.10 shows that if $\varphi(\mathbf{y})$ and its normal derivative at the boundary $\partial\Omega$ are known, the value of $\varphi(\mathbf{x})$ at any interior point $\mathbf{x} \in \Omega$ can be obtained via the surface integral. This boundary integral representation is particularly useful for solving boundary-value problems for the Poisson equation, since it transforms a PDE into an integral equation only at the boundary.

BEM discretizes $\partial\Omega$ into N' boundary elements, typically line segments in 2D or surface panels in 3D. Within each element, the boundary fields (such as φ or its normal derivative) are approximated by shape functions $N'_i(\mathbf{y})$. For example

$$\varphi(\mathbf{y}) \approx \sum_{i=1}^{N'} \varphi_i N'_i(\mathbf{y}), \quad \frac{\partial \varphi}{\partial n}(\mathbf{y}) \approx \sum_{i=1}^{N'} \left(\frac{\partial \varphi}{\partial n} \right)_i N'_i(\mathbf{y}), \quad (4.12)$$

where φ_i and $(\partial\varphi/\partial n)_i$ are the unknown nodal values. Substituting these expansions into the boundary integral equation 4.10, and collocating at selected boundary points reduces the problem to a linear algebraic system in terms of φ_i and $(\partial\varphi/\partial n)_i$. Depending on whether Dirichlet or Neumann boundary conditions are applied (see Sec. 4.3), a set of these nodal fields may be known a priori, simplifying the system [150].

In micromagnetism, one of the most prominent uses of BEM is to handle the nonlocal dipolar field. Instead of solving magnetostatic potentials throughout the entire volume, BEM forms an integral equation at the boundary (or outer surface) to determine the scalar potential φ [153]. This approach can be more efficient than volume discretization when large parts of the domain are effectively vacuum or extend to infinity, since BEM only needs to discretize the interface between magnetic and nonmagnetic regions. Many modern micromagnetic codes and specialized solvers use hybrid techniques – FEM/FDM for exchange and anisotropy terms, and BEM for dipolar fields – to exploit on the efficiency of boundary-only representations.

4.2 Time-stepping approaches

An essential aspect of solving the LLG equation – and, more generally, any time-dependent system – is the choice of time-stepping method [88, 154, 155]. This section presents several time-stepping approaches commonly used in micromagnetic simulations, all of which I have used in the course of my research. These methods have been implemented in several simulation environments, each with different strengths and numerical capabilities.

A key distinction between these approaches is whether they are *explicit* or *implicit*. In explicit methods, the solution at the next time step is computed directly from the known values at the current (or previous) steps, making them computationally simple, but often limited by

stability constraints that require relatively small time-step sizes. Typical explicit methods used in micromagnetism include forward Euler, Runge–Kutta (RK), and Adams–Bashforth (AB) schemes. In contrast, implicit methods require that the unknown future state satisfy an equation that includes its own value, necessitating the solution of a system of equations at each time step. Although more computationally expensive, implicit methods such as backward Euler, backward differentiation formulas (BDF), and generalized- α , often allow for larger time steps and improved numerical stability.

In micromagnetic simulations, certain problems can be *stiff*, meaning that they involve rapidly varying fields or contain widely separated time scales (e.g., one part of the solution evolves much faster than another). Such stiffness often requires more stable (implicit) methods to proceed efficiently without extremely small time steps. Conversely, *non-stiff* problems can be effectively addressed by explicit schemes, which may be more computationally efficient if small time steps are acceptable. Table 4.1 summarizes some key differences between explicit and implicit methods, along with representative examples. Since micromagnetic simulations can exhibit stiff

Table 4.1 Concise comparison of explicit and implicit numerical methods used in simulations.

Aspect	Explicit methods	Implicit methods
Definition	Next-step solution calculated from known past/current values	Next-step solution calculated from unknown future values
Computational cost	Lower per-step cost (no large system of equations to solve)	Higher per-step cost (requires solving a nonlinear equations)
Stability	Conditionally stable (demands smaller time steps)	Unconditionally stable (allows larger time steps)
Implementation	Straightforward (no solver or iteration needed)	Complex (requires iterative or direct solvers)
Applicability	For non-stiff problems or when temporal resolution is feasible	For stiff problems or large time steps
Examples	Forward Euler, RK, AB	Backward Euler, BDF, generalized- α

or non-stiff behavior, having access to both explicit and implicit time-stepping techniques is useful for balancing computational efficiency and stability. The following subsections provide a detailed description of each of the aforementioned methods, outline their theoretical foundations, and discuss practical considerations related to their implementation in MuMax3, COMSOL, and tetmag.

4.2.1 Runge–Kutta methods

A generic system of ODEs can be written in the form:

$$\frac{dy}{dt} = \mathbf{f}(t, \mathbf{y}), \quad (4.13)$$

where $\mathbf{y} = (y_1, y_2, \dots, y_n)^\top$ depends on t . Let $t_n = n\Delta t$, where Δt is the time step, and $\mathbf{y}_n \approx \mathbf{y}(t_n)$ is the numerical approximation of the solution at time t_n . The classical fourth-order Runge–Kutta method (RK4) updates \mathbf{y}_n to \mathbf{y}_{n+1} via four intermediate ‘slopes’ $\mathbf{k}_1, \mathbf{k}_2, \mathbf{k}_3, \mathbf{k}_4$. Specifically,

$$\mathbf{k}_1 = \mathbf{f}(t_n, \mathbf{y}_n) \quad \text{slope at the beginning of the interval, using } \mathbf{y} \text{ (Euler method),} \quad (4.14)$$

$$\mathbf{k}_2 = \mathbf{f}(t_n + \frac{1}{2}\Delta t, \mathbf{y}_n + \frac{1}{2}\Delta t \mathbf{k}_1) \quad \text{slope in the middle of the interval, using } \mathbf{y} \text{ and } \mathbf{k}_1, \quad (4.15)$$

$$\mathbf{k}_3 = \mathbf{f}(t_n + \frac{1}{2}\Delta t, \mathbf{y}_n + \frac{1}{2}\Delta t \mathbf{k}_2) \quad \text{slope in the middle of the interval, using } \mathbf{y} \text{ and } \mathbf{k}_2, \quad (4.16)$$

$$\mathbf{k}_4 = \mathbf{f}(t_n + \Delta t, \mathbf{y}_n + \Delta t \mathbf{k}_3) \quad \text{slope at the end of the interval, using } \mathbf{y} \text{ and } \mathbf{k}_3. \quad (4.17)$$

More information about the Euler methods can be found in Sec. 4.2.3. Finally, the new step solution is updated by

$$\mathbf{y}_{n+1} = \mathbf{y}_n + \frac{\Delta t}{6} (\mathbf{k}_1 + 2\mathbf{k}_2 + 2\mathbf{k}_3 + \mathbf{k}_4). \quad (4.18)$$

In the context of the LLG equation, it is advantageous to use the form that explicitly isolates the time derivative $\partial \mathbf{M} / \partial t$ as a function of the magnetization vector \mathbf{M} and the effective magnetic field \mathbf{H}_{eff} – Eq. 3.20. As explained in Sec. 3.2.2, this arrangement facilitates the direct application of numerical integration schemes by adapting the LLG equation to the standard first-order ODE structure introduced in Eq. 4.13, allowing it to be expressed in generic form:

$$\mathbf{y} \equiv \mathbf{M}, \quad \mathbf{f}(t, \mathbf{M}) = -\frac{|\gamma|\mu_0}{1 + \alpha^2} (\mathbf{M} \times \mathbf{H}_{\text{eff}}) - \frac{\alpha|\gamma|\mu_0}{(1 + \alpha^2)M_s} [\mathbf{M} \times (\mathbf{M} \times \mathbf{H}_{\text{eff}})]. \quad (4.19)$$

Then, given a time step Δt and a known approximation \mathbf{M}_n of $\mathbf{M}(t_n)$, we apply the Eq. 4.19 to the RK4 methodology from Eq. 4.17, and compute:

$$\mathbf{k}_1 = \mathbf{f}(\mathbf{M}_n, t_n), \quad (4.20)$$

$$\mathbf{k}_2 = \mathbf{f}(\mathbf{M}_n + \frac{1}{2}\Delta t \mathbf{k}_1, t_n + \frac{1}{2}\Delta t), \quad (4.21)$$

$$\mathbf{k}_3 = \mathbf{f}(\mathbf{M}_n + \frac{1}{2}\Delta t \mathbf{k}_2, t_n + \frac{1}{2}\Delta t), \quad (4.22)$$

$$\mathbf{k}_4 = \mathbf{f}(\mathbf{M}_n + \Delta t \mathbf{k}_3, t_n + \Delta t). \quad (4.23)$$

In this way, $\mathbf{M}(t)$ at discrete times $t_{n+1} = t_n + \Delta t$ can be solved numerically:

$$\mathbf{M}_{n+1} = \mathbf{M}_n + \frac{\Delta t}{6} (\mathbf{k}_1 + 2\mathbf{k}_2 + 2\mathbf{k}_3 + \mathbf{k}_4). \quad (4.24)$$

Since LLG describes a rotational dynamics (plus damping) of the magnetization vector, some methods are specifically designed to preserve $\|\mathbf{M}\|$ (or keep it close to its saturation value M_s). The standard RK4 method does not strictly preserve $\|\mathbf{M}\|$ unless additional constraints or projections are used (see Eq. 4.49). In practice, \mathbf{M}_{n+1} is often renormalized after each step, or alternative geometric integration schemes are used that better preserve the magnetization norm [156, 157].

In summary, the classical RK4 method is straightforward to implement and achieves fourth-order accuracy in time. When applied to the LLG equation, it provides an explicit way to step the magnetization forward in time in a manner that is accurate for moderate step sizes. Although more specialized integrators exist (in particular, those that preserve geometric properties and introduce adaptive time steps), RK4 remains a popular choice for its simplicity and generally good performance.

Adaptive RK methods. The RK methods family, introduced above, is widely used for solving ODEs and PDEs due to its versatility and accuracy. The methods approximate solutions by evaluating the function at multiple points within each time step, allowing for a better estimate of the solution [158, 159]. RK4 refers to the classical, fixed-step fourth-order RK scheme applied to a spatially discretized PDE. In other words, once the PDE is transformed into a large system of ODEs, the solution evolves in time without adaptive error control, using a fixed time-step size. In contrast, the adaptive RK methods (such as RK34 and RK45) are general-purpose explicit ODE solvers that incorporate embedded error estimation within each time step. By comparing the higher- and lower-order solutions, the solvers dynamically adjust the time-step size, refining the solution where rapid changes occur and coarsening the time steps where the solution varies more slowly. This adaptive feature can significantly improve computational efficiency while maintaining a desired level of accuracy.

- **RK34:** Building on the classical RK4 approach, the embedded RK34 scheme provides both third- and fourth-order solutions within each step. The difference between these solutions serves as an error estimate and guides the automatic adjustment of the time step. RK34 is well suited for non-stiff problems that do not require the highest possible accuracy, but still benefit from a reliable way to control local errors.
- **RK45:** A more common adaptive strategy uses an embedded fourth-order approximation alongside a fifth-order approximation, collectively referred to as ‘RK45’ [155, 160]. There are several sets of coefficients under this category, each balancing efficiency and accuracy differently:
 - **Cash–Karp 5 (CK5):** A fifth-order RK method paired with a fourth-order solution for error estimation. The local truncation error is evaluated by comparing the fifth-order and fourth-order solutions at each step, allowing precise control over time-step adjustments. CK5 is efficient for moderate to high accuracy requirements in non-stiff problems, where an implicit solver would be unnecessary.

- **Dormand–Prince 5 (DP5):** Another well-known RK45-type scheme. Like CK5, DP5 uses a fifth-order solution with an embedded fourth-order estimate, but its coefficients are chosen specifically to optimize the accuracy of the fifth-order solution rather than the embedded approximation. This design choice often results in slightly better efficiency in cases where high accuracy of the main solution is a priority over very long time integrations. In practice, DP5 is a popular default in many software packages due to its robustness and favorable accuracy-per-function-call characteristics.

4.2.2 Adams–Bashforth method

The AB family of methods belongs to the class of linear multistep ODE solvers. Consider a general system of ODEs in first-order form (see Eq. 4.13) with discrete times $t_n = t_0 + n \Delta t$ and approximate solutions $\mathbf{y}_n \approx \mathbf{y}(t_n)$. While one-step methods like RK depend only on the solution at the current time step to move forward, the linear multistep method uses information from several previous time steps. The k -step AB method can be derived by using an interpolating polynomial to approximate the integral

$$\mathbf{y}(t_{n+1}) = \mathbf{y}(t_n) + \int_{t_n}^{t_{n+1}} \mathbf{f}(t, \mathbf{y}(t)) dt, \quad (4.25)$$

and then replacing the t -dependency by values of \mathbf{f} at previously known times. In its explicit form, the k -step AB formula can be written as

$$\mathbf{y}_{n+1} = \mathbf{y}_n + \Delta t \sum_{j=0}^{k-1} \beta_j \mathbf{f}(t_{n-j}, \mathbf{y}_{n-j}), \quad (4.26)$$

where the coefficients β_j are determined by integrating an interpolating polynomial of degree- k over the interval $[t_n, t_{n+1}]$. Table 4.2 lists the coefficients for the AB methods of orders $1 \leq k \leq 4$.

Table 4.2 Coefficients β_j for the AB family (up to fourth order).

order k	β_0	β_1	β_2	β_3
1 (Euler method)	1	0	—	—
2	$3/2$	$-1/2$	0	—
3	$23/12$	$-16/12$	$5/12$	0
4	$55/24$	$-59/24$	$37/24$	$-9/24$

For example, the two-step AB method is

$$\mathbf{y}_{n+1} = \mathbf{y}_n + \Delta t \left(\frac{3}{2} \mathbf{f}(t_n, \mathbf{y}_n) - \frac{1}{2} \mathbf{f}(t_{n-1}, \mathbf{y}_{n-1}) \right), \quad (4.27)$$

and the four-step:

$$\mathbf{y}_{n+1} = \mathbf{y}_n + \Delta t \left(\frac{55}{24} \mathbf{f}(t_n, \mathbf{y}_n) - \frac{59}{24} \mathbf{f}(t_{n-1}, \mathbf{y}_{n-1}) + \frac{37}{24} \mathbf{f}(t_{n-2}, \mathbf{y}_{n-2}) - \frac{9}{24} \mathbf{f}(t_{n-3}, \mathbf{y}_{n-3}) \right). \quad (4.28)$$

A k -step scheme uses k past solution values or function evaluations, so a dedicated ‘starting procedure’ is needed to initialize the first few steps. Often, a one-step method such as the RK4 is used for this, before the AB method can be applied in a pure multistep fashion.

To numerically integrate the LLG equation using the AB method, the general multistep formula given in Eq. 4.26 is applied directly to the magnetization vector \mathbf{M}_n , choosing the desired order k based on the required accuracy and available previous evaluations of the right-hand side. For example, employing the second-order scheme ($k = 2$), the update step becomes:

1. Initialize \mathbf{M}_0 and compute \mathbf{M}_1 with a one-step method (like RK4) so that \mathbf{f}_0 and \mathbf{f}_1 are known.
2. For $n \geq 1$, update:

$$\mathbf{M}_{n+1} = \mathbf{M}_n + \Delta t \left(\frac{3}{2} \mathbf{f}_n - \frac{1}{2} \mathbf{f}_{n-1} \right).$$

3. Evaluate $\mathbf{f}_{n+1} = \mathbf{F}(\mathbf{M}_{n+1}, t_{n+1})$ in preparation for the next time step.

For higher-order AB schemes, Eq. 4.26 is used analogously with the appropriate coefficients (given in Table 4.2), again ensuring that enough initial steps are computed by a one-step method.

As with RK, standard AB methods do not strictly preserve the $\|\mathbf{M}(t)\| \approx M_s$ norm, also requiring the normalization step after each update or using special geometric integrators.

4.2.3 Euler methods

In finite element micromagnetism, a robust time-integration scheme is essential to handle the rapid precessional motion of the magnetization and the strong nonlinearity arising from the LLG equation. While various algorithms (including RK or AB) can be used in principle, FEM implementations generally favor implicit solvers to achieve better stability for moderately large time steps [88].

The most basic time-integration scheme is the Euler method³, of which there are two main variants described below.

Forward Euler (explicit):

$$\mathbf{M}^{n+1} = \mathbf{M}^n + \Delta t \mathbf{f}(\mathbf{M}^n, \mathbf{H}_{\text{eff}}^n). \quad (4.29)$$

³In this section, time-step indices are written as superscripts to avoid confusion with subscripts used for other quantities. In other sections, where there is no such ambiguity, the subscript notation is used.

Here, the right-hand side is evaluated at the known state \mathbf{M}^n . This approach is computationally cheap per step (only \mathbf{f} needs to be evaluated), but is conditionally stable and often requires very small Δt to capture the fast gyromagnetic dynamics without numerical blowing up. It is generally not favored in FEM micromagnetism due to severe time-step constraints and stability issues.

Backward Euler (implicit):

$$\mathbf{M}^{n+1} = \mathbf{M}^n + \Delta t \mathbf{f}(\mathbf{M}^{n+1}, \mathbf{H}_{\text{eff}}^{n+1}). \quad (4.30)$$

Note that \mathbf{M}^{n+1} appears inside the function \mathbf{f} on the right-hand side – this makes the scheme implicit. Consequently, at each time step, a nonlinear system of equations must be solved to find \mathbf{M}^{n+1} .

For micromagnetic simulations where \mathbf{M} can change rapidly and nonlinearly, backward Euler and related implicit methods offer a pragmatic balance between stability and cost, allowing larger time steps while accurately tracking the magnetization dynamics [88].

4.2.4 Backward differentiation formulas

The BDF is a family of implicit, linear, multistep methods that are particularly well suited for stiff differential equations [158, 161, 162]. In FEM software such as COMSOL, the BDF scheme is implemented in an adaptive manner: both the time step Δt and the method order p can change dynamically based on local error estimates. This adaptability is highly advantageous in micromagnetic simulations, where the LLG equation can be stiff, with fast precessional modes alongside slower magnetization relaxation dynamics.

In analogy to Eq. 4.13, a generic initial-value problem is

$$\frac{du}{dt} = f(t, u(t)), \quad u(t_0) = u_0. \quad (4.31)$$

A BDF scheme of order p approximates du/dt at the current time t_n by referencing the solution values at p previous time steps:

$$\left. \frac{du}{dt} \right|_{t_n} \approx \frac{1}{\Delta t} \sum_{i=0}^p \xi_i u_{n-i}, \quad (4.32)$$

where $\Delta t = t_n - t_{n-1}$ is the time step (which can be adjusted from one step to the next), and ξ_i are coefficients of order p . In practice, this discrete approximation is then implicitly combined with the original differential equation:

$$\sum_{i=0}^p \xi_i u_{n-i} = \Delta t \mathbf{f}(t_n, u_n). \quad (4.33)$$

Since u_n (the unknown at time t_n) appears on the right-hand side, each step involves solving a (potentially nonlinear) algebraic system for u_n . If \mathbf{f} is nonlinear, methods such as Newton's iteration are used (see Sec. 4.4.3.6).

A-stability and L-stability. BDF schemes up to a certain order (especially BDF₁ and BDF₂) have *A-stability*, i.e., they do not introduce artificial growth in solutions for stiff problems whose eigenvalues have non-positive real parts. Some BDF variants also have *L-stability*, which enhances A-stability by further damping transient high-frequency modes. These stability properties are important in micromagnetism, where rapid oscillations can coexist with slower, more dissipative processes [158].

During micromagnetic simulations (e.g., magnetization relaxation), the LLG equation can behave in a stiff manner: high damping can cause fast initial transients, while the system eventually evolves slowly toward an equilibrium state. BDF methods handle such stiffness by allowing relatively large time steps Δt without sacrificing stability. In COMSOL's adaptive BDF solver, both Δt and the method order p are automatically selected to balance accuracy and efficiency.

Because of these properties, BDF methods have been the primary choice for my time-domain simulations in COMSOL, especially for magnetization relaxation. Their implicit multistep nature, coupled with A/L-stability, provides a reliable way to handle the stiffness of the LLG equation while maintaining a practical compromise between accuracy, stability, and computational cost.

4.2.5 Generalized- α method

The generalized- α method was originally developed for second-order problems in structural dynamics [163, 164]. However, its ability to introduce user-controllable numerical damping at high frequencies makes it attractive also for transient micromagnetic simulations, where rapid magnetization oscillations can coexist with slower relaxation processes. By tuning two parameters, α_m and α_f , high-frequency noise can be suppressed without excessively damping lower-frequency modes, thereby preserving long-time accuracy. Moreover, this implicit approach handles stiffness well and impose fewer restrictions on the time step Δt than typical explicit methods.

While the method is most commonly used for second-order systems (e.g., structural vibration with mass, damping, and stiffness matrices), it can be adapted to first-order problems such as the LLG equation. In the standard second-order form, α_m and α_f are used to evaluate the system at 'intermediate' time steps:

$$\left. \frac{du}{dt} \right|_{t_n + \alpha_m} = (1 - \alpha_m) \left. \frac{du}{dt} \right|_{t_n} + \alpha_m \left. \frac{du}{dt} \right|_{t_{n+1}}, \quad (4.34)$$

$$u(t_{n+\alpha_f}) = (1 - \alpha_f) u(t_n) + \alpha_f u(t_{n+1}). \quad (4.35)$$

In the micromagnetic context, where the magnetization $\mathbf{M}(\mathbf{r}, t)$ satisfies a first-order partial differential equation in time, the generalized- α method can be applied directly by interpreting $u \rightarrow \mathbf{M}$ and $du/dt \rightarrow \partial \mathbf{M} / \partial t$ in the Eqs. 4.34 and 4.35. The core idea remains unchanged: the method introduces intermediate evaluations of both the solution and its time derivative – specifically at $t_{n+\alpha_f}$ and $t_{n+\alpha_m}$, respectively – by forming convex combinations of their values at the previous and current time steps. These interpolated states are then used to evaluate the effective magnetic field and any nonlinear contributions in the LLG equation. The result is a nonlinear, implicit system for \mathbf{M}_{n+1} , that must be solved at each time step. By tuning the parameters α_m and α_f , the numerical damping of high-frequency modes can be controlled (and reduced if unwanted) while preserving the accuracy of physically relevant dynamics.

While BDF remains a ‘go-to’ method for highly stiff problems, generalized- α can be advantageous when a controlled damping of high-frequency components is desired, or when slightly lower computational cost is beneficial.

4.3 Boundary conditions

Appropriate boundary conditions are essential for realistic simulations. Three typical classes are:

- **Periodic boundary conditions (PBCs)**, used in simulations of translational symmetry systems such as photonic, phononic, or magnonic crystals. They assume that the field is invariant under translations by lattice vectors, effectively modeling an infinite periodic medium using a single unit cell. This can be expressed as:

$$u(\mathbf{r} + \mathbf{R}) = u(\mathbf{r}), \quad (4.36)$$

where $u(\mathbf{r})$ is a scalar or vector field, and \mathbf{R} is any lattice translation vector (e.g., $\mathbf{R} = n_x L_x \hat{\mathbf{x}} + n_y L_y \hat{\mathbf{y}} + n_z L_z \hat{\mathbf{z}}$ with integers n_x, n_y, n_z and unit cell dimensions L_x, L_y, L_z). These conditions allow a finite computational domain to mimic the behavior of an infinite periodic system.

- **Bloch/Floquet⁴ boundary conditions** which extend the PBC concept by including a phase relationship between opposite faces of a periodic unit cell. Formally, these conditions are

$$u(\mathbf{r}_1) = u(\mathbf{r}_2) e^{i\mathbf{k} \cdot (\mathbf{r}_2 - \mathbf{r}_1)}, \quad (4.37)$$

where $u(\mathbf{r}_1)$ and $u(\mathbf{r}_2)$ are the field values at the corresponding points \mathbf{r}_1 and \mathbf{r}_2 on opposite sides, and \mathbf{k} is the wavevector capturing the phase shift between them. This approach is particularly relevant for the analysis of wave propagation and dispersion in periodic media.

⁴Bloch’s theorem (commonly used in solid-state physics) and Floquet’s theorem (from the mathematical theory of differential equations) describe essentially the same concept in the context of solutions with periodic structures; hence the terms ‘Bloch boundary conditions’ and ‘Floquet boundary conditions’ are often used interchangeably.

- **Free boundary conditions**, which represent the absence of external constraints at the boundaries of the simulation domain. They allow the field – whether magnetization, displacement, or any other physical quantity – to evolve naturally at the boundaries, without forcing continuity or fixed values. This approach is particularly useful for modeling finite, isolated systems such as nanostructures or localized excitations, where boundary effects are important.
- **Absorbing boundary conditions** are used to minimize the reflections of spin waves or other excitations at the simulation boundaries. They effectively ‘absorb’ energy at the boundaries, preventing artificial reflections that could affect the simulation results.

4.4 Overview of software tools for micromagnetic simulations

This section provides an overview of three software packages that I have used for micromagnetic simulations: MuMax3, tetmag, and COMSOL Multiphysics. Each of these tools employs a distinct numerical formulation and excels in addressing specific classes of problems, offering comprehensive support for both time- and frequency-domain simulations. Moreover, they collectively incorporate all the time-integration and spatial discretization methods discussed earlier in this chapter. By leveraging their complementary solver capabilities, it becomes possible to simulate a wide range of advanced micromagnetic systems. The insights gained from working with these diverse tools have significantly broadened the scope of this research, enabling more robust and detailed analyses of complex magnetization dynamics.

4.4.1 MuMax3 (used in P1, P2, P3, P6)

MuMax3 is a highly optimized GPU-accelerated micromagnetic simulation software that solves the LLG equation in the time domain using the FDM [146]. It is specifically designed to handle extensive simulations by GPU parallelization, which significantly reduces the computation time. This section describes how MuMax3 implements the core components of the micromagnetic model used to perform the simulations for papers P1–3 and P6.

The kernel uses a one-size cubic grid to discretize the entire simulation domain. Each cell holds the local magnetization vector and material properties (such as M_s and A_{ex}), and its uniform shape ensures that each simulated region has identical resolution, which is optimal for GPU-based parallel computation. Although the grid simplifies the implementation, it is crucial to ensure that the spacing is fine enough to resolve important magnetic length scales, depending on the specifics of the simulation. For simulations involving short spin waves (such as dipole–exchange or pure exchange modes), or in systems with highly noncollinear static magnetization configurations, the discretization cell size must be sufficiently small to accurately capture these spatial variations and avoid numerical artifacts. In the one-dimensional case, the exchange length ℓ_{ex} (see Eq. 3.3) provides an inherent scale for setting the spatial resolution. A

generally accepted condition [165] is that the cell size Δx should satisfy

$$\Delta x < \ell_{\text{ex}}. \quad (4.38)$$

This criterion ensures that the exchange interaction is properly captured within the numerical mesh and that the spatial features of the magnetization are well resolved. It should be noted, however, that this condition is not universally required. For uniformly magnetized systems, or for long wavelength excitations, a coarser discretization may still give accurate and stable results.

According to the Nyquist–Shannon sampling criterion [166], to resolve a wave propagating in x direction of wavelength λ in a discrete mesh, the cell size must also satisfy

$$\Delta x \leq \frac{\lambda}{2}. \quad (4.39)$$

By ensuring this condition, the simulation correctly captures wave propagation and dispersion. If Δx is greater than half of the wavelength, the mesh will effectively ‘undersample’ the spin wave, resulting in aliasing or even inability to detect these excitations.

There is also the Courant–Friedrichs–Lewy (CFL) condition [167], which ensures numerical stability in time-dependent PDE solvers. It is particularly relevant in FDM, especially when applied to hyperbolic PDEs such as wave equations. The condition states that the time step must be sufficiently small relative to the spatial discretization to maintain stability. In its basic one-dimensional form for a wave equation, the CFL condition is expressed as

$$\Delta t \leq \frac{\Delta x}{v_{\text{max}}}, \quad (4.40)$$

where v_{max} is the maximum wave propagation speed along the x -axis. This requirement ensures that a numerical wave does not travel more than one spatial grid cell during a single time step, thereby preserving stability and accuracy in the simulation. If this condition is violated, the simulation may become numerically unstable, leading to unphysical results. In micromagnetic simulations, the effective speed of wave propagation is given by the spin-wave group velocity. Thus, the time step Δt must be carefully chosen to always satisfy the Eq. 4.40 for a given velocity and spatial discretization Δx . In MuMax3, the RK45 adaptive time-stepping scheme [155, 160] generally handles this by dynamically adjusting the time step to ensure stability. However, if a user manually sets a time step in MuMax3 (e.g., using fixed-step methods), the CFL condition should be considered. If the time step is too large, the simulated system may “skip” important dynamics.

MuMax3 efficiently calculates the demagnetizing (dipolar) field using the fast Fourier transform (FFT). Its long-range nature makes it computationally expensive, but MuMax3 reduces the complexity from $\mathcal{O}(\tilde{N}^2)$ to $\mathcal{O}(\tilde{N} \log \tilde{N})$, where \tilde{N} is the number of grid cells, applying FFT-based convolution techniques⁵. For dipolar interactions, a naive approach requires computing pairwise

⁵In computational complexity, the notation \mathcal{O} describes how the runtime or resource consumption of an algorithm scales with the size of the problem.

interactions between all \tilde{N} grid cells, resulting in a quadratic scaling of computation, expressed as $\mathcal{O}(\tilde{N}^2)$. However, specialized algorithms (such as those using FFTs) can reduce this complexity to $\mathcal{O}(\tilde{N} \log \tilde{N})$. This means that as \tilde{N} grows, the computational complexity of FFT-based methods increases more slowly than that of direct pairwise computations, making large-scale simulations more computationally feasible. This enables the MuMax3 software to simulate such systems while accurately accounting for the nonlocal nature of the dipolar field. For time integration, however, this software uses the adaptive RK45 method described in Sec. 4.2.1.

For efficient energy minimization of the magnetic system, MuMax3 provides a built-in `relax()` function [146]. It modifies the LLG equation by disabling all precessional terms, thereby transforming it into a dissipative form. As a result, the magnetization evolves directly along the gradient of decreasing total energy, allowing rapid convergence to a stable equilibrium. The system is first allowed to evolve over time until the total magnetic energy drops to the level of numerical noise, indicating that it has nearly reached equilibrium. The algorithm then begins to track the magnitude of the torque, which decreases steadily near equilibrium. The minimization process is terminated once the torque falls below a predefined threshold, indicating convergence. This method ensures that the system settles into a locally stable energy minimum before any dynamic simulations are initiated.

In most of my FDM simulations, I used PBCs and absorbing boundary conditions simultaneously. For example, to reproduce the magnetization patterns of the Talbot ‘carpet’ (publications P1–P3), it was necessary to simulate a quasi-infinite one-dimensional array of apertures. Meanwhile, along the boundary perpendicular to this array, spin waves had to be absorbed to prevent reflections that would otherwise interfere with the results. In MuMax3, absorbing boundary conditions are typically implemented by gradually increasing the Gilbert damping parameter α near the edges of the simulation domain to ensure that spin waves are absorbed when they reach the boundary. Specifically, α is increased from its bulk value α_0 to a larger value α_{\max} according to

$$\alpha(x) = \alpha_0 + (\alpha_{\max} - \alpha_0) \left(\frac{x - x_0}{d} \right), \quad (4.41)$$

where x_0 is the coordinate that marks the start of the absorbing, and d is the distance over which the damping increases. This gradual transition prevents reflection artifacts that might occur if the damping were increased abruptly.

Equipped with FDM, appropriate time integrators, and customizable boundary conditions, MuMax3 is a well-established numerical framework for micromagnetic simulations. Its simplicity, combined with GPU acceleration, provides a powerful tool for modeling spin-wave phenomena, magnetic domain evolution, and other nanoscale magnetic behaviors.

4.4.2 Tetmag (used in P7)

In my research P7, I used the open-source GPU-accelerated micromagnetic finite element micromagnetic solver called tetmag [148]. It simultaneously employs both FEM and BEM concepts (see Secs. 4.1.2 and 4.1.3) to handle complex nanomagnetic geometries. As discussed earlier,

FEM offers flexibility in capturing curved or irregular boundaries, while tetmag further enhances this with a hybrid finite/boundary element approach (FEM–BEM) for efficient magnetostatic computations in open-boundary conditions [168].

A key feature of its performance is the hierarchical \mathcal{H}^2 -matrix technique, which significantly reduces the computational cost of large-scale magnetostatic field calculations (described below). Classical solvers often face an $\mathcal{O}(\tilde{N}^2)$ complexity when considering all pairwise interactions among \tilde{N} elements. To address this problem, tetmag also uses finite elements within the magnetic domain and boundary elements on the surfaces, thus limiting the region that must be discretized for long-range field calculations [168]. This approach implies that the finite-element domain only represents the magnetic body itself, while the BEM handles the outer boundaries, thus ensuring physically correct open-boundary conditions without the need for large artificial vacuum extensions.

4.4.2.1 Hierarchical \mathcal{H}^2 -matrices algorithm.

The largest computational cost in magnetostatic analysis comes from the dense matrix operations required to capture interactions among all pairs of elements (or surface panels). Tetmag overcomes the $\mathcal{O}(\tilde{N}^2)$ bottleneck by using FEM–BEM formalism, as well as by adopting \mathcal{H}^2 -matrices [168]. This approach approximates far-field interactions (where elements are spatially distant) by low-rank factorizations while preserving near-field interactions in full detail. In particular, the global interaction block A_{ij} between the element clusters i and j can be approximated by a low-rank factorization:

$$A_{ij} \approx U_i B_{ij} V_j^T, \quad (4.42)$$

where U_i and V_j^T are low-rank basis matrices associated with clusters i and j , respectively, and B_{ij} is a small coupling matrix. This structure allows efficient representation of long-range interactions by reusing basis matrices across multiple blocks⁶.

By organizing these approximations hierarchically, the memory and computational cost is reduced to $\mathcal{O}(\tilde{N} \log \tilde{N})$, while maintaining good accuracy for large problems. This makes it possible to simulate micromagnetic systems with tens or hundreds of millions of degrees of freedom on modern GPU-accelerated platforms.

In practice, my simulations with tetmag for work P7 proceeded in two main phases:

1. **Magnetization relaxation.** The solver first increases the damping parameter α in the dynamic equation, driving the magnetization to a stable equilibrium under a given external field. Once the torque falls below a threshold, the damping is reset to its nominal value.
2. **Dynamic perturbation.** After relaxation, the specialized frequency-domain algorithm (proposed by d’Aquino et al. [156, 169]) is used to study FMR-like excitations. Although not part of the tetmag kernel, this algorithm is integrated into the simulation workflow.

⁶The block A_{ij} is the submatrix of the global matrix A , which represents interactions between all elements in clusters i and j .

For time integration, tetmag uses the SUNDIALS/CVODE library [170], which provides adaptive time stepping through robust implicit solvers, well-suited for stiff micromagnetic systems. This allows to accurately capture complex dynamics, even in cases with strong exchange interactions or magnetic anisotropy.

By combining the FEM–BEM approach with \mathcal{H}^2 -matrices, tetmag achieves high efficiency and scalability for open-boundary nanomagnetic simulations. This architecture enabled the large-scale computations presented in P7, where the solver accurately modeled magnetization distributions and resonance phenomena in geometrically complex gyroidal nanostructures.

4.4.3 COMSOL Multiphysics (used in P4, P5, P8, P9)

COMSOL Multiphysics has been my primary tool for conducting micromagnetic simulations [147]. Its strength lies in its ability to accurately model and solve complex physical phenomena while integrating multiple physics modules within a finite-element-based framework. For example, it can capture magneto-elastic interactions, thermal effects, and electrical phenomena such as STT or magnetoresistance – all in addition to standard magnetization dynamics. These capabilities make COMSOL a powerful and versatile micromagnetic simulation tool for detailed analysis of magnetization interactions and dynamics in time and/or frequency domain. Furthermore, COMSOL allows for manual definition and customization of the governing equations through the interface Coefficient Form PDE.

This section explains how the LLG equation is implemented in the software, focusing on time-domain, eigenfrequency, and frequency-domain simulations. It also covers the numerical methods used and how the environment manages error control to ensure accurate outcomes.

4.4.3.1 Coefficient Form PDE

The Coefficient Form PDE in COMSOL allows users to manually implement custom PDEs by specifying various terms and coefficients. It provides the flexibility to work with custom equations, or simply those not included in the built-in physics modules, as in this case. They are expressed in a general form with up to second-order derivatives in time and space, which is suitable for the LLG equation. The Coefficient Form PDE is represented as:

$$e_a \frac{\partial^2 u}{\partial t^2} + d_a \frac{\partial u}{\partial t} + \nabla \cdot (-c \nabla u - \alpha' u + \gamma') + \beta \cdot \nabla u + au = f \quad \text{in } \Omega, \quad (4.43)$$

$$\mathbf{n} \cdot (c \nabla u + \alpha u - \gamma') = g - qu + h^T \mu \quad \text{on } \partial\Omega, \quad (4.44)$$

$$0 = R \quad \text{on } \partial\Omega_c, \quad (4.45)$$

$$u = r \quad \text{on } \partial\Omega_d, \quad (4.46)$$

where u is the dependent variable, corresponding here to components of magnetization \mathbf{M} . In Eq. 4.43, from left to right, there are several coefficients which represent to the following physical terms:

- e_a – mass coefficient,
- d_a – damping or mass coefficient,
- c – diffusion coefficient,
- α' – conservative flux convection coefficient (not to be confused with Gilbert damping α),
- β – convection coefficient,
- a – absorption coefficient,
- γ' – conservative flux source term (not to be confused with gyromagnetic ratio γ),
- f – source term.

Equation 4.44 represents a generalized form of the Neumann boundary condition, that must be satisfied at the domain boundary $\partial\Omega$, where:

- \mathbf{n} denotes the outward-pointing unit normal vector at the boundary $\partial\Omega$,
- g is the boundary source term,
- q is the boundary absorption coefficient.

Equations 4.45 and 4.46 represent a general constraint, with a Dirichlet boundary condition as a special case, respectively, where R and r are predefined boundary terms.

In the context of my calculations of the LLG equation, the Coefficient Form PDE was used to manually define the cross-product term $\mathbf{M} \times \mathbf{H}_{\text{eff}}$, and the damping term $\mathbf{M} \times \partial\mathbf{M}/\partial t$. The spatial and time derivatives were computed in the FEM framework, and the various contributions to the effective magnetic field \mathbf{H}_{eff} were taken from the Eqs. 3.1 and 3.14. Its final form is

$$\mathbf{H}_{\text{eff}} = H_0 \hat{\mathbf{r}} + \frac{2A_{\text{ex}}}{\mu_0 M_s^2} \nabla^2 \mathbf{M} - \nabla \varphi, \quad (4.47)$$

and contains, in order, components responsible for magnetization interactions with the external field (Zeeman energy – Sec. 3.1.4), exchange interactions (Sec. 3.1.1) and dipole interactions (Secs. 2.8 and 3.1.2). To represent LLG with the assumed effective field (Eq. 4.47), the following matrix form coefficients were adapted to the Eq. 4.43:

$$\begin{aligned} d_a &= \frac{\alpha}{M_s} \begin{pmatrix} 1 & m_z & -m_y \\ -m_z & 1 & m_x \\ m_y & -m_x & 1 \end{pmatrix}, & a &= |\gamma| \mu_0 H_0 \begin{pmatrix} 0 & \hat{\mathbf{z}} & -\hat{\mathbf{y}} \\ -\hat{\mathbf{z}} & 0 & \hat{\mathbf{x}} \\ \hat{\mathbf{y}} & -\hat{\mathbf{x}} & 0 \end{pmatrix}, \\ c &= \frac{2A_{\text{ex}} |\gamma|}{M_s^2} \begin{pmatrix} 0 & m_z & -m_y \\ -m_z & 0 & m_x \\ m_y & -m_x & 0 \end{pmatrix}, & f &= |\gamma| \mu_0 \begin{pmatrix} m_y \frac{\partial \varphi}{\partial z} - m_z \frac{\partial \varphi}{\partial y} \\ m_z \frac{\partial \varphi}{\partial x} - m_x \frac{\partial \varphi}{\partial z} \\ m_x \frac{\partial \varphi}{\partial y} - m_y \frac{\partial \varphi}{\partial x} \end{pmatrix}. \end{aligned} \quad (4.48)$$

All other undefined coefficients from Eq. 4.43 are equal to 0. To ensure the physical consistency of the simulations, it was also necessary to impose a condition that preserves the magnitude of

the magnetization vector throughout each stage of the simulation:

$$m_x^2 + m_y^2 + m_z^2 = M_s^2. \quad (4.49)$$

4.4.3.2 Implementation of boundary conditions in COMSOL

FEM handles boundary conditions naturally through its variational (or weak) formulation. For example, Dirichlet conditions can be enforced by specifying nodal values along the domain edges or faces, and Neumann conditions (typically involving the normal derivative $\partial \mathbf{M} / \partial n$) appear as flux terms in surface integrals (more details in Sec. 4.3). The resulting constraints affect the global system $\mathbf{KM} = \mathbf{F}$ (see Sec. 4.1.2.1) by modifying rows or columns corresponding to boundary nodes.

This process results in an algebraic system that captures both the internal physics and the boundary conditions. At each time step (once the global system is assembled), it is solved using iterative methods (e.g., the conjugate gradient, more in Sec. 4.4.3.6) or direct factorization techniques, depending on the size and stiffness of the problem. The result is a piecewise polynomial approximation of the magnetization vector \mathbf{M} that naturally satisfies the geometry and boundary conditions, providing greater flexibility than uniform-grid approaches. However, as with FDM, cell sizes must be carefully chosen to resolve the relevant magnetic lengths, ensuring that the solution accurately captures domain walls, spin waves, or vortex cores.

The boundary conditions used in my COMSOL simulations depend on whether the system is finite or quasi-infinite/periodic. For the former, I used zero flux boundary conditions (as described in Sec. 4.3) to represent open boundaries. This condition ensures that no magnetic flux crosses the domain boundary, allowing magnetization dynamics (such as spin waves) to exit the simulation region with minimal reflection. Mathematically, this boundary condition can be expressed as a modification of Eq. 4.45:

$$\mathbf{n} \cdot (c \nabla u + \alpha' u - \gamma') = 0 \quad \text{on } \partial \Omega. \quad (4.50)$$

In addition, accurate convergence of micromagnetic simulations in pure FEM requires surrounding the magnetic structure with a sufficiently large non-magnetic volume (typically air or vacuum) in which the static magnetic potential can dissipate and decay smoothly. To ensure that the simulation results are unperturbed by boundary effects, Dirichlet conditions are applied to the outer boundaries Ω_c of this surrounding domain ($\varphi = 0$ on Ω_c). They eliminate the magnetic field at the boundaries, thus preventing reflections or artifacts that could interfere with the magnetic behavior of the system under study.

For periodic systems, such as those used to study FMR modes in P9, PBCs have been applied by matching magnetization values at opposite edges (see Eq. 4.36), effectively simulating an infinitely repeating structure. However, for dispersion relations in periodic structures, COMSOL's Pointwise Constraint Boundary node proved more suitable. This tool allows the constraint to be defined between corresponding points on opposite sides of the unit cell, effectively extending the

standard PBCs by enforcing phase continuity across boundaries. In doing so, it implements the Bloch/Floquet boundary condition (Eq. 4.37), as discussed in Sec. 4.3.

4.4.3.3 Time-domain solver

COMSOL Multiphysics offers many time-stepping methods suitable for both stiff and non-stiff systems, including those described earlier – such as RK, Euler, BDF, and the generalized- α (see Sec. 4.2). When solving micromagnetic or other coupled multiphysics systems, the stability and convergence of the solution are highly sensitive to the choice of time-integration scheme. As outlined in the Tab. 4.1, for stiff problems, implicit methods like BDF or generalized- α provide the robustness needed for stable and accurate results. In contrast, for non-stiff scenarios, explicit methods such as RK or Euler may offer a more efficient solution strategy due to their lower computational cost.

4.4.3.4 Frequency-domain solver

The frequency-domain solver in COMSOL computes the steady-state magnetization response under harmonically varying external fields, making it well-suited for simulating spin-wave propagation and resonance phenomena in dynamically excited magnetic materials. In this formulation, the magnetization \mathbf{M} oscillates about an equilibrium configuration \mathbf{M}_0 according to Eq. 3.36. The solver iterates over a specified frequency range, treating ω as a parameter in the governing equations and solving for $\delta\mathbf{M}(x,y,z)$ at each frequency. By capturing the steady-state harmonic solution, it shows how the system's resonances and spin-wave modes depend on ω . Key results include amplitude and phase distributions of $\delta\mathbf{M}$ from which damping or band structures relevant to spin-wave dispersion can be identified. This method complements time-domain analysis by allowing direct mapping of the magnetic response over a range of frequencies, rather than simulating the entire transient process.

It is important to note, however, that unlike the eigenfrequency solver (described in the next section), the results obtained with this approach are inherently dependent on the specific form of the applied excitation field. This field can be designed to approximate experimental measurement techniques, such as coplanar waveguides (CPW), thus allowing a more accurate comparison between numerical simulations and experimental observations. Because the solver linearizes the dynamical equations around \mathbf{M}_0 (see Sec. 3.2.2.2), it remains efficient for exploring spin-wave behavior for sufficiently small-amplitude oscillations. For nonlinear or large-amplitude excitations, time-domain or nonlinear methods (Sec. 4.4.3.6) are more appropriate, but for a broad class of small-signal analyses, the frequency-domain approach provides a direct and efficient path to understanding the spectral characteristics of spin waves and other magnetization dynamics [73, 113].

4.4.3.5 Eigenfrequency solver

The eigenfrequency solver in COMSOL computes natural frequencies (eigenfrequencies) and associated eigenmodes (vector fields) by solving large-scale eigenvalue problems, typical of finite element formulations. It is based on the ARnoldi PACKAge (ARPACK), which focuses on finding a selected subset of eigenvalues and eigenvectors in sparse eigenvalue problems [171, 172]. ARPACK employs the implicitly restarted Arnoldi method (IRAM), an iterative procedure that approximates eigenvalues for large sparse matrices with reduced computational cost. In scenarios involving harmonic oscillations, it is convenient to use COMSOL's eigenvalue version of the Coefficient Form PDE to solve the eigenfunction u :

$$\nabla \cdot (-c \nabla u - \alpha' u) + \beta \cdot \nabla u + a u = \lambda d_a u - \lambda^2 e_a u, \quad (4.51)$$

where λ is the complex eigenfrequency, while d_a and e_a capture the linear and quadratic frequency dependencies that are crucial for the oscillatory behavior. The imaginary part of λ represents the decay rate, while the real part corresponds to the oscillation frequency ω . The eigensolver was applied to the linearized LLG equation to determine the eigenmodes and corresponding eigenfrequencies of the magnetization dynamics. The coefficients were then defined analogously to those in Eqs. 4.43–4.46.

Generalized eigenvalue problem. In finite element contexts, an eigenvalue problem often appears in the generalized form:

$$A u = \kappa B u, \quad (4.52)$$

where A and B are typically stiffness- and mass-like matrices, respectively, and eigenvalues κ correspond to the squares of the angular frequencies, $\kappa = \omega^2$. Direct diagonalization of such large sparse matrices is computationally expensive, so COMSOL implements iterative methods, notably IRAM, which projects the problem onto a lower-dimensional Krylov subspace:

$$K_m(A, v) = \text{span}\{v, Av, A^2v, \dots, A^{m-1}v\}, \quad (4.53)$$

where v is an initial vector, and the term span refers to the set of all possible linear combinations of the listed vectors. The method constructs an $m \times m$ Hessenberg matrix H_m so that

$$A V_m = V_m H_m, \quad (4.54)$$

with V_m forming an orthonormal basis of the subspace. Then a smaller eigenvalue problem with H_m is solved, and the corresponding eigenvalues approximate those of A . IRAM periodically restarts with a smaller basis to focus on the relevant part of the spectrum, reducing memory and computational cost while accurately converging to the target eigenvalues [171, 172].

Search methods. In COMSOL, the eigenfrequency solver has three main search methods that control how ARPACK finds the desired eigenvalues:

1. *Manual search.* The user specifies a shift σ , which prompts the solver to apply shift and inverse transformations:

$$(A - \sigma B)^{-1} B u = \mu_e u, \quad \lambda = \sigma + \frac{1}{\mu_e}, \quad (4.55)$$

where μ_e is the transformed eigenvalue. Eigenvalues near σ dominate, enabling efficient convergence in a specified frequency range.

2. *Region search.* The region search method limits ARPACK to a complex rectangular region:

$$\Re(\lambda) \in [\Re_{\min}, \Re_{\max}], \quad \Im(\lambda) \in [\Im_{\min}, \Im_{\max}], \quad (4.56)$$

extracting eigenvalues within user-defined real and imaginary boundaries. It is especially useful for systems with damping or complex frequency response.

3. *All (filled matrix).* This method attempts to capture the entire spectral range by constructing a broader Krylov space, effectively extracting many eigenvalues. Although computationally expensive, this approach is suitable for problems requiring extensive modal analysis over a wide range of frequencies.

In my research P4, P5, P8, and P9, ARPACK's IRAM proved to be sufficient to accurately capture the relevant eigenmodes in the simulated systems.

4.4.3.6 Linear and nonlinear methods

In COMSOL, the choice of linear or nonlinear solution methods is determined by the characteristics of the analyzed system. Linear methods are appropriate when the model can be represented by a constant coefficient matrix, while nonlinear methods are required when responses depend on the current state, demanding iterative refinement. This distinction has a significant impact on computational cost, convergence, and accuracy.

Linear solvers. For systems of the form $Ax = b$, where A is a constant matrix (independent of the vector of unknowns x), and b is known, COMSOL provides a set of linear solvers:

- **LU decomposition:** A direct method factorizing A into lower (L) and upper (U) triangular matrices such that $A = LU$. Solving $Ly = b$ then $Ux = y$ gives x . Although robust, it can be memory intensive for large, sparse systems.
- **Generalized minimal residual method (GMRES):** An iterative solver suitable for large, sparse, and nonsymmetric matrices. It minimizes the residual $\|b - Ax\|$ within a Krylov subspace generated by successive applications of A . Restarted versions limit the growth of the subspace to save memory [173].

- **Conjugate gradient (CG):** The conjugate gradient method targets symmetric positive-definite matrices by minimizing $f(x) = 1/2 x^T A x - b^T x$. Its efficiency and speed make it attractive for problems with suitable symmetry [174].

Nonlinear solvers. If the system has a nonlinear dependence on unknown variables, it can be written in the general form $\mathbf{F}(u) = 0$ (discretized residual form of the PDE and boundary conditions). Here, u can represent an equilibrium solution of a PDE or a set of unknown parameters in a nonlinear boundary-value problem. To solve such systems, COMSOL uses a Newton-based approach: it linearizes $\mathbf{F}(u)$ around the current approximation $u^{(k)}$ by constructing the Jacobian matrix

$$J = \left. \frac{\partial \mathbf{F}}{\partial u} \right|_{u^{(k)}} \quad (4.57)$$

and then solving a sequence of linearized subproblems at each iteration k to progressively improve the solution. While this approach is more computationally intensive than solving linear systems, it is critical for accurately handling strongly nonlinear material models, complex boundary conditions, and multiphysics couplings.

To improve the stability of these iterations, COMSOL uses the **damped Newton method** [175]:

$$u^{(k+1)} = u^{(k)} - \alpha_D J^{-1} \mathbf{F}(u^{(k)}), \quad (4.58)$$

where α_D is a damping factor that is dynamically adjusted to ensure that each update reduces the residual. This helps avoid large, destabilizing adjustments when improvements in the solution are marginal. Such damping also helps prevent divergence in regimes characterized by high nonlinearity, ensuring a more stable convergence to the accurate solution.

COMSOL also offers two main strategies for handling systems of multiple coupled equations:

- **Fully coupled method.** All equations are solved simultaneously within each iteration. This maximizes accuracy for strongly coupled problems but can be computationally and memory intensive.
- **Segregated method.** Equations are partitioned into smaller subsets that are iterated sequentially. This approach reduces memory requirements and often speeds up convergence for weakly coupled systems or very large models [175].

4.4.3.7 Termination criteria

COMSOL's iterative solvers stop searching for a solution when certain convergence conditions are met or when further progress is deemed unlikely. Standard termination checks include

- **Tolerance on residual norm.** The solver monitors the residual vector $\mathbf{r}(u)$ (e.g., $\mathbf{r}(u) = A u - b$ in a linear system) and stops when the norm $\|\mathbf{r}(u)\| < \epsilon_{\text{abs}}$, where ϵ_{abs} is a user-defined absolute tolerance. This threshold indicates that the steady state has effectively been reached, such that additional iterations will yield negligible improvement in $\mathbf{r}(u)$.

- **Relative tolerance.** Convergence can also be checked by examining the ratio of successive solution updates:

$$\frac{\| (u^{(k+1)} - u^{(k)}) \|}{\| (u^{(k)}) \|} < \epsilon_{\text{rel}}, \quad (4.59)$$

where ϵ_{rel} is a user-defined relative tolerance. If this ratio falls below ϵ_{rel} , the solver assumes that further iterations would only marginally improve to the solution.

- **Maximum number of iterations.** Each solver iteration requires computation to assemble and/or invert matrices. Therefore, COMSOL enforces a practical upper limit on the number of iterations. If neither the residual norm criterion nor the relative tolerance criterion is met before this limit is reached, the solver terminates. In such cases, users may need to:

- refine the mesh or initial guess,
- adjust solver settings (e.g., damping factors or step sizes),
- or modify model parameters (such as boundary conditions or material properties) to improve convergence.

These termination checks – along with automatic selection of linear vs. nonlinear solvers, adaptive damping strategies for stability, and adaptive time stepping – allow COMSOL to balance accuracy and computational cost for a wide range of applications [173, 175].

4.4.4 Concluding comparison

The FDM in MuMax3, FEM–BEM in tetmag and FEM in COMSOL Multiphysics offer different approaches to simulating micromagnetic phenomena, with each approach optimized for specific applications and geometries.

In terms of discretization, the FDM in MuMax3 operates on a uniform cubic grid, which makes it computationally efficient for large-scale and periodic simulations. However, this regular grid structure also comes with limitations: it struggles to accurately represent complex, non-rectangular geometries, as it cannot easily conform to curved or irregular boundaries (see Fig. 4.1). In contrast, FEM in tetmag and COMSOL allows for highly customizable meshes that enable accurate modeling of complex 3D nanostructures with irregular boundaries.

Boundary conditions are another area where each method has distinct advantages. MuMax3 applies PBCs efficiently, but to approximate the open boundaries, it requires a gradual increase in Gilbert damping near the domain edges – a method that may not eliminate reflections sufficiently for systems sensitive to wave dynamics. In contrast, finite-element-based tools such as tetmag and COMSOL offer more precise control over boundary conditions, including direct implementation of Dirichlet and Neumann conditions, allowing more accurate modeling of open or constrained domains.

MuMax3 solves the full LLG equation in the time domain, tetmag originally has only the time domain, but with an add-on module (used in my research) it allows for frequency-domain capabilities. COMSOL Multiphysics, on the other hand, in addition to the standard

time domain for full LLG, has native frequency-domain and eigenfrequency solvers that can linearize the LLG equation around a given steady-state solution. This is enhanced by the ability to define custom PDEs, further extending the versatility of FEM in this environment. By calculating the eigenvalues and eigenvectors of the linearized system, COMSOL can identify all intrinsic magnetic modes independently of any specific driving field. This eigenfrequency analysis provides a comprehensive characterization of the system's resonant behavior, making it particularly valuable for identifying fundamental spin-wave modes and their corresponding eigenfrequencies.

In terms of computational efficiency, MuMax3 benefits significantly from GPU acceleration, enabling fast simulations in extensive domains. This makes it ideal for studies of large domain dynamics, where geometric complexity is limited. Tetmag, while also GPU-accelerated, generally demands more memory and processing power due to the complex structure and elements of FEM. The use of \mathcal{H}^2 -matrices helps reduce the computational cost, but FEM still requires more resources per degree of freedom than FDM. The FEM solver used in COMSOL is CPU-based, so the computation time can be relatively long, especially for large or highly dynamic systems.

For time stepping, MuMax3 uses an explicit RK45 method, which provides good accuracy but requires smaller time steps in stiff systems. Both tetmag and COMSOL use implicit methods by default, which handle stiffness more effectively. The BDF and generalized- α methods, for example, allow larger time steps in stiff systems and provide stability for highly dynamic conditions, but at a higher computational cost. Although computationally intensive, COMSOL is well-suited for applications requiring complex boundary control, multiphysics coupling, and, most importantly (from my perspective), a dedicated frequency-domain and eigenfrequency solver with the ARPACK algorithm. The options for targeted resonance studies are particularly useful for analyzing frequency-dependent behavior in complex nanostructures.

The exploration of numerical methods in micromagnetism reveals a rich and intricate field, with each approach offering unique strengths suited to different types of simulations. The methods presented in this chapter illustrate the variety of numerical techniques available to researchers. Whether it is the GPU acceleration of MuMax3, the open-boundary treatment of tetmag's hybrid FEM–BEM approach, or the advanced frequency-domain analysis capabilities of COMSOL Multiphysics, each software tool has unique strengths that allow different facets of micromagnetic phenomena to be investigated with efficiency and precision.

The development and application of numerical methods in micromagnetic simulations play a crucial role in advancing both the theoretical and applied aspects of magnetism. By bridging complex physical theories with practical computational tools, these methods allow us to study magnetic behaviors that are difficult to capture experimentally, especially at the nanoscale.

Chapter 5

Research

This chapter presents the core publications that form the foundation of my Ph.D. research, each addressing specific aspects of spin-wave dynamics and their control in nanostructured magnetic systems. These studies cover a spectrum of topics ranging from planar waveguide simulations with 1D diffraction gratings to spin-wave behavior in complex 3D architectures. Each publication is preceded by a short introduction summarizing the objectives, methodology, and main results of the study, followed by a brief statement outlining my contributions to the given work.

The research sequence reflects a structured progression from fundamental analyses of spin waves obstructed by 1D antidot arrays and their unique interference patterns, through dynamics in 2D systems such as ADLs and crescent-profile waveguides, to explorations of more advanced multidimensional and periodic 3D structures, including gyroid and scaffold-like networks. However, it is important to note that the chronological order of the studies is reflected by the labels P1–P9, which follow the sequence of their publication dates.

This collection demonstrates how targeted nanoscale structuring enhances control over magnetic and spin-wave properties, providing insights relevant to the development of magnonic devices and spin-based computing applications.

5.1 One-dimensional nanostructures

By introducing periodic modulations in magnetic properties or geometry, 1D nanostructures act as engineered scattering centers, selectively influencing spin-wave modes and enabling tailored dispersion characteristics. In particular, diffraction gratings exploit periodicity to create resonant conditions that enable unique wave interactions, including diffraction, bandgap formation, and mode coupling. In magnonics, such structures can support phenomena analogous to those in optics. In my research, diffraction gratings serve as a platform for studying complex wave phenomena, such as the Talbot effect, where self-imaging of wavefronts can occur under certain conditions. These effects provide fundamental insights into wave behavior in structured magnetic systems and offer practical applications by creating reconfigurable magnonic interference patterns that hold promise for future spintronic and magnonic computing architectures.

Although the waveguides are modeled using 2D micromagnetic simulations, the self-imaging patterns observed in this research are governed by the one-dimensional diffraction grating (or 1D array of single-mode input waveguides), justifying the categorization of this work as focused on 1D textures.

5.1.1 Demonstration of spin-wave self-imaging effect (P1)

This paper investigates the self-imaging phenomenon, or Talbot effect, for spin waves – a novel demonstration of this well-known wave phenomenon outside the field of optics. By introducing a 1D diffraction grating in a thin ferromagnetic film, we show through LLG-based micromagnetic simulations that spin waves can undergo self-imaging, a behavior typically associated with light waves. To our knowledge, this study is the first to establish and describe the Talbot effect for spin waves, and to show that the resulting Talbot ‘carpets’ can be effectively characterized using approximate analytical expressions adapted from general wave theory. This work not only opens avenues for the experimental realization of spin-wave self-imaging, but also highlights potential applications in magnonics, where structured interference patterns could be exploited for wave-based data processing.

Contribution of the Author

In this publication, I have systematically collected, structured, and adapted theoretical concepts from physical optics and wave theory, adapting them to provide a comprehensive framework for describing the Talbot effect in the context of magnonics. I also performed all the micromagnetic simulations using MuMax3, post-processed the data, and contributed to the interpretation of the results in collaboration with M. Krawczyk and P. Gruszecki. Finally, I wrote the first draft of the manuscript, managed its submission to the journal, and corresponded with the reviewers throughout the review process.

The article reprinted with permission from Gołębiewski, M.; Gruszecki, P.; Krawczyk, M.; Serebryannikov, A. E. *Physical Review B* **102**, 13, 134402 (2020) ©2020 American Physical Society. License number: RNP/25/FEB/088088.

Spin-wave Talbot effect in a thin ferromagnetic film

Mateusz Gołębiewski ^{1,*}, Paweł Gruszecki ^{1,2}, Maciej Krawczyk ^{1,†} and Andriy E. Serebryannikov¹

¹*Faculty of Physics, Adam Mickiewicz University, Uniwersytetu Poznańskiego 2, 61-614 Poznań, Poland*

²*Institute of Molecular Physics, Polish Academy of Sciences, Mariana Smoluchowskiego 17, 60-179 Poznań, Poland*



(Received 8 March 2020; revised 15 May 2020; accepted 26 August 2020; published 5 October 2020)

The Talbot effect has been known in linear optics since the 19th century and has found various technological applications. In this paper, with the help of micromagnetic simulations, we demonstrate the self-imaging phenomenon for spin waves in a thin, out-of-plane and in-plane magnetized ferromagnetic film whose propagation is described by the Landau-Lifshitz nonlinear equation. We show that the main features of the obtained Talbot carpets for spin waves can be described, to a large extent, by the approximate analytical formulas yielded by the general analysis of the wave phenomena. Our results indicate a route to a feasible experimental realization of the Talbot effect at low and high frequencies and offer interesting effects and possible applications in magnonics.

DOI: [10.1103/PhysRevB.102.134402](https://doi.org/10.1103/PhysRevB.102.134402)

I. INTRODUCTION

Spin waves (SWs) are coherent disturbances of the magnetization which may propagate in magnetic material as waves. In ferromagnetic materials, the SW dynamics is determined by strong isotropic exchange interactions coexisting with anisotropic magnetostatic interactions. In thin ferromagnetic films, the magnetostatic interactions cause the SW properties to be strongly dependent on the magnetization orientation with respect to the film plane and also dependent on the relative orientation of the propagation direction and the static magnetization vector. This makes the studies of SWs interesting and offers properties uncommon for other types of waves, such as negative group velocity, caustics, and dynamic reconfigurability control. Their frequency spans range from a few to hundreds of gigahertz, with the corresponding wavelength range extending from micrometers to tens of nanometers, which makes them very attractive for applications in microwave technology. In this context, it is interesting to test in magnonics the basic laws that govern wave phenomena and search for analogs of the effects known for electromagnetic or acoustic waves. Basic equations describing propagation of SWs differ from those for electromagnetic and acoustic waves, so that justification of an analog of each phenomenon known for the latter invokes a solution of the Landau-Lifshitz equation for the former—this approach was used in demonstration of the SW graded index lenses [1], SW Luneburg lenses [2], and SW Fourier optics [3], to name a few. Recently, Snell's law for SWs in thin ferromagnetic films [4], the mirage effect [5], and the spin-wave Goos-Hänchen effect has been predicted and demonstrated [6,7]. Also, self-focusing of SWs [8], SW diffraction on gratings [9], and formation of the SW beams [10–12] have found experimental confirmation. The analogs of the graded refractive index structures [1,13,14],

metamaterials [15,16], and metasurfaces [17] have recently been introduced to magnonics. Thus it may be expected that other phenomena and concepts are also transferable to magnonics, but these need to be verified. Among them, the Talbot effect (self-imaging effect) should be mentioned.

The Talbot effect was observed for light in the 19th century [18] and then explained in Ref. [19]. In recent years, this effect has been extensively revisited, e.g., see [20] and references therein. It has been used to improve x-ray imaging [21] and advance the process of lithographic patterning [22–24], and proposed for the realization of some physical models and computing scenarios [25–27], the applications of which can be interesting also for magnonics. Apart from electromagnetic waves propagating in a medium, the Talbot effect has already been demonstrated for plasmons [28], waves in fluids [29,30], and exciton polaritons [31], but for SWs it has not been shown so far.

In this paper we demonstrate the Talbot effect with the use of micromagnetic simulations for SWs propagating in a thin ferromagnetic film magnetized out of plane. We show that the diffraction grating created by the periodically located holes in a thin ferromagnetic film allows obtaining Talbot carpets, which are formed by the SWs propagating in the film and passing through the grating. The demonstration is presented at high frequencies where the exchange interactions dominate and at low frequencies where the magnetostatic interactions also contribute. Furthermore, we study also the influence of SW damping on the Talbot effect to show the possibility for its experimental verification, and we perform simulations of the Talbot effect for in-plane magnetized permalloy (Py) film in order to check the impact of changing the external magnetic field direction on the Talbot carpets and the possibility of using smaller field values.

The structure of the paper is as follows. In Sec. II we present derivation of the main parameters of the Talbot pattern based on the wave optics model. Then we focus on the case of out-of-plane magnetization. In Sec. III we present the results of micromagnetic simulations for short and long

*matgol2@amu.edu.pl

†krawczyk@amu.edu.pl

SWs, in Sec. IV we study the impact of SW damping on potential applications, and in Sec. V we carry out simulations for in-plane magnetization. Finally, we summarize our results in Sec. VI. The Appendixes are put at the end, which present the model development and analysis of some issues presented in the main part of the paper.

II. TALBOT EFFECT-MODEL DESCRIPTION

A. Talbot length

The phenomenon of self-imaging, known as the Talbot effect, results from the interference of a plane wave passed through an array of the periodically arranged objects, which often represents a diffraction grating. Using the knowledge that SWs may behave similarly to electromagnetic and acoustic waves, we can explain the essence of the SW Talbot effect with the help of an analysis of the basic wave phenomena, such as diffraction and interference. According to the principle formulated by Christian Huygens [32] and later supplemented by Augustin Fresnel [33],

Each unobstructed point of the wavefront at a given moment acts as a source of secondary spherical elementary waves with the same frequency as the primary wave. The amplitude of the resultant field at any other point is the superposition of all these elementary waves taking into account their amplitudes and relative phase differences.

This principle is particularly important not only for understanding the phenomenon of wave diffraction, but first of all, for the design of the simulation system and building a suitable mathematical model. It can be used when an aperture width is comparable to a length of incident plane wave. An angle of secondary waves is so large that this aperture can be treated as an elementary source of circular waves (or cylindrical in a two-dimensional view), and the entire diffraction grating can be treated as a one-dimensional infinite matrix of the periodically spaced elementary sources of circular waves. The presented concept of diffraction grating allows us to describe its effects and thus the diffraction field with a high accuracy by means of the superposition principle.

Repetitive modulation of intensity occurring along the propagation direction of the waves diffracted on periodic obstacles, i.e., the Talbot self-imaging effect we study, defines the length parameter also called from his name. The Talbot length determines the period over which secondary beams refocus their source image, i.e., when the diffraction image is created after passing through a diffraction grating, at a certain, precisely determined distance z_T in the direction perpendicular to the grating plane, an image identical to our original grating is formed. The classical formula for the Talbot length [19] can be derived based on the geometrical consideration, which is known from wave optics. It yields

$$z_T = m \frac{d^2}{\lambda}, \quad (1)$$

where m is an integer specifying the number of subsequent self-images, d is a diffraction grating period, and λ is an incident wavelength. For even m values, we obtain the distance between the primary (basic), not laterally shifted in phase Talbot images, whereas for odd m values we observe

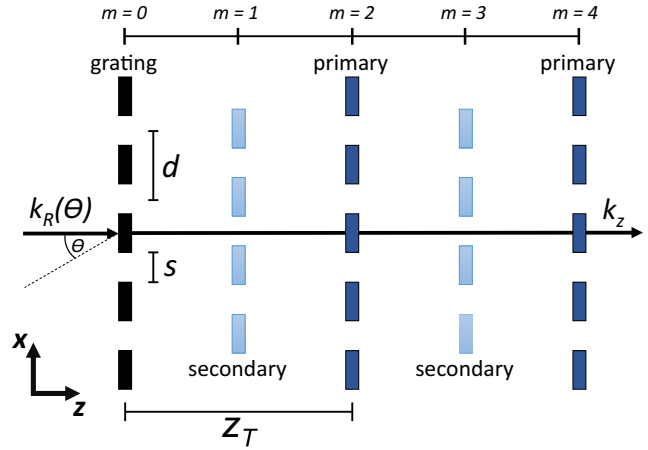


FIG. 1. Diagram of self-images arising behind the diffraction grating with indicated Talbot length z_T , diffraction grating constant d , aperture width s , wave vector k_R as a function of incident angle θ , and wave vector k_z propagating along the z axis.

the secondary Talbot images laterally shifted in phase by half the period of the diffraction grating, as shown in Fig. 1. More details are given in Appendixes A and B.

B. Talbot carpet

In order to obtain an analytical expression for the intensity distribution of the waves after passing through a periodic, infinitesimally thin diffraction grating, we start with writing [34] the transformation equation at the grating in $z = 0$:

$$\psi(x, z = +0) = \psi(x, z = -0)t(x), \quad (2)$$

where $\psi(x, z)$ represents incident wave and $t(x)$ is a periodic grating transmission function. The term $z = -0$ means the coordinate $z = 0$ at the incidence side of the diffraction grating, and $z = +0$ similarly means the coordinate $z = 0$ at the transmission side of the grating. Under assumptions that the one-dimensional periodic structure has an infinite length along the x axis and the incident beam is a plane wave propagating along the normal towards the grating, the transmittance of the diffraction grating $t(x)$ can be defined as

$$t(x) = \sum_{n=-\infty}^{\infty} A_n \exp\left[\frac{2\pi i n x}{d}\right]. \quad (3)$$

Formula (3) is a so-called rectangular function, which means it has a “binary” nature, i.e., a plane wave passes through the structure when its transparent parts are illuminated, with the maximum value [$t(x) = 1$], and does not pass through it when its opaque parts are illuminated [$t(x) = 0$]. For the unlimited ($\max|n| = \infty$) rectangular function along the x axis, components of the Fourier decomposition A_n are described by the formulas

$$A_n = \text{sinc}\left(\frac{n\pi s}{d}\right), \quad (4)$$

where $\text{sinc}(w) = \sin w / w$, and

$$A_0 = s/d. \quad (5)$$

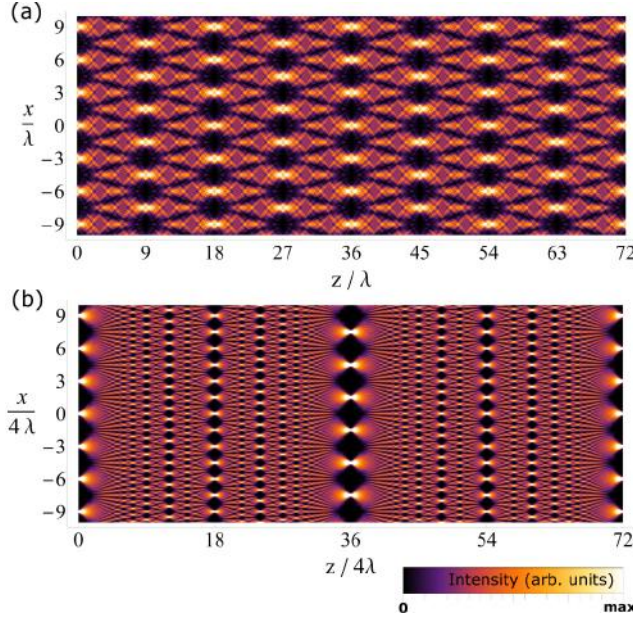


FIG. 2. Talbot carpets obtained from Eqs. (12) and (13) for 31 sum terms and (a) the aperture width $s = \lambda = 1$ [arb. units] and diffraction grating constant $d = 3\lambda$, and (b) $s = \lambda = 0.25$ [arb. units], $d = 12\lambda$. The grating is located at the left edge of each plot.

Substituting Eq. (3) into Eq. (2), using a plane-wave equation as $\psi(x, z = -0)$, and remembering that instead of the wave vector $k = 2\pi/\lambda$, its projection on the x axis depending on the incidence angle θ , $k_R = k \sin \theta$, should be taken into account, we get

$$\psi(x, z = +0) = \sum_{n=-\infty}^{\infty} A_n \exp[ix(k_d n + k_R)], \quad (6)$$

where $k_d = 2\pi/d$.

Next we extend the function ψ to describe the wave propagation in the direction of positive z values by

$$\psi(z) = \exp(ik_z z), \quad (7)$$

where k_z is the axial wave vector associated with propagation along the z axis.

Therefore the complete expression describing the plane wave after passing through the diffraction grating at an arbitrary distance from it can be written as

$$\psi(x, z) = \sum_{n=-\infty}^{\infty} A_n \exp[ix(k_d n + k_R) + ik_z z]. \quad (8)$$

The axial wave number k_z can be expressed as the function of the wave vector k as follows:

$$k^2 = k_z^2 + (k_d n + k_R)^2 \rightarrow k_z = \sqrt{k^2 - (k_d n + k_R)^2}. \quad (9)$$

Assuming that $k \gg (k_d n + k_R)$ and using the Taylor's expansion so that

$$k \sqrt{1 - \left(\frac{k_d n + k_R}{k}\right)^2} \approx k \left[1 - \frac{1}{2} \left(\frac{k_d n + k_R}{k}\right)^2\right], \quad (10)$$

we finally obtain

$$k_z \approx k - \frac{(k_d n + k_R)^2}{2k}. \quad (11)$$

For the purposes of numerical study, we assume that the initial plane wave incident along the normal to the diffraction grating plane ($\theta = 0$). Then we obtain the following formula:

$$\psi(x, z) \approx \sum_{n=-\infty}^{\infty} A_n \exp \left[ixn \frac{2\pi}{d} + iz \left(\frac{2\pi}{\lambda} - \frac{n^2 \lambda}{d^2} \right) \right]. \quad (12)$$

Here, the last term contains the inverse Talbot length formula, see Eq. (1) for $m = 1$. To generate energy density graphs in the near diffraction field, we calculate the field intensity function, i.e.,

$$I(x, z) = \psi(x, z) \times \psi^*(x, z). \quad (13)$$

The theoretical results are shown in Fig. 2 for the selected parameters set and 31 sum components in order to demonstrate the basic features of these Talbot carpets. They clearly show the primary and secondary Talbot images, as well as the lower orders of these images [visible especially in Fig. 2(b)], which testify to the fractal nature of the effect [35]. Being obtained with the use of a rather general formalism, these results form the basis for the understanding of and comparing with the numerical results presented for SWs in the next section.

III. MICROMAGNETIC SIMULATIONS

To demonstrate the Talbot effect for SWs and examine the theoretical assumptions and predictions of Sec. II B, we have conducted a series of micromagnetic simulations by taking into account dipolar interactions and employing MUMAX3 software [36]. The simulations have been performed for a uniformly out-of-plane magnetized 5-nm-thick permalloy (Py) film, which is characterized by the following magnetic parameters: saturation magnetization $M_S = 860$ kA/m, exchange stiffness $A_{ex} = 13$ pJ/m, gyrometric ratio $\gamma = 176$ rad GHz/T, and damping constant $\alpha = 0.0001$. The film has been uniformly magnetized by an external magnetic field, $\mu_0 H_0 = 1.1$ T ($H_0 > M_S$), which is directed perpendicular to the film's plane. The above given magnetic parameters are kept the same for all performed numerical simulations. We compute the diffraction of normally incident plane SWs of frequencies 3 and 40 GHz for various parameter sets of a diffraction grating. The distance between individual holes creating the diffraction grating is adjusted to approximately correspond to the incident SW wavelength (it is calculated analytically in Appendix E). The simulated steady state, i.e., the state with a fully evolved interference pattern, is analyzed. For better visualization of the Talbot effect, the periodic boundary conditions have been also used along the z axis (i.e., perpendicular to the grating plane), at the edges of the simulated area, so that the diffraction grating was much longer compared to the near diffraction field range. Further details of simulations can be found in Appendix D.

A. Spin-wave Talbot carpets and Talbot length

The simulated Talbot carpets are presented as the SW intensity maps, i.e., averaged in time, squared dynamic in-plane

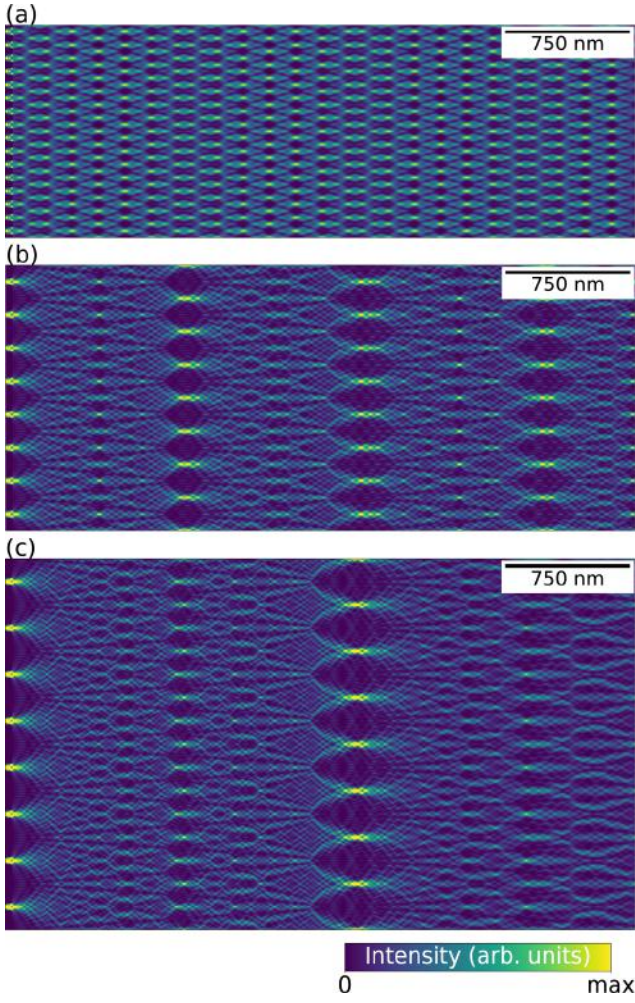


FIG. 3. Spin-wave intensity distribution at frequency of 40 GHz after passing through a one-dimensional diffraction grating with period of (a) 80, (b) 200, and (c) 280 nm. The grating is located at the left edge of each plot.

component of the magnetization, $\langle m_x^2 \rangle$. These diffraction fields for SWs of frequencies 40 and 3 GHz and for different values of d are shown in Figs. 3 and 4, respectively. To make a comparison of interference images for both frequencies more direct, every periods of the analyzed diffraction gratings were selected so that for each pair of results plotted in Figs. 3 and 4, the same kind of scaling takes place. In other words, visually the same (or very similar) carpets can be obtained for different choices of period and frequency. For more clarity, compare the peaks in the reciprocal (wave-vector) space, see Fig. 7. They approximately correspond to the same angle for 40 and 3 GHz, while geometrical parameters were selected depending on frequency.

Figure 3 shows the well-resolved Talbot carpets for SWs excited at frequency 40 GHz. It is observed that with the increasing period of the grating the Talbot length increases as well, and the effect of self-imaging is well recognizable in the form of bright focal points. The resulting diffraction field obtained for 3-GHz SWs (shown in Fig. 4) presents similar Talbot carpets. However, Talbot carpets for 3 GHz are slightly

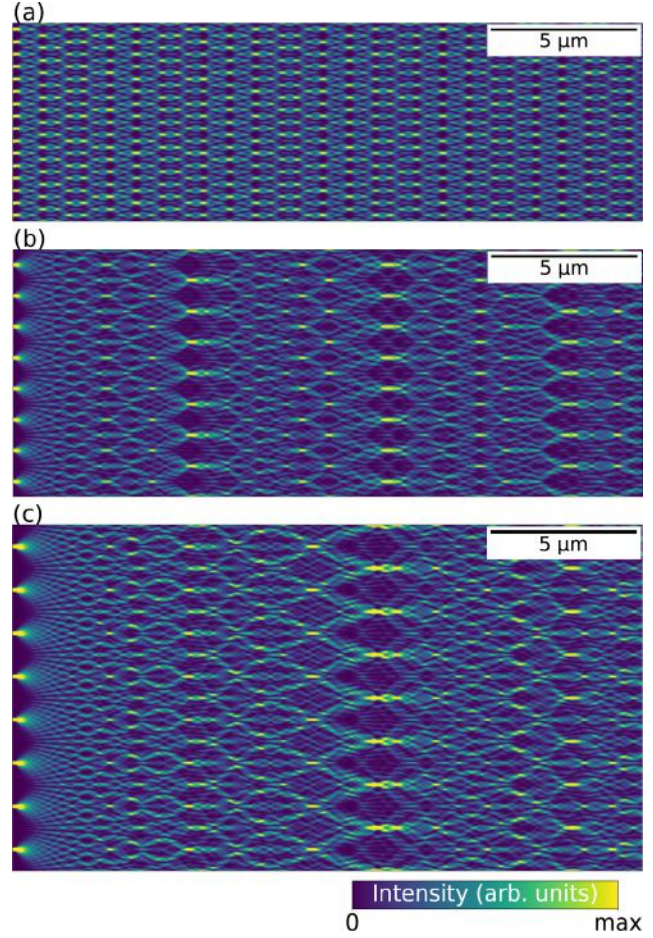


FIG. 4. Spin-wave intensity distribution field at frequency of 3 GHz after passing through a one-dimensional diffraction grating with period of (a) 400, (b) 1000, and (c) 1400 nm. The grating is located at the left edge of each plot.

less regular than in the case of 40 GHz. Later in this paper we will prove that both Talbot carpets for SWs are consistent with theoretical predictions, in spite of the above-mentioned irregularity.

The first, naturally occurring compliance test for the obtained numerical results is to compare the distance between the primary self-images (Fig. 1), Talbot length, with the theoretical predictions. For this purpose we use Eq. (1) as the function of d for the two selected frequencies. As can be seen in Fig. 5, the simulation results well coincide with the general theory given in Sec. II A. Therefore the simulated interference patterns behave very similarly to the Talbot carpets theoretically described in Sec. II B. The Talbot lengths data used in Fig. 5 come from the simulations carried out in an identical manner to those shown in Figs. 3 and 4. The distances between primary Talbot images were measured by analyzing the lengths between individual subsequent intensity maximums [i.e., between each pair of integers, m and $m + 2$, see Eq. (1) and Fig. 1] on the two-dimensional Talbot carpets. The measured lengths were averaged to obtain one, possibly accurate value of Talbot length for each of the selected values of d .

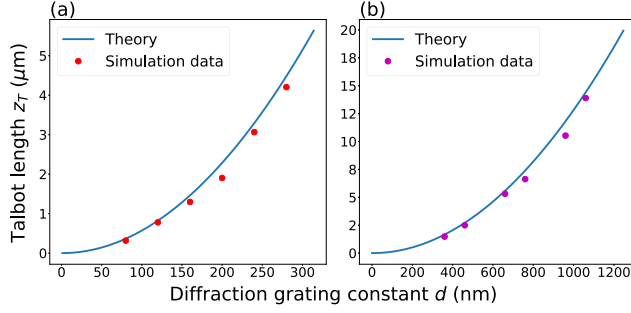


FIG. 5. Functions representing the Talbot length depending on the diffraction grating period from Eq. (1) together with the data taken from micromagnetic simulations for (a) 40 and (b) 3 GHz.

The obtained results show that the resulting SW Talbot carpets are in good agreement with the theoretical description of wave optics. The visualizations in Figs. 3 and 4 show the distribution of SW intensity in the diffraction field according to Eq. (12), which has been proven by comparing the numerically obtained and theoretically predicted Talbot lengths in Fig. 5.

B. Talbot carpets in wave-vector space

The next stage of the results analysis is to apply Fast Fourier transform (FFT) to the obtained Talbot carpet visualizations in order to transform the results from the space domain to the wave-vector domain.

To maintain greater accuracy, the absolute amplitude values of the FFT results (along the z axis) were averaged over a perpendicular axis. The purpose of this averaging was to confirm that the frequency set used in the simulations corresponds to the theoretical values of the wavelengths given by the analytical dispersion relation [37] and observe the discrete components of perpendicular wave vectors (i.e., transverse modes). In Fig. 6 we can see that for frequency of 40 GHz, the wavelength is about 30 nm, while for 3 GHz its value oscillates at around 160 nm. These values satisfactorily coincide with those obtained from the dispersion relation, see Appendix E. Attention should also be paid here to the peaks occurring at larger wavelengths: they are associated with the transition of the plane SW through the periodic object. It is clear that the larger the value of d is, the more pronounced the transverse components of the wave vector in our Talbot carpets are. A plane wave after encountering an obstacle (in our case, in the form of a hole array) gains a nonzero component of the wave vector k_x perpendicular to its propagation direction. Due to the nature of the obstacle, it also has discrete values being a multiple of $2\pi/d$; see Sec. II B for details.

To find transverse components of the wave vector coexisting with the Talbot carpets, we perform two-dimensional FFT. In Fig. 7, we can see the wave-vector-space maps of SW amplitude, on the left side for 40 GHz and on the right side for 3 GHz, along with the marked isofrequency contours of the dispersion relation lines (IFDRLs) for the given frequency, and the lines specific for the quantized wave vector k_d (located on the k_x axis). As we can read from these figures, the results obtained from the simulations agree very well with the

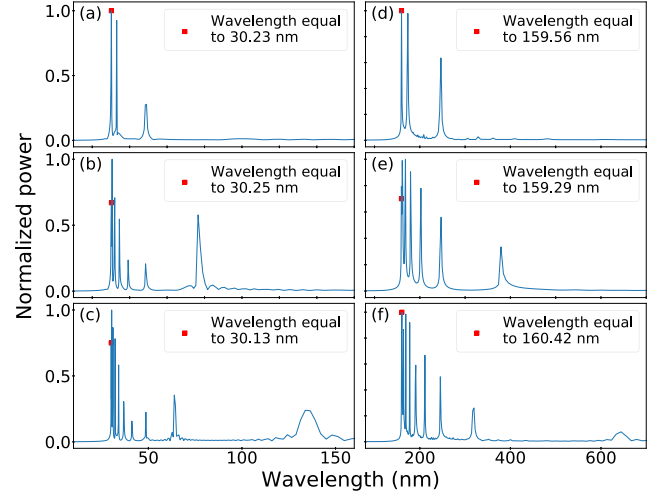


FIG. 6. SW spectra with marked first peaks responsible for the propagation direction wavelength. On the left panel there are spectra from simulations performed for 40 GHz for period d , which is equal to (a) 80, (b) 200, and (c) 280 nm. On the right panel, we have analogous results for 3 GHz for period of (d) 400, (e) 1000, and (f) 1400 nm.

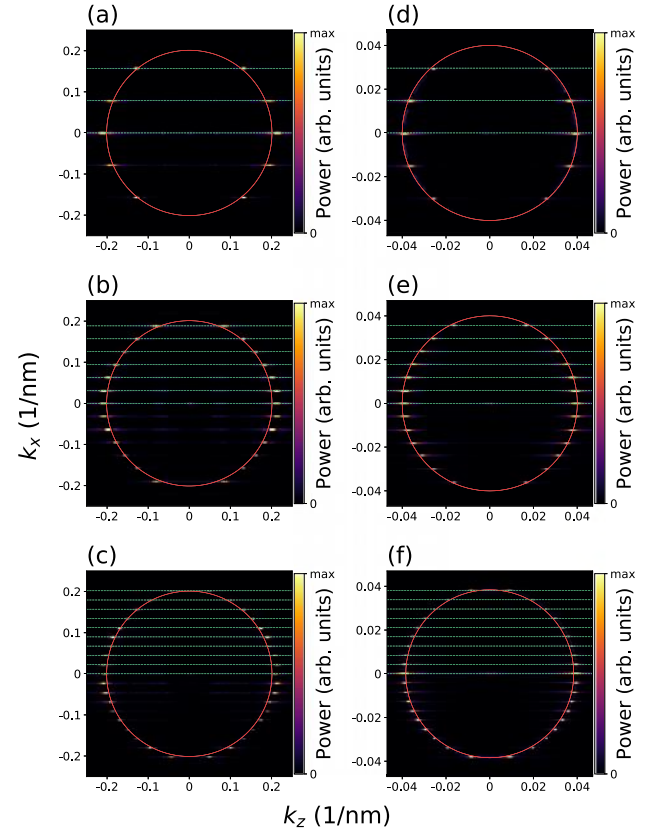


FIG. 7. Reciprocal-space maps of SW amplitude distribution at 40 GHz for the grating period equal to (a) 80, (b) 200, and (c) 280 nm, and at 3 GHz for the period equal to (d) 400, (e) 1000, and (f) 1400 nm. Isofrequency contours are presented as red circles. The quantized wave-vector lines are shown in green.

theoretical data. Indeed, the individual peaks in the (k_z, k_x) planes perfectly match the straight lines corresponding to the multiples of $2\pi/d$ provided in Eq. (12). They are also located directly on the circular isofrequency lines, which confirms that the simulated propagation of SWs in a thin Py film is isotropic.

The results directly show that the Talbot effect can be successfully developed with SWs for its subsequent use for applications. The outcome visible in Fig. 7 also indicates that by manipulating the reciprocal space of the diffraction image we can predict its properties and shape in the real space. This feature is particularly useful, because it opens a way for the use of the Talbot effect for SWs in the systems, in which the location of self-images may provide information about the input signal or the nature of the previously encountered obstacle.

IV. EXPERIMENTAL FEASIBILITY

The purpose of this work was, among others, to demonstrate the Talbot effect for SWs and to test its compliance with theoretical predictions derived from standard wave optics. For this reason, the system used for micromagnetic simulations assumed a very small damping constant ($\alpha = 0.0001$) as a factor not significant from the viewpoint of the SW Talbot effect demonstration. As we have successfully shown and described the effect, the next step was to test it in terms of real application, so we decided to increase the damping constant, as an inevitable parameter in magnonics, to a value of $\alpha = 0.005$, being characteristic for a thin Py film [38]. The simulation results are shown in Fig. 8.

Based on the simulation results for systems with a higher damping constant, we can see that the Talbot effect is clearly visible until the first secondary self-image is formed, so the diffraction field effective range for this specific set of parameters can be estimated by calculating the Talbot length formula (1). It is worth emphasizing that the SW intensity

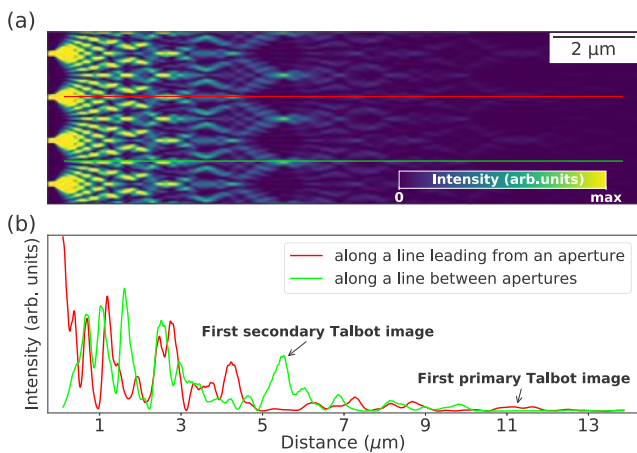


FIG. 8. Spin-wave Talbot effect in thin Py film with damping constant $\alpha = 0.005$ for 3 GHz and diffraction grating period $d = 1000$ nm as (a) a 2D intensity plot with mapped two lines (red and green) along which (b) 1D intensity plots were created. Diffraction grating is located at the left edge, and the line colors are analogous on both graphs.

level on the first secondary self-image should be measurable using microfocus Brillouin light scattering (micro-BLS) [39,40]. The simulation carried out shows that this effect, although significantly limited, can be observed in systems with higher damping, and its effectiveness will strongly depend on the choice of material, its dimensions, and geometry of the diffraction grating.

V. IN-PLANE MAGNETIZATION

The demonstration of the Talbot effect for SWs was carried out so far for out-of-plane magnetization due to the isotropic properties of SW dynamics in this configuration—and thus the closest to electromagnetic waves in an optically homogeneous medium. The proof of this can be seen directly in Fig. 7 in the form of circular IFDRLs matching with simulations data. This situation changes if the applied external magnetic field saturating magnetization is directed parallel (or nonperpendicular) to the plane of the film—then we will observe, especially in the regime where dipolar interactions play a significant role, an anisotropy in SW propagation and related caustic effects [41,42]. We have performed simulations of the Talbot effect for SWs in Damon-Eshbach (DE) and the backward volume (BV) magnetostatic wave geometry, where propagation of SWs is perpendicular and parallel, respectively, to the direction of external magnetic field, 0.1 T. The results are shown in Fig. 9, for the frequency equal to 15 GHz, for which the system anisotropy is already clearly visible in these magnetization configurations. The material parameters remain unchanged compared to the simulations in the Sec. III.

The simulations show that it is possible to obtain SW self-imaging also in much lower fields than required in out-of-plane cases. This property can be decisive when it comes to

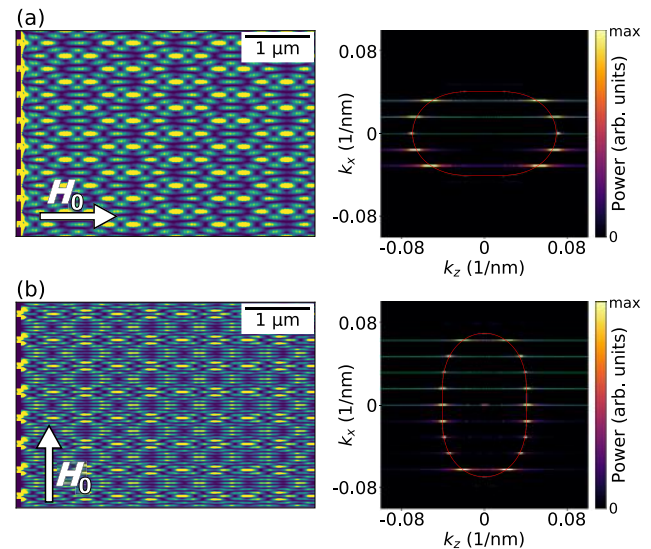


FIG. 9. Spin-wave intensity distribution fields after passing through a diffraction grating $d = 500$ nm with corresponding representations in reciprocal spaces at frequency of 15 GHz for (a) BV and (b) DE geometry. Analytical isofrequency contours are presented as red ellipses, and quantized wave-vector lines separated by $\delta k_x = 2\pi/d$ are shown in green.

the use of magnonic systems based on the Talbot effect in real devices. We can see that Talbot carpets obtained for exactly the same material parameters differ significantly only under the change of the external magnetic field configuration. The anisotropy of SW dynamics brings additional challenges, but it also extends the possibilities of controlling and manipulating SWs through an additional degree of freedom, such as an external magnetic field orientation. This opens the way for further research, e.g., on magnonic logic devices that can perform more than one function by changing the angle or the value of the external magnetic field, thus changing the distribution of self-images, which in turn will result in a different signal at the output. This is a clear benefit of using the Talbot effect for SWs and is in contrast to analogous devices in photonics and electronics that cannot be programmed in this way.

The analysis of anisotropic effects associated with the use of lower frequencies in DE and BV geometries, in combination with counteracting the damping impact [11], provides a very interesting issue for further work of the Talbot effect in magnonics.

VI. CONCLUSIONS

In this paper we have shown by using micromagnetic simulations based on solutions of the Landau-Lifshitz equation that the Talbot effect occurs when SWs propagate in a thin ferromagnetic film after passing through a periodic diffraction grating created in the film. We demonstrated that the properties of SW self-imaging are consistent with the theoretical predictions based on the general formalism of wave optics. Thus it can be used to describe this phenomenon quite accurately in the considered range of parameter variation. This compliance cannot be introduced in advance, i.e., based on the knowledge of the Talbot effect in optics that is described by Maxwell equations. Rather, the Landau-Lifshitz nonlinear equation describing SW propagation must be solved for this purpose. This has systematically been done in our study. By performing micromagnetic simulations in Py film with characteristic damping, we showed that the observation of the first secondary Talbot images shall be feasible with standard micro-BLS. We expect that in yttrium iron garnet thin films, the (first) primary images can be reached due to ten times smaller damping [43]. Moreover, we demonstrated that the Talbot effect exists for SWs in the out-of-plane magnetized and in-plane magnetized film when the SW isofrequency contours of the dispersion relation are isotropic and anisotropic, respectively.

The obtained results open an avenue to practical applications of the Talbot effect in future magnonic devices. Indeed, it is a promising phenomenon from the viewpoint of analysis, control, and manipulation of SW propagation. That is why it may find applications in magnonics, where devices of such a type could be used in signal processing, e.g., in logic circuits and SW analyzers. In the coming years, further theoretical research, experimental demonstration, and development of prototypes of magnonic devices based on the SW Talbot effect are expected to occur. This work is the first step in understanding the main features and assessing the potential of the studied effects.

ACKNOWLEDGMENTS

The research leading to these results has received funding from the National Science Centre of Poland, Project No. UMO-2015/17/B/ST3/00118. The simulations were partially performed at the Poznan Supercomputing and Networking Center (Grant No. 398). P.G. acknowledges support from the National Science Centre of Poland under OPUS funding, Project No. UMO-2019/33/B/ST5/02013.

APPENDIX A: DERIVATION OF THE TALBOT LENGTH—MODEL ANALYSIS I

In order to determine the Talbot length, we analyze the intensity (distribution of a flux density) as a function of a distance between the grating and a given observation point P in the diffraction field according to Refs. [44–46].

At point P away from the source (being one of the apertures, see Fig. 10) by distance r_n , the resulting wave $\Psi(\vec{r}, t)$ can be written as a superposition of the N waves in the following form:

$$\Psi(r, t) = \Re \left(\sum_{n=-(N-1)/2}^{(N-1)/2} C_n e^{-i\omega t} [\cos(kr_n) + i \sin(kr_n)] \right). \quad (\text{A1})$$

Then the intensity can be defined as follows:

$$I(r) = \langle \Psi^2(r, t) \rangle_t = \frac{(NC)^2}{2} \left(\sum_{n=-(N-1)/2}^{(N-1)/2} \cos(kr_n) \right)^2, \quad (\text{A2})$$

where

$$r_n = \sqrt{z^2 + (nd + x)^2}. \quad (\text{A3})$$

In order to simplify further analysis, we neglect the constant $(NC)^2/2$, remembering that N is the number of apertures of the diffraction grating, C is a numerical factor, and we consider the calculations for the point P such that $x = 0$ (as shown in Fig. 10). This results in the distribution of intensity

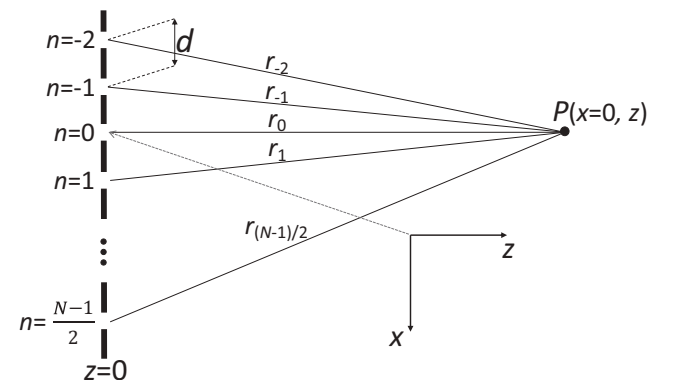


FIG. 10. Diagram showing the situation described in this section together with relevant markings—a diffraction grating consisting of N sources distant from the analyzed point P by r_n , where n is a number indicating the given aperture. The center of the coordinate system is in the aperture $n = 0$.

in the diffraction field being a function of the z coordinate:

$$I(z, x=0) = \left(\sum_{n=-(N-1)/2}^{(N-1)/2} \cos \left(\frac{2\pi}{\lambda} \sqrt{z^2 + (nd)^2} \right) \right)^2. \quad (\text{A4})$$

To examine the course of the expression (A4), the following substitution has been made:

$$U_n = \frac{2\pi}{\lambda} \sqrt{z^2 + (nd)^2}. \quad (\text{A5})$$

As we are looking for the maximum of the (A4) expression in the z function (self-image of the source intensity), $\cos^2(U_n)$ has to take the value 1 (for any n). We can easily see that it takes place only when $U_n = \pi b$, for b being a natural number ($b = 0, 1, 2, \dots$). To extract the classical formula for the Talbot length, now we assume that

$$\left(\frac{nd}{z} \right)^2 \ll 1 \quad (\text{A6})$$

and use Taylor's expansion as follows:

$$\sqrt{1 + \left(\frac{nd}{z} \right)^2} \approx 1 + \frac{1}{2} \left(\frac{nd}{z} \right)^2. \quad (\text{A7})$$

All terms of the Taylor series above the second one were omitted. We can now substitute the approximate result of (A7)–(A5), and remembering that $U_n = \pi b$, we get the condition

$$\frac{2z}{\lambda} + \frac{(nd)^2}{\lambda z} = b. \quad (\text{A8})$$

Note that the fraction $2z/\lambda$ is, in fact, a certain integer indicating the doubled number of wavelengths λ along the z axis. We can therefore substitute $2z/\lambda = b_0$, thanks to which we get

$$z = \frac{n^2}{b - b_0} \frac{d^2}{\lambda}. \quad (\text{A9})$$

Since for all n there exists an integer $b - b_0$ that satisfies Eq. (A9), every aperture (i.e., every circular wave source) contributes to the resulting phase at a certain position, which can be finally found by using the following formula for the Talbot length:

$$z_T = m \frac{d^2}{\lambda}, \quad (\text{A10})$$

where m is an integer specifying the number of subsequent self-images.

APPENDIX B: DERIVATION OF THE TALBOT LENGTH—MODEL ANALYSIS II

Another, slightly more intuitive method of determining the Talbot length [45,47] uses the fact that each order (greater than 0) of the wave front which has passed through the diffraction grating must have, in the direction parallel to the apertures plane (i.e., along x axis), a period that is a natural multiple of the distance between them:

$$b\lambda_x = d, \quad (\text{B1})$$

where b denotes natural numbers, $b = 0, 1, 2, \dots$, and λ_x is the distance between wave fronts along the x axis (x direction

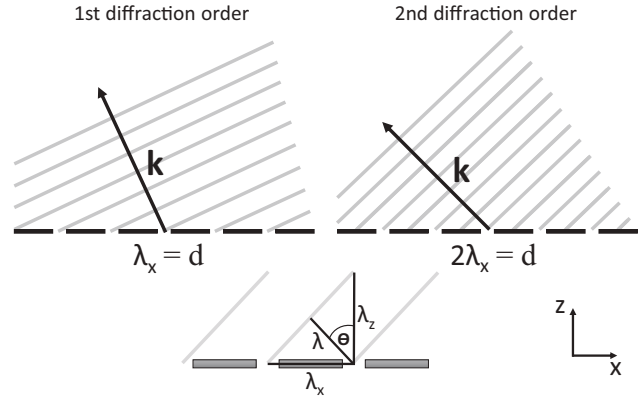


FIG. 11. Propagation scheme of two diffraction orders of the plane wave fronts behind a diffraction grating, in accordance with the rule described by Eq. (B1). Gray lines are the wave fronts with equal phases, while the black arrows indicate the wave-vector directions. Wavelength representations on the axes are marked below.

modulation, for simplicity called “horizontal wavelength,” while λ_z is the “vertical wavelength,” remembering that they are not wavelength projections). The described physical situation is presented in Fig. 11.

In order to find the dependence between those particular wavelengths, the geometrical property presented in Fig. 11 is used, from which a simple relationship can be obtained as follows:

$$\frac{1}{\lambda^2} = \frac{1}{\lambda_x^2} + \frac{1}{\lambda_z^2}. \quad (\text{B2})$$

Using the above introduced Eq. (B1) and simple mathematical derivations, we get the following formula for the “vertical wavelength”:

$$\lambda_z = \frac{\lambda}{\sqrt{1 - \left(\frac{\lambda b}{d} \right)^2}}. \quad (\text{B3})$$

As we know, a period of repetitive intensity modulation in the direction parallel to the z axis, after passing through the periodic structure, has a strictly defined value. Therefore we considered points on this axis for which the secondary waves coming from each of the apertures will have the same phase—it is the condition of occurrence of the constructive interference. The phase distribution of the waves along the z axis is introduced as

$$\phi_z = k_z z = \frac{2\pi}{\lambda_z} z. \quad (\text{B4})$$

For the points on the z axis that are a multiple of the wavelength λ_z , the phase will be constant and equal to 2π . By combining Eqs. (B3) and (B4), we obtain the phase distribution of the diffraction image along the z axis:

$$\phi_z = \frac{2\pi z}{\lambda} \sqrt{1 - \left(\frac{\lambda n}{d} \right)^2}. \quad (\text{B5})$$

Assuming that the grating constant is much larger than the wavelength, it can be written

$$\left(\frac{\lambda n}{d}\right)^2 \ll 1. \quad (\text{B6})$$

Next, again using Taylor's expansion, we obtain

$$\phi_z \approx \frac{2\pi z}{\lambda} \left[1 - \frac{1}{2} \left(\frac{\lambda n}{d}\right)^2 \right] = \frac{2\pi z}{\lambda} - \frac{\pi n^2 \lambda z}{d^2}. \quad (\text{B7})$$

Having already expressed the phase distribution in the diffraction field along the z axis, we could think about particular points we are interested in. As we know, the Talbot length determines the distance between the successive maxima of intensity perpendicular to the diffraction grating plane and coming from one of the apertures. Obviously, the maximum intensity also occurs on the apertures themselves (at $x = 0$). Therefore their subsequent repetitive modulation will be the reproduction of the image from the beginning of the system, and thus the reconstruction of the diffraction grating itself (self-imaging) takes place. We are looking for a constructive interference along the z axis for each of the values $x = nd$, which correspond to the subsequent apertures positions. The first term on the right-hand side of Eq. (B7) does not depend on which aperture we choose as a reference point, so we should make its second term a multiple of the full period. Then, this formula could fulfill the condition of constructive interference, so we can write in our case

$$\phi_z = \frac{2\pi z}{\lambda} - 2\pi n^2. \quad (\text{B8})$$

Comparing Eq. (B7) with the above-given condition of constructive interference, we can see that they are identical only if $\lambda z/2d^2 = 1$, which leads us to the desired Talbot length, i.e.,

$$z_T = \frac{2d^2}{\lambda}. \quad (\text{B9})$$

In Eq. (B9) the obtained Talbot length is multiplied by 2, which can be omitted in the general case. As we can see in Eq. (1), the factor by which d^2/λ is multiplied determines only the order, i.e., the number of the Talbot image analyzed in the sequence, and the fact whether the self-image is shifted laterally in a phase (secondary image, for an odd factor) regarding the original image or is it the phase compatible with that image (primary image, for an even factor), see Fig. 1. Equation (B9) gives the distance between the source and the first-order primary self-image.

The laterally shifted Talbot image would be, in turn, extinguished by taking over the condition for destructive interference,

$$\phi_z = \frac{2\pi z}{\lambda} - \pi n^2, \quad (\text{B10})$$

which yields

$$z_T = \frac{d^2}{\lambda}, \quad (\text{B11})$$

being the Talbot length for the odd factor $m = 1$, according to Eq. (1).

APPENDIX C: ANALYSIS OF COMPUTATIONAL UNCERTAINTIES

It should be emphasized [48] that the analytical formulas obtained in Appendix A and Appendix B give correct results in the systems for which the approximations

$$d \gg \lambda \quad (\text{C1})$$

and

$$z \gg d \quad (\text{C2})$$

are applicable. Thanks to them, it was possible to apply Taylor's expansion in each of the cases described by Eqs. (10), (A7), and (B7). While the condition (C2) can be easily met in most cases, the condition (C1) is no longer so obvious. Indeed, for diffraction gratings whose spatial period is comparable to a given wavelength, then Eq. (B9) can cause significant discrepancies as compared to experimental or numerical data.

In the case when $d \approx \lambda$, the verification of experimental and numerical results is based on the exact, general solution derived by Lord Rayleigh in 1881 [19], defining the Talbot length as

$$z_{T_{\text{gen}}} = \frac{\lambda}{1 - \sqrt{1 - (\frac{\lambda}{d})^2}}. \quad (\text{C3})$$

To quantify the difference of results obtained from Eqs. (B9) and (C3), a graph of the function $z_T(d)$ generated from the both equations is presented in Fig. 12.

The discrepancy function (expressed in percent) is defined as the relative difference of values obtained from Eqs. (C3) and (B9):

$$\delta = \frac{|z_{T_{\text{gen}}} - z_T|}{z_{T_{\text{gen}}}} \times 100\%. \quad (\text{C4})$$

Analyzing the results presented in Fig. 12, we can conclude that the discrepancy function increases as the diffraction grating period decreases and reaches 100% when $d = \lambda$. Thus it is justified to use Eq. (B9) only in the systems where the grating constant is properly greater than the incident wavelength; otherwise it is necessary to use its general form (C3).

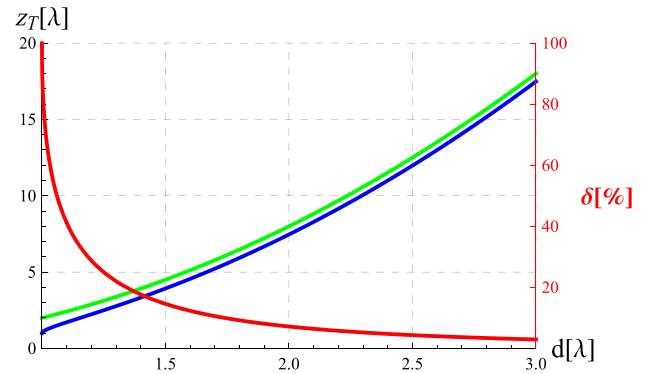


FIG. 12. Graph of the Talbot length as a function of the diffraction grating constant. The general form and the form derived in this paper are shown by blue and green lines. The discrepancy function is shown by the red line.

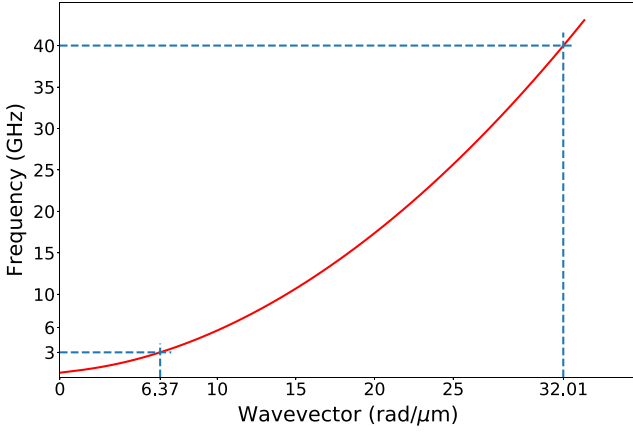


FIG. 13. The dispersion relation for 5-nm-thick Py film in the presence of a 1.1-T out-of-plane magnetic field. The two marked values of the wave vector correspond to 3- and 40-GHz frequencies.

APPENDIX D: SIMULATIONS DETAILS

The performed simulations consist of two parts. First, the static magnetic configuration has been reached which, in turn, was perturbed by a source emitting plane SWs incident normally on the grating. SWs have been excited by the continuously applied RF field, localized on the left side of the diffraction grating within a 15-nm-wide region. SWs have been continuously induced until reaching the resultant steady state, i.e., the state when a fully evolved interference pattern is formed. Along the film's edges perpendicular to the grating, the periodic boundary conditions have been introduced to mimic an infinitely long diffraction grating. In contrast, at the edges parallel to the grating, the absorbing boundary conditions with a gradually increasing damping constant have been used [49]. The out-of-plane simulations have been performed for two frequencies, 40 and 3 GHz, which correspond to the wavelengths 31.2 and 156.9 nm, respectively (see Appendix E). Pure exchange SWs are definitely easier to model for higher frequencies, since the wavelength for 40 GHz is only a few times greater than the exchange length [$l_{\text{ex}} = \sqrt{2A_{\text{ex}}/(\mu_0 M_S^2)} = 6$ nm]. However, this case is not yet accessible experimentally. Therefore we have decided to perform simulations for a more realistic regime to check whether this effect is obtainable for frequencies and wavelengths available in contemporary laboratories, which would

directly affect its application potential. We also investigated the spin-wave Talbot effect in BV and DE configurations for 15 GHz, where the isofrequency contours indicate that the calculations were made for the dipole-exchange regime, i.e., both dipole and exchange interactions play a significant role. A much smaller required external magnetic field (in plane, 11 times smaller than out-of-plane in our simulations) is a step towards experimental prototypes.

For each analyzed SW frequency, the studied system was discretized by the $5 \times 5 \times 5$ nm³ unit cells.

APPENDIX E: SPIN-WAVE DISPERSION

The analytical theory of SWs in thin ferromagnetic films was developed by Kalinikos and Slavin in Ref. [37]. Following that theory, in the linear approximation the dispersion relation, where wave vector k propagates in the film plane at an angle φ with respect to the direction of the external magnetic field H_0 projected onto the film plane, and the H_0 and static magnetization vector M_S form an angle ϑ with the normal to the film plane, takes the form

$$\omega^2 = (\omega_H + l_{\text{ex}}^2 \omega_M k^2)(\omega_H + l_{\text{ex}}^2 \omega_M k^2 + \omega_M F(\varphi, \vartheta)), \quad (\text{E1})$$

where $\omega = 2\pi f$ is the angular frequency of SWs, f is the frequency, μ_0 is the vacuum permeability, $\omega_H = |\gamma| \mu_0 (H_0 - M_S)$, $\omega_M = \gamma \mu_0 M_S$, and the function $F(\varphi, \vartheta)$ is defined as

$$F(\varphi, \vartheta) = P + \sin^2(\vartheta) \times \left[1 - P \left(1 + \cos^2(\varphi) + M_S \frac{P(1-P) \sin^2(\varphi)}{H_0 + l_{\text{ex}}^2 M_S} \right) \right], \quad (\text{E2})$$

where

$$P = 1 - \frac{1 - e^{-kL}}{kL}, \quad (\text{E3})$$

and L is the thickness of the analyzed ferromagnetic film. The contribution of dipolar interactions to the SWs dynamics is expressed by the term $F(\varphi, \vartheta)$, and the effect of the exchange interaction is represented in Eq. (E1) by the terms proportional to k^2 .

The dispersion relation of the simulated Py film is presented in Fig. 13. We can see that for 40 GHz the wave-vector value along the z axis k_z is equal to 32.01 rad/ μ m, which corresponds to the wavelength $\lambda_z = 31.24$ nm. For 3 GHz, $k_z = 6.37$ rad/ μ m, so $\lambda_z = 156.92$ nm.

- [1] N. J. Whitehead, S. A. R. Horsley, T. G. Philbin, and V. V. Kruglyak, *Phys. Rev. B* **100**, 094404 (2019).
- [2] N. J. Whitehead, S. A. R. Horsley, T. G. Philbin, and V. V. Kruglyak, *Appl. Phys. Lett.* **113**, 212404 (2018).
- [3] M. Vogel, B. Hillebrands, and G. von Freymann, *Appl. Phys. Lett.* **116**, 262404 (2020).
- [4] J. Stigloher, M. Decker, H. S. Körner, K. Tanabe, T. Moriyama, T. Taniguchi, H. Hata, M. Madami, G. Gubbiotti, K. Kobayashi, T. Ono, and C. H. Back, *Phys. Rev. Lett.* **117**, 037204 (2016).
- [5] P. Gruszecki and M. Krawczyk, *Phys. Rev. B* **97**, 094424 (2018).

- [6] P. Gruszecki, M. Mailyan, O. Gorobets, and M. Krawczyk, *Phys. Rev. B* **95**, 014421 (2017).
- [7] J. Stigloher, T. Taniguchi, H. S. Körner, M. Decker, T. Moriyama, T. Ono, and C. H. Back, *Phys. Rev. Lett.* **121**, 137201 (2018).
- [8] V. E. Demidov, S. O. Demokritov, K. Rott, P. Krzysteczko, and G. Reiss, *Phys. Rev. B* **77**, 064406 (2008).
- [9] S. Mansfeld, J. Topp, K. Martens, J. N. Toedt, W. Hansen, D. Heitmann, and S. Mendach, *Phys. Rev. Lett.* **108**, 047204 (2012).
- [10] R. Khomeriki, *Eur. Phys. J. B* **41**, 219 (2004).

- [11] R. Gieniusz, P. Gruszecki, M. Krawczyk, U. Guzowska, A. Stognij, and A. Maziewski, *Sci. Rep.* **7**, 8771 (2017).
- [12] H. S. Körner, J. Stigloher, and C. H. Back, *Phys. Rev. B* **96**, 100401(R) (2017).
- [13] C. S. Davies, A. Francis, A. V. Sadovnikov, S. V. Chertopalov, M. T. Bryan, S. V. Grishin, D. A. Allwood, Y. P. Sharaevskii, S. A. Nikitov, and V. V. Kruglyak, *Phys. Rev. B* **92**, 020408(R) (2015).
- [14] M. Vogel, R. Aßmann, P. Pirro, A. V. Chumak, B. Hillebrands, and G. von Freymann, *Sci. Rep.* **8**, 11099 (2018).
- [15] R. V. Mikhaylovskiy, E. Hendry, and V. V. Kruglyak, *Phys. Rev. B* **82**, 195446 (2010).
- [16] M. Mruczkiewicz, M. Krawczyk, R. V. Mikhaylovskiy, and V. V. Kruglyak, *Phys. Rev. B* **86**, 024425 (2012).
- [17] M. Zelent, M. Mailyan, V. Vashistha, P. Gruszecki, O. Y. Gorobets, Y. I. Gorobets, and M. Krawczyk, *Nanoscale* **11**, 9743 (2019).
- [18] H. Talbot, *The London, Edinburgh, and Dublin Philos. Magazine J. Sci.* **9**, 401 (1836).
- [19] L. Rayleigh, *Philos. Mag.* **11**, 196 (1881).
- [20] J. Wen, Y. Zhang, and M. Xiao, *Adv. Opt. Photon.* **5**, 83 (2013).
- [21] A. Bravin, P. Coan, and P. Suortti, *Phys. Med. Biology* **58**, R1 (2012).
- [22] T. Sato, *Microelectron. Eng.* **123**, 80 (2014).
- [23] S. Zhou, J. Liu, Q. Deng, C. Xie, and M. Chan, *IEEE Photon. Technol. Lett.* **28**, 2491 (2016).
- [24] A. Vetter, R. Kirner, D. Opalevs, M. Scholz, P. Leisching, T. Scharf, W. Noell, C. Rockstuhl, and R. Voelkel, *Opt. Express* **26**, 22218 (2018).
- [25] D. Bigourd, B. Chatel, W. P. Schleich, and B. Girard, *Phys. Rev. Lett.* **100**, 030202 (2008).
- [26] O. J. Farias, F. de Melo, P. Milman, and S. P. Walborn, *Phys. Rev. A* **91**, 062328 (2015).
- [27] K. Sawada and S. P. Walborn, *J. Opt.* **20**, 075201 (2018).
- [28] M. R. Dennis, N. I. Zheludev, and F. J. G. de Abajo, *Opt. Express* **15**, 9692 (2007).
- [29] N. Sungar, J. Sharpe, J. Pilgram, J. Bernard, and L. Tambasco, *Chaos* **28**, 096101 (2018).
- [30] A. Bakman, S. Fishman, M. Fink, E. Fort, and S. Wildeman, *Am. J. Phys.* **87**, 38 (2019).
- [31] T. Gao, E. Estrecho, G. Li, O. A. Egorov, X. Ma, K. Winkler, M. Kamp, C. Schneider, S. Höfling, A. G. Truscott, and E. A. Ostrovskaya, *Phys. Rev. Lett.* **117**, 097403 (2016).
- [32] C. Huygens, *Traite de la lumiere* (Chez Pierre vander Aa marchand libraire, 1690) [translated in english by S. P. Thompson, *Treatise on Light*, Project Gutenberg edition (Macmillan and Co., London, 1690), p. 19].
- [33] A. J. Fresnel, *Oeuvres Comp.* **1**, 247 (1819).
- [34] S. D. William Case, Mathias Tomandl, and M. Arndt, *Opt. Express* **17**, 20966 (2009).
- [35] M. V. Berry and S. Klein, *J. Mod. Opt.* **43**, 2139 (1996).
- [36] A. Vansteenkiste, J. Leliaert, M. Dvornik, M. Helsen, F. Garcia-Sanchez, and B. Van Waeyenberge, *AIP Adv.* **4**, 107133 (2014).
- [37] B. Kalinikos and A. Slavin, *J. Phys. C: Solid State Phys.* **19**, 7013 (1986).
- [38] K. Kobayashi, N. Inaba, N. Fujita, Y. Sudo, T. Tanaka, M. Ohtake, M. Futamoto, and F. Kirino, *IEEE Trans. Magn.* **45**, 2541 (2009).
- [39] G. A. Riley, H. J. Jason Liu, M. A. Asmat-Uceda, A. Haldar, and K. S. Buchanan, *Phys. Rev. B* **92**, 064423 (2015).
- [40] T. Sebastian, K. Schultheiss, B. Obry, B. Hillebrands, and H. Schultheiss, *Front. Phys.* **3**, 35 (2015).
- [41] V. Veerakumar and R. E. Camley, *Phys. Rev. B* **74**, 214401 (2006).
- [42] R. Gieniusz, H. Ulrichs, V. Bessonov, U. Guzowska, and A. Stognij, *Appl. Phys. Lett.* **102**, 102409 (2013).
- [43] G. Schmidt, C. Hauser, P. Trempler, M. Paleschke, and E. T. Papaioannou, *Phys. Status Solidi B* **257**, 1900644 (2020).
- [44] E. A. Hiedemann and M. A. Breazeale, *J. Opt. Soc. Am.* **49**, 372 (1959).
- [45] J. T. Winthrop and C. R. Worthington, *J. Opt. Soc. Am.* **55**, 373 (1965).
- [46] W. D. Montgomery, *J. Opt. Soc. Am.* **57**, 772 (1967).
- [47] J. M. Cowley and A. F. Moodie, *Proc. Phys. Soc. Sec. B* **70**, 486 (1957).
- [48] M.-S. Kim, T. Scharf, C. Rockstuhl, and H. Herzig, *Prog. Opt.* **58**, 115 (2013).
- [49] G. Venkat, H. Fangohr, and A. Prabhakar, *J. Mag. Magn. Mater.* **450**, 34 (2018).

5.1.2 Spin-wave Talbot effect in various multimode waveguides (P2)

Building on previous work demonstrating the Talbot effect for spin waves (P1), this paper advances the study by investigating self-imaging in various multimode waveguides. We consider thin ferromagnetic films with a series of single-mode spin-wave sources/inputs, and investigate how these sources induce the self-imaging effect. Through micromagnetic simulations, we systematically analyze how the phenomenon depends on key parameters, including the waveguide width, the number of inputs, and their spatial periodicity. These findings lay the foundation for the development of advanced magnonic devices that exploit the Talbot effect, such as the logic systems discussed in the next section (paper P3).

Contribution of the Author

Building on the results published in *Physical Review B*, I initiated and designed a systematic study of this effect in different multimode waveguides, exploring its dependence on key parameters such as waveguide width, the spacing between single-mode inputs, and their number. I also performed all the micromagnetic simulations in MuMax3, and processed the data. I collaborated with M. Krawczyk and P. Gruszecki on the interpretation of the results, and I took primary responsibility for writing the manuscript, handling its submission to the journal, and managing correspondence with the reviewers.

Due to IEEE copyright requirements, I have included only the accepted version of the publication. ©2022 IEEE. Reprinted, with permission, from M. Gołębiewski, P. Gruszecki, and M. Krawczyk, Self-Imaging of Spin Waves in Thin, Multimode Ferromagnetic Waveguides, *IEEE Transactions on Magnetics*, vol. 58, no. 8, pp. 1–5, Aug. 2022.

Self-imaging of spin waves in thin, multimode ferromagnetic waveguides

Mateusz Gołębiewski^{*,†}, Paweł Gruszecki^{*} and Maciej Krawczyk^{*}

^{*}Institute of Spintronics and Quantum Information, Faculty of Physics,

Adam Mickiewicz University, Poznań, Uniwersytetu Poznańskiego 2, 61-614 Poznań, Poland

[†]matgol2@amu.edu.pl

Abstract—Self-imaging of waves is an intriguing and spectacular effect. The phenomenon was first observed for light in 1836 by Henry Fox Talbot and to this day is the subject of research in many areas of physics, for various types of waves and in terms of different applications. This paper is a Talbot-effect study for spin waves in systems composed of a thin, ferromagnetic waveguide with a series of single-mode sources of spin waves flowing into it. The proposed systems are studied with the use of micromagnetic simulations, and the spin wave self-imaging dependencies on many parameters are examined. We formulated conditions required for the formation of self-images and suitable for experimental realization. The results of the research form the basis for the further development of self-imaging-based magnonic devices.

Index Terms—magnonics, spin waves, Talbot effect, self-imaging, waveguides.

I. INTRODUCTION

Due to their unique properties, such as a strong dependence on the material parameters and the magnetization orientation in relation to the direction of propagation or the film plane, spin waves (SWs, i.e. coherent magnetization disturbances propagating in magnetic materials in the form of waves) are a fascinating research object[1]. Their dynamic properties are related to coexisting short-range, strong, and isotropic exchange interactions and long-range, weak, and anisotropic magnetostatic interactions. Moreover, one of the essential advantages of SWs as an information carrier is the fact that their frequency spans range from a few to hundreds of gigahertz, with the corresponding wavelength range extending from micrometers to tens of nanometers. All this adds up to the type of medium that can be influenced and configurable on many levels, making them flexible for applications in devices that can potentially support or replace conventional electronic solutions[2], [3].

Usually, the transmission and processing of SWs in narrow waveguides[4], [5] that are often coupled[6] are considered in magnonics. Another promising line of research is the use of elements much wider than the waveguides themselves to redirect[7], [8], [9] and process SWs[10], [11], [12], [13], [14]. These elements, being multimode waveguides, can be referred to as processing blocks. Most commonly, SWs are delivered to these elements via a single or a group of narrow waveguides. Subsequently, these entering SWs interfere with each other. Moreover, this interference can be further molded in processing blocks by properly modifying

the medium where SWs propagate. It can be achieved by the introduction of defects[14], programmable magnetic elements on top of that region[12], or utilization of noncolinear magnetization textures[15]. The main advantage of this approach is the possibility of using interference effects to process SW-carried information[12], [13], [14].

It is important to note that as waves fall into the processing block from a group of evenly spaced waveguides, the interference image with the same symmetry as the waveguide array is formed. There is a strong analogy to the Talbot effect[16], [17] that was firstly observed for electromagnetic waves. It results from waves interference coming from a series of periodically arranged sources. The most visible distribution of self-images, the so-called Talbot carpet, is created for infinitely many sources, corresponding to an infinitely long diffraction grating through which a plane wave passes. This phenomenon is extensively studied in recent years for many types of waves[18] and found already applications, for instance to improve x-ray imaging[19]. It has been theoretically demonstrated that this effect can occur also for SWs[20]. However, the conditions of the formation of the SWs' self-images in a thin ferromagnetic multimode waveguide have never been studied.

In this paper, we numerically investigate prototypes of SW multimode waveguides with multiple input single-mode stripes (see Fig. 2) and use the phenomenon of multimode interference (MMI). The fact that self-imaging is here an inherent property of the system allows assuming that in this type of device the interference images will form patterns analogous to the classic Talbot carpets. We will analyze how the width of the multimode waveguide, the number and separations between input waveguides influence the interference pattern, and finally we will discuss prospects for applications. We believe that due to the advantage of magnonic systems over the photonic ones in terms of miniaturization, the self-imaging effect may result in efficient magnonic devices, such as logic gates, couplers, multi-/demultiplexers, or phase controllers.

The paper is organized as follows. In Section II we describe system and method used in our investigations. In Section III we present the simulation results for different geometrical parameters and in Section IV we discuss the influence of damping on formation of the self-images. The paper is finishing with conclusions of the results.

II. MODEL DESCRIPTION

A. Self-imaging

The phenomenon of the self-imaging of waves is well described and widely used today [18], [21]. It dates back to the early 19th century when Henry Fox Talbot first observed it for light passing through a diffraction grating and a lens with high magnifying power [16]. The Talbot effect is the result of waves' interference as they pass through any periodic aperture. In its close diffraction field, at strictly defined distances from the sources, replication of the periodic structure – self-imaging will take place [see Fig. 1(a)]. The effect is the more visible, the wider diffraction grating is in relation to the wavelength of waves passing through it. For an infinitely long periodic grating (or sources array), one can obtain the Talbot carpet – ideal and repeated recreations of the periodic structure in every period, so-called Talbot lengths, described by a formula

$$z_T = nd^2/\lambda, \quad (1)$$

where n is an integer specifying the number of subsequent self-images, d is a period of the object, and λ is a wavelength. The theory of the Talbot effect has been described many times for various types of interactions [20], so in this paper, we will limit it only to the general description.

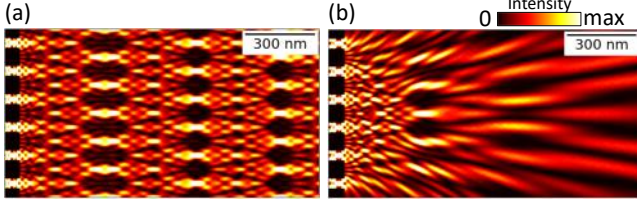


Figure 1. Illustrative self-imaging representation for (a) an infinitely long array of sources on the left and (b) for a finite number of inputs, where the near diffraction field quickly turns into the far diffraction field, and the Talbot effect disappears. In both cases, SW frequency is equal to 40 GHz, inputs period is 120 nm and infinitely wide waveguides were assumed.

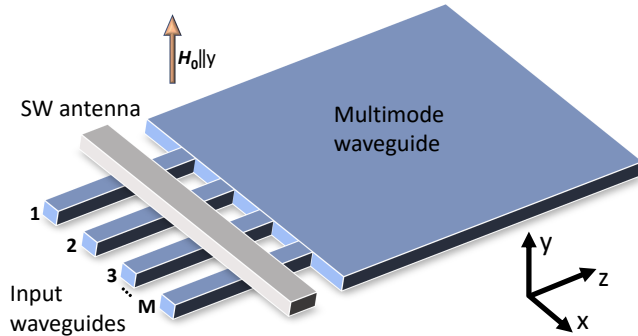


Figure 2. Scheme of a M -input multimode device.

B. Micromagnetic simulations

In order to present magnonic systems based on the self-imaging effect with MMI, the micromagnetic package

MUMAX3 was used [22]. The studied systems were discretized uniformly by $5 \times 5 \times 5 \text{ nm}^3$ unit cells, with one cell per thickness. The following magnetic parameters were applied in the simulations: saturation magnetization of $M_S = 860 \text{ kA/m}$, an exchange constant of $A = 13 \text{ pJ/m}$, these are the parameters related to permalloy, and initially negligibly low damping constant $\alpha = 10^{-5}$. In each of the analyzed cases, the waveguide was homogeneously magnetized by the external magnetic field of the value $\mu_0 H_0 = 1.1 \text{ T}$ ($H_0 > M_S$), directed perpendicular to the plane of the system. Low amplitude harmonic SWs were excited continuously by a microwave antenna placed on each of the input single-mode waveguides of 40 nm width, at a distance of 90 nm from the multimode part (see Fig. 2), until the system reached a steady state, i.e. a state where the interference image in the multimode layer is no longer dependent on time. The analyzed frequency of the SWs in our systems is 40 GHz enabling to excite exchange interaction dominated SWs of the wavelength ($\lambda = 68.83 \text{ nm}$) only a dozen times greater than the exchange length ($l_{\text{ex}} = \sqrt{2A/(\mu_0 M_S^2)} = 6 \text{ nm}$). To illustrate the propagation of SWs through the system, the intensity maps were calculated as the square of the m_x -component of magnetization and averaged over time $\langle m_x^2 \rangle_t$ after reaching the steady state.

III. MULTIPLE, LONG-RANGE SELF-IMAGING IN MULTIMODE WAVEGUIDES

The simulations were divided into three parts, where the Talbot effect in the M -input MMI systems was examined in terms of parameters like the distance between the inputs, the number of inputs, and the multimode waveguide width. In each of the presented cases, the impact of changing only one of these parameters was analyzed, leaving the other unchanged. This allows to access the possibilities of manipulating interference images in terms of their best use in future magnonic devices.

1) *Variable distance between inputs:* The first studies are for systems with a variable distance between the inputs while maintaining a constant number of them and unchanged width of the system. We assume $M=8$ inputs and the waveguide width equal $1.64 \text{ }\mu\text{m}$.

The analysis of the SW interference images in the multimode layer in Fig. 3 clearly shows that the interference first causes the formation of self-images in the near diffraction field, then due to the MMI, the structure is reconstructed further away from the source. As the distance between the inputs increases, so does the distance at which the *reproductions* of Talbot carpets appear. By further increasing the distance between the inputs while keeping the condition of their number and system width constant, we will come to the point where the series of inputs will span the entire width of the waveguide (see Fig. 4).

For large distances, when the inputs fill whole waveguide width, it can be noticed, that in near field the self-imaging effect is very clear. The first Talbot images (a series of first reproductions of periodic sources, laterally shifted in phase

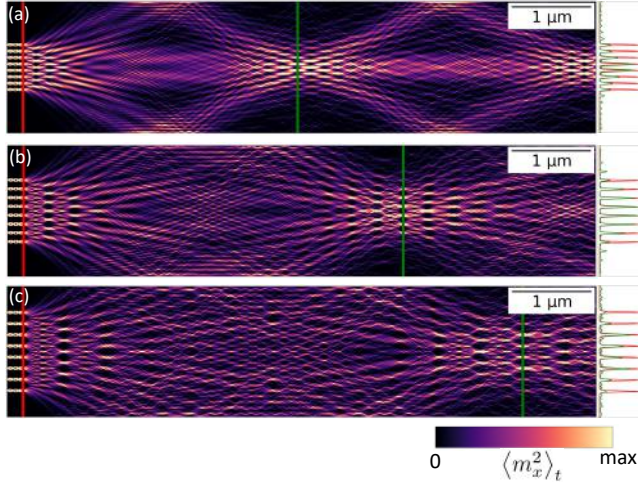


Figure 3. Intensity maps of SWs entering from a series of 8 single-mode 40 nm wide waveguides (on the left) into a 1.64 μm wide multimode film. The distance between the sources is respectively (a) 80 nm, (b) 110 nm, and (c) 140 nm. The red and green vertical lines represent the cross-section along which the normalized SW intensities as a function of width are plotted (on right).

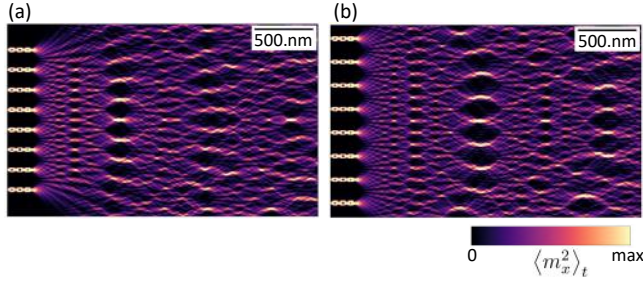


Figure 4. Intensity maps of SWs in the near diffraction field of multimode, 1.64 μm wide waveguides, with 8 inputs separated by (a) 170 nm and (b) 200 nm.

by half of their period) are very similar to the theoretical ones [see Fig. 1(a)], despite the finite dimensions of the system. The difference is only visible at the edges of the system, where the resulting SW focus points are clearly out of line with the others, disturbing the self-imaging. For the first two Talbot lengths (see Eq. 1), this disturbance does not significantly affect the phenomenon, however, for further distances the pattern regularity is increasingly disturbed. Nevertheless, due to reflections from the waveguide edges, the reproductions of the entire patterns are created also at a distance of a dozen μm. However, the self-images resulting from the Talbot effect in the near field are more interesting from the application point of view, because they maintain their regularity and high intensity (see the insets on the right side of Fig. 3), even in materials with relatively high damping, as will be discussed in Section IV.

2) *Variable number of inputs:* The second type of numerical simulation is performed to check how the change in the number of single-mode inputs affects the formation of both Talbot carpets and their reproductions on the further sections of multimode waveguide. Analogically to

the previous paragraph, the width of the system and the distance between the sources will remain unchanged here, i.e., 80 nm and 1.64 μm, respectively.

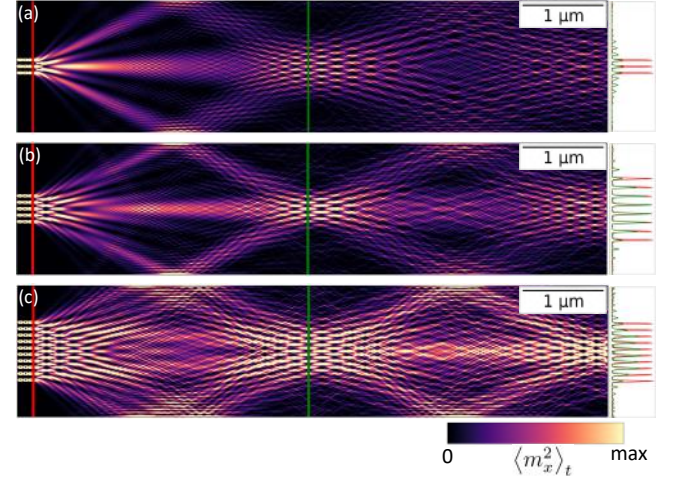


Figure 5. Intensity maps of SWs in a 1.64 μm wide multimode film coming from (a) 3, (b) 5, and (c) 10 single-mode inputs, separated by 80 nm. The red and green lines represent the cross-section along which the normalized SW intensities as a function of width are plotted (on right).

In Fig. 5 it can be seen that, in contrast to the distance between the inputs, their number does not affect the distance at which the Talbot pattern is reconstructed in a multimode waveguide. However, for a small number of sources, this self-imaging in far field practically does not occur – for three sources in Fig. 5(a), a specific interference pattern can be seen, but with significantly lower intensity. Only in the case of 5 or more sources, we can observe the reproduction of the near diffraction field.

3) *Variable MMI waveguide width:* The last type of system in which we decided to analyze SW self-imaging are multimode waveguides with different widths. Here again, as in the previous cases, the remaining parameters tested, i.e., the number and the distance between the inputs, are constant, $M=10$ and 80 nm, respectively.

The simulation results presented in Fig. 6 clearly show, following the intuition from geometric optics, the tendency of the SWs' re-focus area to move away from the inputs with increasing width of the waveguide. It points that the width of the multimode waveguide and its edges are important factors influencing reproduction of the pattern in far field. Comparing Figs. 6(a)-(c), it can be seen that the interference image shown in Fig. 6(a) most closely resembles the classical Talbot image, a similar conclusion may be drawn from comparing Fig. 3(a)-(c). This indicates that by properly choosing the width of the multimode waveguide, the number and a separation between the input single-mode waveguides, one can reproduce a Talbot carpet in relatively far distances in multimode waveguides, the same as for an infinite number of periodically arranged SW sources. This is because, the lateral edges on which reflections occur can act similarly to periodic boundary conditions. This means that for materials with low damping, it can be possible

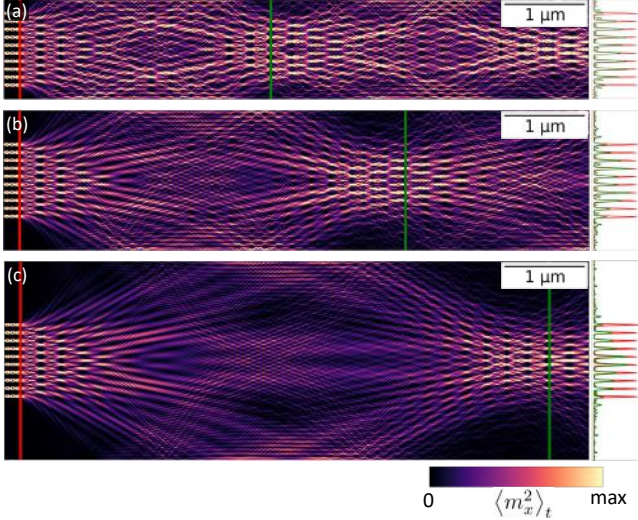


Figure 6. Intensity maps of SWs entering from a series of 10 single-mode 40 nm wide waveguides (on the left) into a (a) 1.25 μm, (b) 1.75 μm and (c) 2.5 μm wide multimode film. The distance between the sources is equal in all cases 100 nm. The red and green lines represent the cross-section along which the normalized SW intensities as a function of width are plotted (on right).

to transmit information about a geometry of a diffraction grating/array of sources over long distances thanks to the self-imaging phenomenon.

IV. IMPACT OF GILBERT DAMPING ON THE SELF-IMAGING EFFECT

The Talbot effect in finite systems of thin ferromagnetic layers can be used in two ways. (i) At short distances from the source array, as we have presented in Fig. 4 for a wide distribution of a number of sources. Here the near diffraction field is distributed over the width of the multimode waveguide and is close to the classic Talbot carpet, and it doesn't significantly depend on the edges of the waveguide (see Figs. 3-6). (ii) As we presented in the other examples, where the near field pattern is reproduced over longer distances. Of course, especially the latter case raises the question of the SW damping and whether this effect is achievable experimentally.

On the basis of micromagnetic simulations, we analyzed the influence of a damping constant on the self-imaging effect, by simulations with the two values of α : 3.2×10^{-4} [characteristic for yttrium iron garnet (YIG)], and $\alpha = 5 \times 10^{-3}$ (permalloy). The remaining material parameters, characteristic for permalloy, are unchanged in relation to the previous simulations. YIG and permalloy are some of the most popular magnetic materials in magnonics due to low damping; therefore, the choice the tabular damping values characteristic for these materials as an example is justified.

Figure 7 shows the SW amplitude distribution for two types of system geometries, with smaller separation between the inputs [(a) and (c)] and large separation [(b) and (d)], for the two values of α . The conclusion that arises

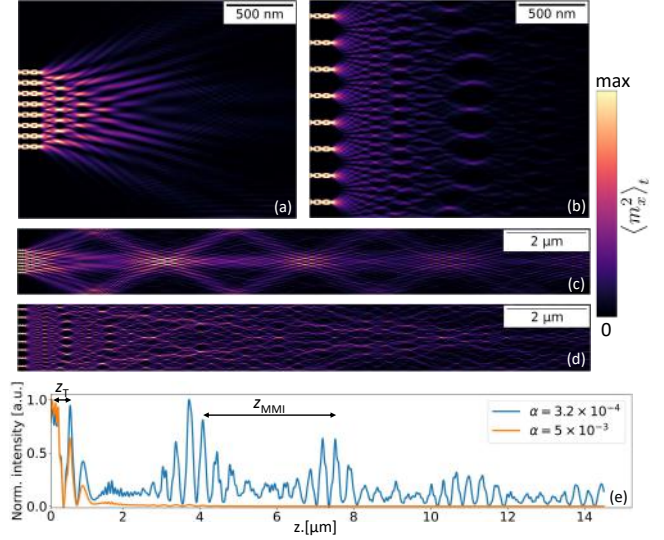


Figure 7. SW intensity maps in multimode waveguides with Gilbert damping factors equal to (a), (b) $\alpha = 5 \times 10^{-3}$ and (c), (d) $\alpha = 3.2 \times 10^{-4}$. The graph (e) shows the intensity of SWs on a line from the fourth source for both analyzed damping values (and smaller input period cases). The Talbot length is marked as z_T , while the length of reproducing self-images as z_{MMI} .

is certainly a large decrease in the intensity of self-images in the far diffraction field for the α of permalloy – here detection by measuring techniques such as micro-BLS may be limited only to classic Talbot images formed near the source array. However, in systems with small damping, the situation is much more promising – reproductions at the distance of even a few μm from the sources should be measurable using standard techniques for measuring the dynamics of magnetization.

Figure 7(e) shows the SW intensity as a function of the distance from the array sources along the line crossing the fourth source. It can be clearly seen that in the system with the damping constant characteristic for permalloy (orange line) the decrease in SW energy by 50% occurs after around 700 nm, thus only classic Talbot effect (z_T) can be exploited. For YIG-value of damping the signal decreases by 50% only after around 8 μm, which allows for observation at least 3 reproduced Talbot images ($3z_{MMI}$) and makes it a good candidate for applications. It is also important to point out that both YIG, permalloy, and materials with a slightly higher damping factor can be used in systems where the Talbot effect in the near field will be used. This is especially promising for future potential magnonic devices where miniaturization, e.g. computing systems, will be a key.

V. CONCLUSIONS

The propagation of high-frequency SWs in multimode structures is of a great interest. Such studies allow understanding the dynamics of SWs in structures that can replace conventional CMOS systems in high-speed signal processing, logic circuits, and information storage technologies in the near future. Using different types of system geometry,

materials and changing the direction and value of the external magnetic field, we can manipulate the interference field generated in the multimode part.

The combination of the Talbot effect with MMI was the core of the structures proposed in this paper. We showed that a series of single-mode SW sources causes the formation of self-images in multimode waveguides in the near diffraction field and also to be transferred for much further distances creating reproduced Talbot carpets due to MMI. The quality of these reproduced carpets depends on the multimode waveguide widths, edges and the arrangement of single-mode waveguides. In materials with low Gilbert damping, this may result in focusing SW beams at far distances from the sources, while the near diffraction field may retain properties close to the theoretical undisturbed Talbot carpets even for moderate values of damping.

The out-of-plane alignment of the magnetization used in the paper is advantageous in the analysis of Talbot phenomena due to the circular shape of isofrequency contours. It makes the analyzed magnonic systems a good analogue of the systems known from photonics. However, there are still a number of technical issues, including high frequency and the value of the external magnetic field assumed in our simulations required to uniformly magnetize the system. One of the solutions may be the use of in-plane magnetized ferromagnetic layer, which would certainly contribute to lowering these two parameters, but at the same time introducing an anisotropy to the system.

We hope that this work will draw the attention of the magnonic community to the potential of SW self-imaging in many sorts of future technological solutions.

ACKNOWLEDGMENT

The research leading to these results has received funding from the National Science Centre of Poland, project no. 2019/35/D/ST3/03729. The simulations were partially performed at the Poznan Supercomputing and Networking Center (Grant No. 398).

REFERENCES

- [1] A. G. Gurevich and G. A. Melkov, *Magnetization oscillations and waves*. CRC Press, Boca Raton, 1996.
- [2] A. Barman, S. Mondal, S. Sahoo, and A. De, "Magnetization dynamics of nanoscale magnetic materials: A perspective," *J. Appl. Phys.*, vol. 128, no. 17, p. 170901, 2020.
- [3] A. Chumak, V. Vasyuchka, A. Serga, and B. Hillebrands, "Magnon spintronics," *Nat. Phys.*, vol. 11, no. 6, pp. 453–461, 2015.
- [4] V. E. Demidov and S. O. Demokritov, "Magnonic waveguides studied by microfocus Brillouin light scattering," *IEEE Transactions on Magnetics*, vol. 51, no. 4, pp. 1–15, 2015.
- [5] Q. Wang, B. Heinz, R. Verba, M. Kewenig, P. Pirro, M. Schneider, T. Meyer, B. Lagel, C. Dubs, T. Bracher, and A. V. Chumak, "Spin pinning and spin-wave dispersion in nanoscopic ferromagnetic waveguides," *Phys. Rev. Lett.*, vol. 122, p. 247202, Jun 2019.
- [6] U. Garlando, Q. Wang, O. Dobrovolskiy, A. Chumak, and F. Ri-ente, "Numerical model for 32-bit magnonic ripple carry adder," *arXiv preprint arXiv:2109.12973*, 2021.
- [7] F. Heussner, M. Nabinger, T. Fischer, T. Bracher, A. A. Serga, B. Hillebrands, and P. Pirro, "Frequency-division multiplexing in magnonic logic networks based on caustic-like spin-wave beams," *physica status solidi (RRL)–Rapid Research Letters*, vol. 12, no. 12, p. 1800409, 2018.
- [8] F. Heussner, G. Talmelli, M. Geilen, B. Heinz, T. Bracher, T. Meyer, F. Ciubotaru, C. Adelman, K. Yamamoto, A. A. Serga *et al.*, "Experimental realization of a passive gigahertz frequency-division demultiplexer for magnonic logic networks," *physica status solidi (RRL)–Rapid Research Letters*, vol. 14, no. 4, p. 1900695, 2020.
- [9] J. Grafe, P. Gruszecki, M. Zelent, M. Decker, K. Keskinbora, M. Noske, P. Gawronski, H. Stoll, M. Weigand, M. Krawczyk, C. H. Back, E. J. Goering, and G. Schutz, "Direct observation of spin-wave focusing by a fresnel lens," *Phys. Rev. B*, vol. 102, p. 024420, Jul 2020.
- [10] . Papp, W. Porod, . I. Csurgay, and G. Csaba, "Nanoscale spectrum analyzer based on spin-wave interference," *Scientific reports*, vol. 7, no. 1, pp. 1–9, 2017.
- [11] . Papp, M. Kiechle, S. Mendisch, V. Ahrens, L. Sahin, L. Seitner, W. Porod, G. Csaba, and M. Becherer, "Experimental demonstration of a concave grating for spin waves in the Rowland arrangement," *Scientific Reports*, vol. 11, no. 1, pp. 1–8, 2021.
- [12] . Papp, W. Porod, and G. Csaba, "Nanoscale neural network using non-linear spin-wave interference," *arXiv preprint arXiv:2012.04594*, 2020.
- [13] . Papp, G. Csaba, and W. Porod, "Characterization of nonlinear spin-wave interference by reservoir-computing metrics," *Applied Physics Letters*, vol. 119, no. 11, p. 112403, 2021.
- [14] Q. Wang, A. V. Chumak, and P. Pirro, "Inverse-design magnonic devices," *Nature Communications*, vol. 12, no. 1, pp. 1–9, 2021.
- [15] D. Prychynenko, M. Sitte, K. Litzius, B. Kruger, G. Bourianoff, M. Klaui, J. Sinova, and K. Everschor-Sitte, "Magnetic skyrmion as a nonlinear resistive element: a potential building block for reservoir computing," *Physical Review Applied*, vol. 9, no. 1, p. 014034, 2018.
- [16] H. Talbot, "Lxxvi. facts relating to optical science. no. iv," *The London, Edinburgh, and Dublin Philosophical Magazine and Journal of Science*, vol. 9, no. 56, pp. 401–407, 1836.
- [17] L. Rayleigh, "On copying diffraction gratings and on some phenomenon connected therewith," *Phil. Mag.*, vol. 11, p. 196, 1881.
- [18] J. Wen, Y. Zhang, and M. Xiao, "The Talbot effect: recent advances in classical optics, nonlinear optics, and quantum optics," *Adv. Opt. Photon.*, vol. 5, no. 1, pp. 83–130, Mar 2013.
- [19] A. Bravin, P. Coan, and P. Suortti, "X-ray phase-contrast imaging: from pre-clinical applications towards clinics," *Physics in Medicine and Biology*, vol. 58, no. 1, pp. R1–R35, 2012.
- [20] M. Golebiewski, P. Gruszecki, M. Krawczyk, and A. E. Serebryanikov, "Spin-wave Talbot effect in a thin ferromagnetic film," *Phys. Rev. B*, vol. 102, p. 134402, Oct 2020.
- [21] X. Wang, H. Chen, H. Liu, L. Xu, C. Sheng, and S. Zhu, "Self-focusing and the Talbot effect in conformal transformation optics," *Phys. Rev. Lett.*, vol. 119, p. 033902, Jul 2017.
- [22] A. Vansteenkiste, J. Leliaert, M. Dvornik, M. Helsen, F. Garcia-Sanchez, and B. Van Waeyenberge, "The design and verification of mumax3," *AIP Advances*, vol. 4, no. 10, p. 107133, 2014.

5.1.3 Concept of a magnonic logic device based on the self-imaging phenomenon (P3)

This work explores a novel approach to incorporate spin waves into the computing paradigm, with the goal of advancing the integration of magnonics with conventional complementary metal-oxide-semiconductor (CMOS) technology. We exploit the Talbot effect in the spin-wave domain to design and simulate interference-based logic systems. By utilizing self-imaging phenomena in thin, ferromagnetic multimode waveguides, we demonstrate that it can be effectively used to implement fundamental logic operations – a concept that, to the best of our knowledge, has not yet been explored. Using micromagnetic simulations, we design and evaluate spin-wave-based lookup tables (LUTs) that exploit self-imaging and demonstrate its high degree of programmability and scalability. This design allows for flexible control of spin-wave phases and amplitudes, a capability essential for implementing a variety of logic operations. The ability of these LUTs to support multiple logic configurations makes them highly suitable for field-programmable gate array (FPGA) applications where reconfigurability is essential. This work presents a novel use of spin-wave self-imaging as a mechanism for logic reconfiguration. Such functionality has the potential to complement conventional CMOS technology and pave the way for energy-efficient, magnon-based computing architectures.

Contribution of the Author

In this work, together with P. Gruszecki, I developed the original concept of spin-wave self-imaging-based logic devices and designed the corresponding structures to implement this functionality. I performed all micromagnetic simulations using MuMax3 and, based on a convolution-based code originally developed by P. Gruszecki, I adapted and extended it to efficiently generate interference patterns specific to this work, thereby avoiding the need for repeated micromagnetic simulations. I post-processed the data, contributed to the interpretation of the results in collaboration with M. Krawczyk and P. Gruszecki, and took primary responsibility for writing the manuscript, managing its submission to the journal, and handling correspondence with the reviewers.

©2022 The Authors. *Advanced Electronic Materials* published by Wiley-VCH GmbH. The paper was published under the CC-BY 4.0 license.

Self-Imaging Based Programmable Spin-Wave Lookup Tables

Mateusz Gołębiewski,* Paweł Gruszecki, and Maciej Krawczyk

Inclusion of spin waves into the computing paradigm, where complementary metal-oxide-semiconductor devices are still at the fore, is now a challenge for scientists around the world. In this work, a wave phenomenon that has not yet been used in magnonics-self-imaging, also known as the Talbot effect, to design and simulate the operation of interference systems that perform logic functions on spin waves in thin ferromagnetic multimode waveguides is utilized. Lookup tables operating in this way are characterized by high programmability and scalability; thanks to which they are promising for their implementation in field-programmable gate arrays circuits, where multiple logic realizations can be obtained.

1. Introduction

Over the last decades, there has been a steady increase in the demand for computing power and multipurpose systems for information processing. One of the strategies is the utilization of reprogrammable integrated circuits whose functionality can be determined and changed multiple times after manufacturing. The most popular class of such circuits are field-programmable gate arrays (FPGAs),^[1] which allow for hardware implementation of customer-specified functions. Moreover, FPGA-based devices can on-demand, partially or even entirely, change their configuration during their operation. In a nutshell, an FPGA is made up of interconnected (by routing channels) configurable logic blocks (CLBs) that perform specific logic functions (see **Figure 1**). FPGA structures contain from tens to thousands of CLBs with a very diverse structure. The essential elements of the CLBs are multi-input RAM-memory-based lookup tables (LUTs) that realize the array indexing operation, that is, they can be used to implement any logic function.

Reprogrammable logic circuits such as FPGA could benefit greatly from using beyond-CMOS solutions such as the replacement of the electric charge as an information carrier, by spin waves (SWs) that are coherent and precessive magnetization

oscillations propagating without charge transfer in magnetic materials.^[2–5] This property, combined with a wider range of available frequencies than in electronics and the ability to encode information both in amplitude and phase, makes SWs an important candidate for an information carrier in a new generation of computing devices, where Joule–Lenz heat and other obstacles may be significantly reduced.^[6–9]

Magnonic circuits (systems utilizing SWs)^[10,11] may consist of waveguides through which SWs propagate,^[12–15] and interference areas at crossings, for example, for creating majority gates.^[16–20]

The waveguides may also couple with other waveguides^[21,22] to implement a logical operation. In this manner, it has been possible to demonstrate a 32-bit magnonic full adder^[21] and SW-based approximate 4:2 compressor.^[23] Another strategy is to use wide ferromagnetic film areas for SW operation and narrow waveguides as SW inputs. This approach was used to redirect^[24–26] and process SWs.^[27–32] Operation of these systems is based on the interference of incoming SWs. Therefore, a local modification of the medium (the magnonic equivalent of the refractive index) in which SWs propagate is crucial to design and optimize its functionality. It was recently shown that it could be achieved by an introduction of defects in so-called inverse design approach,^[32] placement of programmable magnetic elements on top of that region,^[30] or utilization of non-collinear magnetization textures.^[33–35] This interference based strategy appears promising also for the realization of physical neural networks operating on SWs.^[30,33] Thereby, interference effects open a promising avenue for the development of SW-based beyond-CMOS solutions.

A plane wave passing through a system of periodically spaced obstacles (diffraction gratings or holes) interferes, creating a characteristic diffraction pattern in the near field, reproducing the grating image at specific distances from the input apertures. This phenomenon is known as the Talbot or the self-imaging effect, and was observed for light already in the 19th century.^[36] The resulting interference pattern is called a Talbot carpet, and we have recently theoretically demonstrated that this effect can also occur for SWs.^[37] The properties of Talbot carpets created by SWs strongly depend on material parameters, geometry, type, thickness of a magnetic material, and on dynamic parameters such as wavelength, orientation, and the value of an external magnetic field.

Here, we exploit the self-imaging phenomenon occurring in a thin ferromagnetic multimode waveguide with SWs introduced by periodically spaced single-mode input waveguides. SWs entering the multimode waveguide have a controllable phase. In particular, we present a new class of reprogrammable magnonic blocks implementing array indexing operations.

M. Gołębiewski, P. Gruszecki, M. Krawczyk
 Faculty of Physics
 Institute of Spintronics and Quantum Information
 Adam Mickiewicz University in Poznań
 Uniwersytetu Poznańskiego 2, Poznań 61-614, Poland
 E-mail: mateusz.golebiewski@amu.edu.pl

 The ORCID identification number(s) for the author(s) of this article can be found under <https://doi.org/10.1002/aelm.202200373>.

© 2022 The Authors. Advanced Electronic Materials published by Wiley-VCH GmbH. This is an open access article under the terms of the Creative Commons Attribution-NonCommercial License, which permits use, distribution and reproduction in any medium, provided the original work is properly cited and is not used for commercial purposes.

DOI: 10.1002/aelm.202200373

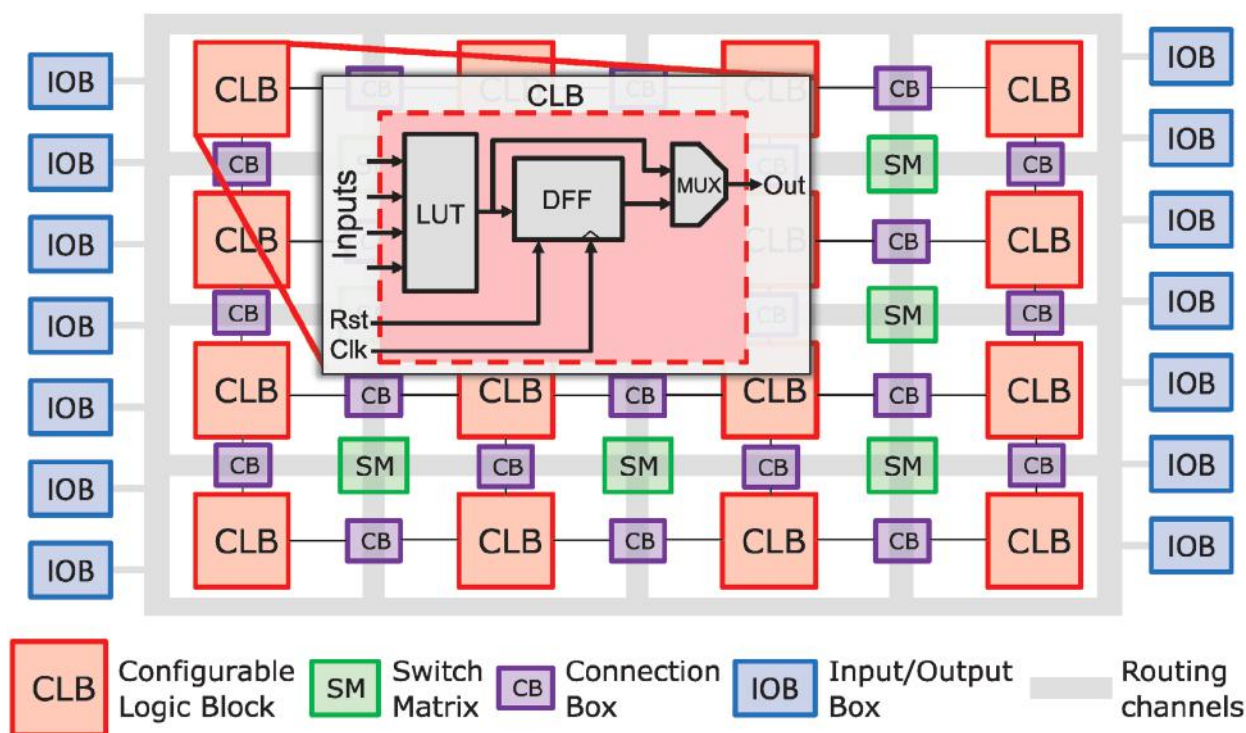


Figure 1. Schematic structure of the FPGA matrix with the CLB build inset (DFF: “delay” flip-flop circuit; MUX: multiplexer; Clk: clock; Rst: reset).

Therefore, we propose a fully magnonic LUT, an essential FPGA building block. We show that our device can be relatively easily configurable by dynamic parameters, that is, without the need to physically change the structure. More specifically, in the paper we describe a logic block with eight magnonic input waveguides—six of them having a control function (control input), that is, the responsibility for defining the functionality of our device and the other two feeding the SW carrying information. On the opposite side of the device, in well-defined positions, there are five outputs. Our LUT is programmed by the phase of the SWs entering the control inputs, and the output logic level is encoded in the SW amplitude. Therefore, we demonstrate 2-input and 5-output LUT. The proposed idea of the self-imaging magnonic LUT can be further developed to include more inputs/outputs and integrate them into CLB and FPGA circuits. In addition, most of the research provided here was obtained using an efficient technique for calculating the steady-state SW amplitude distribution, specifically developed for this purpose. This method provides a satisfactory approximation of full micromagnetic simulations and, at the same time, is several orders of magnitude faster.

2. Results

2.1. Talbot Carpet from a Finite Source Sequence

Let us consider a 5 nm thick yttrium iron garnet (YIG) film, uniformly magnetized by the out-of-plane magnetic field of value $\mu_0 H = 1.1$ T with μ_0 being the permeability of the vacuum, where SWs propagate at frequency $f = 40$ GHz (see the magnetic parameters and simulation details in Experimental

Section). We have chosen this arrangement for the simplicity of calculation, and it guarantees the isotropic propagation of SWs of several dozens of nanometers (i.e., in the so-called exchange regime). The effect of the anisotropy of the dispersion relation on self-imaging is discussed in ref. [37].

First, let us analyze the Talbot carpet obtained by interference of incident SWs at $f = 40$ GHz from a finite sequence of periodically arranged 40 nm wide waveguides with a period equal to 200 nm, supplying SWs to a thin film. We study the effect of small changes in the width of a thin film on the quality of the interference pattern (as shown in **Figure 2**). It is clearly visible that the self-images obtained in the systems with the width equal to the exact multiple of the period (multiplied by the number of inputs), here being 1.60 μm , are the most accurate and closest to those with an infinitely wide layout for which the Talbot effect is theoretically described.^[36] A slight change in this parameter causes the interference pattern to become distorted (Figure 2a,b), and the self-images are less accurate. In this analysis, the most significant result is that, despite the disturbance of the arrangement that may occur in experimental implementations, the Talbot images remain at the same distance from the sources, and their distribution is qualitatively similar (green dashed rectangle in Figure 2) after spatial averaging by the detectors. Despite the high sensitivity to geometric changes, the Talbot effect retains its properties, especially as we analyze changes in the intensity of the self-images in relation to their calibration distribution rather than the top-down values.

Due to the limited dimensions and the number of sources entering the multimode waveguide, it is not possible to recreate an ideal Talbot carpet in a waveguide with finite widths. However, it is visible that the self-imaging effect is almost

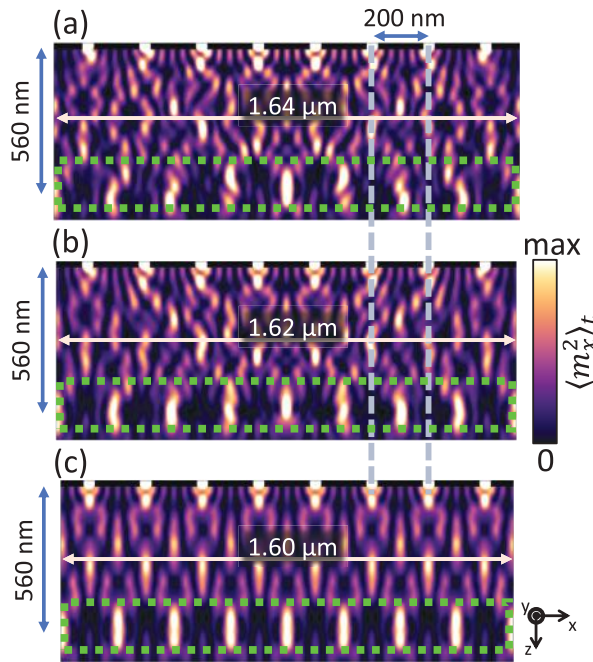


Figure 2. Comparison of Talbot carpets (SW intensity distribution in a near diffraction field) obtained from micromagnetic simulations for the same parameters except for the system width. In (a–c), the width is successively reduced by 20 nm for an unchanged input period of 200 nm. The region of self-image occurrence (each time at a distance of 560 nm) is marked with a green dashed rectangle. In each picture the input source is placed at the top.

perfect when the sources are spread over the entire width of the system.^[38] Consequently, we are able to acquire high-quality self-images at a distance as close to the Talbot theoretical length as possible, which is described by the following equation

$$z_T = nd^2/\lambda \quad (1)$$

where d is the period of the input waveguides, λ is the wavelength, and n is an integer specifying the number of subsequent self-images (here we consider only $n = 1$). It is crucial that z_T depends only on the period and wavelength of the waves that creates the interference pattern.

It is also worth emphasizing the scalability of this effect—the presented results are correct for each range of system dimensions/spin wavelengths, where the proportions remain the same as long as the propagation of SWs is isotropic and are only limited by technical capabilities. In this paper, we analyze systems with sources distributed over the entire width of the waveguide, with the distance between them equal to 200 nm. This is justified by the need to control and manipulate self-images, which is favored by a Talbot length that is at least an order of magnitude longer than the wavelength. These issues will be discussed in the following parts of this paper.

The linear approximation of the Kalinikos–Slavin (K–S) SW dispersion relation^[39] for out-of-plane magnetized ferromagnetic thin films is described by the equation

$$\omega^2 = (\omega_H + l_{\text{ex}}^2 \omega_M k^2) (\omega_H + l_{\text{ex}}^2 \omega_M k^2 + \omega_M F(kL)) \quad (2)$$

where $\omega = 2\pi f$ is the angular frequency, L is a film thickness, $\omega_H = |\gamma| \mu_0 (H - M_S)$, $\omega_M = \gamma \mu_0 M_S$, k is the wavenumber, γ is the gyromagnetic factor, l_{ex} is the exchange length, M_S is the magnetization saturation and

$$F(kL) = 1 - \frac{(1 - e^{-kL})}{kL} \quad (3)$$

We can use Equation (2) to estimate the value of the wavelength and the group velocity of SWs that have a direct impact on the speed of the device. Furthermore, the equation for the Talbot length (Equation (1)) can be used to verify whether this distance agrees with the simulations. After substituting all the data, we get the group velocity $v_{\text{gr}} = d\omega/dk = 1.9 \text{ km s}^{-1}$, the wavelength $\lambda = 67 \text{ nm}$, and thus z_T ($n = 1$) = 581 nm. As we can see in Figures 2 and 5, this corresponds well to the distance at which we analyze the refocusing of SWs.

2.2. Input Phase Coherence Control

Knowing that self-imaging of waves from a number of sources is very sensitive to any incoherence, we can first analyze Talbot carpets and self-images from this point of view. We use Huygens–Fresnel principle-based calculations (HFPBC) to make these calculations. This method provides a satisfactory approximation of the interference patterns in waveguides created by various apertures of the incoming SWs. At the same time, HFPBC is a few orders of magnitude faster than the conventional full micromagnetic simulations (see Experimental Section).

If N coherent in phase and amplitude signals enters a multimode waveguide, then at distance z_T we get $N - 1$ readings with the possibility of reusing them. The single-signal loss results from the lateral shift of the Talbot images (characteristic for odd n values—see Equation (1)) and the finite width of the functional area. If, on the other hand, signals with slight incoherence enter the system, then we expect the output readings to be disturbed. Indeed, a phase shift of random three out of ten sources by $\varphi = \pi/4$ causes a significant change in the output amplitude, as can be seen in Figure 3b. The sensitivity of such a system would clearly depend on the detector accuracy, but after appropriate calibration, when even one source is out of phase with the others, the amplitude of at least one detector will be significantly different from the reference one.

As can be seen in Figure 3, the configuration of such a device is very similar to a LUT with eight inputs and seven outputs, and the functional area is a multimode waveguide in which self-imaging occurs. This perfectly shows the huge potential and flexibility of the effect. This property can be used in many types of magnonic devices, where high accuracy and coherence of the source signals are required. For instance, we can combine the operation of logic gates and phase control functionality in one system, and even use it to calibrate and estimate, before logic operations, the system's geometry regularity, whether the expected wavelength is propagating, and, finally, whether the sources are coherent in phase.

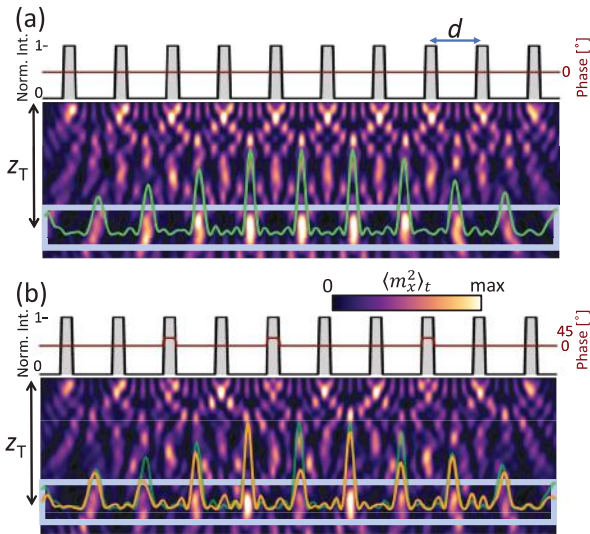


Figure 3. Functionality of the proposed phase coherence controller calculated using HFPBC. In (a) we have the reference state where the input signals (on the top) are perfectly coherent in phase and amplitude. Therefore, the functional area reproduces the exact Talbot carpet with regular and symmetrical distribution of self-image intensities. In (b), we can see the disturbed phase coherence controller, where three of the input signals entering the functional area have shifted phase by $\pi/4$. Afterward, irregular self-images appear in the diffraction pattern. In both figures there is a line graph showing the averaged and normalized intensity of SWs from the marked rectangular area (green line – reference, orange line – disturbance).

2.3. Spin-Wave Lookup Table

For a given SW wavelength and a period of sources, the Talbot length z_T is fixed (see Equation (1)). However, by changing the phase and amplitude of the SWs coming out of the individual input waveguides, the near diffraction field of SWs may be manipulated. Let us discuss the functionality of these changes in the context of their application as logic elements. In the prepared models, we directly use the first Talbot images indicated by the marked region in Figure 2a and analyze how the amplitude of SWs in the location spots of subsequent input self-images varies. The Talbot effect theory, described in more detail in ref. [37], does not quantify the amplitude distribution on consecutive self-images, but is limited only to the Talbot length z_T (1), which defines the distance at which self-images appear from a series of input sources depending on their period, wavelength, etc. By manipulating the input phase, we do not change the distance, but we influence the amplitude distribution at individual focal points, which is crucial for the functionality presented. In order to be able to quantify them, without carrying out separate micro-magnetic simulations each time, we use the HFPBC method. All the calculations presented in this section are obtained using HFPBC.

A typical modern FPGA is built of four input LUTs. However, for simplicity, let us examine here only a simpler version of LUTs consisting of two inputs. In the following sections, we present two examples of 2-input and 5-output programmable LUTs operating on SWs. In both examples, two of the input waveguides act as logic inputs, while the other waveguides

act as control inputs that are used to steer the functionality of the element. The type of operation the devices provide can be changed by the modulation of the amplitude and phase SWs incoming from the control waveguides. Furthermore, one of the biggest challenges is the interconnection of individual CLBs (or LUTs). Potentially, this could be accomplished using fully magnonic components (which seems to be a big challenge at the moment) or electronic circuits similar to those in co-sensor FPGAs. However, this issue is beyond the scope of this paper and we will not explore it.

2.3.1. Example 1 – Symmetric Geometry

The schematic diagram of the first exemplary LUT is shown in Figure 4. The device consists of two inputs I1 and I2, which are maximally separated from each other, and a series of coherent control inputs CIs, necessary to induce and control the Talbot effect in the functional area. The five outputs O1–O5 are defined by the location spots of subsequent self-images of the source waveguides at $z = z_T = 581$ nm.

There are two main options for programming a LUT—by defining a logic value at the input in the SW phase or amplitude. However, in the case of the self-imaging phenomenon, the amplitude manipulation on inputs seems to be less effective, so we decided to use the phase to encode the input information. At the same time, at the output, there are threshold detectors analyzing the amplitudes of SWs, assigning them an appropriate logic value. It is possible to design systems where both the phase and the amplitude of the inputs would be the information carrier, but this is beyond the scope of this work.

In amplitude SW logic gates, a certain threshold value of the magnetization precession angle (MPA) is defined,^[40] above which we treat the output signal as logic “1”, and below it as “0”. The magnetization amplitude can then be defined as

$$\text{MPA} = \arctan \left(\frac{\sqrt{\bar{m}_x^2 + \bar{m}_y^2}}{M_s} \right) \quad (4)$$

where \bar{m}_x and \bar{m}_y denote magnetization mean components in the waveguide plane and M_s is the saturation magnetization. In turn, the information on the inputs is encoded in the SW

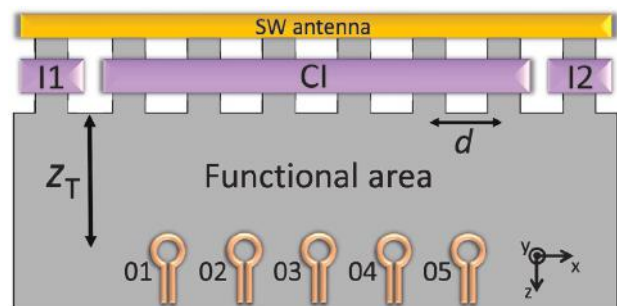


Figure 4. Scheme of the symmetric SW LUT with the first ($n = 1$) Talbot length z_T and the inputs period d marked. CI denotes the control input and the numbered markings I and O denote the inputs and outputs, respectively.

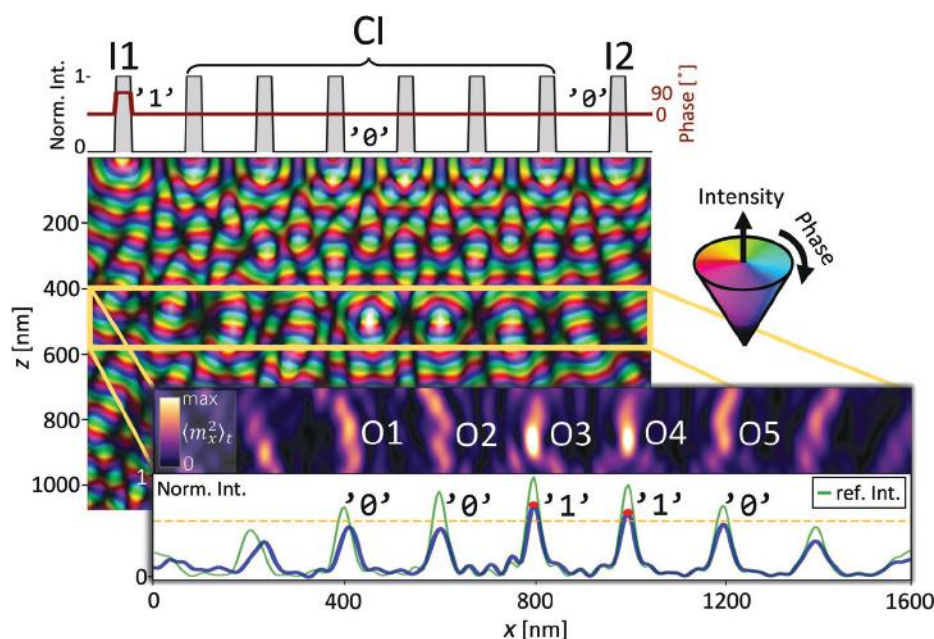


Figure 5. HFPBC results showing the operation of a logic gate based on the self-imaging of SWs (state for inputs $I1=“1”$, $I2=“0”$, $CI=“0”$, see Table 1). The upper part shows the intensity distribution on the inputs (the gray columns) and their phase shift (the maroon line). Below is a colormap representing the amplitude and phase of SWs (color and its intensity denote the phase and amplitude of SWs, respectively) of the functional area where the inputs are on the top edge. The inset at the bottom zooms in on the region where self-imaging takes place. It contains normalized graphs of MPA in 2D and the averaged one in 1D. The orange dashed line indicates the predefined threshold value.

phase, which can be controlled by phase shifters placed behind the spin plane-wave source (Figure 4). We can separately set a phase shift in $I1$ and $I2$ and arbitrarily change the logic value of the CI switch. Thus, in our simulations we assume that the phase shift $\varphi = \pi/2$ determines logic “1”, and no shift ($\varphi = 0$) is logic “0”. So, we have a two-input system with a CI switch, which can also have many states—in our case, it will be responsible for the phase shift of $\varphi = \pi/4$ or no such shift. This allows to programme the LUT and obtain completely new functionality by changing only one switch parameter.

The situation shown in Figure 5 visualizes the system response to the input signal $[1,0]$ and $CI=“0”$ ($\varphi = 0$)—then we

get the output array $[0,0,1,1,0]$. This result is strictly dependent on the threshold value selection, which should be calibrated/normalized in relation to the intensity plot for an undisturbed Talbot carpet ($I1 = I2 = CI = “0”$)—the green line in the inset in Figure 5, visualized also in Figure 3a. In this simulation, the threshold value is equal to 55% of the maximum self-image MPA of the calibration pattern.

The described example was examined for all possible combinations of input signals and the truth tables of two binary variables were made (Table 1). Each individual output (self-image) performs a separate logic function that can be programmed via CI switches. Therefore, with five outputs, we can get a system

Table 1. Two-input five-output symmetric LUT behavior for $CI=“0”$ and $CI=“1”$. Symbols \nrightarrow , \Leftarrow , and \neg stand for material nonimplication, converse nonimplication, and negation, respectively—glossary of terms in Table S1, Supporting Information.

$I1$	$I2$	CI	$O1$	$O2$	$O3$	$O4$	$O5$
1	1	0	0	0	1	0	0
1	0	0	0	0	1	1	0
0	1	0	0	1	1	0	0
0	0	0	1	1	1	1	1
Logic func.:			NOR	$\neg I1$	TRUE	$\neg I2$	NOR
1	1	1	0	0	1	0	0
1	0	1	1	1	1	1	0
0	1	1	0	1	1	1	1
0	0	1	0	1	1	1	0
Logic func.:			\nrightarrow	NAND	TRUE	NAND	\Leftarrow

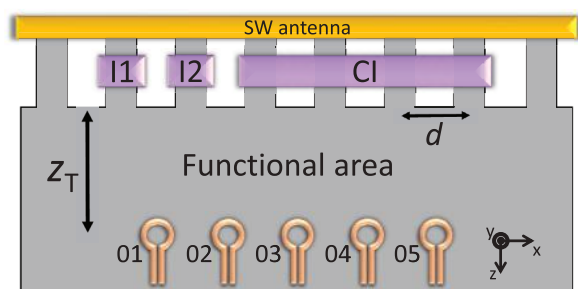


Figure 6. Scheme of the asymmetric SW LUT with the first ($n = 1$) Talbot length z_T and the inputs period d marked. The CI mark denotes the control input, and the numbered I and O denote inputs and outputs, respectively.

that performs up to ten logic operations without the need to interfere with physical parameters.

2.3.2. Example 2 – Asymmetric Geometry

The second example of an SW LUT functionality based on the self-imaging effect is to use an asymmetric arrangement of sources and switches in relation to the array of outputs so that the resulting self-image amplitudes are more varied. In Table 1 we can see that the logic functions performed in the outputs [O1–O5] are mirrored, which is clearly due to the symmetrical arrangement of the inputs. Here, we propose a model that disrupts this symmetry to see how the system behaves in a different configuration.

All the HFPBC simulation parameters of the model in Figure 6 remain identical to the previous example for symmetric geometry. We can see that here the sources I1 and I2 are placed next to each other, and the CI switch does not cover all other inputs—two most distant waveguides remain inactive regarding information transmission, but they are important from the viewpoint of creating self-images (so that the Talbot carpet is the closest to the theory, the sources should be distributed as widely as possible along the multimode waveguide, as in Figure 2).

Based on the truth tables presented in Table 2 for the asymmetric model, we see that the implemented logic functions are no longer mirrored on the outputs, which proves that it is possible to create a 2-in 5-out magnonic logic gate based on

the Talbot effect, carrying out five different functions simultaneously (not counting the switch functionality). The above example, for both $CI=0$ and $CI=1$, performs only four logic functions each, but it results from the difficulty to find a suitable configuration from the numerous possibilities of parameter choice. The optimization of the obtained functionality in terms of the most efficient use of self-imaging for logic operations in magnonics certainly requires development and extensive research. Visualization of the diffraction field intensity distributions for each of the configurations shown in Tables 1 and 2 are provided in Figures S1 and S2, Supporting Information.

3. Discussion

Analysis of computing system functionality requires taking into account the potential speed of operation of such a device. It is a complex task since it depends on i) the group velocity of information-carrying wave packets (which depends on the wavelength), ii) the frequency of propagating waves (the carrier wave frequency should be larger than the information frequency), and iii) on the geometry of the system (in the presented case here, in particular, the Talbot length). The maximal speed of the LUT can be estimated by testing the time in which the system stabilizes after the change of state at the input, that is, how quickly the output reaches a new logic level after the “instantaneous” input change. This responsiveness plays a key role in the design of all types of processors and is often visualized by a waveform chart.

A simple calculation allows estimating that due to the input/output time-delay t_d of around 0.3 ns visible in Figure 7, the presented device allows for the implementation of logic functions with an operating frequency up to roughly 3.3 GHz. However, it should be emphasized that the device can be optimized to a great extent. It includes reducing the duration of one logic level at the input to the smallest value that still maintains the stability of the device, by device miniaturization and shortening z_T , or increasing the group velocity. The Talbot length can be decreased by either decreasing the period of the input waveguides or increasing the wavelength. The group velocity of SWs in our system is $\approx 1.90 \text{ km s}^{-1}$ (according to Equation (2)). Simply, for dipolar SWs (long wavelengths with negligible

Table 2. Two-input five-output asymmetric LUT behavior for $CI=0$ and $CI=1$. The symbols \rightarrow and \leftarrow stand for material implication and converse, respectively—glossary of terms are in Table S1, Supporting Information.

I1	I2	CI	O1	O2	O3	O4	O5
1	1	0	0	1	1	1	1
1	0	0	0	0	0	1	0
0	1	0	0	0	1	0	1
0	0	0	1	1	1	1	1
Logic func.:			NOR	XNOR	\rightarrow	\leftarrow	\rightarrow
1	1	1	0	1	1	1	1
1	0	1	0	1	0	1	0
0	1	1	0	1	1	1	1
0	0	1	1	1	1	1	0
Logic func.:			NOR	TRUE	\rightarrow	TRUE	12

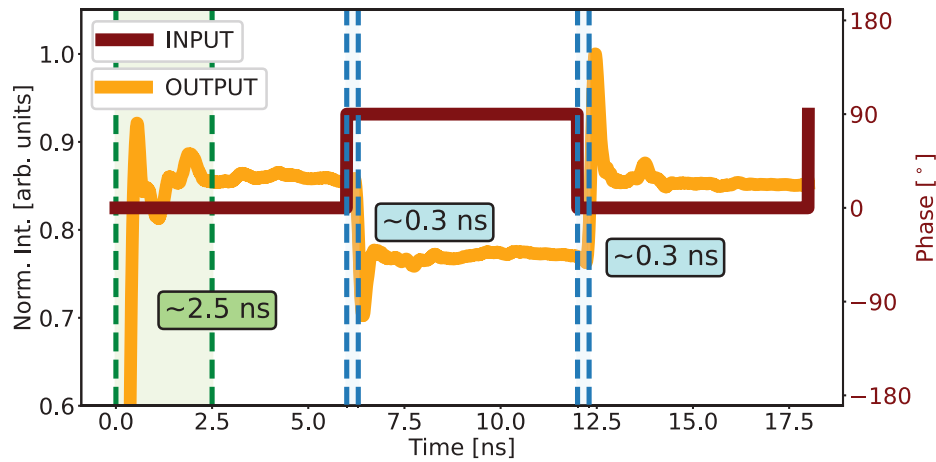


Figure 7. Waveform of one of the input/output pairs of the proposed logic gate, where the $\pi/2$ phase shift causes a decrease in self-image intensity by about 10%. The figure shows the time-delay areas of device initialization until the amplitude stabilizes (in green) and the output change response to the input change of both the “0”/“1” and “1”/“0” logic levels (in blue). The duration of one logic state is 4.5 ns.

exchange interactions), the group velocity increases while kL decreases, for example, at fixed k the thicker film, the larger v_g . In the case of short-wavelength exchange SWs that are more suitable for LUTs, the group velocity is proportional to $\lambda_{ex}k$, where $\lambda_{ex} = l_{ex}^2 M_S$ is the exchange stiffness constant. Therefore, we can increase the group velocity at kept wavelengths, by increasing the value of λ_{ex} . An integral factor in determining the device's operation speed and its time-delay is also the length of the input waveguide, that is, the distance from the SW source to the multimode waveguide (functional area). This factor must be added to the Talbot length when designing

LUTs based on self-imaging to determine their response time to the input signal. In the present discussion (Figure 8 and Equation (5)), the length of single-mode waveguides has been neglected for the sake of clarity. Making the Talbot length dependent on the parameter $M = d/\lambda$ and the wavenumber k , we can also derive the formula for the time-delay ($t_d = z_T/v_{gr}$) of devices based on self-imaging in the exchange interactions regime, where $\omega \approx l_{ex}^2 \omega_M k^2$, getting

$$t_d = \frac{z_T(M)}{v_{gr}} = \frac{\pi M^2}{\gamma \lambda_{ex}} \frac{1}{k^2} \quad (5)$$

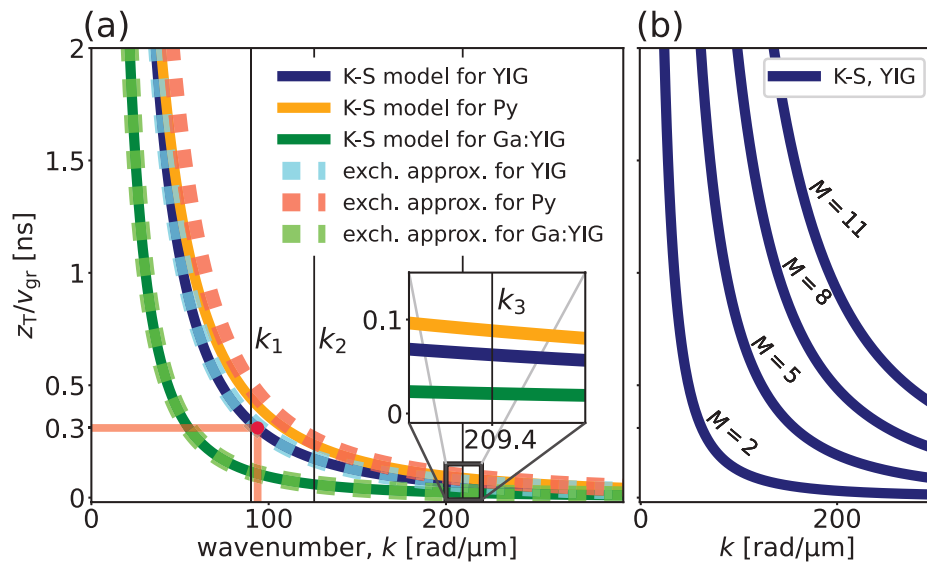


Figure 8. The time-delay $t_d (=z_T/v_{gr})$ dependence on the wave vector. a) $t_d(k)$ dependencies for the same ratio $M = d/\lambda$ (here equals three) and three different materials, that is, YIG, Py ($M_S = 800 \text{ kA m}^{-1}$, $A_{ex} = 16 \text{ pJ m}^{-1}$) and Ga-substituted YIG ($M_S = 15.9 \text{ kA m}^{-1}$, $A_{ex} = 1.37 \text{ pJ m}^{-1}$).^[41] The solid lines represent the results obtained assuming dispersion relation described by Equation (2)) whereas the dashed lines represent the exchange approximation (Equation (5)). b) $t_d(k)$ dependencies for different M values. The positions corresponding to the wave vectors k_1 , k_2 , and k_3 are marked with black, vertical lines for SWs of wavelengths 70, 50, and 30 nm, respectively. The red dot marks the parameters used in this work (40 GHz SWs in YIG) and the corresponding time-delay.

To validate these predictions, we calculate the relationship between the Talbot length values and the group velocity characteristic for a given material ($t_d = z_T/v_{gr}$) as a function of the wave vector. We perform this analysis assuming $M = 3$ and comparing results for films of thickness $L = 5$ nm made of three different materials, that is, YIG, permalloy (Py) and Ga-substituted YIG (Ga:YIG),^[41] see Figure 8a.

The results displayed in Figure 8a confirm that the adopted exchange approximation works very well for the simulated scenario and the resulting time-delay for YIG agrees with the estimated value in Figure 7 for 40 GHz. We can see that the time-delay t_d decreases with increasing wave vector, and therefore frequency. Finally, one may conclude that the higher value of λ_{ex} the better performance of the designed LUT. This indicates that films made of Ga:YIG are the best candidates for these types of application. The vertical black lines in Figure 8a correspond to the wavenumbers k_1 , k_2 , and k_3 to show the potential resulting from the reduction in the spin wavelength. It is evident in the inset for k_3 ($\lambda = 30$ nm), where for Py, YIG, and Ga:YIG, t_d is equal to 0.089, 0.063, and 0.021 ns, respectively, which, in turn, correspond to frequencies of 11.24, 15.87, and 47.62 GHz. The analysis shows that, by using Ga:YIG in the presented design, we are able to obtain about three times higher device clock speed than in YIG and more than four times higher than in Py, for the same wavenumber.

Figure 8b illustrates the impact of the M coefficient, that is, the geometry of the input period with respect to the applied spin wavelength. One may notice that the smaller it is (i.e., the closer the period is to the wavelength), the shorter the time-delay and the better the LUTs efficiency. The limit for this parameter is around $M = 1$, which is directly related to the geometry of a series of single-mode inputs, the width of which must be comparable to the wavelength and to the Talbot length formula applicability used in this analysis (discussed in more detail in ref. [37]).

Another important topic worth discussing is how we estimate the logic output level in our system. Adopting a certain, strictly defined thresholding intensity value of SWs is a solution well known in this type of systems and, apart from the phase shift, is the basic method of determining the logic value. Of course, as in the case of the time-delay and the resulting maximum speed of information processing, we can also optimize the system by selecting the device parameters appropriate for a given application. The thresholding value common to all outputs, despite its simplicity, may prove problematic due to the different level of the reference intensity of the self-images (see Figures 5 or 3a). Selecting it in such a way that the difference between logic “1” and “0” is significant in each output needs further optimization of the system and requires sensitive detection methods. The functionality of the device can also be expanded by increasing the number of input/output waveguides and by appropriately defining functional inputs, control inputs, or inputs not involved in the information processing (such as the two edge inputs in the scheme of Figure 6). Neither the Talbot effect nor the HSPBC method we use limit the geometry in this way, and the configuration we chose is an example. Nevertheless, any change in the SW LUT system will result in a different intensity distribution at the output. If we keep the wavelength and the period constant, the Talbot length does not change, as described earlier, but the amplitude

distribution may. As such, it will be necessary to choose an appropriate threshold amplitude for each device configuration separately to fulfill the expected logical functions. As alternative ideas, we can propose separate thresholding for each output or a detection based not on a threshold intensity, but on its change in relation to the previous value. It is called an edge-triggered circuit,^[42] and the coding is as follows: if the signal is higher (from the previous value by at least a given value), we get logic “1”, and if it is lower, “0”. The last idea points to a possibility of using the proposed SW self-imaging system to design magnonic flip-flop circuits. A possible solution is also to encode information in both the input and output phases. It would be a much more complicated task than conventional amplitude detection, but it would certainly simplify the system and most likely reduce its energy consumption, especially in the application of many interference gates based on self-imaging in one, purely magnonic circuit.

Our study focuses on linear effects, however, we believe that the non-linear regime for SW self-imaging is very interesting, albeit a separate topic for further research. In a sense, the functionality we propose is essentially a generalization of SW majority gates (as shown in refs. [16–20]), but with the possibility of any increase in the number of inputs/outputs of the system. The flexibility and scalability of the Talbot effect for SWs allows to create a gate for any logic function, while majority gates generally implement one functionality (majority function). We believe that this will interest the magnonic community in the use of the Talbot effect in information processing.

4. Conclusions

In this paper, we demonstrate the operation of magnonic LUTs based on the self-imaging effect of SWs in a thin ferromagnetic multimode waveguide. For this purpose, we used micromagnetic simulations and Huygens–Fresnel principle based calculations. The results were presented in the form of truth tables with binary logic operators and SW intensity maps in the functional areas, confirming them. The obtained results show the great potential of the Talbot effect in magnonics, especially in the context of computational wave-based systems and controlling SWs.

The LUTs presented in this paper process by converting the information encoded in the SW phase at the input into information contained in its amplitude at the output. In the functional area, there is interference of waves from a number of input sources, which forms a Talbot carpet. It is characterized by the reproduction of the input amplitude distribution at a specific distance. We showed that, as a result of individual input wave manipulation, it is possible to influence these reproductions without changing the distance of their creation. The flexibility of this effect allows for implementation in various types of computing system that can perform any logic function. Thanks to the use of control input, we can dynamically change the functionality of the system, which would be crucial for potential applications in FPGA circuits. The programmable LUTs proposed here can be an alternative to modern transistor-based systems, in terms of increased

operation speed, greater miniaturization, and reduced energy consumption.

Wave self-imaging is a general phenomenon, and because of its scalability and controllability, it can be used almost anywhere where wave interference occurs. The logic device operation presented in this paper is an example of such an implementation, additionally, to control the coherence of input SWs with their subsequent reconstruction. In addition, its scalability and simplicity allow it to be widely used in a new generation of magnonic devices. We expect a continuation and increased interest in SWs' self-imaging in the next years.

5. Experimental Section

Micromagnetic Simulations: Micromagnetic simulations were used to solve the full Landau–Lifshitz equation using the finite-difference time domain method.^[43] The MuMax3 software used for this purpose calculated this equation in the following explicit form

$$\frac{dm}{dt} = \gamma \frac{1}{1 + \alpha^2} (\mathbf{m} \times \mathbf{B}_{\text{eff}} + \alpha (\mathbf{m} \times (\mathbf{m} \times \mathbf{B}_{\text{eff}}))) \quad (6)$$

where dm/dt is the time evolution of the reduced magnetization $m(x, z)$, γ is the gyromagnetic ratio, and α stands for dimensionless damping coefficient. The effective field \mathbf{B}_{eff} , around which the magnetization precess forming SWs, may contain many components depending on the system characteristics. In this case, the effective field consisted of an externally applied field \mathbf{B}_{ext} , magnetostatic field $\mathbf{B}_{\text{demag}}$ and a Heisenberg exchange field \mathbf{B}_{exch} , that is,

$$\mathbf{B}_{\text{eff}} = \mathbf{B}_{\text{ext}} + \mathbf{B}_{\text{demag}} + \mathbf{B}_{\text{exch}} \quad (7)$$

A 1.60 μm wide, around 600 nm long waveguide with an array of eight 40 nm wide and 300 nm long narrower input waveguides was considered. The distance between them was equal to $d = 200\text{ nm}$. The entire system had a uniform thickness of 5 nm and was made of YIG with the following magnetic parameters: the saturation magnetization $M_s = 137\text{ kA m}^{-1}$, the exchange constant $A_{\text{ex}} = 4\text{ pJ m}^{-1}$, and the gyromagnetic ratio $|\gamma| = 176\text{ GHz rad T}^{-1}$. The geometry was uniformly discretized by $5 \times 5 \times 5\text{ nm}^3$ unit cells, while the exchange length $l_{\text{ex}} = \sqrt{2A_{\text{ex}}/(\mu_0 M_s^2)} = 18\text{ nm}$ (μ_0 is the vacuum permeability). An out-of-plane applied external magnetic field of $\mu_0 H_0 = 1.1\text{ T}$ being enough to uniformly magnetize the sample in this direction was assumed. Therefore, SW in the so-called forward volume (FV) geometry, which is the only scenario where the propagation of SWs is fully isotropic, that is, the wavelength does not depend on the direction of propagation, was considered.^[44]

SWs were excited only in narrow waveguides by locally applying a magnetic microwave field of frequency $f_0 = 40\text{ GHz}$ polarized along the x -axis in the region of a width 10 nm located 290 nm from the entrance to the functional block (wide waveguide) (see Figures 4 or 6). To obtain the steady-state, SWs were continuously emitted by 2.5 ns. At the top and bottom sides of the system the 65 and 260 nm-wide absorbing boundary layers were assumed, respectively, to neglect the influence of backward reflection of SWs from there and mimic the propagation of SWs only downward. In this region, the damping coefficient increased quadratically up to the value of $\alpha = 0.099$ at the outer domain boundaries. The issue of SW damping for Talbot effect in the analyzed multimode waveguide had already been analyzed in detail in refs. [37,38], where it was showed that after appropriate selection of parameters, the detection of at least the first order of self-images was possible. Therefore, the authors found it better to focus on functionality itself in this paper, leaving the damping constant negligibly small.

Huygens–Fresnel Principle Based Calculations: Micromagnetic simulations of SW propagation in large planar magnetic systems are time- and resource-consuming. Knowing i) the distribution of the

complex amplitude of SWs emitted by an ideal point source $s(x, z)$, and ii) the function describing the amplitude and phase of waves entering the system (aperture function, $a(x) = |a(x)|\exp[i\varphi(x)]$), one can quickly calculate the resulting distribution of SW amplitude in a steady-state utilizing Huygens–Fresnel principle. In this paper, this method is referred as the HFPBC. That is, the complex profile of SWs, $m(x, z)$, emitted by a series of sources, spanned along the x -axis and located at $z = z_0$, could be described by the integral $m(x, z) \propto \int_{-\infty}^{\infty} a(x') s(x - x', z - z_0) dx'$. The aperture function describing the profile, amplitude and phase of the SWs emitted from the line located at $z = z_0$ could be derived analytically or numerically. Here, similarly in ref. [26], the distribution of a complex amplitude of the SWs emitted by the point source based on the results of micromagnetic simulations was determined. First, the steady-state of SWs emitted at frequency f_0 was obtained, which was sampled at a frequency of $4f_0$. Subsequently, a fast Fourier transform was performed over time and the result was left corresponding to the frequency f_0 . This allowed to obtain the SW amplitude distribution in the complex form ($m(x, z) \in \mathbb{C}$) required to solve the above integral equation.

The finite width of the waveguide was taken into account by folding the distribution of $m(x, z)$ multiple times for a waveguide of given widths. To represent SW reflections from the edges, the distribution of the complex SW amplitude should be determined over a region much wider than the width of that waveguide. However, in this case, the width of the wave profile from a point SW source was equal to the width of the subsequently folded system with eight input sources (1.60 μm). The reason for this was that in the analysis of the first Talbot image case, the distance from the sources was small and reflections did not play a significant role in their formation, especially when self-images near the side edges were not taken into account.

This method gave almost the same results as full micromagnetic simulations; see the comparison in Figure S3, Supporting Information. Potential differences between these methods might arise from i) differences in the representation of reflections from the waveguide edges; ii) an incorrectly chosen aperture function and; iii) imperfections in the prepared composite amplitude distribution of SWs emitted by the point source. The proposed method worked very well for homogeneous systems, where a diffraction field would be affected only by the interference of waves propagating from (several) source waveguides and from edge reflections. The HFPBC was therefore ineffective in the case of SWs propagating in systems with different magnetic parameters within it, such as for example, magnonic crystals. However, the method was significantly faster than conventional micromagnetic simulations. For comparison, using this method, one steady-state could be obtained in seconds. At the same time, a complete micromagnetic simulation of the same system, the results of which still need to be processed, takes a couple of minutes.^[45] This means an acceleration of the calculations by about two orders of magnitude. The Talbot effect was presented in this paper as a way to obtain amplified and localized spin wave beams at precisely defined and predictable points in a multimode waveguide. Since this was purely a wave phenomenon and had already been described using the analogous nomenclature for both electromagnetic and SWs, the HFPBC tool was used as an approximation of full micromagnetic simulations. The Huygens–Fresnel principle described wave propagation in the near and far diffraction field, taking into account the laws of interference and reflection. Basically, it stated that every point on a wavefront can be considered a source of spherical waves, and the secondary waves that arise from different points interfere with each other. Combined, these spherical wavelets form a wavefront. This justified the use of the HFPBC method to analyze the self-imaging effect for SWs, where a series of single-mode input waveguides could, with high accuracy, be treated as a series of point sources of circular SWs, which then interfered and created diffraction patterns. Therefore, this approach is much better suited for prototyping logic circuits. In this work, most of the results were obtained using this method, and full micromagnetic simulations were used to confirm only the most important one.

Code Availability: The source code of the HFPBC technique is available in the HFPBC-code repository <https://github.com/mateusz-golebiewski/hfpbc-code.git>.

Supporting Information

Supporting Information is available from the Wiley Online Library or from the author.

Acknowledgements

This research had received funding from the National Science Centre of Poland, project nos. 2019/35/D/ST3/03729 and 2018/30/Q/ST3/00416. The simulations were partially performed at the Poznan Supercomputing and Networking Center (Grant No. 398).

Conflict of Interest

The authors declare no conflict of interest.

Author Contributions

M.G. conceptualized and conceived the research and performed simulations. P.G. developed the HFPBC method. M.K. supervised the work. The paper was written by M.G. with input from P.G. and M.K. All authors contributed to the discussion and analyses of the data and approved the final version.

Data Availability Statement

The data that support the findings of this study are available from the corresponding author upon reasonable request.

Keywords

interference computation, lookup tables, magnonics, self-imaging, Talbot effect, spin-wave logic gates

Received: April 1, 2022
Revised: June 13, 2022
Published online:

- [1] S. M. Trimberger, *Field-Programmable Gate Array Technology*, Springer Science & Business Media, Berlin **2012**.
- [2] D. Nikonov, I. Young, *Proc. IEEE* **2013**, *101*, 2498.
- [3] S. Manipatruni, D. E. Nikonov, I. A. Young, *Nat. Phys.* **2018**, *14*, 338.
- [4] G. Csaba, Ádám Papp, W. Porod, *Phys. Lett. A* **2017**, *381*, 1471.
- [5] A. V. Chumak, P. Kabos, M. Wu, C. Abert, C. Adelman, A. O. Adeyeye, J. Åkerman, F. G. Aliev, A. Anane, A. Awad, C. H. Back, A. Barman, G. E. W. Bauer, M. Becherer, E. N. Beginin, V. A. S. V. Bittencourt, Y. M. Blanter, P. Bortolotti, I. Bovenster, D. A. Bozhko, S. A. Bunyayev, J. J. Carmiggelt, R. R. Cheenikundil, F. Ciubotaru, S. Cotozana, G. Csaba, O. V. Dobrovolskiy, C. Dubs, M. Elyasi, K. G. Fripp, H. Fulara, et al., *IEEE Trans. Magn.* **2022**, *58*, 0800172.
- [6] A. V. Chumak, V. I. Vasyuchka, A. A. Serga, B. Hillebrands, *Nat. Phys.* **2015**, *11*, 453.
- [7] B. Dieny, I. L. Prejbeanu, K. Garello, P. Gambardella, P. Freitas, R. Lehnndorff, W. Raberg, U. Ebels, S. O. Demokritov, J. Åkerman, A. Deac, P. Pirro, C. Adelman, A. Anane, A. V. Chumak, A. Hirohata, S. Mangin, S. O. Valenzuela, M. C. Onbaşlı, M. d'Aquino, G. Prenat, G. Finocchio, L. Lopez-Díaz, R. Chantrell, O. Chubykalo-Fesenko, P. Bortolotti, *Nat. Electron.* **2020**, *3*, 446.
- [8] S. Wintz, V. Tiberkevich, M. Weigand, J. Raabe, J. Lindner, A. Erbe, A. Slavin, J. Fassbender, *Nat. Nanotechnol.* **2016**, *11*, 948.
- [9] W. Yu, J. Lan, J. Xiao, *Phys. Rev. Appl.* **2020**, *13*, 024055.
- [10] A. Mahmoud, F. Ciubotaru, F. Vanderveken, A. V. Chumak, S. Hamdioui, C. Adelman, S. Cotozana, *J. Appl. Phys.* **2020**, *128*, 161101.
- [11] X. S. Wang, H. W. Zhang, X. R. Wang, *Phys. Rev. Appl.* **2018**, *9*, 024029.
- [12] V. E. Demidov, S. O. Demokritov, *IEEE Trans. Magn.* **2015**, *51*, 0800215.
- [13] Q. Wang, B. Heinz, R. Verba, M. Kewenig, P. Pirro, M. Schneider, T. Meyer, B. Lägler, C. Dubs, T. Brächer, A. V. Chumak, *Phys. Rev. Lett.* **2019**, *122*, 247202.
- [14] J. Chen, H. Wang, T. Hula, C. Liu, S. Liu, T. Liu, H. Jia, Q. Song, C. Guo, Y. Zhang, J. Zhang, X. Han, D. Yu, M. Wu, H. Schultheiss, H. Yu, *Nano Lett.* **2021**, *21*, 6237.
- [15] C. Liu, J. Chen, T. Liu, F. Heimbach, H. Yu, Y. Xiao, J. Hu, M. Liu, H. Chang, T. Stueckler, S. Tu, Y. Zhang, Y. Zhang, P. Gao, Z. Liao, D. Yu, K. Xia, N. Lei, W. Zhao, M. Wu, *Nat. Commun.* **2018**, *9*, 738.
- [16] T. Fischer, M. Kewenig, D. Bozhko, A. Serga, I. Syvorotka, F. Ciubotaru, C. Adelman, B. Hillebrands, A. Chumak, *Appl. Phys. Lett.* **2017**, *110*, 152401.
- [17] S. Klingler, P. Pirro, T. Brächer, B. Leven, B. Hillebrands, A. V. Chumak, *Appl. Phys. Lett.* **2014**, *105*, 152410.
- [18] O. Zografos, S. Dutta, M. Manfrini, A. Vaysset, B. Sorée, A. Naeemi, P. Raghavan, R. Lauwereins, I. P. Radu, *AIP Adv.* **2017**, *7*, 056020.
- [19] G. Talmelli, T. Devolder, N. Träger, J. Förster, S. Wintz, M. Weigand, H. Stoll, M. Heyns, G. Schütz, I. P. Radu, J. Gräfe, F. Ciubotaru, C. Adelman, *Sci. Adv.* **2020**, *6*, eabb4042.
- [20] A. Mahmoud, F. Vanderveken, C. Adelman, F. Ciubotaru, S. Hamdioui, S. Cotozana, *AIP Adv.* **2020**, *10*, 035119.
- [21] U. Garlando, Q. Wang, O. Dobrovolskiy, A. Chumak, F. Riente, *arXiv:2109.12973*, **2021**.
- [22] R. Hertel, W. Wulfhekel, J. Kirschner, *Phys. Rev. Lett.* **2004**, *93*, 257202.
- [23] A. N. Mahmoud, F. Vanderveken, F. Ciubotaru, C. Adelman, S. Hamdioui, S. Cotozana, *IEEE Nanotechnol. Mag.* **2022**, *16*, 47.
- [24] F. Heussner, M. Nabinger, T. Fischer, T. Brächer, A. A. Serga, B. Hillebrands, P. Pirro, *Phys. Status Solidi RRL* **2018**, *12*, 1800409.
- [25] F. Heussner, G. Talmelli, M. Geilen, B. Heinz, T. Brächer, T. Meyer, F. Ciubotaru, C. Adelman, K. Yamamoto, A. A. Serga, B. Hillebrands, P. Pirro, *Phys. Status Solidi RRL* **2020**, *14*, 1900695.
- [26] J. Gräfe, P. Gruszecki, M. Zelent, M. Decker, K. Keskinbora, M. Noske, P. Gawronski, H. Stoll, M. Weigand, M. Krawczyk, C. H. Back, E. J. Goering, G. Schütz, *Phys. Rev. B* **2020**, *102*, 024420.
- [27] M. Vogel, B. Hillebrands, G. von Freymann, *Appl. Phys. Lett.* **2020**, *116*, 262404.
- [28] Á. Papp, W. Porod, Á. I. Csurgay, G. Csaba, *Sci. Rep.* **2017**, *7*, 9245.
- [29] Á. Papp, M. Kiechle, S. Mendisch, V. Ahrens, L. Sahin, L. Seitner, W. Porod, G. Csaba, M. Becherer, *Sci. Rep.* **2021**, *11*, 14239.
- [30] A. Papp, W. Porod, G. Csaba, *arXiv:2012.04594*, **2020**.
- [31] A. Papp, G. Csaba, W. Porod, *Appl. Phys. Lett.* **2021**, *119*, 112403.
- [32] Q. Wang, A. V. Chumak, P. Pirro, *Nat. Commun.* **2021**, *12*, 2636.
- [33] D. Prychynenko, M. Sitte, K. Litzius, B. Krüger, G. Bourianoff, M. Kläui, J. Sinova, K. Everschor-Sitte, *Phys. Rev. Appl.* **2018**, *9*, 014034.

- [34] P. Borys, F. Garcia-Sanchez, J.-V. Kim, R. L. Stamps, *Adv. Electron. Mater.* **2016**, 2, 1500202.
- [35] V. Laliena, J. Campo, *Adv. Electron. Mater.* **2022**, 8, 2100782.
- [36] H. Talbot, *London, Edinburgh, Dublin Philos. Mag. J. Sci.* **1836**, 9, 401.
- [37] M. Gołębiewski, P. Gruszecki, M. Krawczyk, A. E. Serebryannikov, *Phys. Rev. B* **2020**, 102, 134402.
- [38] M. Gołębiewski, P. Gruszecki, M. Krawczyk, *IEEE Trans. Magn.* **2022**, <https://doi.org/10.1109/TMAG.2022.3140280>.
- [39] B. Kalinikos, A. Slavin, *J. Phys. C: Solid State Phys.* **1986**, 19, 7013.
- [40] A. Mahmoud, F. Vanderveken, C. Adelman, F. Ciubotaru, S. Hamdioui, S. Cotofana, *arXiv:2011.11316*, **2021**.
- [41] T. Böttcher, M. Ruhwedel, K. Levchenko, Q. Wang, H. Chumak, M. Popov, I. Zavislyak, C. Dubs, O. Surzhenko, B. Hillebrands, A. V. Chumak, P. Pirro, *Appl. Phys. Lett.* **2022**, 120, 102401.
- [42] S. Dutta, S.-C. Chang, N. Kani, D. Nikonov, S. Manipatruni, I. Young, A. Naeemi, *Sci. Rep.* **2015**, 5, 9861.
- [43] A. Vansteenkiste, J. Leliaert, M. Dvornik, M. Helsen, F. Garcia-Sanchez, B. Van Waeyenberge, *AIP Adv.* **2014**, 4, 107133.
- [44] A. Prabhakar, D. D. Stancil, *Spin Waves: Theory and Applications*, Springer, US **2009**.
- [45] Calculated in Poznan Supercomputing and Networking Center (PSNC) – GPU: NVIDIA V100.

Supporting Information

for *Adv. Electron. Mater.*, DOI: 10.1002/aelm.202200373

Self-Imaging Based Programmable Spin-Wave Lookup Tables

Mateusz Gołębiewski, Paweł Gruszecki, and Maciej
Krawczyk*

Supporting Information

Self-imaging based programmable spin-wave lookup tables

Mateusz Gołębiewski,^{1,*} Paweł Gruszecki,¹ and Maciej Krawczyk¹

¹*Institute of Spintronics and Quantum Information, Faculty of Physics,
Adam Mickiewicz University, Uniwersytetu Poznańskiego 2, 61-614 Poznań, Poland*

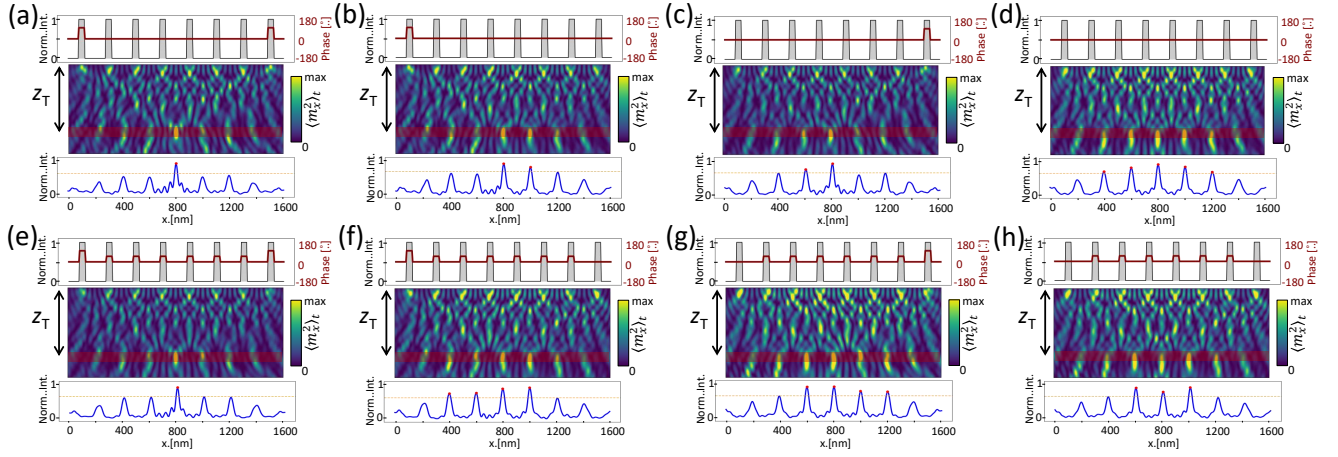


Fig. S1. Visualisations of all numerical simulations performed for the cases described in Table 1 (a)-(d) and Table 2 (e)-(h). The upper parts of each subfigure show the intensity distribution on the inputs (grey columns) and their phase shift (maroon line). In the middle, there are intensity maps of the functional areas (with inputs at the top edge). In turn, below are normalised plots of the dynamic magnetisation intensity averaged over the red region. The orange dashed lines indicate the predefined threshold value.

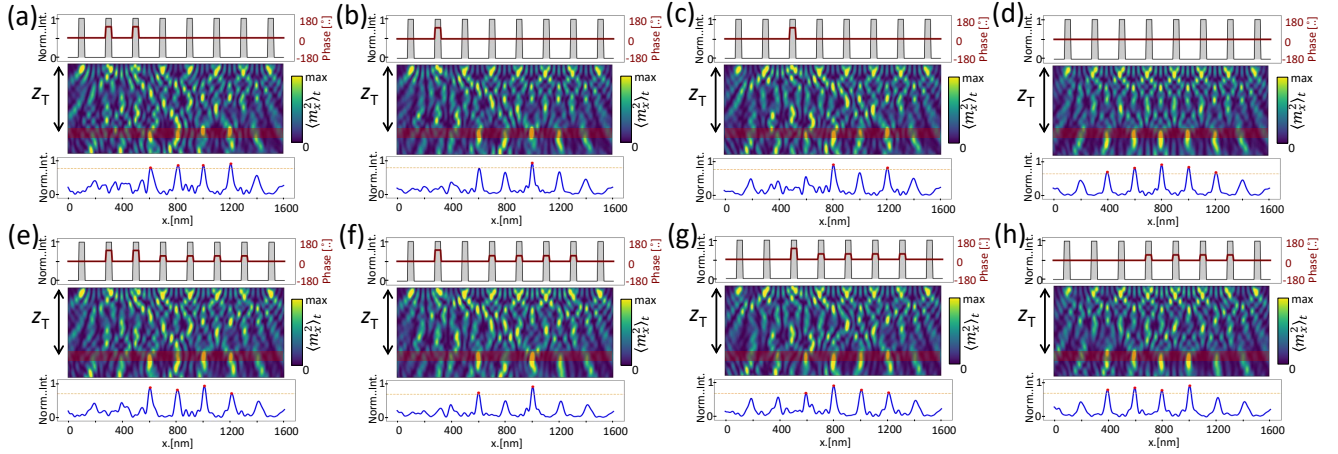


Fig. S2. Visualisations of all numerical simulations performed for the cases described in Table 3 (a)-(d) and Table 4 (e)-(h). The upper parts of each subfigure show the intensity distribution on the inputs (grey columns) and their phase shift (maroon line). In the middle, there are intensity maps of the functional areas (with inputs at the top edge). In turn, below are normalised plots of the dynamic magnetisation intensity averaged over the red region. The orange dashed lines indicate the predefined threshold value.

* Corresponding author, email: mateusz.golebiewski@amu.edu.pl

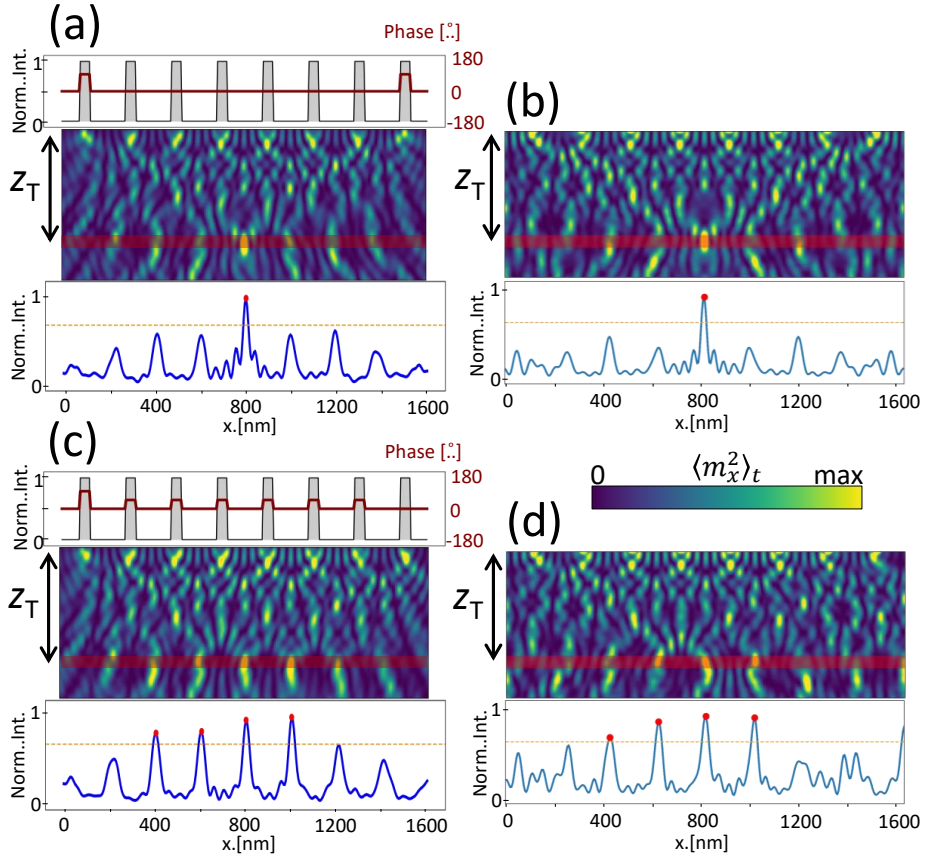


Fig. S3. Comparison of exemplary simulations carried out with the HFPBC method used to quickly obtain Talbot carpets (a),(c) with the results directly from MuMax3 (b),(d).

Tab. S1. Truth table for all 16 possible logic functions of two binary variables

p	q	F	NOR	\leftarrow	$\neg p$	$\neg \rightarrow$	$\neg q$	XOR	NAND	AND	XNOR	q	\rightarrow	p	\leftarrow	OR	T
1	1	0	0	0	0	0	0	0	0	1	1	1	1	1	1	1	1
1	0	0	0	0	0	1	1	1	1	0	0	0	0	1	1	1	1
0	1	0	0	1	1	0	0	1	1	0	0	1	1	0	0	1	1
0	0	0	1	0	1	0	1	0	1	0	1	0	1	0	1	0	1

where:

p – first argument/input

q – second argument/input

T – true

F – false

\neg – negation, returns '1' when its argument is '0', and '0' when its argument is '1'

OR – returns '1' unless both of its arguments are '0'

NOR – negation of logical **OR**

XOR – returns '1' whenever the arguments differ

XNOR – returns '1' if and only if both arguments are '0' or both arguments are '1'

AND – returns '1' if and only if both of its arguments are '1'

NAND – negation of logical **AND**

\rightarrow – material implication, returns '1' unless **p** is '1' and **q** is '0'

\nrightarrow – material nonimplication, negation of material implication

\leftarrow – converse, returns '1' when **p** is '1' if and only if **q** is also '1'

\nleftarrow – converse nonimplication, negation of converse

5.1.4 Experimental demonstration of spin-wave self-imaging (P6)

Building on previous theoretical and simulation studies of the Talbot effect in magnonics, this work presents the first experimental verification of this phenomenon in a magnetic system. The experimental part of this work has been carried out by the research group from Białystok, whose contributions have been instrumental in validating the theoretical predictions and numerical simulations developed by our group. Using an in-plane magnetized YIG film, we demonstrate and analyze spin-wave self-imaging in a configuration where plane spin waves propagate through a diffraction grating, and the resulting interference pattern is captured by Brillouin light scattering microscopy. By varying the frequency of the dynamic magnetic field, we investigate the influence of the anisotropic dispersion relation and the caustic effect on the self-imaging.

Contribution of the Author

In this work, together with M. Krawczyk, I co-supervised the first author, U. Makartsou. I introduced him to the topic of the spin-wave self-imaging effect and contributed to the interpretation of his micromagnetic simulations, as well as to the analysis of experimental results provided by the collaborating team (U. Guzowska, A. Stognij, R. Gieniusz). I assisted in the preparation of the manuscript, managed its submission to the journal, and handled correspondence with the reviewers throughout the peer-review process.

The article reprinted from Makartsou, U.; Gołębiewski, M.; Guzowska, U.; Stognij, A.; Gieniusz, R.; Krawczyk, M. *Applied Physics Letters* **124**, 19, 192406 (2024), with the permission of AIP Publishing. ©2024 Authors. License number: 5965900682142.

RESEARCH ARTICLE | MAY 09 2024

Spin-wave self-imaging: Experimental and numerical demonstration of caustic and Talbot-like diffraction patterns



Uladzislau Makartsou ; Mateusz Gołębiewski ; Urszula Guzowska ; Alexander Stognij ; Ryszard Gieniusz ; Maciej Krawczyk



Appl. Phys. Lett. 124, 192406 (2024)

<https://doi.org/10.1063/5.0195099>



09 May 2024 18:42:27

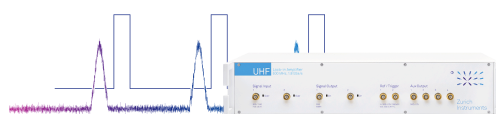


Lock-in Amplifier



Find out more

Boost Your Optics and Photonics Measurements



Boxcar Averager

Spin-wave self-imaging: Experimental and numerical demonstration of caustic and Talbot-like diffraction patterns

Cite as: Appl. Phys. Lett. **124**, 192406 (2024); doi: [10.1063/5.0195099](https://doi.org/10.1063/5.0195099)

Submitted: 30 December 2023 · Accepted: 29 April 2024 ·

Published Online: 9 May 2024



Uladzislau Makartsou,^{1,a)} Mateusz Gołębiewski,^{1,a)} Urszula Guzowska,² Alexander Stognij,^{3,b)} Ryszard Gieniusz,² and Maciej Krawczyk¹

AFFILIATIONS

¹Institute of Spintronics and Quantum Information, Faculty of Physics, Adam Mickiewicz University, Uniwersytetu Poznańskiego 2, 61-614 Poznań, Poland

²Department of Physics of Magnetism, Faculty of Physics, University of Białystok, Konstantego Ciołkowskiego 1L, 15-245 Białystok, Poland

³Scientific-Practical Materials Research Center at National Academy of Sciences of Belarus, Pietrusia Broŭki 19, 220072 Minsk, Belarus

Note: This paper is part of the APL Special Collection on Magnonics.

^{a)}Authors to whom correspondence should be addressed: ulamak@amu.edu.pl and mateusz.golebiewski@amu.edu.pl

^{b)}Deceased.

ABSTRACT

Extending the scope of the self-imaging phenomenon, traditionally associated with linear optics, to the domain of magnonics, this study presents the experimental demonstration and numerical analysis of spin-wave (SW) self-imaging in an in-plane magnetized yttrium iron garnet film. We explore this phenomenon using a setup in which a plane SW passes through a diffraction grating, and the resulting interference pattern is detected using Brillouin light scattering. We have varied the frequencies of the source dynamic magnetic field to discern the influence of the anisotropic dispersion relation and the caustic effect on the analyzed phenomenon. We found that at low frequencies and diffraction fields, the caustics determine the interference pattern. However, at large distances from the grating, when the waves of high diffraction order and number of slits contribute to the interference pattern, the self-imaging phenomenon and Talbot-like patterns are formed. This methodological approach not only sheds light on the behavior of SW interference under different conditions but also enhances our understanding of the SW self-imaging process in both isotropic and anisotropic media.

Published under an exclusive license by AIP Publishing. <https://doi.org/10.1063/5.0195099>

Spin waves (SWs) represent coherent magnetization disturbances that propagate in magnetic materials as waveforms. In ferromagnetic materials, SW dynamics is shaped by a blend of strong isotropic exchange and anisotropic magnetostatic interactions.^{1,2} Particularly in thin films, the magnetostatic interactions render SW properties highly sensitive to the orientation of magnetization relative to the film plane as well as to the alignment of the propagation direction with the static magnetization vector.^{3–6} This interplay of factors makes the study of SWs interesting, endowing them with distinct properties uncommon in other wave types, such as negative group velocity, the formation of caustics,⁷ and dynamic reconfigurability control.⁸

The governing equations for SW propagation diverge from those of electromagnetic and acoustic waves, thereby each analogy, such as those found in SW graded index lenses,^{9,10} SW Luneburg lenses,¹¹ and

SW Fourier optics,¹² necessitates solving the Landau–Lifshitz equation. Notable and related advances also include the numerical or experimental demonstration of phenomena such as self-focusing of SWs,¹³ SW diffraction on gratings,¹⁴ and the formation of SW beams.^{15–17} Ferromagnetic films with a line of nanodots, analogous to those in this paper, have also been used to observe the phenomenon known in the literature as total non-reflection of SWs.¹⁸

The self-imaging effect, often referred to as the Talbot effect, first observed in the 19th century for light¹⁹ and later elucidated in Ref. 20 has recently experienced a renewed research interest, as outlined in Ref. 21 and associated references. When a plane wave passes through a system of periodically spaced obstacles, it interferes, creating a characteristic diffraction pattern and reproducing the obstacles image at specific distances from the input.

Its applications have been diverse, ranging from enhancing x-ray imaging²² to advancing lithographic patterning,^{23–25} and even extending to the realization of certain physical models and computing scenarios.^{26–28} Beyond electromagnetic waves, the Talbot effect has been demonstrated in diverse mediums, including plasmons,²⁹ fluid waves,^{30,31} and exciton-polaritons.³² Theoretical explorations suggest that this effect is also feasible for SWs,^{33,34} with proposed logic scenarios in the magnonic domain.³⁵

In this paper, we take a step forward by experimentally and numerically demonstrating the self-imaging effect resulting from the diffraction of SWs on a one-dimensional antidot array, with dimensions comparable to the SW wavelength, in a yttrium iron garnet (YIG) film in the Damon–Eshbach (DE) configuration. The simulations, performed at various frequencies, different antidot periods, and two antidot shapes, i.e., circular and square, and juxtaposed with experimental analogs, allow an understanding of the interference patterns in the transition of the caustic and self-imaging effects.

The samples measured were monocrystalline YIG, 4.5 μm thick films (see Fig. 1) grown by liquid phase epitaxy on transparent gadolinium gallium garnet substrates. A one-dimensional array of antidots was chemically etched on the surface of the films, functioning as a diffraction grating. In the two systems analyzed, we make use of an 5-element array of square antidots [50 \times 50 μm —scheme in Fig. 1(a)] with period $d = 100 \mu\text{m}$, and a 10-element array of circular antidots [diameter equal to 50 μm —scheme in Fig. 1(b)] with period $d = 150 \mu\text{m}$. The samples were magnetized by the external magnetic field B_{ext} directed along the line of the antidots (y -axis). We use 36 and 98 mT fields for the samples with square and circular antidots, respectively. Magnetostatic SWs were excited using a 50 μm wide microstrip antenna deposited on a light-opaque dielectric substrate, below the YIG film, and placed about 185 μm in front of the grating, with a continuous-mode microwave generator (see Fig. 1).

The interaction of SWs with the line of antidots was visualized using a Brillouin light scattering (BLS) spectrometer with a spatial

resolution of 30 μm . Measurements are made in the reflection configuration due to the opaque substrate used to mount the microwave antenna. A laser beam with a wavelength of 532 nm was scanned over the area around the line of antidots and the interference area behind the grating with 20 μm step, and the BLS intensity was recorded at each point. This technique provides a 2D color map of the amplitude of the magnetostatic SWs scattered on the line of antidots [see Figs. 3(b), 3(c), and 5(a)].

Simulations were carried out using MuMax3, a GPU-accelerated micromagnetic simulation software.³⁶ The implemented simulation system ($100 \times 100 \times 4.5 \mu\text{m}^3$) was discretized with $512 \times 512 \times 10$ computational cells, giving a size of about $195.3 \times 195.3 \times 450.0 \text{ nm}^3$ each. The cell size clearly exceeds the length of the exchange interaction for YIG films due to computational limitations. However, according to the dispersion relation graphs (see the supplementary material, Fig. S1), the discrepancies are insignificant for small wavevectors, justifying the use of numerical methods for this research.

To replicate the SWs excited by the microstrip in the experiment, in micromagnetic simulations, we employ the dynamic magnetic field $\mathbf{h}(x, t)$, homogeneous in the area of width $w = 50 \mu\text{m}$ along the x -axis (extended along the y direction and across the film thickness) and placed at $x_0 = 185 \mu\text{m}$ before the grating. The microwave field is expressed as

$$\mathbf{h}(x, t) = [h_0, 0, h_0] \sin(2\pi ft), \quad (1)$$

where h_0 is the amplitude of the dynamic magnetic field ($h_0 = 0.0014 B_{\text{ext}}$).

The distribution of the SW intensity within the magnetic material is determined by averaging the magnetization component m_z over the thickness of the material (along the z -axis) and integrating its squared value over time t . The SW intensity I is then quantified by the following equation:

$$I = \int \langle m_z(t) \rangle_z^2 dt. \quad (2)$$

This method effectively captures the spatial intensity distribution of SWs in the material, allowing for direct comparison with BLS measurement results.

In the simulations, we use geometries shown in Fig. 1, with dimensions matching those of our experiment. In all cases, we implemented absorbing boundary conditions along the x -axis (at the end of a system). These are characterized by an exponential increase in the damping factor α , approaching a maximum value of 1 at the edges. Additionally, to better visualize the diffraction patterns formed behind the grating, periodic boundary conditions (PBCs) along the y -axis were used in most simulations (indicated if not). It enabled the imitation of an infinitely wide film and an array of antidots, extending a given SW diffraction field to longer distances. The YIG is characterized by the following magnetic parameters: saturation magnetization $M_s = 139 \text{ kA/m}$, exchange constant $A_{\text{ex}} = 4 \text{ pJ/m}$, $|\gamma| = 176 \text{ GHz} \cdot \text{rad/T}$, and reduced Gilbert damping $\alpha = 1 \times 10^{-7}$.

Previous investigations of the self-imaging of SWs, manifesting the Talbot effect,^{33,34} have extensively utilized the out-of-plane magnetic field configuration, i.e., forward volume SWs. In this orientation, the isofrequency lines tend to be circular due to the symmetry of the applied field with respect to the film plane, leading to the isotropic propagation characteristics of SWs. This isotropic nature facilitates the

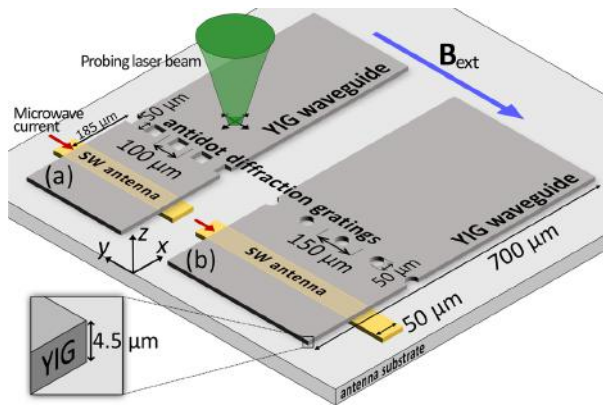


FIG. 1. Schematic representations of two YIG-samples and BLS measurement configuration used in the research, with the major dimensions marked. Image (a) shows the system with a diffraction grating made of square-shaped antidots, while (b) shows one made of circular antidots. In all experimental measurements and finite-width simulations, the square and circular antidot arrays contain 5 and 10 elements, respectively.

formation of distinct interference patterns, critical for achieving the clear SW Talbot effect, also in relatively thick YIG films, considered in this paper (see Fig. S2 in the supplementary material). However, the out-of-plane magnetic field configuration has several disadvantages when applied to thin magnetic films. A primary limitation is the need for high magnetic field values or strong out-of-plane anisotropy to saturate the magnetization. They impose practical limitations on the generation and control of large magnetic fields in experiments, and thus in potential applications, where compact and efficient magnetic field generation is critical. These challenges underscore the importance of exploring alternative configurations, such as the in-plane magnetic field orientation.

Avoiding the high magnetic field requirements associated with the forward volume SW configuration is a key feature of the DE configuration. However, this naturally leads to anisotropic SW propagation due to the asymmetry introduced by the in-plane magnetic field.³⁷ This anisotropy results in hyperbolic isofrequency contours at small wavenumbers (Fig. 2), offering directional control over SW propagation.³⁸ When studying the dynamics of SWs in ferromagnetic films with a thickness of 4.5 μm in an in-plane magnetic field configuration, the interplay between the magnetic field magnitude, SWs frequency, and diffraction grating period together is of primary importance on the interference pattern, which determines the appearance of caustic waves or the Talbot effect.

At lower magnetic field values and SW frequencies, the system with hyperbolic isofrequency lines predominantly forms caustic beams post-interaction with a narrow slot.^{39,40} When a plane SW passes through a diffraction grating, its wavefront is modulated, resulting in a discrete spectrum of wavevectors.¹⁴ As these diffracted waves propagate through the magnetic medium, their paths are influenced by the strong anisotropic dispersion relation (Fig. 2). It causes the SWs to focus along certain trajectories, leading to the convergence of the waves at specific focal points or lines.^{41,42} This convergence is the fundamental mechanism behind the formation of caustic beams, where the wave intensity is significantly amplified.

A theoretical model for caustic beam formation is usually based on analysis of the function $f(\mathbf{k})$ and the angle ϕ , representing the orientation of the group velocity \mathbf{v}_{gr} relative to the external magnetic field \mathbf{B}_{ext} ,^{40,43,44}

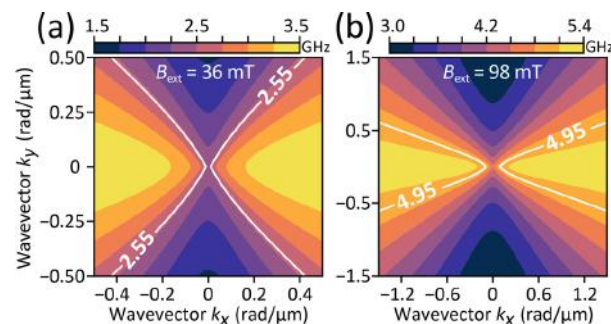


FIG. 2. Diagram of the SW dispersion relation for an external magnetic field of (a) $B_{\text{ext}} = 36$ mT and (b) $B_{\text{ext}} = 98$ mT applied in-plane of the YIG film and along the y direction. The highlighted isofrequency lines correspond to the values used in the study and are obtained from the analytical model of Ref. 37 with free boundary conditions.

$$\phi = \arctan(v_{\text{gr},y}/v_{\text{gr},x}) = -\arctan(dk_x/dk_y). \quad (3)$$

At each point, the SW group velocity is indicated by the normal to the isofrequency curve. Caustic rays are formed when the direction of the group velocity, defined by the angle ϕ , remains constant for SWs with different wavevectors \mathbf{k} . This specific condition for caustic beam emergence is mathematically expressed as $\frac{d\phi}{dk_x} = 0$, which ensures that SWs with different wavevectors maintain a uniform group velocity direction, resulting in wave convergence. When a plane wave passes through a periodic structure, such as the one-dimensional antidot array in our study, it acquires a distinct transverse wavevector component k_y , quantized as multiples of $2\pi/d$. Depending on the change in angle ϕ for the surface wavefront and its intensity for a discrete set of k_y , one of the aforementioned patterns—caustic rays, diffractive self-imaging effect, or a combination of them—is obtained.

Figure 3(a) shows the amplitude-frequency characteristic of the sample with square antidots at $B_{\text{ext}} = 36$ mT. In the experiment,

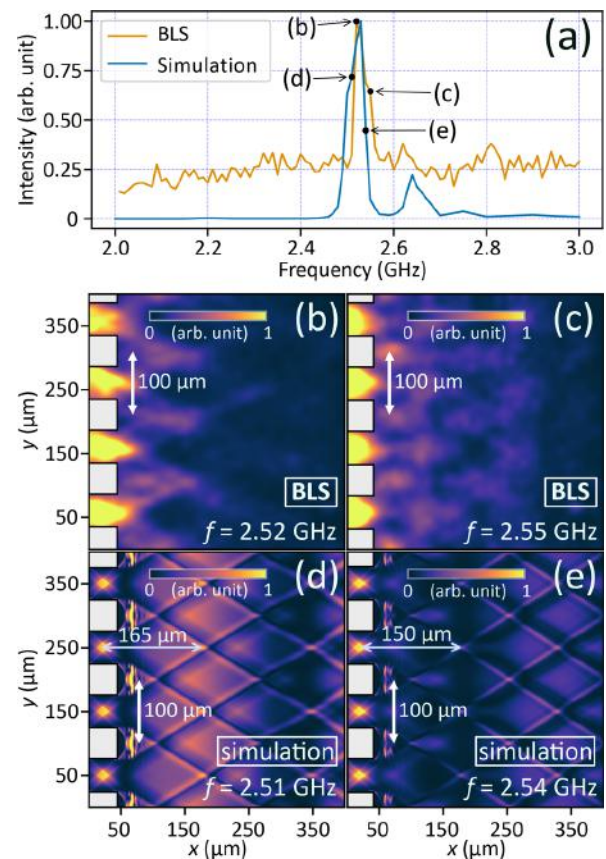


FIG. 3. Experimental and simulation results for a diffraction grating composed of square antidots [Fig. 1(a)] at a magnetic field $B_{\text{ext}} = 36$ mT. Panel (a) shows the amplitude-frequency characteristic of the excited SWs in the interference region. Panels (b) and (c) show the dynamic magnetization pattern obtained from BLS measurements, while panels (d) and (e) display the SW intensity distribution [see Eq. (2)] calculated by MuMax3 for $f = 2.51$ and 2.54 GHz, respectively. The vertical arrows indicate the distances to the nearest caustic beam intersections.

which is well reproduced in the simulations, frequencies in the range of 2.5–2.6 GHz exhibit the most efficient excitation. In addition, these frequencies are slightly higher than the ferromagnetic resonance frequencies, which can be attributed to the selectivity of the antenna in exciting SWs with non-zero wavevectors.

In Fig. 3, we see the results of both the experimental studies (b) and (c) and micromagnetic simulations (d) and (e) of plane wave propagation through a diffraction grating with square antidots [scheme shown in Fig. 1(a)]. The choice of frequencies in the simulations slightly shifted from those of the experiment (by 10 MHz each) is determined by the best fit of the rhombic pattern to that of the experiment. In addition, the goal was also to show the difference in the distance at which the caustic beams intersect for two different, excited SW frequencies from the region of high excitation [marked with arrows in Figs. 3(d) and 3(e)]. For example, in Fig. 3(a), we see that at 2.55 GHz, the experimental intensity is high, but in the simulations, it is already quenched, hence the need for a slight offset. The chosen SW frequencies ($f = 2.51$ GHz and $f = 2.54$ GHz) fit for the high transmission range at $B_{\text{ext}} = 36$ mT [Fig. 3(a)] and allow us to observe the caustic, non-diffractive propagation of the beam after passing through the obstacles.

As seen in Fig. 2(a), the isofrequency lines are nearly straight. It is confirmed by a two-dimensional Fourier transform of the SW signal performed over the simulation area behind the grating shown in Fig. 4(a). It allows to extract of the individual sets of wavevectors involved in the formation of the diffraction images.⁴⁵ Each of the visible intensity peaks corresponds to a packet of wavevectors with very similar angles and group velocity vector values that can independently produce a caustic effect. In the experiment and simulations, Fig. 3, we see a blend of several such packets with varying intensities, producing a complex combination of caustic and interference effects. In the spectra from Fig. 4(a) at 2.53 GHz, we see that the difference between the angles $\Delta\phi$ for the group velocity vectors \mathbf{v}_{gr} for the second and fourth diffraction spots (range of most intensive high order diffraction) is only 2.7° , which explains the clear observation of the caustic effect for this configuration. The discrepancy between them is closely related to the difference in the diffraction angle of the passed waves, and its value is a function of the excited plane wave's frequency (see also Fig. S3 in the supplementary material).

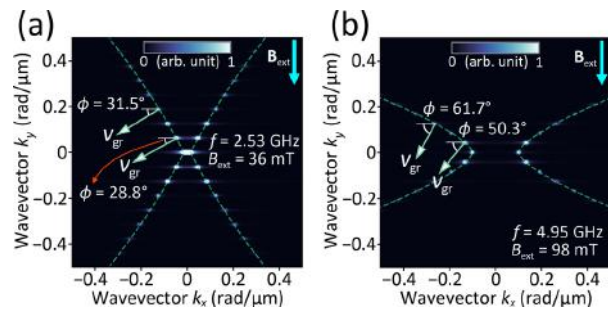


FIG. 4. Reciprocal space maps of the simulated SW intensity distribution after passing the grating for the two cases analyzed: (a) the $100\ \mu\text{m}$ period square grating and (b) the $150\ \mu\text{m}$ period circular grating. The graphs illustrate the group velocity vectors for selected peaks and their slope ϕ [see Eq. (3)] with respect to the SW propagation direction. Interpolated isofrequency contours are shown as green dashed lines.

It is expected that at higher frequencies, as the caustic conditions weaken, the system will begin to exhibit behavior similar to the Talbot effect. This will be the case if the group velocity direction angles differ for each excited wavevector, i.e., the isofrequency curve becomes more parabolic than hyperbolic, as shown in Fig. 2(b) and also in Fig. 4(b) for $B_{\text{ext}} = 98$ mT at $f = 4.95$ GHz ($\lambda = 84.4\ \mu\text{m}$). For these parameters, the self-imaging effect shall be more pronounced due to larger differences in the group velocity angles than in the pure caustic case, still being below the caustic angle $\phi_C = 69.3^\circ$ (obtained from the linearly interpolated dispersion relation from Fig. 2 for k_x up to $3.5\ \text{rad}/\mu\text{m}$). For $B_{\text{ext}} = 36$ mT and a frequency of 2.53 GHz, this angle was only $\phi_C = 44.7^\circ$. This combination of factors allows us to observe periodic diffraction patterns of SWs and the Talbot-like effect. Experimentally, however, these observations were only possible for the circular antidots sample with $150\ \mu\text{m}$ period. Therefore, in the following analysis, we present the experimental and simulation results for this separation at $B_{\text{ext}} = 98$ mT and 4.95 GHz.

As shown in Fig. 5, initially, after passing through the diffraction grating, the SW beams still have a caustic nature. However, as the distance from the grating increases, these beams gradually form the interference pattern. This is due to the increasing influence of larger wavevectors with distance from the source, which no longer satisfies the causticity condition described earlier [see Fig. 4(b)], where $\Delta\phi = 11.4^\circ$ between the spots of the second and fourth diffraction order. Nevertheless, it is clear, especially from the micromagnetic simulations (see Fig. S4 in the supplementary material) that caustic beams and self-imaging coexist even at large distances from the grating. The Talbot-like effect observed in the simulations [Figs. 5(b) and 5(c)] agrees well with the BLS measurements shown in Fig. 5(a). Experimentally, the interference pattern is limited to a triangular shape due to the finite number (10) of circular antidots used in the sample. This limitation is replicated in simulations [Fig. 5(b)] with 10 antidots and absorbing boundaries at the edges.

Comparing the interference patterns obtained in micromagnetic simulations for diffraction on circular and square antidots for the same period, field, and frequency, we found that the self-imaging patterns are very similar (see Fig. S5 in the supplementary material). However, a more intense signal is obtained for the circular antidots. This difference between the shapes can be attributed to the difference in the demagnetization fields near the antidots.⁴⁵ Furthermore, this may be an additional reason for the difficulties in measuring self-imaging patterns in the sample with square antidots discussed earlier for higher frequencies.

In summary, this paper provides a numerical and experimental analysis of SW self-imaging by a diffraction grating in the in-plane magnetized thin YIG films, traversing the intricate transition from caustic beam formation to the Talbot-like effect and demonstrating the nuanced interplay between anisotropic SW dynamics, magnetic field configurations, and diffraction grating geometries. We explore SW behavior at static magnetic field values of 36 and 98 mT and, sequentially, excited SW frequencies of (2.51 GHz) 2.53 and 4.95 GHz, respectively.

At lower fields and frequencies, we observed the formation of caustic beams, a phenomenon emerging due to the strong anisotropic nature of SW propagation in the DE configuration. As we increase the magnetic field strength and SW frequency, a transition to diffractive

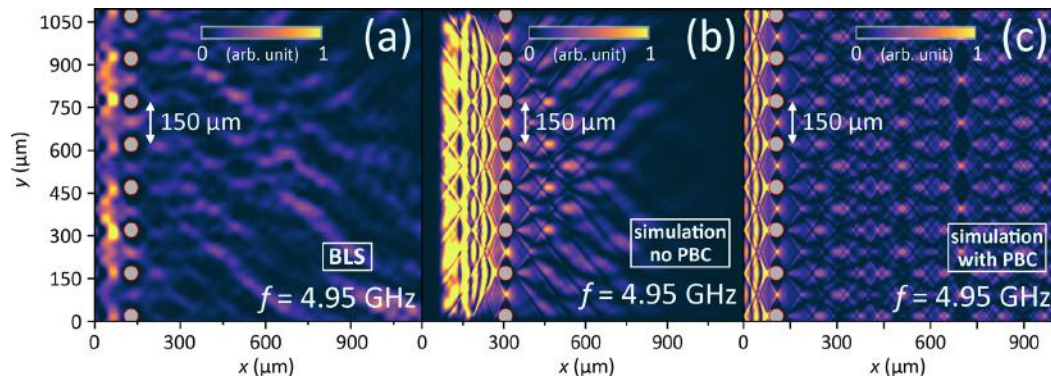


FIG. 5. The SW field intensity distributions at $B_{\text{ext}} = 98$ mT and $f = 4.95$ GHz in the in-plane external magnetic field of 98 mT. Panel (a) shows the results of BLS measurements, and (b) the corresponding micromagnetic simulation, where a finite-length diffraction grating was used. In the SW intensity plot (c), PBC is applied along the y -axis, revealing a clear SW self-imaging effect. All the results were obtained for a diffraction grating composed of 10 circular antidots [Fig. 1(b)] separated by 150 nm. Due to matching zooms from the experiment, the visualizations show only eight nanodots.

self-imaging patterns is observed. This switch from caustic beams to the interference self-imaging not only exemplifies complex wave dynamics in magnonic systems but also enhances our understanding of SW diffraction mechanisms in ferromagnetic films.

See the supplementary material for additional data, including numerical results of the dispersion relations and their comparison with theoretical predictions. These data confirm the accuracy of the numerical approaches and discretization methods used. In addition, it includes extended results from micromagnetic simulations of diffraction fields, specifically illustrating the Talbot effect over various magnetic field configurations, diffraction grating constants, and nanodot geometries.

This work was supported by the National Science Centre Poland project OPUS-LAP under No. 2020/39/I/ST3/02413 and project M-ERA.NET 3 under No. 2022/04/Y/ST5/00164. The authors thank Andrzej Maziewski for valuable discussions.

AUTHOR DECLARATIONS

Conflict of Interest

The authors have no conflicts to disclose.

Author Contributions

Uladzislau Makartsou: Conceptualization (equal); Data curation (equal); Formal analysis (equal); Methodology (lead); Software (lead); Validation (lead); Visualization (lead); Writing – original draft (equal). **Mateusz Gołębiewski:** Conceptualization (equal); Methodology (equal); Supervision (equal); Validation (equal); Visualization (supporting); Writing – original draft (lead); Writing – review & editing (equal). **Urszula Guzowska:** Data curation (equal); Validation (equal); Visualization (equal); Writing – review & editing (supporting). **Alexander Stognij:** Data curation (equal); Resources (equal). **Ryszard Gieniusz:** Conceptualization (equal); Data curation (equal); Writing – review & editing (supporting). **Maciej Krawczyk:** Conceptualization (equal); Formal analysis (equal); Funding acquisition (lead);

Methodology (equal); Supervision (lead); Writing – original draft (equal); Writing – review & editing (equal).

DATA AVAILABILITY

The data that support the findings of this study are openly available on Zenodo at <https://doi.org/10.5281/zenodo.10962369>, Ref. 46.

REFERENCES

- D. D. Stancil and A. Prabhakar, *Spin Waves: Theory and Applications* (Springer US, 2009), pp. 1–355.
- A. G. Gurevich and G. A. Melkov, *Magnetization Oscillations and Waves* (CRC Press, Boca Raton, 1996).
- F. Garcia-Sanchez, P. Borys, R. Soucaille, J. P. Adam, R. L. Stamps, and J. V. Kim, “Narrow magnonic waveguides based on domain walls,” *Phys. Rev. Lett.* **114**, 247206 (2015).
- K. Wagner, A. Kákay, K. Schultheiss, A. Henschke, T. Sebastian, and H. Schultheiss, “Magnetic domain walls as reconfigurable spin-wave nanochannels,” *Nat. Nanotech.* **11**, 432–436 (2016).
- G. Duerr, K. Thurner, J. Topp, R. Huber, and D. Grundler, “Enhanced transmission through squeezed modes in a self-cladding magnonic waveguide,” *Phys. Rev. Lett.* **108**, 227202 (2012).
- J. Lan, W. Yu, R. Wu, and J. Xiao, “Spin-wave diode,” *Phys. Rev. X* **5**, 041049 (2015).
- A. Y. Annenkov, S. V. Gerus, and E. H. Lock, “Superdirectional beam of surface spin wave,” *Europhys. Lett.* **123**, 44003 (2018).
- P. Pirro, V. I. Vasyuchka, A. A. Serga, and B. Hillebrands, “Advances in coherent magnonics,” *Nat. Rev. Mater.* **6**, 1114–1135 (2021).
- N. J. Whitehead, S. A. R. Horsley, T. G. Philbin, and V. V. Kruglyak, “Graded index lenses for spin wave steering,” *Phys. Rev. B* **100**, 094404 (2019).
- M. Kiechle, A. Papp, S. Mendisch, V. Ahrens, M. Golibrzuch, G. H. Bernstein, W. Porod, G. Csaba, and M. Becherer, “Spin-wave optics in YIG realized by ion-beam irradiation,” *Small* **19**, 2207293 (2023).
- N. J. Whitehead, S. A. R. Horsley, T. G. Philbin, and V. V. Kruglyak, “A lense-burg lens for spin waves,” *Appl. Phys. Lett.* **113**, 212404 (2018).
- M. Vogel, B. Hillebrands, and G. von Freymann, “Optical elements for anisotropic spin-wave propagation,” *Appl. Phys. Lett.* **116**, 262404 (2020).
- V. E. Demidov, S. O. Demokritov, K. Rott, P. Krzytyczko, and G. Reiss, “Mode interference and periodic self-focusing of spin waves in permalloy micro-strips,” *Phys. Rev. B* **77**, 064406 (2008).
- S. Mansfeld, J. Topp, K. Martens, J. N. Toedt, W. Hansen, D. Heitmann, and S. Mendach, “Spin wave diffraction and perfect imaging of a grating,” *Phys. Rev. Lett.* **108**, 047204 (2012).

- ¹⁵R. Khomeriki, "Self-focusing magnetostatic beams in thin magnetic films," *Eur. Phys. J. B* **41**, 219–222 (2004).
- ¹⁶R. Gieniusz, P. Gruszecki, M. Krawczyk, U. Guzowska, A. Stognij, and A. Maziewski, "The switching of strong spin wave beams in patterned garnet films," *Sci. Rep.* **7**, 8771 (2017).
- ¹⁷H. Körner, J. Stigloher, and C. Back, "Excitation and tailoring of diffractive spin-wave beams in nife using nonuniform microwave antennas," *Phys. Rev. B* **96**, 100401 (2017).
- ¹⁸R. Gieniusz, V. D. Bessonov, U. Guzowska, A. I. Stognii, and A. Maziewski, "An antidot array as an edge for total non-reflection of spin waves in yttrium iron garnet films," *Appl. Phys. Lett.* **104**, 082412 (2014).
- ¹⁹H. Talbot, "Lxxxvi. Facts relating to optical science. No. iv," *London, Edinburgh Dublin Philos. Mag. J. Sci.* **9**, 401–407 (1836).
- ²⁰L. Rayleigh, "On copying diffraction gratings and on some phenomenon connected therewith," *Philos. Mag.* **11**, 196 (1881).
- ²¹J. Wen, Y. Zhang, and M. Xiao, "The Talbot effect: Recent advances in classical optics, nonlinear optics, and quantum optics," *Adv. Opt. Photonics* **5**, 83–130 (2013).
- ²²A. Bravin, P. Coan, and P. Suortti, "X-ray phase-contrast imaging: From pre-clinical applications towards clinics," *Phys. Med. Biol.* **58**, R1–R35 (2012).
- ²³T. Sato, "Focus position and depth of two-dimensional patterning by Talbot effect lithography," *Microelectron. Eng.* **123**, 80–83 (2014).
- ²⁴S. Zhou, J. Liu, Q. Deng, C. Xie, and M. Chan, "Depth-of-focus determination for Talbot lithography of large-scale free-standing periodic features," *IEEE Photonics Technol. Lett.* **28**, 2491–2494 (2016).
- ²⁵A. Vetter, R. Kirner, D. Opalevs, M. Scholz, P. Leisching, T. Scharf, W. Noell, C. Rockstuhl, and R. Voelkel, "Printing sub-micron structures using Talbot mask-aligner lithography with a 193 nm CW laser light source," *Opt. Express* **26**, 22218–22233 (2018).
- ²⁶D. Bigourd, B. Chatel, W. P. Schleich, and B. Girard, "Factorization of numbers with the temporal Talbot effect: Optical implementation by a sequence of shaped ultrashort pulses," *Phys. Rev. Lett.* **100**, 030202 (2008).
- ²⁷O. J. Farias, F. de Melo, P. Milman, and S. P. Walborn, "Quantum information processing by weaving quantum Talbot carpets," *Phys. Rev. A* **91**, 062328 (2015).
- ²⁸K. Sawada and S. P. Walborn, "Experimental quantum information processing with the Talbot effect," *J. Opt.* **20**, 075201 (2018).
- ²⁹M. R. Dennis, N. I. Zheludev, and F. J. G. de Abajo, "The plasmon Talbot effect," *Opt. Express* **15**, 9692–9700 (2007).
- ³⁰N. Sungar, J. Sharpe, J. Pilgram, J. Bernard, and L. Tambasco, "Faraday–Talbot effect: Alternating phase and circular arrays," *Chaos* **28**, 096101 (2018).
- ³¹A. Bakman, S. Fishman, M. Fink, E. Fort, and S. Wildeman, "Observation of the Talbot effect with water waves," *Am. J. Phys.* **87**, 38–43 (2019).
- ³²T. Gao, E. Estrecho, G. Li, O. A. Egorov, X. Ma, K. Winkler, M. Kamp, C. Schneider, S. Höfling, A. G. Truscott, and E. A. Ostrovskaya, "Talbot effect for exciton polaritons," *Phys. Rev. Lett.* **117**, 097403 (2016).
- ³³M. Gołbiewski, P. Gruszecki, M. Krawczyk, and A. E. Serebryannikov, "Spin-wave Talbot effect in a thin ferromagnetic film," *Phys. Rev. B* **102**, 134402 (2020).
- ³⁴M. Gołbiewski, P. Gruszecki, and M. Krawczyk, "Self-imaging of spin waves in thin, multimode ferromagnetic waveguides," *IEEE Trans. Magn.* **58**, 1–5 (2022).
- ³⁵M. Gołbiewski, P. Gruszecki, and M. Krawczyk, "Self-imaging based programmable spin-wave lookup tables," *Adv. Electrode Mater.* **8**, 2200373 (2022).
- ³⁶A. Vansteenkiste, J. Leliaert, M. Dvornik, M. Helsen, F. Garcia-Sanchez, and B. Van Waeyenberge, "The design and verification of mumax3," *AIP Adv.* **4**, 107133 (2014).
- ³⁷B. A. Kalinikos and A. N. Slavin, "Theory of dipole-exchange spin wave spectrum for ferromagnetic films with mixed exchange boundary conditions," *J. Phys. C: Solid State Phys.* **19**, 7013 (1986).
- ³⁸T. Ogasawara, "Time-resolved vector-field imaging of spin-wave propagation in permalloy stripes using wide-field magneto-optical Kerr microscopy," *Phys. Rev. Appl.* **20**, 024010 (2023).
- ³⁹V. Veerakumar and R. E. Camley, "Magnon focusing in thin ferromagnetic films," *Phys. Rev. B* **74**, 214401 (2006).
- ⁴⁰T. Schneider, A. A. Serga, A. V. Chumak, C. W. Sandweg, S. Trudel, S. Wolff, M. P. Kostylev, V. S. Tiberkevich, A. N. Slavin, and B. Hillebrands, "Nondiffractive subwavelength wave beams in a medium with externally controlled anisotropy," *Phys. Rev. Lett.* **104**, 197203 (2010).
- ⁴¹R. Gieniusz, H. Ulrichs, V. D. Bessonov, U. Guzowska, A. I. Stognii, and A. Maziewski, "Single antidot as a passive way to create caustic spin-wave beams in yttrium iron garnet films," *Appl. Phys. Lett.* **102**, 102409 (2013).
- ⁴²S. Muralidhar, R. Khymyn, A. A. Awad, A. Alemán, D. Hanstorp, and J. Åkerman, "Femtosecond laser pulse driven caustic spin wave beams," *Phys. Rev. Lett.* **126**, 037204 (2021).
- ⁴³O. Büttner, M. Bauer, S. O. Demokritov, B. Hillebrands, Y. S. Kivshar, V. Grimalsky, Y. Rapoport, and A. N. Slavin, "Linear and nonlinear diffraction of dipolar spin waves in yttrium iron garnet films observed by space- and time-resolved Brillouin light scattering," *Phys. Rev. B* **61**, 11576–11587 (2000).
- ⁴⁴A. Wartelle, F. Vilsmeier, T. Taniguchi, and C. H. Back, "Caustic spin wave beams in soft thin films: Properties and classification," *Phys. Rev. B* **107**, 144431 (2023).
- ⁴⁵J. Gräfe, P. Gruszecki, M. Zelent, M. Decker, K. Keskinbora, M. Noske, P. Gawronski, H. Stoll, M. Weigand, M. Krawczyk, C. H. Back, E. J. Goering, and G. Schütz, "Direct observation of spin-wave focusing by a Fresnel lens," *Phys. Rev. B* **102**, 024420 (2020).
- ⁴⁶U. Makartsou *et al.* (2024). "Spin-wave self-imaging: Experimental and numerical demonstration of caustic and talbot-like diffraction patterns," Zenodo. <https://doi.org/10.5281/zenodo.10962369>

SUPPLEMENTARY MATERIAL

Spin-Wave Self-Imaging: Experimental and Numerical Demonstration of Caustic and Talbot-like Diffraction Patterns

Uladzislau Makartsou,¹ Mateusz Gołębiewski,¹ Urszula Guzowska,² Alexander Stognij,^{3, a)} Ryszard Gieniusz,² and Maciej Krawczyk¹

¹⁾*Institute of Spintronics and Quantum Information, Faculty of Physics, Adam Mickiewicz University, Uniwersytetu Poznańskiego 2, 61-614 Poznań, Poland*

²⁾*Department of Physics of Magnetism, Faculty of Physics, University of Białystok, Konstantego Ciołkowskiego 1L, 15-245 Białystok, Poland*

³⁾*Scientific-Practical Materials Research Center at National Academy of Sciences of Belarus, Pietrusia Broŭki 19, 220072 Minsk, Belarus*

(*Electronic mail: ulamak@amu.edu.pl)

I. DISPERSION RELATION AND VALIDATION OF THE DISCRETIZATION IN MICROMAGNETIC SIMULATIONS

In Fig. S1 we show the spin wave (SW) dispersion relations for two different configurations and different magnetic field values obtained in numerical simulations (MuMax3) and analytical model (based on Ref. [s1]) for 4.5 μm thick YIG film. Fig. S1(a) shows the dispersion for the forward volume (FV) configuration (magnetic field and the magnetization perpendicular to the film plane), where the discrepancies between the methods are minimal and mainly due to the coarse discretization along the film thickness. The dispersions in Fig. S1(b,c) are for the Damon-Eshbach (DE) configuration (propagation direction perpendicular to the in-plane magnetization and the external magnetic field) and two different values of the applied external magnetic field. The plots also show non-dispersive signals from thickness quantized SW modes, the so-called perpendicular standing SWs (PPSWs). Again, we obtained a very good fit to the theoretical model for small wavevectors close to zero, validating the numerical approach used in the micromagnetic simulations.

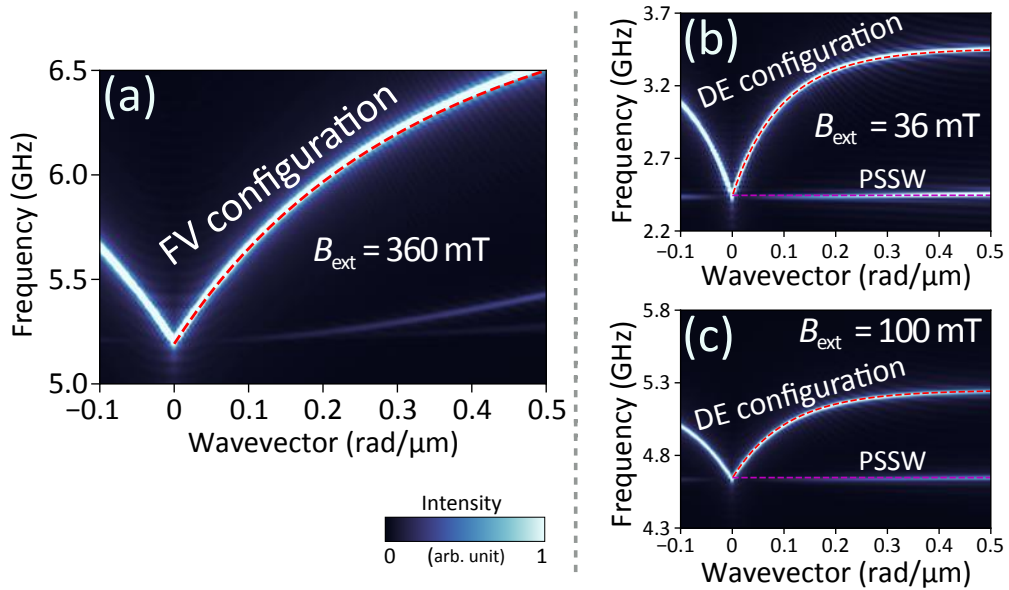


FIG. S1. The dispersion relations for SWs in two different magnetic configurations and different external magnetic field values. (a) Dispersion curve for the FV configuration under a magnetic field of 360 mT. (b) Dispersion in the DE configuration under an external field of 36 mT and PPSW signal lines are visible. (c) DE and PPSW signals for an enhanced field of 100 mT, showing a significant shift in the frequency values. In all panels, the dashed lines represent the analytical calculations based on Ref. [s1].

^{a)}Deceased.

The process of calculating the SW dispersions using Mumax³ involved three main steps:

1. **System Initialization:** Prompting the system to relax into a stable magnetic ground state for selected configurations.
2. **SW excitation:** The SWs were excited from the central part of the waveguide by applying the time- and space-dependent dynamic magnetic field \mathbf{h} , defined as: $\mathbf{h}(x, t) = [h_0, h_0, h_0] \cdot \text{sinc}(2\pi k_{\text{cut}} x) \cdot \text{sinc}(2\pi f_{\text{cut}} t)$, where $h_0 = 0.015 H_{\text{ext}}$. By using this equation, we can apply broadband SW excitation within the frequency range $f \in [0, f_{\text{cut}}]$ and wavevectors along the x -axis $k_x \in [-k_{\text{cut}}, k_{\text{cut}}]$.
3. **Data Analysis:** The dispersion relations were extracted by applying a 2D Fast Fourier Transform to the space and time resolved magnetization data using Python with the NumPy package. This analysis was further refined by evaluating the SW width profiles over the m_x component across the width of the waveguides using a single frequency excitation.

The dispersion relations from micromagnetic simulations and analytical calculations match precisely for the fundamental mode, as indicated in Fig. S1. In the simulations with DE configuration, a low-frequency branch emerges due to quantization effects within the significant thickness (4.5 μm) of the YIG sample, visible in Fig. S1(b,c). The theoretical curve was calculated using the formula (22) from Ref. [s2]. The results demonstrate the agreement between MuMax3 simulations and the analytical dispersion relation based on Refs. [s1 and s2]. The simulation cell size used is $195.3 \times 195.3 \times 450.0 \text{ nm}^3$.

II. TALBOT EFFECT IN A FORWARD VOLUME CONFIGURATION – SIMULATION RESULTS

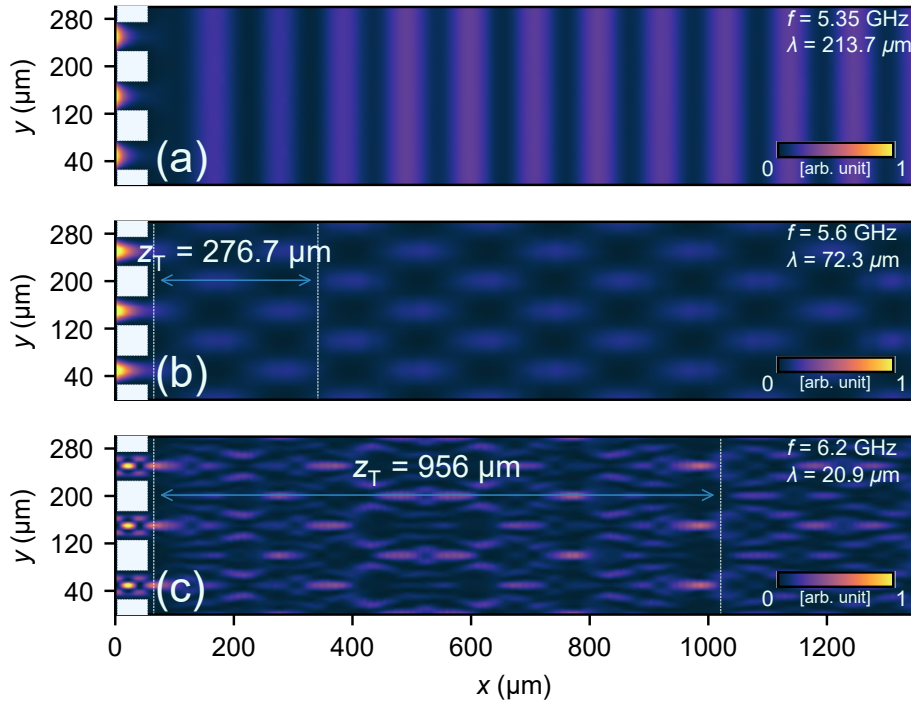


FIG. S2. The evolution of the SW interference pattern after passing through a diffraction grating with a square antidot structure and a period of 100 μm . These micromagnetic simulations were performed in an FV configuration at different frequencies (5.35, 5.6 and 6.2 GHz) and for $B_{\text{ext}} = 100 \text{ mT}$. Panel (a) shows SWs with a wavelength of 213 μm propagating unaffected by the obstacle, and (b) visualizes the generation of the Talbot effect after the passage of 72.3 μm long SWs through a diffraction grating. Panel (c) shows the Talbot effect at a much shorter wavelength of 20.9 μm , resulting in a more pronounced self-imaging effect. Periodic boundary conditions along the diffraction grating (y -axis) were applied to each of these simulations.

The Talbot effect in magnonics has been numerically demonstrated for the configuration with the isotropic dispersion relation, i.e., in the FV configuration for the thin ferromagnetic films^{s3,s4}. In Fig. S2 we show the numerical results indicating the possibility of observing the Talbot effect in a 4.5 μm thick YIG film, a system considered in this paper, with a line of antidots

of square shape ($50 \times 50 \mu\text{m}$) and the period of $100 \mu\text{m}$. We can see that the diffraction of SWs with wavelengths similar to the grating period forms self-imaging patterns (Fig. S2(a,b)), which is the Talbot effect, and it is more clear for shorter SWs as shown in Fig. S2(c). In Fig. S2(c) we observe clear self-repeating patterns over a longer distance (the Talbot length $z_T = 956 \mu\text{m}$) than in Fig. S2(b) ($z_T = 276.7 \mu\text{m}$) with SW wavelengths of $20.9 \mu\text{m}$ and $72.3 \mu\text{m}$, respectively.

III. DAMON-ESHBACH CONFIGURATION

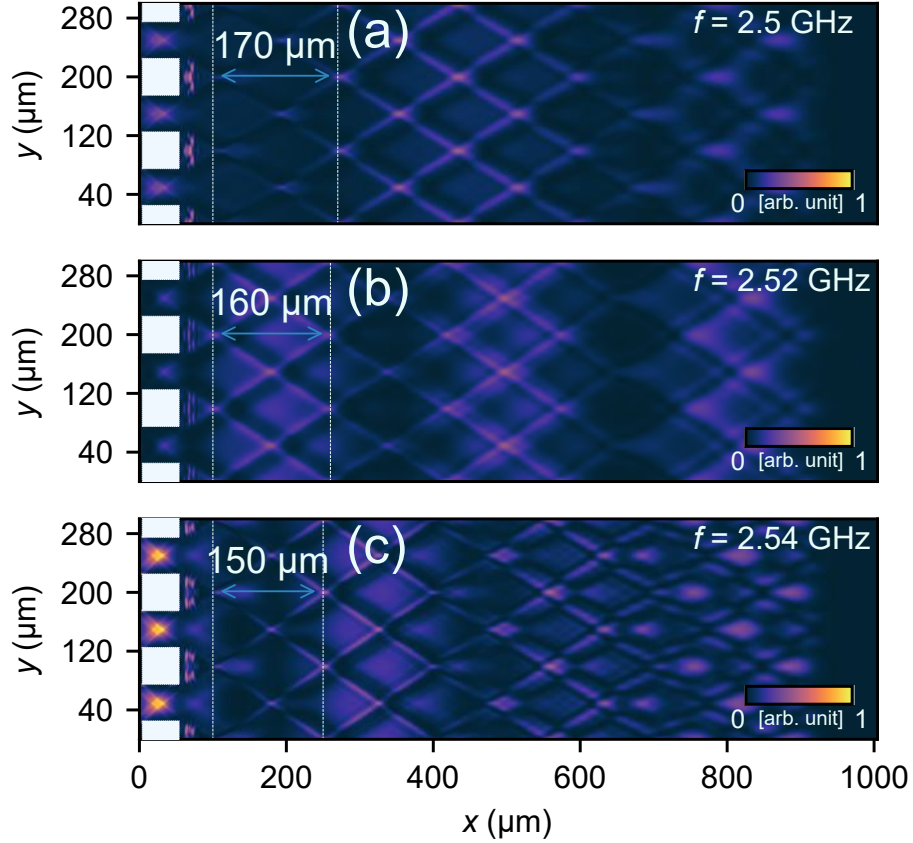


FIG. S3. The SW interference pattern after passing through a diffraction grating with a square antidot structure and a period of $100 \mu\text{m}$. The micromagnetic simulations were performed in a DE configuration for the frequencies 2.50, 2.52 and 2.54 GHz and for $B_{\text{ext}} = 36 \text{ mT}$.

In Fig. S3 we show the extended progression of SWs following diffraction on square antidots in the in-plane magnetized YIG film in DE configuration. The analysis is performed over a larger spatial domain compared to the figures in the main text, allowing a comprehensive observation of the SW pattern evolution. Fig. S3 shows the micromagnetic simulation results for SWs at 2.50, 2.52, and 2.54 GHz for $B_{\text{ext}} = 36 \text{ mT}$. The dominant behavior of the SWs is characterized by the caustic effect, as shown in Fig. S3(a). However, as the frequency increases (wavelength shortens), the angle of caustic beam propagation increases, resulting in a decrease in the distance of crossing beams from adjacent slits along the propagation axis, from 170 to $150 \mu\text{m}$ with the frequency change of 40 MHz, leading to a more complex picture, as shown in Fig. S3(b,c). Furthermore, in Fig. S4 for circular antidots and $150 \mu\text{m}$ period, we show the diffraction of SWs at a higher frequency (4.95 GHz) and a larger external magnetic field strength ($B_{\text{ext}} = 98 \text{ mT}$). This corresponds to exciting SWs with different group velocity angles, resulting in even more complex and periodically repeating patterns.

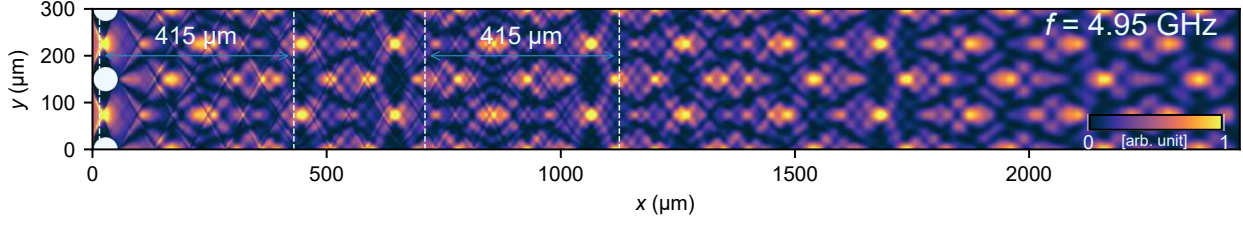


FIG. S4. The SW interference pattern after passing through a diffraction grating with a circular antidot structure and a period of 150 μm . These micromagnetic simulations were performed in a DE configuration for frequency 4.95 GHz and for $B_{\text{ext}} = 98$ mT.

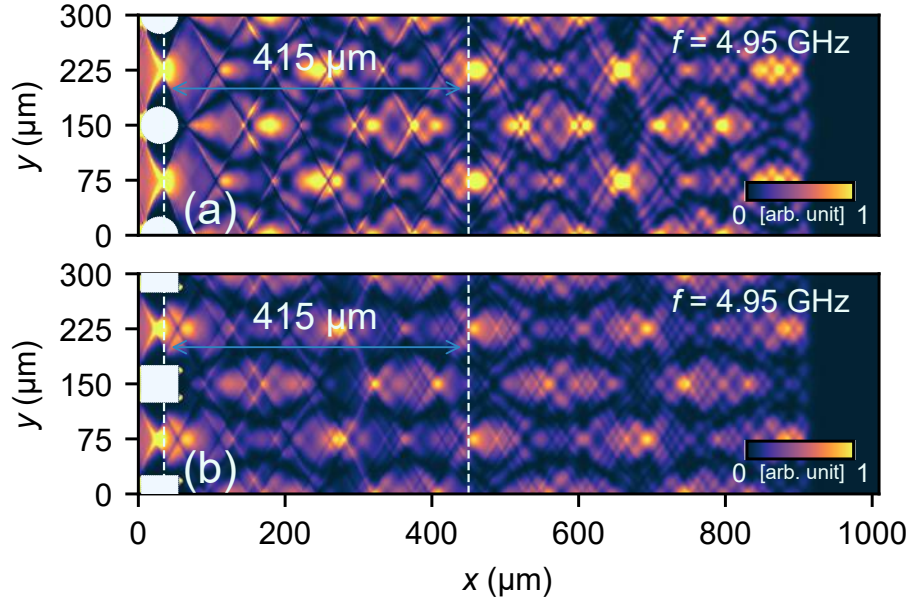


FIG. S5. Panel (a) shows a section of the simulation from Fig. S4 with a circular grating having a period of 150 μm . Panel (b) shows the interference pattern formed by SWs passing through a square antidot grating having the same period of 150 μm .

IV. INFLUENCE OF ANTIDOT SHAPE ON SELF-IMAGE

We changed the shape of the antidots to investigate their effect on the SW propagation in a YIG film and the formation of the self-image pattern. We use the same parameters as in the simulation in Fig. S4 (lattice period 150 μm , frequency 4.95 GHz, and $B_{\text{ext}} = 98$ mT), and the obtained pattern with the circular antidots as a reference image. By changing the antidot shapes from circles [Fig. S5(a)] to squares [Fig. S5(b)], we preserve the self-image pattern in diffraction with the same distance between repetitions, i.e., 415 μm . However, the circular antidot grating provides better signal quality, resulting in the formation of clearer patterns. This difference between the shapes of the antidots can be attributed to the difference in the demagnetization field near the holes^{s5}.

- [s1] B. A. Kalinikos and A. N. Slavin, "Theory of dipole-exchange spin wave spectrum for ferromagnetic films with mixed exchange boundary conditions," *Journal of Physics C: Solid State Physics* **19**, 7013 (1986).
- [s2] K. Szulc, J. Kharlan, P. Bondarenko, E. V. Tartakovskaya, and M. Krawczyk, "Impact of surface anisotropy on the spin-wave dynamics in a thin ferromagnetic film," *Phys. Rev. B* **109**, 054430 (2024).
- [s3] M. Gołębiewski, P. Gruszecki, M. Krawczyk, and A. E. Serebryannikov, "Spin-wave Talbot effect in a thin ferromagnetic film," *Phys. Rev. B* **102**, 134402 (2020).
- [s4] M. Gołębiewski, P. Gruszecki, and M. Krawczyk, "Self-imaging of spin waves in thin, multimode ferromagnetic waveguides," *IEEE Transactions on Magnetics* **58**, 1–5 (2022).
- [s5] J. Gräfe, P. Gruszecki, M. Zelen, M. Decker, K. Keskinbora, M. Noske, P. Gawronski, H. Stoll, M. Weigand, M. Krawczyk, C. H. Back, E. J. Goering, and G. Schütz, "Direct observation of spin-wave focusing by a Fresnel lens," *Phys. Rev. B* **102**, 024420 (2020).

5.2 Two-dimensional systems

In line with the goals of my Ph.D. research plan, the natural continuation of the study of one-dimensional textured systems is to extend the investigation to two-dimensional nanostructures.

This transition enables the study of spin-wave phenomena in more complex geometries, such as waveguides with crescent-shaped cross section and ADLs, in line with the broader goal of advancing functional magnonic architectures. These structures are considered two-dimensional in this study, because the spatial variation of their physical parameters is confined to two dimensions, while the third dimension is held constant and/or excluded from the analysis. For example, we model an infinitely long structure where the cross section is crescent-shaped, meaning that properties such as magnetization and material composition can only change within the profile (in two dimensions) but remain uniform along the length of the waveguide.

ADL's micromagnetic simulations are in fact fully 3D because they include out-of-plane boundary conditions that make the structure finite in the thickness direction. However, the periodicity and primary magnetic behavior are restricted to the in-plane dimensions, with a single unit cell across the thickness of a film (same as in the MuMax3 simulations for Talbot effect studies). Although the out-of-plane thickness affects the spin-wave dynamics, there are no structural variations occurring along this direction, allowing the main effects to be accurately described in a two-dimensional context.

The structures manipulate spin waves in a planar framework, allowing for precise control over wave confinement, propagation, and interference within the plane, which is invaluable for designing efficient magnonic devices.

Two-dimensional nanostructures, such as ADLs with periodic arrays of dots, create frequency-selective channels by establishing tunable bandgaps. These bandgaps filter spin waves according to their frequency, making ADLs highly effective for frequency-selective applications. Similarly, crescent-shaped waveguides exploit structural asymmetry to achieve tailored propagation modes, further extending the ability to control spin-wave behavior.

The research presented in this section builds on the principles established in 1D studies and extends them to more complex geometries that enable sophisticated wave manipulation and open new avenues for applied magnonics.

5.2.1 Spin-wave localization and dynamics in crescent cross-section nanorods under geometric and field manipulations (P4)

This research investigates the properties of spin waves in crescent-shaped waveguides – structures that are inherently three-dimensional due to their curved, asymmetric cross-sectional geometry. However, to focus specifically on the cross-sectional dynamics of magnetization, we perform micromagnetic simulations in two dimensions, modeling the waveguide as infinitely long.

The study shows that changing the direction of the applied magnetic field breaks the inherent symmetry of the crescent-shaped waveguide, which in turn shifts the localization of the spin-wave modes with respect to the static demagnetizing field. This shift affects the frequencies of the

spin waves and provides a way to control the mode confinement. These results demonstrate that such sophisticated waveguides support chirality-based, nonreciprocal dispersion relations for high-frequency spin waves that can be tuned by changing both the direction and the strength of the magnetic field.


This work was carried out in an international collaboration with research groups from the United Kingdom and India, bringing together advanced theoretical expertise and experimental methodologies. It highlights the potential of crescent-shaped waveguides as two-dimensionally textured but fundamentally three-dimensional magnetic structures with tunable spin-wave properties. Such architectures are promising for applications in spintronic and magnonic devices, where precise control of the wave behavior by field and geometry offers new functionalities.

Contribution of the Author

In this publication, I co-supervised the work of the student H. Reshetniak (the second author), and was primarily responsible for the execution of the micromagnetic simulations in COMSOL Multiphysics, which we performed together. I also participated in the interpretation of the simulation results (from COMSOL and from MuMax3 performed by U. Makartsou), established and maintained the international collaboration for this project (with A. van den Berg, S. Ladak, and A. Barman), post-processed the data, wrote the first draft, managed the submission of the manuscript to the journal, and handled all correspondence with the reviewers.

The article reprinted with permission from Gołębiewski, M.; Reshetniak, H.; Makartsou, U.; Krawczyk, M.; van den Berg, A.; Ladak, S.; Barman, A. *Physical Review Applied* **19**, 6, 2200373 (2023) ©2023 American Physical Society. License number: RNP/25/FEB/088094.

Spin-Wave Spectral Analysis in Crescent-Shaped Ferromagnetic Nanorods

Mateusz Gołębiewski^{1,*}, Hanna Reshetniak¹, Uladzislau Makartsou¹, Maciej Krawczyk¹, Arjen van den Berg², Sam Ladak², and Anjan Barman³¹*Institute of Spintronics and Quantum Information, Faculty of Physics, Adam Mickiewicz University, Uniwersytetu Poznańskiego 2, Poznań 61-614, Poland*²*School of Physics and Astronomy, Cardiff University, The Parade, Cardiff CF24 3AA, United Kingdom*³*Department of Condensed Matter and Materials Physics, S. N. Bose National Centre for Basic Sciences, Block JD, Sector III, Salt Lake, Kolkata 700 106, India* (Received 22 November 2022; revised 25 April 2023; accepted 28 April 2023; published 14 June 2023)

The research on the properties of spin waves (SWs) in three-dimensional nanosystems is an innovative idea in the field of magnonics. Mastering and understanding the nature of magnetization dynamics and binding of SWs at surfaces, edges, and in-volume parts of three-dimensional magnetic systems enables the discovery of alternative phenomena and suggests other possibilities for their use in magnonic and spintronic devices. In this work, we use numerical methods to study the effect of geometry and external magnetic field manipulations on the localization and dynamics of SWs in crescent-shaped (CS) waveguides. It is shown that changing the magnetic field direction in these waveguides breaks the symmetry and affects the localization of eigenmodes with respect to the static demagnetizing field. This, in turn, has a direct effect on their frequency. Furthermore, CS structures are found to be characterized by significant saturation at certain field orientations, resulting in a cylindrical magnetization distribution. Thus, we present chirality-based nonreciprocal dispersion relations for high-frequency SWs, which can be controlled by the field direction (shape symmetry) and its amplitude (saturation).

DOI: [10.1103/PhysRevApplied.19.064045](https://doi.org/10.1103/PhysRevApplied.19.064045)

I. INTRODUCTION

Today, the topic of spin waves (SWs) and their control in magnetic materials covers a broad spectrum of research. The technological potential of signal transport without the emission of Joule-Lenz heat [1–3], the wavelength of SWs from micrometers to tens of nanometers for frequencies from few GHz to several hundred GHz [4–7], the ability to control the dispersion and group velocity of magnons [8–11], and high-energy efficiency without compromising the conversion speed [1,12–14], make them a desirable successor to conventional electric currents, among others in computing, memory, and various types of microwave systems [15–20].

It is promising to design advanced magnonic systems where, thanks to static (e.g., geometry, topology, material properties, magnetization texture) and dynamic factors (e.g., frequency of SWs, dynamic couplings, and direction of the external magnetic field), it is possible to control magnons and adjust their dynamics to the given goals. In ferromagnetic materials, the properties of SWs are determined by strong isotropic exchange interactions coexisting

with anisotropic magnetostatic interactions. The localization of SWs is a natural consequence of the development and miniaturization of nanoscale magnetic systems and attempts to manipulate their magnetization. One example of such localizations is the edge mode [21–35], where SWs are bound or propagate only along the outer parts of a system. The strong heterogeneity of the internal demagnetizing field at the edges perpendicular to the magnetization allows the localization of SWs in these regions, and the localization allows the trapped wave modes to act as information carriers or sensitive probes of the magnetic properties of an entire system.

In recent years, there has been significant development of alternative fabrication techniques, such as two-photon lithography and focused electron-beam-induced deposition, which now allow the fabrication and analysis of complex three-dimensional (3D) structures at the nanometer scale [36–41]. Understanding the influence of geometric and topological properties on the propagation of SWs in 3D systems is at a very early stage of research. Exciting effects are shown by crescent-shaped (CS) nanowires arranged in diamond bondlike networks, i.e., enabling the analysis of states close to degeneration and providing a platform for reconfigurable magnonic devices [42–46]. In the above research, the nanorods are building blocks of

*mateusz.golebiewski@amu.edu.pl

more complex systems, demonstrating the existing implementation of CS structures in experimental and theoretical studies. A single CS waveguide may also be of interest in its own right. Moreover, the knowledge of single nanowires will provide a better understanding of the complex dynamics of magnetization in 3D structures' entire system.

This study investigates the shape and curvature of CS nanowires to determine how they affect the magnetization dynamics. In this context, there are key studies showing effective Dzyaloshinskii-Moriya and anisotropy interactions associated with curvature, as proposed in Ref. [47]. There are also numerous other intriguing effects in curved magnetic wires and films [48], the understanding of which opens other research avenues and motivates the systematic analysis of the CS structures performed in this work.

The geometry of the simulated structure is shown in Fig. 1, where the coordinate system and field direction are defined. The SW modes have different spatial distributions in the described structure, ranging from localized to volumetric, spreading throughout the volume, and having different quantization numbers and properties. We study two types of nanorods with CS cross sections—those with rounded edges and those with sharp edges. With this approach, we combine the practical and theoretical analysis of eigenmodes and determine the range where and to what extent the contribution of the edge changes the results for the whole nanorod. In addition, the SW propagation and its dependence on the transverse localization of the modes have been analyzed. The obtained dispersion relations show interesting nonreciprocal properties that can be used for dynamic manipulation of SWs in these waveguides.

The structure of the paper is as follows. First, we describe the system geometry (Sec. II) and the numerical methods used in the simulations (Sec. III). In Sec. IV we present the results and analyze the SW spectra. The results obtained in magnetization saturation at different external field orientations with respect to the CS nanorod axis are presented in Sec. IV A. The SW spectrum in the continuous transformation from elliptic to CS nanorod is shown in Sec. IV B, and we conclude how the edge sharpness influences the magnonic response of the structure in Sec. IV C. In Sec. IV D we study the effect of decreasing magnetic field and static magnetization distribution. Finally, in Sec. IV E we examine the influence of the magnetic field orientation on the dispersion relation of the SWs along the long axis. The last section is a summary of the paper.

II. GEOMETRY AND MATERIAL PARAMETERS

In this research, infinitely long ferromagnetic nanorods with CS cross sections (Fig. 1) are studied. Thus, the magnetic properties (magnetization, demagnetizing field, etc.) are considered to be homogeneous along the z axis.

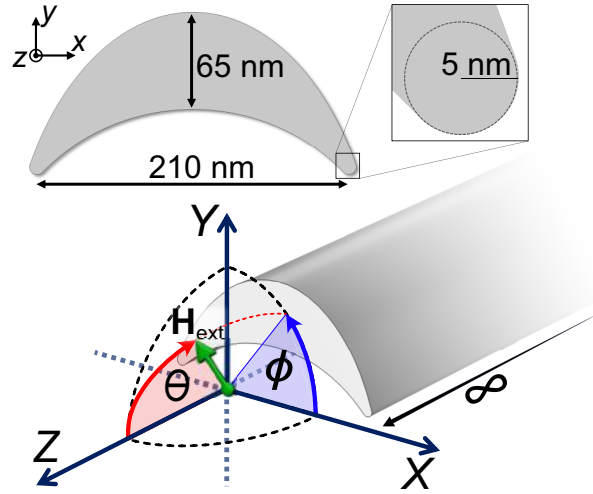


FIG. 1. Model of the nanorod with a CS section. Spherical coordinates for the external magnetic field \mathbf{H}_{ext} and the main dimensions are marked.

Such nanowires can be realized using a combination of two-photon lithography and evaporation [42–45].

The simulation model has 65 nm at the thickest point, the width between the edges is 210 nm, and their rounding radius is 5 nm. Rounded edges of the waveguide are closely related to maintaining the integrity of the simulation by avoiding too thin elements. In addition, as shown in Ref. [42], it is experimentally justified, and its simulated edge modes retain their physical properties. We use the following parameters of permalloy (Py): the saturation magnetization $M_S = 800$ kA/m, the exchange constant $A_{\text{ex}} = 13$ pJ/m, and the gyromagnetic ratio $|\gamma| = 176$ GHz rad/T. To saturate the sample at all analyzed angles, we use an external magnetic field of $\mu_0 \mathbf{H}_{\text{ext}} = 3$ T.

III. MICROMAGNETIC SIMULATIONS

To comprehensively analyze the properties of the SW modes in the CS nanorod, we perform a series of numerical simulations in the COMSOL Multiphysics software. It uses the finite-element method (FEM) to solve coupled systems of partial differential equations, including the Landau-Lifshitz equation and Maxwell equations in the magnetostatic approximation.

All magnetic moments in numerically defined unit cells are modeled in the simulations as normalized unit vectors $\mathbf{m} = \mathbf{M}/M_S$, where \mathbf{M} is the spatiotemporal distribution function of the total magnetization. Then, neglecting damping as a parameter irrelevant to our analysis, the Landau-Lifshitz equation takes the form:

$$\frac{d\mathbf{m}}{dt} = -\gamma [\mathbf{m} \times \mathbf{B}_{\text{eff}}], \quad (1)$$

where $d\mathbf{m}/dt$ is the time evolution of the reduced magnetization. The effective magnetic flux density field \mathbf{B}_{eff} determines the direction around which the magnetization precesses and contains many system-related magnetic components. In our simulations we assume only the influence of the external magnetic field, exchange interactions, and demagnetization.

The demagnetizing field \mathbf{H}_d , contributes to the shape anisotropy in ferromagnets and to the SW dynamics. Since it is governed by Ampère's law ($\nabla \times \mathbf{H}_d = 0$), the demagnetizing field can be derived from a gradient of the magnetic scalar potential U_m :

$$\mathbf{H}_d = -\nabla U_m, \quad (2)$$

which, inside the magnetic body, yields

$$\nabla^2 U_m = \nabla \cdot \mathbf{M}. \quad (3)$$

All presented equations have been implemented in COMSOL to solve the eigenproblem derived from Eqs. (1)–(3), assuming full magnetization saturation by the magnetic field, linear approximation, and analyzing only the CS planes. Assuming that ferromagnetic materials are saturated along the i axis (orientation of \mathbf{H}_{ext}), a linear approximation can be used to split the magnetization vector into static and dynamic (time t - and position \mathbf{r} -dependent) components $\mathbf{m}(\mathbf{r}, t) = m_i \hat{i} + \delta\mathbf{m}(\mathbf{r}, t) \forall (\delta\mathbf{m} \perp \hat{i})$, neglecting all nonlinear terms in the dynamic magnetization $\delta\mathbf{m}(\mathbf{r}, t)$. For further methodological details, see Refs. [49,50]. Therefore, the numerical simulations are performed in two spatial dimensions with a triangular discretization of nearly 10 000 cells. To visualize the static demagnetizing field on a two-dimensional xy area in the form of a color map, we use the formula for its module:

$$H_d(x, y) = \sqrt{(dU_m/dx)^2 + (dU_m/dy)^2}. \quad (4)$$

To elucidate the SW spectra and SW dispersion relation in unsaturated CS nanorods, we use the finite-difference method based micromagnetic simulation package—Mumax3 [51]. Here we solve the Landau-Lifshitz equation with the damping term (assuming damping coefficient $\alpha = 0.0001$), leaving other \mathbf{B}_{eff} terms the same as in COMSOL simulations. To calculate the ferromagnetic resonance intensity spectra (Fig. 8) and dispersion relations (Fig. 9), we apply the fast Fourier transform (FFT). By applying the FFT, we are able to convert the time- and space-domain signals from our simulations into frequency and wave-vector domain spectra and determine the resonant frequencies and SW mode profiles of CS waveguides.

Mumax3 field-rotation simulations are discretized by $256 \times 128 \times 1$ cells, each $0.92 \times 0.90 \times 1$ nm³ in size, along the x , y , and z axes, respectively. Periodic boundary conditions (PBC) are applied along the z axis to

mimic an infinitely long system. To excite the SW dynamics, we use a homogeneous in-space microwave magnetic field $\mathbf{h}(z, t) = [h_0, h_0, h_0]\text{sinc}(2\pi f_{\text{cut}}t)$ with amplitude $h_0 = 0.015H_{\text{ext}}$ and $f_{\text{cut}} = 100$ GHz.

For the dispersion relation simulation, however, the computational volume without PBC had to be increased to $20 \mu\text{m}$, which required the discretization reduction to $64 \times 64 \times 5120$ cells. To avoid reflections of SWs at the waveguide ends, an absorbing boundary condition is assumed. These adjustments did not affect the mode profiles, although a minimal shift in frequencies is observed. Of note, in none of the simulations is the unit cell larger than the exchange length, which is 5.69 nm for Py. The SWs are excited from the central part of the waveguide by applying the time- and space-dependent dynamic component of the magnetic field \mathbf{h} , defined as

$$\mathbf{h}(z, t) = [h_0, h_0, h_0]\text{sinc}(2\pi k_{\text{cut}}z)\text{sinc}(2\pi f_{\text{cut}}t), \quad (5)$$

where $h_0 = 0.015H_{\text{ext}}$. By using Eq. (5), we can apply broadband SW excitation in ranges of frequencies $f \in [0, f_{\text{cut}}]$ and wave vectors along the z axis $k_z \in [-k_{\text{cut}}, k_{\text{cut}}]$.

IV. RESULTS

A. Dependence of SW spectra on the orientation of the magnetic field

We analyze the SW eigenmodes of the system shown in Fig. 1, saturated by the external magnetic field (3 T) directed at different angles ϕ and θ . The results are shown in Figs. 2–4. They reveal interesting changes in the frequencies and distribution of the SW amplitude for different field configurations.

The analysis of changing the azimuth angle ϕ (at $\theta = 90^\circ$) on the SW eigenmodes in Fig. 2 shows the evident influence of the system symmetry on their properties. This is manifested by the edge localization of some modes and the bulk concentration of others. The frequency shift with increasing ϕ is nonmonotonic, revealing more and less favorable configurations for some applications. At $\phi = 0^\circ$, the two low-frequency modes [see mode 1 in Figs. 2(a) and 2(b)] are the edge-localized SWs with antisymmetric and symmetric oscillations at the opposite edges of the nanorod, see Fig. 3(a). Their frequency difference is only 100 MHz, indicating a weak coupling between the SW oscillations at the opposite edges. Interestingly, their responses to field rotation vary significantly, as the frequency of the symmetry branch increases linearly with increasing angle, from 75.76 GHz at 0° to approximately 88 GHz at 30° . The antisymmetric branch shows a completely different trend. We observe the transition from edge mode at $\phi = 0^\circ$ (no. 1), to asymmetric single-edge localization at $\phi = 45^\circ$ (no. 3), to low-frequency volume mode at $\phi = 90^\circ$ (no. 5). The edge localization and its changes with magnetic field rotation can be explained by

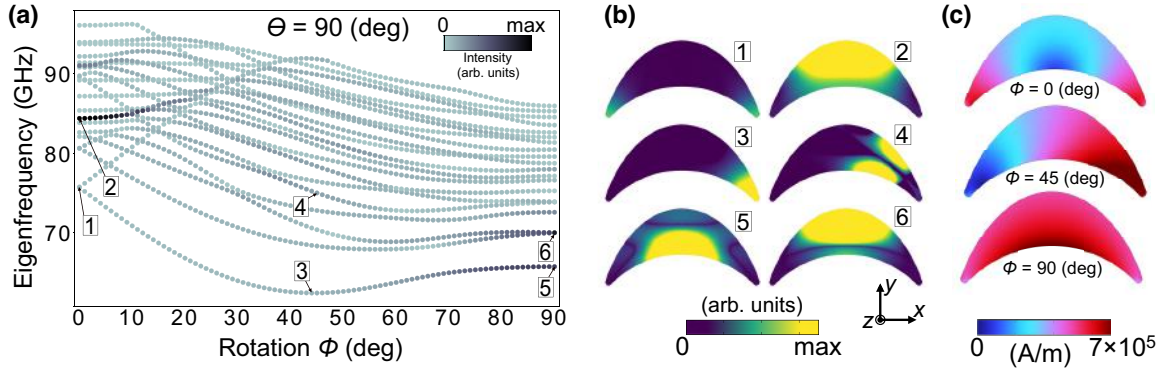


FIG. 2. Eigenanalysis of the CS nanowire as a function of the changing direction of the external magnetic field that saturates the magnetization, $\mu_0 H_{\text{ext}} = 3$ T. Plot (a) shows the dependence of the eigenfrequencies on the azimuthal angle ϕ in the range 0 – 90° for the polar angle $\theta = 90^\circ$. The colors correspond to the intensities of the individual eigenmodes according to Eq. (6). In (b) we can see the distribution of the magnetization precession intensity, while in (c) the static magnetizing fields, Eq. (4), are shown for the selected ϕ values. The number insets in the plots refer to the eigenmode visualizations.

the enhancement of the demagnetizing field, which locally reduces the internal magnetic field, as shown in Fig. 2(c). Thus, the observed transition is strongly associated with the breaking of the symmetry of the internal magnetic field and the associated changes in the demagnetizing field. For the examples in Fig. 2 labeled 3 and 4, we see that the demagnetizing field is strongly localized at the right edge; therefore, mode no. 3 has a lower frequency. On the other hand, modes 5 and 6 are volumetric, but both the magnetization and the demagnetizing field are not uniformly distributed over the cross section, which results in a lower frequency of mode 5 than 6, since the peak of the magnetization intensity coincides with the rise of the demagnetizing field. Thus, the minima in the band structure for the polar angle $\phi = 45^\circ$ are also related to the localization of these low-frequency modes in one half of the CS, e.g., see mode no. 3 in Fig. 2(b). The demagnetizing field in the CS nanorod fluctuates with changing ϕ , so does the frequency of the modes. Thus, the graph presented in Fig. 2(a) shows some crossing and anticrossing between different modes, but we have left their origin and interpretation for further study. Instead, in this paper we

focus on analyzing the effect of field rotation on the CS system eigenfrequencies and SW propagation in them.

The above analysis of the external magnetic field rotation reveals the decoupling of the edge-localized SW modes. Consequently, the two edges can behave as separate, weakly dipolar coupled paths for SW guiding along the nanorod, with their frequencies controlled by the magnitude and orientation of the field. Furthermore, after the field rotation breaks the symmetry, CS nanorods can be used as two-channel SW waveguides capable of simultaneously supporting different frequencies on both sides.

Qualitatively, the situation is very similar for polar angles θ other than 90° , while the eigenfrequency values

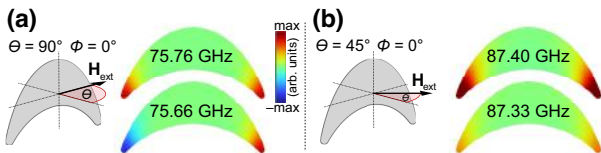


FIG. 3. Edge-mode amplitude distribution for the first two eigenfrequencies and external magnetic field polar angle equal to (a) 90° and (b) 45° . In both cases the azimuthal angle remains 0° , and the colors represent the sum of the dynamic components of the magnetization.

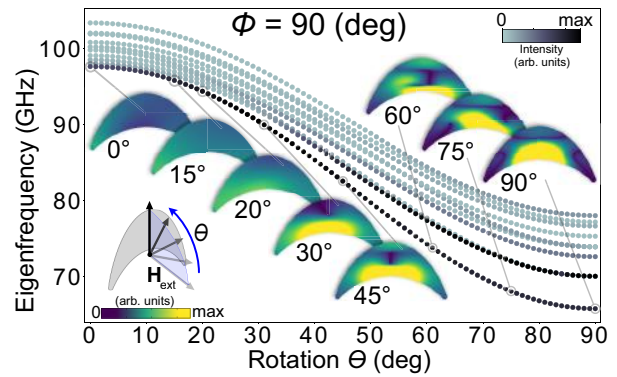


FIG. 4. Frequencies of the SWs in the CS nanowire as a function of the polar angle θ for a constant azimuthal angle $\phi = 90^\circ$ of the 3-T external magnetic field (auxiliary diagram in the lower-left corner). The dark color of the dots represents the resulting intensity of the eigenmodes calculated according to Eq. (6). The images of the cross sections show the distribution of the magnetization precession intensity for successively marked values of θ .

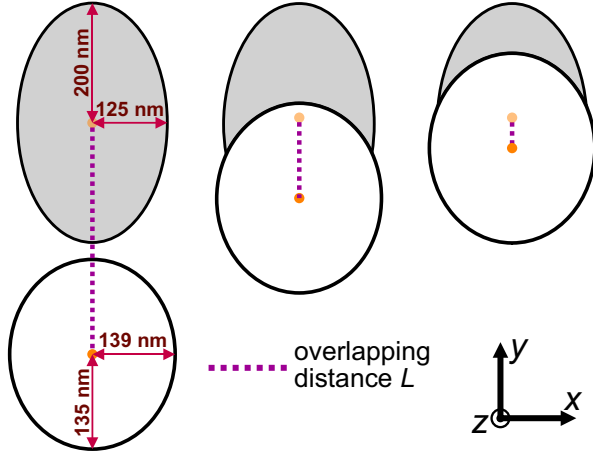


FIG. 5. Scheme of the analyzed shape transformation—from ellipse to the crescent.

change significantly. In particular, the frequency of the edge mode increases from approximately 76 to approximately 88 GHz with a rotating magnetic field from $\theta = 90$ to 45° (Fig. 3), since decreasing the demagnetizing field results in increasing the internal field. By changing θ from 90 to 45° (and keeping $\phi = 0^\circ$), we drive the first edge eigenmode to change its nature from antisymmetric to symmetric.

For this reason, we also decide to study the influence of the polar angle θ on the response of the ferromagnetic system. In this case, the symmetry between the geometry and the external magnetic field is maintained, i.e., for the constant angle $\phi = 90^\circ$.

Figure 4 shows the distinct and monotonic frequency drop (by approximately 30 GHz for the lowest mode)

along with the “skew” of the external magnetic field from the long axis of the nanowire. As for the variation of ϕ , one can also observe a transition from the edge mode for small θ values to the volume mode already formed at about $\theta = 20^\circ$. The frequency drop is also accompanied by a greater separation of eigenmodes, especially the low-frequency ones, compared to the others. This is related to the increasing propensity of the system to generate an intense fundamental mode as θ grows. Furthermore, homogeneously precessing magnetization vectors are energetically more favorable for the field directed along a volume section of finite thickness. It will therefore oscillate with greater intensity and lower frequency.

In addition, the data markers on the frequency plots, Figs. 2(a) and 4, are colored according to values of the following formula:

$$I = \left(\frac{1}{S} \int_S \delta \mathbf{m}(\mathbf{r}, t) dS \right)^2, \quad (6)$$

where S is an area of the nanorod's CS cross section. It defines the intensity of the eigenmodes, formulated to estimate their visibility in experiments, e.g., ferromagnetic resonance measurements. The most intense lines are associated with the fundamental mode (no phase change in the nanorod cross section); see mode 2 in Figs. 2(a) and 2(b). This is predictable since symmetric edge modes are enhanced by a strong demagnetization field, while volume modes occur over a larger area. However, azimuthal rotation of the field reduces the intensity and is only restored at $\phi > 70^\circ$. Here we have two modes of comparable intensity at 65 and 70 GHz [see modes 5 and 6 in Fig. 2(b)]. These modes have amplitudes concentrated in different parts of the inner and central parts of the nanorod with a nodal line perpendicular to \mathbf{H}_{ext} . Their frequency splitting is due to

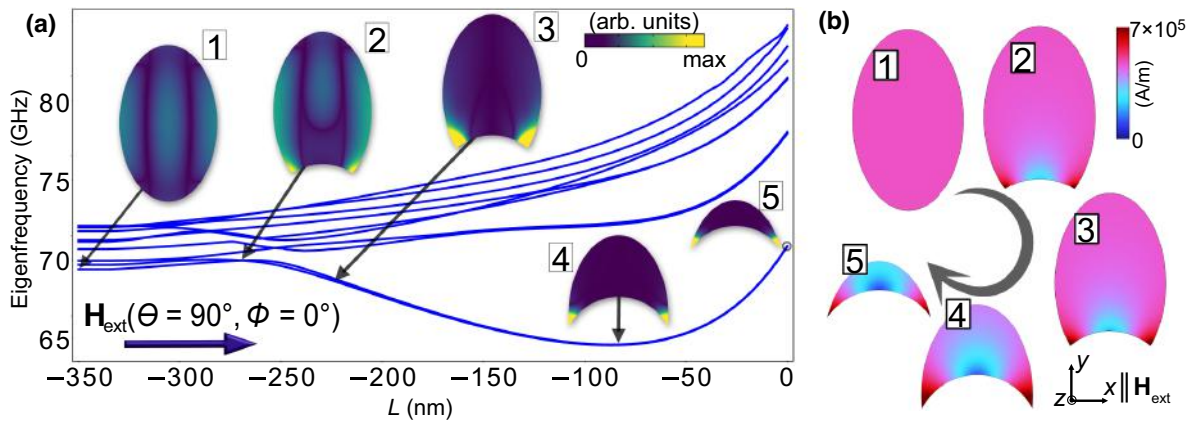


FIG. 6. Eigenanalysis of a variably shaped nanowire going from a full ellipse to the CS cross section (according to Fig. 5). In (a), the magnetization precession intensity distributions for the lowest eigenfrequency branch are shown for the five selected steps of overlapping distance $|L| = 350, 270, 240, 90$, and 0 nm. In (b) the distributions of the static demagnetizing field [see Eq. (4)] are presented.

different curvatures of the lower and upper nanorod edges and thus different demagnetizing fields (see Fig. 2(c) at $\phi = 90^\circ$). Interestingly, rotating the field along the long axis (from $\theta = 90^\circ$ to 0°) decreases the intensity as they transform to the edge-type mode (see Fig. 4).

B. Crescent-ellipse shape transformation

We further investigate the shape and curvature dependence of the analyzed cross section on the formation of low-frequency modes. Therefore, we perform a series of simulations for different geometries resulting from the superposition of two elliptical shapes, from a full ellipse to the crescent shape, controlled by a single parameter L . The scheme of the reasoning is shown in Fig. 5. This allows us to capture the transition of the localization of the modes. In addition, we could also observe the effect of changing the geometry on the demagnetizing field. This analysis is performed for the 3-T external magnetic field along the x axis.

In Fig. 6 it can be seen that the crossings of the individual frequency branches occur at the moment of transition, at $L \approx -270$ nm. Notable is also the nonmonotonic dependence of the lowest-frequency branches. By choosing the appropriate shape of the cross section, we can significantly influence their energy without changing the character of the modes (in this case, the edge-mode excitation at the lowest frequency, i.e., 64.81 GHz, occurs for $L \approx -90$ nm). For $L > -90$ nm, the frequency of all modes increases with increasing L , indicating the dominant role of exchange interactions. An interesting phenomenon is also found for the first three pairs of eigenmodes—we see that as the cross section is brought closer to the crescent shape, these modes degenerate. This is opposite to the behavior of Fig. 2, where symmetric and antisymmetric edge modes split. It is also interesting from the point of view of designing such structures, since the geometry can tune the coupling between modes localized on opposite sides.

C. Edge sharpness impact

Comparing the simulations for $\theta = 90^\circ$ and $\phi = 0^\circ$, we see that the first edge and volume modes (numbered 1 and 2 in Fig. 2) appear at 75.66 and 84.39 GHz, respectively. In the sharp-edged case (analogous to $L = 0$ nm), the first eigenmode appears already at 70.88 GHz and is strictly localized at the edges. It shows a strong edge geometry and sharpness dependence of the eigenfrequencies obtained. This property provides another degree of freedom in this system to tune a magnonic spectrum. However, unlike the thickness, curvature and length of the nanowire, the shape of the edges is difficult to control experimentally. Therefore, in this analysis we examine only what differences can be expected and how essential this element is for the results of micromagnetic simulations. From experimental

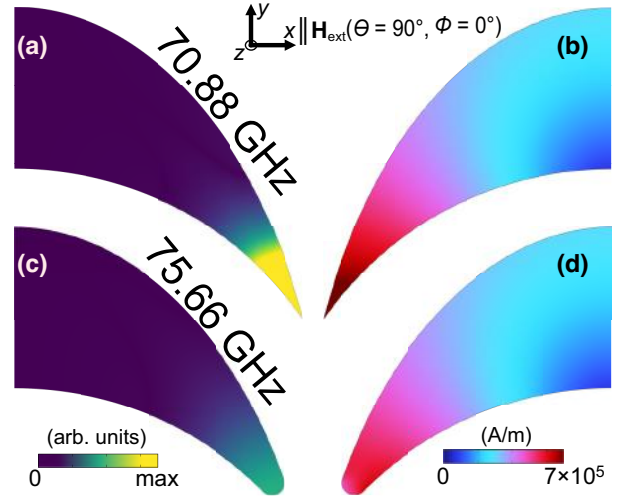


FIG. 7. Comparison of the localization of the SW modes and their frequencies (a),(c) depending on the different edge sharpness and comparison with the corresponding demagnetizing fields (b),(d). The color distributions for the modes represent the magnetization precession intensity from Eq. (6), while the demagnetizing field is from Eq. (4).

studies, it can be observed that the evaporation of a material on a polymer framework with an elliptical cross section [42] leads to the formation of CS nanowires with partially rounded edges. This is mainly due to the roughness of the underlying resist of about 5 nm.

In Fig. 7 it is evident that for the illustrative example ($\phi = 0^\circ$, $\theta = 90^\circ$), where the first eigenmodes are edge localized, there are obvious differences in their distribution and oscillation frequency, up to 4.78 GHz. As shown in the previous section, a strong demagnetizing field in thin regions, relative to a normally oriented magnetic field, causes the modes to be localized there. The crucial observation from Fig. 7 is that the frequency decreases significantly for the sharper edge case. This most likely means that the localization is still forced by the demagnetizing field (magnetostatic effect), since the exchange contribution would increase the frequency with persistent phase or amplitude inhomogeneities in the edge region.

D. Unsaturated system

The eigenproblem simulations in COMSOL assume a uniform static magnetization and focus on the change of field direction and its influence on the localization of harmonic SW modes and their frequencies. For this reason, a large 3-T magnetic field is assumed. An interesting observation is made when comparing the results of the frequency-domain simulation with the results obtained in Mumax3 with the relaxation of the static magnetization distribution. As shown in Fig. 8 (right panels), even at 3-T field, the

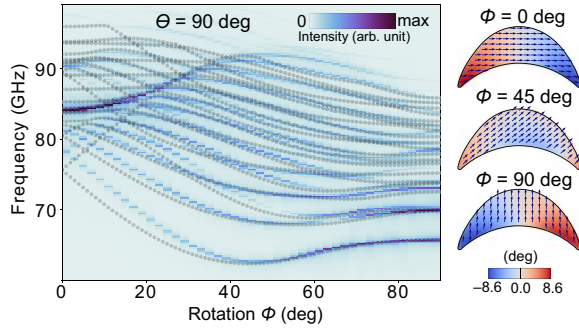


FIG. 8. Comparison of the CS nanowire's eigenanalysis results from COMSOL (gray dots) and time-domain simulation results from Mumax3 (color scale) as a function of the azimuthal angle ϕ for the polar angle $\theta = 90^\circ$ at external magnetic field 3 T. On the right, the static magnetization plots of the CS cross section from Mumax3 for three magnetic field configurations are shown. The color map visualizes the angle deviation of the static magnetization vector (arrows) from the direction of the external magnetic field.

infinite CS nanowire still maintains a nonuniform magnetization (up to 8.6° from the magnetic field orientation at the edges of the CS nanowire for $\phi = 0^\circ$ and 90°), the strength and distribution of which vary with the magnetic field orientation. This leads to slight frequency differences (up to 2.5%) between the Mumax3 and COMSOL calculations (for low-frequency modes at $\phi = 0^\circ$ and higher frequency at $\phi = 90^\circ$), while maintaining their qualitative agreement, as seen in Fig. 8 (left panel). The intensity of a mode is also correlated for both solvers, which can be seen by comparing the intensity of the color map in Fig. 8 with the intensity of the dots in Fig. 2(a). The unexpectedly large saturation field drew our attention to the use of CS waveguides for the propagation of high-frequency SWs, whose frequency will be strongly tunable with the propagation direction (chiral anisotropy) and the value and direction of the external field.

E. Dispersion relation

Curvilinear magnetism, and in particular the propagation of SWs in cylindrical nanotubes, is the subject of analysis in recent studies [47,52–54]. They focus on the influence of the magnetization chirality, forced by the geometry, on the dispersion relation of SWs, obtaining different frequency values with the same wave number but propagating in opposite directions. By analogy with the cylindrical cross section of a nanotube, we can assume that the magnetization in the CS nanorods spreads along their curvature at low magnetic fields, giving rise to SWs with chiral properties. In Fig. 9 we show the dispersion relations for a wave vector directed along the z axis for two values of the external magnetic field, 1 T and 3 T, and its two orientations, $\phi = 0$ and 90° (for both $\theta = 90^\circ$).

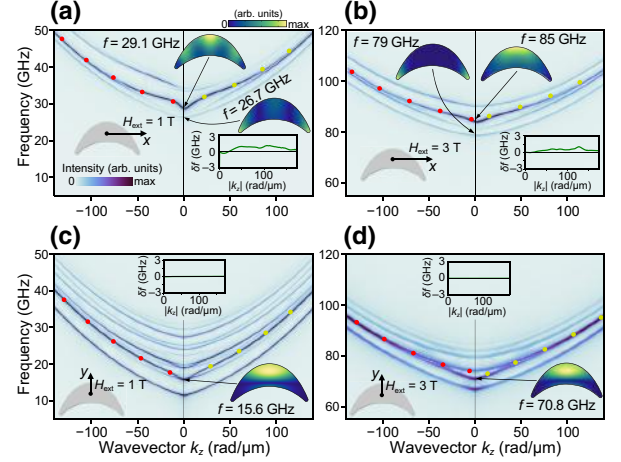


FIG. 9. Dispersion relations of CS nanorods for (a),(c) 1-T and (b),(d) 3-T external magnetic field directed along the x axis (a),(b) and the y axis (c),(d) for 1 T and (d) for 3 T. The wave vector is directed along the z axis. Nonreciprocity is shown in insets as the frequency differences δf between the most intense branches for positive (yellow dots) and negative (red dots) wave vectors. The plots also include visualizations of volumetric and edge modes (where they occur) for $k_z = 0$.

The results for the field directed along the x axis [Figs. 9(a) and 9(b)] show a clear, field-value-dependent nonreciprocity for the bulk mode, represented by the inset plots $\delta f(|k_z|) = f(k_z) - f(-k_z)$. The highest value of this function for the bulk mode at 1 T along the x axis is $\max(\delta f) \approx 1.35$ GHz, and for the analogous case at 3 T— $\max(\delta f) \approx 1.03$ GHz. Interestingly, as we can see in Figs. 9(a) and 9(b), the lowest frequency bands are the edge modes. In the case of 3 T [Fig. 9(b)], this mode is strictly edge localized (see also mode no. 1 in Fig. 2). Simulations also show that this mode has a symmetric parabolic dispersion relation, indicating the propagation nature of this excitation, which supports the thesis of a two-channel SW conductor in structures with CS cross sections. For smaller fields [e.g., 1 T in Fig. 9(a)], the demagnetization exceeds the external magnetic field and the magnetization rotates tangentially to the edge of the nanowire, causing the amplitude to spread over the volume and lose its edge character. This results in a small nonreciprocity also for this mode. On the other hand, at the vertical magnetic field orientation, shown in Figs. 9(c) and 9(d), there is a perfectly symmetric dispersion relation for both 1-T and 3-T field values.

The peculiar dependence of the SW dispersion relation on the value and direction of the magnetic field described in this section is a direct effect of the curvature when the magnetic field breaks the shape symmetry and its low amplitude does not allow it to saturate, leading to a

quasichiral magnetization distribution. Therefore, the nonreciprocity can be explained by the fact that the static magnetization is distributed in a nonlinear way—the smaller the field value, the more significant the nonreciprocity. Interestingly, we are still able to observe detectable nonreciprocity in the CS nanorods at fields as high as 3 T (asymmetrically directed). A feature of the presented systems is the wide operating frequency range and the dynamic tunability using an external magnetic field. Another interesting step may be to test their operation in small fields (or even remanence), where the chirality and thus the nonreciprocity should be stronger and the SW frequencies lower. In addition, it is worth noting that the fabrication of structures with a CS cross section is less expensive than that of nanotubes, which is also an invaluable parameter for future applications.

V. CONCLUSIONS

In this study, an infinitely long waveguide with a CS cross section is investigated. The magnetic response of the system is examined (by eigenfrequency analysis) for different angles of the external magnetic field and the ratio of the edge curvature to the total volume of the cross section. From the obtained results we conclude that the dynamic manipulation of the field direction significantly changes the frequency and character of the eigenmodes, especially the low-frequency ones, shifting from edge to volume localization. The critical factor in this transition is the effect of the symmetry breaking and the magnitude of the internal demagnetizing field in the edge and volume regions, respectively. An analogous transition from the low-frequency edge to the volume mode is observed by gradually changing the cross section from an elliptical to a narrow crescent. However, the relationship between shape and frequency remained nonmonotonic, allowing the identification of the parameters analyzed to obtain the desired SW localization at a given frequency.

The analysis of CS structures is based on experimental research. Here, we numerically demonstrate that very long nanowires with such cross sections are interesting objects of study, allowing us to better understand magnonic effects in complex nanostructures. In 3D systems, where the nanorod elements are oriented at different angles to the external magnetic field, the magnetic effects resulting from the cross sections have a crucial impact on the global dynamic properties. There are also interesting aspects of CS waveguides whose magnetization is not fully saturated and is distributed along the curvature of the structure. For certain angles of incidence of the external magnetic field (in particular, $\phi = 0^\circ$ and $\theta = 90^\circ$) it corresponds to a quasi-chiral-like texture and thus to an asymmetric dispersion relation for SWs propagating along its long axis. In addition, it is found that the saturation of this structure (in

this configuration) is surprisingly high, which may favor the nonreciprocal propagation of high-frequency SWs.

An in-depth understanding of SW performance in waveguides with nontrivial shapes and cross sections is essential to understand the collective effects and advantages of using them in complex magnonic circuits. Ultimately, this research demonstrates the unique nature of CS-section nanorods and their real potential for use in future magnonic devices, where waveguides enabling advanced SW dynamics control will be critical.

The data that support the findings of this study are available from the corresponding author upon reasonable request.

ACKNOWLEDGMENTS

The research leading to these results is funded by the National Science Centre of Poland, Project No. UMO-2020/39/I/ST3/02413. H.R., U.M., and M.K. acknowledge the financial support of the Ministry of Science and Higher Education in Poland, Grant No. MEiN/2022/DIR/3203. S.L. acknowledges support from the Leverhulme Trust (RPG-2021-139) and EPSRC (EP/R009147/1). A.B. gratefully acknowledges funding from Nano Mission, DST, India, under Grant No. DST/NM/TUE/QM-3/2019-1CSNB.

M.G.: conceptualization (equal); formal analysis (equal); methodology (equal); project administration (equal); software (lead); validation (equal); visualization (lead); writing—original draft preparation (lead); writing—review and editing (equal). H.R.: conceptualization (equal); formal analysis (equal); methodology (supporting); software (equal), visualization (equal); writing—original draft preparation (supporting). U.M.: formal analysis (supporting); software (lead); validation (supporting); visualization (equal); writing—original draft preparation (supporting). A.v.B.: methodology (equal), software (equal). S.L.: conceptualization (equal); methodology (equal); project administration (equal); supervision (equal); validation (equal); writing—review and editing (equal). A.B.: conceptualization (equal); methodology (equal); project administration (equal); supervision (equal); validation (equal); writing—review and editing (equal). M.K.: conceptualization (equal); formal analysis (equal); funding acquisition (lead); methodology (equal); project administration (lead); resources (lead); supervision (lead); validation (supporting); writing—review and editing (equal).

The authors have no conflicts to disclose.

-
- [1] A. A. Serga, A. V. Chumak, and B. Hillebrands, YIG magnonics, *J. Phys. D: Appl. Phys.* **43**, 264002 (2010).

- [2] P. Yan and G. E. Bauer, Magnonic Domain Wall Heat Conductance in Ferromagnetic Wires, *Phys. Rev. Lett.* **109**, 087202 (2012).
- [3] J. Barker and G. E. Bauer, Thermal Spin Dynamics of Yttrium Iron Garnet, *Phys. Rev. Lett.* **117**, 217201 (2016).
- [4] T. Schneider, A. A. Serga, B. Leven, B. Hillebrands, R. L. Stamps, and M. P. Kostylev, Realization of spin-wave logic gates, *Appl. Phys. Lett.* **92**, 022505 (2008).
- [5] Y. Kajiwara, K. Harii, S. Takahashi, J. Ohe, K. Uchida, M. Mizuguchi, H. Umezawa, H. Kawai, K. Ando, K. Takanashi, S. Maekawa, and E. Saitoh, Transmission of electrical signals by spin-wave interconversion in a magnetic insulator, *Nature* **464**, 262 (2010).
- [6] H. Yu, O. D'Allivy Kelly, V. Cros, R. Bernard, P. Bortolotti, A. Anane, F. Brandl, R. Huber, I. Stasinopoulos, and D. Grundler, Magnetic thin-film insulator with ultra-low spin wave damping for coherent nanomagnonics, *Sci. Rep.* **4**, 1 (2014).
- [7] S. Maendl, I. Stasinopoulos, and D. Grundler, Spin waves with large decay length and few 100 nm wavelengths in thin yttrium iron garnet grown at the wafer scale, *Appl. Phys. Lett.* **111**, 012403 (2017).
- [8] F. Garcia-Sanchez, P. Borys, R. Soucaille, J. P. Adam, R. L. Stamps, and J. V. Kim, Narrow Magnonic Waveguides Based on Domain Walls, *Phys. Rev. Lett.* **114**, 247206 (2015).
- [9] K. Wagner, A. Kákay, K. Schultheiss, A. Henschke, T. Sebastian, and H. Schultheiss, Magnetic domain walls as reconfigurable spin-wave nanochannels, *Nat. Nanotechnol.* **11**, 432 (2016).
- [10] G. Duerr, K. Thurner, J. Topp, R. Huber, and D. Grundler, Enhanced Transmission Through Squeezed Modes in a Self-Cladding Magnonic Waveguide, *Phys. Rev. Lett.* **108**, 227202 (2012).
- [11] J. Lan, W. Yu, R. Wu, and J. Xiao, Spin-Wave Diode, *Phys. Rev. X* **5**, 041049 (2015).
- [12] A. V. Chumak, V. I. Vasyuchka, A. A. Serga, and B. Hillebrands, Magnon spintronics, *Nat. Phys.* **11**, 453 (2015).
- [13] M. V. V. Kruglyak, S. O. Demokritov, and D. Grundler, Magnonics, *J. Phys. D: Appl. Phys.* **43**, 264001 (2010).
- [14] B. Lenk, H. Ulrichs, F. Garbs, and M. Münzenberg, The building blocks of magnonics, *Phys. Rep.* **507**, 107 (2011).
- [15] P. Pirro, V. I. Vasyuchka, A. A. Serga, and B. Hillebrands, Advances in coherent magnonics, *Nat. Rev. Mater.* **6**, 1114 (2021).
- [16] A. V. Chumak, in *Spintronics Handbook: Spin Transport and Magnetism*, edited by E. Y. Tsybaland I. Žutić (CRC Press, Boca Raton, 2019) 2nd ed., Chap. 6, p. 247.
- [17] S. A. Nikitov, D. V. Kalyabin, I. V. Lisenkov, A. Slavin, Y. N. Barabanenkov, S. A. Osokin, A. V. Sadovnikov, E. N. Beginin, M. A. Morozova, Y. A. Filimonov, Y. V. Khivintsev, S. L. Vysotsky, V. K. Sakharov, and E. S. Pavlov, Magnonics: A new research area in spintronics and spin wave electronics, *Physics-Uspekhi* **58**, 1002 (2015).
- [18] A. Mahmoud, F. Ciubotaru, F. Vanderveken, A. V. Chumak, S. Hamdioui, C. Adelmann, and S. Cotozana, Introduction to spin wave computing, *J. Appl. Phys.* **128**, 161101 (2020).
- [19] A. Barman *et al.*, The 2021 Magnonics Roadmap, *J. Phys.: Condens. Matter* **33**, 413001 (2021).
- [20] A. V. Chumak *et al.*, Advances in Magnetism Roadmap on Spin-Wave Computing, *IEEE. Trans. Magn.* **58**, 1 (2022).
- [21] J. Jorzick, S. O. Demokritov, B. Hillebrands, M. Bailleul, C. Fermon, K. Y. Guslienko, A. N. Slavin, D. V. Berkov, and N. L. Gorn, Spin Wave Wells in Nonellipsoidal Micrometer Size Magnetic Elements, *Phys. Rev. Lett.* **88**, 047204 (2002).
- [22] J. P. Park, P. Eames, D. M. Engebretson, J. Berezovsky, and P. A. Crowell, Spatially Resolved Dynamics of Localized Spin-Wave Modes in Ferromagnetic Wires, *Phys. Rev. Lett.* **89**, 277201 (2002).
- [23] C. Bayer, S. O. Demokritov, B. Hillebrands, and A. N. Slavin, Spin-wave wells with multiple states created in small magnetic elements, *Appl. Phys. Lett.* **82**, 607 (2003).
- [24] M. Bailleul, D. Olligs, and C. Fermon, Micromagnetic Phase Transitions and Spin Wave Excitations in a Ferromagnetic Stripe, *Phys. Rev. Lett.* **91**, 137204 (2003).
- [25] C. Bayer, J. P. Park, H. Wang, M. Yan, C. E. Campbell, and P. A. Crowell, Spin waves in an inhomogeneously magnetized stripe, *Phys. Rev. B* **69**, 134401 (2004).
- [26] R. D. McMichael and B. B. Maranville, Edge saturation fields and dynamic edge modes in ideal and nonideal magnetic film edges, *Phys. Rev. B - Condens. Matter Mater. Phys.* **74**, 024424 (2006).
- [27] B. B. Maranville, R. D. McMichael, S. A. Kim, W. L. Johnson, C. A. Ross, and J. Y. Cheng, Characterization of magnetic properties at edges by edge-mode dynamics, *J. Appl. Phys.* **99**, 08C703 (2006).
- [28] V. V. Kruglyak, P. S. Keatley, R. J. Hicken, J. R. Childress, and J. A. Katine, Time resolved studies of edge modes in magnetic nanoelements (invited), *J. Appl. Phys.* **99**, 08F306 (2006).
- [29] V. E. Demidov, M. Buchmeier, K. Rott, P. Krzysteczko, J. Münchenberger, G. Reiss, and S. O. Demokritov, Non-linear Hybridization of the Fundamental Eigenmodes of Microscopic Ferromagnetic Ellipses, *Phys. Rev. Lett.* **104**, 217203 (2010).
- [30] B. B. Maranville, R. D. McMichael, and D. W. Abraham, Variation of thin film edge magnetic properties with patterning process conditions in $\text{Ni}_8\text{OFe}_2\text{O}$ stripes, *Appl. Phys. Lett.* **90**, 232504 (2007).
- [31] M. Zhu and R. D. McMichael, Modification of edge mode dynamics by oxidation in $\text{Ni}_8\text{OFe}_2\text{O}$ thin film edges, *J. Appl. Phys.* **107**, 103908 (2010).
- [32] J. M. Shaw, T. J. Silva, M. L. Schneider, and R. D. McMichael, Spin dynamics and mode structure in nanomagnet arrays: Effects of size and thickness on linewidth and damping, *Phys. Rev. B - Condens. Matter Mater. Phys.* **79**, 184404 (2009).
- [33] H. T. Nembach, J. M. Shaw, T. J. Silva, W. L. Johnson, S. A. Kim, R. D. McMichael, and P. Kabos, Effects of shape distortions and imperfections on mode frequencies and collective linewidths in nanomagnets, *Phys. Rev. B - Condens. Matter Mater. Phys.* **83**, 094427 (2011).
- [34] V. V. Kruglyak, A. Barman, R. J. Hicken, J. R. Childress, and J. A. Katine, Picosecond magnetization dynamics in nanomagnets: Crossover to nonuniform precession, *Phys. Rev. B - Condens. Matter Mater. Phys.* **71**, 220409 (2005).
- [35] R. D. McMichael, C. A. Ross, and V. P. Chuang, Thickness dependence of magnetic film edge properties in $\text{Ni}_8\text{OFe}_2\text{O}$ stripes, *J. Appl. Phys.* **103**, 07C505 (2008).

- [36] A. Fernández-Pacheco, R. Streubel, O. Fruchart, R. Hertel, P. Fischer, and R. P. Cowburn, Three-dimensional nanomagnetism, *Nat. Commun.* **8**, 1 (2017).
- [37] C. Donnelly, A. Hierro-Rodríguez, C. Abert, K. Witte, L. Skoric, D. Sanz-Hernández, S. Finizio, F. Meng, S. McVitie, J. Raabe, D. Suess, R. Cowburn, and A. Fernández-Pacheco, Complex free-space magnetic field textures induced by three-dimensional magnetic nanostructures, *Nat. Nanotechnol.* **17**, 136 (2021).
- [38] M. Hunt, M. Taverne, J. Askey, A. May, A. Van Den Berg, Y. L. D. Ho, J. Rarity, and S. Ladak, Harnessing multiphoton absorption to produce three-dimensional magnetic structures at the nanoscale, *Materials* **13**, 761 (2020).
- [39] A. van den Berg, M. Caruel, M. Hunt, and S. Ladak, Combining two-photon lithography with laser ablation of sacrificial layers: A route to isolated 3D magnetic nanostructures, *Nano Res.* **16**, 1441 (2023).
- [40] P. Fischer, D. Sanz-Hernández, R. Streubel, and A. Fernández-Pacheco, Launching a new dimension with 3D magnetic nanostructures, *APL Mater.* **8**, 010701 (2020).
- [41] D. Makarov, O. M. Volkov, A. Kákay, O. V. Pylypovskyi, B. Budinská, O. V. Dobrovolskiy, D. Makarov, O. M. Volkov, A. Kákay, O. V. Pylypovskyi, and H.-Z. Dresden Rossendorf, New dimension in magnetism and superconductivity: 3D and curvilinear nanoarchitectures, *Adv. Mater.* **34**, 2101758 (2022).
- [42] A. May, M. Hunt, A. Van Den Berg, A. Hejazi, and S. Ladak, Realisation of a frustrated 3D magnetic nanowire lattice, *Commun. Phys.* **2**, 1 (2019).
- [43] J. C. Gartside, S. G. Jung, S. Y. Yoo, D. M. Arroo, A. Vanstone, T. Dion, K. D. Stenning, and W. R. Branford, Current-controlled nanomagnetic writing for reconfigurable magnonic crystals, *Commun. Phys.* **3**, 1 (2020).
- [44] S. Sahoo, A. May, A. Van Den Berg, A. K. Mondal, S. Ladak, and A. Barman, Observation of coherent spin waves in a three-dimensional artificial spin ice structure, *Nano Lett.* **21**, 4629 (2021).
- [45] A. May, M. Saccone, A. van den Berg, J. Askey, M. Hunt, and S. Ladak, Magnetic charge propagation upon a 3D artificial spin-ice, *Nat. Commun.* **12**, 1 (2021).
- [46] S. Sahoo, S. Mondal, G. Williams, A. May, S. Ladak, and A. Barman, Ultrafast magnetization dynamics in a nanoscale three-dimensional cobalt tetrapod structure, *Nanoscale* **10**, 9981 (2018).
- [47] R. Streubel, P. Fischer, F. Kronast, V. P. Kravchuk, D. D. Sheka, Y. Gaididei, O. G. Schmidt, and D. Makarov, Magnetism in curved geometries, *J. Phys. D: Appl. Phys.* **49**, 363001 (2016).
- [48] D. D. Sheka, A perspective on curvilinear magnetism, *Appl. Phys. Lett.* **118**, 230502 (2021).
- [49] M. Mruczkiewicz, M. Krawczyk, V. K. Sakharov, Y. V. Khivintsev, Y. A. Filimonov, and S. A. Nikitov, Standing spin waves in magnonic crystals, *J. Appl. Phys.* **113**, 093908 (2013).
- [50] J. Rychly, V. S. Tkachenko, J. W. Klos, A. Kuchko, and M. Krawczyk, Spin wave modes in a cylindrical nanowire in crossover dipolar-exchange regime, *J. Phys. D: Appl. Phys.* **52**, 075003 (2018).
- [51] A. Vansteenkiste, J. Leliaert, M. Dvornik, M. Helsen, F. Garcia-Sanchez, and B. Van Waeyenberge, The design and verification of MuMax3, *AIP Adv.* **4**, 107133 (2014).
- [52] J. A. Otálora, M. Yan, H. Schultheiss, R. Hertel, and A. Kákay, Curvature-Induced Asymmetric Spin-Wave Dispersion, *Phys. Rev. Lett.* **117**, 227203 (2016).
- [53] J. A. Otálora, M. Yan, H. Schultheiss, R. Hertel, and A. Kákay, Asymmetric spin-wave dispersion in ferromagnetic nanotubes induced by surface curvature, *Phys. Rev. B* **95**, 184415 (2017).
- [54] L. Körber, R. Verba, J. A. Otálora, V. Kravchuk, J. Lindner, J. Fassbender, and A. Kákay, Curvilinear spin-wave dynamics beyond the thin-shell approximation: Magnetic nanotubes as a case study, *Phys. Rev. B* **106**, 014405 (2022).

5.2.2 Thin-film magnonic crystals for high-frequency spin-wave generation (P5)

This paper explores the potential of spin waves for high-frequency signal processing, highlighting the role of two-dimensional texturing in achieving nano-wavelength confinement and high-frequency operation. Using a periodic ADL – a two-dimensional magnonic crystal structure – we demonstrate through micromagnetic simulations that a microwave-pumped spin-wave mode, confined within the lattice cavity (region in ADL without the antidots – a defect), can generate spin waves with frequencies in the tens of GHz and wavelengths below 50 nm. This represents a significant advance in the generation of high-frequency, short-wavelength spin waves.

The 2D texturing by the ADL creates a magnonic bandgap that overlaps the frequency of the cavity mode, enhancing confinement and enabling magnetic field tunability. We find that higher harmonics emerge when the RF amplitude exceeds a certain threshold, indicating nonlinear magnetization dynamics. The cavity mode frequency is aligned with the FMR frequency of the planar ferromagnetic film, providing a stable mechanism for wave generation and control.

This study highlights the importance of two-dimensional texturization for high-frequency spin-wave applications and presents a scalable method for generating short spin waves, underscoring the potential of magnonic crystals in advanced magnonic and quantum technologies.

Contribution of the Author

In this publication, I performed the COMSOL part of the micromagnetic simulations (band structures and spectra of the ADLs), contributed to the discussion and interpretation of the results, assisted in the post-processing of the simulation data, and supported the writing and review of the manuscript.

©2024 The Authors. *Advanced Quantum Technologies* published by Wiley-VCH GmbH. The paper was published under the CC-BY 4.0 license.

Exciting High-Frequency Short-Wavelength Spin Waves using High Harmonics of a Magnonic Cavity Mode

Nikhil Kumar, Paweł Gruszecki, Mateusz Gołębiewski, Jarosław W. Kłos, and Maciej Krawczyk*

Spin waves (SWs) are promising objects for signal processing and future quantum technologies due to their high microwave frequencies with corresponding nanoscale wavelengths. However, the nano-wavelength SWs generated so far are limited to low frequencies. In the paper, using micromagnetic simulations, it is shown that a microwave-pumped SW mode confined to the cavity of a thin film magnonic crystal (MC) can be used to generate waves at tens of GHz and wavelengths well below 50 nm. These multi-frequency harmonics of the fundamental cavity mode are generated when the amplitude of the pumping microwave field exceeds a threshold, and their intensities then scale linearly with the field intensity. The frequency of the cavity mode is equal to the ferromagnetic resonance frequency of the planar ferromagnetic film, which overlaps with the magnonic bandgap, providing an efficient mechanism for confinement and magnetic field tunability. The effect reaches saturation when the microstrip feed line covers the entire cavity, making the system feasible for realization.

electronics and photonics in terms of high operating frequency, low power consumption, and miniaturization.^[2,7–11] MCs are the magnetic equivalent of photonic or phononic crystals, which are important elements of photonic^[12,13] and phononic^[14,15] technologies, respectively, and are also considered to be an important element of future magnonic circuits.^[16–19] The characteristic in-plane sizes of planar MCs are in the range of tens or single hundreds of nanometers, while the thicknesses are about a few or tens of nanometers. In this context, the SW modes in antidot lattices (ADLs), i.e. thin ferromagnetic films periodically structured with holes (antdots), have attracted considerable interest^[20–27] and were used for controlling SW velocity,^[28] exploiting magnonic bandgaps and SW diffraction.^[29–31]

However, the fundamental obstacles in the design of magnonic devices are, among

1. Introduction

Magnonics, which uses SWs to transmit and process information, is one of the fastest developing areas of research in modern magnetism.^[1–6] It covers a wide frequency range from sub-GHz to tens of THz, with corresponding wavelengths from micrometers to nanometers, and is free of translational electron motion and Joule heating. This makes it a promising alternative to

others, difficulties related to the excitation of SWs, especially of high frequency and short wavelengths. To excite short SWs, i.e. with wavelengths below 100 nm, the use of (a) microwave strip lines,^[32] (b) magnetic solitons (domain wall^[33] or vortex in a single or double ferromagnetic layer^[34,35]), (c) ferromagnetic strips magnetostatically coupled to the ferromagnetic conduit,^[36] (d) 2D grating couplers^[37] or (f) inhomogeneity of the internal magnetic field^[38] has been proposed. The first approach (a) requires ultra-narrow metallic strips that limit the transmitted power, and the latter three (b–d) are used at low frequencies that are limited by the natural oscillations of the magnetic solitons or ferromagnetic nanoelements (ferromagnetic resonance frequency). In the latter case (d), the frequencies of the locally modified internal magnetic field are usually below or around the ferromagnetic resonance frequency of the respective bulk material. More recently, in the out-of-plane magnetized film, the local reduction of the demagnetization field due to high-angle magnetization oscillations allowed the excitation of SWs with wavelengths down to 200 nm.^[39] Although a simple microstrip is used to transmit microwaves to the SW, the nonlinear effect involved and the proposed conversion are limited to low frequencies, hardly accessible for shorter SWs, and effective only in the assumed geometry.

By introducing a defect into the ADL, e.g., in the form of a filled hole (or a few filled holes), we can trap SW energy in this region whenever a resonant frequency of the cavity falls into the magnonic bandgap of the MC.^[40–43] Such a magnonic cavity

N. Kumar
Electronics and Communication Engineering Department
National Institute of Technology Calicut
Kozhikode 673 601, India

P. Gruszecki, M. Gołębiewski, J. W. Kłos, M. Krawczyk
Institute of Spintronics and Quantum Information
Faculty of Physics
Adam Mickiewicz University
Poznań, Uniwersytetu Poznańskiego 2, Poznań 61-614, Poland
E-mail: krawczyk@amu.edu.pl

The ORCID identification number(s) for the author(s) of this article can be found under <https://doi.org/10.1002/qute.202400015>

© 2024 The Authors. Advanced Quantum Technologies published by Wiley-VCH GmbH. This is an open access article under the terms of the [Creative Commons Attribution](#) License, which permits use, distribution and reproduction in any medium, provided the original work is properly cited.

DOI: 10.1002/qute.202400015

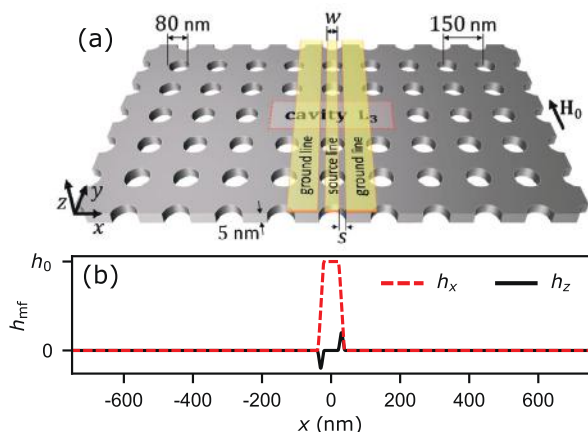


Figure 1. a) Schematic of the device – an ADL with a three-hole defect cavity (L_3) centered at $x = 0$ and $y = 0$. MC is made of a 5 nm thick Py-film with magnetization saturated by the magnetic field H_0 directed along the y -axis, the diameter of the antidots is 80 nm and the lattice constant is 150 nm. A CPW antenna is placed just above the film, centered at x_0 (in the plot $x_0 = 0$), and consists of a source line of width w and two ground lines, which are separated from the source line by gaps of width s . b) The SWs are excited by the x and z components of the microwave frequency magnetic field h_{mf} of amplitude h_{mf} produced by CPW. The calculated field distribution from CPW with $w = 40$ nm and $s = 20$ nm is shown.

allows building-up of SW amplitude,^[44,45] similar to electromagnetic waves in a photonic crystal cavity,^[12] when externally pumped at the cavity resonant frequency. Finally, at sufficiently high wave amplitudes, nonlinear processes are initiated. This effect is widely studied and exploited in photonics cavities, in particular, to enhance the generation of 2nd and 3rd harmonics.^[13,46]

Recently, multi-frequency generation in magnonics has also been demonstrated.^[47–50] However, the frequency of the generated SW modes hardly exceeds 10 GHz. In particular, the results of time-resolved scanning transmission X-ray microscopy measurements demonstrate the generation of SW high harmonics, up to 7th order, in ADL based on 50 nm thick Py film.^[50] The pumping microwave field frequency is only 0.93 GHz, so the 7th order harmonic frequency is only 6.51 GHz.

In our work, we further exploit ADL by combining it with the defects forming magnonic cavities to enhance nonlinear processes, in particular high-frequency harmonic generation. To this end, we introduce into ADL an L_3 cavity (a homogeneous region where three successive antidots are absent). In order to concentrate and enhance the SW amplitude inside the cavity, which is required to cross the nonlinearity threshold, we need to choose an ADL with a full frequency gap in which the fundamental mode of the cavity exists. This condition is satisfied for a Py-based ADL with cylindrical antidots arranged in a square lattice—see **Figure 1**. Here, the gap width is 1.9 GHz at 0.5 T magnetic field and can be further optimized by changing the lattice type, shape, and size of the antidots. The fundamental mode frequency of the L_3 cavity corresponds to the ferromagnetic resonance (FMR) frequency of the uniform Py layer, and this frequency is within the magnonic bandgap of the ADL. This allows a wide frequency tunability by the magnetic field: changing it from 200 mT to 1 T results in the 2nd and 3rd harmonics in the fre-

quency ranges 28–80 GHz and 42–120 GHz, respectively, while keeping the SW wavelength below 62 and 40 nm, respectively. The presented mechanism of high-frequency short-wavelength SW generation demonstrates its general character and the feasibility of its experimental realization by using a standard coplanar waveguide (CPW) to pump the fundamental cavity mode.

2. Device Model

The device geometry is shown in **Figure 1a**. It is an ADL with a square lattice of antidots in a 5 nm thick Py film, with an antidot diameter of 80 nm and a lattice constant of $a = 150$ nm. A three-antidot defect L_3 (i.e., the area of three unit cells without the holes) is introduced in this structure. The system is uniformly magnetized by an in-plane bias magnetic field $\mu_0 H_0 > 0.2$ T directed along the y -axis (μ_0 is the permeability of the vacuum). The SWs are excited by a microwave frequency magnetic field (h_{mf}) generated by a CPW consisting of a signal line of width w separated by $s = 20$ nm gaps from two identical ground lines (much wider than w), and centered at x_0 .

Two simulation methods are used. Comsol Multiphysics package is used to calculate the magnonic band structure and cavity modes. Here, we use the finite element method (FEM) to solve the eigenproblem obtained from the linearized Landau-Lifshitz equation in real space and the frequency domain. The nonlinear effects are simulated in the real space and time domain (with finite difference time domain method, FDTD) using the Mumax3 micromagnetic solver,^[51] which solves the full Landau-Lifshitz-Gilbert equation. The methods are described in Section 5. We use typical material parameters for Py, i.e., the saturation magnetization $M_s = 800$ kAm⁻¹, the exchange constant $A = 13$ pJm⁻¹, and in FDTD simulations the damping $\alpha = 0.01$. We assume the free electron gyromagnetic ratio, $\gamma = 176$ rad GHzT⁻¹. The magnetization dynamics inside the cavity are studied by probing the magnetization amplitude over 450×150 nm area, i.e., three unit cells along the x -axis and one along the y -axis.

3. Results

3.1. Band Structure and the Resonance Spectra

Magnonic band structure of the ADL (without the defect) is shown in **Figure 2a** and is obtained by FEM at 0.5 T. The dispersion relation is over the path Γ -Y-X-M-Y in the first Brillouin zone (see the inset). Importantly, we see a well-defined full bandgap, ranging from 23.05 to 24.95 GHz. The two bands below the bandgap originate in the edge modes, i.e., the modes with the amplitude concentrated near the antidot edges, while the bands above are bulk modes, with the first one a fundamental mode of the ADL.^[27]

The resonance response of the ADL, ADL with the L_3 cavity, and as a reference of the plain Py film are shown in **Figure 2b**. The results are obtained with FDTD method by applying a spatially uniform broadband microwave magnetic field linearly polarized along the z -axis:

$$h_{mf} = h_{mf} \text{sinc}(2\pi f_{\text{cut}}(t - t_0)) [0, 0, 1] \quad (1)$$

where, the amplitude of microwave field $\mu_0 h_{mf} = 1$ mT, $f_{\text{cut}} = 40$ GHz, and $t_0 = 8/f_{\text{cut}}$. The intensity is calculated by integrating

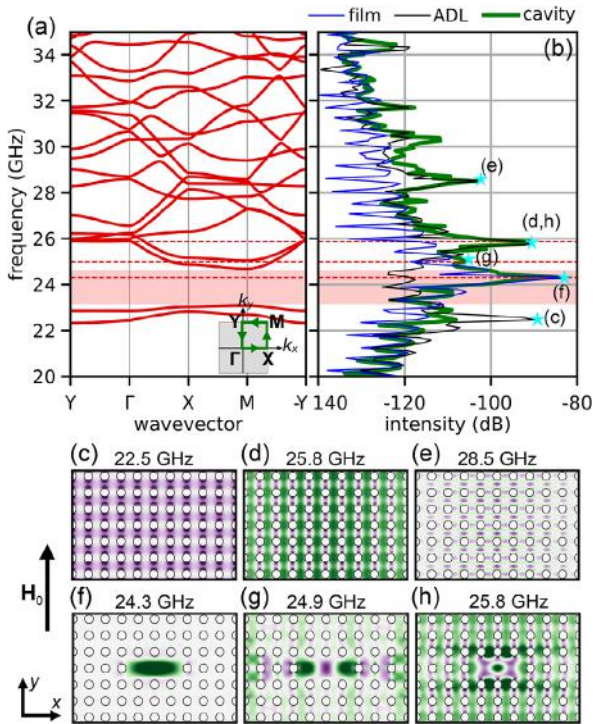


Figure 2. a) Dispersion relation of SWs over the Y-Γ-X-M-Y path in the first Brillouin zone (as indicated in the inset) in the 2D ADL calculated with FEM. The magnonic bandgap is marked in transparent red. b) Spin-wave spectra obtained using FDTD using broadband excitation ($\mu_0 h_{\text{mf}} = 1$ mT) by a spatially uniform microwave field for a uniform Py film (the blue line), an ADL (the black line), and an ADL with the L₃ cavity (the thick green line). The cyan stars indicate the mode profiles displayed in (c–h). Eigenmodes in the ADL are demonstrated in (c–e), while mode profiles for the ADL with L₃ cavity are presented in (f–h). The color utilized represents the amplitude of the out-of-plane component of the magnetization in arbitrary units. The external magnetic field $\mu_0 H_0 = 0.5$ T is applied along the y-axis.

the square of the normalized z component of the magnetization vector ($m_z \equiv M_z/M_s$) over the cavity region (i.e., the area of L₃) in a steady state. For presenting intensity, we use a logarithmic scale: $20 \log_{10}(|m_z|)$ in dB units.

For a plain Py film, we have only one distinctive peak at 24.3 GHz, corresponding to its FMR frequency. In the ADL there are several intense peaks,^[27] the most intense are shown in Figure 2c,d: c) the symmetric edge mode at 22.5 GHz (1st band), d) the fundamental excitation of the ADL at 25.8 GHz, and e) a higher order SW at 28.5 GHz. This is in full agreement with the dispersion relation presented in Figure 2a. For the ADL with the cavity, we obtain the spectrum (green line in Figure 2b), which is quite similar to the undefected ADL, but with a well-defined peak at $f_0 = 24.3$ GHz, i.e., in the bandgap of the ADL. The peak represents the fundamental cavity mode (see Figure 2f), which oscillates in phase, and its amplitude is confined inside the cavity. Interestingly, the frequency of this mode is the same as the FMR of a uniform Py film (see green and blue lines in Figure 2b). There are also high-frequency resonant modes in the cavity with enhanced SW amplitude inside the cavity as shown in Figure 2g,h. However, their frequencies overlap with the continuous bands of

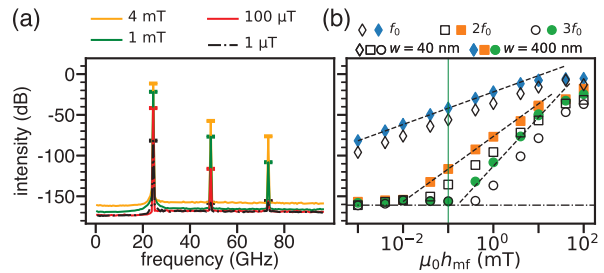


Figure 3. a) The SW spectra ($\propto m_z^2$) in the L₃ cavity excited with CPW of $w = 400$ nm, located at $x_0 = 0$ at frequency 24.3 GHz and amplitude of microwave field $\mu_0 h_{\text{mf}}$: 1 μT (the black-dashed line), 0.1 mT (the red line), 1 mT (the green line), and 4 mT (the orange line). b) Intensity ($\propto m_z^2$) of the fundamental cavity mode ($f_0 = 24.3$ GHz), and its second ($f_2 \equiv 2f_0 = 48.6$ GHz), and third ($f_3 \equiv 3f_0 = 72.9$ GHz) harmonics on the microwave excitation field strength h_{mf} from CPWs with signal line widths $w = 40$ nm and 400 nm represented as open and closed points, respectively. The black dashed lines represent the fitted dependencies from Equation (2), whereas the vertical narrow green line represents the field of value 0.1 mT used in Figure 5. Simulations with FDTD were performed at $\mu_0 H_0 = 0.5$ T.

the ADL, and for that reason, the SW amplitude of these modes spread over the entire ADL.

Learned from photonics, the enhancement of the pumping power on the cavity mode shall result in entering into nonlinear regime whenever the cavity is a medium possessing some kind of nonlinearity.^[13,46] In magnetism, nonlinearity is its inherent property.^[52] Therefore, in the following part of the manuscript, we will focus on the fundamental cavity mode pumped by the microwave magnetic field generated by CPW at 24.3 GHz and at high amplitudes, unless otherwise noted.

3.2. Nonlinear Dynamics

Frequency spectra of the ADL cavity system are shown in Figure 3a. The calculations were performed for 0.5 T magnetic field and the CPW of $w = 400$ nm wide, located at the center of the cavity ($x_0 = 0$), which generate the fields $h_{\text{mf}} = 1$ μT, 100 μT, 1 mT, and 4 mT. Three peaks, corresponding to the frequencies $f_0 = 24.3$ GHz, $f_2 = 48.6$ GHz, and $f_3 = 72.9$ GHz, are clearly visible at higher amplitudes of the microwave field, except the lowest considered value $h_{\text{mf}} = 1$ μT, where f_2 and f_3 are at the base signal level below −150 dB. These frequencies correspond to the excitation of the fundamental cavity mode (f_0) and its second ($f_2 \equiv 2f_0$) and third ($f_3 \equiv 3f_0$) harmonics, respectively. The higher the amplitude of the microwave field, the higher the intensities of the modes. However, there are significant changes in the relative peak amplitudes between the fundamental cavity mode and its harmonics. For the fundamental cavity mode, there is an increase of 70 dB in the peak as we increase the microwave amplitude from 1 μT to 4 mT, whereas for the second and third harmonics, there is an increase of approximately 100 and 80 dB, respectively.

To shed more light on the efficiency of the SW excitations we perform systematic simulations with increased h_{mf} from 1 μT to 0.1 T using the same CPW antenna. The results are shown in Figure 3b. The intensity of the fundamental cavity mode increases from −80 dB at 10^{-3} mT till −10 dB at 10 mT, and saturates with a further increase of h_{mf} . The intensities of the 2nd and

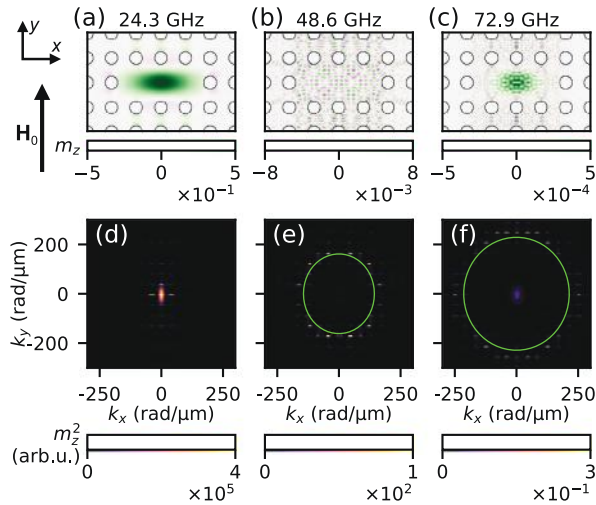


Figure 4. a–c) Spatial distributions of amplitudes of the perpendicular component of reduced magnetization m_z of the SW modes corresponding to the (a) fundamental cavity mode (24.3 GHz), and its (b) second (48.6 GHz), and (c) third (72.9 GHz) harmonics. FDTD results are obtained with the CPW of $w = 400$ nm, $x_0 = 0$, $h_{\text{mf}} = 4$ mT, and $\mu_0 H_0 = 0.5$ T. d–f) Representation of the modes from (a–c) in the reciprocal space. The size of the Brillouin zone is ca. $42 \text{ rad}/\mu\text{m}^{-1}$. The green lines in (e) and (f) represent analytical^[54] isofrequency contours for uniform Py film at frequencies 48.6 and 72.9 GHz, respectively.

3^{rd} harmonics start to grow at about 0.01 and 0.1 mT, respectively, grow almost linearly in this double logarithmic scale, and both reach an intensity only 20 dB less than the f_0 mode at 40 mT.

This means that the effectiveness of the nonlinear processes increases according to the square and cubic function of h_{mf} , with different threshold amplitudes of h_{mf} . This is according to the theoretical predictions for the plane film and plane waves^[52] indicating that the intensity of the n^{th} harmonics:

$$I^{(n)} \propto \left(\frac{h_{\text{mf}}}{H_0} \right)^n \quad (2)$$

Similar behavior has already been observed experimentally in the microwave pumping of the elliptical Py nanodot saturated along the long axis.^[53] However, in Ref. [53] the excitation was off-resonant, i.e., the generation of the 2^{nd} and 3^{rd} harmonic was only observed at $2f_{\text{ex},1}$ and $3f_{\text{ex},2}$, with the pumping field frequency $f_{\text{ex},1}$ and $f_{\text{ex},2}$, respectively. Here, $2f_{\text{ex},1}$ and $3f_{\text{ex},2}$ correspond to the frequency of the antisymmetric (with the nodal line along the long axis of the ellipse) and symmetric (fundamental) eigenmode of the nanodot, respectively. This means that for a given frequency of the microwave field $f_{\text{ex},1}$ or $f_{\text{ex},2}$ only the 2^{nd} or 3^{rd} harmonic can be observed.

The spatial distributions of the fundamental cavity mode (f_0), mode f_2 and f_3 at a microwave excitation field of $h_{\text{mf}} = 4.0$ mT are displayed in Figure 4a,b,c. The figures present a neat, undulating pattern at 48.6 and 72.9 GHz indicating a short wavelength of excited SWs. Notably, the amplitude of these harmonics extends from the cavity to the ADL as the magnonic bands in the ADL at these high frequencies are very dense, and come from the distant Brillouin zones. A slight amplitude increase occurs along

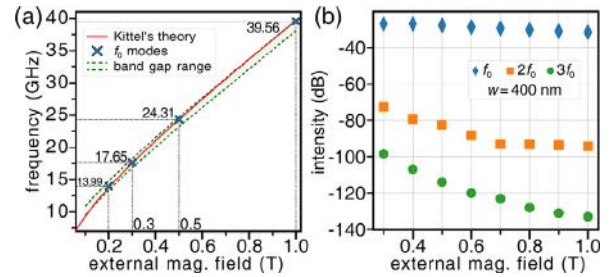


Figure 5. a) Dependence of the fundamental cavity mode frequency on external static magnetic field magnitude, H_0 . The crosses mark the frequency of the cavity mode obtained from FEM in the supercell approach, while the red line represents the FMR frequency of the plain Py film from the Kittel's formulae.^[57] The green dotted lines indicate the edges of the bandgap obtained from FEM. b) Intensity of the fundamental cavity mode (f_0) and its second ($2f_0$) and third harmonics ($3f_0$) as a function of H_0 obtained by FDTD. The markers indicate the intensities obtained by excitation with a CPW line $w = 400$ nm wide, positioned at $x_0 = 0$, at $\mu_0 h_{\text{mf}} = 0.1$ mT at frequencies following the red line in (a).

the y-axis, suggesting that utilizing these modes could be useful for wave propagation. In fact, as seen in Figure 4e,f, the 2^{nd} and 3^{rd} harmonics possess discrete spectra in reciprocal space with regularly spaced spots at high wavenumbers. This pattern is related to the structure's periodicity and the discrete values of its reciprocal lattice vectors. The bright spots are located around the almost circular isofrequency contours of SWs in the plain Py film at 48.6 and 72.9 GHz. For f_2 and f_3 , their radius is 180 and $220 \text{ rad}/\mu\text{m}^{-1}$, respectively, which corresponds to the SWs at wavelengths as short as 35 and 29 nm. The spots have larger intensities along the direction of H_0 that indicate the preferred direction of SW distribution from the cavity in the ADL, consistent with the observation in Figure 4b,c. In the future, designing isofrequency contours of the ADL at pertinent frequencies could enable tailoring of the propagation direction of nonlinearly excited high-frequency SWs outside of the ADL. This objective can be accomplished through appropriate ADL geometry design and tailored magnonic band structure.^[55,56]

According to Equation (2), the effectiveness of the nonlinear process can also be increased by decreasing H_0 . However, to maintain similar conditions for the ADL cavity system at different values of H_0 , the frequency of the fundamental cavity mode must follow the magnonic bandgap as the magnetic field is varied. We already indicated that the f_0 coincides with FMR frequency of the Py film. In Figure 5a, we show that it is also in a wide range of fields, i.e., from 0.2 to 1 T. Moreover, the frequency of this mode (increasing from 13.99 to 39.56 GHz, respectively) falls into the magnonic bandgap, which also depends on H_0 . Taking the frequencies of the FMR mode with increasing H_0 , assuming a pumped microwave magnetic field amplitude $h_{\text{mf}} = 0.1$ mT, we perform FDTD simulations. The results are shown in Figure 5b. We see that as the magnetic field decreases from 1 to 0.3 T, the intensity of the 2^{nd} and 3^{rd} harmonics increases by 21.7 and 34.5 dB, respectively. However, there is a downside to decreasing H_0 , it is that a lower frequency means longer wavelengths. In particular, at 1 T the 2^{nd} and 3^{rd} harmonics are at 79.12 and 118.68 GHz with wavelengths of 31.1 and 21.6 nm respectively, while at 0.2 T they are at 27.98 and 41.97 GHz and wavelengths of 61.4 and 39.8 nm, respectively.

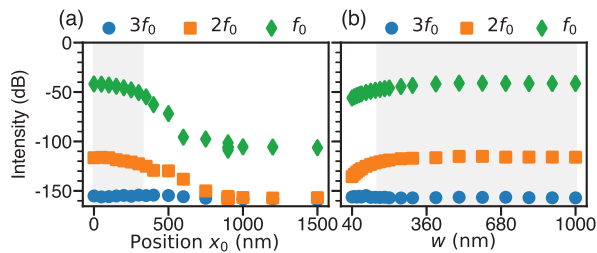


Figure 6. The dependence of the SW intensities ($\propto m_z^2$) at $f_0 = 24.3$ GHz, $f_2 = 2 \times 24.3$ GHz, and $f_3 = 3 \times 24.3$ GHz on (a) the position of the CPW antenna x_0 with respect of cavity center ($w = 400$ nm and $h_{mf} = 0.1$ mT), and (b) the CPW signal line width w ($x_0 = 0$ and $h_{mf} = 0.1$ mT). The gray area in (a) denotes region with $x_0 \in [0, 300]$ nm], whereas in (b) are with $w > 150$ nm.

3.3. Getting Ready to Experiment

The type of the ADL considered in this paper has been broadly investigated in the last few years,^[27,28,50,58,59] so the nonlinear effects presented above should be feasible for experimental realization with current technology. To make our idea closer to realization, we studied the influence of the CPW width and position with respect to the cavity center on the frequency multiplication.

The dependence of the SW intensity at f_0, f_2, f_3 on the position of the CPW ($w = 400$ nm emitting a microwave magnetic field $h_{mf} = 0.1$ mT) at $\mu_0 H_0 = 0.5$ T is shown in Figure 6a. Since h_{mf} is below the threshold for f_3 , the discussion below relates directly to f_0 and f_2 , but similar dependencies were also found at higher values of h_{mf} for f_3 . As expected, the intensities of the SWs decrease as the CPW signal line is moved away from the center of the cavity. The rate of decrease accelerates significantly at $x_0 > 425$ nm. This is due to the fact that, from this position, the emission occurs outside the cavity, and the excitation of the cavity mode is only via evanescent SW modes in the ADL at the frequency of 24.3 GHz, which is in the bandgap. The study shows that the $x_0 \approx 0$ is the most appropriate for excitation of SWs inside the cavity for CPW narrower than the cavity length.

The influence of the width of the CPW signal line on the intensity of the excited SW modes is shown in Figure 6b. We place the CPW centrally over the cavity and increase w starting at $w = 40$ nm, we keep $h_{mf} = 0.1$ mT. The intensity of f_0 and f_2 mode increases with w , and as expected saturates when the signal line covers the entire cavity.

We conclude that the optimal conditions for multi-frequency SW mode generation are when the cavity is completely covered by the signal line, regardless of its position relative to the cavity center. However, if the signal line is narrower than the cavity, the intensity of the excited SW modes becomes sensitive to x_0 and w . Moreover, their values influence also the threshold field values for the generation of high-frequency harmonics. As shown in Figure 3b the threshold fields are 0.04 and 0.4 mT for CPW with $w = 40$ nm (empty symbols), which are higher than for $w = 400$ nm, (solid symbols), 0.01 and 0.1 T, respectively.

The important element for the realization of the demonstrated effects is a full magnonic bandgap, in particular, its width and the frequency position of the fundamental cavity mode, which determine the mode confinement. In the dipole-exchange regime in the in-plane magnetized ferromagnetic film, the case studied in

our work, the SW dispersion is strongly anisotropic, resulting in the complex band structure, hardly suitable for the full magnonic bandgap.^[60–63] Nevertheless, in ADL, due to the demagnetizing fields from the antidot edges, the lowest frequency SW bands are formed by the modes confined to the edges of the antidots. However, the small separation between the antidots leads to the overlapping of the demagnetization field of the neighboring antidots and the formation of the collective propagating modes, which coupled with the fundamental ADL mode and finally close the gap.^[27] On the other hand, a large lattice constant leads to the low-frequency flat edge mode bands and the decrease of the frequency of the lowest bulk band (a fundamental mode of the ADL) to the FMR frequency of the film, thus a loss of cavity mode confinement. Thus, the SW mode confinement in the ADL requires a moderate lattice constant, which ensures that the edge mode bands are well separated from the fundamental bulk mode of the ADL, and at the same time, the bottom frequency of the bulk band is above the FMR frequency of the plane film. Nevertheless, it gives a wide spectrum for the tuning of the magnonic bandgap in ADL to enhance the SW mode localization by the changes in the lattice type, lattice constant, filling fraction, antidot shape, or materials used for ADL preparation.

4. Conclusion

In summary, we describe a method to enhance the SW energy confined in an MC cavity created in a thin Py-film based ADL to enter the nonlinear regime. We have shown that the microwave-pumped fundamental cavity mode, which has the frequency of the plain film FMR fitting into a complete bandgap, can easily reach the nonlinearity threshold leading to the generation of modes at multiple frequencies. Thus, we propose a way to generate high-frequency SWs in the range of 28 to 79 GHz and 42 to 119 GHz with very short wavelengths of 62 to 31 nm and 40 to 22 nm for the 2nd and 3rd harmonics, respectively, by decreasing the external magnetic field from 1 to 0.3 T. The harmonics follow known dependencies on the amplitude of the pumped microwave field and the magnitude of the static magnetic field,^[52] allowing the effectiveness of multi-frequency mode generation to be significantly enhanced. The effects demonstrated in this paper can be achieved in standard ADLs using a simple CPW antenna, whose main limitation is the overlap of the signal line with the cavity surface. This provides an opportunity to investigate magnonics applications at high frequencies, which overlap with 6G microwave bands and have very short wavelengths, up to 100,000 times shorter than the wavelength of microwaves at these frequencies.

Further optimization of the MC structure can even increase the demonstrated conversion efficiency of FMR oscillations to high-frequency oscillations. This can be achieved if, instead of using a cavity to confine only the SW at the input frequency (fundamental cavity mode), the structure also allows the mode to be confined at the output frequency(s) (high-frequency harmonics). Learning from photonics, not only can the power consumption be greatly reduced, but in principle 100% conversion can be achieved.^[64,65]

Such high efficiencies can be particularly useful for hybrid magnonics, the systems that have attracted much interest for their potential applications in quantum sensing, communication, and information.^[66] In particular, hybrid designs that

combine the spin of nitrogen-vacancy (NV) centers in diamonds with other materials and physical systems have been shown to enhance quantum sensing and information applications. By increasing the local microwave magnetic field by orders of magnitude, surface-limited SWs generated in the cavity of a thin film MC can greatly enhance the interactions between the SW and the NV spin, or the spin–spin coupling mediated by SWs.^[67,68] In addition, high-amplitude SW oscillations enhance nonlinear effects that can be exploited to further enhance photon–magnon coupling.^[69,70] Thus, our simple-geometry device is a promising hybrid magnon platform suitable for integrating magnons for quantum and analog information processing.

5. Experimental Section

Micromagnetic Simulations: To achieve precise outcomes for the ADL's dispersion relations and to gain a better understanding of the complexity of the SW modes inside the crystal cavity, FEM and FDTD methods were utilized to solve the Landau-Lifshitz and Maxwell equations. Within simulations, every magnetic moment in the predefined unit cells is given by normalized unit vectors $m = M/M_s$, where M is the total magnetization, and M_s is the saturation magnetization of the ferromagnetic material. The approach then focuses on solving the Landau-Lifshitz-Gilbert (LLG) equation:

$$\frac{dm}{dt} = \gamma \frac{1}{1 + \alpha^2} (m \times B_{\text{eff}} + \alpha (m \times (m \times B_{\text{eff}}))) \quad (3)$$

where γ is the gyromagnetic ratio and α is the dimensionless damping coefficient. The effective magnetic flux density field, B_{eff} includes externally applied field, $B_0 \equiv \mu_0 H_0$, together with the magnetostatic demagnetization, B_d , and the exchange field, B_{exch} :

$$B_{\text{eff}} = B_{\text{ext}} + B_d + B_{\text{exch}} \quad (4)$$

All micromagnetic simulations are performed at 0 K.

Finite Element Method: In the FEM analysis implemented with Comsol Multiphysics, the eigenproblem derived from Equations (3) and (4) was addressed, neglecting damping, i.e., $\alpha = 0$, and defining the demagnetizing field amplitude, $H_d \equiv B_d/\mu_0$, as the gradient of the magnetic scalar potential, U_m : $H_d = -\nabla U_m$, which inside a magnetic body fulfill the equation: $\nabla^2 U_m = \nabla \cdot M$. By considering full magnetization saturation along the direction \hat{i} and utilizing a linear approximation, the magnetization vector could be separated into its static and dynamic (dependent on time t and position r) components as $m(r, t) = m_i \hat{i} + \delta m(r, t) \forall (\delta m \perp \hat{i})$, neglecting all nonlinear terms in the dynamic magnetization $\delta m(r, t)$. Additional information on this methodology can be found in Refs. [71, 72].

Using Bloch-Floquet boundary conditions (BC) on the unit cell boundaries:

$$m_{\text{dst}} = m_{\text{src}} e^{-ik \cdot (r_{\text{dst}} - r_{\text{src}})} \quad (5)$$

an infinite MC layer is modeled. Here, k is the 2D Bloch wavenumber, m is the normalized magnetic moment defined both at the target (dst) and source (src), r are the spatial coordinates of the boundaries where the BCs are applied, and i is the imaginary unit. By parametrically sweeping the wavenumber, eigenfrequencies are determined at each interval. The resulting wavenumber versus frequency plots yield the dispersion curves for the periodic structure.^[73,74]

For planes perpendicular to the plane of the MC layer, Dirichlet BCs were applied to suppress the scalar magnetic potential (U_m) at its out-of-plane boundaries. To ensure the physical accuracy and convergence of the simulation, it was crucial to position the conditions sufficiently far from the specimen. In this simulations, the cell's height was set to be ten times the layer's unit cell width (1.5 μm). The average quality of the tetrahedral

discretization mesh, as determined by the volume-to-length parameter, is 0.91. This results in a mesh comprising 13630 prisms for the MCs unit cell, with one element per thickness and excluding the surrounding environment. The cavity mode simulations in Comsol Multiphysics (Figure 5) used the unit supercell approach, which consists of a cavity surrounded by six (parallel to the long side) and eight (perpendicular) antidotes. This results in a symmetrical size of the supercell with a side equal to 1.35 μm . In this case, the height of the environment was 20 times this width (27 μm), and the amount of mesh elements of this supercell was 37330 with an average quality of 0.82 (and with one prism per thickness).

Finite Difference Time Domain Method: The time domain simulations in the paper had been obtained with the open-source software MuMax3 employing the FDTD method^[51] with the RK45 solver (based on Dormand-Prince method)^[75] to solve Equation (3). The micromagnetic cell size was taken as $5 \times 5 \times 5 \text{ nm}^3$ with cell dimensions smaller than the exchange length ($l_{\text{ex}} = 5.7 \text{ nm}$ for Py). The in-plane periodic boundary condition (PBC) was used, i.e., the supercell of dimension $4.5 \mu\text{m} \times 3 \mu\text{m}$ had been multiplied 10 and 50 times along the x and y directions, respectively. To get the mode profiles, the pointwise FFT over time was calculated for each magnetization component, and the real part corresponding to a particular resonance frequency was then visualized, see details in Ref. [76].

The nonlinear response of the system excited by a single frequency microwave source was analyzed accordingly with the methodology used in Ref. [77].

The mf current transmitted along the y axis generates a magnetic field \mathbf{h}_{mf} , which exerts a torque on the magnetization in Py. The dependence of \mathbf{h}_{mf} with peak amplitude h_{mf} on x coordinate can be approximated by the equation:^[78]

$$\mathbf{h}_{\text{mf}}(x) = h_{\text{mf}} \begin{bmatrix} \frac{1}{2} + \frac{1}{2} \cos \left[\frac{\pi}{s} (|x| - \frac{w}{2}) \right] \\ 0 \\ \frac{1}{5} \text{sign}(x) \left\{ \frac{1}{2} + \frac{1}{2} \cos \left[\frac{2\pi}{s} (|x| - \frac{w}{2} - \frac{s}{2}) \right] \right\} \end{bmatrix} \quad (6)$$

for $|x| > w/2$ and $\mathbf{h}_{\text{mf}}(x) = [1, 0, 0]^T$ for $|x| \leq w/2$.

Acknowledgements

This work was supported in part by the National Science Center Poland projects nos 2020/39/1/ST3/02413 and 2019/35/D/ST3/03729. The simulations were partially performed at Poznań Supercomputing and Networking Center and at the National Institute of Technology Calicut, India.

Correction added on 25 May 2024, after first online publication: Article title was updated.

Conflict of Interest

The authors declare no conflict of interest.

Data Availability Statement

The data that support the findings of this study are available at Zenodo, <https://zenodo.org/doi/10.5281/zenodo.10792491>.

Keywords

cavity, high-harmonic generation, magnonic crystal, magnonics, nonlinearity, spin wave

Received: January 9, 2024
Revised: February 8, 2024
Published online: March 29, 2024

[1] V. Kruglyak, S. Demokritov, D. Grundler, *J. Phys. D: Appl. Phys.* **2010**, 43, 264001.

- [2] A. Mahmoud, F. Ciubotaru, F. Vanderveken, A. V. Chumak, S. Hamdioui, C. Adelman, S. Cotozana, *J. Appl. Phys.* **2020**, 128, 161101.
- [3] S. A. Nikitov, D. V. Kalyabin, I. V. Lisenkov, A. N. Slavin, Y. N. Barabanenkov, S. A. Osokin, A. V. Sadovnikov, E. N. Beginin, M. A. Morozova, Y. P. Sharaevskiy, Y. A. Filimonov, Y. V. Khivintsev, S. L. Vysotsky, V. K. Sakharov, E. S. Pavlov, *Phys.-Uspekhi* **2015**, 58, 1002.
- [4] A. V. Chumak, H. Schultheiss, *J. Phys. D: Appl. Phys.* **2017**, 50, 300201.
- [5] A. Barman, G. Gubbiotti, S. Ladak, A. O. Adeyeye, M. Krawczyk, J. Grafe, C. Adelman, S. Cotozana, A. Naeemi, V. I. Vasyuchka, B. Hillebrands, S. A. Nikitov, H. Yu, D. Grundler, A. V. Sadovnikov, A. A. Grachev, S. E. Sheshukova, J.-Y. Duquesne, M. Marangolo, G. Csaba, W. Porod, V. E. Demidov, S. O. Demokritov, E. Albisetti, D. Petti, R. Bertacco, H. Schultheiss, V. V. Kruglyak, V. D. Poimanov, et al., *J. Phys.: Condens. Matter* **2021**, 33, 413001.
- [6] B. Flebus, S. M. Rezende, D. Grundler, A. Barman, *J. Appl. Phys.* **2023**, 133, 160401.
- [7] G. Csaba, A. Papp, W. Porod, *Phys. Lett. A* **2017**, 381, 1471.
- [8] B. Dieny, I. L. Prejbeanu, K. Garello, P. Gambardella, P. Freitas, R. Lehnndorff, W. Raberg, U. Ebels, S. O. Demokritov, J. Akerman, A. Deac, P. Pirro, C. Adelman, A. Anane, A. V. Chumak, A. Hirohata, S. Mangin, S. O. Valenzuela, M. Cengiz Onbasli, M. d'Aquino, G. Prenat, G. Finocchio, L. Lopez-Diaz, R. Chantrell, O. Chubykalo-Fesenko, P. Bortolotti, *Nat. Electron.* **2020**, 3, 446.
- [9] A. Hirohata, K. Yamada, Y. Nakatani, I.-L. Prejbeanu, B. Dieny, P. Pirro, B. Hillebrands, *J. Magn. Magn. Mater.* **2020**, 509, 166711.
- [10] P. Pirro, V. I. Vasyuchka, A. A. Serga, B. Hillebrands, *Nat. Rev. Mater.* **2021**, 6, 1114.
- [11] A. V. Chumak, P. Kabos, M. Wu, C. Abert, C. Adelman, A. Adeyeye, J. Åkerman, F. G. Aliev, A. Anane, A. Awad, C. H. Back, A. Barman, G. E. W. Bauer, M. Becherer, E. N. Beginin, V. A. S. V. Bittencourt, Y. M. Blanter, P. Bortolotti, I. Bovenster, D. A. Bozhko, S. A. Bunyayev, J. J. Carmiggelt, R. R. Cheenikundil, F. Ciubotaru, S. Cotozana, G. Csaba, O. V. Dobrovolskiy, C. Dubs, M. Elyasi, K. G. Fripp, et al., *IEEE Trans. Magn.* **2022**, 58, 1.
- [12] J. Ioannopoulos, S. G. Johnson, J. N. Winn, R. D. Meade, *Photonic Crystals: Molding the Flow of Light*, Princeton University Press, Princeton **2008**.
- [13] M. Soljačić, J. D. Ioannopoulos, *Nat. Mater.* **2004**, 3, 211.
- [14] M. Maldovan, *Nature* **2013**, 503, 209.
- [15] T. Vasileiadis, J. Varghese, V. Babacic, J. Gomis-Bresco, D. N. Urrios, B. Graczykowski, *J. Appl. Phys.* **2021**, 129, 160901.
- [16] M. Krawczyk, H. Puszkarski, *Phys. Rev. B* **2008**, 77, 054437.
- [17] B. Lenk, H. Ulrichs, F. Garbs, M. Munzenberg, *Phys. Rep.* **2011**, 507, 107.
- [18] M. Krawczyk, D. Grundler, *J. Phys.: Condens. Matter* **2014**, 26, 123202.
- [19] A. Chumak, A. Serga, B. Hillebrands, *J. Phys. D: Appl. Phys.* **2017**, 50, 244001.
- [20] S. Vysotskii, S. Nikitov, Y. A. Filimonov, *J. Exp. Theor. Phys.* **2005**, 101, 547.
- [21] M. Yu, L. Malkinski, L. Spinu, W. Zhou, S. Whittenburg, *J. Appl. Phys.* **2007**, 101, 09F501.
- [22] M. J. Pechan, C. Yu, R. Compton, J. Park, P. Crowell, *J. Appl. Phys.* **2005**, 97, 10J90.
- [23] S. McPhail, C. Gürtler, J. Shilton, N. Curson, J. Bland, *Phys. Rev. B* **2005**, 72, 094414.
- [24] M. Kostylev, G. Gubbiotti, G. Carlotti, G. Socino, S. Tacchi, C. Wang, N. Singh, A. O. Adeyeye, R. L. Stamps, *J. Appl. Phys.* **2008**, 103, 07C507.
- [25] H. Ulrichs, B. Lenk, M. Münzenberg, *Appl. Phys. Lett.* **2010**, 97, 092506.
- [26] C.-L. Hu, R. Magaraggia, H.-Y. Yuan, C. Chang, M. Kostylev, D. Tripathy, A. Adeyeye, R. Stamps, *Appl. Phys. Lett.* **2011**, 98, 262508.
- [27] S. Tacchi, P. Gruszecki, M. Madami, G. Carlotti, J. W. Klos, M. Krawczyk, A. Adeyeye, G. Gubbiotti, *Sci. Rep.* **2015**, 5, 10367.
- [28] S. Neusser, G. Duerr, S. Tacchi, M. Madami, M. Sokolovskiy, G. Gubbiotti, M. Krawczyk, D. Grundler, *Phys. Rev. B* **2011**, 84, 094454.
- [29] R. Gieniusz, P. Gruszecki, M. Krawczyk, U. Guzowska, A. Stognij, A. Maziewski, *Sci. Rep.* **2017**, 7, 8771.
- [30] M. Gołębiewski, P. Gruszecki, M. Krawczyk, A. E. Serebryannikov, *Phys. Rev. B* **2020**, 102, 134402.
- [31] C. Riedel, T. Taniguchi, L. Korber, A. Kakay, C. H. Back, *Adv. Phys. Res.* **2023**, 2, 2200104.
- [32] F. Ciubotaru, T. Devolder, M. Manfrini, C. Adelman, I. P. Radu, *Appl. Phys. Lett.* **2016**, 109, 012403.
- [33] S. Woo, T. Delaney, G. S. D. Beach, *Nat. Phys.* **2017**, 13, 448.
- [34] S. Wintz, V. Tiberkevich, M. Weigand, J. Raabe, J. Lindner, A. Erbe, A. Slavin, J. Fassbender, *Nat. Nanotechnol.* **2016**, 11, 948.
- [35] G. Dieterle, J. Förster, H. Stoll, A. S. Semisalova, S. Finizio, A. Gangwar, M. Weigand, M. Noske, M. Fähnle, I. Bykova, J. Gräfe, D. A. Bozhko, H. Y. Musienko-Shmarova, V. Tiberkevich, A. N. Slavin, C. H. Back, J. Raabe, G. Schütz, S. Wintz, *Phys. Rev. Lett.* **2019**, 122, 117202.
- [36] C. Liu, J. Chen, T. Liu, F. Heimbach, H. Yu, Y. Xiao, J. Hu, M. Liu, H. Chang, T. Stueckler, S. Tu, Y. Zhang, Y. Zhang, P. Gao, Z. Liao, D. Yu, K. Xia, N. Lei, W. Zhao, M. Wu, *Nat. Commun.* **2018**, 9, 738.
- [37] H. Yu, O. Allivy Kelly, V. Cros, R. Bernard, P. Bortolotti, A. Anane, F. Brandl, F. Heimbach, D. Grundler, *Nat. Commun.* **2016**, 7, 11255.
- [38] F. B. Mushenok, R. Dost, C. S. Davies, D. A. Allwood, B. J. Inkson, G. Hrkac, V. V. Kruglyak, *Appl. Phys. Lett.* **2017**, 111, 042404.
- [39] Q. Wang, R. Verba, B. Heinz, M. Schneider, O. Wojewoda, K. Davidková, K. Levchenko, C. Dubs, N. J. Mauser, M. Urbanek, P. Pirro, A. V. Chumak, *Sci. Adv.* **2023**, 9, eadg4609.
- [40] V. V. Kruglyak, M. L. Sokolovskii, V. S. Tkachenko, A. N. Kuchko, *J. Appl. Phys.* **2006**, 99, 08C906.
- [41] J. W. Klos, V. S. Tkachenko, *J. Appl. Phys.* **2013**, 113, 133907.
- [42] K. Di, V. L. Zhang, M. H. Kuok, H. S. Lim, S. C. Ng, K. Narayanapillai, H. Yang, *Phys. Rev. B* **2014**, 90, 060405.
- [43] M. A. Morozova, S. V. Grishin, A. V. Sadovnikov, D. V. Romanenko, Y. P. Sharaevskii, S. A. Nikitov, *Appl. Phys. Lett.* **2015**, 107, 242402.
- [44] N. Kumar, A. Prabhakar, *J. Magn. Magn. Mater.* **2018**, 450, 46.
- [45] N. Kumar, *Phys. B: Condens. Matter* **2022**, 645, 414248.
- [46] P. Lalanne, C. Sauvan, J. Hugonin, *Laser Photonics Rev.* **2008**, 2, 514.
- [47] K. Schultheiss, R. Verba, F. Wehrmann, K. Wagner, L. Körber, T. Hula, T. Hache, A. Kákay, A. A. Awad, V. Tiberkevich, A. N. Slavin, J. Fassbender, H. Schultheiss, *Phys. Rev. Lett.* **2019**, 122, 097202.
- [48] C. Koerner, R. Dreyer, M. Wagener, N. Liebing, H. G. Bauer, G. Woltersdorf, *Science* **2022**, 375, 1165.
- [49] T. Hula, K. Schultheiss, F. J. T. Gonçalves, L. Körber, M. Bejarano, M. Copus, L. Flacke, L. Liensberger, A. Buzdakov, A. Kákay, M. Weiler, R. Camley, J. Fassbender, H. Schultheiss, *Appl. Phys. Lett.* **2022**, 121, 112404.
- [50] F. Groß, M. Weigand, A. Gangwar, M. Werner, G. Schütz, E. J. Goering, C. H. Back, J. Gräfe, *Phys. Rev. B* **2022**, 106, 014426.
- [51] A. Vansteenkiste, J. Leliaert, M. Dvornik, M. Helsen, F. Garcia-Sanchez, B. Van Waeyenberge, *AIP Adv.* **2014**, 4, 107133.
- [52] A. G. Gurevich, G. A. Melkov, *Magnetization Oscillations and Waves*, CRC Press, Boca Raton **1996**.
- [53] V. E. Demidov, H. Ulrichs, S. O. Demokritov, V. Bessonov, R. Gieniusz, A. Maziewski, *Appl. Phys. Lett.* **2011**, 99, 012505.
- [54] B. Kalinikos, A. Slavin, *J. Phys. C: Solid State Phys.* **1986**, 19, 7013.
- [55] J. W. Klos, P. Gruszecki, A. E. Serebryannikov, M. Krawczyk, *IEEE Magn. Lett.* **2015**, 6, 1.
- [56] A. V. Sadovnikov, E. N. Beginin, S. A. Odincov, S. E. Sheshukova, Y. P. Sharaevskii, A. I. Stognij, S. A. Nikitov, *Appl. Phys. Lett.* **2016**, 108, 172411.

- [57] C. Kittel, *Phys. Rev.* **1946**, 70, 965.
- [58] S. Neusser, B. Botters, M. Becherer, D. Schmitt-Landsiedel, D. Grundler, *Appl. Phys. Lett.* **2008**, 93, 12.
- [59] M. Zelent, N. Tahir, R. Gieniusz, J. W. Kłos, T. Wojciechowski, U. Guzowska, A. Maziewski, J. Ding, A. O. Adeyeye, M. Krawczyk, *J. Phys. D: Appl. Phys.* **2017**, 50, 185003.
- [60] J. W. Kłos, M. L. Sokolovskyy, S. Mamica, M. Krawczyk, *J. Appl. Phys.* **2012**, 111, 123910.
- [61] S. Tacchi, B. Botters, M. Madami, J. W. Kłos, M. L. Sokolovskyy, M. Krawczyk, G. Gubbiotti, G. Carlotti, A. O. Adeyeye, S. Neusser, D. Grundler, *Phys. Rev. B* **2012**, 86, 014417.
- [62] M. Krawczyk, S. Mamica, M. Mruczkiewicz, J. W. Kłos, S. Tacchi, M. Madami, G. Gubbiotti, G. Duerr, D. Grundler, *J. Phys. D: Appl. Phys.* **2013**, 46, 495003.
- [63] S. Tacchi, G. Gubbiotti, M. Madami, G. Carlotti, *J. Phys.: Condens. Matter* **2016**, 29, 073001.
- [64] J. Bravo-Abad, A. Rodriguez, P. Bermel, S. G. Johnson, J. D. Joannopoulos, M. Soljačić, *Opt. Express* **2007**, 15, 16161.
- [65] A. Rodriguez, M. Soljačić, J. D. Joannopoulos, S. G. Johnson, *Opt. Express* **2007**, 15, 7303.
- [66] Z. Jiang, J. Lim, Y. Li, W. Pfaff, T.-H. Lo, J. Qian, A. Schleife, J.-M. Zuo, V. Novosad, A. Hoffmann, *Appl. Phys. Lett.* **2023**, 123, 130501.
- [67] D. Kikuchi, D. Prananto, K. Hayashi, A. Laraoui, N. Mizuochi, M. Hatano, E. Saitoh, Y. Kim, C. A. Meriles, T. An, *Appl. Phys. Express* **2017**, 10, 103004.
- [68] M. Fukami, J. C. Marcks, D. R. Candido, L. R. Weiss, B. Soloway, S. E. Sullivan, N. Deegan, F. J. Heremans, M. E. Flatté, D. D. Awschalom, *Proc. Nat. Acad. Sci.* **2024**, 121, e2313754120.
- [69] W. Xiong, M. Tian, G.-Q. Zhang, J. Q. You, *Phys. Rev. B* **2022**, 105, 245310.
- [70] F.-Z. Ji, J.-H. An, *Phys. Rev. B* **2023**, 108, L180409.
- [71] M. Mruczkiewicz, M. Krawczyk, V. K. Sakharov, Y. V. Khivintsev, Y. A. Filimonov, S. A. Nikitov, *J. Appl. Phys.* **2013**, 113, 093908.
- [72] J. Rychły, V. S. Tkachenko, J. W. Kłos, A. Kuchko, M. Krawczyk, *J. Phys. D: Appl. Phys.* **2018**, 52, 075003.
- [73] C. Hakoda, J. Rose, P. Shokouhi, C. Lissenden, *AIP Conf. Proc.* **2018**, 1949, 020016.
- [74] M. Collet, M. Ouisse, M. Ruzzene, M. Ichchou, *Int. J. Solids Struct.* **2011**, 48, 2837.
- [75] J. R. Dormand, P. J. Prince, *J. Comput. Appl. Math.* **1980**, 6, 19.
- [76] P. Gruszecki, J. Kisielewski, *Sci. Rep.* **2023**, 13, 1218.
- [77] P. Gruszecki, K. Y. Guslienko, I. L. Lyubchanskii, M. Krawczyk, *Phys. Rev. Appl.* **2022**, 17, 044038.
- [78] P. Gruszecki, M. Kasprzak, A. E. Serebryannikov, M. Krawczyk, W. Śmigaj, *Sci. Rep.* **2016**, 6, 22367.

5.3 Three-dimensional architectures

As a natural progression from one- and two-dimensional systems, this section explores the study of three-dimensional ferromagnetic nanostructures in magnonics. Extending spin-wave studies to fully 3D nontrivial systems opens up new possibilities for manipulating wave behavior in ways that are not possible in planar structures. The introduction of additional degrees of freedom through complex architectures enables sophisticated functionalities, such as unidirectional and/or guided propagation, dynamic mode localization, and overall better control over spin-wave confinement and dispersion in all spatial directions.

The growing popularity of 3D nanostructures in magnonics stems from two key advancements: improved fabrication techniques and enhanced capabilities of numerical simulations. Atomic layer deposition and self-assembled block copolymer templating enable the creation of intricate, highly ordered 3D geometries with nanoscale precision. The former allows for the conformal coating of complex woodpile or scaffold-like structures, while the latter provides scalable routes to the formation of periodic structures, including gyroids. Concurrently, the development of numerical methods and computational power has made it feasible to model and simulate these complex 3D structures with unprecedented detail (a main aspect of my contribution to this field).

During my six-month internship in Strasbourg under the supervision of R. Hertel, I became familiar with tetmag, a micromagnetic software well-suited for 3D magnetization dynamics. This experience gave me with a comprehensive understanding of advanced finite-element methods which, in turn, helped me to develop my own simulation approach in COMSOL. This expertise expanded my modeling capabilities and provided a solid foundation for investigating complex 3D spin-wave phenomena.

The advanced simulation tools allow us to capture the complex interactions within 3D nanostructures, including the effects of geometry, boundary conditions, and field dependencies on spin-wave dynamics. This computational approach also allows us to study spin-wave behaviors that are otherwise difficult to measure experimentally, supporting collaborations with experimental groups.

In this section, I present my research on how the dimensionality and geometry of three-dimensional ferromagnetic nanostructures can extend the capabilities and potential of magnonic devices. Through a combination of theoretical modeling, comprehensive numerical simulations, and close experimental collaboration, we aim to understand the role of 3D architectures in enabling novel functionalities for spin-wave-based computing and communication systems, bringing us one step closer to a new generation of magnonic and spintronic technologies.

5.3.1 Theoretical and experimental investigation of gyroid networks: localized spin-wave excitations and crystallography-dependent ferromagnetic responses (P7)

This paper is the result of a broad international collaboration, involving theoretical research teams from Poland (us) and France, and experimental teams from Italy, Germany and Japan. It investigates the dynamic behavior of spin waves in three-dimensional gyroid nanostructures – a unique periodic chiral architecture with nanoscale triple junctions. Our study combines micromagnetic simulations with FMR measurements to investigate how the crystallographic orientation of these gyroid structures in relation to the applied external magnetic fields influences their magnetic response. The results show that this directional sensitivity enables control over spin-wave localization and collective excitations within the network, suggesting applications for gyroids as reconfigurable metamaterial-like microwave antennas. Gyroids, characterized by their periodic and chiral three-dimensional architecture, act as magnetic metamaterials by exhibiting an effective magnetization and a tunable magnetic response that is primarily governed by their geometric filling factor rather than solely by the intrinsic properties of the base material.

This work advances the understanding of 3D magnonics and highlights gyroid nanostructures as versatile platforms for tunable FMR applications that can contribute to the development of next-generation adaptive, frequency-selective devices in microwave and spintronic technologies.

Contribution of the Author

In this publication, I conceived and designed detailed computational FEM models of gyroidal nanostructures and, with the scientific guidance and technical assistance of R. Hertel, performed both time- and frequency-domain micromagnetic simulations of the cubic gyroidal models using tetmag. I coordinated an extensive international collaboration, overseeing the organization of meetings, managing ongoing correspondence, and facilitating research visits to support effective scientific exchange. I actively participated in the discussion and interpretation of both simulation and experimental results, post-processed the data, wrote the first draft, submitted the manuscript, and handled all correspondence with reviewers.

Copyright ©2024 The Authors. *ACS Applied Materials & Interfaces* published by the American Chemical Society. The paper was published under the CC-BY 4.0 license.

Collective Spin-Wave Dynamics in Gyroid Ferromagnetic Nanostructures

Mateusz Gołębiewski,* Riccardo Hertel, Massimiliano d'Aquino, Vitaliy Vasyuchka, Mathias Weiler, Philipp Pirro, Maciej Krawczyk, Shunsuke Fukami, Hideo Ohno, and Justin Llandro



Cite This: *ACS Appl. Mater. Interfaces* 2024, 16, 22177–22188



Read Online

ACCESS |



Metrics & More



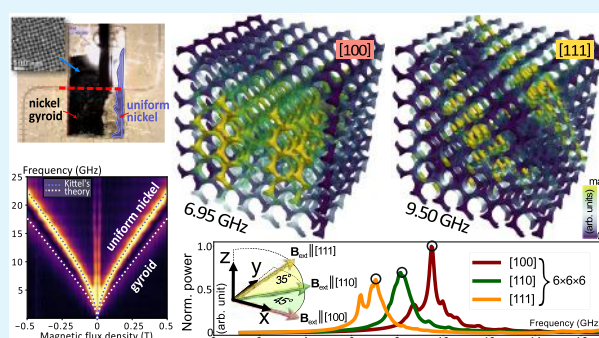
Article Recommendations



Supporting Information

ABSTRACT: Expanding upon the burgeoning discipline of magnonics, this research elucidates the intricate dynamics of spin waves (SWs) within three-dimensional nanoenvironments. It marks a shift from traditionally used planar systems to exploration of magnetization configurations and the resulting dynamics within 3D nanostructures. This study deploys micromagnetic simulations alongside ferromagnetic resonance measurements to scrutinize magnetic gyroids, periodic chiral configurations composed of chiral triple junctions with a period in nanoscale. Our findings uncover distinctive attributes intrinsic to the gyroid network, most notably the localization of collective SW excitations and the sensitivity of the gyroid's ferromagnetic response to the orientation of the static magnetic field, a correlation closely tied to the crystallographic alignment of the structure. Furthermore, we show that for the ferromagnetic resonance, multidomain gyroid films can be treated as a magnonic material with effective magnetization scaled by its filling factor. The implications of our research carry the potential for practical uses such as an effective, metamaterial-like substitute for ferromagnetic parts and lay the groundwork for radio frequency filters. The growing areas of 3D magnonics and spintronics present exciting opportunities to investigate and utilize gyroid nanostructures for signal processing purposes.

KEYWORDS: gyroids, 3D nanostructures, magnonics, ferromagnetic resonance, micromagnetic simulations, spin-wave modes



1. INTRODUCTION

Spin waves (SWs) and their intricate manipulation in magnetic materials constitute a significant part of the contemporary research. In ferromagnetic systems, the complex dynamics of SWs arises from the coexistence of magnetostatic and exchange interactions. The magnetostatic interactions, being highly anisotropic in thin structures, induce a profound dependence of SW properties on the relative orientation of magnetization and wavevector. This gives them a number of properties that are conspicuously absent in other types of waves, including negative group velocity, caustics, readily accessible non-linearity, and dynamic reconfigurability control.¹ The potential applications are myriad, ranging from signal propagation without Joule–Lenz heat dissipation,^{2,3} to the tunability of dispersion and group velocity.^{4,5} The construction of magnonic systems, known for their enhanced efficiency, further emphasizes the unique properties of SWs and provides a compelling rationale for their extensive exploration.^{2,6,7} Thus, the focus of current research is to harness and adapt magnetization dynamics for sophisticated industrial applications, a goal underscored by recent advances and roadmaps.^{8,9}

Nanostructured 3D networks may give rise to topological and geometrical effects and emergent material properties,

offering new possibilities for SW manipulation.^{10–12} A fully interconnected 3D system opens up a new degree of freedom for novel phenomena, allowing interactions and collective effects in all three dimensions.^{13–15} In recent years, there has been significant development of fabrication techniques such as two-photon lithography, focused electron beam deposition, and block copolymer templating, which now allow the fabrication and measurement of complex 3D structures on the nanometer scale.^{16–19}

This paper analyzes a promising yet hardly explored structure in magnetism called a gyroid, which was discovered and first presented in 1970.²⁰ It is defined by chiral triple junctions and periodicity in all three spatial directions, classified as *I*4₃₂ space group (no. 214).²¹ In recent years, many studies have been published describing gyroids in the field of photonics, where they have been presented as potential

Received: February 9, 2024

Revised: April 3, 2024

Accepted: April 5, 2024

Published: April 22, 2024



chiral beamsplitters,²² nonlinear optical metamaterials,^{23,24} or photonic crystals.^{25–27} It has also inspired many research groups into the fabrication of artificial systems based on this geometry.^{22–24,28–34} The 3D structural unit of magnetic gyroids is in nanoscale and has both chirality and curvature, which has been shown to be highly effective in controlling noncollinear spin textures.³⁵ Recently, numerical and experimental visualization of the magnetic structure in a single and double Ni₇₅Fe₂₅ gyroid network has also been performed.¹⁶ The effective Dzyaloshinskii–Moriya interaction and the curvature-related anisotropy are further important research topics in this context.^{36–39} Curved magnetic wires and films also exhibit novel physical effects,⁴⁰ which together with chiral and topological properties,^{41,42} open new avenues for future research.

SWs have been extensively researched in 2D structures; however, there are limited studies on artificial ferromagnetic systems in full 3D^{43,44} and a lack of experimental research on the collective dynamics of SW in 3D nanostructures. Gyroids, due to their unique geometry and dimensions comparable to the exchange length, bear multidimensional properties of interactions with SWs through shape anisotropy, an inhomogeneous demagnetization field, and chirality. They are an intriguing candidate for the realization of artificial 3D magnonic crystals with highly coupled geometric and magnetic states.^{12,45–47} Furthermore, gyroids, with a significant number of energetically equivalent stable states, may have the potential for artificial spin ice systems and active elements in unconventional computing architectures.⁴⁸

Approaching these structures from a magnonics perspective, we employ micromagnetic simulations to delve into the collective SW dynamics. Our investigation scrutinizes the alignment of the external magnetic field in relation to the gyroid's crystallographic axes, offering an insightful perspective on the impact of their geometry on shaping collective magnetization dynamics. To complement our simulation-based findings, we performed experimental broadband ferromagnetic resonance (BBFMR) measurements on the nickel (Ni) gyroid structure. This empirical approach enhances our numerical observations, specifically in terms of the frequencies and intensities of resonances excited at a given external magnetic field and the impact of various crystallographic domains on the half-width of the signals measured in the sample. Furthermore, the measured magnetic field dependencies suggest that the gyroid structure exhibits magnonic metamaterial-like properties. This combination of simulation and empirical experimentation fosters a comprehensive understanding of the multifaceted dynamics within these unique 3D nanostructures, highlighting their potential applications and motivating further research.

2. GEOMETRY AND MATERIAL PARAMETERS

The gyroidal surface was given for the first time using conjugate surface construction,⁴⁹ and in ref 50 its embedding was subsequently proved. The volume fractions of minimal and constant mean curvature gyroids have been further investigated numerically⁵¹ with the constant mean curvature variants of the geometry.

In other fields, the gyroid is referred to as Laves' graph of girth ten⁵² and the K_4 crystal.⁵³ It consists of cubic unit cells composed of triple bonds connected by nanorods with elliptical cross sections for the nonzero volume filling fraction ϕ , the range of which is described in ref 24. For $\phi = 0\%$ (see

Figure 1), a gyroid surface divides space into two labyrinths of paths oriented in opposite directions. The empty, unobstructed

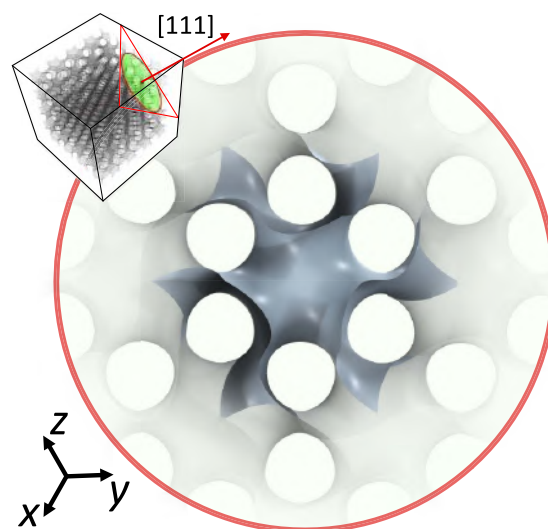


Figure 1. Representation of the gyroid surface model ($\phi = 0\%$), highlighting the unit cell structure. The illustration accentuates the unit cell configuration along the crystallographic [111] direction in orthographic projection, unveiling the hexagonal organization inherent in the gyroid's channels.

channels pass through the gyroid labyrinths in directions [100] and [111], and the paths emerge at 70.5° angles to any given channel as it passes through. Circling or gyrating down the channel in this way gives rise to the term “gyroid”. Interestingly, gyroids exist in several Schwarz surface families that preserve different symmetries of triply periodic minimal surfaces and, like many others, can be approximated by a trigonometrical equation

$$\begin{aligned} &\sin(2\pi x/L)\cos(2\pi y/L) + \sin(2\pi y/L)\cos(2\pi z/L) \\ &\quad + \sin(2\pi z/L)\cos(2\pi x/L) \\ &\leq (101.5 - 2\phi)/68.1 \end{aligned} \quad (1)$$

where L is the gyroid's unit cell length.

The studied gyroid nanostructure was constructed by solvent vapor annealing, selective dissolution, and electrodeposition of a block copolymer template, following the protocol described in ref 16. The gyroidal structure was fabricated by applying polyisoprene-*b*-polystyrene-*b*-poly(ethylene oxide) (ISO) triblock terpolymers with block volume fractions of $\phi_{PI} = 0.30$, $\phi_{PS} = 0.53$, and $\phi_{PEO} = 0.17$ to fluorine-doped tin oxide (FTO)-coated glass substrates. Initial cleaning with Piranha solution at 80 °C for 15 min prepared the substrates, which were then treated with octyltrichlorosilane. A 1 μm BCP film was spin-coated from a 10 wt % anhydrous anisole solution and formed into the gyroid morphology by solvent vapor annealing under nitrogen saturated with chloroform vapor at 26 °C. After annealing, the PI block was removed by UV exposure and immersion in ethanol to form gyroid polymer templates. Ni electrodeposition from a commercial solution followed in a three-electrode cell, filling the voided single-gyroid network with Ni under a constant potential at -1.05 V while monitoring the deposition charge. This method efficiently produces gyroid

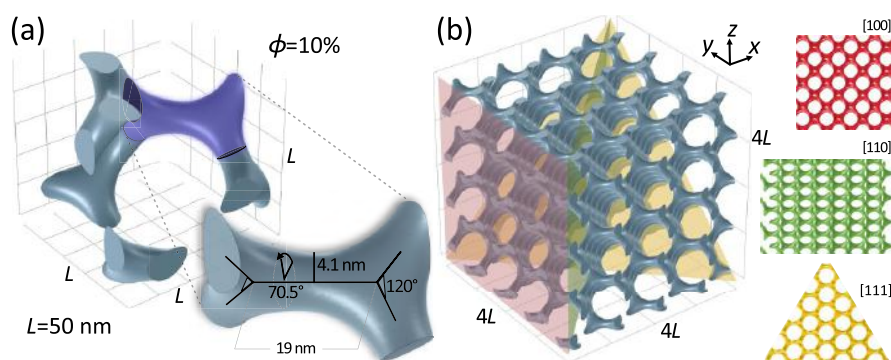


Figure 2. Depiction of the gyroid unit cell and geometric modeling for micromagnetic simulations. The focus of our investigation is a cubic gyroid unit cell measuring $L = 50$ nm, featuring a volume fraction $\phi = 10\%$ as depicted in (a). For the purpose of micromagnetic simulations, a geometric model consisting of an aggregate $4 \times 4 \times 4$ unit cells, or equivalently $200 \times 200 \times 200$ [nm], was employed, as displayed in (b). Illustrated alongside are the three principal high-symmetry directions of the gyroid structure ([111]—yellow triangle, [110]—green rectangle, and [100]—red square) which are color-coordinated to match the planes intersecting the structure. Each direction reveals the unique distribution and shape of the gyroid's channels: the [111] direction displays a hexagonal pattern and round holes, the [110] direction exhibits a square pattern and lenticular holes, while the [100] direction showcases a square pattern and round holes.

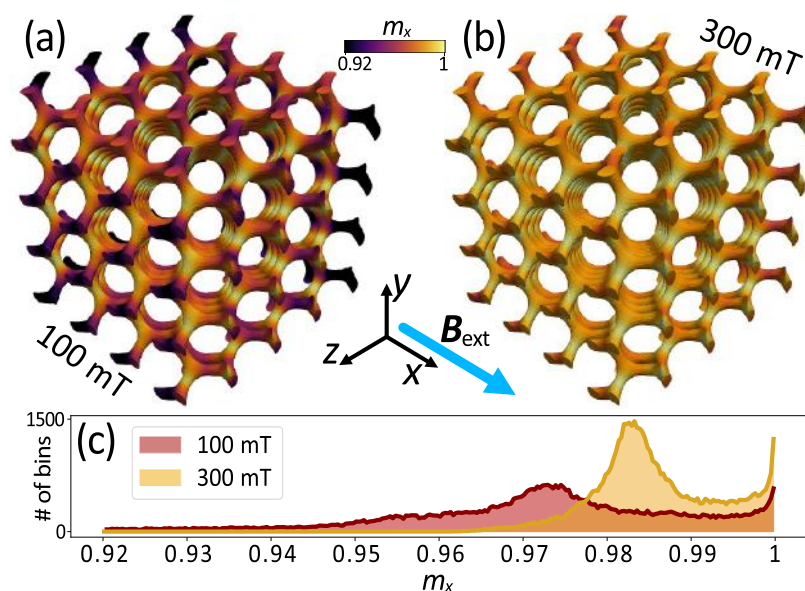


Figure 3. Images of the postrelaxation static configurations of the reduced magnetization component $m_x (\equiv M_x/M_s)$ parallel to the external magnetic field, aligned in the crystallographic direction [100]. Panel (a) displays the case when $B_{\text{ext}} = 100$ mT. The deviation of the magnetization vector from the x -direction is notably larger compared to (b) with $B_{\text{ext}} = 300$ mT, where the magnetization distribution is nearly uniformly oriented along the direction of the external magnetic field. (c) Histogram (number of numerically calculated magnetic moments falling within specific ranges of m_x) of the reduced magnetization component distribution m_x in the simulated gyroid model for both magnetic field magnitudes. The number of bins indicates the number of elementary simulation elements (tetrahedrons).

structures with precise Ni insertion. The material parameters used in the micromagnetic simulations represent those of Ni utilized in the fabrication of the sample, i.e., saturation magnetization $M_s = 480$ kA/m, exchange stiffness $A_{\text{ex}} = 8.6$ pJ/m, and g -factor equal to 2.14.⁵⁴ In each relaxation simulation, the Gilbert damping was set to a large value of $\alpha = 0.5$ to obtain fast convergence to the equilibrium state. Then, for all frequency-domain simulations, this parameter was set to a low value of 0.01.

The unit cell of the investigated gyroid sample measures 50 nm in each direction and has a volume fraction (ϕ) of approximately 10%, which here corresponds to a cross-sectional radius of a single gyroid node of about 4.1 nm (where it is oval in shape) and an arm length of about 19 nm.

The geometric parameters of the gyroid unit cell are described in Figure 2a and are the same for all models analyzed in this work. In the experimental portion of this investigation, the gyroid sample comprises 12 unit cells of height, resulting in an overall thickness of 600 nm. Consequently, individual strut diameters are on the order of single nanometers, mirroring intrinsic magnetic length scales, including exchange length, domain wall width, and SW wavelength.

3. MICROMAGNETIC SIMULATIONS

To unravel the magnetic phenomena transpiring within nanoscale gyroidal struts, we perform comprehensive micromagnetic simulations of the system, taking into account dipole

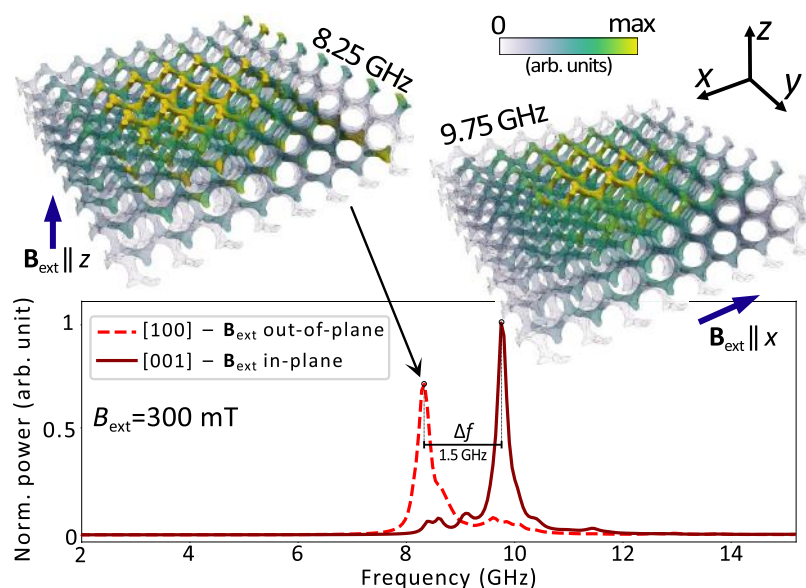


Figure 4. Resonance frequency spectra of $8 \times 8 \times 2$ gyroid structures obtained from micromagnetic simulation. The graphical representations showcase the resonance derived from two different orientations of an applied magnetic field: a dashed line represents the signal from a sample subjected to a 300 mT field, directed out-of-plane (along the z -axis); the solid line, meanwhile, illustrates the response of the sample magnetized in the in-plane (x -axis) direction. The employed color scale is representative of the imaginary part of magnetic susceptibility.

and exchange interactions. In this endeavor, we harness the capabilities of our GPU-accelerated open-source finite-element (FEM) micromagnetic solver *tetmag*.⁵⁵ A remarkable feature of *tetmag* is its proficiency at resolving magnetostatic open boundary problems in large-scale micromagnetic simulations via a hybrid finite-element/boundary-element (FEM-BEM) formalism.⁵⁶ Notably, we forego the assumption of periodic boundary conditions in all of the simulations presented herein.

All of the following micromagnetic simulations are performed in two steps, where the first step is to calculate the stable (relaxed) magnetic configuration at a given field strength (see, e.g., Figure 3a,b). After the magnetization relaxation, we performed simulations of the ferromagnetic resonance using a dedicated frequency domain algorithm⁵⁷ based on a formulation proposed by d'Aquino et al. in ref 58.

The low-amplitude alternating, and homogeneous in space, magnetic field applied in the frequency domain simulations generates a response of the magnetic system in the form of stationary magnetization oscillations with the frequency of the applied field. The magnetic susceptibility $\chi(\omega)$ describes the frequency-dependent relation between the externally applied oscillating field δH and the dynamic component of magnetization δM . For a more detailed discussion of the dynamic susceptibility and its definition, see ref 57.

In the linear-response theory, the imaginary component of the susceptibility is related to dissipative processes in which the sample absorbs energy from the applied field. These absorption peaks denote resonances and generally coincide with frequencies of the maximum oscillation amplitude of the dynamic magnetization. For the case of a spatially homogeneous harmonic magnetic field applied in the simulations, we can thus analyze the spatial distribution of the magnetization oscillation amplitude at these absorption peaks to identify the modes developing at these resonances. The colors in the mode visualizations (Figures 4–6) refer to the imaginary magnetic susceptibility component of the gyroid structure, which in this

case is analogous to the modulus of the dynamic components of the magnetization.

Initially, our simulation work involves the comparative analysis of the ferromagnetic response within the planar system geometry for both in-plane and out-of-plane directed fields to ascertain if a planar gyroid network exhibits macroscopic shape anisotropy. Our experimental sample, possessing a near-planar macroscopic geometry, boasts a lateral dimension spanning a few millimeters and a thickness in the submicron range (see Figure 7).

Therefore, first we analyze a quasi-planar $8 \times 8 \times 2$ gyroid model (number of the unit cells along the x , y , and z , respectively) to verify the influence of external shape anisotropy on resonant frequencies. The model here is $400 \times 400 \times 100$ nm in size (see Figure 4) and consists of about 366,000 tetrahedral discretization cells (~ 2860 per unit cell). We consider two cases where the external magnetic field is directed out-of-plane and in-plane: [100] and [001], respectively, which are crystallographically identical. We see in Figure 4 an apparent anisotropy in the spectrum that changes in both field directions. The maximum absorption frequency shifts from about 8.25 GHz in the out-of-plane scenario to about 9.75 GHz in the in-plane scenario ($\Delta f = 1.5$ GHz). It can therefore be concluded that when simulating gyroids in a cubic simulation volume, as shown in Figure 2b, we can expect resonant frequencies with values lower than those obtained from experiments due to the significant influence of macroscopic shape anisotropy. The most accurate results of micromagnetic simulations could be obtained by simulating a much larger structure. However, due to limited computational resources and simulation time, it was necessary to limit the size of simulated structures.

To study gyroid-based effects at the nanometer scale, the model with dimensions of $4 \times 4 \times 4$ unit cells ($200 \times 200 \times 200$ nm; see Figure 2b) was used in the second stage of micromagnetic simulations, consisting of about 171,000

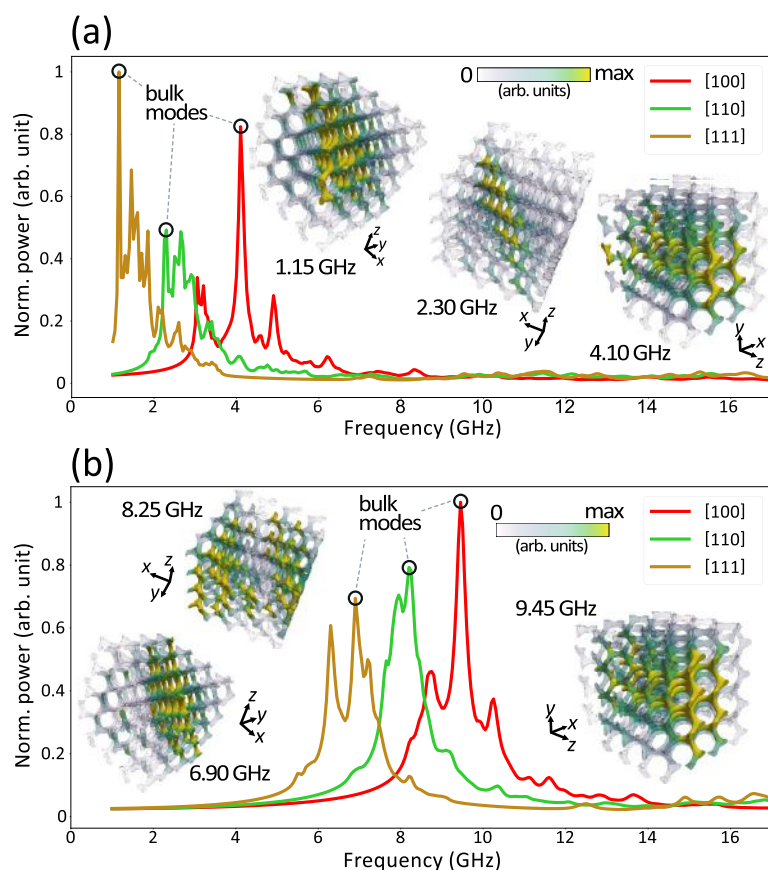


Figure 5. Micromagnetic simulation-derived resonance frequency spectra for $4 \times 4 \times 4$ gyroid constructs. The spectra are derived from two scenarios: (a) in which the applied external magnetic field has a strength of 100 mT and (b) where it measures 300 mT. Within each plot, different color coding indicates the crystallographic direction in which the field is applied, with the specific points encircled on the graph signifying the ferromagnetic resonance. Visual illustrations and resonance frequency values, in sequential order of their appearance, are exhibited as insets within the plots. The coloring scheme used here corresponds directly to the imaginary component of the magnetic susceptibility.

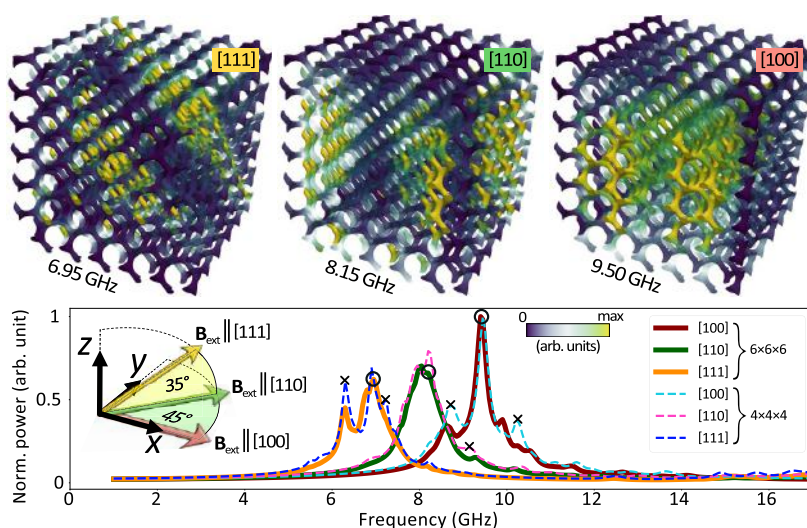


Figure 6. Spectral examination of high-intensity volume modes within a $6 \times 6 \times 6$ gyroid structure. The lower section of the figure presents a plotted distribution of the frequency spectra, with the high-intensity volume modes depicted in the upper part distinctly marked by black circles. For the purpose of comparison, spectra corresponding to more compact structures (illustrated as dotted lines) are superimposed on the graph, thereby clearly demonstrating a marked decline in the intensity of edge modes (denoted with crosses) commensurate with the enlargement of the structure dimensions. The color gradation utilized in the visual representation of the modes is proportional to the imaginary component of the magnetic susceptibility.

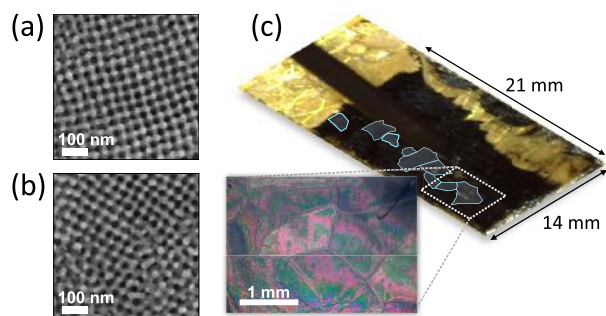


Figure 7. Multidomain gyroid structure employed in BBFMR measurements, illustrating the complex and varied nature of the sample. In panels (a) and (b), scanning electron microscope (SEM) topographical images offer detailed views of two distinct sample regions, characterized by different crystallographic directions and varying degrees of amorphousness. Panel (c) showcases a photograph of the entire sample, annotated with the approximate locations of several prominent domains. These domains were identified and characterized through polarized light microscopy.

tetrahedral discretization cells (~ 2670 per unit cell). The cubic shape of the structure allows a more accurate analysis of the dynamic magnetization distribution and insights into the effects associated with gyroid crystallography.

In this examination, we scrutinize three crystallographic directions, namely, [100], [110], and [111], as illustrated in Figure 2b. We further engage with two distinct magnitudes of the external static magnetic field B_{ext} , set at 100 and 300 mT, as depicted in Figure 5. The considerable computational power and time demanded by the simulations of such complex structures necessitate this restricted selection of parameters.

As shown in Figure 5, magnetic resonance simulations of gyroid structures reveal their pronounced geometric anisotropy. Upon juxtaposition of these plots with those for the planar structure depicted in Figure 4, Figure 5 exhibits a substantially richer spectrum for both external magnetic field values. This richness originates from the increased prominence of edge modes within the overall signal, a characteristic feature of cubic structures. Visual representations of these can be accessed in the Supporting Information (Figures S2 and S3). Through the identification and visualization of bulk modes, we observe that these predominantly emerge within the structure's inner part. This observation suggests that their existence can be primarily attributed to the intrinsic gyroid geometry rather than edge features or artifacts produced in the cutting region, underscoring the distinctive and influential role that the gyroid geometry plays in modulating the magnetic response of these 3D structures. Consequently, our analysis focuses solely on the resonant modes linked to the volumetric portion of the structure, disregarding the discernible satellite peaks attributable to the edge modes.

The resonance spectra findings unequivocally assign the shifting resonance signals observed in the rotating gyroid sample to the crystallographic anisotropy, as evidenced by the plots displayed in Figure 5. A comparative assessment of the plots corresponding to 100 mT in Figure 5a and 300 mT in Figure 5b, reveals a discernible increase of frequencies. However, the order and dispersion of the resonance frequency peaks remain invariant, with the two most distal bulk modes (1.15 GHz, 4.10 GHz in Figure 5a and 6.90 GHz, 9.45 GHz in Figure 5b) separated by 2.95 and 2.55 GHz, respectively. Those separations emphasize the pivotal role played by gyroid

geometry in dictating the system's magnonic properties, demonstrating that these features are not merely a consequence of extrinsic variables.

In the final stage of our simulations, we conducted an analysis of a larger cubic gyroid structure. In the course of visualizing the modes via micromagnetic simulations (Figure 5), we uncovered a compelling localization of high-amplitude magnetization precession. In order to enhance the visibility of these modes vis-à-vis smaller structures and to incrementally amplify the signal of volume modes in relation to satellite ones, we proceeded to simulate and scrutinize a gyroid structure comprising $6 \times 6 \times 6$ unit cells. This extensive structure was discretized into upward of 638,000 finite elements (~ 2950 per unit cell). The resultant magnetization intensity distribution (Figure 6 top row) distinctly delineates planes orthogonal to the 300 mT external magnetic field axis, manifest at modes 6.95 GHz for [100], 8.15 GHz for [110], and 9.50 GHz for [111]. Furthermore, in the case of the field-aligned along [100] and [110], the modes manifest a periodicity (see the top row showing the spatial distribution of the imaginary component of the magnetic susceptibility), a characteristic not previously discernible in the $4 \times 4 \times 4$ structure. The graph depicted at the bottom of Figure 6 showcases the FMR spectrum derived from simulations of the $6 \times 6 \times 6$ model across the three investigated crystallographic directions. To facilitate comparison with corresponding calculations for a more diminutive structure (Figure 5b), the outcomes of these simulations were superimposed on the graph as dashed lines. It becomes evident that the influence of edge modes (denoted with a cross) in most cases diminishes in correlation with the model dimensions' expansion, yielding a decrease of about 28% when increasing the layout from $4 \times 4 \times 4$ to $6 \times 6 \times 6$ unit cells, i.e., 3.375-fold. The normalized intensity of the volume modes (denoted by a circle) remains unchanged for the cases [100] and [111], but is slightly reduced for [110], most likely due to its coupling with the edge mode and/or its localization at the corners of the structure.

4. EXPERIMENT

The main conclusion elucidated from our simulations is the intrinsic relationship between the ferromagnetic response of the gyroid network and its orientation to the axis of the static magnetic field. Figure 7 indicates that the sample embodies multiple domains, manifested as gyroid patches with varying crystallographic orientations relative to a consistent reference point. The varied orientations significantly influence the material's magnetic response, adding complexity to its behavior in a magnetic field.

In Figure 7b, a distinct transition is observed from top to bottom, ranging from a well-defined, highly oriented region to an irregular, less-structured domain. This transition can be construed as the domain wall within the complex gyroid structure. As shown in the simulations, each distinct crystallographic orientation of the gyroid with respect to the externally applied magnetic field may lead to a nuanced alteration in the resonance response. Owing to the substantial multiplicity of domains, the anticipated FMR signal will manifest as an averaged and diluted amalgamation of contributions from individual domains.

Through the application of polarized light spectroscopy, the research facilitated the estimation of the individual domains of the gyroid structure; that is, the regions exhibiting homogeneous crystallographic alignment. As depicted in Figure 7c, the

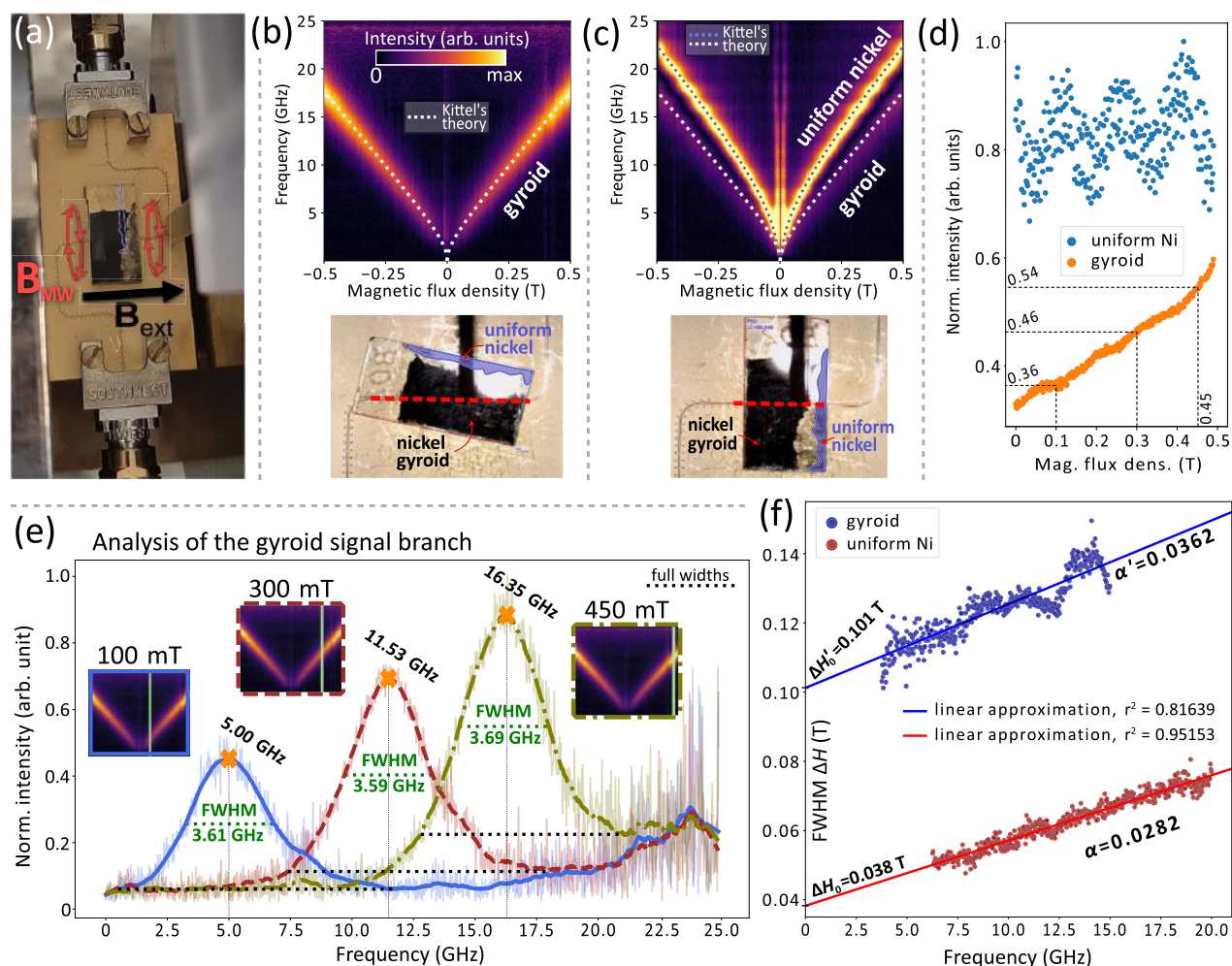


Figure 8. BBFMR measurement conducted on the Ni gyroid structure. The sample underwent repositioning with respect to the CPW to elucidate the effect of an additional homogeneous Ni layer present within the specimen. In two distinct configurations, separate assessments were made of the energy absorption stemming from the microwave field B_{MW} , applied perpendicular to the external static magnetic field (a). The resultant plots of dynamic magnetization amplitude as functions of static magnetic flux density and frequency for selected sample configurations are depicted in (b,c). These render a conspicuous signal attributed to the gyroid layer when the CPW is in direct alignment below it (b), and an additional, higher-frequency signal emanating from the uniform Ni layer (c) when the CPW (as delineated by the red dashed line) intersects its projected position (highlighted in purple on the sample). The dotted lines in the graphs represent the theoretical fit derived from the Kittel formula (see eq 2). For uniform Ni, parameters from micromagnetic simulations were used, while for gyroid, we implemented the calculated effective parameters, i.e., saturation magnetization $M_{\text{eff}} = 132$ kA/m, and the g -factor of 2.2. Plot (d) shows a summary of the peak intensities calculations of FMR signals (blue dots for uniform Ni, and orange dots for gyroid) as a function of the external magnetic field strength. Normalized intensity values for 100, 300, and 450 mT fields are indicated. In graph (e), a cross-sectional analysis of the BBFMR signals is depicted for distinct values of the external magnetic field, where the solid blue line corresponds to $B_{\text{ext}} = 100$ mT, the dashed brown line to $B_{\text{ext}} = 300$ mT, and the dash-dotted green line to $B_{\text{ext}} = 450$ mT. Additionally, horizontal dashed green lines mark the full width at half-maximum (FWHM) for each section, providing quantitative insights into the resonance line widths along with their respective values. The orange crosses signify peak maxima and their corresponding frequencies, pinpointing the resonant behavior within the explored frequency range. Insets furnish intensity plots from the BBFMR measurements, with the green vertical lines highlighting the specific locations of the sections for each magnetic field value. Finally, plot (f) shows the magnetic field FWHM's as a function of frequency for BBFMR signals of gyroid (purple dots) and uniform Ni (dark red dots). Based on the experimental data and using eq 3, a linear regression was performed and the values of the determination coefficient r^2 , ΔH_0 (from the abscissa of the lines) and the eq 3-derived damping values α (from the slope of the lines) were estimated. Parameters related to the gyroid structure are marked with a prim (').

dimensions of the largest domains extend to the millimeter scale. However, it must be acknowledged that these particular measurements do not allow for the determination of the specific crystallography present within each domain. In an effort to achieve a dynamic magnetic characterization of the Ni gyroid sample, BBFMR measurements were executed in the frequency range of 0.1 to 25 GHz, following the methodology delineated by Heinrich.⁵⁹ This involved the utilization of a

two-port vector network analyzer, with connections established to opposite ends of a coplanar waveguide (CPW) in accordance with the techniques described by Montoya.⁶⁰

The gyroid probe was mounted on a CPW with a 80 μm wide center conductor facing downward to ensure maximum coupling with the microwave field⁶¹ and the static external magnetic field applied within the sample plane, along the CPW center conductor (Figure 8a). We tested several orientations of

the specimen with respect to the CPW line and discovered a signal from both gyroid-structured Ni and a uniform layer of this material (Figure 8b,c). Measurement data from more sample orientations relative to CPW are provided in the Supporting Information (Figure S1). Indeed, the precise manipulation of the sample's position on the CPW elucidated the presence of a higher frequency signal that is uniquely associated with the homogeneous Ni layer present at one of the sample's edge. This distinct relationship was substantiated by an excellent agreement between the observed signal and the theoretical prediction derived from the Kittel formula

$$f = \frac{\gamma}{2\pi} \sqrt{B_{\text{ext}}(B_{\text{ext}} + \mu_0 M_s)} \quad (2)$$

where f is the resonance frequency, μ_0 is a vacuum permeability ($\sim 4\pi \times 10^{-7}$ T m/A), and γ is the gyromagnetic ratio. For the comparative calculations, we employed identical magnetic parameters as in the numerical simulations, specifically, the g -factor of 2.14 and saturation magnetization $M_s = 480$ kA/m. Contrarily, the lower frequency signal is consistently identified with the gyroid-structured region of the sample, a correlation supported by its sustained presence irrespective of orientation relative to the CPW.

Using eq 2, we not only fitted the resonance signal derived from the homogeneous Ni structure but also attempted to fit it to the experimental signal in the gyroids and estimated the effective values of the saturation magnetization and the g -factor.

As a result, a satisfactory fit of the Kittel curve to the gyroidal resonance signal for different sample orientations relative to the CPW (see Figure S4 in the Supporting Information) was obtained using $M_{\text{eff}} = 0.275M_s = 132$ kA/m, and $g_{\text{eff}} = 1.028g = 2.2$, as shown in Figure 8b,c with a white dotted line. Such findings suggest that the given 3D structure exhibits magnonics' metamaterial-like properties, so far considered only for the planar structures,^{62–66} capable of modulating (specifically, decreasing) the effective saturation magnetization and the dynamical response of the structure in a methodical and foreseeable manner. The effective magnetization, which is higher than expected with only a 10% filling fraction, implies that the gyroid structure may have anisotropy. It can be indicative of a strong shape anisotropy inherent to the particular nanoelements of this structure, which 'anchors' the magnetization in place until it is forced to switch due to a change in the field direction.

To facilitate a qualitative comparison between the results of the experiment and simulation, we examined the FWHM's. Figure 8 reveals that the signal from gyroid exhibits a broader frequency FWHM than in Ni, e.g., at 450 mT field it is 3.69 GHz for gyroid and 3.09 GHz for homogeneous Ni. This phenomenon is likely attributable to the multidomain nature of the sample. That is, the signal observed from the gyroid is the average value coming from several different domains located above the CPW and differing in crystallographic orientation. We deduce from the BBFMR measurements depicted in Figure 8e an average difference between the FWHM's of 1.3 GHz over different values of the external magnetic field. The micromagnetic simulations for the cube shape (Figure 5) reveal a maximum peak separation of 2.55 and 2.95 GHz for the field of 300 and 100 mT, respectively (in both cases between [100] and [111] crystallographic directions). Our simulations meticulously evaluated the crystallographic directions that represent the most disparate configurations of the

gyroid lattice relative to the field, most likely resulting in the largest feasible separation of resonant frequencies.

In field-swept FMR experiments conducted at a fixed frequency, the absorption line FWHM conforms to $\mu_0 \Delta H = 4\pi\alpha/\gamma$. This occurs when the magnetization vector is aligned with the applied magnetic field, either in the plane or perpendicular to it. Such alignment results in a line width that scales proportionally with frequency, where the slope of this scaling is defined by the Gilbert damping parameter α .⁶⁷ Beyond this intrinsic contribution, empirical data also indicate the presence of a frequency-independent term

$$\Delta H = \Delta H_0 + \frac{4\pi\alpha}{\mu_0\gamma} f \quad (3)$$

denoted by ΔH_0 that represents the inhomogeneous contributions, which add to the overall line width observed in the experiments.

Experimental investigations have enabled a linear regression analysis of FWHM across a spectrum of B_{MW} frequencies, as depicted in Figure 8f for the designated orientations of the sample over CPW. This analytical approach is instrumental in ascertaining the damping values α and the inhomogeneous line width contribution ΔH_0 for both the homogeneous Ni layer and the gyroidal structure, respectively, employing eq 3. In the first case, the derived values are $\alpha = 0.0282 \pm 2.54\%$ and $\Delta H_0 = 0.038 \pm 1.28\%$ T, with a coefficient of determination of $r^2 = 0.95153$. Comparatively, the gyroidal structure exhibits $\alpha' = 0.0362 \pm 6.49\%$ and $\Delta H'_0 = 0.101 \pm 1.05\%$ T, with $r^2 = 0.81639$. The damping constants for Ni align with previously reported values.⁶⁸ The 95% confidence interval was used to calculate the range of estimates for the values. Larger α' for the gyroid structure is likely attributable to the scattering of SW modes within the nanowires, which are much thinner than the bulk Ni and exhibit complex noncollinear interconnections. This difference varies with the sample's orientation relative to the CPW, as further exemplified in the Supporting Information (Figure S4). The examples there, however, are subject to considerable uncertainty due to the nonlinearity of $\Delta H(f)$ for gyroid structures.

The disparity in the ΔH_0 values between the homogeneous Ni layer and the gyroidal structure is also noteworthy. Such variations in the material's magnetic properties, including anisotropy, manifest as a frequency-independent line width.⁶⁷ The pronounced $\Delta H'_0$ in gyroid structures corroborates the influence of crystallographic orientation on the system's resonant frequencies, as confirmed by micromagnetic simulations and indicated in the earlier discussion. It is that, experimentally, in a multimode sample scenario depicted in Figure 7, the inhomogeneous contribution to the effective FWHM is an aggregate effect of the various crystallographic orientations present, and $\Delta H'_0$ emerges from the superposition of all resonant peaks within the spectrum bounded by the extremities observed in Figures 5 and 6 (the maximum separation between FMR peaks for the studied crystallographies in the 100 mT field is 2.95 GHz, while in the 300 mT field, 2.60 GHz).

The next step is to compare the frequencies. In the experiment, the maximum intensity at $B_{\text{ext}} = 300$ mT is at 11.53 GHz (Figure 8d), while in the simulations for the gyroid of cubic shape, it is at 8.25 GHz for the [110] field orientation (among the orientations analyzed, in accordance with the above discussion about FWHM, we chose the orientation with

the medium frequency, Figure 5b), giving a difference of 3.28 GHz. At 100 mT this difference decreases to 2.7 GHz (Figure 5a). The results in Figure 4 indicate that the macroscopic shape of the gyroid contributes to the results. In these simulations, considering a relatively small thin cuboid shape, the FMR frequency separation between orthogonal field orientations is $\Delta f = 1.5$ GHz. However, when considering a bulk thin film ferromagnet of $M_{\text{eff}} = 132$ kA/m, the maximum influence of shape (i.e., FMR between in-plane and out-of-plane magnetic field orientations) can reach over 4 GHz. Therefore, it is reasonable to expect that the resonant frequencies in simulations will be lower than those obtained in experiments due to the significant influence of the macroscopic shape anisotropy.

A noteworthy distinction between the gyroid and homogeneous Ni signals also arises with respect to their measured intensities as a function of the external magnetic field. In the case of the gyroid structure, it shows an almost linear increase (Figure 8d), giving an almost 30% increase in intensity between 100 and 300 mT magnetic fields (and 50% between 100 and 450 mT), while for homogeneous Ni it remains fairly irregular. This intriguing behavior may reflect the intricate influence of the complex gyroid geometry on the internal demagnetization field and magnetization orientation. Such complexity may counteract the orthogonal orientation of the dynamic magnetization components with respect to the static field, thus attenuating their detectability by the microwave field, B_{MW} . Upon increasing the field, the sample leads to a parallel orientation of the magnetization vectors, as shown in Figure 3c, thereby increasing the detectability of the magnetization precession at resonance. From this graph it can be seen that most of the bins (elementary simulation cells) are almost completely saturated for a field of 100 mT (for example, at least 94% saturation has been reached in 89% of the gyroid volume: 56,463 bins, and at 300 mT the >94% saturation is already in 100% of the structure: 63,274 bins). However, a comprehensive understanding of the FMR intensities in gyroids for larger fields would require further investigation that falls outside the scope of this paper.

5. DISCUSSION

Owing to the inherently multidomain architecture of the sample under investigation, the task of identifying a singular dominant crystallography and quantifying its direct influence on the resonance spectrum presents a formidable challenge. Recognizing this complexity, the study has embraced a numerical approach, rigorously testing the three selected field directions ([100], [110], and [111]) in the finite-size gyroid, to elucidate the extent to which the structure's intrinsic complexity governs resonance frequency variations. It is imperative to note that beyond the irregular shape, size, and interfaces of the domains, which relate to the shape anisotropy, fabrication of such an intricate structure encompasses numerous factors that elude accurate prediction and, consequently, integration within the simulation framework. Such factors include, but are not limited to, irregularities and impurities in both the shape and thickness of the nanorods, compounded by a paucity of definitive information concerning the sample's dominant crystallographic orientation in each experimental configuration. A full experimental validation of the phenomena predicted by our micromagnetic simulations is beyond the scope of this work. However, we expect that these effects will soon be observable in experiments with directed

self-assembly gyroids.⁶⁹ Our experimental results provide the basis for this since the signs of the predicted phenomena have already been detected.

The research presented here highlights several emerging avenues for the application and practical use of 3D gyroidal nanostructures. By controlling ϕ , one could modulate the effective saturation magnetization, offering magnonic metamaterial of effective dynamical properties. Traditionally, the construction of artificial photonic or phononic crystals requires the use of different materials, each characterized by unique properties, e.g., dielectric constant or elastic properties. However, our results suggest that a gyroidal structure with a tunable filling factor could serve as an effective substitute for 3D magnonic crystals. This paradigm shift in fabrication methodology heralds a transition from 2D to 3D magnonic nanostructures with a wide range of novel applications and functionalities.

Due to the random distribution, shape, and size of the gyroid domains in the experiment, the sample can be approximated to a porous structure when examined collectively.⁷⁰ This simplification, however, nullifies the interpretation of the relationship between the field direction and the frequency of SWs. This may ultimately be shown in future studies e.g. by using Brillouin light scattering for individual gyroid domains.

Some of the visible SW bulk modes presented in this work show also an intriguing surface character, localizing on the sides perpendicular to the direction of the magnetic field—see, e.g. Figures 4, 6 ([110] and [100]), and in the Supporting Information Figure S2 (modes no. 7 and 8) and Figure S3 (modes no. 1 and 5). This may be the result of an additional effect arising from the strong influence of crystallography and the shape anisotropy on the localization of resonant modes in different regions and probably on the chirality of the system. However, the analysis of these effects, although interesting, is beyond the scope of this work, since it is necessary to perform micromagnetic simulations with periodic boundary conditions and to conduct experiments of a different type, where the sample containing the single-domain gyroidal structure could be selectively analyzed on a much smaller scale.

In addition, the distinct mode spectrum observed in our research has direct implications for radio frequency filtering applications. The presence of a singular bulk mode in both BBFMR experiments (as an effective response from a multidomain structure) or simulations (a strong resonance in a single domain) enables the design of selective filter systems. They could be tailored to isolate specific FMR frequencies depending on factors such as crystallographic orientation relative to the incident signal and filling factor. In addition, the three-dimensional magnonic structures are expected to exhibit superior absorption properties compared to their two-dimensional counterparts, as supported by previous studies.⁴⁴

6. CONCLUSIONS

In the investigation, a comprehensive ferromagnetic resonance analysis was conducted on three-dimensional gyroidal Ni nanostructures, delving into the complex interplay between magnetic properties and structural geometry. Utilizing FEM micromagnetic simulations in the time domain to determine the static magnetization structures⁵⁵ and in the frequency domain to investigate their oscillatory, magnonic properties,⁵⁷ the study embarked on a multifaceted exploration aimed not merely at interpreting experimental results but also at

unraveling the intricate magnetization distribution within the gyroid nanostructure.

A major result that emerges from our simulations is the importance of the crystallographic orientation of the gyroid, relative to the magnetic field's direction, on a frequency and spatial distribution of the collective magnetization oscillations. Complementing these simulations, experimental measurements were executed using BBFMR, where a multidomain gyroid sample was positioned on a CPW line, enabling analysis of differences and relationships between the solid, uniform Ni layer and the gyroid-structured portion of the sample. Although the measurements were not able to study individual crystallographic domains of the gyroid and thus confirm all simulation predictions, based on our findings, gyroid films can be conceptualized as homogeneous materials, i.e., magnonic metamaterials, where the effective saturation magnetization is reduced by the gyroid filling factor and the FMR signal line width encapsulates more than the inherent damping properties of the material; it is also intricately linked to the particular geometry and crystallographic orientation of the structure.

Collectively, these discoveries show a new frontier in the realm of 3D magnonics, positing the gyroid structure as a potential cornerstone in the field. The results not only augment our theoretical and experimental grasp of the magnetization dynamics in complex nanostructures but also open up promising avenues for practical applications, imbuing the gyroid configuration with the potential to become an elemental building block in emerging magnetic technologies. We propose a gyroidal structure with a tunable filling factor as a magnonic crystal and as the basis for novel 3D radio frequency filters. The study's interdisciplinary approach, bridging numerical simulations with empirical investigation, marks a significant stride toward the comprehensive understanding and manipulation of magnetic resonance in three-dimensional architectures.

■ ASSOCIATED CONTENT

Data Availability Statement

The data underlying this study are openly available in Zenodo at <https://doi.org/10.5281/zenodo.11004007>.

■ Supporting Information

The Supporting Information is available free of charge at <https://pubs.acs.org/doi/10.1021/acsami.4c02366>.

BBFMR gyroid structure analysis under in-plane field rotation in 40° increments over 180° relative to the CPW; micromagnetic results of 4 × 4 × 4 gyroid spectra at 100 mT: detailed focus on satellite peaks; micromagnetic results of 4 × 4 × 4 gyroid spectra at 300 mT: detailed focus on satellite peaks; and FWHM vs frequency: comparison of BBFMR signals of gyroids and uniform Ni, under sample rotations on CPW, revealing the variation in the resulting effective parameters of damping and inhomogeneous contributions to the line width (PDF)

■ AUTHOR INFORMATION

Corresponding Author

Mateusz Golebiewski – *Institute of Spintronics and Quantum Information, Faculty of Physics, Adam Mickiewicz University, 61-614 Poznań, Poland*; orcid.org/0000-0002-1948-0652; Email: mateusz.golebiewski@amu.edu.pl

Authors

Riccardo Hertel – *Université de Strasbourg, CNRS, Institut de Physique et Chimie des Matériaux de Strasbourg, F-67000 Strasbourg, France*

Massimiliano d'Aquino – *Department of Electrical Engineering and ICT, University of Naples Federico II, 80125 Naples, Italy*

Vitaliy Vasyuchka – *Fachbereich Physik und Landesforschungszentrum OPTIMAS, Rheinland-Pfälzische Technische Universität Kaiserslautern-Landau, 67663 Kaiserslautern, Germany*

Mathias Weiler – *Fachbereich Physik und Landesforschungszentrum OPTIMAS, Rheinland-Pfälzische Technische Universität Kaiserslautern-Landau, 67663 Kaiserslautern, Germany*

Philipp Pirro – *Fachbereich Physik und Landesforschungszentrum OPTIMAS, Rheinland-Pfälzische Technische Universität Kaiserslautern-Landau, 67663 Kaiserslautern, Germany*

Maciej Krawczyk – *Institute of Spintronics and Quantum Information, Faculty of Physics, Adam Mickiewicz University, 61-614 Poznań, Poland*; orcid.org/0000-0002-0870-717X

Shunsuke Fukami – *Research Institute of Electrical Communication (RIEC), Tohoku University, Sendai-shi, Miyagi 980-8577, Japan; Center for Science and Innovation in Spintronics (CSIS), Tohoku University, 980-8577 Sendai, Japan; Center for Innovative Integrated Electronic Systems (CIES), Tohoku University, 980-0845 Sendai, Japan; WPI Advanced Institute for Materials Research, Tohoku University, 980-8577 Sendai, Japan; Inamori Research Institute for Science, 600-8411 Kyoto, Japan*

Hideo Ohno – *Research Institute of Electrical Communication (RIEC), Tohoku University, Sendai-shi, Miyagi 980-8577, Japan; Center for Science and Innovation in Spintronics (CSIS), Tohoku University, 980-8577 Sendai, Japan; Center for Innovative Integrated Electronic Systems (CIES), Tohoku University, 980-0845 Sendai, Japan; WPI Advanced Institute for Materials Research, Tohoku University, 980-8577 Sendai, Japan*

Justin Llandro – *Research Institute of Electrical Communication (RIEC), Tohoku University, Sendai-shi, Miyagi 980-8577, Japan; Center for Science and Innovation in Spintronics (CSIS), Tohoku University, 980-8577 Sendai, Japan*

Complete contact information is available at: <https://pubs.acs.org/doi/10.1021/acsami.4c02366>

Notes

The authors declare no competing financial interest.

■ ACKNOWLEDGMENTS

The research was funded by the National Science Centre of Poland, Projects nos. UMO-2020/39/I/ST3/02413 and UMO-2023/49/N/ST3/03032. J.L. and S.F. acknowledge support from the Japan Society for the Promotion of Science (JSPS) under KAKENHI 21K04816 and 19H05622, Cooperative Research Projects of CSIS, Tohoku University, and the Graduate Program for Spintronics (GP-Spin), Tohoku University. R.H. acknowledges the High Performance Computing center of the University of Strasbourg for supporting this work by providing access to computing

resources. M.W., V.V., and P.P. acknowledge funding by the Deutsche Forschungsgemeinschaft (DFG, German Research Foundation)—TRR 173/3—268565370 Spin+X (Projects B01 and B13). The authors thank Dr. J. Dolan for sample preparation, Dr. I. Gunkel and Dr. Naëmi Leo for providing domain images, and Prof. T. Dietl and Prof. B. Hillebrands for insightful discussions.

REFERENCES

- (1) Pirro, P.; Vasyuchka, V. I.; Serga, A. A.; Hillebrands, B. Advances in coherent magnonics. *Nat. Rev. Mater.* **2021**, *6*, 1114–1135.
- (2) Serga, A. A.; Chumak, A. V.; Hillebrands, B. YIG magnonics. *J. Phys. D: Appl. Phys.* **2010**, *43*, 264002.
- (3) Yan, P.; Bauer, G. E. Magnon mediated domain wall heat conductance in ferromagnetic wires. *IEEE Trans. Magn.* **2013**, *49*, 3109–3112.
- (4) Garcia-Sanchez, F.; Borys, P.; Soucaille, R.; Adam, J. P.; Stamps, R. L.; Kim, J. V. Narrow Magnonic Waveguides Based on Domain Walls. *Phys. Rev. Lett.* **2015**, *114*, 247206.
- (5) Wagner, K.; Kákay, A.; Schultheiss, K.; Henschke, A.; Sebastian, T.; Schultheiss, H. Magnetic domain walls as reconfigurable spin-wave nanochannels. *Nat. Nanotechnol.* **2016**, *11*, 432–436.
- (6) Chumak, A. V.; Vasyuchka, V. I.; Serga, A. A.; Hillebrands, B. Magnon spintronics. *Nat. Phys.* **2015**, *11*, 453–461.
- (7) Kruglyak, V. V.; Demokritov, S. O.; Grundler, D. Magnonics. *J. Phys. D: Appl. Phys.* **2010**, *43*, 264001.
- (8) Barman, A.; Gubbiotti, G.; Ladak, S.; Adeyeye, A. O.; Krawczyk, M.; Gräfe, J.; Adelman, C.; Cotofana, S.; Naeemi, A.; Vasyuchka, V. I.; et al. The 2021 Magnonics Roadmap. *J. Phys.: Condens. Matter* **2021**, *33*, 413001.
- (9) Chumak, A. V.; Kabos, P.; Wu, M.; Abert, C.; Adelman, C.; Adeyeye, A. O.; Akerman, J.; Aliev, F. G.; Anane, A.; Awad, A.; et al. Advances in Magnetics Roadmap on Spin-Wave Computing. *IEEE Trans. Magn.* **2022**, *58*, 1–72.
- (10) Gubbiotti, G. In *Three-Dimensional Magnonics*, 1st ed.; Gubbiotti, G., Ed.; Jenny Stanford Publishing: New York, 2019.
- (11) Cheenikundil, R.; d'Aquino, M.; Hertel, R. Defect-sensitive High-frequency Modes in a Three-Dimensional Artificial Magnetic Crystal. *arXiv* **2023**, arXiv:2312.08415. preprint
- (12) Krawczyk, M.; Grundler, D. Review and prospects of magnonic crystals and devices with reprogrammable band structure. *J. Phys.: Condens. Matter* **2014**, *26*, 123202.
- (13) Makarov, D.; Volkov, O. M.; Kákay, A.; Pylypovskiy, O. V.; Budinská, B.; Dobrovolskiy, O. V. New Dimension in Magnetism and Superconductivity: 3D and Curvilinear Nanoarchitectures. *Adv. Mater.* **2022**, *34*, 2101758.
- (14) Cheenikundil, R.; Bauer, J.; Goharyan, M.; d'Aquino, M.; Hertel, R. High-frequency modes in a magnetic buckyball nano-architecture. *APL Mater.* **2022**, *10*, 81106.
- (15) Cheenikundil, R.; d'Aquino, M.; Hertel, R. Magnetization dynamics in a three-dimensional interconnected nanowire array. *arXiv* **2023**, arXiv:2306.00174. preprint
- (16) Llandro, J.; Love, D. M.; Kovács, A.; Caron, J.; Vyas, K. N.; Kákay, A.; Salikhov, R.; Lenz, K.; Fassbender, J.; Scherer, M. R. J.; et al. Visualizing magnetic structure in 3d nanoscale ni-fe gyroid networks. *Nano Lett.* **2020**, *20*, 3642–3650.
- (17) Fernández-Pacheco, A.; Streubel, R.; Fruchart, O.; Hertel, R.; Fischer, P.; Cowburn, R. P. Three-dimensional nanomagnetism. *Nat. Commun.* **2017**, *8*, 15756.
- (18) Donnelly, C.; Hierro-Rodríguez, A.; Abert, C.; Witte, K.; Skoric, L.; Sanz-Hernández, D.; Finizio, S.; Meng, F.; McVitie, S.; Raabe, J.; Suess, D.; Cowburn, R.; Fernández-Pacheco, A. Complex free-space magnetic field textures induced by three-dimensional magnetic nanostructures. *Nat. Nanotechnol.* **2022**, *17*, 136–142.
- (19) van den Berg, A.; Caruel, M.; Hunt, M.; Ladak, S. Combining two-photon lithography with laser ablation of sacrificial layers: A route to isolated 3D magnetic nanostructures. *Nano Res.* **2023**, *16*, 1441–1447.
- (20) Schoen, A. H. *Infinite periodic minimal surfaces without self-intersections*; National Aeronautics and Space Administration, 1970.
- (21) Lambert, C. A.; Radzilowski, L. H.; Thomas, E. L. Triply periodic level surfaces as models for cubic tricontinuous block copolymer morphologies. *Philos. Trans. R. Soc., A* **1996**, *354*, 2009–2023.
- (22) Turner, M. D.; Saba, M.; Zhang, Q.; Cumming, B. P.; Schröder-Turk, G. E.; Gu, M. Miniature chiral beamsplitter based on gyroid photonic crystals. *Nat. Photonics* **2013**, *7*, 801–805.
- (23) Vignolini, S.; Yufa, N. A.; Cunha, P. S.; Guldin, S.; Rushkin, I.; Stefik, M.; Hur, K.; Wiesner, U.; Baumberg, J. J.; Steiner, U. A 3D optical metamaterial made by self-assembly. *Adv. Mater.* **2012**, *24*, OP23–OP27.
- (24) Dolan, J. A.; Wilts, B. D.; Vignolini, S.; Baumberg, J. J.; Steiner, U.; Wilkinson, T. D. Optical Properties of Gyroid Structured Materials: From Photonic Crystals to Metamaterials. *Adv. Opt. Mater.* **2015**, *3*, 12–32.
- (25) Michiels, K.; Stavenga, D. G. Gyroid cuticular structures in butterfly wing scales: Biological photonic crystals. *J. R. Soc., Interface* **2008**, *5*, 85–94.
- (26) Saranathan, V.; Osuji, C. O.; Mochrie, S. G.; Noh, H.; Narayanan, S.; Sandy, A.; Dufresne, E. R.; Prum, R. O. Structure, function, and self-assembly of single network gyroid (14 132) photonic crystals in butterfly wing scales. *Proc. Natl. Acad. Sci. U.S.A.* **2010**, *107*, 11676–11681.
- (27) Schröder-Turk, G.; Wickham, S.; Averdunk, H.; Brink, F.; Fitz Gerald, J. D.; Poladian, L.; Large, M. C.; Hyde, S. T. The chiral structure of porous chitin within the wing-scales of *Callophrys rubi*. *J. Struct. Biol.* **2011**, *174*, 290–295.
- (28) Yan, C.; Hao, L.; Hussein, A.; Raymont, D. Evaluations of cellular lattice structures manufactured using selective laser melting. *Int. J. Mach. Tool Manufact.* **2012**, *62*, 32–38.
- (29) Yáñez, A.; Herrera, A.; Martel, O.; Monopoli, D.; Afonso, H. Compressive behaviour of gyroid lattice structures for human cancellous bone implant applications. *Mater. Sci. Eng., C* **2016**, *68*, 445–448.
- (30) Armatas, G. S.; Kanatzidis, M. G. Mesosstructured germanium with cubic pore symmetry. *Nature* **2006**, *441*, 1122–1125.
- (31) Hajduk, D. A.; Harper, P. E.; Gruner, S. M.; Honeker, C. C.; Kim, G.; Thomas, E. L.; Kim, G. The Gyroid: A New Equilibrium Morphology in Weakly Segregated Diblock Copolymers. *Macromolecules* **1994**, *27*, 4063–4075.
- (32) Kim, J. K.; Yang, S. Y.; Lee, Y.; Kim, Y. Functional nanomaterials based on block copolymer self-assembly. *Prog. Polym. Sci.* **2010**, *35*, 1325–1349.
- (33) Bai, W.; Hannon, A. F.; Gotrik, K. W.; Choi, H. K.; Aissou, K.; Lontos, G.; Ntetsikas, K.; Alexander-Katz, A.; Avgeropoulos, A.; Ross, C. A. Thin film morphologies of bulk-gyroid polystyrene-block-polydimethylsiloxane under solvent vapor annealing. *Macromolecules* **2014**, *47*, 6000–6008.
- (34) Hsueh, H. Y.; Yao, C. T.; Ho, R. M. Well-ordered nanohybrids and nanoporous materials from gyroid block copolymer templates. *Chem. Soc. Rev.* **2015**, *44*, 1974–2018.
- (35) Lich, L. V.; Hue, D. T. H.; Giang, D. T. H.; Duc, N. H.; Shimada, T.; Kitamura, T.; Dinh, V. H. Formation and switching of chiral magnetic field textures in three-dimensional gyroid nanostructures. *Acta Mater.* **2023**, *249*, 118802.
- (36) Hertel, R. Curvature-induced magnetochirality. *SPIN* **2013**, *03*, 1340009.
- (37) Gaididei, Y.; Kravchuk, V. P.; Sheka, D. D. Curvature Effects in Thin Magnetic Shells. *Phys. Rev. Lett.* **2014**, *112*, 257203.
- (38) Streubel, R.; Fischer, P.; Kronast, F.; Kravchuk, V. P.; Sheka, D. D.; Gaididei, Y.; Schmidt, O. G.; Makarov, D. Magnetism in curved geometries. *J. Phys. D: Appl. Phys.* **2016**, *49*, 363001.
- (39) Sander, D.; Valenzuela, S. O.; Makarov, D.; Marrows, C. H.; Fullerton, E. E.; Fischer, P.; McCord, J.; Vavassori, P.; Mangin, S.; Pirro, P.; et al. The 2017 Magnetism Roadmap. *J. Phys. D: Appl. Phys.* **2017**, *50*, 363001.

- (40) Sheka, D. D. A perspective on curvilinear magnetism. *Appl. Phys. Lett.* **2021**, *118*, 230502.
- (41) Shindou, R.; Matsumoto, R.; Murakami, S.; Ohe, J. I. Topological chiral magnonic edge mode in a magnonic crystal. *Phys. Rev. B: Condens. Matter Mater. Phys.* **2013**, *87*, 174427.
- (42) McClarty, P. A. Topological Magnons: A Review. *Annu. Rev. Condens. Matter Phys.* **2022**, *13*, 171–190.
- (43) May, A.; Saccone, M.; van den Berg, A.; Askey, J.; Hunt, M.; Ladak, S. Magnetic charge propagation upon a 3D artificial spin-ice. *Nat. Commun.* **2021**, *12*, 3217–3310.
- (44) Guo, H.; Deenen, A. J. M.; Xu, M.; Hamdi, M.; Grundler, D. Realization and Control of Bulk and Surface Modes in 3D Nanomagnonic Networks by Additive Manufacturing of Ferromagnets. *Adv. Mater.* **2023**, *35*, 2303292.
- (45) Krawczyk, M.; Puzkarski, H. Magnonic crystal theory of the spin-wave frequency gap in low-doped manganites. *J. Appl. Phys.* **2006**, *100*, 073905.
- (46) Krawczyk, M.; Puzkarski, H. Plane-wave theory of three-dimensional magnonic crystals. *Phys. Rev. B: Condens. Matter Mater. Phys.* **2008**, *77*, 054437.
- (47) Volkov, O. M.; Röbber, U. K.; Fassbender, J.; Makarov, D. Concept of artificial magnetoelectric materials via geometrically controlling curvilinear helimagnets. *J. Phys. D: Appl. Phys.* **2019**, *52*, 345001.
- (48) Hopfield, J. J. Neural networks and physical systems with emergent collective computational abilities. *Proc. Natl. Acad. Sci. U.S.A.* **1982**, *79*, 2554–2558.
- (49) Karcher, H. The triply periodic minimal surfaces of Alan Schoen and their constant mean curvature companions. *Manuscripta Math.* **1989**, *64*, 291–357.
- (50) Große-Brauckmann, K.; Wohlgemuth, M. The gyroid is embedded and has constant mean curvature companions. *Calc. Var. Partial Differ. Equ.* **1996**, *4*, 499–523.
- (51) Große-Brauckmann, K. Gyroids of constant mean curvature. *Exp. Math.* **1997**, *6*, 33–50.
- (52) Sunada, T. Crystals That Nature Might Miss Creating. *Not. AMS* **2008**, *55*, 208–215.
- (53) Hyde, S. T.; O’Keeffe, M.; Proserpio, D. M. A short history of an elusive yet ubiquitous structure in chemistry, materials, and mathematics. *Angew. Chem., Int. Ed.* **2008**, *47*, 7996–8000.
- (54) Coey, J. M. *Magnetism and Magnetic Materials*; Cambridge University Press, 2010; pp 1–617.
- (55) Hertel, R. tetmag. 2023, <https://github.com/R-Hertel/tetmag>.
- (56) Hertel, R.; Christophersen, S.; Börm, S. Large-scale magnetostatic field calculation in finite element micromagnetics with H²-matrices. *J. Magn. Magn. Mater.* **2019**, *477*, 118–123.
- (57) d’Aquino, M.; Hertel, R. Micromagnetic frequency-domain simulation methods for magnonic systems. *J. Appl. Phys.* **2023**, *133*, 033902.
- (58) d’Aquino, M.; Serpico, C.; Miano, G.; Forestiere, C. A novel formulation for the numerical computation of magnetization modes in complex micromagnetic systems. *J. Comput. Phys.* **2009**, *228*, 6130–6149. Number: 17.
- (59) Heinrich, B. In *Ultrathin Magnetic Structures II* Heinrich, B., Bland, J., Eds.; Springer: Berlin, Heidelberg, 1994; pp 195–296.
- (60) Montoya, E.; McKinnon, T.; Zamani, A.; Girt, E.; Heinrich, B. Broadband ferromagnetic resonance system and methods for ultrathin magnetic films. *J. Magn. Magn. Mater.* **2014**, *356*, 12–20.
- (61) Dubowik, J.; Głowiński, H. Broad-Band Ferromagnetic Resonance in Thin Magnetic Films and Nanostructures. *Current Topics in Biophysics* **2010**, *33*, 43–45.
- (62) Mikhaylovskiy, R. V.; Hendry, E.; Kruglyak, V. V. Negative permeability due to exchange spin-wave resonances in thin magnetic films with surface pinning. *Phys. Rev. B: Condens. Matter Mater. Phys.* **2010**, *82*, 195446.
- (63) Mruczkiewicz, M.; Krawczyk, M.; Mikhaylovskiy, R. V.; Kruglyak, V. V. Towards high-frequency negative permeability using magnonic crystals in metamaterial design. *Phys. Rev. B: Condens. Matter Mater. Phys.* **2012**, *86*, 024425.
- (64) Kruglyak, V.; et al. In *Metamaterial*; Jiang, X.-Y., Ed.; IntechOpen: Rijeka, 2012; Chapter 14.
- (65) Zhuo, F.; Li, H.; Cheng, Z.; Manchon, A. Magnonic Metamaterials for Spin-Wave Control with Inhomogeneous Dzyaloshinskii-Moriya Interactions. *Nanomaterials* **2022**, *12*, 1159.
- (66) Haldar, A.; Adeyeye, A. O. Reconfigurable and self-biased magnonic metamaterials. *J. Appl. Phys.* **2020**, *128*, 240902.
- (67) Beaujour, J.-M.; Ravelosona, D.; Tudosa, I.; Fullerton, E. E.; Kent, A. D. Ferromagnetic resonance linewidth in ultrathin films with perpendicular magnetic anisotropy. *Phys. Rev. B: Condens. Matter Mater. Phys.* **2009**, *80*, 180415.
- (68) Walowski, J.; Kaufmann, M. D.; Lenk, B.; Hamann, C.; McCord, J.; Münzenberg, M. Intrinsic and non-local Gilbert damping in polycrystalline nickel studied by Ti: sapphire laser fs spectroscopy. *J. Phys. D: Appl. Phys.* **2008**, *41*, 164016.
- (69) Abdelrahman, D.; Iseli, R.; Musya, M.; Jinnai, B.; Fukami, S.; Yuasa, T.; Sai, H.; Wiesner, U. B.; Saba, M.; Wilts, B. D.; Steiner, U.; Llandro, J.; Gunkel, I. Directed Self-Assembly of Diamond Networks in Triblock Terpolymer Films on Patterned Substrates. *ACS Appl. Mater. Interfaces* **2023**, *15*, 57981–57991.
- (70) Gurevich, A.; Melkov, G. *Magnetization Oscillations and Waves*; Taylor & Francis, 1996.

Supporting Information:

Collective Spin-Wave Dynamics in Gyroid Ferromagnetic Nanostructures

Mateusz Gołębiewski,^{*,†} Riccardo Hertel,[‡] Massimiliano d'Aquino,[¶] Vitaliy Vasyuchka,[§] Mathias Weiler,[§] Philipp Pirro,[§] Maciej Krawczyk,[†] Shunsuke Fukami,^{||,⊥,#,@,△} Hideo Ohno,^{||,⊥,#,@} and Justin Llandro^{||,⊥}

[†]*Institute of Spintronics and Quantum Information, Faculty of Physics, Adam Mickiewicz University,
Uniwersytetu Poznańskiego 2, 61-614 Poznań, Poland*

[‡]*Université de Strasbourg, CNRS, Institut de Physique et Chimie des Matériaux de Strasbourg, F-67000
Strasbourg, France*

[¶]*Department of Electrical Engineering and ICT, University of Naples Federico II, 80125 Naples, Italy
§Fachbereich Physik und Landesforschungszentrum OPTIMAS, Rheinland-Pfälzische Technische
Universität Kaiserslautern-Landau, Erwin-Schrödinger-Straße 56, 67663 Kaiserslautern, Germany*

^{||}*Research Institute of Electrical Communication (RIEC), Tohoku University, 2-1-1 Katahira, Aoba-ku,
980-8577 Sendai-shi Miyagi, Japan*

[⊥]*Center for Science and Innovation in Spintronics (CSIS), Tohoku University, 980-8577 Sendai, Japan*

[#]*Center for Innovative Integrated Electronic Systems (CIES), Tohoku University, 468-1 Aramaki Aza
Aoba, Aoba-ku, 980-0845 Sendai, Japan*

[@]*WPI Advanced Institute for Materials Research, Tohoku University, 2-1-1 Katahira, Aoba-ku, 980-8577
Sendai, Japan*

[△]*Inamori Research Institute for Science, 600-8411 Kyoto, Japan*

E-mail: mateusz.golebiewski@amu.edu.pl

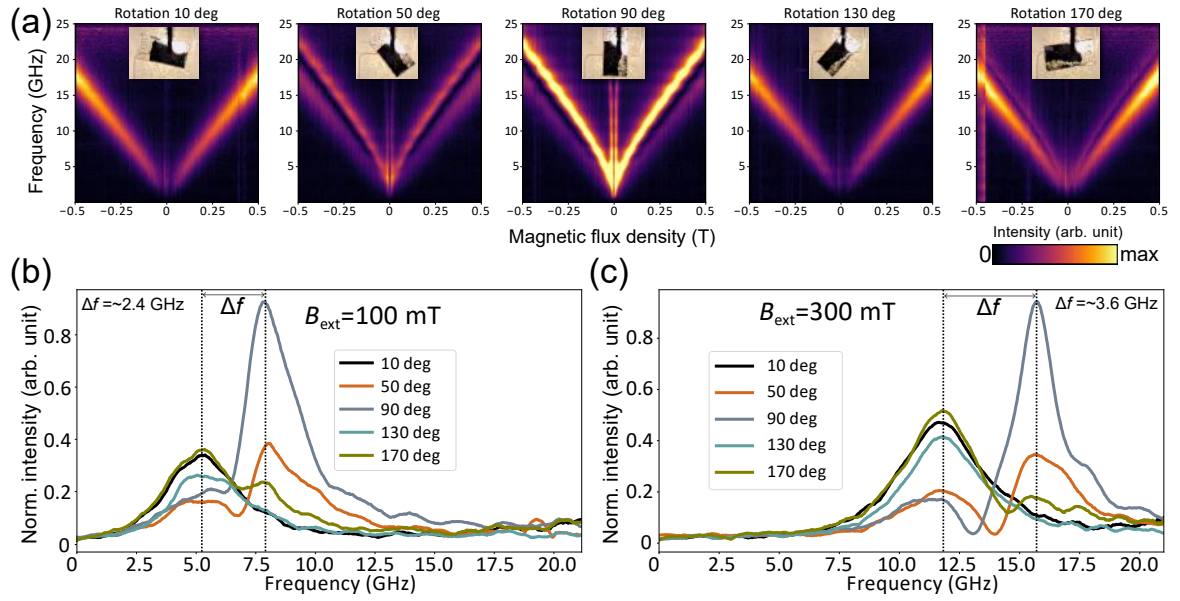


Figure S1: BBFMR measurement of the gyroid structure. The sample was rotated 180 deg relative to the CPW in 40 deg steps. For each configuration, a separate measurement of the energy absorption from the microwave field applied perpendicular to the static external magnetic field was performed as shown in (a). Plots of the FMR intensity as a function of frequency (for $B_{\text{ext}} = 100$ mT and $B_{\text{ext}} = 300$ mT) for selected angles are presented in (b) and (c), respectively. They show a clear and cyclic transition of spectral weight from the lower frequency branch from gyroidal sample's zone (high intensity at 10 deg) to the higher one from uniform Ni (high intensity at 90 deg). The separation between the bands (Δf) are measured to be 2.64 GHz and 3.89 GHz, respectively, as the field increases. Unlike amplitude, Δf is independent of rotation angle. The assumed values of the angles are conventional and do not refer to the crystallographic axes of the gyroid.

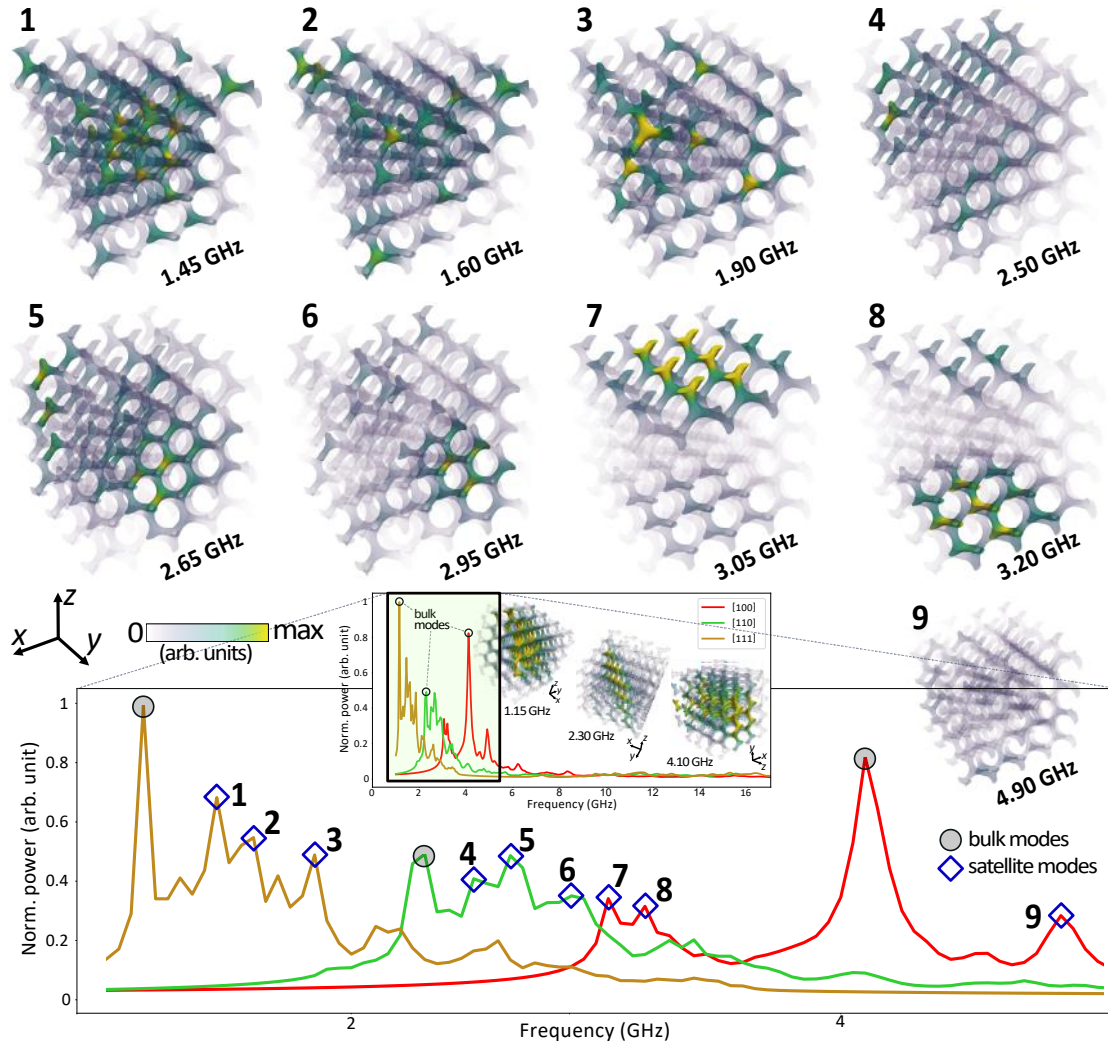


Figure S2: Micromagnetic simulation-derived resonance frequency spectra for $4 \times 4 \times 4$ gyroid constructs in which the applied external magnetic field has a strength of 100 mT. The spectrum used in the main part of the work has been enlarged, focusing on each individual satellite peaks. Different color coding in the plot indicates the crystallographic direction in which the field is applied, with the specific points marked on the plot indicating all significant satellite/edge ferromagnetic modes (diamonds) and volumetric modes (gray circles). Each satellite mode is numbered according to the visualization of the respective module with its frequency values above. The color scheme used here corresponds directly to the imaginary part of the magnetic susceptibility.

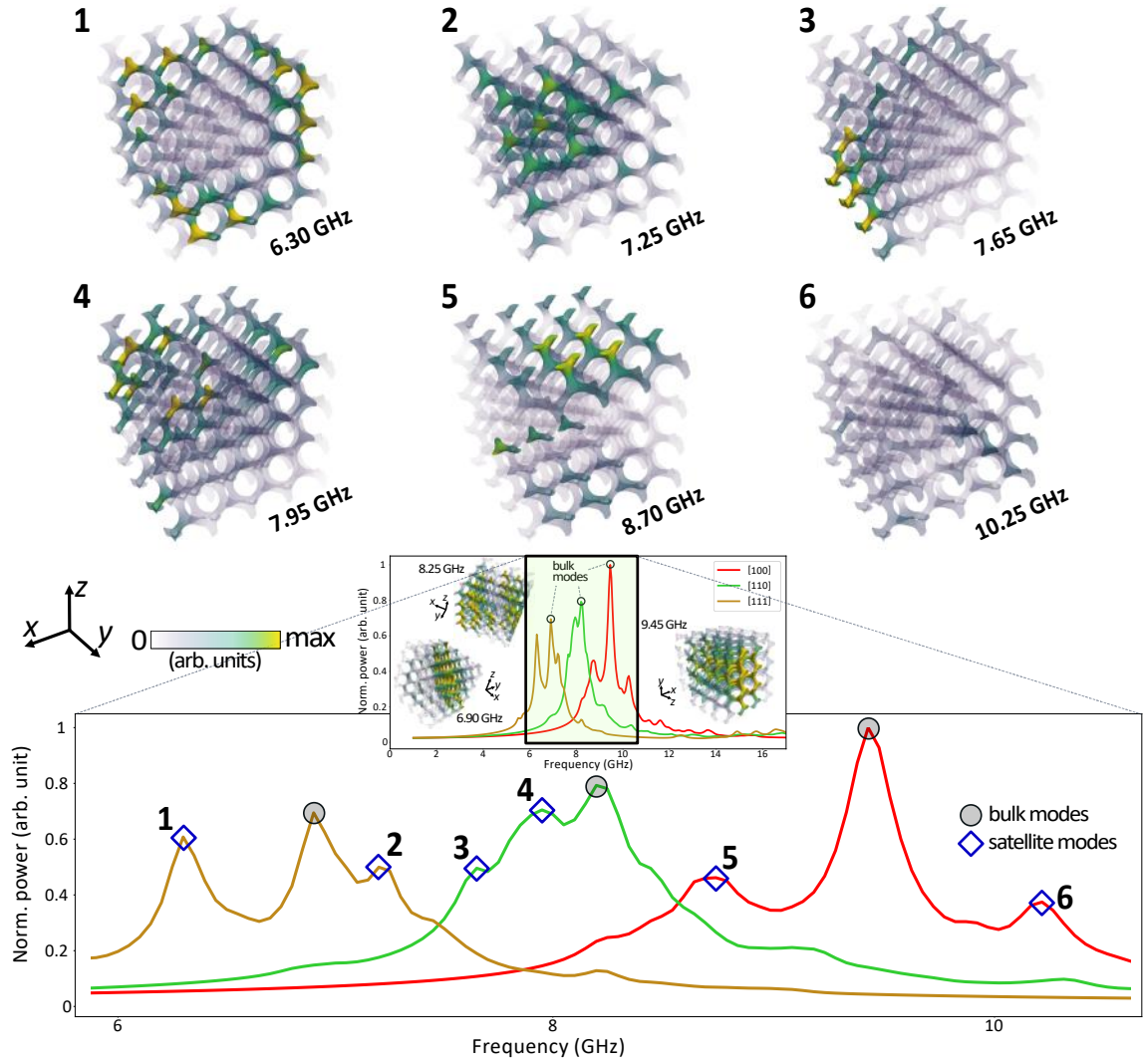


Figure S3: Micromagnetic simulation-derived resonance frequency spectra for $4 \times 4 \times 4$ gyroid constructs in which the applied external magnetic field has a strength of 300 mT. The spectrum used in the main part of the work has been enlarged, focusing on each individual satellite peaks. Different color coding in the plot indicates the crystallographic direction in which the field is applied, with the specific points marked on the plot indicating all significant satellite/edge ferromagnetic modes (diamonds) and volumetric modes (gray circles). Each satellite mode is numbered according to the visualization of the respective module with its frequency values above. The color scheme used here corresponds directly to the imaginary part of the magnetic susceptibility.

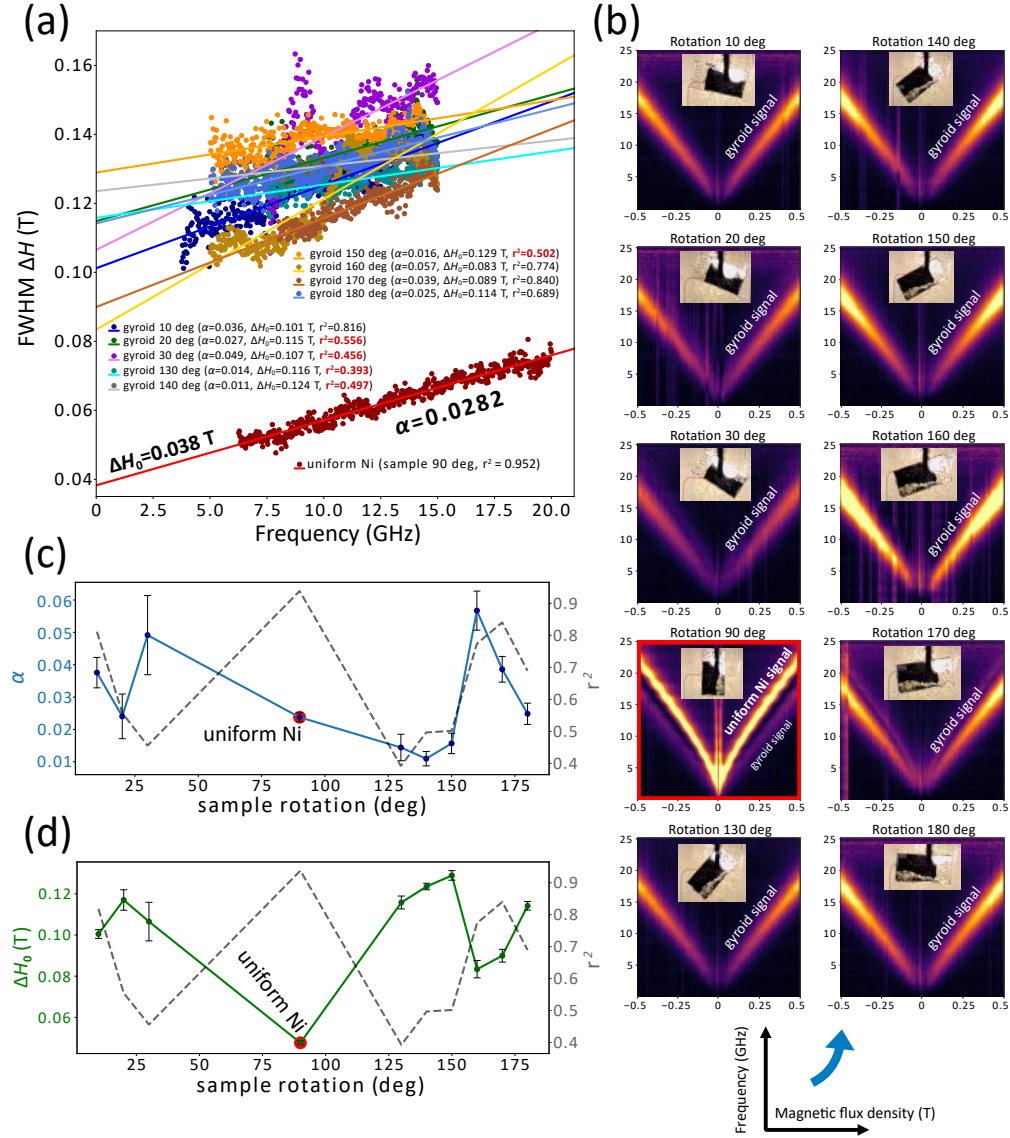


Figure S4: Plot (a) shows the FWHM values as a function of frequency, comparing BBFMR signals from gyroidal Ni and uniform Ni (represented by dark red dots). Several signals from gyroids were obtained by rotating the sample on the CPW, as illustrated in Figure S1, effectively obtaining a signal from various domains with different crystallography. Based on the experimental results and using Equation 3 from the main manuscript, linear regressions were performed on each set of data. The estimated values of the determination coefficient r^2 , inhomogeneous contributions to the linewidth ΔH_0 (measured from the abscissa of the lines), and the damping values α (derived from the slope of the lines) were estimated. (b) illustrates BBFMR measurements of dynamic magnetization intensities as functions of static magnetic flux density and frequency for selected sample configurations. The gyroid signal dominates all of them except for the 90-deg rotation, which is indicated by the red box. The changes in α and ΔH_0 as a function of sample rotation relative to the CPW with corresponding statistical error-bars are presented in (c) and (d). The curves with the values of the coefficient of determination r^2 for the measured configurations are additionally plotted on the graphs, showing their strongly nonlinear/irregular nature for some of the measurements [the lowest quality r^2 values are highlighted in red in (a)]. In the main manuscript, configurations with reliable linear regression fits were used, marked here with angles of 10 deg (for gyroid signal analysis) and 90 deg (for homogeneous Ni signal analysis).

5.3.2 Comprehensive overview of state-of-the-art research on magnetic gyroid structures: from mathematical foundations and fabrication to experimental characterization and numerical simulations (P8)

This chapter, submitted to the book *2D and 3D Nanostructures: Structure, Properties and Applications* by Jenny Stanford Publishing Pte Ltd (edited by J.-C. S. Lévy), provides a roadmap and comprehensive review of the magnetic properties of ferromagnetic gyroidal nanostructures, integrating insights from the recent literature along with my own research. In particular, I review how static and dynamic magnetization studies have revealed that distinctive features of gyroids – such as nontrivial shape anisotropy, inherent chirality, and inhomogeneous demagnetizing fields – can facilitate the formation of low-energy magnetization textures, localized spin-wave modes, and controllable spin-wave dispersions and propagation paths. Within this broader context, I place my own contributions and highlight promising research directions that build upon these insights.

Contribution of the Author

To prepare this chapter, I conducted a comprehensive review of the relevant literature and state-of-the-art research on gyroidal structures. With the assistance of M. Krawczyk, I systematically organized, classified, and synthesized these findings to ensure a coherent and structured presentation within the manuscript. For our original research contributions, I performed the micromagnetic simulations, discussed the results with M. Krawczyk, and post-processed the data. I was also responsible for writing the first draft and revising the chapter.

The draft included in this dissertation has undergone minor formatting adjustments, including changes in margin sizes and alignment of Fig. 1.10, compared to the version published on *arXiv* and submitted to *2D and 3D Nanostructures: Structure, Properties and Applications*. These changes were made solely to optimize the document layout and to avoid excessive white space, thus ensuring a more compact thesis file. Importantly, the content of the manuscript remains unchanged. Copyright ©2024 The Authors. Published on *arXiv* under the CC-BY 4.0 license.

Chapter 1

Gyroid ferromagnetic nanostructures in 3D magnonics

Mateusz Gołębiewski^a and Maciej Krawczyk^a

^a*Institute of Spintronics and Quantum Information, Faculty of Physics, Adam Mickiewicz University, Uniwersytetu Poznańskiego 2, 61-614 Poznań, Poland*
mateusz.golebiewski@amu.edu.pl

Abstract

This chapter provides a comprehensive analysis of the magnetic properties of ferromagnetic gyroidal nanostructures, based on both original research and a review of the state-of-the-art literature in the field of 3D magnonics. Through static and dynamic magnetization studies, we highlight how unique features such as non-trivial shape anisotropy, chirality, and inhomogeneous demagnetization fields within gyroidal structures contribute to the formation of low-energy magnetization textures, spin-wave mode localization, and controllable spin-wave propagation. In addition, the chapter reviews key studies on the magnetic behavior of individual gyroidal components, such as unit cells and vertices, further advancing our understanding of the gyroid's interactions with external fields and its effective magnetic properties. The combination of original research with a review of recent advances contributes to the ongoing exploration of complex gyroidal systems and their potential in 3D magnonics and spintronics.

1.1 Introduction

The exploration of spin waves (SWs) and their interactions within magnetic materials covers the interdisciplinary fields of magnonics and spintronics [Kruglyak *et al.* (2010); Chumak (2019); Dieny *et al.* (2020)]. This convergence has opened avenues for advanced research, particularly in harnessing SWs for signal transport avoiding Joule-Lenz heat emission [Serga *et al.* (2010); Yan and Bauer (2013); Barker and Bauer (2016)]. The spectrum of SW wavelengths, ranging from micrometers to tens of nanometers, and corresponding to frequencies from a few to hundreds of GHz [Schneider

et al. (2008); Maendl *et al.* (2017)], also promises advances in microwave technologies with a versatile platform for manipulating their dispersion and group velocities [Garcia-Sanchez *et al.* (2015); Wagner *et al.* (2016); Duerr *et al.* (2012); Lan *et al.* (2015); Krawczyk and Grundler (2014)]. This versatility, combined with high energy efficiency without sacrificing processing speed [Chumak *et al.* (2015); Kruglyak *et al.* (2010); Serga *et al.* (2010); Lenk *et al.* (2011); Mahmoud *et al.* (2020)] positions SWs as a compelling alternative to traditional electric currents, especially in computing and microwave systems.

The design of advanced magnonic systems integrates multiple factors, such as geometry, topology, and material properties. Together with the magnitude and direction of the external magnetic field, these factors influence key properties of SWs, including supported SW frequencies, their anisotropy, and ferromagnetic response. This integrated approach enables precise control of magnon dynamics for targeted applications. Magnonic crystals (MCs) represent an innovative intersection of magnetic film technology and periodic patterning, serving as a platform for exploring wave dynamics in both two-dimensional (2D) and three-dimensional (3D) domains [Krawczyk and Grundler (2014); Chumak *et al.* (2017)]. In the case of 2D MCs, the characteristic in-plane dimensions usually span several hundred nanometers, while the magnetic films maintain thicknesses on the order of tens of nanometers [Rychly *et al.* (2015); Mamica *et al.* (2019)]. In these ferromagnetic materials, the dynamics of SWs are primarily governed by isotropic exchange and anisotropic magnetostatic interactions [Krawczyk *et al.* (2013)], making the physics of the system more complex than that of their photonic (light-based) [Butt *et al.* (2021)] and phononic (sound or elastic wave-based) [Vasileiadis *et al.* (2021)] counterparts. Similar to other periodic composites, MCs allow for customization of the dispersion relation through structural and material composition adjustments, allowing for precise control over the velocity, direction, and magnonic gap width of propagating SWs [Krawczyk and Grundler (2014)]. However, magnetism provides a broad mechanism for manipulating the dynamics of SWs that is not present in other types of artificial crystals and waves. A notable aspect of MCs is the way the SWs are affected by the geometry of the system through the internal magnetic fields. This is called the demagnetization field and can be tuned by the orientation of an external magnetic field, often resulting in a reduction of symmetry compared to the original structural design [Neusser *et al.* (2011); Tacchi *et al.* (2015); Gross *et al.* (2021); Ji *et al.* (2022); Mamica (2023)]. The other possibility, unique to MC, is the modulation of the SW properties by the magnetization texture, with or without nanostructuralization. For example, the magnetization domain structure in the form of periodic stripes can have a periodicity up to 100 nm, forming a periodic potential for the propagation of SWs, which can be considered as a fully reprogrammable MC [Banerjee *et al.* (2017); Gruszecki *et al.* (2019); Yu *et al.* (2021); Petti *et al.* (2022); Szulc *et al.* (2022)]. In 1D and 2D, the MC can be also formed by the chain [Ma *et al.* (2015); Mruczkiewicz *et al.* (2016); Szulc *et al.* (2024)] or the array [Wang *et al.* (2020); Tang *et al.* (2023)] of skyrmions, due to the small skyrmion size, they are also stabilized with the period in deep nanoscale.

The MCs discussed above are predominantly planar structures that are uniform along the thickness, and due to the small thickness, the magnetization is also largely homogeneous. If the geometrical inhomogeneity or the magnetization texture becomes inhomogeneous along the thickness, we can call the system 3D [Beginin *et al.* (2019); Gubbiotti *et al.* (2021); Sadovnikov *et al.* (2022); Girardi *et al.* (2024)]. Strictly speaking, however, 3D MCs are characterized by a three-dimensional periodic distribution of two materials consisting of inclusion and matrix. Enriched by the additional

dimension, the properties of these systems were the focus of theoretical studies, including the exploration of magnonic bandgap phenomena [Krawczyk and Puzskarski (2006); Mamica *et al.* (2012); Romero Vivas *et al.* (2012)]. They have demonstrated critical aspects such as the threshold of magnetic contrast required between the constituent materials to open a band gap and its dependence on the crystallographic structure of the crystal [Krawczyk *et al.* (2010)]. In addition, it has been shown that the selection of an appropriate MC structure and filling fraction can lead to the design of anisotropic and strongly wavevector-dependent effective damping [Romero Vivas *et al.* (2012)], demonstrating the potential of 3D MCs to advance the field of magnonics and spintronics through nuanced control of wave propagation mechanisms in 3D space [Gubbiotti (2019)].

In addition to propagating waves that create bands in an MC and occupy the whole magnetic volume, an important aspect of the nanoscale magnonic systems is also the phenomenon of SW localization inside the 3D nanostructure or at the surfaces [Serha *et al.* (2022); Liu *et al.* (2020)]. A well-described type of SW localization already occurs on the surface of thin films in the Damon-Eshbach (DE) configuration [Damon and Eshbach (1961); Hurben and Patton (1995)], i.e., when the propagation of SWs is perpendicular to an applied external magnetic field that lies in the plane of the film and saturate the sample. The interplay between the dynamic stray fields from the surface and volume magnetic charges formed by oscillating magnetization in the film geometry leads to an asymmetry in the internal magnetic field distribution, creating a gradient in the effective magnetic field across the thickness (the non-zero wavenumber k is required for this effect). As a result, the SWs have a higher intensity near one of the surfaces of the film compared to the inner part and opposite surface. The intensity of these surface-localized modes decays exponentially from the surface of the film toward its center, with the decay length depending on the SW wavelength, i.e., being proportional to k . The side of localization changes with the reversal of the direction of the wavevector (or magnetic field orientation). This type of SW localization offers several advantages for magnonic applications, e.g., increasing the efficiency of SW excitation with inherent nonreciprocity and detection at the film surfaces [Schneider *et al.* (2008); Jamali *et al.* (2013)], which is particularly beneficial for devices that rely on surface-based SW manipulation [Inoue *et al.* (2011); Bessonov *et al.* (2015)]. In addition, confining the SWs to the surfaces reduces volumetric scattering and damping, potentially leading to lower energy loss and improved propagation characteristics [Yamamoto *et al.* (2019)]. Finally, the DE configuration enables the design of devices with directional propagation properties, i.e., nonreciprocal, which can be exploited in the development of directional magnonic waveguides and logic elements.

SW localization can also be caused by static demagnetization fields. A notable manifestation of this is the emergence of edge modes [Jorzick *et al.* (2002); Park *et al.* (2002); Bayer *et al.* (2006); Bailleul *et al.* (2003); Kruglyak *et al.* (2006)], where SWs are confined or propagated [Gruszecki *et al.* (2021, 2022)] along the edges of a system, to which static magnetization is perpendicular. The reduction of the internal magnetic field at the edges of the ferromagnetic element can be modified by the magnetization orientation and the shape of the edge, allowing to increase or decrease the localization of low-frequency SWs [Gołębiewski *et al.* (2023)]. This makes the edge SWs sensitive to the properties at the very edge of ferromagnets, which allows us to use them for sensing the magnetic properties [Maranville *et al.* (2006, 2007)].

Another interesting type of localization is the topologically protected propagation of SWs along customized paths, facilitated by the MC edges or interfaces between two MCs with different

topologies [Shindou *et al.* (2013b,a); Li *et al.* (2018); McClarty (2022); Zhuo *et al.* (2023)]. These edges or interfaces act as ideal waveguides, guiding the SWs in one direction and being immune to backscattering, resulting in high coherence even along sharply curved paths [Wang *et al.* (2018); Feilhauer *et al.* (2023)]. Such topological phases are characterized by so-called topological invariants [Kane and Mele (2005b,a); König *et al.* (2007)], such as Chern numbers, which describe the topological connection between bulk and boundary dynamics [Bansil *et al.* (2016)]. Recently, an extension to higher-order topological states has become cutting-edge research [Schindler *et al.* (2018)], realized especially with the use of the artificial crystal in photonics [El Hassan *et al.* (2019)] or acoustics [Ni *et al.* (2019)], and only initiated in magnonics showing corner SWs in 2D antiskyrmion crystal [Hirosawa *et al.* (2020)], and remains completely unexplored in 3D magnonic systems.

The study of 3D MCs holds great promise not only for SW localization phenomena. By tuning the geometry and lattice periods of their unit cells, these structures introduce an additional dimension for novel interactions, including various topological and geometric effects, and emergent material properties [Gubbiotti (2019); Fischer *et al.* (2020); Makarov *et al.* (2022); Cheenikundil *et al.* (2022); Fernández-Pacheco *et al.* (2017)]. Recent advancements in techniques such as X-ray vector nanotomography [Donnelly *et al.* (2017)], magnetic laminography [Donnelly *et al.* (2022)], two-photon lithography [Hunt *et al.* (2020); van den Berg *et al.* (2023)], focused electron beam deposition [Skoric *et al.* (2020)], and block copolymer templating [Llandro *et al.* (2020)] have enabled the fabrication of complex 3D magnetic systems at the nanoscale, providing the potential for rapid development of the field. Intriguing effects have already been observed in nanorods arranged in diamond-bond networks [May *et al.* (2019); Stenning *et al.* (2023)], facilitating the analysis of near-degenerate states and laying the groundwork for reconfigurable magnonic devices. Recently, gyroids [Luzzati and Spegt (1967); Schoen (1970); Han and Che (2018)], characterized by their chiral triple junctions and fully interconnected 3D network, have been fabricated from ferromagnetic metals [Llandro *et al.* (2020)]. Due to the interplay of geometric, chiral and potential topological properties in the nanoscale, the ferromagnetic gyroids can be regarded as 3D MCs possessing all the above-mentioned properties, making them an ideal structure for studying SW dynamics [Gołębiewski *et al.* (2024)]. In this chapter, we summarize the current state of research on ferromagnetic gyroids and present our preliminary results on SW dynamics within these structures.

1.2 Geometric properties of gyroidal networks

Since their discovery in 1970 [Schoen (1970)], gyroids have been of interest to research in mathematics, material engineering, and photonics. These structures, belonging to the $I4_132$ space group (No. 214) [Lambert *et al.* (1996)], owe their unique morphology to the cooperative formation at inorganic-organic interfaces, as evidenced in surfactant-silicate mesostructures [Monnier *et al.* (1993)]. This architecture has inspired a variety of studies in photonics, where gyroids have been employed as chiral beamsplitters, nonlinear optical metamaterials, and photonic crystals [Turner *et al.* (2013); Vignolini *et al.* (2012); Dolan *et al.* (2015); Michielsen and Stavenga (2008)]. Recent advancements in fabrication techniques (see Introduction 1.1) have also facilitated the creation of artificial systems inspired by gyroid geometry [Yan *et al.* (2012); Yáñez *et al.* (2016); Turner *et al.* (2013)].

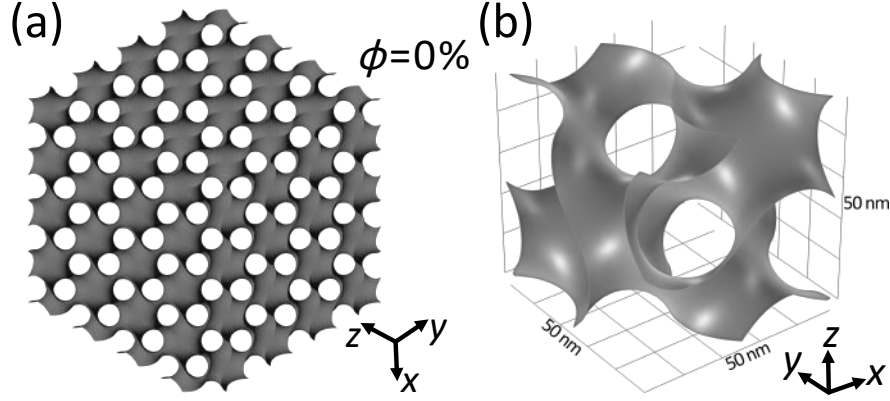


Figure 1.1 The gyroid surface model, illustrating the arrangement along the [111] crystallographic direction through an orthographic projection (a), revealing the hexagonal patterning inherent to the interconnected channels of the system. Panel (b) shows the unit cell in a perspective projection, providing a dynamic view of its geometric configuration.

As detailed in Refs. [Schoen (1970, 2012); Rosi *et al.* (2020)], the gyroid is characterized as a unique triple periodic minimal surface (see Fig. 1.1). Its most notable property is its zero mean curvature, meaning that each point on the surface functions as a saddle point with equal and opposite principal curvatures [Dacorogna (2014)]. This surface extends periodically along three orthogonal vectors and exhibits inherent chirality, lacking any symmetry plane or center, yet retaining rotational symmetry elements [Wohlgemuth *et al.* (2001)]. Due to its triple periodic nature, the gyroid is conceptualized as a crystalline structure [Chen *et al.* (2013)], adhering to the body-centered cubic (bcc) Bravais lattice and associated with the point group O , or described as $I4_132$ in Hermann-Mauguin notation. This cubic group, being purely rotational, emphasizes the chiral nature of the gyroid, and the prefix I indicates a body-centered arrangement, suggesting a non-primitive, body-centered conventional unit cell.

Historically, the gyroidal surface was first described using the conjugate surface construction method [Karcher (1989)], with its embedding later confirmed theoretically in Ref. [Große-Brauckmann and Wohlgemuth (1996)]. Subsequent studies dealt with the volume fractions of gyroids, especially those with constant mean curvature [Große-Brauckmann (1997)]. In a broader scientific context, the gyroid is recognized as Laves' graph of girth ten [Sunada (2008)] and the K_4 crystal [Hyde *et al.* (2008); Mizuno *et al.* (2019)], known for their efficient space-filling properties and high symmetry. The connection to Laves' graph comes from the gyroid's intricate network of vertices and edges, which mimics the uniformity and connectivity of the graph. Similarly, the local arrangement of atoms in materials that form gyroid structures may be analogous to the tetrahedral coordination of the K_4 crystal.

Its complex design features cubic unit cells interconnected by elliptical cross-section nanorods, as detailed in Ref. [Dolan *et al.* (2015)]. With a volume filling fraction of $\phi = 0\%$, shown in Fig. 1.1, the gyroid surface divides space into two distinct labyrinths, intersecting at 70.5° . Their mathematical

$$\begin{aligned} & \sin(2\pi x/L) \cos(2\pi y/L) + \\ & \sin(2\pi y/L) \cos(2\pi z/L) + \\ & \sin(2\pi z/L) \cos(2\pi x/L) < (101.5 - 2\phi)/68.1, \end{aligned} \quad (1.1)$$

1.2.1 Block copolymer self-assembly and fabrication techniques

Diagram illustrating the classification of copolymers based on their sequence:

- homopolymer
- alternating
- AB block
- ABA block
- ABC block

The last three categories (alternating, AB block, ABA block, and ABC block) are collectively labeled as **copolymers**.

Figure 1.2 Schematic illustration of various polymer types. Block copolymers consist of two or more homopolymer segments (A) connected by covalent bonds. Diblock copolymers contain two distinct segments (AB), while triblock copolymers have three (ABC). A block is technically defined as a segment of a macromolecule, made up of numerous repeating units, with at least one characteristic absent in adjacent segments.

Due to their customizable chemical compositions and the ability to form a wide array of structures, block copolymers have found applications across numerous fields. They can be tailored for use in nanoscale templates for electronic devices, photonic crystals, drug delivery systems, and materials with specific mechanical, optical, or conductive properties. The versatility and tunability of block copolymers, due to the variety of monomers from which they can be made and their unique self-assembly properties, make them a powerful tool in materials science and nanotechnology. For a comprehensive overview, refer to [Dolan *et al.* (2015); Hyde *et al.* (1997c,b,a); Segalman (2005); Cheng *et al.* (2006)].

A simple example of covalently bonded homopolymers are the linear AB diblock copolymers, representing the essential behavior of more complex systems like linear triblock terpolymers. The morphology of diblock copolymers in thermodynamic equilibrium is influenced by three key parameters: N (total degree of polymerization, i.e., the number of monomer units in a polymer chain), f_A or f_B (volume fractions of each homopolymer), and χ (the Flory-Huggins interaction parameter, indicating monomer repulsion). In block copolymers, a higher χ value signifies greater incompatibility between the blocks, driving them to segregate and self-assemble into complex structures to minimize the free energy of the system, e.g., gyroids (Fig. 1.3 – G/G'). The interplay between χ , which promotes phase separation, and N , which influences the entropy and enthalpy of the system, guides the self-assembly process.

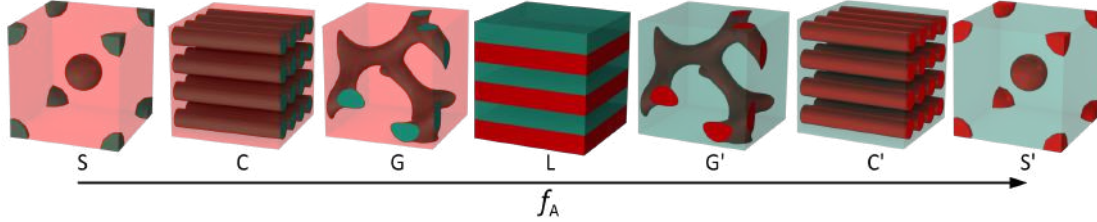


Figure 1.3 Equilibrium morphologies of AB diblock copolymers in a bulk, varying as a function of the volume fraction f_A of the blocks and the interaction parameter χ . The morphologies are categorized as follows S/S' – body-centered cubic spheres, C/C' – hexagonally packed cylinders, G/G' – bicontinuous gyroids, and L – lamellae.

As the block copolymers self-organize, the gyroid structure emerges as a result of the balance between the repulsive interactions (dictated by χ) and the chain length of the polymers (defined by N). This balance leads to the formation of continuous, triple periodic minimal surfaces, which are characteristic of the gyroid structure. This architecture, with interconnected labyrinths of both materials, is thus a direct consequence of the molecular properties of the block copolymers and their drive to achieve a thermodynamically favorable configuration. Larger gyroid structures, scaling from millimeters to sub-millimeters, are typically fabricated using top-down methods [Yan *et al.* (2012); Yáñez *et al.* (2016); Turner *et al.* (2013); Gan *et al.* (2016)]. Conversely, the creation of nanostructures with unit cells below 100 nm is predominantly achieved through bottom-up techniques [Armatas and Kanatzidis (2006); Kresge *et al.* (1992)]. The process involves microphase separation in copolymers, resulting in gyroid networks of a minority polymer block within a majority block matrix [Ross *et al.* (2014); She *et al.* (2013)].

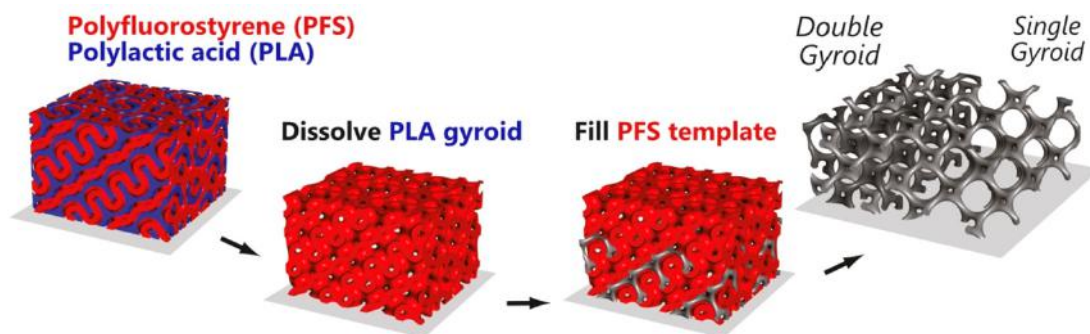


Figure 1.4 Fabrication and structural characterization of gyroid nanostructures. This scheme shows the process for creating free-standing metallic gyroid nanostructures, involving the thermal annealing of a block copolymer template, followed by the selective removal of the minority block and subsequent electrodeposition. Reprinted (adapted) with permission from *Nano Lett.* 2020, 20, 5, 3642-3650. Copyright 2024 American Chemical Society.

The formation of complex structures using block copolymers as templates involves a multi-step process that exploits the self-assembly properties of block copolymers and the technique of electrodeposition to introduce ferromagnetic materials, such as permalloy (Py) or nickel (Ni), into the predetermined patterns. One of the polymer blocks is selectively removed to create a porous template that retains the architecture. This can be achieved by various methods, including chemical etching or UV degradation, depending on the nature of the block copolymer. With the porous template in place, electrodeposition is used to fill the voids with a ferromagnetic material, as illustrated in Fig. 1.4. In this instance, a diblock copolymer of poly(4-fluorostyrene) (PFS) and 38% poly(lactic acid) (PLA) is employed, with PFS and PLA serving as the majority and minority blocks, respectively [Scherer *et al.* (2014); Llandro *et al.* (2020)]. During electrodeposition, the template is immersed in an electrolytic solution containing ions of the ferromagnetic material. When a voltage is applied, the ions are reduced and deposited onto the conductive areas of the template, gradually filling the structure. After the electrodeposition process is complete, the remaining block copolymer template is removed, often by solvent washing or thermal decomposition, leaving a freestanding structure composed entirely of the ferromagnetic material. The end product is a 3D structure of ferromagnetic material that replicates the geometry of the original template.

In Fig. 1.4, the fabrication of magnetic (based on Ni) gyroid nanostructures from Ref. [Llandro *et al.* (2020)], featuring unit cell dimensions smaller than 50 nm, is demonstrated. These nanostructures are realized through electrodeposition into block copolymer templates, yielding $\text{Ni}_{75}\text{Fe}_{25}$ gyroids. The self-assembly of 3D nanostructures, especially when integrated with inorganic components [Simon *et al.* (2001)], allows unprecedented morphological control at the nanoscale, opening new avenues for magnetism and magnonics. The SW interactions within gyroids are complex and involve, among others, shape anisotropy, inhomogeneous demagnetization fields, curved surfaces, and chirality. Our research aims to show the complexity of these interactions, provide an understanding of the magnetic behavior in gyroids, and lay the framework for future explorations and use of 3D ferromagnetic magnonics.

1.3 Gyroid structures in magnetism

Short SWs, with their nanoscale wavelengths and microwave frequencies, enable high-density, high-frequency applications of miniaturized magnonic devices [Chumak *et al.* (2015)]. The concepts of SWs in connection with the chirality inherent in the magnetization dynamics, as discussed above and reviewed in Ref. [Kruglyak (2021)], on the one hand, and introduced by the Dzyaloshinskii-Moriya interaction (DMI) [Tacchi *et al.* (2023)] or geometric curvature [Otálora *et al.* (2017); Sheka *et al.* (2022)], on the other hand, may play an important role in the further development of information processing technologies based on magnonics [Chen *et al.* (2020, 2021)]. Chirality, which refers to the preference of spin structures to twist in a particular direction, facilitates also directional SW propagation, opening the door to non-reciprocal devices. DMI, which exists in systems with broken inversion symmetry [Gan *et al.* (2016)], stabilizes chiral magnetic textures, improving control over spin structure and enabling the design of robust, energy-efficient memory devices, the structures which can also be exploited for magnonics [Garcia-Sanchez *et al.* (2014)]. Similar properties are expected to exist in curvilinear ferromagnetic systems, since curvature, when introduced on a length comparable to the exchange length, introduces the anisotropic exchange in the same form as DMI [Sheka *et al.* (2022)]. Therefore, the complex architecture of gyroidal structures, with the 3D gyroid elementary cell characterized by curvature and chirality (see Figs. 1.1 and 1.6), provides a unique, three-dimensional platform for exploiting all of these phenomena, making it a good candidate for further research, and promising applications. Nonetheless, the study of magnetization dynamics within periodic 3D nanostructures is still in its early stages. While extensive research exists on SWs in uniform, 1D and 2D structures, investigations into collective SW dynamics in 3D artificial systems [May *et al.* (2021); Guo *et al.* (2023); Gubbiotti (2019); Fernández-Pacheco *et al.* (2017)], particularly gyroids [Gołębiewski *et al.* (2024)], remain limited. We attempt to summarize existing and explore new research directions on the collective dynamics of SWs in gyroidal nanostructures.

As described above, the inherent chirality and curvature of nanoscale magnetic gyroids offer a promising pathway for controlling non-collinear spin textures. Recent studies have underscored this potential [Lich *et al.* (2023)], and the experimental visualization of magnetic structures in $\text{Ni}_{75}\text{Fe}_{25}$ gyroid networks has provided further evidence [Llandro *et al.* (2020)]. However, the DMI and curvature-induced anisotropy, which add another layer of complexity to research in 3D ferromagnetic structures [Hertel (2013); Gaididei *et al.* (2014)], have not yet been explored in gyroidal structures. Similarly, novel physical effects observed in curved magnetic wires and films [Sheka (2021)], and the integration of chiral and topological properties [Shindou *et al.* (2013b); McClarty (2022)], have not been tested in gyroids. Furthermore, the potential of gyroids extends further, with the numerous energetically equivalent stable states, suggesting suitability for the realization of artificial spin-ice systems in 3D. Indeed, gyroidal magnetic nanostructures, particularly those with at least one dimension in the exchange length scale, have emerged as key to the realization of in-volume system phenomena such as monopole-type excitations [Wannier (1950); Diep (2013); Lacroix *et al.* (2011)], which were previously observed only in two-dimensional (2D) systems [Skjærvø *et al.* (2020); Nisoli *et al.* (2017)].

Taking the magnonic perspective, we use micromagnetic simulations to reveal the collective dynamics of SWs in gyroids. This approach is consistent with the findings in Ref. [Demidov *et al.*

(2010)], where the importance of direct observation and mapping of SWs, especially in nano-oscillators, is highlighted. An interesting aspect of our investigations is to study the ferromagnetic resonance and SW dispersion within gyroids. The frequency-wavevector relationship of SWs is of particular interest in complex 3D geometries, where the multidimensional nature introduces additional complexities in SW propagation, potentially leading to tunable, magnetic field-directed band gaps, mode crossings/hybridizations, and unconventional group velocities. By analyzing these properties, we aim to unveil the potential of gyroids as magnonic metamaterials and efficient SW carriers.

1.3.1 Static magnetization configuration

The study of static magnetization in 3D gyroidal ferromagnetic nanostructures apart from learning the specifics of these structures, also can advance our understanding of complex magnetic systems in general, and open up new technological possibilities, as they have already been recognized for their intricate, frustrated remanent states [Llandro *et al.* (2020)]. These states are inherently ferromagnetic, but do not conform to a unique equilibrium configuration. The detailed imaging and mapping of gyroids, shown in Fig. 1.5, provide a deeper insight into their magnetic structure, highlighting the complex interplay between the magnetic fields and the intricate single and double gyroid architecture. Figure 1.5(b) shows the magnetic induction map of the double-gyroid nanostructure. The external stray field surrounding the gyroid exhibits dipole-like behavior aligned with the saturating field (\mathbf{H}). Within the structure, multiple flux-closed loops are evident, some of which enclose only a single unit cell. However, identifying the chirality of these loops is challenging due to the integration of the magnetic induction map across the thickness of several unit cells and the entangled nature of the double-gyroid networks.

In the single-gyroid region [Fig. 1.5(d)], the correlation between the structure and the magnetization of the ferromagnetic gyroid becomes more pronounced. The external stray field remains dipole-like, but the remanent state of the single gyroid is more complex than a simple network of flux-closed loops. The contours are generally aligned with the structure, but in some regions (marked with the arrows) the flux lines cut directly across the struts, implying that the magnetization is transverse to the strut axis. In other regions, the flux contours encircle specific vertices, possibly indicating that the magnetization of the three constituent struts converge or diverge from the vertex center.

In Ref. [Lich *et al.* (2023)], the authors have presented an insightful analysis through phase-field simulation studies, focusing on the formation and switching behavior of magnetization textures within Py gyroid nanostructures with a periodicity of 50 nm. The study uncovers the coexistence of left-handed (LH) and right-handed (RH) helices in these structures, a feature particularly pronounced in gyroids with small solid volume fractions. Moreover, it has been demonstrated that at small ϕ , the magnetization textures conform to the ice rule. However, as ϕ increases, this rule is disrupted, leading to magnetic field texture frustration, a phenomenon that becomes prominent at a critical volume fraction of about 30%. Furthermore, the findings indicate an increase in the coercive field as the volume fraction rises from 10 to 50%, followed by a reversal of this trend with further increases in ϕ . This behavior is attributed to the balance between LH and RH magnetic helices, with global switching events occurring near $\phi = 50\%$, while local switching is observed in other volume

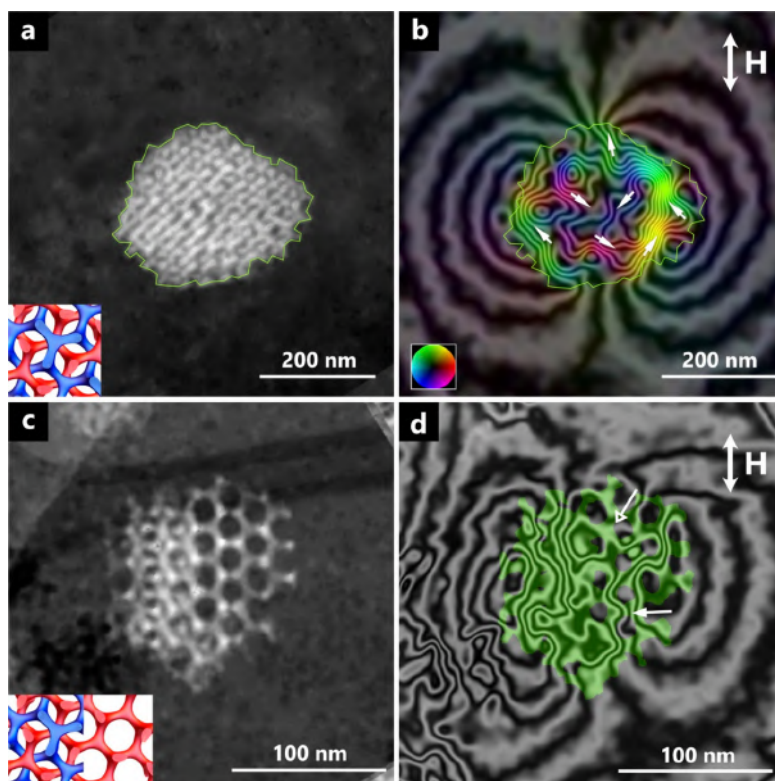


Figure 1.5 Magnetographic analysis of Py double and single gyroid structures with unit cell size $L = 42$ nm: insets illustrate simulated models of double-gyroids and hybrid double/single-gyroid structures, with each gyroid network marked in red and blue. Panels (a) and (b) display the phase contribution of the mean inner potential and the map of magnetic induction for a double-gyroids. Bidirectional arrows indicate the saturation magnetic field (\mathbf{H}) direction. Stray magnetic fields around the structure are traced by contour lines, which within the struts is non-uniform, as indicated by unidirectional arrows representing varied field directions. The structure's outline, derived from the phase shift's mean inner potential contribution, is shown in (b). In panels (c) and (d), the phase contribution of the mean inner potential and the corresponding magnetic flux contour map are depicted for a sample containing both double-gyroid and single-gyroid regions. In (d), the gyroid particle is masked in green and superimposed with contour lines to illustrate the relationship between field lines and gyroid struts. Points where flux contours intersect gyroid struts or loop around vertices are marked with closed and open unidirectional arrows, respectively. The contour interval for both (b) and (d) is set at $2\pi/64$ radians. Reprinted (adapted) with permission from *Nano Lett.* 2020, 20, 5, 3642-3650. Copyright 2024 American Chemical Society.

fractions. They summarize the relationship between solid volume fraction and static magnetization distribution in gyroids.

Exploring the realm of static magnetism within complex 3D structures [Hsueh *et al.* (2011)] opens up promising avenues of research, particularly in the creation and control of topological spin textures such as skyrmions, torons [Ji *et al.* (2022)] and hopfions [Tai and Smalyukh (2018)] and

others [Wu and Smalyukh (2022)]. The curvature and topology inherent in gyroids provide a novel platform for studying how these structures can stabilize such textures. Additional research focusing on static magnetization configurations under external fields could deepen our understanding of domain distribution and orientation. Also, the process of magnetization reversal in gyroids, influenced by geometry and thermal fluctuations, could provide valuable insights into material optimization for precise magnetic switching. Broadening the scope to include hybrid structures by integrating materials such as superconductors or topological insulators with gyroidal ferromagnets opens up other research opportunities.

Studying the magnetization texture and dynamics at the level of individual nanostructures, unit cells, vertices and struts, is essential for a comprehensive understanding of their magnetic behavior. Current research suggests the possibility of multiple equivalent magnetization configurations within the 3D gyroid network, which is particularly promising for applications such as reservoir computing [Tanaka *et al.* (2019)], where systems benefit from high interconnectivity and a variety of stable states. The ability to access and manipulate these different states could enable new paradigms in nanoscale computing by exploiting the properties of these complex magnetic 3D structures.

1.3.2 Magnetization dynamics

As already mentioned in the Introduction, the study of SW dynamics in 3D nanostructures is at a very early stage [Gubbiotti (2019); Cheenikundil *et al.* (2022); Li *et al.* (2023)], especially experimentally [Sahoo *et al.* (2018); Donnelly *et al.* (2020); Guo *et al.* (2023); Girardi *et al.* (2024)]. In the following subsections, we will summarize our research on Ni-based gyroids, including experimental ferromagnetic resonance (FMR) studies and numerical simulations. Here, the gyroid sample's unit cell is defined with a dimension of 50 nm and $\phi = 10\%$, as shown in Fig. 1.6. This specific dimensionality leads to strut diameters that align with crucial nanoscale measures, e.g., the exchange length (around 9 nm for Ni). This congruence highlights the profound impact of nanoscale features on the magnetic dynamics and properties we observe.

1.3.2.1 Gyroidal crystallography vs. ferromagnetic response

Our recent work [Gołębiewski *et al.* (2024)] presents a synergistic approach combining micromagnetic simulations and FMR measurements, employed to examine the magnetic properties of three-dimensional gyroidal Ni nanostructures. This investigation reveals several distinctive characteristics of the gyroid network, particularly the pronounced influence of the static, external magnetic field orientation on the ferromagnetic response. This relationship is closely linked to the crystallographic alignment of the gyroid structure, as presented in Fig. 1.7.

We utilize the finite element method (FEM) micromagnetic simulations in *tetmag*, both in the time domain for determining static magnetization structures [Hertel (2023)], and, using add-on algorithm, in the frequency domain for analyzing oscillatory, magnonic properties [d'Aquino and Hertel (2023)] – see more details in Appendix A.1. The following, Ni material parameters have been used: the saturation magnetization $M_S = 480$ kA/m, the exchange stiffness $A_{\text{ex}} = 13$ pJ/m, the Gilbert damping coefficient $\alpha = 0.008$, and the g -factor of 2.14 [Coey (2010); Singh *et al.* (1976)].

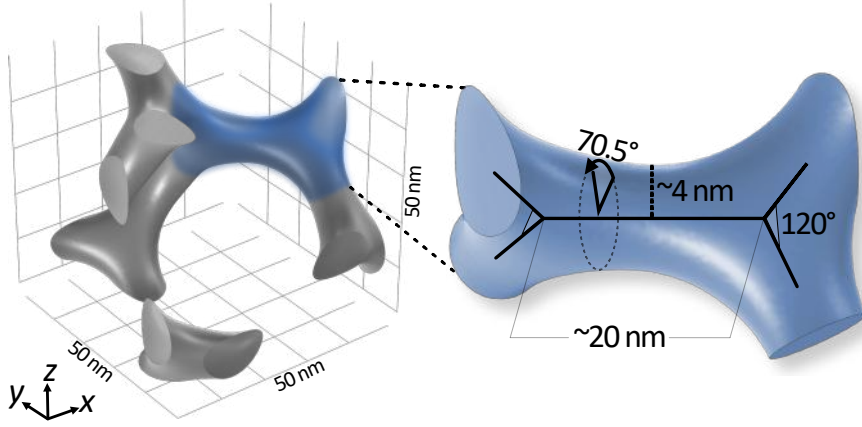


Figure 1.6 Illustration of the cubic gyroid unit cell tailored for micromagnetic simulations, with dimensions $L = 50$ nm and a volume fraction of $\phi = 10\%$. An enlarged inset highlights the chiral linkage between two primary gyroid nodes, emphasizing key geometric features.

We examine the impact of three specific field directions, aligned with the crystallographic axes $[100]$, $[110]$, and $[111]$, on finite-sized gyroids, see Fig. 1.7. The findings from the resonance spectra simulations attribute the observed shifts in resonance signals in the rotating gyroid sample to crystallographic anisotropy. Moreover, several bulk SW modes, as identified in this work, exhibit a predominantly localization on the different regions across the perpendicular axis of the gyroid structure, on the facets perpendicular to the $[110]$ and $[100]$ magnetic field directions. This behavior likely stems from a combined effect of crystallographic influence and shape anisotropy impacting the localization of resonant modes across various regions, potentially influenced by the system's chirality. Furthermore, we identified some SW modes localized on the outer surfaces of the gyroid structure (see the modes marked with 'x' in the spectra shown in Fig. 1.7). This also indicates the important influence of the shape and outer surfaces of the 3D nanostructure on the SW dynamics. This observation prompts us to investigate the surface effects further. The preliminary results of our numerical studies of surface-localized SW modes are summarized in the next section.

The *tetmag* simulations were complemented by meticulous experimental measurements using broadband FMR, where a multi-domain (multiple, interconnected sub-parts with different crystallographic orientations) gyroid sample was positioned on a coplanar waveguide (CPW) line. This setup facilitated the analysis of distinctions and correlations between a solid, uniform Ni layer and the gyroid-structured segment of the sample. The Ni gyroid nanostructure analyzed was fabricated through the thermal annealing of a block copolymer template [detailed in Sec. 1.2.1 (Fig. 1.4) and Ref. [Llandro *et al.* (2020)]], followed by selective dissolution of one of the gyroid-forming blocks and filling the resultant right-handed gyroid network with Ni by electrodeposition ($L = 50$ nm, $\phi = 10\%$). Performed measurements and provided numerical analysis allow us to conceptualize gyroid films as homogeneous materials or magnonic metamaterials, where the effective saturation magnetization is reduced in proportion to the gyroid's filling factor – see Fig. 1.8. We can see, that the gyroid signal exhibits a broader frequency full-width at half-maximum (FWHM)

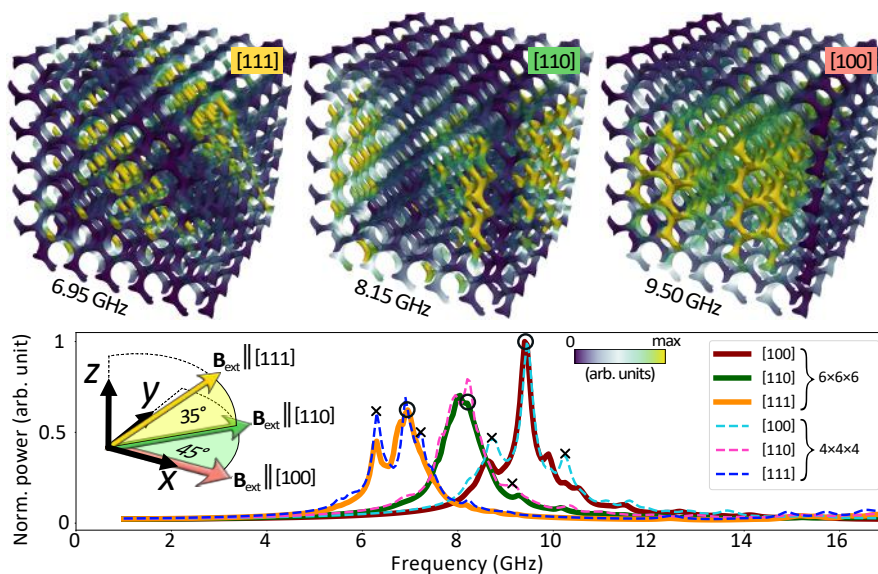


Figure 1.7 Spectral analysis of SW modes in a $6 \times 6 \times 6$ gyroid structure. The lower part of the figure shows the frequency spectra with high-intensity volume modes highlighted by black circles. For comparison, spectra of more compact structures (dotted lines) are superimposed, showing a significant reduction in the intensity of edge modes (indicated by crosses) with increasing structure size. The color gradient in the mode visualization corresponds to the imaginary part of the magnetic susceptibility. Reprinted (adapted) with permission from *ACS Appl. Mater. Interfaces* 2024, 16, 17, 22177-22188 licensed under CC-BY 4.0. Copyright 2024 American Chemical Society.

compared to that of homogeneous Ni. For instance, at a magnetic field of 450 mT, the FWHM is 3.69 GHz for the gyroid and 3.09 GHz for Ni. This broader signal is likely due to the multidomain nature of the sample. Specifically, the observed signal from the gyroid represents an average from multiple domains with varying crystallographic orientations located above the CPW. From the FMR measurements shown in Fig. 1.8(e), we deduce an average FWHM difference of 1.3 GHz across various external magnetic field values. Micromagnetic simulations for a cube-shaped sample (Fig. 1.7) indicate a maximum peak separation of 2.95 GHz at 300 mT, specifically between the [100] and [111] crystallographic directions. These simulations evaluated the crystallographic orientations that represent the most divergent configurations of the gyroid lattice relative to the applied field, resulting in the largest possible separation of resonant frequencies. In field-swept FMR experiments conducted at a fixed frequency, the absorption line FWHM conforms to the equation $\mu_0 \Delta H = 4\pi\alpha f/\gamma$. This relationship holds when the magnetization vector is aligned with the applied magnetic field, either in-plane or perpendicular to it, leading to a linewidth that scales proportionally with frequency. The slope of this scaling is defined by the Gilbert damping parameter α . In addition to this intrinsic contribution, empirical data suggest the presence of a frequency-independent term (see Eq. A.7), which contributes to the overall linewidth observed in the experiments. Experimental investigations have also enabled a linear regression analysis of FWHM across a spectrum of B_{MW} frequencies, as depicted in Fig. 1.8(f) for the designated orientations of the sample over CPW. This analytical

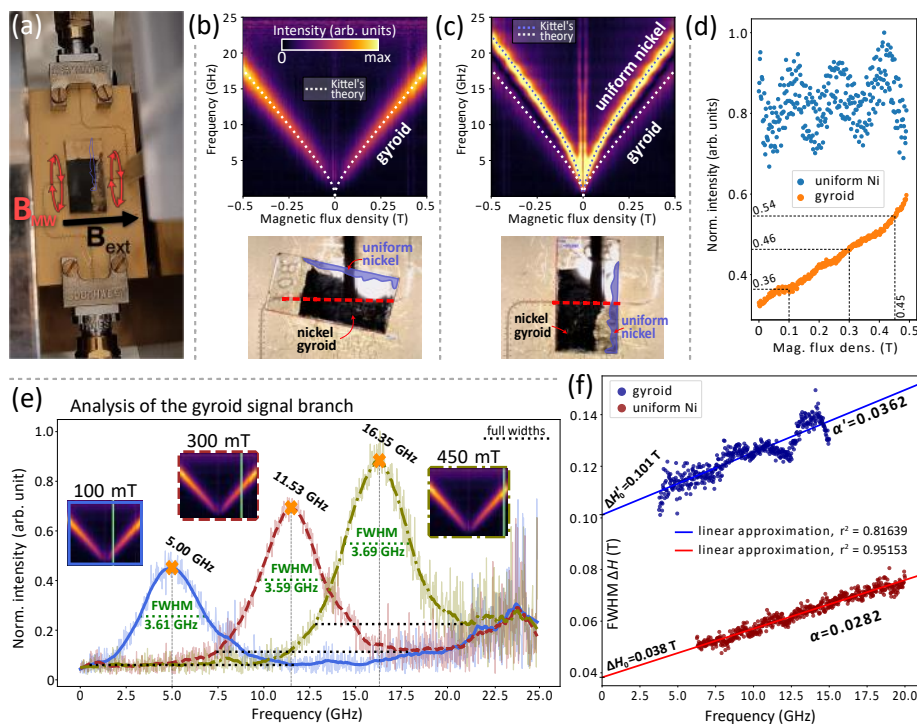


Figure 1.8 A broadband FMR measurement on a Ni gyroid structure. The sample was repositioned relative to the CPW to study the effect of an additional homogeneous Ni layer. Two configurations were used to assess energy absorption from the microwave field B_{MW} , applied perpendicular to the static magnetic field (a). Dynamic magnetization amplitude as a function of static magnetic flux density and frequency for selected configurations are shown in (b) and (c). A strong signal from the gyroid layer appears when the CPW aligns directly below it (b), while a higher-frequency signal from the uniform Ni layer is observed when the CPW intersects its projected position (highlighted in purple) (c). Dotted lines represent theoretical fits using the Kittel formula (Eq. A.6). For the uniform Ni, parameters from micromagnetic simulations were used; for the gyroid, calculated effective parameters ($M_{eff} = 132$ kA/m, g -factor of 2.2) were applied to the formula. Plot (d) summarizes peak intensities of FMR signals (blue dots for uniform Ni, orange dots for gyroid) as a function of external magnetic field strength, with normalized values for 100 mT, 300 mT, and 45 mT. Plot (e) provides a cross-sectional analysis of FMR signals at different external magnetic fields: solid blue line for $B_{ext} = 100$ mT, dashed brown line for $B_{ext} = 300$ mT, and dash-dotted green line for $B_{ext} = 450$ mT. Horizontal dashed green lines indicate the FWHM for each section. Orange crosses mark peak maxima and corresponding frequencies. Insets show intensity plots from FMR measurements with green vertical lines marking specific section locations. Plot (f) shows the magnetic field FWHMs as a function of frequency for FMR signals of gyroid (purple dots) and uniform Ni (dark red dots). Linear regression, based on experimental data and Eq. A.7, estimates determination coefficient r^2 , ΔH_0 (from the abscissa), and damping values α (from the slope). Parameters for the gyroid are marked with a prime ('). Reprinted (adapted) with permission from *ACS Appl. Mater. Interfaces* 2024, 16, 17, 22177-22188 licensed under CC-BY 4.0. Copyright 2024 American Chemical Society.

approach is instrumental in ascertaining the damping values α and the inhomogeneous linewidth contribution ΔH_0 for both the homogeneous Ni layer and the gyroidal structure, respectively. In the first case, the derived values are $\alpha = 0.0282 \pm 2.54\%$ and $\Delta H_0 = 0.038 \pm 1.28\%$ T. Comparatively, the gyroidal structure exhibits $\alpha' = 0.0362 \pm 6.49\%$ and $\Delta H'_0 = 0.101 \pm 1.05\%$ T. Larger α' for the gyroid structure is likely attributable to the scattering of SW modes within the nanowires, which are much thinner than the bulk Ni and exhibit complex noncollinear interconnections.

1.3.2.2 Localization properties

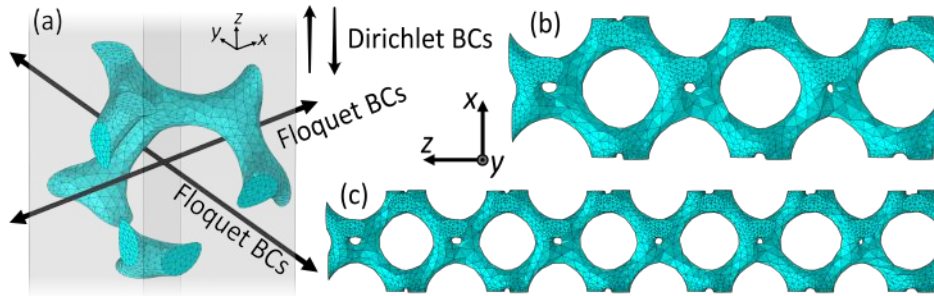


Figure 1.9 Visualization of discretization grids for gyroid structures utilized in Comsol micromagnetic simulations. Arrows indicate the Bloch-Floquet boundary conditions (BCs) along the x and y axes, defining the structure's plane. In contrast, along the z -axis, perpendicular and at a significant distance from the plane, Dirichlet boundary conditions (BCs) are implemented. This setup is exemplified for a single-unit thick ($1 \times 1 \times 1$) gyroid layer in (a), and similarly for other models: $1 \times 1 \times 3$ in (b), and $1 \times 1 \times 6$ in (c). Note that the relative sizes of the structures are not to scale in this representation.

To study surface effects in gyroids, we simulate the gyroid in a thin film geometry in dependence on the thickness of the gyroid structure and the orientation of the external magnetic field. To avoid the influence of the lateral edges effects on the SW spectra we employ Bloch-Floquet boundary conditions at the unit cell boundaries. The simulations are performed with Comsol Multiphysics software. In this implementation, we assume full magnetization saturation and solve the Landau-Lifshitz-Gilbert equations in the linear approximation as an eigenproblem. Further details about this numerical approach can be found in Refs [Mruczkiewicz *et al.* (2013); Rychly *et al.* (2018)] in 2D implementation, and in the Appendix A.1. With that, we model an infinite gyroidal plane with varying thicknesses: 1, 3, and 6 unit cells, corresponding to dimensions of 50, 150, and 300 nm, respectively (Fig. 1.9). Material parameters identical to those in the previous section were used. Throughout our simulations, the external magnetic field, \mathbf{B}_{ext} , was maintained constant at 500 mT and oriented in the plane of the gyroidal plane along the crystallographic direction [100]. This field strength, corroborated by Ref. [Llandro *et al.* (2020)], supports our assumption of complete saturation of the structure aligned with the external magnetic field's direction.

During the analysis of the micromagnetic simulation results, a surprising pattern emerged in the behavior of the lowest frequency mode, which exhibited the highest intensity, particularly under the influence of the rotating in-plane magnetic field. It is, an intriguing switch in the area of localization

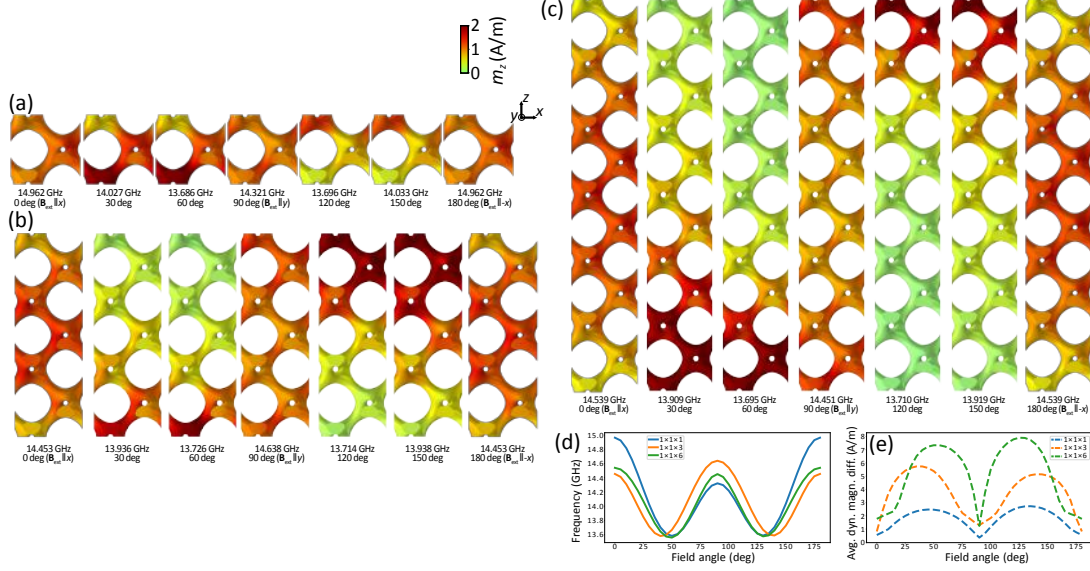


Figure 1.10 Distribution of low frequency, the most intensive mode in (a) $1 \times 1 \times 1$, (b) $1 \times 1 \times 3$, and $1 \times 1 \times 6$ gyroids ($\phi = 10\%$) and their localization as a function of magnetic field rotation ($B_{\text{ext}} = 0.5$ T) with respect to the x -axis. The plots below illustrate the impact of the rotating field's angle relative to the structure on the eigenfrequency (d) and the variation between the minimum and maximum dynamic magnetization components within the unit cell (e).

of SWs from the bottom [at 30 and 60 deg in Fig. 1.10(b) and (c)] to the top of the layer (at 120 and 150 deg). Between these angles, specifically at 0, 90, and 180 degrees, this mode exhibits a bulk character. This shift in mode amplitude concentration regions suggests a complex interplay between magnetic field orientation and intrinsic properties of the gyroid structure, involving dipolar and exchange interactions. The change of the amplitude localization is followed by the change of the resonance frequency [see Fig. 1.10(d)], the lowest (about 13.6 GHz at the field angle of 45-50 deg and 125-130 deg) occurs when the mode has a surface character and increases with the transition into the bulk region.

Preliminary analysis indicates that this localization phenomenon is more pronounced in structures with increased thickness, i.e., characterized by a higher number of unit cells per thickness, as can be seen by comprising SW amplitude distribution in Fig. 1.10(a)-(c). This has been quantified by plotting the difference between the maximum and minimum value of the dynamic magnetization component in the unit cell in Fig. 1.10(d). The largest value of this difference indicates stronger amplitude localization. Interestingly, the angle at which maximum localization occurs also shifts with changes in film thickness. In such cases, the crystallography exerts a greater influence on the SW amplitude distribution and indicates a possible influence of chirality.

The findings described are intriguing and require further investigation to unravel the complex interactions that govern these phenomena. Understanding the dynamics controlling the localization

of SW modes in these structures has the potential to open up new applications in 3D magnonics, such as sensing or controlling dynamical coupling by rotating the magnetic field.

1.3.2.3 Dispersion relation

The surface character of the SW mode at $k = 0$ has not been found in homogeneous thin ferromagnetic films so far. Thus, it is interesting to see how this and other modes in the gyroid structure evolve with the wavevector. The introduced Bloch-Floquet boundary conditions in Comsol MultiPhysics are very well suited for the calculation of the dispersion relation, just by parametrize the solution with the Bloch wavevector, k .

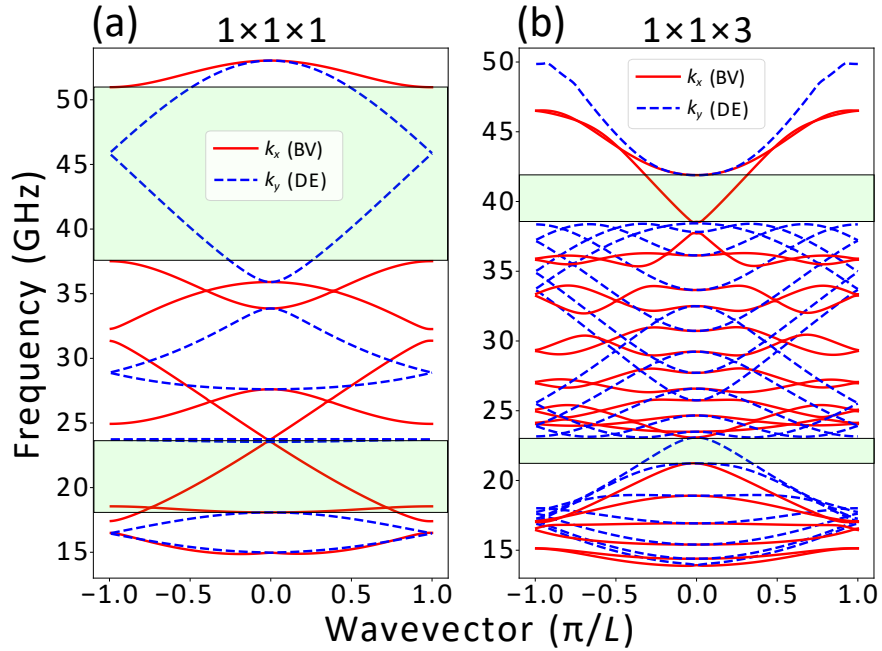


Figure 1.11 The dispersion relations within the 1st Brillouin zone for a gyroid structure along the x -axis ([100] crystallographic direction), characterized by a 10% filling factor and 1 (a), and 3 (b) unit cells per thickness. The data is color-coded to distinguish between different configurations: the BV configuration is represented in red, while the DE configuration is depicted in blue. These plots have been generated in the presence of an in-plane external magnetic field, $B_{\text{ext}} = 0.5$ T, oriented along the x -axis. Wider band gaps specific to one of the configurations are highlighted using green rectangles.

In reciprocal lattice space, the range $-\pi/L < k < \pi/L$ defines the 1st Brillouin zone along the main direction of the cubic lattice. The primary focus is on the 1st Brillouin zone, as the bands from the subsequent zones are folded back to the 1st zone, and the whole magnonic band structure has a periodicity with the period equal to the reciprocal lattice vector $2\pi/L$. Our research delves into the SW dispersion in a thin film based on the gyroid structure, defined in the previous section. It displays dispersion relations similar to those of traditional magnonic crystals but with specific

features. As evidenced in Fig. 1.11, the direction of the magnetic field relative to SW propagation significantly influences the gyroid's band structure, leading to the opening and closing of band gaps. This phenomenon is exemplified in our simulations of the $1 \times 1 \times 1$ [Fig. 1.11(a)] and $1 \times 1 \times 3$ [Fig. 1.11(b)] gyroid structures for two relative orientations of the in-plane magnetic field and wavevector, i.e., DE configuration in which both directions are orthogonal, and backward volume (BV) configuration in which these vectors are parallel. In the DE configuration, in $1 \times 1 \times 1$ structure, we observe a wide band gap from 18.1 to 23.6 GHz, limited by the flat band, and another band gap just above, from about 23.8 to 27.9 GHz. On the other hand, in BV configuration, there are only two very narrow gaps at low frequencies and a wide band gap between 37.6 GHz and 51.2 GHz. The spectra change significantly when we increase the film thickness to 3 unit cells [Fig. 1.11(b)]. In this case, the band structure is much denser due to the decreasing frequency of the SW modes quantized along the thickness. The band gaps at low frequencies are now closed for DE, but it is opened for BV configuration, although it is rather small, only 1.8 GHz wide (around 22 GHz). In higher frequencies, the band gap in DE configuration opens (38.6-41.9 GHz). Interestingly, in the frequency range from 23 to 38.6 GHz, the DE bands show a pronounced slope with numerous crossings but no hybridizations, whereas in the BV configuration, extensive hybridizations result in a wavy band structure as a function of k , separated by distinct band gaps.

The preliminary analyses reveal the complexities of SW propagation in thin films based on gyroid structures, such as the emergence of band gaps and the crossing of different modes. The distinctive dispersion properties of gyroids, as highlighted in our results, hold great promise for further research aimed at improving the transmission capabilities of magnonic 3D devices.

1.4 Conclusions

To summarize the research described in this chapter, it is evident that ferromagnetic gyroidal nanostructures exhibit interesting properties with significant implications for the field of 3D magnonics. The presented studies, both static and dynamic magnetization based, have shown that factors such as non-trivial shape anisotropy, chirality, and inhomogeneous demagnetization fields within gyroidal structures are determined by the specific crystallography, and can lead to the creation of multiple low-energy state magnetization textures, SW mode localization, and controllable SW propagation. Though preliminary, these investigations have begun to unveil the substantial potential inherent in these structures.

Further studies of individual nanostructures forming gyroids, such as unit cells, vertices, and struts, are crucial for a comprehensive understanding of the magnetic behavior of gyroids and their interactions with external fields. Much like how micro/nano texturing in metamaterials influences their macroscopic effective properties, these detailed investigations are crucial for elucidating the intricate relationships between gyroid geometry, chirality, and their effective magnetic properties, particularly at microwave frequencies. This is evidenced by the study of resonance frequencies in gyroid samples under rotational field manipulation, demonstrating the significant influence of geometric anisotropy on the FMR signal strength and the structure's effective properties. Gyroids, with their inherently chiral structure, nanoscale unit cell dimensions, and exchange-length bond sizes, show promise for 3D spin-ice systems, exhibiting intriguing collective SW properties such as

band gaps and magnon mode hybridizations. However, further experimental studies are essential to validate these properties and demonstrate their practical applications. Thus, the results presented in this chapter establish our current understanding of ferromagnetic gyroidal nanostructures and pave the way for their further investigation. In conclusion, research on ferromagnetic gyroidal nanostructures reveals intriguing properties and novel phenomena, underscoring their potential to advance the fields of 3D magnonics and spintronics.

Acknowledgments

The research leading to these results was funded by the National Science Centre of Poland, Projects No. UMO-2020/39/I/ST3/02413 and No. UMO-2023/49/N/ST3/03032.

Conflict of Interest

The authors have no conflicts to disclose.

Data Availability Statement

The data underlying this study are openly available in Zenodo at <https://doi.org/10.5281/zenodo.13143799>.

Appendix A

Appendix

A.1 Micromagnetic Simulations

In Sec. 1.3.2.1, for the numerical investigation, we used *tetmag* – the GPU-accelerated open-source FEM micromagnetic solver [Hertel (2023)]. We exploit its ability to solve magnetostatic open boundary problems in large-scale micromagnetic simulations via a hybrid finite-element/boundary-element formalism [Hertel *et al.* (2019)]. In this analysis, however, we do not assume periodic boundary conditions. All *tetmag*-based micromagnetic simulations were performed in two steps, where the first one was to compute the stable magnetic configuration at a given field value. After the magnetization relaxation, we conducted simulations of the ferromagnetic resonance using a dedicated frequency domain algorithm [d’Aquino and Hertel (2023)] based on a formulation proposed by [d’Aquino *et al.* (2009)].

To investigate the SW modes within the gyroid structure described in Secs. 1.3.2.2 and 1.3.2.3, we utilized the capabilities of Comsol Multiphysics software. It employs the finite element method (FEM) to solve complex systems of coupled partial differential equations. This includes both the Landau-Lifshitz-Gilbert (LLG) equation and the Maxwell equations under the magnetostatic approximation. In these simulations, each magnetic moment within the unit cells of the gyroid is represented as a normalized unit vector denoted by $\mathbf{m} = \mathbf{M}/M_S$, where \mathbf{M} is the magnetization distribution function in space and time, and M_S is the saturation magnetization of the ferromagnetic material.

The core of our approach is solving the LLG equation in its explicit form:

$$\frac{d\mathbf{m}}{dt} = \gamma \frac{1}{1 + \alpha^2} (\mathbf{m} \times \mathbf{B}_{\text{eff}} + \alpha (\mathbf{m} \times (\mathbf{m} \times \mathbf{B}_{\text{eff}}))), \quad (\text{A.1})$$

where $d\mathbf{m}/dt$ is the time evolution of the reduced magnetization, γ is the gyromagnetic ratio, and α represents the dimensionless damping coefficient. The effective magnetic flux density field, \mathbf{B}_{eff} , integrates the externally applied field, \mathbf{B}_{ext} , with the magnetostatic demagnetizing field, \mathbf{B}_d , and

the Heisenberg exchange field, \mathbf{B}_{exch} :

$$\mathbf{B}_{\text{eff}} = \mathbf{B}_{\text{ext}} + \mathbf{B}_{\text{d}} + \mathbf{B}_{\text{exch}}. \quad (\text{A.2})$$

The demagnetizing field strength, \mathbf{H}_{d} (equivalent to $\mathbf{B}_{\text{d}}/\mu_0$, where μ_0 is the vacuum permeability), is governed by Ampère's law, and is derived from the magnetic scalar potential gradient, U_{m} :

$$\mathbf{H}_{\text{d}} = -\nabla U_{\text{m}}, \quad (\text{A.3})$$

which further evolves within the magnetic body as:

$$\nabla^2 U_{\text{m}} = \nabla \cdot \mathbf{M}. \quad (\text{A.4})$$

In our Comsol implementation, we addressed the eigenproblem derived from Eqs. A.1-A.4. Assuming complete magnetization saturation by the magnetic field, we adopted a linear approximation to decompose the magnetization vector into static and dynamic components $\mathbf{m}(\mathbf{r}, t) = m_i \hat{i} + \delta \mathbf{m}(\mathbf{r}, t) \forall (\delta \mathbf{m} \perp \hat{i})$, disregarding all nonlinear terms in the dynamic magnetization $\delta \mathbf{m}(\mathbf{r}, t)$. This method aligns with foundational research such as Refs. [Mruczkiewicz *et al.* (2013); Rychlý *et al.* (2018)], which provides a comprehensive understanding of the underlying physical principles.

The Bloch-Floquet boundary conditions, applied to parallel surfaces on the opposite sides of the unit cell, are defined as:

$$\delta \mathbf{m}_{\text{dst}} = \delta \mathbf{m}_{\text{src}} e^{-ik(r_{\text{dst}} - r_{\text{src}})} \quad (\text{A.5})$$

where k represents the wavenumber, $\delta \mathbf{m}$ is the normalized dynamic component of the magnetization vector at both sides of the unit cell: the destination (dst) and the source (src), r denotes the spatial coordinates of the boundaries where the boundary conditions are applied, and i is the imaginary unit. For a unit cell encompassing periodicity, these boundary conditions are applied to its corresponding parallel faces (as illustrated in Fig. 1.9). By sweeping the wavenumber parametrically, eigenfrequencies are calculated at each interval, resulting in wavenumber versus frequency plots that reveal the dispersion curves for the periodic structure [Hakoda *et al.* (2018); Collet *et al.* (2011)]. These curves characteristically show periodicity in relation to the wavenumber, with a repeating pattern every $2\pi/L$.

For the distant planes parallel to the axes of the examined gyroid layer, Dirichlet boundary conditions are implemented to nullify the scalar magnetic potential, U_{m} . These first-type boundary conditions specify the precise value a variable must take at the boundary during the PDE solution process. Here, we set $U_{\text{m}}|_{\text{src}} = U_{\text{m}}|_{\text{dst}} = 0$. To ensure the simulation's physical fidelity and convergence, these conditions are placed sufficiently far from the specimen. In our Comsol simulations, the cell's height was configured to be 40 times the thickness of the gyroid layer.

A.2 Broadband FMR experiment

By adjusting the position of the sample on the CPW, as described in Sec. 1.3.2.1, apart from gyroidal structures, we observed a higher frequency signal specifically associated with the homogeneous Ni layer at one edge of the sample. It was confirmed by a good match between the detected signal and the theoretical prediction from the Kittel formula for the resonance frequency:

$$f = \frac{\gamma}{2\pi} \sqrt{B_{\text{ext}}(B_{\text{ext}} + \mu_0 M_{\text{s}})}. \quad (\text{A.6})$$

In field-swept broadband FMR experiments at a fixed microwave field frequency, the FWHM of the absorption linewidth follows $\mu_0\Delta H = 4\pi\alpha f/\gamma$. This relationship holds when the magnetization vector aligns with the applied magnetic field, either in-plane or perpendicular. The linewidth scales linearly with frequency, with the slope determined by the Gilbert damping parameter α . Besides this, empirical data show an additional frequency-independent term:

$$\Delta H = \Delta H_0 + \frac{4\pi\alpha}{\mu_0\gamma}f, \quad (\text{A.7})$$

where ΔH_0 represents inhomogeneous contributions, adding to the overall linewidth observed in the experiments.



Bibliography

- Armatas, G. S. and Kanatzidis, M. G. (2006). Mesosstructured germanium with cubic pore symmetry, *Nature* **441**, 7097, p. 1122—1125.
- Bailleul, M., Olligs, D. and Fermon, C. (2003). Micromagnetic phase transitions and spin wave excitations in a ferromagnetic stripe, *Phys. Rev. Lett.* **91**, p. 137204.
- Banerjee, C., Gruszecki, P., Kłos, J. W., Hellwig, O., Krawczyk, M. and Barman, A. (2017). Magnonic band structure in a Co/Pd stripe domain system investigated by brillouin light scattering and micromagnetic simulations, *Phys. Rev. B* **96**, p. 024421.
- Bansil, A., Lin, H. and Das, T. (2016). Colloquium: Topological band theory, *Rev. Mod. Phys.* **88**, p. 021004.
- Barker, J. and Bauer, G. E. (2016). Thermal spin dynamics of yttrium iron garnet, *Phys. Rev. Lett.* **117**, 21, p. 217201.
- Bayer, C., Jorzick, J., Demokritov, S. O., Slavin, A. N., Guslienko, K. Y., Berkov, D. V., Gorn, N. L., Kostylev, M. P. and Hillebrands, B. (2006). *Spin-Wave Excitations in Finite Rectangular Elements* (Springer Berlin Heidelberg, Berlin, Heidelberg), ISBN 978-3-540-39842-4, pp. 57–103.
- Beginin, E., Sadovnikov, A., Sakharov, V., Stognij, A., Khivintsev, Y. and Nikitov, S. (2019). Collective and localized modes in 3D magnonic crystals, *J. Magn. Magn. Mater.* **492**, p. 165647.
- Bessonov, V. D., Mruczkiewicz, M., Gieniusz, R., Guzowska, U., Maziewski, A., Stognij, A. I. and Krawczyk, M. (2015). Magnonic band gaps in YIG-based one-dimensional magnonic crystals: An array of grooves versus an array of metallic stripes, *Phys. Rev. B* **91**, p. 104421.
- Butt, M., Khonina, S. and Kazanskiy, N. (2021). Recent advances in photonic crystal optical devices: A review, *Optics and Laser Technology* **142**, p. 107265.
- Cheenkundil, R., Bauer, J., Goharyan, M., d’Aquino, M. and Hertel, R. (2022). High-frequency modes in a magnetic buckyball nanoarchitecture, *APL Mater.* **10**, 8, p. 081106.
- Chen, J., Hu, J. and Yu, H. (2020). Chiral magnonics: Reprogrammable nanoscale spin wave networks based on chiral domain walls, *iScience* **23**, 6, p. 101153.
- Chen, J., Yu, H. and Gubbiotti, G. (2021). Unidirectional spin-wave propagation and devices, *J. Phys. D: Appl. Phys.* **55**, 12, p. 123001.
- Chen, Y., Yao, H. and Wang, L. (2013). Acoustic band gaps of three-dimensional periodic polymer cellular solids with cubic symmetry, *J. Appl. Phys.* **114**, 4, p. 043521.
- Cheng, J., Ross, C., Smith, H. and Thomas, E. (2006). Templated self-assembly of block copolymers: Top-down helps bottom-up, *Adv. Mater.* **18**, 19, pp. 2505–2521.
- Chumak, A. V. (2019). Magnon spintronics, in E. Y. Tsymlal and I. Žutić (eds.), *Spintronics Handbook: Spin Transport and Magnetism, Second Edition*, 2nd edn., chap. 6 (CRC Press, Boca Raton), ISBN 9780429423079, pp. 247–302.
- Chumak, A. V., Serga, A. A. and Hillebrands, B. (2017). Magnonic crystals for data processing, *J. Phys. D: Appl. Phys.* **50**, 24, p. 244001.
- Chumak, A. V., Vasyuchka, V. I., Serga, A. A. and Hillebrands, B. (2015). Magnon spintronics, *Nat. Phys.* **11**, 6, pp. 453–461.
- Coey, J. M. (2010). *Magnetism and magnetic materials* (Cambridge University Press), ISBN 9780511845000.
- Collet, M., Ouisse, M., Ruzzene, M. and Ichchou, M. (2011). Floquet–Bloch decomposition for the computation of dispersion of two-dimensional periodic, damped mechanical systems, *Int. J. Solids*

- Struct.* **48**, 20, pp. 2837–2848.
- Dacorogna, B. (2014). *Introduction to the calculus of variations*, 3rd edn. (Imperial College Press).
- Damon, R. and Eshbach, J. (1961). Magnetostatic modes of a ferromagnet slab, *Journal of Physics and Chemistry of Solids* **19**, 3, pp. 308–320.
- d’Aquino, M. and Hertel, R. (2023). Micromagnetic frequency-domain simulation methods for magnonic systems, *J. Appl. Phys.* **133**, 3, p. 033902.
- Demidov, V. E., Urazhdin, S. and Demokritov, S. O. (2010). Direct observation and mapping of spin waves emitted by spin-torque nano-oscillators, *Nat. Mater.* **9**, pp. 984–988.
- Dieny, B., Prejbeanu, I. L., Garello, K., Gambardella, P., Freitas, P., Lehnendorff, R., Raberg, W., Ebels, U., Demokritov, S. O., Akerman, J., Deac, A., Pirro, P., Adelmann, C., Anane, A., Chumak, A. V., Hirohata, A., Mangin, S., Valenzuela, S. O., Onbasli, M. C., d’Aquino, M., Prenat, G., Finocchio, G., Lopez-Diaz, L., Chantrell, R., Chubykalo-Fesenko, O. and Bortolotti, P. (2020). Opportunities and challenges for spintronics in the microelectronics industry, *Nature Electronics* **3**, 8, pp. 446–459.
- Diep, H. (2013). *Frustrated Spin Systems* (World Scientific), ISBN 9789814440745.
- Dolan, J. A., Wilts, B. D., Vignolini, S., Baumberg, J. J., Steiner, U. and Wilkinson, T. D. (2015). Optical properties of gyroid structured materials: From photonic crystals to metamaterials, *Adv. Opt. Mater.* **3**, 1, pp. 12–32.
- Donnelly, C., Finizio, S., Gliga, S., Holler, M., Hrabec, A., Odstrcil, M., Mayr, S., Scagnoli, V., Heyderman, L. J., Guizar-Sicairos, M. and Raabe, J. (2020). Time-resolved imaging of three-dimensional nanoscale magnetization dynamics, *Nat. Nanotechnol.* **15**, 5, pp. 356–360.
- Donnelly, C., Guizar-Sicairos, M., Scagnoli, V., Gliga, S., Holler, M., Raabe, J. and Heyderman, L. (2017). Three-dimensional magnetization structures revealed with X-ray vector nanotomography, *Nature* **547**, pp. 328–331.
- Donnelly, C., Hierro-Rodríguez, A., Abert, C., Witte, K., Skoric, L., Sanz-Hernández, D., Finizio, S., Meng, F., McVitie, S., Raabe, J., Suess, D., Cowburn, R. and Fernández-Pacheco, A. (2022). Complex free-space magnetic field textures induced by three-dimensional magnetic nanostructures, *Nat. Nanotechnol.* **17**, 2, pp. 136–142.
- Duerr, G., Thurner, K., Topp, J., Huber, R. and Grundler, D. (2012). Enhanced transmission through squeezed modes in a self-cladding magnonic waveguide, *Phys. Rev. Lett.* **108**, 22, p. 227202.
- d’Aquino, M., Serpico, C., Miano, G. and Forestiere, C. (2009). A novel formulation for the numerical computation of magnetization modes in complex micromagnetic systems, *J. Comput. Phys.* **228**, 17, pp. 6130–6149.
- El Hassan, A., Kunst, F. K., Moritz, A., Andler, G., Bergholtz, E. J. and Bourennane, M. (2019). Corner states of light in photonic waveguides, *Nat. Photonics* **13**, 10, pp. 697–700.
- Feilhauer, J., Zelent, M., Zhang, Z., Christensen, J. and Mruczkiewicz, M. (2023). Unidirectional spin-wave edge modes in magnonic crystal, *APL Mater.* **11**, 2, p. 021104.
- Feng, H., Lu, X., Wang, W., Kang, N.-G. and Mays, J. W. (2017). Block copolymers: Synthesis, self-assembly, and applications, *Polymers* **9**, 10.
- Fernández-Pacheco, A., Streubel, R., Fruchart, O., Hertel, R., Fischer, P. and Cowburn, R. P. (2017). Three-dimensional nanomagnetism, *Nat. Commun.* **8**, 1, pp. 1–14.
- Fischer, P., Sanz-Hernández, D., Streubel, R. and Fernández-Pacheco, A. (2020). Launching a new dimension with 3D magnetic nanostructures, *APL Mater.* **8**, 1, p. 010701.
- Gaididei, Y., Kravchuk, V. P. and Sheka, D. D. (2014). Curvature effects in thin magnetic shells, *Phys. Rev. Lett.* **112**, 25, p. 257203, publisher: American Physical Society.
- Gan, Z., Turner, M. D. and Gu, M. (2016). Biomimetic gyroid nanostructures exceeding their natural origins, *Sci. Adv.* **2**, 5, p. e1600084.
- Garcia-Sanchez, F., Borys, P., Soucaille, R., Adam, J. P., Stamps, R. L. and Kim, J. V. (2015). Narrow magnonic waveguides based on domain walls, *Phys. Rev. Lett.* **114**, 24, p. 247206.
- Garcia-Sanchez, F., Borys, P., Vansteenkiste, A., Kim, J.-V. and Stamps, R. L. (2014). Nonreciprocal spin-wave channeling along textures driven by the Dzyaloshinskii-Moriya interaction, *Phys. Rev. B* **89**, p.

- 224408.
- Girardi, D., Finizio, S., Donnelly, C., Rubini, G., Mayr, S., Levati, V., Cuccurullo, S., Maspero, F., Raabe, J., Petti, D. and Albisetti, E. (2024). Three-dimensional spin-wave dynamics, localization and interference in a synthetic antiferromagnet, *Nat. Commun.* **15**, 1, p. 3057.
- Gołębiewski, M., Hertel, R., d'Aquino, M., Vasyuchka, V., Weiler, M., Pirro, P., Krawczyk, M., Fukami, S., Ohno, H. and Llandro, J. (2024). Collective spin-wave dynamics in gyroid ferromagnetic nanostructures, *ACS Appl. Mater. Interfaces* **16**, 17, pp. 22177–22188.
- Gołębiewski, M., Reshetniak, H., Makartsou, U., Krawczyk, M., van den Berg, A., Ladak, S. and Barman, A. (2023). Spin-wave spectral analysis in crescent-shaped ferromagnetic nanorods, *Phys. Rev. Appl.* **19**, p. 064045.
- Gross, F., Zelent, M., Gangwar, A., Mamica, S., Gruszecki, P., Werner, M., Schütz, G., Weigand, M., Goering, E. J., Back, C. H., Krawczyk, M. and Gräfe, J. (2021). Phase resolved observation of spin wave modes in antidot lattices, *Appl. Phys. Lett.* **118**, 23, p. 232403.
- Große-Brauckmann, K. (1997). Gyroids of constant mean curvature, *Exp. Math.* **6**, 1, pp. 33–50.
- Große-Brauckmann, K. and Wohlgemuth, M. (1996). The gyroid is embedded and has constant mean curvature companions, *Calc. Var. Partial Differ. Equ.* **4**, 6, pp. 499–523.
- Gruszecki, P., Banerjee, C., Mruczkiewicz, M., Hellwig, O., Barman, A. and Krawczyk, M. (2019). Chapter two - the influence of the internal domain wall structure on spin wave band structure in periodic magnetic stripe domain patterns, in R. L. Stamps and H. Schultheiß (eds.), *Recent Advances in Topological Ferroics and their Dynamics, Solid State Physics*, Vol. 70 (Academic Press), pp. 79–132.
- Gruszecki, P., Guslienko, K. Y., Lyubchanskii, I. L. and Krawczyk, M. (2022). Inelastic spin-wave beam scattering by edge-localized spin waves in a ferromagnetic thin film, *Phys. Rev. Appl.* **17**, p. 044038.
- Gruszecki, P., Lyubchanskii, I. L., Guslienko, K. Y. and Krawczyk, M. (2021). Local non-linear excitation of sub-100 nm bulk-type spin waves by edge-localized spin waves in magnetic films, *Appl. Phys. Lett.* **118**, 6, p. 062408.
- Gubbiotti, G. (2019). *Three-Dimensional Magnonics*, 1st edn. (Jenny Stanford Publishing, New York), ISBN 9780429299155.
- Gubbiotti, G., Sadovnikov, A., Beginin, E., Nikitov, S., Wan, D., Gupta, A., Kundu, S., Talmelli, G., Carpenter, R., Asselberghs, I., Radu, I. P., Adelmann, C. and Ciubotaru, F. (2021). Magnonic band structure in vertical meander-shaped $\text{Co}_{40}\text{Fe}_{40}\text{B}_{20}$ thin films, *Phys. Rev. Appl.* **15**, p. 014061.
- Guo, H., Deenen, A. J. M., Xu, M., Hamdi, M. and Grundler, D. (2023). Realization and control of bulk and surface modes in 3D nanomagnonic networks by additive manufacturing of ferromagnets, *Adv. Mater.*, p. 2303292.
- Hakoda, C., Rose, J., Shokouhi, P. and Lissenden, C. (2018). Using Floquet periodicity to easily calculate dispersion curves and wave structures of homogeneous waveguides, *AIP Conf. Proc.* **1949**, 1, p. 020016.
- Han, L. and Che, S. (2018). An overview of materials with triply periodic minimal surfaces and related geometry: From biological structures to self-assembled systems, *Adv. Mater.* **30**, 17, p. 1705708.
- Hertel, R. (2013). Curvature-induced magnetochirality, *SPIN* **03**, 03, p. 1340009, publisher: World Scientific Publishing Co.
- Hertel, R. (2023). tetmag, <https://github.com/R-Hertel/tetmag>.
- Hertel, R., Christophersen, S. and Börm, S. (2019). Large-scale magnetostatic field calculation in finite element micromagnetics with H2-matrices, *J. Magn. Magn. Mater.* **477**, pp. 118–123.
- Hirosawa, T., Díaz, S. A., Klinovaja, J. and Loss, D. (2020). Magnonic quadrupole topological insulator in antiskyrmion crystals, *Phys. Rev. Lett.* **125**, p. 207204.
- Hsueh, H.-Y., Huang, Y.-C., Ho, R.-M., Lai, C.-H., Makida, T. and Hasegawa, H. (2011). Nanoporous gyroid nickel from block copolymer templates via electroless plating, *Adv. Mater.* **23**, 27, pp. 3041–3046.
- Hunt, M., Taverne, M., Askey, J., May, A., Van Den Berg, A., Ho, Y. L. D., Rarity, J. and Ladak, S. (2020). Harnessing multi-photon absorption to produce three-dimensional magnetic structures at the nanoscale, *Materials* **13**, 3, p. 761.

- Hurben, M. and Patton, C. (1995). Theory of magnetostatic waves for in-plane magnetized isotropic films, *J. Magn. Magn. Mater.* **139**, 3, pp. 263–291.
- Hyde, S., Ninham, B. W., Andersson, S., Larsson, K., Landh, T., Blum, Z. and Lidin, S. (1997a). Chapter 1 - the mathematics of curvature, in S. Hyde, B. W. Ninham, S. Andersson, K. Larsson, T. Landh, Z. Blum and S. Lidin (eds.), *The Language of Shape* (Elsevier Science B.V., Amsterdam), ISBN 978-0-444-81538-5, pp. 1–42.
- Hyde, S., Ninham, B. W., Andersson, S., Larsson, K., Landh, T., Blum, Z. and Lidin, S. (1997b). Chapter 3 - molecular forces and self-assembly, in S. Hyde, B. W. Ninham, S. Andersson, K. Larsson, T. Landh, Z. Blum and S. Lidin (eds.), *The Language of Shape* (Elsevier Science B.V., Amsterdam), ISBN 978-0-444-81538-5, pp. 87–140.
- Hyde, S., Ninham, B. W., Andersson, S., Larsson, K., Landh, T., Blum, Z. and Lidin, S. (1997c). Chapter 4 - beyond flatland: The geometric forms due to self-assembly, in S. Hyde, B. W. Ninham, S. Andersson, K. Larsson, T. Landh, Z. Blum and S. Lidin (eds.), *The Language of Shape* (Elsevier Science B.V., Amsterdam), ISBN 978-0-444-81538-5, pp. 141–197.
- Hyde, S. T., O’Keeffe, M. and Proserpio, D. M. (2008). A short history of an elusive yet ubiquitous structure in chemistry, materials, and mathematics, *Angewandte Chemie - International Edition* **47**, 42, pp. 7996–8000.
- Inoue, M., Baryshev, A., Takagi, H., Lim, P. B., Hatafuku, K., Noda, J. and Togo, K. (2011). Investigating the use of magnonic crystals as extremely sensitive magnetic field sensors at room temperature, *Appl. Phys. Lett.* **98**, 13, p. 132511.
- Jamali, M., Kwon, J. H., Seo, S.-M., Lee, K.-J. and Yang, H. (2013). Spin wave nonreciprocity for logic device applications, *Scientific Reports* **3**, 1, p. 3160.
- Ji, L., Zhao, R., Hu, X., Hu, C., Shen, X., Liu, X., Zhao, X., Zhang, J., Chen, W. and Zhang, X. (2022). Reconfigurable ferromagnetic resonances by engineering inhomogeneous magnetic textures in artificial magnonic crystals, *Advanced Functional Materials* **32**, 20, p. 2112956.
- Jorzick, J., Demokritov, S. O., Hillebrands, B., Bailleul, M., Fermon, C., Guslienko, K. Y., Slavin, A. N., Berkov, D. V. and Gorn, N. L. (2002). Spin wave wells in nonellipsoidal micrometer size magnetic elements, *Phys. Rev. Lett.* **88**, p. 047204.
- Kane, C. L. and Mele, E. J. (2005a). Quantum spin Hall effect in graphene, *Phys. Rev. Lett.* **95**, p. 226801.
- Kane, C. L. and Mele, E. J. (2005b). Z_2 topological order and the quantum spin Hall effect, *Phys. Rev. Lett.* **95**, p. 146802.
- Karcher, H. (1989). The triply periodic minimal surfaces of Alan Schoen and their constant mean curvature companions, *Manuscripta Math.* **64**, 3, pp. 291–357.
- König, M., Wiedmann, S., Brüne, C., Roth, A., Buhmann, H., Molenkamp, L. W., Qi, X.-L. and Zhang, S.-C. (2007). Quantum spin Hall insulator state in hgte quantum wells, *Science* **318**, 5851, p. 766–770.
- Krawczyk, M. and Grundler, D. (2014). Review and prospects of magnonic crystals and devices with reprogrammable band structure, *J. Phys. Condens. Matter* **26**, 12, p. 123202.
- Krawczyk, M., Kłos, J., Sokolovskyy, M. L. and Mamica, S. (2010). Materials optimization of the magnonic gap in three-dimensional magnonic crystals with spheres in hexagonal structure, *J. Appl. Phys.* **108**, 9, p. 093909.
- Krawczyk, M., Mamica, S., Mruczkiewicz, M., Kłos, J. W., Tacchi, S., Madami, M., Gubbiotti, G., Duerr, G. and Grundler, D. (2013). Magnonic band structures in two-dimensional bi-component magnonic crystals with in-plane magnetization, *J. Phys. D: Appl. Phys.* **46**, 49, p. 495003.
- Krawczyk, M. and Puzkarski, H. (2006). Magnonic excitations versus three-dimensional structural periodicity in magnetic composites, *Crystal Research and Technology* **41**, 6, pp. 547–552.
- Kresge, C. T., Leonowicz, M. E., Roth, W. J., Vartuli, J. C. and Beck, J. S. (1992). Ordered mesoporous molecular sieves synthesized by a liquid-crystal template mechanism, *Nature* **359**, 6397, pp. 710–712.
- Kruglyak, V. V. (2021). Chiral magnonic resonators: Rediscovering the basic magnetic chirality in magnonics, *Appl. Phys. Lett.* **119**, 20, p. 200502.

- Kruglyak, V. V., Demokritov, S. O. and Grundler, D. (2010). Magnonics, *J. Phys. D: Appl. Phys.* **43**, 26, p. 264001.
- Kruglyak, V. V., Keatley, P. S., Hicken, R. J., Childress, J. R. and Katine, J. A. (2006). Time resolved studies of edge modes in magnetic nanoelements, *J. Appl. Phys.* **99**, 8, p. 08F306.
- Lacroix, C., Mendels, P. and Mila, F. (2011). *Introduction to Frustrated Magnetism: Materials, Experiments, Theory*, Springer Series in Solid-State Sciences (Springer Berlin Heidelberg), ISBN 9783642105890.
- Lambert, C. A., Radzilowski, L. H. and Thomas, E. L. (1996). Triply periodic level surfaces as models for cubic tricontinuous block copolymer morphologies, *Philos. Trans. R. Soc. A* **354**, 1715, pp. 2009–2023.
- Lan, J., Yu, W., Wu, R. and Xiao, J. (2015). Spin-wave diode, *Phys. Rev. X* **5**, 4, p. 041049.
- Lenk, B., Ulrichs, H., Garbs, F. and Münzenberg, M. (2011). The building blocks of magnonics, *Phys. Rep.* **507**, 4-5, pp. 107–136.
- Li, X., Wang, Z., Lei, Z., Ding, W., Shi, X., Yan, J. and Ku, J. (2023). Magnetic characterization techniques and micromagnetic simulations of magnetic nanostructures: from zero to three dimensions, *Nanoscale* **15**, pp. 19448–19468.
- Li, Y.-M., Xiao, J. and Chang, K. (2018). Topological magnon modes in patterned ferrimagnetic insulator thin films, *Nano Lett.* **18**.
- Lich, L. V., Hue, D. T. H., Giang, D. T. H., Duc, N. H., Shimada, T., Kitamura, T. and Dinh, V. H. (2023). Formation and switching of chiral magnetic field textures in three-dimensional gyroid nanostructures, *Acta Mater.* **249**, p. 118802.
- Liu, J., Wang, L. and Shen, K. (2020). Dipolar spin waves in uniaxial easy-axis antiferromagnets: A natural topological nodal-line semimetal, *Phys. Rev. Res.* **2**, p. 023282.
- Llandro, J., Love, D. M., Kovács, A., Caron, J., Vyas, K. N., Kákay, A., Salikhov, R., Lenz, K., Fassbender, J., Scherer, M. R., Ciorra, C., Steiner, U., Barnes, C. H., Dunin-Borkowski, R. E., Fukami, S. and Ohno, H. (2020). Visualizing magnetic structure in 3D nanoscale Ni-Fe gyroid networks, *Nano Lett.* **20**, 5, pp. 3642–3650.
- Luzzati, V. and Speg, P. A. (1967). Polymorphism of lipids, *Nature* **215**, pp. 701–704.
- Ma, F., Zhou, Y., Braun, H. B. and Lew, W. S. (2015). Skyrmion-based dynamic magnonic crystal, *Nano Lett.* **15**, 6, pp. 4029–4036.
- Maendl, S., Stasinopoulos, I. and Grundler, D. (2017). Spin waves with large decay length and few 100 nm wavelengths in thin yttrium iron garnet grown at the wafer scale, *Appl. Phys. Lett.* **111**, 1, p. 012403.
- Mahmoud, A., Ciubotaru, F., Vanderveken, F., Chumak, A. V., Hamdioui, S., Adelman, C. and Cotozana, S. (2020). Introduction to spin wave computing, *J. Appl. Phys.* **128**, 16, p. 161101.
- Makarov, D., Volkov, O. M., Kákay, A., Pylypovskyi, O. V., Budinská, B. and Dobrovolskiy, O. V. (2022). New dimension in magnetism and superconductivity: 3D and curvilinear nanoarchitectures, *Adv. Mater.* **34**, 3, p. 2101758.
- Mamica, S. (2023). The influence of the demagnetizing field on the concentration of spin wave energy in two-dimensional magnonic crystals, *J. Magn. Magn. Mater.* **588**, p. 171395.
- Mamica, S., Krawczyk, M. and Grundler, D. (2019). Nonuniform spin-wave softening in two-dimensional magnonic crystals as a tool for opening omnidirectional magnonic band gaps, *Phys. Rev. Appl.* **11**, p. 054011.
- Mamica, S., Krawczyk, M., Sokolovskyy, M. L. and Romero-Vivas, J. (2012). Large magnonic band gaps and spectra evolution in three-dimensional magnonic crystals based on magnetoferritin nanoparticles, *Phys. Rev. B* **86**, p. 144402.
- Maranville, B. B., McMichael, R. D. and Abraham, D. W. (2007). Variation of thin film edge magnetic properties with patterning process conditions in Ni80Fe20 stripes, *Appl. Phys. Lett.* **90**, 23, p. 232504.
- Maranville, B. B., McMichael, R. D., Kim, S. A., Johnson, W. L., Ross, C. A. and Cheng, J. Y. (2006). Characterization of magnetic properties at edges by edge-mode dynamics, *J. Appl. Phys.* **99**, 8, p. 08C703.
- May, A., Hunt, M., van den Berg, A., Hejazi, A. and Ladak, S. (2019). Realisation of a frustrated 3D magnetic nanowire lattice, *Commun. Phys.* **2**.

- May, A., Saccone, M., van den Berg, A., Askey, J., Hunt, M. and Ladak, S. (2021). Magnetic charge propagation upon a 3D artificial spin-ice, *Nat. Commun.* **12**, 1, pp. 1–10.
- McClarty, P. A. (2022). Topological magnons: A review, *Annu. Rev. Condens. Matter Phys.* **13**, 1, pp. 171–190.
- Michielsen, K. and Stavenga, D. G. (2008). Gyroid cuticular structures in butterfly wing scales: Biological photonic crystals, *J. R. Soc. Interface.* **5**, 18, pp. 85–94.
- Mizuno, A., Shuku, Y. and Awaga, K. (2019). Recent developments in molecular spin gyroid research, *Bull. Chem. Soc. Jpn.* **92**, 6, pp. 1068–1093.
- Monnier, A., Schüth, F., Huo, Q., Kumar, D., Margolese, D., Maxwell, R. S., Stucky, G. D., Krishnamurty, M., Petroff, P. M., Firouzi, A., Janicke, M. T. and Chmelka, B. F. (1993). Cooperative formation of inorganic-organic interfaces in the synthesis of silicate mesostructures, *Science* **261**, 5126, pp. 1299–1303.
- Mruczkiewicz, M., Gruszecki, P., Zelent, M. and Krawczyk, M. (2016). Collective dynamical skyrmion excitations in a magnonic crystal, *Phys. Rev. B* **93**, p. 174429.
- Mruczkiewicz, M., Krawczyk, M., Sakharov, V. K., Khivintsev, Y. V., Filimonov, Y. A. and Nikitov, S. A. (2013). Standing spin waves in magnonic crystals, *J. Appl. Phys.* **113**, 9, p. 093908.
- Neusser, S., Duerr, G., Tacchi, S., Madami, M., Sokolovskyy, M. L., Gubbiotti, G., Krawczyk, M. and Grundler, D. (2011). Magnonic minibands in antidot lattices with large spin-wave propagation velocities, *Phys. Rev. B* **84**, p. 094454.
- Ni, X., Weiner, M., Alú, A. and Khanikaev, A. B. (2019). Observation of higher-order topological acoustic states protected by generalized chiral symmetry, *Nat. Mater.* **18**, 2, pp. 113–120.
- Nisoli, C., Kapaklis, V. and Schiffer, P. (2017). Deliberate exotic magnetism via frustration and topology, *Nat. Phys.* **13**, 3, pp. 200–203.
- Otálora, J. A., Yan, M., Schultheiss, H., Hertel, R. and Kákay, A. (2017). Asymmetric spin-wave dispersion in ferromagnetic nanotubes induced by surface curvature, *Phys. Rev. B* **95**, p. 184415.
- Park, J. P., Eames, P., Engebretson, D. M., Berezovsky, J. and Crowell, P. A. (2002). Spatially resolved dynamics of localized spin-wave modes in ferromagnetic wires, *Phys. Rev. Lett.* **89**, p. 277201.
- Petti, D., Tacchi, S. and Albisetti, E. (2022). Review on magnonics with engineered spin textures, *J. Phys. D: Appl. Phys.* **55**, 29, p. 293003.
- Romero Vivas, J., Mamica, S., Krawczyk, M. and Kruglyak, V. V. (2012). Investigation of spin wave damping in three-dimensional magnonic crystals using the plane wave method, *Phys. Rev. B* **86**, p. 144417.
- Rosi, G., Auffray, N. and Combescure, C. (2020). On the failure of classic elasticity in predicting elastic wave propagation in gyroid lattices for very long wavelengths, *Symmetry* **12**, 8.
- Ross, C. A., Berggren, K. K., Cheng, J. Y., Jung, Y. S. and Chang, J.-B. (2014). Three-dimensional nanofabrication by block copolymer self-assembly, *Adv. Mater.* **26**, 25, pp. 4386–4396.
- Rychlý, J., Gruszecki, P., Mruczkiewicz, M., Kłos, J. W., Mamica, S. and Krawczyk, M. (2015). Magnonic crystals – prospective structures for shaping spin waves in nanoscale, *Low Temperature Physics* **41**, 10, pp. 745–759.
- Rychlý, J., Tkachenko, V. S., Kłos, J. W., Kuchko, A. and Krawczyk, M. (2018). Spin wave modes in a cylindrical nanowire in crossover dipolar-exchange regime, *J. Phys. D: Appl. Phys.* **52**, 7, p. 075003.
- Sadovnikov, A., Talmelli, G., Gubbiotti, G., Beginin, E., Sheshukova, S., Nikitov, S., Adelman, C. and Ciubotaru, F. (2022). Reconfigurable 3D magnonic crystal: Tunable and localized spin-wave excitations in CoFeB meander-shaped film, *J. Magn. Magn. Mater.* **544**, p. 168670.
- Sahoo, S., Mondal, S., Williams, G., May, A., Ladak, S. and Barman, A. (2018). Ultrafast magnetization dynamics in a nanoscale three-dimensional cobalt tetrapod structure, *Nanoscale* **10**, pp. 9981–9986.
- Scherer, M. R. J., Cunha, P. M. S. and Steiner, U. (2014). Labyrinth-induced faceted electrochemical growth, *Adv. Mater.* **26**, 15, pp. 2403–2407.
- Schindler, F., Cook, A. M., Vergniory, M. G., Wang, Z., Parkin, S. S. P., Bernevig, B. A. and Neupert, T. (2018). Higher-order topological insulators, *Sci. Adv.* **4**, 6, p. 0346.

- Schneider, T., Serga, A. A., Leven, B., Hillebrands, B., Stamps, R. L. and Kostylev, M. P. (2008). Realization of spin-wave logic gates, *Appl. Phys. Lett.* **92**, 2, p. 022505.
- Schoen, A. H. (1970). Infinite periodic minimal surfaces without self-intersections, Tech. rep., NASA Electronics Research Center, Cambridge.
- Schoen, A. H. (2012). Reflections concerning triply-periodic minimal surfaces, *Interface Focus* **2**, 5, pp. 658–668.
- Segalman, R. A. (2005). Patterning with block copolymer thin films, *Mater. Sci. Eng. R Rep.* **48**, 6, pp. 191–226.
- Serga, A. A., Chumak, A. V. and Hillebrands, B. (2010). YIG magnonics, *J. Phys. D: Appl. Phys.* **43**, 26, p. 264002.
- Serha, R. O., Bozhko, D. A., Agrawal, M., Verba, R. V., Kostylev, M., Vasyuchka, V. I., Hillebrands, B. and Serga, A. A. (2022). Low-damping spin-wave transmission in YIG/Pt-interfaced structures, *Adv. Mater. Interfaces* **9**, 36, p. 2201323.
- She, M.-S., Lo, T.-Y. and Ho, R.-M. (2013). Controlled ordering of block copolymer gyroid thin films by solvent annealing, *Macromolecules* **47**, p. 175–182.
- Sheka, D. D. (2021). A perspective on curvilinear magnetism, *Appl. Phys. Lett.* **118**, 23, p. 230502.
- Sheka, D. D., Pylypovskyi, O. V., Volkov, O. M., Yershov, K. V., Kravchuk, V. P. and Makarov, D. (2022). Fundamentals of curvilinear ferromagnetism: Statics and dynamics of geometrically curved wires and narrow ribbons, *Small* **18**, 12, p. 2105219.
- Shindou, R., Matsumoto, R., Murakami, S. and Ohe, J. I. (2013a). Topological chiral magnonic edge mode in a magnonic crystal, *Phys. Rev. B* **87**, p. 174427.
- Shindou, R., Ohe, J. I., Matsumoto, R., Murakami, S. and Saitoh, E. (2013b). Chiral spin-wave edge modes in dipolar magnetic thin films, *Phys. Rev. B* **87**, p. 174402.
- Simon, P. F. W., Ulrich, R., Spiess, H. W. and Wiesner, U. (2001). Block copolymer-ceramic hybrid materials from organically modified ceramic precursors, *Science* **261**, 5126, pp. 1299–1303.
- Singh, M., Callaway, J. and Wang, C. S. (1976). Calculation of g and g' for iron and nickel, *Phys. Rev. B* **14**, 3, pp. 1214–1220.
- Skjærvø, S. H., Marrows, C. H., Stamps, R. L. and Heyderman, L. J. (2020). Advances in artificial spin ice, *Nat. Rev. Phys.* **2**, pp. 2522–5820.
- Skoric, L., Sanz-Hernández, D., Meng, F., Donnelly, C., Merino-Aceituno, S. and Fernández-Pacheco, A. (2020). Layer-by-layer growth of complex-shaped three-dimensional nanostructures with focused electron beams, *Nano Lett.* **20**, 1, pp. 184–191.
- Stenning, K. D., Xiao, X., Holder, H. H., Gartside, J. C., Vanstone, A., Kennedy, O. W., Oulton, R. F. and Branford, W. R. (2023). Low-power continuous-wave all-optical magnetic switching in ferromagnetic nanoarrays, *Cell Rep. Phys. Sci.* **4**, 3, p. 101291.
- Sunada, T. (2008). Crystals that nature might miss creating, *Not. Am. Math. Soc.* **55**, 2, pp. 208–215.
- Szulc, K., Tacchi, S., Hierro-Rodriguez, A., Diaz, J., Gruszecki, P., Graczyk, P., Quiros, C., Marko, D., Martin, J. I., Vélez, M., Schmool, D. S., Carlotti, G., Krawczyk, M. and Álvarez-Prado, L. M. (2022). Reconfigurable magnonic crystals based on imprinted magnetization textures in hard and soft dipolar-coupled bilayers, *ACS Nano* **16**, 9, pp. 14168–14177.
- Szulc, K., Zelent, M. and Krawczyk, M. (2024). Reconfigurable spin-wave platform based on interplay between nanodots and waveguide in hybrid magnonic crystal, .
- Tacchi, S., Flores-Farias, J., Petti, D., Brevis, F., Cattoni, A., Scaramuzzi, G., Girardi, D., Cortes-Ortuno, D., Gallardo, R. A., Albisetti, E., Carlotti, G. and Landeros, P. (2023). Experimental observation of flat bands in one-dimensional chiral magnonic crystals, *Nano Lett.* **23**, 14, pp. 6776–6783.
- Tacchi, S., Gruszecki, P., Madami, M., Carlotti, G., Klos, J. W., Krawczyk, M., Adeyeye, A. and Gubbiotti, G. (2015). Universal dependence of the spin wave band structure on the geometrical characteristics of two-dimensional magnonic crystals, *Scientific Reports* **5**, 1, p. 10367.
- Tai, J.-S. B. and Smalyukh, I. I. (2018). Static hopf solitons and knotted emergent fields in solid-state noncentrosymmetric magnetic nanostructures, *Phys. Rev. Lett.* **121**, p. 187201.

- Tanaka, G., Yamane, T., Héroux, J. B., Nakane, R., Kanazawa, N., Takeda, S., Numata, H., Nakano, D. and Hirose, A. (2019). Recent advances in physical reservoir computing: A review, *Neural Netw.* **115**, pp. 100–123.
- Tang, N., Liyanage, W. L. N. C., Montoya, S. A., Patel, S., Quigley, L. J., Grutter, A. J., Fitzsimmons, M. R., Sinha, S., Borchers, J. A., Fullerton, E. E., DeBeer-Schmitt, L. and Gilbert, D. A. (2023). Skyrmion-excited spin-wave fractal networks, *Adv. Mater.* **35**, 33, p. 2300416.
- Tselikas, Y., Hadjichristidis, N., Lescanec, R. L., Honeker, C. C., Wohlgemuth, M. and Thomas, E. L. (1996). Architecturally-induced tricontinuous cubic morphology in compositionally symmetric miktoarm starblock copolymers, *Macromolecules* **29**, 10, pp. 3390–3396.
- Turner, M., Saba, M., Zhang, Q., Cumming, B., Schröder-Turk, G. and Gu, M. (2013). Miniature chiral beamsplitter based on gyroid photonic crystals, *Nat. Photonics* **7**, pp. 801–805.
- van den Berg, A., Caruel, M., Hunt, M. and Ladak, S. (2023). Combining two-photon lithography with laser ablation of sacrificial layers: A route to isolated 3D magnetic nanostructures, *Nano Res.* **16**, 1, pp. 1441–1447.
- Vasileiadis, T., Varghese, J., Babacic, V., Gomis-Bresco, J., Navarro Urrios, D. and Graczykowski, B. (2021). Progress and perspectives on phononic crystals, *J. Appl. Phys.* **129**, 16, p. 160901.
- Vignolini, S., Yufa, N. A., Cunha, P. S., Guldin, S., Rushkin, I., Stefik, M., Hur, K., Wiesner, U., Baumberg, J. J. and Steiner, U. (2012). A 3D optical metamaterial made by self-assembly, *Adv. Mater.* **24**, 10, pp. OP23–OP27.
- Wagner, K., Kákay, A., Schultheiss, K., Henschke, A., Sebastian, T. and Schultheiss, H. (2016). Magnetic domain walls as reconfigurable spin-wave nanochannels, *Nat. Nanotechnol.* **11**, 5, pp. 432–436.
- Wang, X.-g., Nie, Y.-Z., Xia, Q.-l. and Guo, G.-h. (2020). Dynamically reconfigurable magnonic crystal composed of artificial magnetic skyrmion lattice, *J. Appl. Phys.* **128**, 6, p. 063901.
- Wang, X. S., Zhang, H. W. and Wang, X. R. (2018). Topological magnonics: A paradigm for spin-wave manipulation and device design, *Phys. Rev. Appl.* **9**, p. 024029.
- Wannier, G. H. (1950). Antiferromagnetism. the triangular Ising net, *Phys. Rev.* **79**, pp. 357–364.
- Wohlgemuth, M., Yufa, N., Hoffman, J. and Thomas, E. L. (2001). Triply periodic bicontinuous cubic microdomain morphologies by symmetries, *Macromolecules* **34**, 17, pp. 6083–6089.
- Wu, J.-S. and Smalyukh, I. I. (2022). Hopfions, heliknotons, skyrmions, torons and both abelian and nonabelian vortices in chiral liquid crystals, *Liquid Crystals Reviews* **10**, 1-2, pp. 34–68.
- Yamamoto, K., Thiang, G. C., Pirro, P., Kim, K.-W., Everschor-Sitte, K. and Saitoh, E. (2019). Topological characterization of classical waves: The topological origin of magnetostatic surface spin waves, *Phys. Rev. Lett.* **122**, p. 217201.
- Yan, C., Hao, L., Hussein, A. and Raymont, D. (2012). Evaluations of cellular lattice structures manufactured using selective laser melting, *Int. J. Mach. Tools Manuf.* **62**, pp. 32–38.
- Yan, P. and Bauer, G. E. (2013). Magnon mediated domain wall heat conductance in ferromagnetic wires, *IEEE Trans. Magn.* **49**, 7, pp. 3109–3112.
- Yáñez, A., Herrera, A., Martel, O., Monopoli, D. and Afonso, H. (2016). Compressive behaviour of gyroid lattice structures for human cancellous bone implant applications, *Mater. Sci. Eng. C* **68**, pp. 445–448.
- Yu, H., Xiao, J. and Schultheiss, H. (2021). Magnetic texture based magnonics, *Phys. Rep.* **905**, pp. 1–59.
- Zhuo, F., Kang, J., Manchon, A. and Cheng, Z. (2023). Topological phases in magnonics, *Advanced Physics Research*, p. 2300054.

5.3.3 Theoretical demonstration of a new type of FMR mode localization in 3D nanostructures (P9)

This work introduces a new type of FMR mode localization in complex three-dimensional nanostructures. Using micromagnetic simulations, I investigate the FMR behavior in scaffold-like architectures and gyroid nanostructures, demonstrating how their unique three-dimensional geometries give rise to surface-localized FMR modes – a phenomenon fundamentally different from conventional spin-wave localization mechanisms reported in the literature. The results show that demagnetizing fields and exchange interactions in these structures produce a highly asymmetric distribution of dynamic magnetization along the vertical axis.

A key discovery is the top-bottom dynamic switching of the surface-mode localization controlled by the orientation of the external magnetic field, revealing a novel mechanism for tuning magnetization dynamics by simply adjusting the field direction. This work demonstrates a new approach to mode localization in 3D nanostructures and lays the foundation for experimental exploration and practical applications in magnonics where tunable spin-wave behavior can be exploited.

Contribution of the Author

For this publication, I discovered the effect and conceptualized the overall study in collaboration with K. Szulc. I also designed the models and performed the numerical simulations in COMSOL Multiphysics. I actively participated in discussions and interpretations of the simulation results with K. Szulc and M. Krawczyk, post-processed the data, and prepared the first draft. I was responsible for submitting the manuscript and managing all correspondence with reviewers throughout the publication process.

©2024 The Authors. Published by Elsevier Ltd on behalf of *Acta Materialia* Inc under the CC-BY 4.0 license.



Contents lists available at ScienceDirect

Acta Materialia

journal homepage: www.elsevier.com/locate/actamat

Full length article



Magnetic field controlled surface localization of ferromagnetic resonance modes in 3D nanostructures

Mateusz Gołębiewski^{a,*}, Krzysztof Szulc^{a,b}, Maciej Krawczyk^a^a Institute of Spintronics and Quantum Information, Faculty of Physics and Astronomy, Adam Mickiewicz University, Uniwersytetu Poznańskiego 2, 61-614, Poznań, Poland^b Institute of Molecular Physics, Polish Academy of Sciences, M. Smoluchowskiego 17, 60-179, Poznań, Poland

ARTICLE INFO

Dataset link: <https://doi.org/10.5281/zenodo.13141840>

Keywords:

3D nanostructures
Micromagnetism
Ferromagnetic
Magnetization profiles
Magnetic shape anisotropy

ABSTRACT

By extending the current understanding and use of magnonics beyond conventional planar systems, we demonstrate the surface localization of ferromagnetic resonance (FMR) modes through the design of complex three-dimensional nanostructures. Using micromagnetic simulations, we systematically investigate woodpile-like scaffolds and gyroids — periodic chiral entities characterized by their triple junctions. The study highlights the critical role of demagnetizing fields and exchange energy in determining the FMR responses of 3D nanosystems, especially the strongly asymmetric distribution of the spin-wave mode over the system's height. Importantly, the top-bottom dynamic switching of the surface mode localization across the structures in response to changes in magnetic field orientation provides a new method for controlling magnetization dynamics. The results demonstrate the critical role of the geometric features in dictating the dynamic magnetic behavior of three-dimensional nanostructures, paving the way for both experimental exploration and practical advances in 3D magnonics.

1. Introduction

Spin waves (SWs), originating from the collective oscillations of magnetic moments, are marked by their intricate dynamics, dependence on material structure, magnetization texture, and profound application potential in IT systems [1]. The properties of SWs are a consequence of the interplay between long-range magnetostatic and short-range exchange interactions. This balance is particularly pronounced when the anisotropy of the magnetostatic interactions introduces a unique dependence of the SW propagation on the alignment between magnetization and SW wavevector. Such dependencies give rise to a number of distinctive SW properties, including negative group velocity, caustics, pronounced nonlinearity, and dynamic reconfigurability [2]. Thus, the current focus of the magnonic research is not only to understand these phenomena, but also to exploit them for digital, analog, non-conventional, and quantum signal processing at high frequencies, from a few to hundreds of GHz, operating at the nanoscale, and consuming less power than other alternative systems [3]. This vision is reflected in recent breakthroughs and strategic roadmaps of the field [4,5].

Nanostructured 3D networks can significantly advance the potential of magnonics, giving rise to topological and geometric effects and emergent material properties that extend existing and offer new

possibilities for SW manipulation [6–8]. For example, by tuning their geometry and lattice period, we obtain control over the magnonic band structure with tailored SW group velocity and collective response to external stimuli in all possible directions of SW propagation and polarization of external fields [8–10]. In addition, 3D magnetic structures provide an opportunity to explore chiral surface, edge, and corner states, characterized by higher-order topology [11,12]. Furthermore, a fully interconnected 3D systems [13–15] open up a new degree of freedom to explore other emerging phenomena in magnetism, such as frustration and magnetic charge isolation, realized with 3D artificial spin-ice systems [16,17]. In recent years, the significant development of new fabrication techniques – such as two-photon lithography, focused-electron-beam deposition, and block-copolymer templating – makes it possible to fabricate and measure complex 3D structures and artificial nanosystems on the nanometer scale [18–23], test them for various applications [24,25], and also start investigations on SW dynamics [26]. However, the study of magnetization dynamics in nanostructures with periodicity in 3D is still in its early stages [16,26].

Gyroids are 3D structures with intriguing properties that have been widely explored in photonics [27–29]. As detailed in Refs. [30–32], the gyroid emerges as a unique triply-periodic minimal surface. Its defining feature is a zero mean curvature, which means that every

* Corresponding author.

E-mail address: mateusz.golebiewski@amu.edu.pl (M. Gołębiewski).<https://doi.org/10.1016/j.actamat.2024.120499>

Received 10 September 2024; Received in revised form 17 October 2024; Accepted 21 October 2024

Available online 29 October 2024

1359-6454/© 2024 The Authors. Published by Elsevier Ltd on behalf of Acta Materialia Inc. This is an open access article under the CC BY license (<http://creativecommons.org/licenses/by/4.0/>).

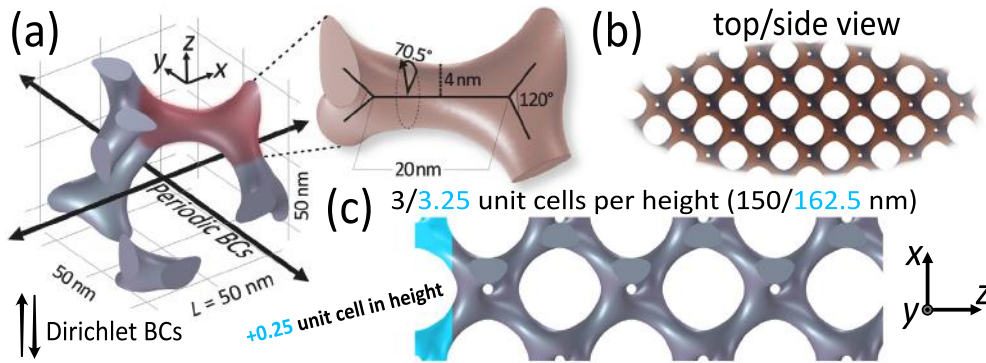


Fig. 1. Visualization of gyroidal systems used in micromagnetic simulations. The cubic gyroidal unit cell (UC) with dimensions $L = 50$ nm and a volume fraction of $\phi = 10\%$ is shown in (a), with the enlarged inset highlighting the chiral linkage between two primary gyroidal nodes. The arrows indicate the direction of application of the periodic boundary conditions (PBCs), which are applied along both the x - and y -axes defining the plane of the structure. Along the z -axis – perpendicular and far from the plane – Dirichlet BCs are assumed [see Methods 6.1]. Panel (b) shows the orthographic projection of the gyroid structure from each side of the analyzed cubic cells (crystallographic normal direction [100]), demonstrating the characteristic square distribution of gyroid channels, rotated 45 deg to the axes. The analyses were performed using models with 3 and 3.25 UCs per height (c), highlighting the influence of the surface shape on the observed effects.

point on the surface acts as a saddle point, characterized by equal and opposite principal curvatures [33]. Its intricate design comprises cubic unit cells (UCs) linked by nanorods with elliptical cross-section [34]. The inherent chirality and curvature of nanoscale gyroids [35] offer a promising avenue also for controlling non-collinear spin textures in magnetism [36]. This potential is further underscored by the visualization of magnetic structures in $\text{Ni}_{75}\text{Fe}_{25}$ gyroid networks [18]. Its chiral structure, well below 100 nm UCs, and the building struts' dimensions close to the exchange length also promise interesting SW dynamics. The effect of Ni gyroid crystallography on resonance frequencies has recently been demonstrated using micromagnetic simulations and broadband ferromagnetic resonance measurements [37].

In this paper, we study the magnetization dynamics in a 3D plane extended and height finite ferromagnetic gyroid nanostructure through theoretical analysis of ferromagnetic resonance (FMR) modes. Unexpectedly, we find that for some specific orientations of the in-plane bias magnetic field, the lowest frequency signal with the highest FMR intensity comes from a surface-localized mode. Since the localized mode has a wavevector of $k = 0$, it clearly indicates that the localization is not associated with any propagating modes, including the Damon–Eshbach type [38]. It is also not a Shockley [39] or topologically protected type of surface state [40], which requires a Bragg bandgap in the SW spectrum. To explain this unusual type of localization, we use a simpler structure with vertically layered, orthogonally alternating cylindrical ferromagnetic nanorods. On this basis, we also reject the hypothesis that this localization is just due to the non-uniformity of the demagnetizing field at the surface of the structure (i.e., edge modes [41]), but we show that the demagnetizing field plays an important role by creating potential barriers for SWs, whose localization is determined by the exchange interaction. Thus, these results provide a new type of SW surface localization with a high absorption intensity of a homogeneous microwave field. Importantly, the localization can be controlled by rotation of the in-plane bias magnetic field as well as by shape manipulation, especially of the surface region of the structures. It allows the SW intensity to be transferred from the bottom surface, through the bulk, to the top surface by simply rotating the sample or the magnetic-field direction [42–44].

2. Gyroid structure and numerical simulations

The gyroidal surface divides space into two contrasting labyrinths that intersect at angles of 70.5 deg [Fig. 1(a)], creating a captivating

geometric pattern. Its representation can be expressed by the trigonometric equation:

$$\begin{aligned} &\sin(2\pi x/L) \cos(2\pi y/L) + \\ &\sin(2\pi y/L) \cos(2\pi z/L) + \\ &\sin(2\pi z/L) \cos(2\pi x/L) \leq (101.5 - 2\phi)/68.1, \end{aligned} \quad (1)$$

where L signifies the gyroid UC length and ϕ is a filling factor. In our research, the UC of the nickel-made gyroid measures 50 nm, as shown in Fig. 1(a), which results in a single strut diameter of 8 nm, thus comparable to the exchange length [18]. It relates to the volume fraction of $\phi = 10\%$. In this work, we study gyroids in the form of a thin films with the [100]-direction normal to the plane [Fig. 1(b)] and with two different heights: 3 UCs (150 nm) and 3.25 UCs (162.5 nm) [Fig. 1(c)].

To study the SW dynamics, we numerically solve an eigenproblem obtained from the Landau–Lifshitz (LL) equation in linear approximation. Using periodic boundary conditions (PBCs) on the UC boundaries along the x - and y -axes, we model infinite gyroidal films (see Fig. 1). Details on the technical and theoretical aspects of the simulations can be found in the Methods, Section 6.1. For each of our simulations, we adopt material parameters typical of nickel (Ni) films: the saturation magnetization $M_s = 480$ kA/m, the exchange stiffness $A_{\text{ex}} = 13$ pJ/m, and the gyromagnetic ratio $\gamma = 176$ rad/s/T [45,46]. The external magnetic field, $\mu_0 H_{\text{ext}}$, remains constant at 500 mT. This magnitude, as supported by Ref. [18], validates our assumption of complete saturation of magnetization in the gyroid structure.

3. Results

3.1. Surface modes in gyroid

We examine the FMR response of the gyroid structure as a function of the external magnetic field (500 mT) direction within its xy -plane. As mentioned above, we consider films with two heights, 150 nm (3 UCs) and 162.5 nm (3.25 UCs), which form angled and parallel patterns on the top and bottom surfaces of the gyroid film, respectively (see the top panels in Fig. 3 showing the struts at the top and bottom of the film as viewed from above). As shown in Fig. 2, the FMR spectra [for 3 UCs (a) and 3.25 UCs (b)] for 0 deg angle of static field orientation consist of only a single peak of high intensity [all spectra intensities were calculated using Eq. (6) based on the response to the homogeneous microwave magnetic field excitation h_{dyn} – see Methods, Section 6.1]. In addition to the frequency decrease, when the field is

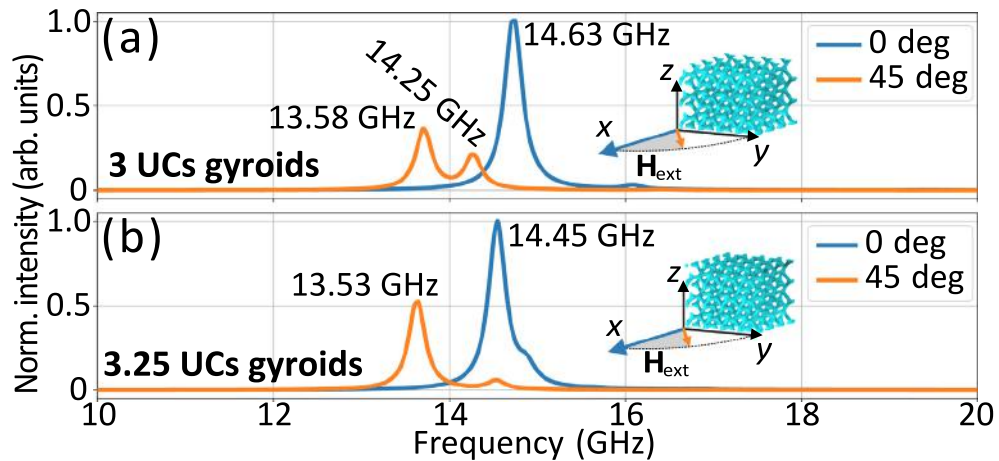


Fig. 2. Normalized FMR spectra of the gyroid structures with 3 UCs (a) and 3.25 UCs (b) per height. The colors indicate various angles of the external magnetic field relative to the x -axis. The values of the corresponding frequencies are given for the high-intensity peaks.

rotated by 45 deg, the spectra in Fig. 2 also clearly show the emergence of a secondary peak of lower intensity. The lowest-frequency, high-intensity peaks are attributed to the modes with in-phase magnetization oscillations over the height, while the secondary peaks are attributed to an asymmetric quantized SW mode [see Fig. S1(a) and (b) in the Supplementary Information]. In the following, we will focus only on the resonant frequency mode, which has the most intense response to the homogeneous microwave magnetic field and is the lowest frequency mode in a given configuration.

Unexpectedly, the rotation of the magnetic field along with the orientation of the outer parts of the gyroid affects not only the frequency but also the amplitude distribution of this SW mode, as shown in Fig. 3. Specifically, when the field aligns with the x -axis for 3 UCs case [Fig. 3(a)], magnetization distribution appears nearly uniform across the layer's entire height, exhibiting a bulk concentration preference, henceforth referred to as a bulk mode (frequency 14.63 GHz). However, for a 3.25 UCs, i.e., where the top and bottom of the structure are oriented the same, we can see the distribution of the magnetization tendency towards localization in the upper level (14.45 GHz). A significant change in amplitude distribution occurs when the field is rotated by 45 deg — the FMR mode is predominantly concentrated in one or both of the surface regions of gyroids for the 3 UCs and 3.25 UCs cases (13.58 and 13.53 GHz), respectively, which we refer to as surface modes. A subsequent rotation by another 45 deg aligns the field along the y -axis [Fig. 3(c)], transitioning the mode back to an almost uniform state for 3 UCs structure (14.43 GHz), albeit with a distinct bias towards both surfaces. For the 3.25 UCs case (14.48 GHz), we again see the tendency of the magnetization to localize, but this time on the bottom of the layer. At 135 deg rotation [Fig. 3(d)], the pattern of strong localization reemerges for 3 UCs structure (13.57 GHz), yet on the opposite surface compared with 45 deg, showcasing a dynamic shift in vertical localization of the FMR mode depending on the field's rotation. At the same time, for a 3.25 UCs structure (13.90 GHz), the field directed at an angle of 135 deg from the x -axis in the plane, causes the magnetization to be concentrated in the inner, bulk part of the structure. Completing the cycle, a 180 deg rotation reinstates the magnetization distribution to its original states observed at 0 deg in both cases.

Gyroidal systems, due to their complexity, significantly complicate the interpretation of the obtained results, therefore to gain a deeper insight into the mode localization phenomena, we propose a model of a simple three-dimensional structure with reduced complexity. As a result of the systematic study (see Supplementary Information, Fig. S6), a woodpile-like scaffold structure, in which the horizontal piles are separated and connected with vertical bars, emerged as an optimal candidate that meets the criteria, notably:

- material continuity essential for facilitating exchange interactions,
- alternating and perpendicular configuration of nanorods designed to influence the modulation of demagnetizing field distribution,
- a size and spacing between nanorods aligning with the order of magnitude of the exchange length $l_{ex} = \sqrt{2A_{ex}/(\mu_0 M_s^2)}$ (≈ 9.5 nm for the Ni parameters).

As we will show, it captures the essential geometric attributes necessary to replicate the magnetic field angle-dependent localization effects observed in gyroids.

3.2. Woodpile-like scaffolds

The proposed woodpile-like scaffold structure is a stack of vertically and orthogonally distributed cylindrical nanorods, as shown in Fig. 4(a,b), with the vertical distance between them defined as d . In the micromagnetic simulations, the radius of cylinders was kept constant at $r = 3$ nm and the width of the UC (nanorod length) at $R = 50$ nm, with PBC in the xy -plane, as in the case of gyroids. The selection of this structural type is driven by the analogies observed in the distribution of critical struts. As depicted in Fig. 4(c), the hard-axis and easy-axis struts are arranged quasi-perpendicularly, functioning as energy barriers under the influence of an external magnetic field in both systems. In addition, the scaffold nanostructures allow fast and efficient analysis of the FMR mode distribution, taking into account an even number of orthogonal rods (asymmetry through height – surface top/bottom bars are perpendicular to each other as in the 3-UCs gyroid structure) and an odd number of them (symmetry through height – surface top/bottom bars are parallel to each other, as in the 3.25-UCs gyroid structure), as shown in Fig. 4(b). Thus, according to the framework established in Section 3.1, the scaffold structure has been categorized into two configurations: symmetric, with an odd number of scaffold levels, and asymmetric, with an even number of levels. In our work, the symmetric configuration is represented by the 156 nm-high structure consisting of 7 levels of nanorods, while the asymmetric configuration measures 184 nm in height with 8 levels of nanorods. Unlike gyroids, the entire structure, not just the surface reconstructions, has inversion symmetry.

The scaffold structure is subjected to micromagnetic simulations similar to those performed on gyroids. We examine the FMR response of the structure as a function of the 500 mT external magnetic field direction within its xy -plane. Representative FMR spectra for the two analyzed scaffold structures in the field at 0 and 45 deg (from x -axis, in-plane) are shown in Fig. 5(a) and (b), respectively. They were

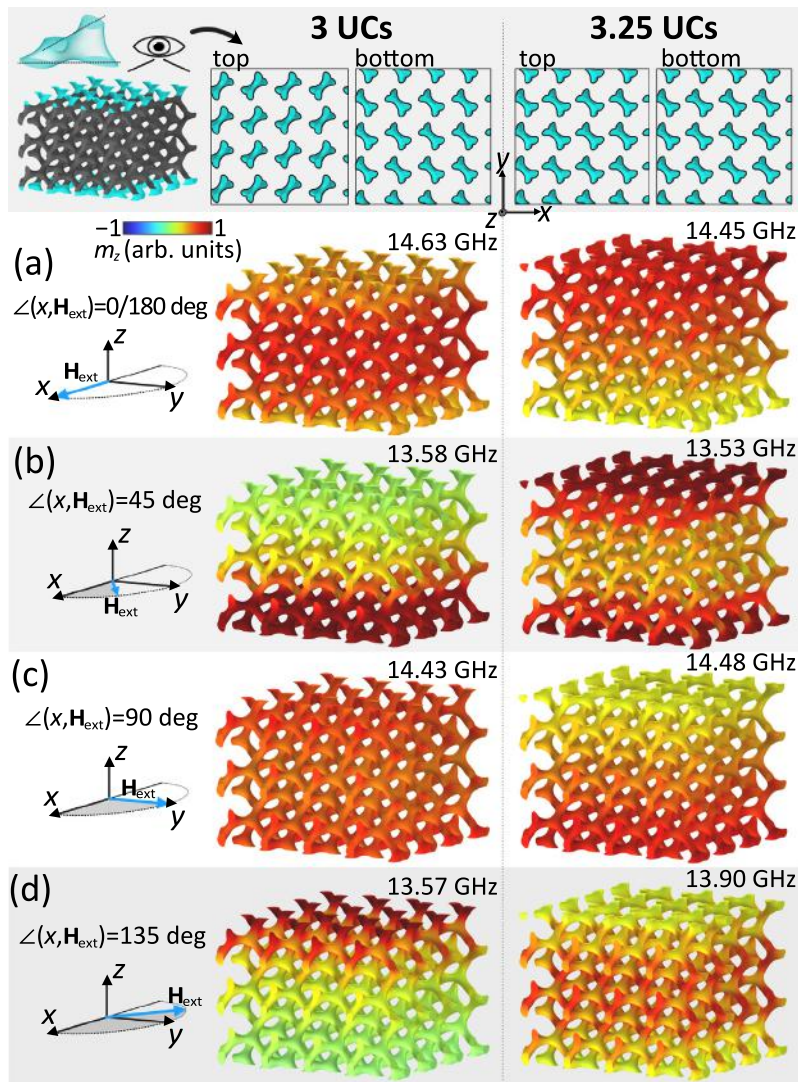


Fig. 3. Distribution of the dynamic component of the magnetization m_z in a gyroid structure with a $\phi = 10\%$ and height of 150 nm (3 UCs — angled surface struts on the top and bottom surface, left side) and 162.5 nm (3.25 UCs, parallel surface struts, right side). Above are the orientations of the outer struts for the two configurations studied (top view). Different configurations of the direction of the external magnetic field in the plane of the layer are shown, demonstrating the differences in the localization of individual FMR modes. For better visibility, the gyroidal arrays consist of 4×4 columns of the UC.

determined using the same technique as described above for the gyroids (Fig. 2) and explained in detail in Methods, Section 6.1. Again, the most intense mode has the lowest frequency and oscillates in phase throughout the volume. There is also the second, slightly weaker peak clearly visible in Fig. 5(a) for a static field angle of 0 deg (blue line, 9.80 GHz), which represents the first, asymmetric SW mode quantized along the z -direction [see Fig. S1(c) and (d) in the Supplementary Information].

Initiating with the field oriented along the x -axis [Fig. 6(a)], the symmetric configuration exhibits bulk localization (frequency 9.79 GHz), namely in nanorods oriented perpendicular to the external field (these include y -axis aligned rods and connecting vertical bars) with almost no intensity in the nanorods aligned with the magnetic field. Conversely, the asymmetric configuration demonstrates energy localization within the upper plane of the film, resulting in a surface mode (9.59 GHz). A 45 deg rotation of the field, [Fig. 6(b)], yields a configuration where the nanorod junctions became focal points for SW amplitude concentration, favoring the bulk section. The orientation of the field along the y -axis [Fig. 6(c), 90 deg] brought forth a critical scenario in this simulation segment. For the symmetric structure, where

the nanorods aligned with the x -axis are present, localization at both surfaces is observed (at 9.58 GHz). In contrast, in the asymmetric structure, the localization is manifested on the bottom surface, i.e., opposite to the x -axis saturation case at 9.59 GHz. Further on, a 135 deg rotation [Fig. 6(d)] repeats the results obtained for 45 deg rotation. The rotation of 180 deg brings back the original structure, completing the cycle.

3.3. SW localization – quantitative analysis

To accurately quantify SW localization, the inverse participation ratio (IPR) serves as a valuable parameter. Traditionally employed in quantum mechanics to assess the localization of wave function [47–50] the IPR is defined as $\text{IPR} = \sum_i |\psi_i|^4 / (\sum_i |\psi_i|^2)^2$, where ψ_i symbolizes the wave function at the i th site or lattice point. This parameter effectively measures how concentrated the wave function is within a given discrete space, providing a scalar value that differentiates localized states from extended ones. In continuous ferromagnetic systems, as in our case, the IPR needs the transition to the continuous form, which requires an integral form [51] and the use of a SW amplitude instead of the

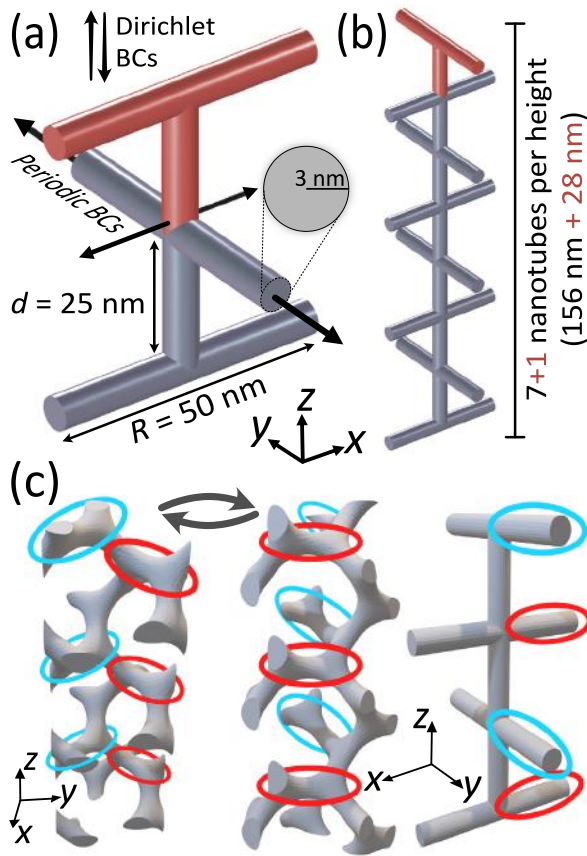


Fig. 4. Visualization of the scaffold models used in the micromagnetic simulations. The enlarged representative cutout in (a) illustrates the main geometric features of the nanorods, including their UC length of $R = 50$ nm, vertical distance $d = 25$ nm, and circular cross-section radius $r = 3$ nm. The arrows indicate the direction of the applied boundary conditions, in the same way as for gyroids (see Fig. 1). The red color marks an additional level used to manipulate the vertical symmetry of the whole structure. Model (b) shows a full-height column used to perform calculations with a symmetric arrangement (with 7 horizontal nanorods) and an asymmetric arrangement (with 8 nanorods), where the bottom one is rotated 90 deg with respect to the top one. In (c), the critical gyroid rods for analysis are highlighted, schematically illustrating the structural similarities between the two systems studied. Blue ellipses indicate the hard-axis struts, while red ellipses mark the easy-axis struts, which act as energy “barriers” under the influence of an external magnetic field oriented parallel to them. (For interpretation of the references to colour in this figure legend, the reader is referred to the web version of this article.)

wave function. Finally, the formula for IPR in magnonic systems can be expressed as:

$$\text{IPR} = \frac{\int_V |m(\mathbf{r})|^4 dV}{(\int_V |m(\mathbf{r})|^2 dV)^2} \cdot V, \quad (2)$$

where $|m(\mathbf{r})| = (m_x(\mathbf{r})m_x^*(\mathbf{r}) + m_y(\mathbf{r})m_y^*(\mathbf{r}) + m_z(\mathbf{r})m_z^*(\mathbf{r}))^{1/2}$ is the position-dependent absolute value of the complex SW amplitude, and the integration is over the volume V of the single UC. An asterisk sign (*) indicates a complex conjugate. For a completely delocalized magnetic excitation, where the amplitude of the SW mode is uniform across the entire volume of the ferromagnet, the IPR yields the value of 1. Conversely, in the case of extreme localization, where the SW mode is concentrated at a single point within the volume, resembling the behavior of a Dirac delta function, the IPR approaches infinity.

Fig. 7(a) provides a quantitative validation of the SW mode localization behavior inferred from the results depicted in Figs. 3 and 6. The IPRs of the scaffold structures (dashed lines) show that the localization of SWs occurs at field angles of 0, 90, and 180 deg. From

Fig. 6, we can see that this corresponds to the top-bottom-top cycle of surface localization in asymmetric scaffolds, and the center-surfaces-center magnetization distribution in symmetric scaffolds, respectively. The lower IPR values for the symmetric structure (red dashed line) are due to the fact that the SW modes are generally distributed over a larger volume than in the asymmetric case (green dashed line). This result further underscores the conclusions of Section 3.2, i.e., the crucial influence of structural symmetry on the magnetization switching within the scaffolds, making the localization on opposite surfaces energetically preferential for the asymmetric structure after a 90-deg field rotation.

The angular dependence of IPR for 3-UCs gyroids [blue solid line in Fig. 7(a)] qualitatively mirrors (with a 45 deg shift) the behavior seen in the asymmetric scaffold structure. However, an IPR maximum is observed at field rotation angles around 55 deg and, due to symmetry, around 125 deg. Conversely, the IPR values decrease at angles of 0, 90, and 180 deg. In the case of 3.25-UCs gyroids (orange solid line), the situation changes significantly — here we have a clear weakening of the IPR (due to both side localization) and a shift of the IPR peaks to the first quarter of the bias field angle, and a flattening of the IPR to a low value between 90 and 180 deg of the bias field orientation. Thus, the two gyroidal structures, which differ in height by only 0.25 UC, show significant differences in these dependencies. This indicates the effect of the surface cut and the breaking of the 90-deg symmetry, suggesting the influence of structural chirality.

The strong influence of the surface cut on the localization phenomenon can be understood by looking carefully at the cuts in Fig. 3 — the top and bottom surface struts have their specific effective directions relative to the external magnetic field. However, the part primarily responsible for the localization is not the outermost surface, but its inner junction towards the center [can be seen well in the upper left corner image in Fig. 3, and the first illustration in Fig. 4(c)], as indicated by the slightly higher SW amplitude. This is due to a larger demagnetizing field as will be discussed later in this paper. Thus, in a system composed of 3 UCs, the line effectively normal to this part of the structure is directed about 125 deg from the x -axis in the upper layer and about 55 deg in the lower layer. For a 3.25 UC high gyroid, the normal to the SW localization inducing part is rotated about 35 and 55 deg from the x -axis for the top and bottom layers, respectively. As can be seen from the plots in Fig. 7(a), this coincides well with the IPR peaks. We can therefore correlate the localization dependence with the demagnetizing field and chirality of the gyroidal structure. It is also worth noting that the effect of SW localization is always present in gyroids — it is only its dependence on the direction of the bias magnetic field that changes (more examples in the Supplementary Information, Sec. II, Figs. S4 and S5).

In Fig. 7(b) we see the resonant frequency of SW cyclically decreasing and increasing with the field rotation, which is clearly associated with the localization peaks in all cases. The maximum frequency variation is approximately 3.5 GHz for scaffolds and 1 GHz for gyroids. There is a one-to-one correspondence between the maximum (minimum) of the IPR and the minimum (maximum) of the FMR frequency for the scaffold structure. Consequently, the frequency dependence is a smooth sine-like function characteristic of the two-axis easy anisotropy system. However, a slight asymmetry is observed for the gyroid (solid orange line) between the orthogonal directions of the magnetic field, again indicating that the chirality of the structure may play a role. Thus, the fourfold symmetry seen in the FMR spectra is also present in the IPR dependence on field orientation for the scaffold structures, but it is lost in gyroids. The drop in the mode frequency with increasing IPR can be understood as an influence of the static demagnetizing field resulting in the accumulation of dynamic magnetization in smaller regions.

3.4. Demagnetizing field effect

Common to woodpile-like systems is that the lowest frequency mode is always localized in the nanorods oriented perpendicular to the

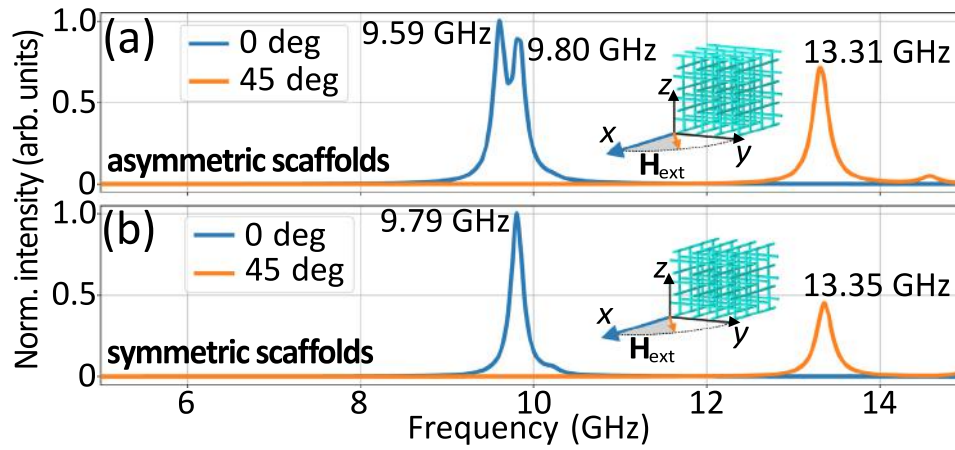


Fig. 5. Normalized FMR spectra of the woodpile-like scaffold structures used in the study — asymmetric with 8 horizontal nanorods (a) and symmetric with 7 horizontal nanorods (b) per height. The colors indicate various angles of the external magnetic field relative to the x-axis. The values of the corresponding frequencies are given for each high-intensity peak.

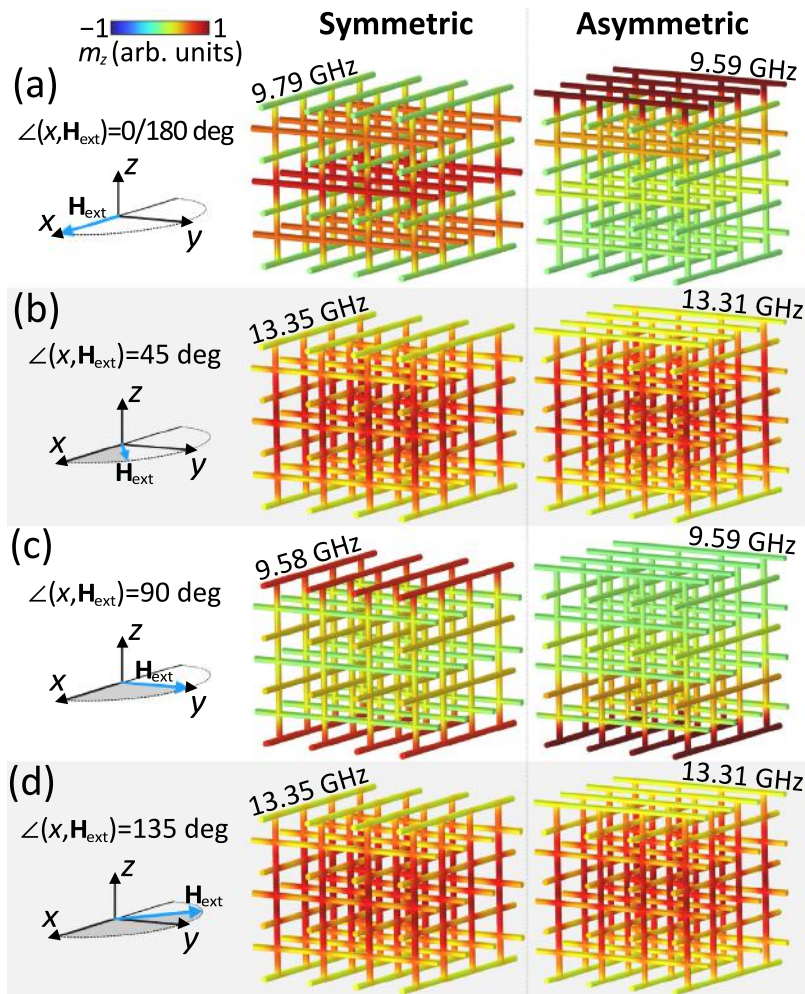


Fig. 6. The dynamic magnetization component distribution, m_z , across scaffold structures featuring symmetric (156 nm height) and asymmetric (184 nm height) configurations, subjected to different orientations of the external magnetic field within the plane, adjusted in 45-deg increments from panels (a) to (d). It showcases the localization patterns of FMR modes under distinct magnetic field configurations, represented within 4×4 column arrays for detailed visual comparison.

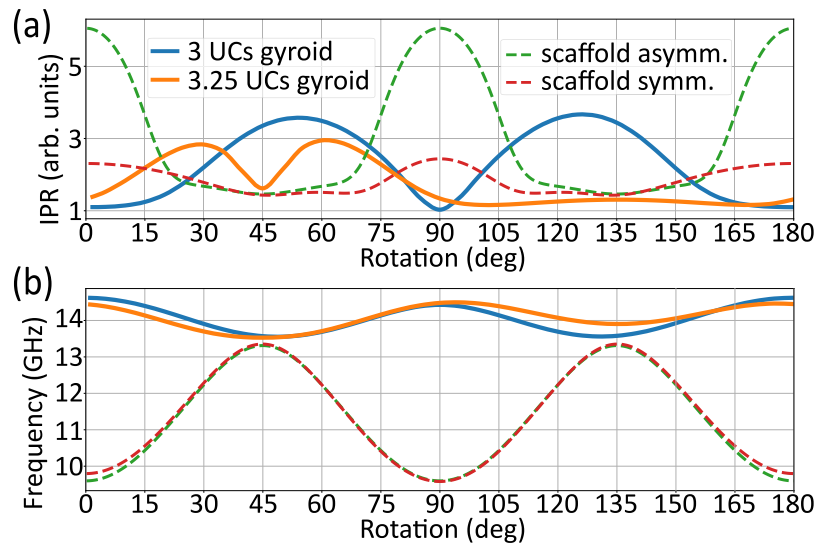


Fig. 7. IPR (a) and FMR frequency (b) as a function of the rotation angle of the external magnetic field over the plane of the analyzed gyroids (solid line) and scaffolds (dashed line) structures. Different colors indicate the asymmetric and symmetric configurations of both nanosystems.

external magnetic field. This is a result of the static demagnetizing field. To better understand this effect, we take the smallest building block of the scaffold structure, which is a single infinitely long nanorod [52]. When the field is parallel to it, the demagnetizing field is not generated, resulting in a high FMR frequency of 22.41 GHz [53]. On the other hand, the external field perpendicular to the rod produces a strong demagnetizing field, resulting in a reduction of the effective magnetic field and lowering the FMR frequency of a single rod to 8.94 GHz. The field rotated by 45 deg to the rod produces a moderate demagnetizing field so that the FMR frequency reaches 16.00 GHz. This behavior is effectively transferred to the scaffold structure, shown in Fig. 6. For 0 and 90 deg, the FMR mode is localized in the levels with rods perpendicular to the external field (9.79 and 9.58 GHz). For 45 and 135 deg configurations (13.35 GHz), only the vertical bars remain perpendicular to the field, and therefore they are the parts with the strongest amplitude of the FMR mode.

As shown in Fig. 4(c), both gyroids and scaffold structures are built from a vertically alternating distribution of bonds. This leads to an analogous dependence of the static demagnetizing field on the external field rotation as for the single nanorod described above. If the field is effectively parallel to the gyroid struts (and at the same time perpendicular for adjacent ones), the local demagnetizing field will be alternately weaker and stronger, creating the potential wells in which the FMR modes are localized. Although perfect alignment is impossible in gyroids due to the lack of straight rods (see Fig. 1), we observe analogous properties of the magnetization distribution as in the scaffold nanostructures.

When discussing the demagnetizing field, we cannot overlook the stray field generated by the nanorods. As an example, let us take the symmetric scaffold structure for the field applied along the x -axis, as depicted in Fig. 6(a). In this case, the rods aligned with the y -axis (with the largest mode amplitude) produce a stray field in the neighboring levels of parallel nanorods, in the direction opposite to the external field. Levels in the center of the structure have two close parallel neighbors compared to one for the surface level, so the stray field is stronger in the center. Since the stray field enhances the effect of the demagnetizing field, the effective field in the center is the smallest, resulting in the lower local FMR frequency and, hence, the largest amplitude. The same reasoning can be applied to the 45 and 135 deg cases. However, the stray field cannot explain the strong surface localization that is present for the 0-deg field in the asymmetric structure and for the 90-deg field in both structures. This is further confirmed

in Fig. 8(c), which shows the UC-averaged internal magnetostatic field \mathbf{H}_d^{\parallel} (including the demagnetization as well as a stray field) along the z -axis for the asymmetric scaffold structure for 0, 45, and 90 deg field orientation. It is clear that the depths in the magnetostatic field are located at the nanorods, which are perpendicular to the bias field at 0 and 90 deg, but their depth is almost the same. Qualitatively similar dependencies of the average magnetostatic field are found in the gyroid [Fig. 8(a,b)]. However, here the field variations are smooth due to the complex geometry and different orientations of the struts. Thus, the inhomogeneity of the internal magnetostatic field determines the type of struts of the FMR mode localization, but does not justify the surface or bulk localization of the SW mode in dependence on the bias field orientation. For more information on the effect of the gyroidal filling factor and its height on localization, see the Supplementary Information, Sec. II.

The results for both scaffold and gyroid structures not only underscore the intricate interplay between geometry, magnetic field orientation, and magnetostatic fields in these advanced magnonic materials but also point to the important role of other interactions in enabling the tunable localization of SW modes. The mode analysis during the design of a woodpile-like structure suitable to reproduce this effect (Supplementary Information, Fig. S6) showed the necessity of its vertical continuity, which led us to conclude that the surface localization in 3D nanostructures is not related to the dynamic stray field, but rather to the exchange interaction. The following section and simulations confirm that exchange-related effects are critical in driving this behavior.

3.5. Exchange interaction and vertical period impact in scaffold structure

Micromagnetic simulations investigating the variation of the vertical distance between neighboring nanorods, d , in asymmetric scaffold structures, as shown in Fig. 9, support our interpretation of the influence of exchange interactions on the observed effects. This analysis focuses on the amplitude distribution of FMR mode and corresponding IPR values as a function of the separation between adjacent perpendicular nanorods. Fig. 9(a) shows a pronounced IPR value for 0 deg (blue line) within the 5–45 nm range of d , with the maximum IPR ≈ 6 at 23 nm, signifying the FMR mode localization on the surface nanorod (see the modes $\langle 1 \rangle$ and $\langle 2 \rangle$). Beyond this optimal distance, the magnetization shifts from a surface localized state to the bulk (mode $\langle 3 \rangle$), saturating IPR value at about 2.5. The bulk mode concentration

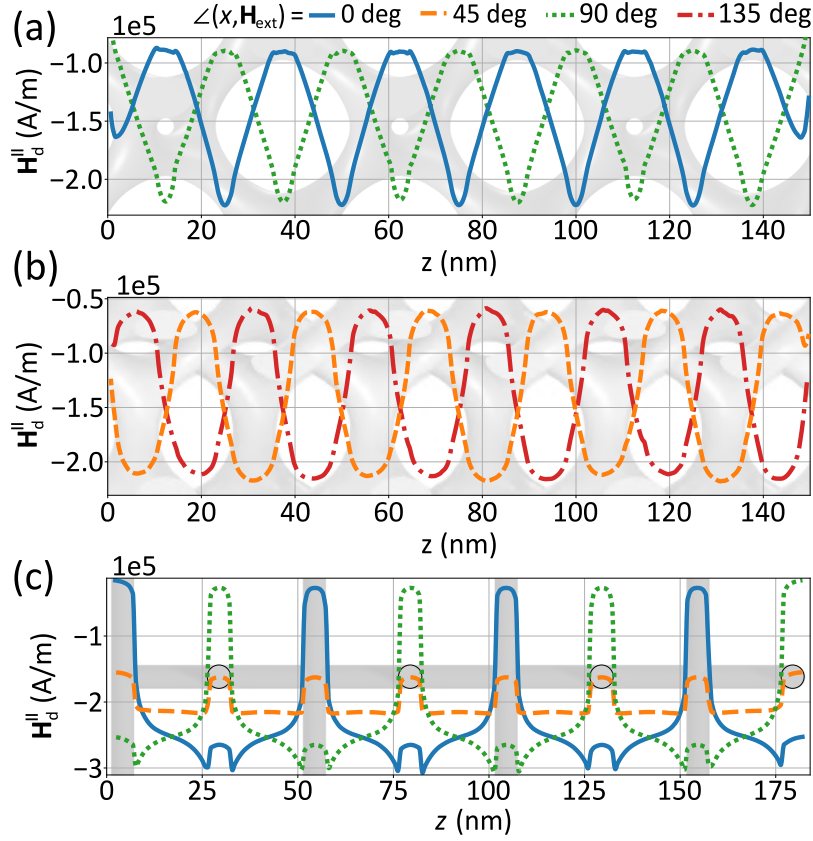


Fig. 8. Plots of the internal magnetostatic field $H_d^||$ (including demagnetizing and stray fields, see Methods 6.1) parallel to the bias field H_{ext} , averaged over the UC and projected here on the z -axis (along its height, $H_d^|| (z) = 1/S \int_S H_d(x, y, z) dx dy$). The different colors correspond to the average distribution of $H_d^||$ for different directions of the static magnetic field H_{ext} relative to the x -axis. Panel (a) shows the demagnetizing field in the 3-UCs gyroid for the H_{ext} field directed at 0 and 90 deg (the corresponding projection of the structure can be seen in the background). In (b) we see the analogous results for angles of 45 and 135 deg, along with the corresponding projection of the gyroid. (c) The $H_d^||$ of the asymmetric scaffold structure, for an external magnetic field directed at angles of 0, 45 and 90 deg (background structure projection for normal along the x -axis).

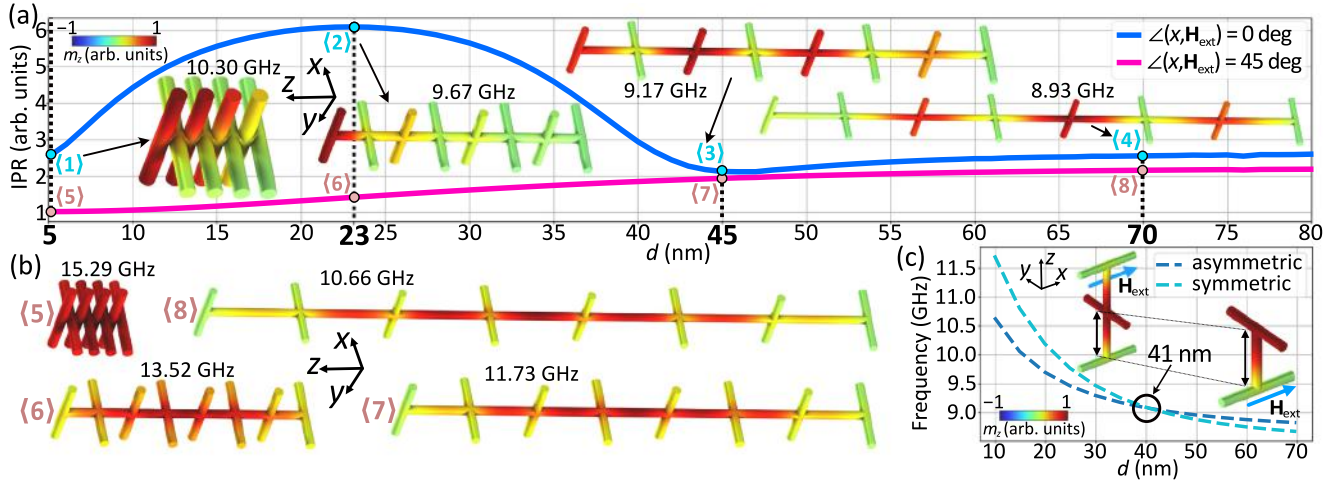


Fig. 9. The ferromagnetic response of the scaffold nanosystem as a function of the distance (d) between adjacent nanorods. Panel (a) presents the IPR against d under two conditions: with the magnetic field aligned along the x -axis (depicted in blue) and with the field rotated by 45 deg within the plane (shown in magenta). The critical points highlighted on this curve correspond to specific distributions of the dynamic magnetization component m_z of the FMR modes within the analyzed nanostructures. These key spots are marked by numbers, with visualizations of the modes for the 45-deg field configuration provided in (b). Panel (c) illustrates how the FMR frequency varies with d for both symmetric and asymmetric one-unit cell high scaffolds, for H_{ext} parallel to the x -axis. It includes depictions of the modes at a significant juncture — where the frequencies of both configurations converge at $d = 41$ nm. (For interpretation of the references to colour in this figure legend, the reader is referred to the web version of this article.)

remains in nanorods, which are perpendicular to the field, reflecting the inherent inability of the structure to adopt a fully delocalized configuration across its volume (mode (4)). For simulations with the

field oriented 45 deg from the x -axis [indicated by the magenta curve in Fig. 9(a)], the response is monotonic, increasing IPR from 1 at $d = 5$ nm up to 2.1 at $d = 80$ nm. This change in IPR is associated with the change

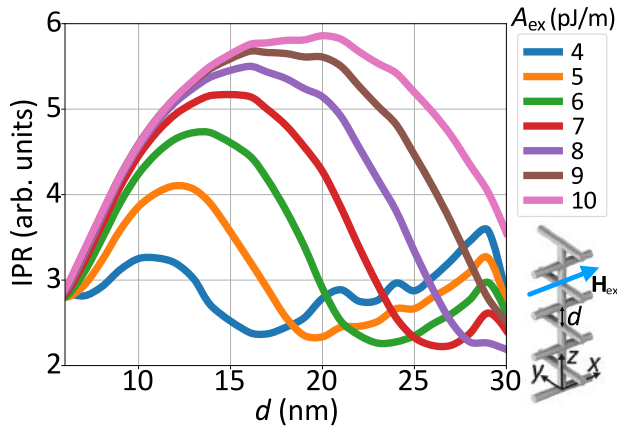


Fig. 10. Plot of IPR variation within the range indicative of surface localization in scaffold structures (asymmetric, H_{ext} along x -axis), as a function of the nanorod separation d , for different values of the exchange constant A_{ex} .

in the SW amplitude distribution from uniform at $d = 5$ nm (mode (5)) to the bulk with amplitude in the nanorod oriented along the z -axis (mode (8)).

In both cases, 0 and 45 deg, the amplitude distribution at $d > 45$ nm corresponds to the H_d^{\parallel} profiles [see Fig. 8(c)], i.e., the maximum of the SW amplitude is concentrated in the regions with the largest H_d^{\parallel} . The proximity between xy -plane-oriented nanorods at $d < 45$ nm narrows these potential wells for SW confinement, increasing their frequency and the leakage of the amplitude into neighboring regions, especially in the case of shallow wells of H_d^{\parallel} , i.e., at 45 deg where well depth is less than 50 kA/m [Fig. 8(c)]. In the case of 0 deg, the potential wells are deep (above 250 kA/m), and the increase in frequency is associated with the transfer of the SW amplitude to the surface, which has a nanorod perpendicular to H_{ext} , since it provides more suitable conditions for the FMR mode than the bulk cells. This is because in a bulk part, each field-orthogonal rod is flanked by two field-parallel “pinning” neighbors, whereas surface nanorods are influenced by only one such neighbor. Thus, this phenomenon can be attributed to the exchange interactions that make the frequency of SWs and their localization dependent on the magnetization pinning at the boundaries: the demagnetizing field wells or surfaces. Consequently, at 0 deg and $d < 45$ nm the only one-sided pinning of the SW amplitude in the surface field-orthogonal nanorod provides the suitable conditions for lowering the frequency of the surface-localized SW [modes (1) and (2) in Fig. 9(a)]. This effect is similar to SW surface localization and SW quantization in thin ferromagnetic films presented in Refs. [54–56]. However, in these works the pinning/unpinning is introduced by surface anisotropy at the surface of the atomic lattice of spins, resulting in bulk/surface SW formation.

Fig. 9(c) illustrates how increasing d influences FMR mode frequencies in both symmetric and asymmetric, 3 and 2 level scaffolds for a bias magnetic field parallel to the x -axis (0 deg). The analysis of a single field-perpendicular rod with one magnetization-fixing rod oriented parallel to the field for the asymmetric case, and two for the symmetric case, excludes the influence of stray magnetostatic field interactions from neighboring field-perpendicular nanorods. This allows an isolated analysis of the effect of the proximity of the adjacent rods. In both configurations, the FMR mode is primarily concentrated in the nanorod oriented perpendicular to the field. In the symmetric structure, it occurs in the bulk, while in the asymmetric structure, it is localized at the surface. Notably, the frequencies of the FMR in both configurations converge at $d = 41$ nm, with the lowest frequency for surface localization at $d < 41$ nm and bulk at $d > 41$ nm. This suggests that the spatial separation along the z -axis between rods reaches a

threshold at $d = 41$ nm, beyond which exchange energy no longer dominates the dynamic magnetization distribution. This observation aligns with Fig. 9(a) for 0 deg field orientation, where the scaffold structure’s localization similarly diminishes around 45 nm, marking the shift of localization from surface to bulk rods, with minor discrepancy in d value.

To further confirm that the surface localization in scaffolds within a small d range is an effect of exchange interaction, we conducted additional simulations varying the exchange constant (A_{ex}), and plotting IPR(d). The results for asymmetric scaffold structure at 0 deg are depicted in Fig. 10. There is a pronounced variation in the IPR values, illustrating ultimately the significant impact of exchange interactions on the localization phenomena. Specifically, at $A_{\text{ex}} = 4$ pJ/m, the IPR profile appears weaker and irregular, indicating subdued surface localization effects. In contrast, at $A_{\text{ex}} = 10$ pJ/m, there emerges a distinct range ($d < 35$ nm), where surface localization is enhanced [$\max(\text{IPR}) \approx 6$], demonstrating a clear and strong SW localization effect. The exchange dominance effects on the surface localization of the FMR mode shown above for the scaffold structure can be related to the gyroid structure and the surface localization observed in Fig. 3, but due to different structures and smooth demagnetizing field variation, it needs additional analysis.

3.6. Effect of exchange interaction on surface localization in gyroids

In scaffolds, we can directly manipulate the structural parameter (d), and its relation to A_{ex} . In gyroids, we can use the filling factor ϕ (see the Supplementary Information, Sec. II.A), but by changing it we collectively affect the entire geometry and the nature of all interactions in it, including magnetostatics, shape anisotropy, and the ratio of the gyroid linear dimensions to the exchange length. In particular, the flattening of the demagnetizing field with increasing ϕ correlates with decreasing IPR and decreasing modulation of the FMR frequency (see Fig. S2 in the Supplementary Information). Thus, in this section, we analyze the gyroid structure with 3 UCs and keep the filling factor at $\phi = 10\%$ (parameters as in Section 3.1).

In Fig. 11, the localization effect is shown in the form of one-dimensional projections of the z -component of the dynamic magnetization along the z -axis, averaged over the UC in the xy -plane. The results of the gyroid [Fig. 11(a)] are juxtaposed with those of the scaffold [Fig. 11(b)] to highlight the differences and similarities of the exchange contribution to the localization effect of the studied SW modes.

In Fig. 11(b) we see the magnetization curves (m_z) for an asymmetric scaffold structure with neighboring rods at $d = 25$ nm. There is a strong dependence of the surface localization on the exchange constant — the transition from the bulk mode for small $A_{\text{ex}} (\leq 5$ pJ/m) to the surface mode for $A_{\text{ex}} \geq 8$ pJ/m. We see a similar, though smaller effect of A_{ex} on the surface localization of the FMR mode in the gyroid. For $A_{\text{ex}} = 2$ pJ/m the SW amplitude is almost equal in the first two perpendicular rods, i.e., a clear shift of the dynamic magnetization towards the center of the layer can be observed [blue line in Fig. 11(a)]. For larger values of the exchange constant, the surface localization is preserved, and the smoothing of the $\langle m_z \rangle$ curves along the z -direction with increasing A_{ex} is observed. A larger exchange ensures that the dynamic magnetization is not only concentrated in bars perpendicular to the field (where the demagnetization is largest), but spreads more homogeneously to neighboring struts, analogously to scaffold structures (for sufficiently small d and large exchange length). A more pronounced effect of the transition from the bulk to the surface state as a function of the exchange constant occurs for a gyroid with a filling of $\phi = 20\%$, for which results can be found in Fig. S3 in the Supplementary Information. In addition, we performed an analysis of the effect of the height of the gyroidal layers (independent of the cut point) on SW localization, which further confirms the influence of exchange energy on the presence of surface localization. The results are shown in the Supplementary Information, Figs. S4 and S5.

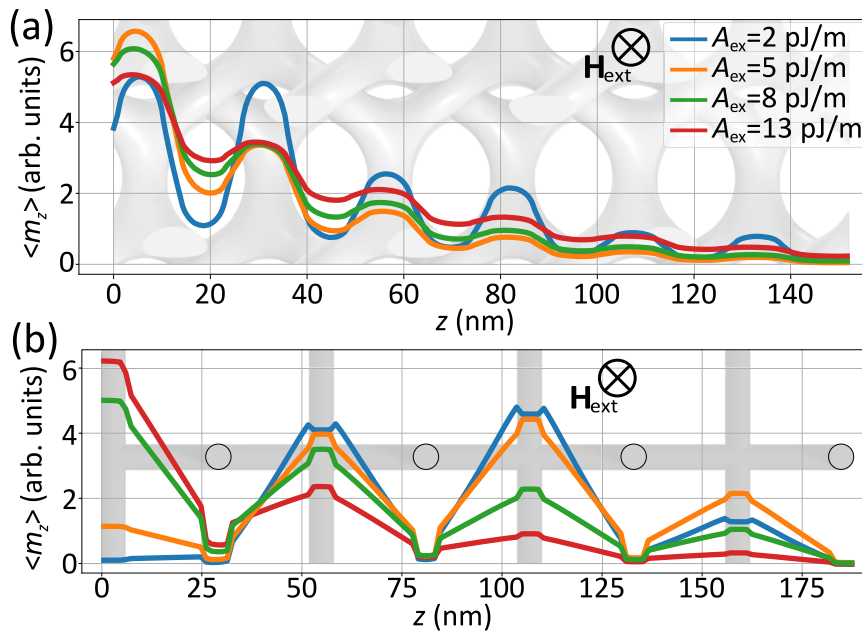


Fig. 11. Plots of the distribution of the dynamic magnetization component m_z , averaged and projected on the z-axis, for the gyroid structure with 3 UCs (a) and the asymmetric scaffold structure (b). For comparison, the case with the field at an angle of 45 deg from the x-axis was used for the gyroid, and for scaffold along the x-axis (0 deg) – both cases show clear surface localization at large A_{ex} (see Figs. 3 and 6). The colors represent different values of the exchange constant A_{ex} , whose legend is common to both plots.

Based on the analysis of the localization of SWs as a function of the exchange constant in the studied gyroid structures and their comparison with the scaffolds along the z-direction, we can conclude that it has a different, though fundamental, influence in both cases. In gyroids, the transition from the bulk to the surface state is determined only for very small values of A_{ex} (a relationship strongly related to the filling factor). A stronger exchange determines the uniformity of magnetization within neighboring nanowires. Woodpile-like scaffolds show a more “stepped” and monotonic A_{ex} -related transition from bulk to surface localization of SWs.

4. Discussion

In this study, we explored surface localization of the FMR mode phenomena within thin films made of gyroid and woodpile-like scaffold three-dimensional ferromagnetic nanostructures, focusing on the effects of the in-plane external magnetic field rotation. Using micromagnetic simulations, we have demonstrated a novel surface localization of SWs that differs from other known wave localization phenomena. Unlike Damon–Eshbach localization, which requires SW propagation, or Shockley and Tamm surface states and topologically protected edge modes, which rely on a Bragg bandgap, this newly observed surface localization does not satisfy these requirements. It also differs from edge-localized magnetostatic modes that occur in the demagnetization wells oriented perpendicular to the surface. Instead, we found that the surface localization in considered 3D structures is a cooperative effect of the magnetostatic (demagnetizing and stray) in-plane field and exchange interactions. The former creates potential wells in the nanorods (gyroid struts) perpendicular to the bias magnetic field, the latter determines the frequency in the well when its width is comparable to the exchange length. As a result, for some bias field orientations and surface cuts the SW localized at the surface UC has only one-sided pinning, which lowers its energy, making it a low-frequency surface-localized FMR mode. Thus, this research highlighted the critical influence of the static demagnetizing fields and the exchange energy in shaping the SW amplitude distribution in the ferromagnetic response of such nanostructures, thereby contributing to our understanding of the magnonic behavior in 3D structures. Furthermore, the intricate

relationship between the magnetic field orientation and the geometry of the structures was revealed, i.e., the surface configuration seemed to strongly influence the SW amplitude concentration along the height of the thin film. Nevertheless, the localization for a given field direction persists over different surface states, demonstrating its universal nature.

Such selective localization of the FMR mode introduces a novel mechanism enabling reconfigurable functionalities. This reveals the potential for enhancing experimental measurements of SWs in three-dimensional structures through localized FMR modes, among others, in the established optical techniques like Brillouin light scattering (BLS) [57] or magneto-optical Kerr effect (MOKE) microscopy [58].

5. Summary

In summary, this research presents a comprehensive investigation of SW dynamics in 3D ferromagnetic nanostructures, shifting the focus from planar systems to complex gyroidal and scaffold-like designs. We demonstrate and analyze a novel type of SW localization using extensive micromagnetic simulations and show how external factors, such as magnetic field orientation, can control the intensity, frequency, and amplitude distribution of localized FMR modes. The universal nature of this surface localization across different structures and configurations, offers significant potential for advancing 3D magnonics, e.g., through improved sensitivity in probing SW dynamics and controllable vertical energy transfer, providing deeper insight into the magnetic properties of complex structures. The knowledge gained from this work may also open new avenues for device design that exploit the properties of gyroids, woodpile-like scaffolds, or other 3D nanoarchitectures to advance the development of next-generation 3D magnonic technologies.

6. Methods

6.1. Micromagnetic simulations

To calculate SW modes within the 3D nanostructures, we employed the COMSOL Multiphysics software. It harnesses the finite-element method (FEM) to provide solutions to complex coupled systems of

partial differential equations. The SW dynamic is framed with the LL equation:

$$\frac{\partial \mathbf{M}}{\partial t} = -\gamma \mu_0 \mathbf{M} \times \mathbf{H}_{\text{eff}} \quad (3)$$

where \mathbf{M} is the magnetization vector, γ denotes the gyromagnetic ratio, μ_0 is the vacuum permeability, and \mathbf{H}_{eff} is the effective magnetic field. The nonuniformity in material properties (e.g., variations in M_s , magnetic anisotropy, or exchange stiffness) is one of the ways that introduces a spatially dependent \mathbf{H}_{eff} that, in turn, affects the localization and dispersion properties of SWs. Here, it merges the externally applied field, \mathbf{H}_{ext} , with the magnetostatic demagnetizing field, \mathbf{H}_d , and the Heisenberg exchange field, \mathbf{H}_{exch} :

$$\mathbf{H}_{\text{eff}} = \mathbf{H}_{\text{ext}} + \mathbf{H}_d + \mathbf{H}_{\text{exch}}. \quad (4)$$

The demagnetizing field is critical for SW dynamics in ferromagnetic materials, especially when it is patterned. Governed by Ampère's law, this field is derived from the gradient of the magnetic scalar potential, $\mathbf{H}_d = -\nabla U_m$. Within the magnetic body, this relationship further evolves in:

$$\nabla^2 U_m = \nabla \cdot \mathbf{M}, \quad (5)$$

while outside it, $\nabla^2 U_m = 0$. In performed COMSOL implementation, we tackled the eigenproblem derived from Eqs. (3), (4), and (5). By presuming full magnetization saturation via the bias magnetic field and adopting a linear approximation, we could dissect the magnetization vector into its static and dynamic (time t and position \mathbf{r} dependent) components $\mathbf{M}(\mathbf{r}, t) = M_s \hat{i} + \delta \mathbf{M}(\mathbf{r}, t) \forall (\delta \mathbf{M} \perp \hat{i})$, neglecting all nonlinear terms in the dynamic magnetization $\delta \mathbf{M}(\mathbf{r}, t)$. Here, we assume that the static component of the magnetization is equal to the saturation magnetization, M_s . This methodology is further explained in Refs. [59, 60].

Using PBCs on the UC boundaries along the x - and y -axes, we model in COMSOL an infinite in-plane gyroidal and scaffold-structured films (see Figs. 1 and 4). The PBCs are defined on both faces to maintain the same values for the magnetization components and magnetic scalar potential. For planes parallel to the surfaces of the films, we implemented Dirichlet boundary conditions aiming to suppress the scalar magnetic potential, $U_m = 0$, at the boundaries of the computational cell. To ensure the simulation's physical accuracy and convergence, it is essential to position these conditions sufficiently far from the specimen. In our simulations, the computational cell's height was set to be 40 times the gyroid/scaffold layer's height.

Throughout the simulations, consistent mesh quality was maintained across the different gyroid and scaffold models. The quality of the tetrahedral discretization mesh, characterized by the volume-to-length parameter, remained stable at an average value of about 0.7. It is based on a ratio of element edge lengths to element volume. This resulted in a scalable mesh of about 55,000 elements for the single cubic $\phi = 10\%$ -gyroid model [as in Fig. 1(a)], and about 85,000 for a 3-level scaffold structure [Fig. 4(a)].

Calculations of the FMR spectra (Figs. 2 and 5) of the studied structures were obtained by simulations in the frequency domain, sweeping the spatially uniform, dynamic microwave field in a given range with a step of 50 MHz. Its magnitude was set to $\mu_0 h_{\text{dyn}} = 0.005 \mu_0 H_0 = 2.5$ mT and was polarized along the y -axis. To determine the macroscopic measure of the global magnetization intensity, the complex dynamic component m_z (perpendicular to both the static and dynamic fields) was multiplied by its conjugated value m_z^* , and integrated over the entire volume of the ferromagnet:

$$I = \int_V m_z m_z^* dV. \quad (6)$$

The plots for each structure have been normalized to the maximum of one of the two spectra (the one with higher maximum intensity), preserving their relative ratio.

CRediT authorship contribution statement

Mateusz Gołębiewski: Writing – original draft, Visualization, Software, Methodology, Investigation, Funding acquisition, Formal analysis, Data curation, Conceptualization. **Krzysztof Szulc:** Writing – review & editing, Validation, Methodology, Investigation, Formal analysis. **Maciej Krawczyk:** Writing – review & editing, Validation, Supervision, Resources, Project administration, Funding acquisition, Conceptualization.

Declaration of competing interest

The authors declare that they have no known competing financial interests or personal relationships that could have appeared to influence the work reported in this paper.

Acknowledgments

The research leading to these results was funded by the National Science Centre of Poland, Projects No. UMO-2020/39/1/ST3/02413 and No. UMO-2023/49/N/ST3/03032.

Appendix A. Supplementary data

Supplementary material related to this article can be found online at <https://doi.org/10.1016/j.actamat.2024.120499>.

Data availability

The data underlying this study are openly available in Zenodo at <https://doi.org/10.5281/zenodo.13141840>.

References

- [1] B. Dieny, I.L. Prejbeanu, K. Garello, P. Gambardella, P. Freitas, R. Lehnndorff, W. Raberg, U. Ebels, S.O. Demokritov, J. Akerman, A. Deac, P. Pirro, C. Adelman, A. Anane, A.V. Chumak, A. Hirohata, S. Mangin, S.O. Valenzuela, M.C. Onbasli, M. d'Aquino, G. Prenat, G. Finocchio, L. Lopez-Diaz, R. Chantrell, O. Chubykalo-Fesenko, P. Bortolotti, Opportunities and challenges for spintronics in the microelectronics industry, *Nat. Electron.* 3 (8) (2020) 446–459.
- [2] P. Pirro, V.I. Vasyuchka, A.A. Serga, B. Hillebrands, *Advances in coherent magnonics*, *Nat. Rev. Mater.* 6 (12) (2021) 1114–1135.
- [3] A.V. Chumak, *Magnon spintronics: Fundamentals of magnon-based computing*, in: *Spintronics Handbook, Second Edition: Spin Transport and Magnetism*, second ed., CRC Press, 2019, p. 56.
- [4] A. Barman, G. Gubbiotti, S. Ladak, A.O. Adeyeye, M. Krawczyk, J. Gräfe, C. Adelman, S. Cotoana, A. Naemi, V.I. Vasyuchka, B. Hillebrands, S.A. Nikitov, H. Yu, D. Grundler, A.V. Sadovnikov, A.A. Grachev, S.E. Sheshukova, J.-Y. Duquesne, M. Marangolo, G. Csaba, W. Porod, V.E. Demidov, S. Urazhdin, S.O. Demokritov, E. Alibisetti, D. Petti, R. Bertacco, H. Schultheiss, V.V. Kruglyak, V.D. Poimanov, S. Sahoo, J. Sinha, H. Yang, M. Münzenberg, T. Moriyama, S. Mizukami, P. Landeros, R.A. Gallardo, G. Carlotti, J.-V. Kim, R.L. Stamps, R.E. Camley, B. Rana, Y. Otani, W. Yu, T. Yu, G.E.W. Bauer, C. Back, G.S. Uhrig, O.V. Dobrovolskiy, B. Budinska, H. Qin, S. van Dijken, A.V. Chumak, A. Khitun, D.E. Nikonov, I.A. Young, B.W. Zingsem, M. Winklhofer, The 2021 magnonics roadmap, *J. Phys.: Condens. Matter* 33 (41) (2021) 413001.
- [5] A.V. Chumak, P. Kabos, M. Wu, C. Abert, C. Adelman, A.O. Adeyeye, J. Akerman, F.G. Aliev, A. Anane, A. Awad, C.H. Back, A. Barman, G.E.W. Bauer, M. Becherer, E.N. Beginin, V.A.S.V. Bittencourt, Y.M. Blanter, P. Bortolotti, I. Boverter, D.A. Bozhko, S.A. Bunyayev, J.J. Carmiggelt, R.R. Cheenikundil, F. Ciubotaru, S. Cotoana, G. Csaba, O.V. Dobrovolskiy, C. Dubs, M. Elyasi, K.G. Fripp, H. Fulara, I.A. Golovchanskiy, C. Gonzalez-Ballester, P. Graczyk, D. Grundler, P. Gruszecki, G. Gubbiotti, K. Guslienko, A. Haldar, S. Hamdioui, R. Hertel, B. Hillebrands, T. Hioki, A. Houshang, C.-M. Hu, H. Huebl, M. Huth, E. Iacocca, M.B. Jungfleisch, G.N. Kakazei, A. Khitun, R. Khymyn, T. Kikkawa, M. Kläui, O. Klein, J.W. Klos, S. Knauer, S. Koraltan, M. Kostylev, M. Krawczyk, I.N. Krivorotov, V.V. Kruglyak, D. Lachance-Quirion, S. Ladak, R. Lebrun, Y. Li, M. Lindner, R. Macêdo, S. Mayr, G.A. Melkov, S. Mieszczyk, Y. Nakamura, H.T. Nembach, A.A. Nikitin, S.A. Nikitov, V. Novosad, J.A. Otálora, Y. Otani, A. Papp, B. Pigeau, P. Pirro, W. Porod, F. Poratti, H. Qin, B. Rana, T. Reimann, F. Riente, O. Romero-Isart, A. Ross, A.V. Sadovnikov, A.R. Safin, E. Saitoh, G. Schmidt, H. Schultheiss, K. Schultheiss, A.A. Serga, S. Sharma, J.M. Shaw, D.

- Suess, O. Surzhenko, K. Szulc, T. Taniguchi, M. Urbánek, K. Usami, A.B. Ustinov, T. van der Sar, S. van Dijken, V.I. Vasychka, R. Verba, S.V. Kusminskiy, Q. Wang, M. Weides, M. Weiler, S. Wintz, S.P. Wolski, X. Zhang, Advances in magnetism roadmap on spin-wave computing, *IEEE Trans. Magn.* 58 (6) (2022) 1–72.
- [6] G. Gubbiotti, *Three-Dimensional Magnonics*, first ed., Jenny Stanford Publishing, New York, 2019.
- [7] R. Hertel, R. Cheenikundil, *Defect-sensitive High-frequency Modes in a Three-Dimensional Artificial Magnetic Crystal*, 2022, PREPRINT (Version 1) available at Research Square <https://doi.org/10.21203/rs.3.rs-846190/v1>.
- [8] M. Krawczyk, D. Grundler, Review and prospects of magnonic crystals and devices with reprogrammable band structure, *J. Phys.: Condens. Matter.* 26 (12) (2014) 123202.
- [9] M. Krawczyk, H. Puzkarski, Plane-wave theory of three-dimensional magnonic crystals, *Phys. Rev. B* 77 (2008) 054437.
- [10] M. Okuda, T. Schwarze, J.-C. Eloi, S.E.W. Jones, P.J. Heard, A. Sarua, E. Ahmad, V.V. Kruglyak, D. Grundler, W. Schwarzacher, Top-down design of magnonic crystals from bottom-up magnetic nanoparticles through protein arrays, *Nanotechnology* 28 (15) (2017) 155301.
- [11] H. Kondo, Y. Akagi, H. Katsura, Three-dimensional topological magnon systems, *Phys. Rev. B* 100 (2019) 144401.
- [12] C.-B. Hua, F. Xiao, Z.-R. Liu, J.-H. Sun, J.-H. Gao, C.-Z. Chen, Q. Tong, B. Zhou, D.-H. Xu, Magnon corner states in twisted bilayer honeycomb magnets, *Phys. Rev. B* 107 (2023) L020404.
- [13] P. Fischer, D. Sanz-Hernández, R. Streubel, A. Fernández-Pacheco, Launching a new dimension with 3D magnetic nanostructures, *APL Mater.* 8 (1) (2020) 010701.
- [14] D. Makarov, O.M. Volkov, A. Kákay, O.V. Pylypovskiy, B. Budinská, O.V. Dobrovolskiy, New dimension in magnetism and superconductivity: 3D and curvilinear nanoarchitectures, *Adv. Mater.* 34 (3) (2022) 2101758.
- [15] R. Cheenikundil, J. Bauer, M. Goharyan, M. D'Aquino, R. Hertel, High-frequency modes in a magnetic buckyball nanoarchitecture, *APL Mater.* 10 (8) (2022) 81106.
- [16] A. May, M. Saccone, A. van den Berg, J. Askey, M. Hunt, S. Ladak, Magnetic charge propagation upon a 3D artificial spin-ice, *Nature Commun.* 12 (1) (2021) 3217.
- [17] M. Saccone, A. Van den Berg, E. Harding, S. Singh, S.R. Giblin, F. Flicker, S. Ladak, Exploring the phase diagram of 3D artificial spin-ice, *Commun. Phys.* 6 (1) (2023) 217.
- [18] J. Llandro, D.M. Love, A. Kovács, J. Caron, K.N. Vyasa, A. Kákay, R. Salikhov, K. Lenz, J. Fassbender, M.R.J. Scherer, C. Cimorra, U. Steiner, C.H.W. Barnes, R.E. Dunin-Borkowski, S. Fukami, H. Ohno, Visualizing magnetic structure in 3D nanoscale Ni-Fe gyroid networks, *Nano Lett.* 20 (5) (2020) 3642–3650.
- [19] A. Fernández-Pacheco, R. Streubel, O. Fruchart, R. Hertel, P. Fischer, R.P. Cowburn, Three-dimensional nanomagnetism, *Nature Commun.* 8 (1) (2017) 136–142.
- [20] C. Donnelly, A. Hierro-Rodríguez, C. Abert, K. Witte, L. Skoric, D. Sanz-Hernández, S. Finizio, F. Meng, S. McVitie, J. Raabe, D. Suess, R. Cowburn, A. Fernández-Pacheco, Complex free-space magnetic field textures induced by three-dimensional magnetic nanostructures, *Nat. Nanotechnol.* 17 (2) (2022) 136–142.
- [21] M. Hunt, M. Taverne, J. Askey, A. May, A. Van Den Berg, Y.L.D. Ho, J. Rarity, S. Ladak, Harnessing multi-photon absorption to produce three-dimensional magnetic structures at the nanoscale, *Materials* 13 (3) (2020) 761.
- [22] A. van den Berg, M. Caruel, M. Hunt, S. Ladak, Combining two-photon lithography with laser ablation of sacrificial layers: A route to isolated 3D magnetic nanostructures, *Nano Res.* 16 (1) (2023) 1441–1447.
- [23] C. Yan, L. Hao, A. Hussein, D. Raymont, Evaluations of cellular lattice structures manufactured using selective laser melting, *Int. J. Mach. Tools Manuf.* 62 (2012) 32–38.
- [24] A. Yáñez, A. Herrera, O. Martel, D. Monopoli, H. Afonso, Compressive behaviour of gyroid lattice structures for human cancellous bone implant applications, *Mater. Sci. Eng. C* 68 (2016) 445–448.
- [25] M.D. Turner, M. Saba, Q. Zhang, B.P. Cumming, G.E. Schröder-Turk, M. Gu, Miniature chiral beamsplitter based on gyroid photonic crystals, *Nat. Photon.* 7 (10) (2013) 801–805.
- [26] H. Guo, A.J.M. Deenen, M. Xu, M. Hamdi, D. Grundler, Realization and control of bulk and surface modes in 3D nanomagnonic networks by additive manufacturing of ferromagnets, *Adv. Mater.* 35 (39) (2023) 2303292.
- [27] M. Saba, M. Thiel, M.D. Turner, S.T. Hyde, M. Gu, K. Grosse-Brauckmann, D.N. Neshev, K. Mecke, G.E. Schröder-Turk, Circular dichroism in biological photonic crystals and cubic chiral nets, *Phys. Rev. Lett.* 106 (2011) 103902.
- [28] W. Flavell, A. Neophytou, A. Demetriadiou, T. Albrecht, D. Chakrabarti, Programmed self-assembly of single colloidal gyroids for chiral photonic crystals, *Adv. Mater.* 35 (23) (2023) 2211197.
- [29] S. Peng, R. Zhang, V.H. Chen, E.T. Khabiboulline, P. Braun, H.A. Atwater, Three-dimensional single gyroid photonic crystals with a mid-infrared bandgap, *ACS Photon.* 3 (6) (2016) 1131–1137.
- [30] A.H. Schoen, *Infinite Periodic Minimal Surfaces Without Self-Intersections*, Tech. rep., NASA Electronics Research Center, Cambridge, 1970.
- [31] A.H. Schoen, Reflections concerning triply-periodic minimal surfaces, *Interface Focus* 2 (5) (2012) 658–668.
- [32] G. Rosi, N. Auffray, C. Combescure, On the failure of classic elasticity in predicting elastic wave propagation in gyroid lattices for very long wavelengths, *Symmetry* (2020).
- [33] Dacorogna B., *Introduction to the Calculus of Variations*, third ed., Imperial College Press, 2014.
- [34] J.A. Dolan, B.D. Wilts, S. Vignolini, J.J. Baumberg, U. Steiner, T.D. Wilkinson, Optical properties of gyroid structured materials: From photonic crystals to metamaterials, *Adv. Opt. Mater.* 3 (1) (2015) 12–32.
- [35] M. Wohlgenuth, N. Yufa, J. Hoffman, E.L. Thomas, Triply periodic bicontinuous cubic microdomain morphologies by symmetries, *Macromolecules* 34 (17) (2001) 6083–6089.
- [36] L.V. Lich, D.T.H. Hue, D.T.H. Giang, N.H. Duc, T. Shimada, T. Kitamura, V.H. Dinh, Formation and switching of chiral magnetic field textures in three-dimensional gyroid nanostructures, *Acta Mater.* 249 (2023) 118802.
- [37] M. Gołębiewski, R. Hertel, M. d'Aquino, V. Vasychka, M. Weiler, P. Pirro, M. Krawczyk, S. Fukami, H. Ohno, J. Llandro, Collective spin-wave dynamics in gyroid ferromagnetic nanostructures, *ACS Appl. Mater. Interfaces* 16 (17) (2024) 22177–22188.
- [38] R. Damon, J. Eshbach, Magnetostatic modes of a ferromagnet slab, *J. Phys. Chem. Solids* 19 (3) (1961) 308–320.
- [39] J. Rychlý, J.W. Klos, Spin wave surface states in 1D planar magnonic crystals, *J. Phys. D: Appl. Phys.* 50 (16) (2017) 164004.
- [40] P.A. McClarty, Topological magnons: A review, *Annu. Rev. Condens. Matter Phys.* 13 (2022) 171–190.
- [41] F. Guo, L.M. Belova, R.D. McMichael, Spectroscopy and imaging of edge modes in permalloy nanodisks, *Phys. Rev. Lett.* 110 (2013) 017601.
- [42] E. Beginin, A. Sadovnikov, V. Sakharov, A. Stognij, Y. Khivintsev, S. Nikitov, Collective and localized modes in 3D magnonic crystals, *J. Magn. Magn. Mater.* 492 (2019) 165647.
- [43] K. Szulc, P. Graczyk, M. Mruczkiewicz, G. Gubbiotti, M. Krawczyk, Spin-wave diode and circulator based on unidirectional coupling, *Phys. Rev. Appl.* 14 (2020) 034063.
- [44] A.A. Martyshevskii, E.N. Beginin, A.V. Sadovnikov, Spin waves transport in 3D magnonic waveguides, *AIP Adv.* 11 (3) (2021) 035024.
- [45] J.M. Coey, *Magnetism and Magnetic Materials*, Cambridge University Press, 2010.
- [46] M. Singh, J. Callaway, C.S. Wang, Calculation of g and g' for iron and nickel, *Phys. Rev. B* 14 (1976) 1214–1220.
- [47] M. Calixto, E. Romera, Inverse participation ratio and localization in topological insulator phase transitions, *J. Stat. Mech. Theory Exp.* 2015 (6) (2015) P06029.
- [48] Y. He, S. Xia, D.G. Angelakis, D. Song, Z. Chen, D. Leykam, Persistent homology analysis of a generalized Aubry–André–Harper model, *Phys. Rev. B* 106 (2022) 054210.
- [49] M. Berciu, R.N. Bhatt, Spin waves in disordered III-V diluted magnetic semiconductors by a modified RPA approach, *Phys. Rev. B* 66 (2002) 085207.
- [50] A. Szallás, A. Jagannathan, Spin waves and local magnetizations on the Penrose tiling, *Phys. Rev. B* 77 (2008) 104427.
- [51] S. Imagawa, K. Edagawa, K. Morita, T. Niino, Y. Kagawa, M. Notomi, Photonic band-gap formation, light diffusion, and localization in photonic amorphous diamond structures, *Phys. Rev. B* 82 (2010) 115116.
- [52] D.-X. Chen, J. Brug, R. Goldfarb, Demagnetizing factors for cylinders, *IEEE Trans. Magn.* 27 (4) (1991) 3601–3619.
- [53] C. Kittel, On the theory of ferromagnetic resonance absorption, *Phys. Rev.* 73 (1948) 155–161.
- [54] J.T. Yu, R.A. Turk, P.E. Wigen, Exchange-dominated surface spin waves in thin yttrium-iron-garnet films, *Phys. Rev. B* 11 (1975) 420–434.
- [55] H. Puzkarski, Theory of surface states in spin wave resonance, *Prog. Surf. Sci.* 9 (5) (1979) 191–247.
- [56] J. Levy, Surface and interface magnons: Magnetic structures near the surface, *Surf. Sci. Rep.* 1 (2) (1981) 39–119.
- [57] T. Sebastian, K. Schultheiss, B. Obry, B. Hillebrands, H. Schultheiss, Micro-focused Brillouin light scattering: imaging spin waves at the nanoscale, *Front. Phys.* 3 (2015).
- [58] K. Perzlmaier, G. Woltersdorf, C.H. Back, Observation of the propagation and interference of spin waves in ferromagnetic thin films, *Phys. Rev. B* 77 (2008) 054425.
- [59] M. Mruczkiewicz, M. Krawczyk, V.K. Sakharov, Y.V. Khivintsev, Y.A. Filimonov, S.A. Nikitov, Standing spin waves in magnonic crystals, *J. Appl. Phys.* 113 (9) (2013) 093908.
- [60] J. Rychlý, V.S. Tkachenko, J.W. Klos, A. Kuchko, M. Krawczyk, Spin wave modes in a cylindrical nanowire in crossover dipolar-exchange regime, *J. Phys. D: Appl. Phys.* 52 (7) (2018) 075003.

SUPPLEMENTARY MATERIAL

Magnetic field controlled surface localization of ferromagnetic resonance modes in 3D nanostructures

Mateusz Gołębiewski,¹ Krzysztof Szulc,^{1,2} and Maciej Krawczyk¹

¹*Institute of Spintronics and Quantum Information,
Faculty of Physics and Astronomy, Adam Mickiewicz University,
Uniwersytetu Poznańskiego 2, 61-614 Poznań, Poland*

²*Institute of Molecular Physics, Polish Academy of Sciences,
M. Smoluchowskiego 17, 60-179 Poznań, Poland*

I. SPECTRAL ANALYSIS OF THE SPIN-WAVE MODES IN GYROID AND SCAFFOLD STRUCTURES

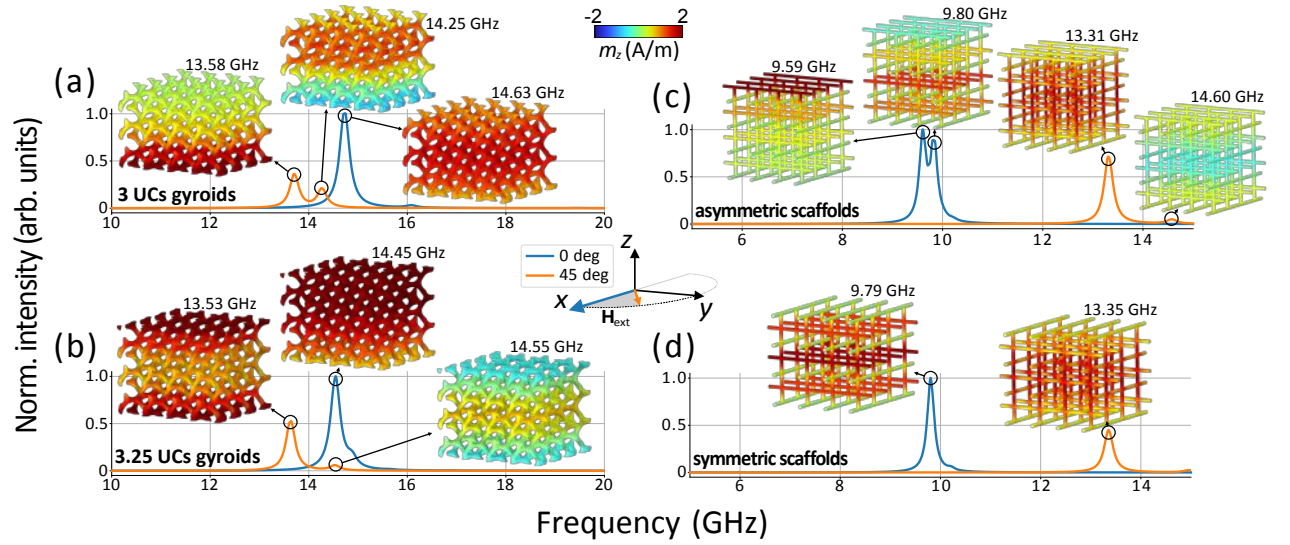


Figure S1. Visualization of higher intensity spin-wave (SW) modes in the investigated structures of gyroids [(a) – 3 unit cells (UCs), (b) – 3.25 UCs] and scaffolds [(c) – asymmetric, (d) – symmetric]. Plots of mode excitation in the structures under magnetic field applied along the x -axis (blue line) and at 45 deg to it in the xy -plane (orange line) are shown on each panel.

II. IMPACT OF OTHER MATERIAL PARAMETERS ON LOCALIZATION IN GYROIDS

A. Filling factor

As the filling factor increases, transitioning the structure towards a more homogeneous nickel layer, the effects of localization and frequency modulation begin to decrease, as shown in Fig. S2. Consequently, the rotation of the external magnetic field will no longer function as a significant modulator of mode localization in the denser structures. This trend highlights the intricate interplay between structural geometry and magnetic properties, where the shape of gyroids appears to favor the modulation of magnetic responses by field orientation adjustments.

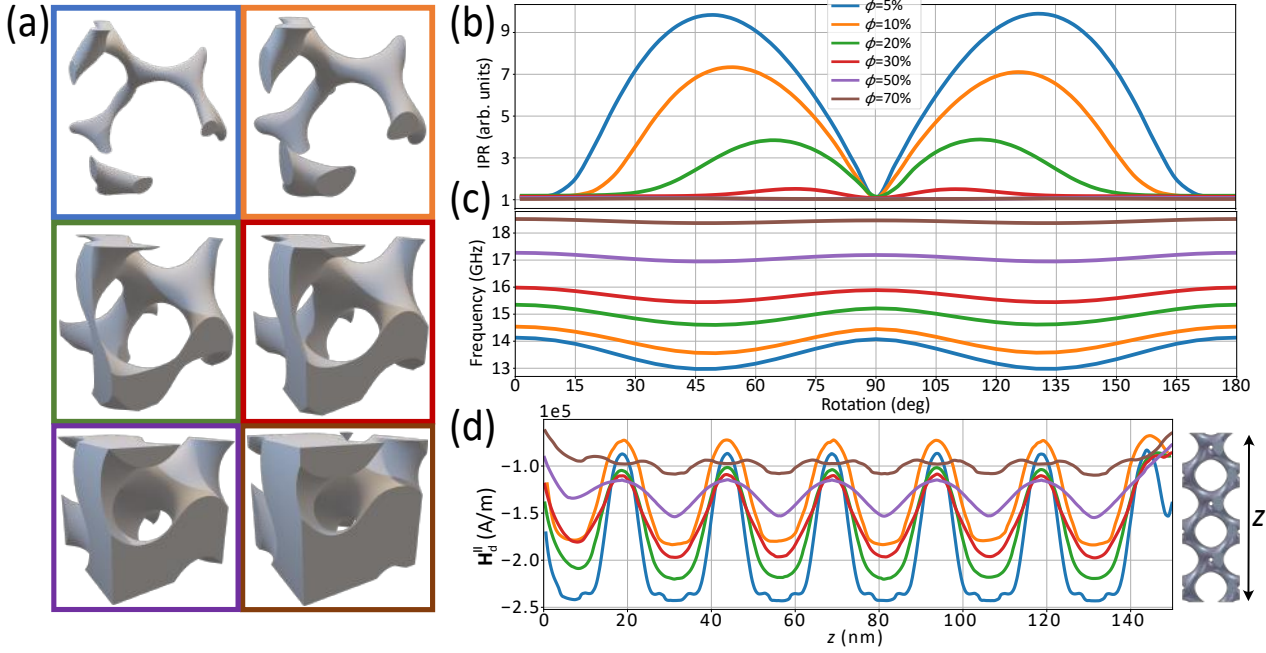


Figure S2. Variation in inverse participation ratio (IPR) (b) and ferromagnetic resonance (FMR) frequency (c) as a function of the rotational angle of the external magnetic field within the planes of gyroid structures, composed of 6 UCs across the height. The colors correspond to different filling factors ϕ of the structures, whose UCs are shown in (a).

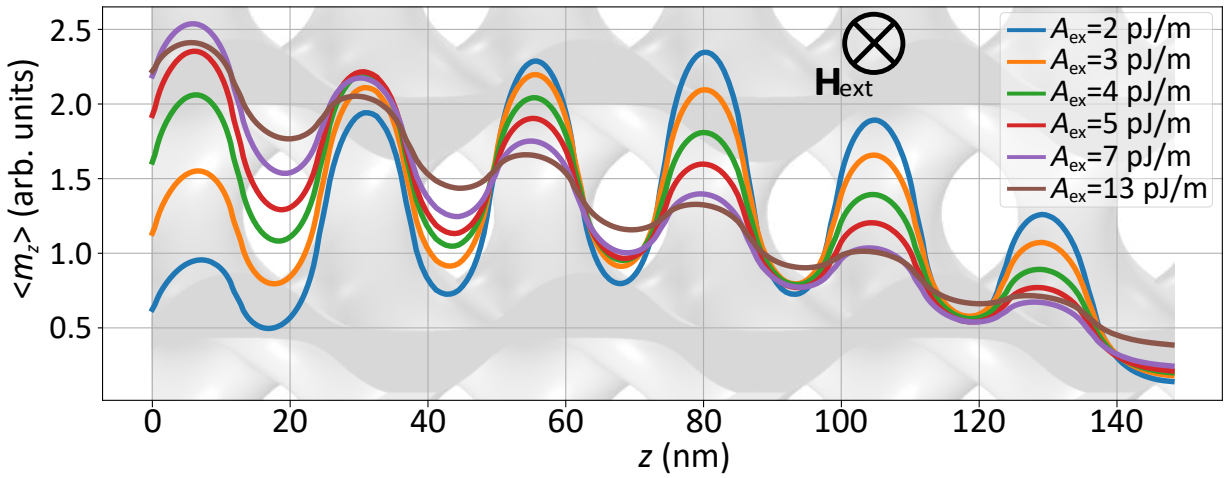


Figure S3. Distribution of the dynamic magnetization component m_z , averaged and projected on the z -axis, for the gyroid structure with 3 UCs and $\phi = 20\%$. The case with the field at an angle of 45 deg from the x -axis was used to show a clear surface localization. The colors represent different values of the exchange constant A_{ex} .

B. Height

Another quantity that could have a significant impact on SW localization is the height of the nanostructures studied. In this paper, we assumed a gyroid height of 3 and 3.25 UCs (150 and 162.5 nm, respectively); however, we also ran simulations for other values – both smaller, to test the potential effect of surface modes interacting with each other, and larger, where the modes are more isolated. The results of these additional simulations are shown for gyroids with perpendicularly oriented surface struts – Fig. S4, and with their parallel orientation – Fig. S5.

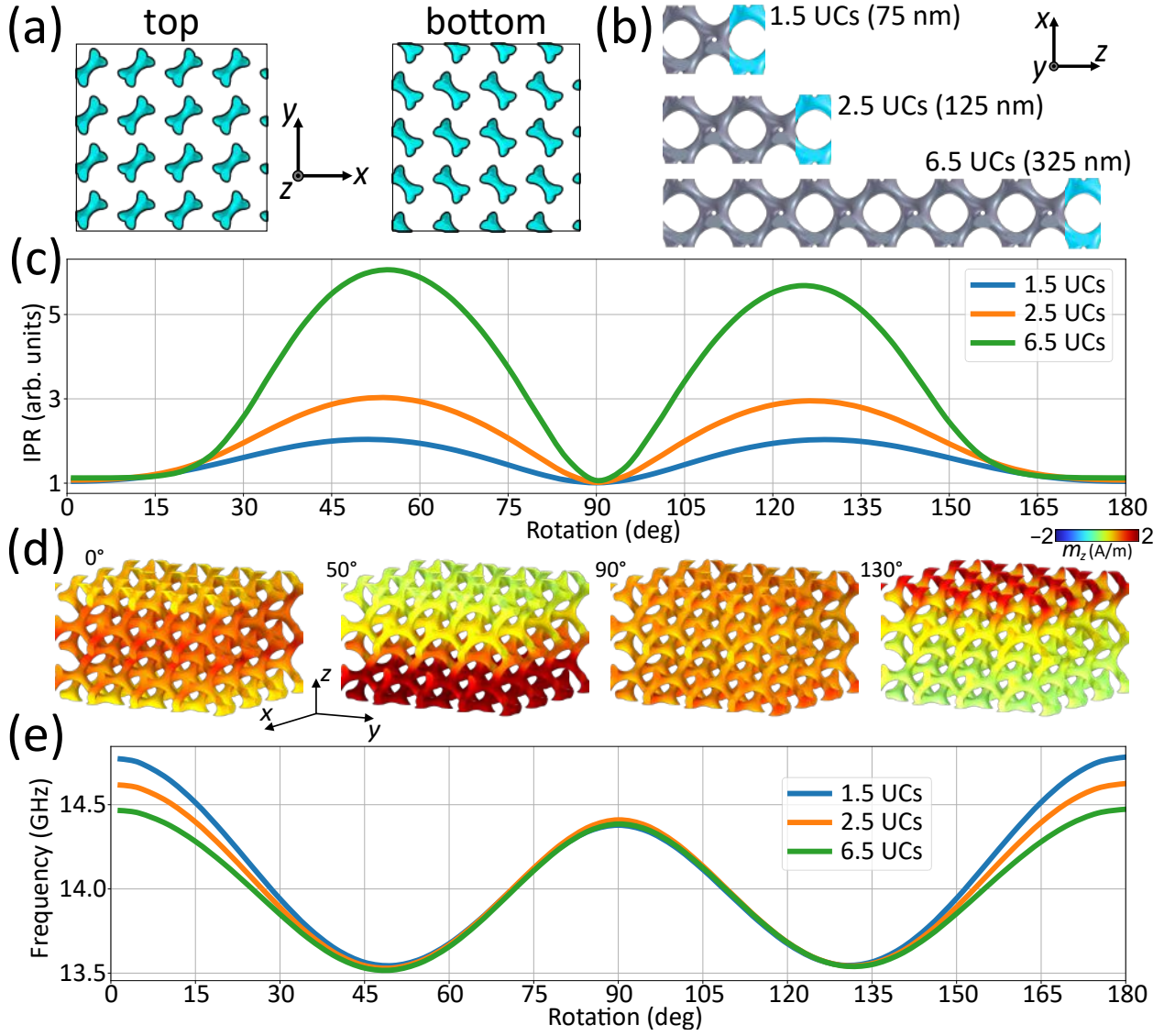


Figure S4. Analysis of the FMR mode localization of SWs for gyroid structures with perpendicular struts on the top and bottom surfaces (a) and for different heights of the structures (b). The results in the form of IPR plots as a function of the angle of rotation of the external magnetic field in the plane of the layers are presented in (c), and selected configurations of the z -component of the magnetization distribution in the 2.5 UCs gyroids are shown in panel (d). The last plot in (e) shows the changes in FMR mode frequencies, analogously as a function of H_{ext} rotation for gyroids of different heights [blue line – 1.5 UCs (75 nm), orange line – 2.5 UCs (125 nm), green line – 6.5 UCs (325 nm)].

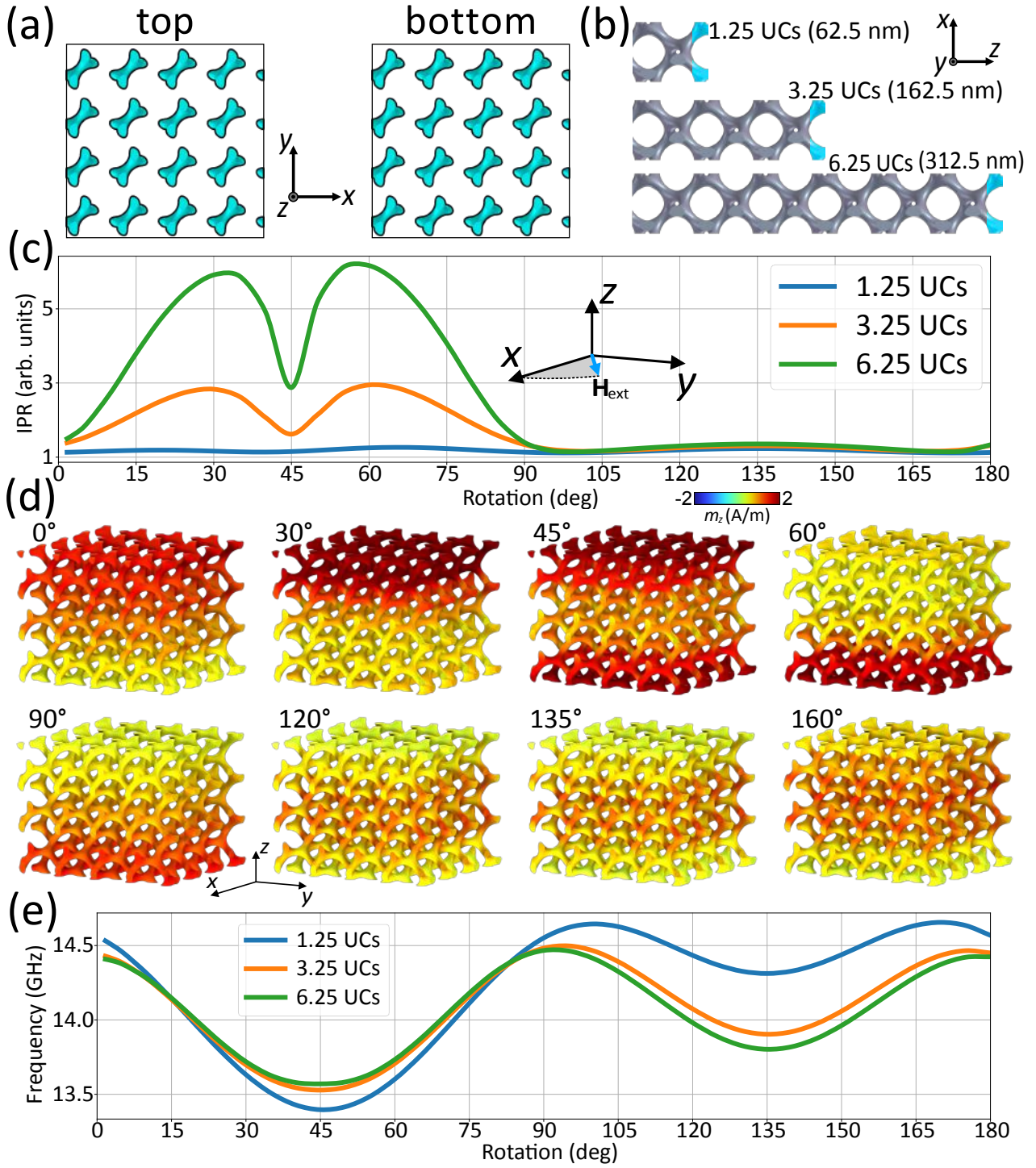


Figure S5. Analysis of the FMR mode localization of SWs for gyroid structures with parallel struts on the top and bottom surfaces (a) and for different heights of the structures (b). The results in the form of IPR plots as a function of the angle of rotation of the external magnetic field (H_{ext}) in the plane of the layers are presented in (c), and selected configurations of the z -component of the magnetization distribution in the 3.25 UCs gyroids are shown in panel (d). The last plot in (e) shows the changes in FMR mode frequencies, analogously as a function of H_{ext} rotation for gyroids of different heights [blue line – 1.25 UCs (62.5 nm), orange line – 3.25 UCs (162.5 nm), green line – 6.25 UCs (312.5 nm)]

III. VARIOUS WOODPILE-LIKE STRUCTURES TESTING

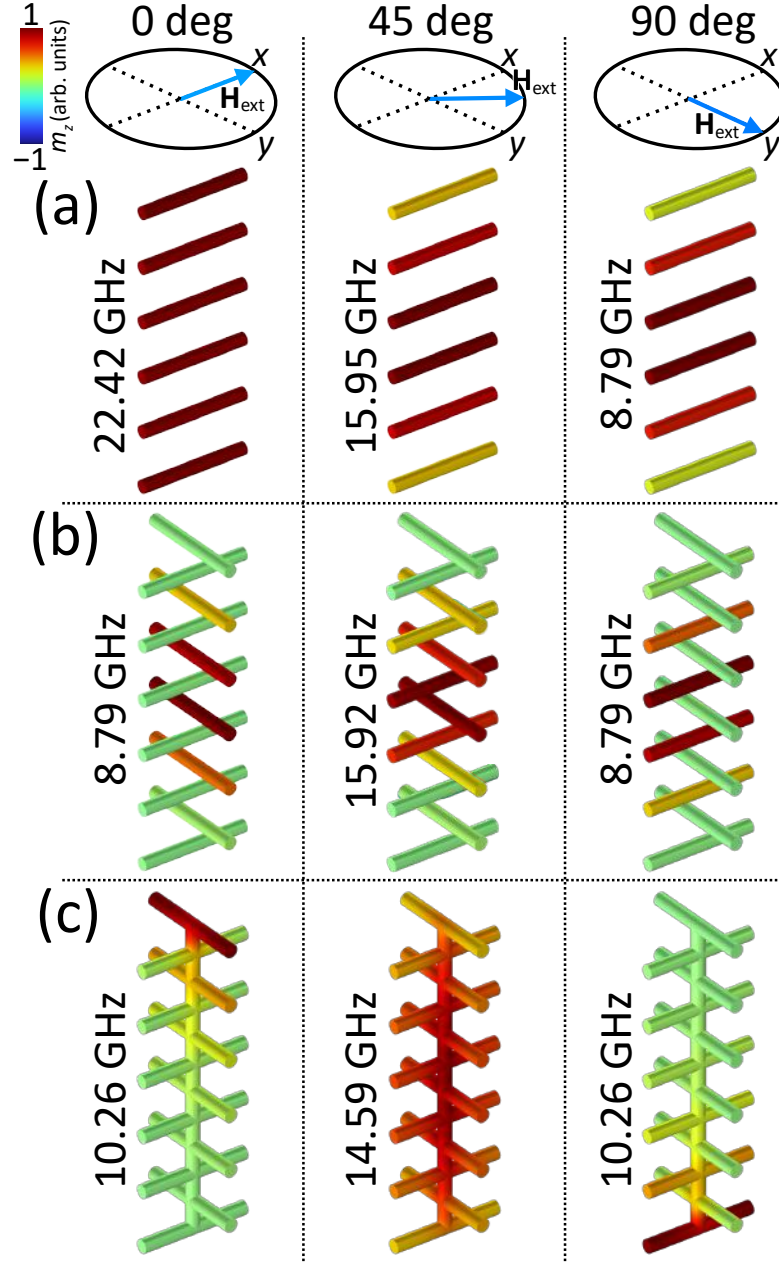


Figure S6. Analysis of the FMR modes for different angles of the external magnetic field oriented in the plane of the layers (0, 45 and 90 deg from the x -axis). Row (a) depicts the dynamic magnetization distribution in unconnected nanorods aligned parallel to each other, showing no surface localization. In (b), unconnected nanorods are arranged perpendicular to adjacent ones, also showing no surface localization. Row (c) presents a scaffold structure used in this study, in which perpendicular nanorods are connected by an out-of-plane rod, revealing the presence of surface localization.

5.4 Co-authorship statements

In this section, I include statements from co-authors of my multi-authored publications, specifically from at least four co-authors in cases where the total number of authors exceeds five. These statements are intended to clarify my individual contributions to each manuscript and to provide a more transparent account of my specific role and efforts within the collaborative research process.

P1 – *Spin-wave Talbot effect in a thin ferromagnetic film*

Oświadczenie o wkładzie do publikacji

Niniejszym oświadczam, że ja,

Maciej Krawczyk,

jestem współautorem publikacji

Gołębiewski, M.; Gruszecki, P.; Krawczyk, M.; Serebryannikov, A. E.
Spin-wave Talbot effect in a thin ferromagnetic film,
Physical Review B **102**, 13, 134402 (2020).

i moim wkładem do tej pracy były:

- konceptualizacja badań,
- nadzór nad realizacją działań badawczych,
- mentoring,
- analiza i dyskusja wyników symulacji,
- korekta manuskryptu.

20.02.2022

Oświadczenie o wkładzie do publikacji

Niniejszym oświadczam, że ja,

Paweł Gruszecki,

jestem współautorem publikacji

Gołębiewski, M.; Gruszecki, P.; Krawczyk, M.; Serebryannikov, A. E.
Spin-wave Talbot effect in a thin ferromagnetic film,
Physical Review B **102**, 13, 134402 (2020).

i moim wkładem do tej pracy były:

- wsparcie programistyczne przy tworzeniu kodu do MuMax3 oraz post-processingu w Pythonie,
- analiza i dyskusja wyników symulacji,
- korekta manuskryptu.

04.02.2025 *Gruszecki*
(data i podpis)

Oświadczenie o wkładzie do publikacji

Niniejszym oświadczam, że ja,

Andriy E. Serebryannikov,

jestem współautorem publikacji

Gołębiewski, M.; Gruszecki, P.; Krawczyk, M.; Serebryannikov, A. E.
Spin-wave Talbot effect in a thin ferromagnetic film,
Physical Review B **102**, 13, 134402 (2020).

i moim wkładem do tej pracy były:

- pozyskanie finansowania dla projektu prowadzącego do tej publikacji,
- analiza i dyskusja wyników symulacji,
- korekta manuskryptu.

04.02.2025



P2 – *Self-imaging of spin waves in thin, multimode ferromagnetic waveguides***Oświadczenie o wkładzie do publikacji**

Niniejszym oświadczam, że ja,

Paweł Gruszecki,

jestem współautorem publikacji

Gołębiewski, M.; Gruszecki, P.; Krawczyk, M.

Self-imaging of spin waves in thin, multimode ferromagnetic waveguides,

IEEE Transactions on Magnetics **58**, 8, 1-5 (2022)

i moim wkładem do tej pracy były:

- wsparcie programistyczne przy tworzeniu kodu do MuMax3 oraz post-processingu w Pythonie,
- analiza i dyskusja wyników symulacji,
- korekta manuskryptu.

04.02.2025 gruszecki
(data i podpis)

Oświadczenie o wkładzie do publikacji

Niniejszym oświadczam, że ja,

Maciej Krawczyk,

jestem współautorem publikacji

Gołębiewski, M.; Gruszecki, P.; Krawczyk, M.

Self-imaging of spin waves in thin, multimode ferromagnetic waveguides,

IEEE Transactions on Magnetism **58**, 8, 1-5 (2022)

i moim wkładem do tej pracy były:

- konceptualizacja badań,
- nadzór nad realizacją działań badawczych,
- mentoring,
- analiza i dyskusja wyników symulacji,
- korekta manuskryptu.



20.02.2025

(data i podpis)

P3 – *Self-imaging based programmable spin-wave lookup tables***Oświadczenie o wkładzie do publikacji**

Niniejszym oświadczam, że ja,

Paweł Gruszecki,

jestem współautorem publikacji

Gołębiewski, M.; Gruszecki, P.; Krawczyk, M.

Self-imaging based programmable spin-wave lookup tables,

Advanced Electronic Materials **8**, 10, 2200373 (2022)

i moim wkładem do tej pracy były:

- konceptualizacja,
- wsparcie programistyczne i metodologiczne (MuMax3, Python),
- wstępne opracowanie metody HFPBC opisanej w pracy,
- analiza i dyskusja wyników symulacji,
- korekta manuskryptu.

04.02.2025 *Gruszecki*
(data i podpis)

Oświadczenie o wkładzie do publikacji

Niniejszym oświadczam, że ja,

Maciej Krawczyk,

jestem współautorem publikacji

Gołębiewski, M.; Gruszecki, P.; Krawczyk, M.

Self-imaging based programmable spin-wave lookup tables,

Advanced Electronic Materials **8**, 10, 2200373 (2022)

i moim wkładem do tej pracy były:

- nadzór nad realizacją działań badawczych,
- mentoring,
- analiza i dyskusja wyników symulacji,
- korekta manuskryptu.

20.02.2025



(data i podpis)

P4 – *Spin-Wave Spectral Analysis in Crescent-Shaped Ferromagnetic Nanorods***Oświadczenie o wkładzie do publikacji**

Niniejszym oświadczam, że ja,

Hanna Reshetniak,

jestem współautorem publikacji

Gołębiewski, M.; Reshetniak, H.; Makartsou, U.; Krawczyk, M.;

van den Berg, A.; Ladak, S.; Barman, A.

Spin-Wave Spectral Analysis in Crescent-Shaped Ferromagnetic Nanorods,
Physical Review Applied **19**, 6, 2200373 (2023)

i moim wkładem do tej pracy były:

- uzupełniające symulacje numeryczne (COMSOL Multiphysics),
- przetwarzanie danych z symulacji,
- analiza i dyskusja wyników symulacji.

5.22.25 Hanna
(data i podpis) Reshetniak

Oświadczenie o wkładzie do publikacji

Niniejszym oświadczam, że ja,

Uladzislau Makartsou,

jestem współautorem publikacji

Gołębiewski, M.; Reshetniak, H.; Makartsou, U.; Krawczyk, M.;

van den Berg, A.; Ladak, S.; Barman, A.

Spin-Wave Spectral Analysis in Crescent-Shaped Ferromagnetic Nanorods,

Physical Review Applied **19**, 6, 2200373 (2023)

i moim wkładem do tej pracy były:

- wszystkie symulacje numeryczne w MuMax3,
- przetwarzanie danych z symulacji z MuMax3,
- wizualizacja tych wyników,
- analiza i dyskusja.

(data i podpis)

04.01.2025 Makartsou

Statement of Contribution to Publication

I hereby declare that I,

Sam Ladak,

I am a co-author of the publication

Gołębiewski, M.; Reshetniak, H.; Makartsou, U.; Krawczyk, M.;
van den Berg, A.; Ladak, S.; Barman, A.

Spin-Wave Spectral Analysis in Crescent-Shaped Ferromagnetic Nanorods,
Physical Review Applied **19**, 6, 2200373 (2023)

and my contributions to this work were:

- conceptualization,
- methodology,
- supervision,
- validation (based on experience from experimental studies of structures with crescent geometries used in this work),
- writing – review & editing.



(S.Ladak, 18.02.2025)

Oświadczenie o wkładzie do publikacji

Niniejszym oświadczam, że ja,

Maciej Krawczyk,

jestem współautorem publikacji

Gołębiewski, M.; Reshetniak, H.; Makartsou, U.; Krawczyk, M.;

van den Berg, A.; Ladak, S.; Barman, A.

Spin-Wave Spectral Analysis in Crescent-Shaped Ferromagnetic Nanorods,

Physical Review Applied **19**, 6, 2200373 (2023)

i moim wkładem do tej pracy były:

- konceptualizacja
- nadzór nad realizacją działań badawczych,
- mentoring,
- analiza i dyskusja wyników symulacji,
- korekta manuskryptu.



20.02.2025

(data i podpis)

P5 – Exciting High-Frequency Short-Wavelength Spin Waves using High Harmonics of a Magnonic Cavity Mode

Statement of Contribution to Publication

I hereby declare that I,

Nikhil Kumar,

I am a co-author of the publication

Kumar, N.; Gruszecki, P.; Gołębiewski, M.; Kłos, J. W.; Krawczyk, M.
*Exciting High-Frequency Short-Wavelength Spin Waves using High Harmonics
of a Magnonic Cavity Mode*, Advanced Quantum Technologies 2400015 (2024)

and my contributions to this work were:

- conceptualization (proposal for research on cavities in antidot lattices)
- numerical investigation in MuMax3
- visualization of the results from MuMax3
- writing – original draft preparation
- writing – review & editing

Nikhil
04/02/2025

(date and signature)



Oświadczenie o wkładzie do publikacji

Niniejszym oświadczam, że ja,

Paweł Gruszecki,

jestem współautorem publikacji

Kumar, N.; Gruszecki, P.; Gołębiewski, M.; Kłos, J. W.; Krawczyk, M.

Exciting High-Frequency Short-Wavelength Spin Waves using High Harmonics of a Magnonic Cavity Mode,

Advanced Quantum Technologies 2400015 (2024)

i moim wkładem do tej pracy były:

- uzupełniające symulacje mikromagnetyczne w MuMax3,
- weryfikacja wyników symulacji mikromagnetycznych,
- analiza i dyskusja wyników symulacji,
- korekta manuskryptu.

04.01.2025. Gruszecki
(data i podpis)

Oświadczenie o wkładzie do publikacji

Niniejszym oświadczam, że ja,

Jarosław W. Kłos,

jestem współautorem publikacji

Kumar, N.; Gruszecki, P.; Gołębiewski, M.; Kłos, J. W.; Krawczyk, M.

*Exciting High-Frequency Short-Wavelength Spin Waves using High Harmonics
of a Magnonic Cavity Mode,*

Advanced Quantum Technologies 2400015 (2024)

i moim wkładem do tej pracy były:

- analiza i dyskusja wyników symulacji,
- korekta manuskryptu.

04.02.2025, Jarosław Kłos
(data i podpis)

Oświadczenie o wkładzie do publikacji

Niniejszym oświadczam, że ja,

Maciej Krawczyk,

jestem współautorem publikacji

Kumar, N.; Gruszecki, P.; Gołębiewski, M.; Kłos, J. W.; Krawczyk, M.

*Exciting High-Frequency Short-Wavelength Spin Waves using High Harmonics
of a Magnonic Cavity Mode,*

Advanced Quantum Technologies 2400015 (2024)

i moim wkładem do tej pracy były:

- konceptualizacja (propozycja badań zjawisk nieliniowych w sieciach antykropek z wnęką rezonansową)
- nadzór nad realizacją działań badawczych,
- analiza i dyskusja wyników symulacji,
- redakcja i korekta manuskryptu.



20.02.2025

(data i podpis)

P6 – *Spin-Wave Self-Imaging: Experimental and Numerical Demonstration of Caustic and Talbot-like Diffraction Patterns*

Oświadczenie o wkładzie do publikacji

Niniejszym oświadczam, że ja,

Uladzislau Makartsou,

jestem współautorem publikacji

Makartsou, U.; Gołębiewski, M.; Guzowska, U.; Stognij, A.; Gieniusz, R.; Krawczyk, M.
Spin-Wave Self-Imaging: Experimental and Numerical Demonstration of Caustic and Talbot-like Diffraction Patterns,
Applied Physics Letters **124**, 19, 192406 (2024)

i moim wkładem do tej pracy były:

- symulacje numeryczne w MuMax3,
- przetwarzanie danych z symulacji,
- wizualizacja wyników,
- analiza i dyskusja wyników symulacji,
- redakcja manuskryptu.

(data i podpis)

04.02.2025 *Makartsou*

Oświadczenie o wkładzie do publikacji

Niniejszym oświadczam, że ja,

Urszula Guzowska,

jestem współautorem publikacji

Makartsou, U.; Gołębiewski, M.; Guzowska, U.; Stognij, A.; Gieniusz, R.; Krawczyk, M.
*Spin-Wave Self-Imaging: Experimental and Numerical Demonstration of Caustic
and Talbot-like Diffraction Patterns*,
Applied Physics Letters **124**, 19, 192406 (2024)

i moim wkładem do tej pracy były:

- badania eksperymentalne (wykonanie pomiarów BLS),
- analiza i dyskusja wyników,
- korekta manuskryptu.

Urszula Guzowska
04/02/2025

Oświadczenie o wkładzie do publikacji

Niniejszym oświadczam, że ja,

Ryszard Gieniusz,

jestem współautorem publikacji

Makartsou, U.; Gołębiewski, M.; Guzowska, U.; Stognij, A.; Gieniusz, R.; Krawczyk, M.

Spin-Wave Self-Imaging: Experimental and Numerical Demonstration of Caustic and Talbot-like Diffraction Patterns,

Applied Physics Letters **124**, 19, 192406 (2024)

i moim wkładem do tej pracy były:

- konceptualizacja badań eksperymentalnych,
- nadzór nad badaniami eksperymentalnymi,
- analiza i dyskusja rezultatów,
- korekta manuskryptu.

04.02.2025. 
(data i podpis)

Oświadczenie o wkładzie do publikacji

Niniejszym oświadczam, że ja,

Maciej Krawczyk,

jestem współautorem publikacji

Makartsou, U.; Gołębiewski, M.; Guzowska, U.; Stognij, A.; Gieniusz, R.; Krawczyk, M.
*Spin-Wave Self-Imaging: Experimental and Numerical Demonstration of Caustic
and Talbot-like Diffraction Patterns*,
Applied Physics Letters **124**, 19, 192406 (2024)

i moim wkładem do tej pracy były:

- konceptualizacja (propozycja zestawienia naszych badań teoretycznych i symulacji numerycznych z istniejącymi już danymi eksperymentalnymi),
- nadzór nad realizacją działań badawczych,
- mentoring,
- analiza i dyskusja wyników symulacji,
- korekta manuskryptu.



20.02.2025

(data i podpis)

P7 – Collective Spin-Wave Dynamics in Gyroid Ferromagnetic Nanostructures**Statement of Contribution to Publication**

I hereby declare that I, the undersigned

Riccardo Hertel

CNRS Senior Scientist at the IPCMS in Strasbourg (France),

am a co-author of the publication

Gołębiewski, M.; Hertel, R.; d'Aquino, M.; Vasyuchka, V.; Weiler, M.; Pirro, P.;
Krawczyk, M.; Fukami, S.; Ohno, H.; Llandro, J.

Collective Spin-Wave Dynamics in Gyroid Ferromagnetic Nanostructures,
ACS Applied Materials & Interfaces **16**, 17, 22177-22188 (2024) .

My contributions to this work were:

- methodology (proposition to use “tetmag” to perform micromagnetic simulations of gyroid structures),
- software (development and provision of the “tetmag” micromagnetic software and a frequency-domain based proprietary software for research purposes),
- supervision (scientific guidance and technical assistance for Mateusz Gołębiewski in conducting micromagnetic simulations),
- simulation studies on flat gyroids to quantify impact of macroscopic shape anisotropy
- analysis and discussion of simulation results,
- writing – review & editing.



Riccardo Hertel

Statement of Contribution to Publication

I hereby declare that I,

Vitaliy Vasyuchka,

I am a co-author of the publication

Gołębiewski, M.; Hertel, R.; d'Aquino, M.; Vasyuchka, V.; Weiler, M.; Pirro, P.;
Krawczyk, M.; Fukami, S.; Ohno, H.; Llandro, J.

Collective Spin-Wave Dynamics in Gyroid Ferromagnetic Nanostructures,
ACS Applied Materials & Interfaces **16**, 17, 22177-22188 (2024)

and my contributions to this work were:

- experimental investigation (ferromagnetic resonance – FMR),
- methodology of the FMR measurements,
- validation of numerical simulation based on experimental expertise,
- writing – review & editing.

06.02.2025



(Vitaliy Vasyuchka)

Statement of Contribution to Publication

I hereby declare that I,

Philipp Pirro,

I am a co-author of the publication

Gołębiewski, M.; Hertel, R.; d'Aquino, M.; Vasyuchka, V.; Weiler, M.; Pirro, P.;
Krawczyk, M.; Fukami, S.; Ohno, H.; Llandro, J.

Collective Spin-Wave Dynamics in Gyroid Ferromagnetic Nanostructures,
ACS Applied Materials & Interfaces **16**, 17, 22177-22188 (2024)

and my contributions to this work were:

- methodology of the FMR measurements,
- visualization of the experimental data,
- validation of numerical simulation based on experimental expertise,
- writing – review & editing.



Kaiserslautern, 04.02.2024

Oświadczenie o wkładzie do publikacji

Niniejszym oświadczam, że ja,

Maciej Krawczyk,

jestem współautorem publikacji

Gołębiewski, M.; Hertel, R.; d'Aquino, M.; Vasyuchka, V.; Weiler, M.; Pirro, P.;
Krawczyk, M.; Fukami, S.; Ohno, H.; Llandro, J.

Collective Spin-Wave Dynamics in Gyroid Ferromagnetic Nanostructures,
ACS Applied Materials & Interfaces **16**, 17, 22177-22188 (2024)

i moim wkładem do tej pracy były:

- nadzór nad realizacją działań badawczych w zakresie symulacji mikromagnetycznych,
- mentoring,
- analiza i dyskusja wyników symulacji i ich zestawienia z eksperymentem,
- korekta manuskryptu.

20.02.2025



(data i podpis)

Statement of Contribution to Publication

I hereby declare that I,

Justin Llandro,

I am a co-author of the publication

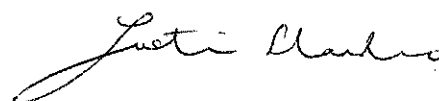
Gołębiewski, M.; Hertel, R.; d'Aquino, M.; Vasyuchka, V.; Weiler, M.; Pirro, P.;
Krawczyk, M.; Fukami, S.; Ohno, H.; Llandro, J.

Collective Spin-Wave Dynamics in Gyroid Ferromagnetic Nanostructures,
ACS Applied Materials & Interfaces **16**, 17, 22177-22188 (2024)

and my contributions to this work were:

- conceptualization (utilization of gyroid structures in magnetic research),
- experimental investigation (fabrication),
- fabrication methodology,
- validation of numerical simulation based on experimental expertise,
- supervision,
- writing – review & editing.

2025 / 2 / 4



P8 – Gyroid ferromagnetic nanostructures in 3D magnonics**Oświadczenie o wkładzie do publikacji**

Niniejszym oświadczam, że ja,

Maciej Krawczyk,

jestem współautorem publikacji

Gołębiewski, M.; Krawczyk, M.

Gyroid ferromagnetic nanostructures in 3D magnonics,

arXiv preprint arXiv:2407.05851 (2024)

i moim wkładem do tej pracy były:

- mentoring,
- analiza i dyskusja badań,
- korekta manuskryptu.



20.02.2025

(data i podpis)

P9 – Magnetic field controlled surface localization of ferromagnetic resonance modes in 3D nanostructures

Oświadczenie o wkładzie do publikacji

Niniejszym oświadczam, że ja,

Krzysztof Szulc,

jestem współautorem publikacji

Gołębiewski, M.; Szulc, K.; Krawczyk, M.

Magnetic field controlled surface localization of ferromagnetic resonance modes in 3D nanostructures,

Acta Materialia **283**, 120499 (2025)

i moim wkładem do tej pracy były:

- konceptualizacja (propozycja demonstracji badanego efektu w nanostrukturze o innej geometrii),
- analiza i dyskusja wyników symulacji,
- korekta manuskryptu.

04.02.2025 Kr. Szulc
(data i podpis)

Oświadczenie o wkładzie do publikacji

Niniejszym oświadczam, że ja,

Maciej Krawczyk,

jestem współautorem publikacji

Gołębiewski, M.; Szulc, K.; Krawczyk, M.

Magnetic field controlled surface localization of ferromagnetic resonance modes in 3D nanostructures,

Acta Materialia **283**, 120499 (2025)

i moim wkładem do tej pracy były:

- udział w konceptualizacji badań,
- nadzór nad realizacją działań badawczych,
- mentoring,
- analiza i dyskusja wyników symulacji,
- korekta manuskryptu.

20.02.2025

(data i podpis)

Scientific perspectives

Building on the progress made during my Ph.D. research, I intend to continue to pursue innovative projects in the field of magnonics. My previous work, including studies on the Talbot effect for spin waves and the exploration of complex three-dimensional ferromagnetic nanostructures, has provided a solid foundation for further investigations. Equipped with the necessary expertise and in close collaboration with leading international research teams, I plan to carry out the research projects outlined below.

Investigations of three-dimensional magnonic nanostructures

Gyroids. One of the most promising directions is the further exploration of gyroidal structures. These intricate three-dimensional nanostructures are expected to exhibit unique spin-wave dispersion relations and remarkable anisotropic magnetoresistance effects. Such properties may enable precise control of spin-wave propagation in three dimensions, opening the way to more advanced, energy-efficient spintronic and beyond-CMOS logic devices. In the context of magnonic crystals, gyroids could serve as the backbone for fully three-dimensional systems, where the geometry inherently allows for versatile band structure engineering. Similar principles have been explored in photonic crystals [176], highlighting how 3D periodic media can yield remarkable wave manipulation capabilities. Translating these concepts to the spin-wave regime holds promise for magnetic metamaterials with tunable microwave and communication functionalities.

Woodpiles. In addition to gyroids, I have initiated a collaboration with Prof. Dirk Grundler's group from the Swiss Federal Institute of Technology (EPFL) in Switzerland and Dr. Kilian Lenz from the Helmholtz-Zentrum Dresden-Rossendorf (HZDR) in Germany to study woodpile-like nanostructures. These architectures – resembling stacks of wooden logs (see Fig. 5.1) – are an exciting avenue for three-dimensional magnonics, as recently highlighted in *Advanced Materials* [177]. In these networks, submicron nanotubes of ferromagnetic material are arranged in a periodic 'woodpile' fashion, allowing excitation of both bulk and surface

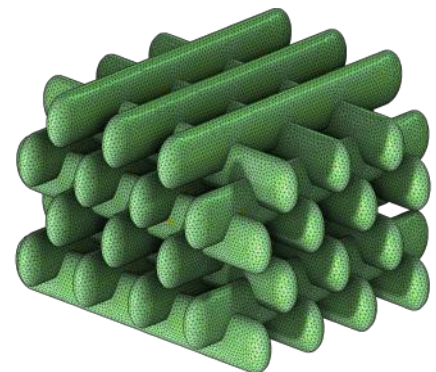


Figure 5.1 Schematic model of the woodpile structure.

spin-wave modes. To strengthen our collaboration, I completed a two-week internship at EPFL, working closely with Prof. Grundler's team.

Building on the initial demonstration in Ref. [177], we are currently investigating the resonant response of these systems using a vector network analyzer (VNA–FMR) within a ring-shaped microresonator while systematically varying the orientation of the static magnetic field. My goal is to accurately reproduce these experimental conditions in micromagnetic simulations, allowing a deeper understanding of the underlying spin-wave dynamics and resonance behavior. Despite the complexity of the geometry and the associated computational challenges, preliminary results indicate a strong agreement between the experimental data and my COMSOL simulations. This research effort, which includes both experimental measurements and numerical computations, aims to understand the collective magnetization dynamics in these systems and to uncover innovative physical effects such as mode hybridization and field-tunable spin-wave confinement.

Buckyballs. To further extend my research into three-dimensional magnonic networks, I have begun simulations of so-called *buckyball* structures in collaboration with Dr. Sebastian Gliga from the Paul Scherrer Institute (PSI) in Switzerland and Dr. Lenz. These nanostructures, analogous in shape to the carbon C_{60} fullerene, consist of a spherical shell with a network of ferromagnetic tubes forming pentagonal and hexagonal facets (see Fig. 5.2). In the magnetic analog, nanofabrication techniques recreate similarly curved architectures, enabling a closed 3D spin-wave network. My main task in this project is to match the field-angle-dependent FMR experimental measurements with micromagnetic simulations. By clarifying how the measured resonances vary with field orientation, the goal is to unravel how the curvature and topology within these spherical lattices can be exploited to engineer custom spin-wave modes and resonant properties.

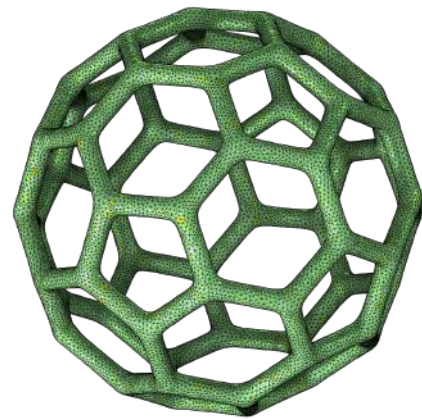


Figure 5.2 Schematic model of the buckyball structure.

Research on antidot lattices

In parallel, I plan to extend my studies of ADLs, that I started in P5. As explained in Sec. 5.2.2, these periodic arrays of nanoscale holes or ‘antidots’ within a magnetic film are known to localize spin waves at their edges, serving as a compelling pathway for the generation of higher-order harmonic emissions. By exploring geometric parameters, lattice periodicity, and applied magnetic fields, I intend to tailor the band structure of spin waves to control nonlinear phenomena. Such investigations may pave the way for fast and nanoscale spin-wave devices capable of high-density information encoding.

Crescent-shaped waveguides and diamond-like networks

I plan to further develop crescent-shaped waveguides, a topic initiated in my *Physical Review Applied* publication P4. Initial results showed that the curved geometry of ferromagnetic nanorods significantly affects mode localization and magnetization dynamics. My next step is to construct and study *diamond-like networks* formed by interconnecting the crescent-shaped waveguides (see Fig. 5.3), as already prototyped at Cardiff University by Prof. Sam Ladak's group [34]. These 3D diamond networks can exhibit coupling and frustration at the vertices, potentially allowing reprogrammable spin-wave spectra and band gap formation under different field configurations [178]. By exploiting curvature-induced anisotropies and frustration effects, I aim to explore reliable spin-wave guiding pathways that could contribute to the development of next-generation magnonic circuits.

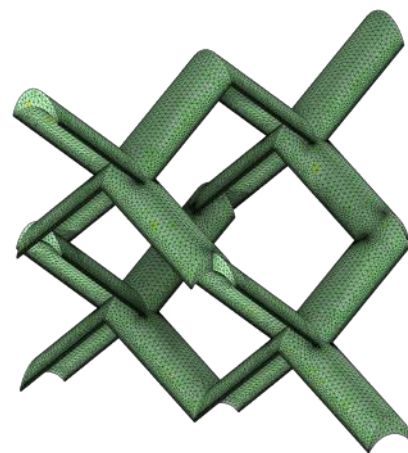


Figure 5.3 Schematic model of the diamond-like lattice constructed from crescent-shaped wires.

Magnonic neural networks based on self-imaging (Talbot effect)

Finally, I intend to build on the concept of the spin-wave Talbot effect, introduced in my paper (P3) in *Advanced Electronic Materials* to develop magnonic neural networks. The self-imaging phenomenon of spin waves, in which periodic wavefronts re-emerge at specific propagation distances, provides a way to generate repeatable interference patterns. This effect suggests the possibility of an entirely new class of neural network architectures based on collective interference states rather than on conventional transistor-based logic. A key aspect of such architectures involves nonlinear activation functions, which are essential for modeling complex relationships in high-dimensional data. The integration of spin-wave nonlinearities into these systems could lead to enhanced computational capabilities and potentially to novel machine-learning algorithms that exploit wave interference [179]. A strong indication of the potential of this approach is the *MANNGA* project, funded by the Horizon Europe PathFinder Challenge, to which I am contributing under the supervision of Prof. Paweł Gruszecki in collaboration with the University of Exeter and Aalto University.

Summary

The collection of scientific studies presented in this thesis encapsulates the trajectory of my Ph.D. research, showing a transition from relatively simple one-dimensional systems to increasingly complex three-dimensional nanostructures. This journey reflects not only the evolution of my own expertise, but also parallels the broader development of the field of magnonics, which is increasingly focused on exploiting multidimensional structuring to achieve precise control over spin-wave dynamics.

My work spans a range of structural dimensionalities, from periodic one-dimensional systems (P1–P3, P6) to complex three-dimensional nanostructures (P7–P9), illustrating how geometry can be used to influence magnetization dynamics. While higher dimensionality offers more design possibilities and opens up new physical phenomena, especially in the context of 3D nanoarchitectures, it does not necessarily guarantee more promising or applicable outcomes. In fact, the relatively simple 1D systems studied in P1–P3, P6 yielded particularly compelling results. Their foundation in fundamental wave physics, combined with computational efficiency and predictability, makes them highly relevant for practical implementation. This highlights an important insight: both low- and high-dimensional systems have distinct advantages, and progress in magnonics depends on exploiting the strengths of each.

Significant progress is also being made in P5, where research is moving from one-dimensional arrays to fully two-dimensional antidot lattices. These more complex geometries introduce additional degrees of freedom and enable new functionalities – most notably the generation of short spin waves through nonlinear effects, including higher harmonic excitation. Such capabilities position antidot lattices as a promising platform for the realization of magnonic neural networks, offering an exciting avenue for future developments in wave-based information processing and unconventional computing.

The crescent-shaped waveguide studied in P4 also serves as a bridge between two-dimensional and fully three-dimensional magnonic systems. Although the geometry may seem unconventional, its relevance is well established in experimental practice. Techniques such as two-photon lithography combined with sputter deposition allow the fabrication of magnetic layers that conform to curved scaffolds, naturally producing crescent-shaped cross sections – much like snow accumulating along a curved railing. Beyond their experimental feasibility, these nontrivial geometries introduce novel physical effects in magnonics, as demonstrated in P4, and provide compelling motivation for further exploration in both theoretical and applied contexts.

P6 provides experimental verification of the Talbot effect for spin waves, previously explored in the theoretical studies of P1–P3. This validation not only reinforces the credibility of the earlier simulations, but also underscores the practical applicability of the effect in real magnonic systems, highlighting its potential for implementation in future wave-based technologies.

Finally, the studies of three-dimensional nanostructures presented in P7–P9 represent the most complex and ambitious investigations within this thesis. These works demonstrate the unique potential of 3D magnonic systems, revealing phenomena such as dynamic spin-wave localization and crystallography-dependent tunable magnetization dynamics. Beyond these core findings, the research also points to several promising directions for future exploration, including magnetoresistance effects.

As emphasized throughout this dissertation, 3D magnonics remains a relatively young field – but one with extraordinary potential. Its rapid development is being driven by advances in fabrication techniques such as atomic layer deposition, two-photon lithography, and self-assembled block copolymer templating, as well as increasingly powerful computational tools for modeling geometrically and magnetically complex systems. This research contributes to the growth of the field by addressing critical challenges related to dimensionality, structural complexity, and their influence on spin-wave behavior, helping to lay the groundwork for future innovations in magnonic technology.

Bringing together a wide range of topics within the field of magnonics, this thesis provides a comprehensive investigation into the control of spin waves in nanostructured ferromagnetic materials. Spanning the theoretical foundations of magnetism, advanced numerical modeling, and experimental validation (enabled by international collaborations), the work demonstrates how spin waves – known for their energy efficiency and wave-based nature – can be harnessed in multidimensional systems to realize novel functionalities and device concepts.

The research underscores the growing importance of magnons in modern science and technology, particularly in light of the increasing demand for low-power alternatives to conventional electronics. In this context, the work contributes to the broader vision of wave-based computing by systematically investigating how structured magnetic media – from simple one-dimensional periodic systems to complex three-dimensional nanoarchitectures – can be designed to tailor spin-wave dynamics.

One of the central approaches in this thesis is the use of advanced numerical methods, which have become a key tool in modern research on magnetism and magnonics – especially where the complexity of real systems makes analytical solutions impractical. Much attention has been paid to the theoretical foundations and practical implementation of the computational techniques, in particular the finite difference and finite element methods, which form the backbone of my micromagnetic simulations. The finite difference method, as used in MuMax3, is particularly suitable for systems with simple geometries and uniform meshing. Its computational efficiency and numerical stability make it ideal for solving the Landau–Lifshitz–Gilbert equation in large-scale simulations. This method proved particularly effective in my studies of one-dimensional

periodic structures in thin films, where the simplicity of the physical geometry matched the strengths of the finite difference method.

In contrast, finite element method, implemented in COMSOL Multiphysics and tetmag, offers the versatility required to model complex geometries and nontrivial boundary conditions. Its capacity for adaptive meshing and localized refinement enables accurate representation of structures where subtle features strongly influence magnetization dynamics and spin-wave behavior. Thus, the finite element method was essential for modeling the crescent-shaped nanorods and fully three-dimensional magnonic networks studied in this thesis. By using both methods strategically, this work demonstrates how appropriate numerical approaches can be matched to specific system geometries to perform efficient and accurate simulations.

This thesis not only applies these numerical methods, but also provides a thorough analysis of their implementation and adaptation to the specific challenges posed by structured ferromagnetic materials. For example, I discuss the role of specific boundary conditions in ensuring physical validity. I also explore the use of special time-stepping algorithms to deal with the stiffness and nonlinearity inherent in magnetic systems. Modeling gyroids and scaffold-like networks required not only computational efficiency but also a deep understanding of how to design and discretize complex geometries to accurately capture their interactions with external magnetic fields. Using the finite element method in COMSOL and tetmag, I explored both the role of demagnetizing fields and exchange interactions in shaping spin-wave behavior.

By placing a strong emphasis on numerical methods, this thesis provides added value compared to more conventional approaches in the field. First, it helps bridge the gap between theory and experiment by allowing the study of systems that are beyond the scope of analytical models. Second, it aims to underscore the important role of numerical simulations in advancing the frontiers of magnetism research and unlocking the potential of complex, multidimensional structures for future spin-wave technologies.

The significance of this research as a Ph.D. thesis lies in its distinctive balance of breadth and depth. It addresses fundamental aspects of magnetization dynamics while also engaging with practical challenges in modeling and experimental validation. By integrating numerical simulations, theoretical analysis, and collaborative experimental efforts, the work establishes a solid foundation that bridges basic scientific inquiry with technological relevance. More broadly, this dissertation contributes to the evolving field of magnonics by providing a comprehensive framework for understanding and controlling spin waves in structured, multidimensional magnetic environments. Through its results, methods, and conceptual insights, this work aims to support future research at the intersection of magnetic media geometry design, magnetization dynamics, numerical methods, and wave-based information processing. It is my hope that these findings will foster continued innovation in functional magnonic systems and advance the development of next-generation technologies.

Bibliography

- [1] A. A. Serga, A. V. Chumak, and B. Hillebrands, “YIG magnonics”, *Journal of Physics D: Applied Physics* **43**, 264002 (2010).
- [2] P. Yan and G. E. W. Bauer, “Magnonic domain wall heat conductance in ferromagnetic wires”, *Physical Review Letters* **109**, 087202 (2012).
- [3] J. Barker and G. E. Bauer, “Thermal spin dynamics of yttrium iron garnet”, *Physical Review Letters* **117**, 217201 (2016).
- [4] A. Khitun, M. Bao, and K. L. Wang, “Magnetic cellular nonlinear network with spin wave bus”, in *12th International Workshop on Cellular Nanoscale Networks and their Applications (CNNA)* (2010), pp. 1–5.
- [5] A. V. Chumak, V. I. Vasyuchka, A. A. Serga, and B. Hillebrands, “Magnon spintronics”, *Nature Physics* **11**, 453–461 (2015).
- [6] V. V. Kruglyak, S. O. Demokritov, and D. Grundler, “Magnonics”, *Journal of Physics D: Applied Physics* **43**, 260301 (2010).
- [7] B. Lenk, H. Ulrichs, F. Garbs, and M. Münzenberg, “The building blocks of magnonics”, *Physics Reports* **507**, 107–136 (2011).
- [8] T. Schneider, A. A. Serga, B. Leven, et al., “Realization of spin-wave logic gates”, *Applied Physics Letters* **92**, 022505 (2008).
- [9] Y. Kajiwara, K. Harii, S. Takahashi, et al., “Transmission of electrical signals by spin-wave interconversion in a magnetic insulator”, *Nature* **464**, 262–266 (2010).
- [10] S. Maendl, I. Stasinopoulos, and D. Grundler, “Spin waves with large decay length and few 100 nm wavelengths in thin yttrium iron garnet grown at the wafer scale”, *Applied Physics Letters* **111**, 012403 (2017).
- [11] F. Garcia-Sanchez, P. Borys, R. Soucaille, et al., “Narrow magnonic waveguides based on domain walls”, *Physical Review Letters* **114**, 247206 (2015).
- [12] K. Wagner, A. Kákay, K. Schultheiss, et al., “Magnetic domain walls as reconfigurable spin-wave nanochannels”, *Nature Nanotechnology* **11**, 432–436 (2016).
- [13] G. Duerr, K. Thurner, J. Topp, R. Huber, and D. Grundler, “Enhanced transmission through squeezed modes in a self-cladding magnonic waveguide”, *Physical Review Letters* **108**, 227202 (2012).
- [14] J. Lan, W. Yu, R. Wu, and J. Xiao, “Spin-wave diode”, *Physical Review X* **5**, 041049 (2015).
- [15] G. Talmelli, T. Devolder, N. Träger, et al., “Reconfigurable submicrometer spin-wave majority gate with electrical transducers”, *Science Advances* **6**, eabb4042 (2020).
- [16] J. Chen, J. Hu, and H. Yu, “Chiral emission of exchange spin waves by magnetic skyrmions”, *ACS Nano* **15**, 4372–4379 (2021).
- [17] Y. Liu, Y. Zhang, and S. Zhang, “Current-controlled propagation of spin waves in antiparallel, coupled domains”, *Nature Nanotechnology* **14**, 691–697 (2019).
- [18] J. Jorzick, S. O. Demokritov, B. Hillebrands, et al., “Spin wave wells in nonellipsoidal micrometer size magnetic elements”, *Physical Review Letters* **88**, 047204 (2002).

- [19] J. P. Park, P. Eames, D. M. Engebretson, J. Berezovsky, and P. A. Crowell, “Spatially resolved dynamics of localized spin-wave modes in ferromagnetic wires”, *Physical Review Letters* **89**, 277201 (2002).
- [20] C. Bayer, S. O. Demokritov, B. Hillebrands, and A. N. Slavin, “Spin-wave wells with multiple states created in small magnetic elements”, *Applied Physics Letters* **82**, 607–609 (2003).
- [21] M. Bailleul, D. Olligs, and C. Fermon, “Micromagnetic phase transitions and spin wave excitations in a ferromagnetic stripe”, *Physical Review Letters* **91**, 137204 (2003).
- [22] R. D. McMichael and B. B. Maranville, “Edge saturation fields and dynamic edge modes in ideal and nonideal magnetic film edges”, *Physical Review B* **74**, 024424 (2006).
- [23] V. V. Kruglyak, P. S. Keatley, R. J. Hicken, J. R. Childress, and J. A. Katine, “Time resolved studies of edge modes in magnetic nanoelements”, *Journal of Applied Physics* **99**, 08F306 (2006).
- [24] V. E. Demidov, M. Buchmeier, K. Rott, et al., “Nonlinear hybridization of the fundamental eigenmodes of microscopic ferromagnetic ellipses”, *Physical Review Letters* **104**, 217203 (2010).
- [25] B. B. Maranville, R. D. McMichael, and D. W. Abraham, “Variation of thin film edge magnetic properties with patterning process conditions in Ni80Fe20 stripes”, *Applied Physics Letters* **90**, 232504 (2007).
- [26] M. Zhu and R. D. McMichael, “Modification of edge mode dynamics of oxidized Ni80Fe20 thin film edges”, *Journal of Applied Physics* **107**, 103908 (2010).
- [27] J. M. Shaw, T. J. Silva, M. L. Schneider, and R. D. McMichael, “Spin dynamics and mode structure in nanomagnet arrays: effects of size and thickness on linewidth and damping”, *Physical Review B* **79**, 184404 (2009).
- [28] H. T. Nembach, J. M. Shaw, T. J. Silva, et al., “Effects of shape distortions and imperfections on mode frequencies and collective linewidths in nanomagnets”, *Physical Review B* **83**, 094427 (2011).
- [29] V. V. Kruglyak, A. Barman, R. J. Hicken, J. R. Childress, and J. A. Katine, “Picosecond magnetization dynamics in nanomagnets: crossover to nonuniform precession”, *Physical Review B* **71**, 220409 (2005).
- [30] R. D. McMichael, C. A. Ross, and V. P. Chuang, “Thickness dependence of magnetic film edge properties in Ni80Fe20 stripes”, *Journal of Applied Physics* **103**, 07C505 (2008).
- [31] B. B. Maranville, R. D. McMichael, S. A. Kim, et al., “Characterization of magnetic properties at edges by edge-mode dynamics”, *Journal of Applied Physics* **99**, 08C703 (2006).
- [32] Z. Zhang, M. Vogel, M. B. Jungfleisch, et al., “Tuning edge-localized spin waves in magnetic microstrips by proximate magnetic structures”, *Physical Review B* **100**, 174434 (2019).
- [33] F. Groß, M. Weigand, A. Gangwar, et al., “Imaging magnonic frequency multiplication in nanostructured antidot lattices”, *Physical Review B* **106**, 014426 (2022).
- [34] A. May, M. Hunt, A. van den Berg, A. Hejazi, and S. Ladak, “Realisation of a frustrated 3D magnetic nanowire lattice”, *Communications Physics* **2**, 13 (2019).
- [35] J. Gartside, S. Jung, S. Yoo, et al., “Current-controlled nanomagnetic writing for reconfigurable magnonic crystals”, *Communications Physics* **3**, 219 (2020).
- [36] V. Luzzati and P. A. Spegt, “Polymorphism of lipids”, *Nature* **215**, 701–704 (1967).
- [37] A. H. Schoen, *Infinite periodic minimal surfaces without self-intersections*, tech. rep. (NASA Electronics Research Center, Cambridge, 1970).
- [38] L. Han and S. Che, “An overview of materials with triply periodic minimal surfaces and related geometry: From biological structures to self-assembled systems”, *Advanced Materials* **30**, 1705708 (2018).
- [39] J. Llandro, D. M. Love, A. Kovács, et al., “Visualizing magnetic structure in 3D nanoscale Ni-Fe gyroid networks”, *Nano Letters* **20**, 3642–3650 (2020).

- [40] S. H. Skjærvø, C. H. Marrows, R. L. Stamps, and L. J. Heyderman, “Advances in artificial spin ice”, *Nature Reviews Physics* **2**, 2522–5820 (2020).
- [41] C. Nisoli, V. Kapaklis, and P. Schiffer, “Deliberate exotic magnetism via frustration and topology”, *Nature Physics* **13**, 200–203 (2017).
- [42] R. Streubel, P. Fischer, F. Kronast, et al., “Magnetism in curved geometries”, *Journal of Physics D: Applied Physics* **49**, 363001 (2016).
- [43] A. Fernández-Pacheco, R. Streubel, O. Fruchart, et al., “Three-dimensional nanomagnetism”, *Nature Communications* **8**, 15756 (2017).
- [44] D. Sander, S. O. Valenzuela, D. Makarov, et al., “The 2017 magnetism roadmap”, *Journal of Physics D: Applied Physics* **50**, 363001 (2017).
- [45] B. D. Cullity and C. D. Graham, *Introduction to magnetic materials*, 2nd ed. (John Wiley & Sons Inc, 2008).
- [46] J. D. Jackson, *Classical electrodynamics*, 3rd ed. (Wiley, 1999).
- [47] G. Gilbert, *De magnete, magneticisque corporibus, et de magno magnete tellure; physiologia nova, plurimis & argumentis, & experimentis demonstrata* (Petrus Short, 1600).
- [48] H. C. Ørsted, “Experiments on the effect of a current of electricity on the magnetic needle”, Royal Danish Academy of Sciences (1820).
- [49] M. Faraday, “Experimental researches in electricity”, *Philosophical Transactions of the Royal Society of London* **122**, 125–162 (1832).
- [50] J. C. Maxwell, *A treatise on electricity and magnetism*, Vol. 1 (Oxford: Clarendon Press, 1873).
- [51] G. E. Uhlenbeck and S. Goudsmit, “Spinning electrons and the structure of spectra”, *Nature* **117**, 264–265 (1926).
- [52] W. Pauli, “Zur Quantenmechanik des magnetischen Elektrons”, *Zeitschrift für Physik* **43**, 601–623 (1927).
- [53] W. Heisenberg, “Zur Theorie des Ferromagnetismus”, *Zeitschrift für Physik* **49**, 619–636 (1928).
- [54] L. Néel, “Propriétés magnétiques des ferrites; ferrimagnétisme et antiferromagnétisme”, *Annales De Physique* **12**, 137–198 (1948).
- [55] E. Ising, “Beitrag zur Theorie des Ferromagnetismus”, *Zeitschrift für Physik* **31**, 253–258 (1925).
- [56] F. Bloch, “Über die Quantenmechanik der Elektronen in Kristallgittern”, *Zeitschrift für Physik* **52**, 555–600 (1929).
- [57] J. C. Slater, “The theory of ferromagnetism: Lowest energy levels”, *Physical Review* **52**, 198–214 (1937).
- [58] J. Hubbard and B. H. Flowers, “Electron correlations in narrow energy bands”, *Proceedings of the Royal Society of London. Series A. Mathematical and Physical Sciences* **276**, 238–257 (1963).
- [59] A. Okamoto and S. Nakagawa, “Development of ferrite materials and their applications”, in *IEEE HISTory of ELectrotechnolgy CONference (HISTELCON)* (2017), pp. 7–12.
- [60] J. M. D. Coey, *Rare-earth iron permanent magnets*, Monographs on the physics and chemistry of materials (Clarendon Press, 1996).
- [61] L. Néel, “Magnetism and the local molecular field”, *Science* **174**, 985–992 (1971).
- [62] L. D. Landau and E. M. Lifshitz, “On the theory of the dispersion of magnetic permeability in ferromagnetic bodies”, *Physikalische Zeitschrift der Sowjetunion* **8**, 153–169 (1935).
- [63] T. L. Gilbert, “A phenomenological theory of damping in ferromagnetic materials”, *IEEE Transactions on Magnetics* **40**, 3443–3449 (2004).
- [64] M. N. Baibich, J. M. Broto, A. Fert, et al., “Giant magnetoresistance of (001)Fe/(001)Cr magnetic superlattices”, *Physical Review Letters* **61**, 2472–2475 (1988).

- [65] G. Binasch, P. Grünberg, F. Saurenbach, and W. Zinn, “Enhanced magnetoresistance in layered magnetic structures with antiferromagnetic interlayer exchange”, *Physical Review B* **39**, 4828–4830 (1989).
- [66] M. Julliere, “Tunneling between ferromagnetic films”, *Physics Letters A* **54**, 225–226 (1975).
- [67] T. Miyazaki and N. Tezuka, “Giant magnetic tunneling effect in Fe/Al₂O₃/Fe junction”, *Journal of Magnetism and Magnetic Materials* **139**, L231–L234 (1995).
- [68] F. Bloch, “Zur Theorie des Ferromagnetismus”, *Zeitschrift für Physik* **61**, 206–219 (1930).
- [69] J. Slonczewski, “Current-driven excitation of magnetic multilayers”, *Journal of Magnetism and Magnetic Materials* **159**, L1–L7 (1996).
- [70] L. Berger, “Emission of spin waves by a magnetic multilayer traversed by a current”, *Physical Review B* **54**, 9353–9358 (1996).
- [71] Y. Tokura and N. Nagaosa, “Nonreciprocal responses from non-centrosymmetric quantum materials”, *Nature Communications* **9**, 3740 (2018).
- [72] S. Blundell, *Magnetism in condensed matter* (Oxford University Press, 2001).
- [73] J. M. D. Coey, *Magnetism and magnetic materials* (Cambridge University Press, 2010).
- [74] N. W. Ashcroft and N. D. Mermin, *Solid state physics*, HRW international editions (Holt, Rinehart and Winston, 1976).
- [75] D. J. Griffiths, *Introduction to electrodynamics*, 4th ed. (Cambridge University Press, 2017).
- [76] W. Meissner and R. Ochsenfeld, “Ein neuer effekt bei eintritt der supraleitfähigkeit”, *Naturwissenschaften* **21**, 787–788 (1933).
- [77] M. Tinkham, *Introduction to superconductivity*, 2nd ed. (Dover Publications, 2004).
- [78] C. Kittel, *Introduction to solid state physics*, 8th ed. (Wiley, 2004).
- [79] L. Šmejkal, J. Sinova, and T. Jungwirth, “Emerging research landscape of altermagnetism”, *Physical Review X* **12**, 040501 (2022).
- [80] L. Šmejkal, Y. Mokrousov, B. Yan, and A. H. MacDonald, “Topological antiferromagnetic spintronics”, *Nature Physics* **14**, 242–251 (2018).
- [81] O. J. Amin, A. Dal Din, E. Golias, et al., “Nanoscale imaging and control of altermagnetism in MnTe”, *Nature* **636**, 348–353 (2024).
- [82] A. Smolyanyuk, I. I. Mazin, L. Garcia-Gassull, and R. Valentí, “Fragility of the magnetic order in the prototypical altermagnet RuO₂”, *Physical Review B* **109**, 134424 (2024).
- [83] O. Fedchenko, J. Minár, A. Akashdeep, et al., “Observation of time-reversal symmetry breaking in the band structure of altermagnetic RuO₂”, *Science Advances* **10**, eadj4883 (2024).
- [84] R. M. Bozorth, *Ferromagnetism*, The Bell Telephone Laboratories series (D. Van Nostrand Company, Inc., 1951).
- [85] S. Chikazumi and C. Graham, *Physics of ferromagnetism*, International Series of Monographs on Physics (Clarendon Press, 1997).
- [86] D. Wei, T. Chin, K. You, et al., “Enhancement of L10 ordered FePt by Pt buffer layer”, *Journal of Magnetism and Magnetic Materials* **303**, The 6th International Symposium on Physics of Magnetic Materials, e265–e269 (2006).
- [87] A. Hubert and R. Schäfer, *Magnetic domains: the analysis of magnetic microstructures*, 1st ed. (Springer, 1998).
- [88] W. Brown, *Micromagnetics*, Interscience tracts on physics and astronomy (Interscience Publishers, 1963).
- [89] J. Oitmaa and W. H. Zheng, “Curie and Néel temperatures of quantum magnets”, *Journal of Physics: Condensed Matter* **16**, 8653–8660 (2004).

- [90] R. M. White, *Quantum theory of magnetism: magnetic properties of materials*, 3rd ed., Springer Series in Solid-State Sciences (Springer, 2007).
- [91] E. C. Stoner, “Collective electron ferromagnetism”, Proceedings of the Royal Society of London. Series A. Mathematical and Physical Sciences **165**, 372–414 (1938).
- [92] R. Winkler, *Spin-orbit coupling effects in two-dimensional electron and hole systems*, Springer Tracts in Modern Physics (Springer Berlin Heidelberg, 2003).
- [93] T. Holstein and H. Primakoff, “Field dependence of the intrinsic domain magnetization of a ferromagnet”, Physical Review **58**, 1098–1113 (1940).
- [94] S. S. P. Parkin, M. Hayashi, and L. Thomas, “Magnetic domain-wall racetrack memory”, Science **320**, 190–194 (2008).
- [95] A. Aharoni, *Introduction to the theory of ferromagnetism*, International Series of Monographs on Physics (Clarendon Press, 2000).
- [96] J. A. Osborn, “Demagnetizing factors of the general ellipsoid”, Physical Review **67**, 351–357 (1945).
- [97] P. Vavassori, V. Bonanni, A. Busato, et al., “Magnetostatic and exchange coupling in the magnetization reversal of trilayer nanodots”, Journal of Physics D: Applied Physics **41**, 134014 (2008).
- [98] M. Fähnle, D. Steiauf, and J. Seib, “The Gilbert equation revisited: anisotropic and nonlocal damping of magnetization dynamics”, Journal of Physics D: Applied Physics **41**, 164014 (2008).
- [99] P. Zeeman, “The effect of magnetisation on the nature of light emitted by a substance”, Nature **55**, 347–347 (1897).
- [100] A. Fert, V. Cros, and J. Sampaio, “Skyrmions on the track”, Nature Nanotechnology **8**, 152–156 (2013).
- [101] M. Bode, M. Heide, K. von Bergmann, et al., “Chiral magnetic order at surfaces driven by inversion asymmetry”, Nature **447**, 190–193 (2007).
- [102] A. Gurevich and G. Melkov, *Magnetization oscillations and waves* (CRC Press, 1996).
- [103] W. M. Lü, S. Saha, X. R. Wang, et al., “Long-range magnetic coupling across a polar insulating layer”, Nature Communications **7**, 11015 (2016).
- [104] A. M. Black-Schaffer, “RKKY coupling in graphene”, Physical Review B **81**, 205416 (2010).
- [105] D. Polishchuk, Y. Tykhonenko-Polishchuk, V. Borynskyi, et al., “Magnetic hysteresis in nanostructures with thermally controlled RKKY coupling”, Nanoscale Research Letters **13**, 245 (2018).
- [106] A. U. Canbolat, H. Sevinçli, and Ö. Çakır, “Indirect exchange interaction in two-dimensional materials with quartic dispersion”, Physical Review B **106**, 104409 (2022).
- [107] M. M. Asmar and W.-K. Tse, “Interlayer RKKY coupling in bulk Rashba semiconductors under topological phase transition”, Physical Review B **100**, 014410 (2019).
- [108] M. Sherafati and S. Satpathy, “On the Ruderman-Kittel-Kasuya-Yosida interaction in graphene”, AIP Conference Proceedings **1461**, 24–33 (2012).
- [109] S. O. Demokritov and A. N. Slavin, *Magnonics: From fundamentals to applications* (Springer, 2017).
- [110] J. Larmor, “A dynamical theory of the electric and luminiferous medium. Part III. Relations with material media”, Philosophical Transactions of the Royal Society of London. Series A, Containing Papers of a Mathematical or Physical Character **190**, 205–300 (1897).
- [111] X. Fan, T. G. Myers, B. A. D. Sukra, and G. Gabrielse, “Measurement of the electron magnetic moment”, Physical Review Letters **130**, 071801 (2023).
- [112] B. Heinrich and J. Cochran, “Ultrathin metallic magnetic films: magnetic anisotropies and exchange interactions”, Advances in Physics **42**, 523–639 (1993).

- [113] D. D. Stancil and A. Prabhakar, *Spin waves: Theory and applications* (Springer, 2009).
- [114] C. Kittel, “On the theory of ferromagnetic resonance absorption”, *Physical Review* **73**, 155–161 (1948).
- [115] R. Damon and J. Eshbach, “Magnetostatic modes of a ferromagnet slab”, *Journal of Physics and Chemistry of Solids* **19**, 308–320 (1961).
- [116] K. Schultheiss, N. Sato, P. Matthies, et al., “Time refraction of spin waves”, *Physical Review Letters* **126**, 137201 (2021).
- [117] V. Sluka, T. Schneider, R. A. Gallardo, et al., “Emission and propagation of 1D and 2D spin waves with nanoscale wavelengths in anisotropic spin textures”, *Nature Nanotechnology* **14**, 328–333 (2019).
- [118] I. Bertelli, J. J. Carmiggelt, T. Yu, et al., “Magnetic resonance imaging of spin-wave transport and interference in a magnetic insulator”, *Science Advances* **6**, eabd3556 (2020).
- [119] I. Lisenkov, A. Jander, and P. Dhagat, “Magnetoelastic parametric instabilities of localized spin waves induced by traveling elastic waves”, *Physical Review B* **99**, 184433 (2019).
- [120] Q. Wang, R. Verba, B. Heinz, et al., “Deeply nonlinear excitation of self-normalized short spin waves”, *Science Advances* **9**, eadg4609 (2023).
- [121] S. Iihama, Y. Sasaki, A. Sugihara, et al., “Quantification of a propagating spin-wave packet created by an ultrashort laser pulse in a thin film of a magnetic metal”, *Physical Review B* **94**, 020401 (2016).
- [122] O. V. Dobrovolskiy, R. Sachser, T. Brächer, et al., “Magnon–fluxon interaction in a ferromagnet/superconductor heterostructure”, *Nature Physics* **15**, 477–482 (2019).
- [123] B. A. Kalinikos and A. N. Slavin, “Theory of dipole-exchange spin wave spectrum for ferromagnetic films with mixed exchange boundary conditions”, *Journal of Physics C: Solid State Physics* **19**, 7013–7033 (1986).
- [124] T. M. Apostol, *Mathematical analysis*, 2nd (Addison-Wesley, 1974).
- [125] K. Szulc, P. Graczyk, M. Mruczkiewicz, G. Gubbiotti, and M. Krawczyk, “Spin-wave diode and circulator based on unidirectional coupling”, *Physical Review Applied* **14**, 034063 (2020).
- [126] D. Sanz-Hernández, A. Hierro-Rodriguez, C. Donnelly, et al., “Artificial double-helix for geometrical control of magnetic chirality”, *ACS Nano* **14**, 8084–8092 (2020).
- [127] J. Lucassen, M. J. Meijer, M. C. H. de Jong, et al., “Stabilizing chiral spin structures via an alternating Dzyaloshinskii-Moriya interaction”, *Physical Review B* **102**, 014451 (2020).
- [128] N. Nagaosa and Y. Tokura, “Topological properties and dynamics of magnetic skyrmions”, *Nature Nanotechnology* **8**, 899–911 (2013).
- [129] L. Zhang, J. Ren, J. S. Wang, and B. Li, “Topological magnon insulator in insulating ferromagnet”, *Physical Review B* **87**, 144101 (2013).
- [130] S. A. Díaz, T. Hirose, J. Klinovaja, and D. Loss, “Chiral magnonic edge states in ferromagnetic skyrmion crystals controlled by magnetic fields”, *Physical Review Research* **2**, 013231 (2020).
- [131] E. Wigner and F. Seitz, “On the constitution of metallic sodium”, *Physical Review* **43**, 804–810 (1933).
- [132] H. Yu, J. Xiao, and H. Schultheiss, “Magnetic texture based magnonics”, *Physics Reports* **905**, 1–59 (2021).
- [133] D. Petti, S. Tacchi, and E. Albisetti, “Review on magnonics with engineered spin textures”, *Journal of Physics D: Applied Physics* **55**, 293003 (2022).
- [134] F. Ma, Y. Zhou, H. B. Braun, and W. S. Lew, “Skyrmion-based dynamic magnonic crystal”, *Nano Letters* **15**, 4029–4036 (2015).

- [135] R. Verba, G. Melkov, V. Tiberkevich, and A. Slavin, “Collective spin-wave excitations in a two-dimensional array of coupled magnetic nanodots”, *Physical Review B* **85**, 014427 (2012).
- [136] G. Gubbiotti, S. Tacchi, M. Madami, et al., “Brillouin light scattering studies of planar metallic magnonic crystals”, *Journal of Physics D: Applied Physics* **43**, 264003 (2010).
- [137] D. A. Abanin, E. Altman, I. Bloch, and M. Serbyn, “Colloquium: Many-body localization, thermalization, and entanglement”, *Reviews of Modern Physics* **91**, 021001 (2019).
- [138] M. Evers, C. A. Müller, and U. Nowak, “Weak localization of magnons in chiral magnets”, *Physical Review B* **97**, 184423 (2018).
- [139] M. F. Jakobsen, A. Qaiumzadeh, and A. Brataas, “Scattering theory of transport through disordered magnets”, *Physical Review B* **100**, 134431 (2019).
- [140] A. V. Chumak, V. S. Tiberkevich, A. D. Karenowska, et al., “All-linear time reversal by a dynamic artificial crystal”, *Nature Communications* **1**, 1142 (2010).
- [141] K. Vogt, F. Fradin, J. Pearson, et al., “Realization of a spin-wave multiplexer”, *Nature Communications* **5**, 3727 (2014).
- [142] Z. Duan, A. Smith, L. Yang, et al., “Nanowire spin torque oscillator driven by spin orbit torques”, *Nature Communications* **5**, 5616 (2014).
- [143] K. A. Rivkin, *Spin wave optics*, arXiv.2404.13882, 2024.
- [144] D. R. Birt, B. O’Gorman, M. Tsoi, et al., “Diffraction of spin waves from a submicrometer-size defect in a microwaveguide”, *Applied Physics Letters* **95**, 122510 (2009).
- [145] D. Sanz-Hernández, R. F. Hamans, J. Osterrieth, et al., “Fabrication of scaffold-based 3D magnetic nanowires for domain wall applications”, *Nanomaterials* **8**, 483 (2018).
- [146] A. Vansteenkiste, J. Leliaert, M. Dvornik, et al., “The design and verification of MuMax3”, *AIP Advances* **4**, 107133 (2014).
- [147] *COMSOL Multiphysics® v. 6.1*, Computer Software, COMSOL AB, Stockholm, Sweden (2024).
- [148] R. Hertel, *tetmag*, <https://github.com/R-Hertel/tetmag>, 2023.
- [149] A. K. Sethi, “Computers and computing”, in *The business of electronics: a concise history* (Palgrave Macmillan US, New York, 2013), pp. 61–86.
- [150] C. Brebbia, “The boundary element method in engineering practice”, *Engineering Analysis* **1**, 3–12 (1984).
- [151] M. Bonnet, “Boundary integral equation methods for solids and fluids”, *Meccanica* **34**, 301–302 (1999).
- [152] R. Kress, *Linear integral equations*, 3rd ed., Applied Mathematical Sciences (Springer, 2013), p. 412.
- [153] E. Abbena, S. Salamon, and A. Gray, *Modern differential geometry of curves and surfaces with mathematica*, 3rd ed., Textbooks in Mathematics (Taylor & Francis, 2006).
- [154] J. D. Hoffman and S. Frankel, *Numerical methods for engineers and scientists*, 2nd ed. (Taylor & Francis, 2001).
- [155] W. H. Press, S. A. Teukolsky, W. T. Vetterling, and B. P. Flannery, *Numerical recipes: The art of scientific computing*, 3rd ed. (Cambridge University Press, 2007).
- [156] M. d’Aquino, C. Serpico, G. Miano, and C. Forestiere, “A novel formulation for the numerical computation of magnetization modes in complex micromagnetic systems”, *Journal of Computational Physics* **228**, 6130–6149 (2009).
- [157] M. d’Aquino, C. Serpico, and G. Miano, “Geometrical integration of Landau–Lifshitz–Gilbert equation based on the mid-point rule”, *Journal of Computational Physics* **209**, 730–753 (2005).
- [158] E. Hairer, S. Nørsett, and G. Wanner, *Solving ordinary differential equations II: Stiff and differential-algebraic problems* (Springer, 1993).

- [159] J. R. Dormand and P. J. Prince, “A family of embedded Runge-Kutta formulae”, *Journal of Computational and Applied Mathematics* **6**, 19–26 (1980).
- [160] E. Fehlberg, *Classical fifth-, sixth-, seventh-, and eighth-order Runge-Kutta formulas with stepsize control*, tech. rep. R-287 (NASA Technical Report, 1968).
- [161] U. Ascher and L. Petzold, *Computer methods for ordinary differential equations and differential-algebraic equations* (Society for Industrial and Applied Mathematics, 1998).
- [162] K. E. Brenan, S. L. Campbell, and L. R. Petzold, *Numerical solution of initial-value problems in differential-algebraic equations* (Society for Industrial and Applied Mathematics, 1995).
- [163] J. Chung and G. M. Hulbert, “A time integration algorithm for structural dynamics with improved numerical dissipation: The generalized- α method”, *Journal of Applied Mechanics* **60**, 371–375 (1993).
- [164] J. Chung and J. M. Lee, “A new family of explicit time integration methods for linear and non-linear structural dynamics”, *International Journal for Numerical Methods in Engineering* **37**, 3961–3976 (1994).
- [165] P. Heistracher, C. Abert, F. Bruckner, T. Schrefl, and D. Suess, “Proposal for a micromagnetic standard problem: Domain wall pinning at phase boundaries”, *Journal of Magnetism and Magnetic Materials* **548**, 168875 (2022).
- [166] C. Shannon, “Communication in the presence of noise”, *Proceedings of the IRE* **37**, 10–21 (1949).
- [167] R. Courant, K. Friedrichs, and H. Lewy, “Über die partiellen Differenzengleichungen der mathematischen Physik”, *Mathematische Annalen* **100**, 32–74 (1928).
- [168] R. Hertel, S. Christophersen, and S. Börm, “Large-scale magnetostatic field calculation in finite element micromagnetics with H2-matrices”, *Journal of Magnetism and Magnetic Materials* **477**, 118–123 (2019).
- [169] M. d’Aquino and R. Hertel, “Micromagnetic frequency-domain simulation methods for magnonic systems”, *Journal of Applied Physics* **133**, 033902 (2023).
- [170] *SUNDIALS: SUite of Nonlinear and Differential/ALgebraic Equation Solvers*, <https://computing.llnl.gov/projects/sundials>, Lawrence Livermore National Laboratory (2024).
- [171] R. B. Lehoucq, D. C. Sorensen, and C. Yang, *ARPACK users’ guide: Solution of large-scale eigenvalue problems with implicitly restarted Arnoldi methods*, Software, Environments, and Tools (Society for Industrial and Applied Mathematics, 1998).
- [172] Y. Saad, *Numerical methods for large eigenvalue problems* (Society for Industrial and Applied Mathematics, 2011).
- [173] Y. Saad, *Iterative methods for sparse linear systems*, 2nd ed. (Society for Industrial and Applied Mathematics, 2003).
- [174] R. Barrett, M. Berry, T. F. Chan, et al., *Templates for the solution of linear systems: Building blocks for iterative methods* (Society for Industrial and Applied Mathematics, 1994).
- [175] C. T. Kelley, *Iterative methods for linear and nonlinear equations* (Society for Industrial and Applied Mathematics, 1995).
- [176] S. John, “Strong localization of photons in certain disordered dielectric superlattices”, *Physical Review Letters* **58**, 2486–2489 (1987).
- [177] H. Guo, A. J. M. Deenen, M. Xu, M. Hamdi, and D. Grundler, “Realization and control of bulk and surface modes in 3D nanomagnonic networks by additive manufacturing of ferromagnets”, *Advanced Materials* **35**, 2303292 (2023).
- [178] S. Ladak, D. E. Read, G. K. Perkins, L. F. Cohen, and W. R. Branford, “Direct observation of magnetic monopole defects in an artificial spin-ice system”, *Nature Physics* **6**, 359–363 (2010).
- [179] A. V. Chumak, P. Kabos, M. Wu, et al., “Advances in magnetics roadmap on spin-wave computing”, *IEEE Transactions on Magnetics* **58**, 1–72 (2022).

About the Author

During my Bachelor's, Master's, and Ph.D. studies in the Department of Physics of Nanostructures at Adam Mickiewicz University in Poznań (Faculty of Physics and Astronomy), I had the privilege of working in an environment that fostered both rigorous scientific inquiry and a passion for innovation.

My research centers on magnetism – particularly magnonics – where I investigate spin-wave-based phenomena as a promising path toward next-generation technologies. A key component of my work involves developing and applying a broad range of numerical methods to model complex geometries in magnetic nanostructures. Throughout my Ph.D. study, I have worked extensively with tools such as COMSOL Multiphysics, tetmag, MuMax3, and various Python libraries. This emphasis on computational techniques not only enables me to explore the fundamental physics of spin-wave dynamics but also serves to bridge theoretical predictions with experimental observations. The challenge of simulating intricate architectures has been both demanding and deeply rewarding, sharpening my computational expertise and reinforcing my commitment to advancing numerical approaches.

I firmly believe that collaboration is fundamental to modern research, which is why I have invested significant effort in attending conferences, and undertaking internships to learn from leading scientists. My internships at IPCMS in Strasbourg, France, and IMEC in Leuven, Belgium were particularly formative, introducing me to advanced computational techniques such as computer-aided design and finite element method simulations. In addition, managing my own PRELUDIUM research grant from the National Science Centre of Poland broadened my skill set by providing hands-on experience in project management and budgeting. Presenting my findings at international conferences and contributing to peer-reviewed journals has also challenged and enriched me, enabling deeper engagement with the global scientific community. These endeavors have underscored the inherently collaborative and interdisciplinary nature of scientific research, where curiosity and open-mindedness drive meaningful progress.

Looking ahead, I aspire to continue refining and expanding these simulation methods to deepen our understanding of spin-based systems. By forging a tighter connection between theory and experiment, I hope to contribute to the broader effort in magnonics – ultimately helping to drive the shift toward spin-based computing and fostering further innovation in the field of nanotechnology.

Career timeline

10.2020 – 09.2025	<i>Studies at the Doctoral School</i> Adam Mickiewicz University in Poznań, Poland Domain: Exact Sciences Discipline: Physical Sciences Supervisor: prof. dr hab. Maciej Krawczyk
07.2020	<i>MSc degree in Physics</i> Adam Mickiewicz University in Poznań, Poland Thesis title: “Spin-wave Talbot effect in thin ferromagnetic film” Supervisor: prof. dr hab. Maciej Krawczyk
10.2018 – 07.2020	<i>Master studies at the Faculty of Physics</i> Adam Mickiewicz University in Poznań, Poland Field of study: Physics Specialization: Physics of Advanced Materials for Energy Processing Conducted solely in the English language Completed with the result: very good
07.2018	<i>BSc degree in Physics</i> Adam Mickiewicz University in Poznań, Poland Thesis title: “The Talbot effect for electromagnetic waves” Supervisor: prof. dr hab. Maciej Krawczyk
10.2015 – 06.2018	<i>Bachelor studies at the Faculty of Physics</i> Adam Mickiewicz University in Poznań, Poland Field of study: Physics Specialization: Nanotechnology Completed with the result: very good

Publications

1. Gołębiewski, M.; Gruszecki, P.; Krawczyk, M.; Serebryannikov, A. E. *Spin-wave Talbot effect in a thin ferromagnetic film*, Phys. Rev. B **102**, 13, 134402 (2020).
2. Gołębiewski, M.; Gruszecki, P.; Krawczyk, M. *Self-imaging of spin waves in thin, multi-mode ferromagnetic waveguides*, IEEE Trans. Magn. **58**, 8, 1–5 (2022).
3. Gołębiewski, M.; Gruszecki, P.; Krawczyk, M. *Self-imaging based programmable spin-wave lookup tables*, Adv. Electron. Mater. **8**, 10, 2200373 (2022).

4. Gołębiewski, M.; Reshetniak, H.; Makartsou, U.; Krawczyk, M.; van den Berg, A.; Ladak, S.; Barman, A. *Spin-Wave Spectral Analysis in Crescent-Shaped Ferromagnetic Nanorods*, Phys. Rev. Appl. **19**, 6, 2200373 (2023).
5. Kumar, N.; Gruszecki, P.; Gołębiewski, M.; Kłos, J. W.; Krawczyk, M. *Exciting High-Frequency Short-Wavelength Spin Waves using High Harmonics of a Magnonic Cavity Mode*, Adv. Quantum Technol. 2400015 (2024).
6. Makartsou, U.; Gołębiewski, M.; Guzowska, U.; Stognij, A.; Gieniusz, R.; Krawczyk, M. *Spin-Wave Self-Imaging: Experimental and Numerical Demonstration of Caustic and Talbot-like Diffraction Patterns*, Applied Physics Letters **124**, 19, 192406 (2024).
7. Gołębiewski, M.; Hertel, R.; d'Aquino, M.; Vasyuchka, V.; Weiler, M.; Pirro, P.; Krawczyk, M.; Fukami, S.; Ohno, H.; Llandro, J. *Collective Spin-Wave Dynamics in Gyroid Ferromagnetic Nanostructures*, ACS Appl. Mater. Interfaces **16**, 17, 22177–22188 (2024).
8. Gołębiewski, M.; Krawczyk, M. *Gyroid ferromagnetic nanostructures in 3D magnonics*, arXiv preprint arXiv:2407.05851 (2024).
9. Memarzadeh, S.; Gołębiewski, M.; Krawczyk, M.; Kłos J. W. *Nucleation and Arrangement of Abrikosov Vortices in Hybrid Superconductor-Ferromagnetic Nanostructure*, arXiv preprint arXiv:2411.12486 (2024).
10. Gołębiewski, M.; Szulc, K.; Krawczyk, M. *Magnetic field controlled surface localization of ferromagnetic resonance modes in 3D nanostructures*, Acta Materialia **283**, 120499 (2025).

Reviews

1. **Advanced Electronic Materials** – 1 review
2. **AIP Advances** – 1 co-review
3. **IEEE Transactions on Magnetism** – 1 co-review
4. **Physical Review Letters** – 1 co-review

Conference presentations

11.2019	Scientific symposium QuTecNOMM 2019, Poznań, Poland Oral presentation: “Spin-wave Talbot effect in thin ferromagnetic film”
12.2020	Joint European Magnetic Symposia (JEMS 2020, on-line) Poster: “Spin-wave Talbot effect in a thin ferromagnetic film”
01.2021	WE Heraeus Seminar (on-line) Poster: “Demonstration and potential application of the spin-wave Talbot effect”
06–07.2021	Physics of Magnetism 2021 (PM’21, on-line) Poster: “Self-imaging of spin waves in thin, multimode ferromagnetic waveguides”
09.2021	Trends in MAGnetism 2020 (TMAG2020), Cefalù, Italy Oral presentation: “Control and manipulation of self-images using phase/amplitude change of input wave fronts and potential application in magnonics”
01.2022	MMM–Intermag 2022, New Orleans, United States of America Oral presentation: “Self-imaging based programmable Spin-wave Logic Gates”
06.2022	Sol-SkyMag 2022, San Sebastian, Spain Oral presentation: “Spin-wave lookup tables”
08.2022	CMD29, Manchester, United Kingdom Oral presentation: “Self-imaging based logic operations”
05.2023	iSIM 2023, Sendai, Japan Poster: “Logic operations based on self-imaging and interference of spin waves”
05.2023	Intermag 2023, Sendai, Japan Oral presentation: “Spin-Wave Dynamics in Ferromagnetic Gyroid Nanostructures”
06.2023	Physics of Magnetism 2023 (PM’23), Poznań, Poland Oral presentation: “Gyroid Nanostructures in Magnonics”
07.2023	MagIC 2023, Będlewo, Poland Poster: “Spin-wave interference control for self-imaging based logic operations”
08.2023	Joint European Magnetic Symposia (JEMS 2023), Madrid, Spain Oral presentation: “Ferromagnetic Resonance in Gyroidal Networks”
09.2023	Trends in MAGnetism 2023 (TMAG2023), Rome, Italy Poster: “Magnonic properties of 3D Nickel Gyroid Networks”
12.2023	I Doctoral Symposium in Exact Science, Dębina, Poland Oral presentation: “Magnonic properties of three-dimensional gyroidal nanostructures”

01.2024	WE Heraeus Seminar, Bad Honnef, Germany Poster: “Collective Spin-Wave Dynamics in Gyroidal Nanostructures”
01.2024	Symposium on Spintronics and Quantum Information 2024, Będlewo, Poland Poster: “Magnonic Properties of Gyroidal Ferromagnetic Networks”
04–05.2024	SPICE–Workshop Nanomagnetism in 3D, Ingelheim, Germany Poster: “Spin-wave FMR Modes Localization and Propagation Properties in Gyroidal Ferromagnetic Networks”
06.2024	Transnational Round Table on Magnonics, High-Frequency Spintronics, and Ultrafast Magnetism (TRTM2024), Exeter, United Kingdom Poster: “Spin-Wave Propagation Properties in Gyroid Nanostructures”
06.2024	Sol-SkyMag 2024, San Sebastian, Spain Oral presentation: “Magnetic Field’s Angle-Dependent Localization of FMR Spin Wave Modes in 3D Nanoarchitectures”
06–07.2024	International Conference on Magnetism (ICM2024), Bologna, Italy Poster: “Localization and Propagation of Spin Waves in Gyroidal Nanostructures”
04–05.2025	International Conference on Superconductivity and Magnetism (ICSM2025) Fethiye–Oludeniz, Turkey Invited talk: “New surface localization mechanism of FMR modes in 3D nanostructures”

Awards, grants, and scholarships

10.2019 – 06.2020	AMU Rector’s Scholarship for the best students
10.2019 – 06.2020	Jan Kulczyk Scholarship for the best students
07.2022 – 12.2022	Abroad internship grant STER NAWA
01.2024 – 01.2026	NCN PRELUDIUM–22 (2023/49/N/ST3/03032) project title: “Three-dimensional complex-geometry ferromagnetic nanostructures in magnonics and spintronics”
10.2024 – 07.2025	AMU Foundation Scholarship for Ph.D. students

Student co-supervision

- Ph.D. student, mgr Hanna Reshetniak

Scientific visits and internships

03.2024	<p>Ecole Polytechnique Fédérale de Lausanne (EPFL) Laboratory of Nanoscale Magnetic Materials and Magnonics Lausanne, Switzerland Prof. Dirk Grundler's group 2-week research visit</p>
02.2023	<p>S. N. Bose National Centre for Basic Sciences (SNBNCBS) Department of Condensed Matter and Materials Physics Kolkata, India Prof. Anjan Barman's group 2-week research visit</p>
10.2022	<p>Rheinland–Pfälzische Technische Universität Kaiserslautern–Landau Kaiserslautern, Germany Prof. Philipp Pirro's group 1-week research visit</p>
07.2022 – 12.2022	<p>Centre national de la recherche scientifique / Université de Strasbourg Institut de physique et chimie des Matériaux de Strasbourg (IPCMS) Strasbourg, France Group: Magnetic Objects on the NanoScale Local supervisor: Prof. Riccardo Hertel 6-month internship</p> <p>Advanced research on gyroid structures for magnonics applications, including preparing and implementing 3D models to numerically solve coupled systems of partial differential equations using the finite element method.</p>
02.2020 – 07.2020	<p>Interuniversitair Micro-Electronica Centrum vzw (IMEC) Leuven, Belgium Sector: Computing and Memory Technologies Local supervisor: Dr. Florin Ciubotaru 5-month internship</p> <p>Insight into the fabrication of magnonic and spintronic devices in clean room laboratories. Participation in scientific research involving numerical simulation of various magnetoelastic systems using COMSOL Multiphysics software.</p>